Award Number DE-NE0000566

Development of LWR Fuels with Enhanced Accident Tolerance

Final Technical Report

RT-TR-15-34

October 30, 2015

Westinghouse Electric Company LLC
1000 Cranberry Woods Drive
Cranberry Woods, PA 16066

Principal Investigator: Edward J. Lahoda
Project Manager: Frank A. Boylan

Team Member Authors

Edison Welding Institute
General Atomics
Idaho National Laboratory
Los Alamos National Laboratory
Massachusetts Institute of Technology
Southern Nuclear Company
Texas A&M University
Westinghouse Electric Company LLC

Table of Contents

List of Tables

Executive Summary

Significant progress was made on the technical, licensing, and business aspects of the Westinghouse Electric Company's Enhanced Accident Tolerant Fuel (ATF) by the Westinghouse ATF team. The fuel pellet options included waterproofed $U^{15}N$ and U_3Si_2 and the cladding options SiC composites and zirconium alloys with surface treatments.

Technology was developed that resulted in U_3Si_2 pellets with densities of >94% being achieved at the Idaho National Laboratory (INL). The use of U_3Si_2 will represent a 15% increase in U235 loadings over those in UO_2 fuel pellets. This technology was then applied to manufacture pellets for 6 test rodlets which were inserted in the Advanced Test Reactor (ATR) in early 2015 in zirconium alloy cladding. The first of these rodlets are expected to be removed in about 2017. Key characteristics to be determined include verification of the centerline temperature calculations, thermal conductivity, fission gas release, swelling and degree of amorphization.

Waterproofed UN pellets have achieved >94% density for a 32% U_3Si_2/68% UN composite pellet at Texas A&M University. This represents a U235 increase of about 31% over current UO_2 pellets.

Pellets and powders of UO_2, UN, and $U_3Si_2$the were tested by Westinghouse and Los Alamos National Laboratory (LANL) using differential scanning calorimetry to determine what their steam and 20% oxygen corrosion temperatures were as compared to UO_2. Results from this work are summarized as follows:

- The oxidation of U_3Si_2 and UN to U_3O_8 occurs by a single step reaction compared to the previously determined 2 step oxidation reaction of UO_2.
- The Westinghouse results of the temperature of oxidation reaction initiation (Tox, i) for these 3 U bearing fuel compounds in powder form can be ranked as follows.
    - Tox, i (20% O_2 in He) = UO_2 < UN < U_3Si_2
    - Tox, i (steam) = UN < U_3Si_2
- The LANL results of the temperature of oxidation reaction initiation (Tox, i) for these 3 U bearing fuel compounds in pellet form can be ranked as follows.
    - Tox, i (synthetic air) = U_3Si_2< UN< UO_2
- The oxidation reaction enthalpy for these 3 U bearing fuel compounds can be ranked as follows.
    - RXN enthalpy (syn. air) = UO_2 << UN < U_3Si_2
- U_3Si_2 and UN when compared to UO_2 are on order of magnitude more reactive during oxidation and the proper precautions should be taken during the processing and handling of U_3Si_2 and UN.

Cold spray application of either the amorphous steel or the Ti_2AlC was successful in forming an adherent ~20 micron coating that remained after testing at 420°C in a steam autoclave. The coatings were limited to 20 microns to minimize their effect on the neutron economy of the fuel since many of the coating components have relatively high thermal neutron cross-sections. Tests at 1200°C in 100% steam on coatings for Zr alloy have not been successful possibly due to the low density of the coatings which allowed steam transport to the base zirconium metal. Further testing supported this hypothesis since

coating thicknesses of ~80 to 90 microns significantly reduced the zirconium oxidation rate. Mechanical testing of the coatings indicated good bonding for the cold-spray applied coatings.

Significant modeling and testing has been carried out for the SiC/SiC composite/SiC monolith structures developed by General Atomics (GA). Early modeling efforts indicated that the original monolith on the inside and composite on the outside would not maintain hermeticity in a neutron flux with a thermal gradient applied. This was due to the fact that both the monolith and the composite had the same swelling characteristics. GA then developed a structure with the monolith on the outside and composite on the inside which is the current baseline structure and a SiC to SiC tube closure approach. GA has also developed permeability tests and mechanical tests to verify the operation of the SiC cladding. Steam autoclave (420°C), high temperature (1200°C) flowing steam tests and quench tests have been carried out at the Massachusetts Institute of Technology (MIT) with minimal corrosion, mechanical or hermeticity degradation effect on the SiC cladding or end plug closure. However, in-reactor loop tests carried out in the MIT reactor indicated an unacceptable degree of corrosion, likely due to the corrosive effect of radiolysis products which attacked the SiC. The approaches being applied to rectify this issue include additional hydrogen overpressure to more quickly react these radiolysis products and the addition of catalysts to further accelerate the reaction between the hydrogen and the radiolysis products.

A detailed, preliminary regulatory examination has also been completed based on the current Westinghouse ATF designs. The following table highlights the estimated regulatory frame work, timeline, and costs required to achieve a lead test rod (LTR) test date of 2022 and full implementation by 2032.

The estimated timeframe is based on a lead test rod (LTR) load date of 2022 with full batch implementation occurring in the 2034 timeframe. Licensing of ATF is feasible. While there are significant challenges to overcome, based on past and ongoing licensing activities associated with fuel changes, these challenges can be overcome. Overcoming these challenges to meet the aggressive schedule outlined here will require successful coordination between industry and the NRC.

We acknowledge that many areas need additional scrutiny and will be improved over time. In terms of further testing, irradiation of the U_3Si_2 and UN with SiC is required to determine the performance aspects of the fuel and cladding individually, as well as a fuel system. Key potential issues to be explored are swelling of the fuel and interactions between the fuel and cladding and the in-reactor corrosion of SiC at pressurized water reactor (PWR) conditions. A testing and verification effort to determine the optimum SiC cladding design and a detailed manufacturing analysis to develop a low cost approach for SiC cladding production is needed to address the current high cost of available production techniques. A robust high density pellet program is needed to achieve optimal performance and economics for any ATF.

Acknowledgment: This material is based upon work supported by the Department of Energy under Award Number DE-NE0000566.

Disclaimer: This report was prepared as an account of work sponsored by an agency of the United States Government. Neither the United States Government nor any agency thereof, nor any of their employees, makes any warranty, express or implied, or assumes any legal liability or responsibility for the accuracy, completeness, or usefulness of any information, apparatus, product, or process disclosed, or represents that its use would not infringe privately owned rights. Reference herein to any specific commercial product, process, or service by trade name, trademark, manufacturer, or otherwise does not necessarily constitute or imply its endorsement, recommendation, or favoring by the United States Government or any agency thereof. The views and opinions of authors expressed herein do not necessarily state or reflect those of the United States Government or any agency thereof.

1. Introduction

The beyond design basis accident at Fukushima Daiichi in March 2011 and the Three Mile Island accident in 1979 imply that severe nuclear accidents may occur at somewhat higher frequencies than previously predicted, and that the financial liabilities of such accidents can cripple a utility [1]. While current fuel is more than adequate for design basis accidents, the potential for harm from beyond design basis accidents has been a driver for Westinghouse development efforts since 2004, and after Fukushima the other fuel vendors, to pursue new fuel materials that provide significant increases in the time for the reactor operator to respond to unforeseen events before significant releases of fuel materials and fission products occur. Any accident tolerant fuel (ATF) products that are developed must provide significant operating cost improvements as well as safety improvements if they are to be commercially successful.

This report documents the engineering, design and testing that occurred during the period October 1, 2012, until September 30, 2015, by the Westinghouse team in the area of accident tolerant fuel. The fuel pellet options included U_3Si_2 and waterproofed $U_3Si_2/U^{15}N$ and the cladding options SiC composites and zirconium alloys with surface treatments.

2. Accident Tolerant Fuel Development Efforts

This report summarizes:

1. Technical concept description of accident tolerant fuel (ATF) (Appendix 1)
2. Description of research and development required to qualify the different ATF technical concepts (Appendix 2)
3. Licensing plan for ATF (Appendix 3)
4. Preliminary business plan for bringing ATF to market (Appendix 4)
5. Details on U_3Si_2 powder manufacture and pelleting (Appendix 5)
6. Details on UN/U_3Si_2 composite pellets manufacture (Appendix 6)
7. Zirconium coatings development, testing and results (Appendix 7)
8. SiC composite cladding development (Appendix 8)
9. In-reactor testing results of SiC composites (Appendix 9)
10. High temperature oxidation tests of SiC composites in steam (Appendix 10)
11. High temperature oxidation tests of UN, U_3Si_2 and UO_2 in steam and synthetic air (Appendix 11)
12. Oxidation tests on U_3Si_2, UN and UO_2 powders in 20% O_2/80% He and steam (Appendix 12)

Details on each of these items can be found in the indicated appendix.

2.1 Proposed ATF Fuel Technical Concept Description

The licensing of new Zr base metallic nuclear fuel cladding has previously been accomplished, in example for alloys such as M5™ and ZIRLO®[1] using criteria and test methods established for Zircaloy-2 and -4 cladding. However, a new advanced fuel and cladding composed of materials other than Zr base alloys and UO_2 fuel offer many potential advantages and challenges specifically with respect to regulatory licensing. An advanced cladding and fuel, composed of either SiC_f/SiC (SiC fiber/SiC matrix) ceramic matrix composite (CMC) cladding or coated Zr alloy cladding, and U_3Si_2 or U_3Si_2 + UN fuel, have many potential advantages compared to the current Zr/UO_2 fuel system. Some of these potential advantages can be summarized as follows;

Cladding

1. Increased fuel rod failure temperature, resistance to thermal cycling and irradiation induced degradation,
2. Decreased thermal neutron cross section for SiC_f/SiC CMC cladding
3. Increased resistance to expansion and warping,
4. Increased thermal conductivity, and
5. Lower rate of oxidation.

Fuel

1. Increased U loading providing increased ^{235}U content at 5 % enrichment,
2. Increased thermal conductivity resulting in lower fuel temperatures,
3. Opportunity for extended fuel cycles due to higher energy content of fuel without higher enrichment cost.

While all of the listed potential advantages of a new advanced fuel could benefit commercial nuclear power generation, application of a new light water reactor (LWR) cladding and fuel will require regulatory modifications. Application of a cladding and fuel that is significantly different from the current Zr/UO_2 fuel system will require modification to the current regulatory bases, establishing new acceptance criteria, and confirmatory testing. Current nuclear power plant licensing requirements are detailed in Part 50 of Title 10 of the Code of Federal Regulations (10 CFR). Additionally, guidelines for evaluating the licensing bases, for example for new fuel, against 10 CFR are provided by the Nuclear Regulatory Commission (NRC). The effort to apply an advanced LWR cladding and fuel will require significant analysis and testing to license this fuel to the satisfaction of the NRC.

As an approach to developing a credible technical concept for new, advanced LWR fuels with enhanced accident tolerance, an analysis was performed of areas critical to the development and potential commercialization of cladding and fuel. For details, please see Appendix 1. This analysis includes the following:

---

[1] ZIRLO is a trademark or registered trademark of Westinghouse Electric Company LLC, its Affiliates and/or its Subsidiaries in the United States of America and may be registered in other countries throughout the world. All rights reserved. Unauthorized use is strictly prohibited. Other names may be trademarks of their respective owners.

1. Discussion of potential NRC requirements for advanced fuel and cladding;
2. A proposed specification for U_3Si_2 and U_3Si_2 – UN advanced non-oxide fuels, SiC_f/SiC cladding, and coated Zr base alloy cladding;
3. Discussion of the architecture of proposed advanced fuel pellets and cladding;
4. Preliminary analysis of the performance of an advanced fuel design including
    a. neutronic and economic analysis
    b. fuel rod performance analysis
    c. thermal – hydraulic analysis
    d. safety analysis including design basis and beyond design basis accidents
    e. shipping, handling, storage, and operational analysis
5. Discussion of fabrication methods, potential external providers of materials or processes, and the supply chain for advanced LWR fuel.

An overview of the required information and experimental data required for commercial implementation of a new LWR cladding and fuel is as follows:

1. For currently used UO_2 fuel, specifications for powder, pellet, and pellet drawings already exist and these have been highly successful in commercial LWR fuel fabrication for many years [2-4]. Therefore, the current UO_2 specifications and drawings will generally be used as a guide in developing proposed specifications for an advanced fuel. Enrichment for an advanced fuel will be assumed to not exceed the current NRC license limit content of 5 wt.% ^{235}U and the exact fuel pellet enrichment (typically below 4.95 wt. % ^{235}U) is determined from neutronic calculations based on the loading of the specific reactor core and is specified in the enriched fuel pellet drawing.
2. Detailed values to be included in a specification for non-oxide fuel, SiC CMC or coated Zr cladding require experimental determination and mostly depend on the fuel design of the specific fuel fabricator.
3. Calculations indicate replacing the current Zr/UO_2 fuel system with a SiC CMC cladding and high density fuel would result in up to 8.8% fuel cycle cost savings.
4. Preliminary fuel rod performance calculations indicate use of UN fuel with SiC CMC or coated Zr cladding would allow for an increase in fuel loading compared to current Zr/UO_2 fuel. Use of U_3Si_2 with SiC CMC or coated Zr cladding would cause a decrease in fuel loading compared to current Zr/UO_2 fuel. However, these results for U_3Si_2 are based on very limited and conservative assumption on fuel swelling data and additional experimental data is required to more accurately predict fuel rod performance using U_3Si_2.
5. Preliminary thermal hydraulic performance analysis indicates a significant benefit is obtained when using UN/SiC CMC fuel compared to current Zr/UO_2 fuel when measured as margin from fuel melting. U_3Si_2/SiC CMC fuel would result in a small penalty at low temperatures and a benefit at high temperatures in margin from fuel melting. When using coated Zr cladding, both U_3Si_2 and UN provide a significant benefit as margin from fuel melting.
6. The use of SiC CMC or coated Zr cladding with both U_3Si_2 and UN would provide significantly better safety performance during station blackout or anticipated transients without scram events. The safety performance of advanced fuel during other fuel rod failure mechanisms or transient events

appears mixed during this preliminary analysis. For many of these failure mechanism and transient events, additional data during normal fissile operation is required to better characterize the safety performance of this new cladding and fuel.

7. Methods to synthesize U_3Si_2 and UN from enriched UF_6 feedstock presently do not exist and need to be developed if either of these fuels is to be fabricated on a commercial manufacturing scale. Once synthesized into powder, both fuels could be fabricated into pellet form using conventional ceramic press and sinter processing. While SiC CMC tubes have been experimentally fabricated into 3 ft. length tubes, significant development is required to fabricate 14 ft. length tubes on a commercial manufacturing scale. Coating deposition processing methods are mature however application to Zr substrates specifically for nuclear application is new and will require development for thin wall Zr tube application. The current nuclear fuel supply chain is specifically for Zr/UO_2 fuel. Transitioning to a new advanced fuel will require some new materials (SiC/SiC composite tubes, UF_6 to UN and/or U_3Si_2 conversion) supply chain of the required nuclear industry quality, safety, and scale.

2.2 Research and Development Required for ATF Commercialization

This report, performed as Task 2 of this program, describes the R&D needed to fully qualify and commercialize this ATF concept describes in Appendix 1. This includes the development and testing needed in the short term (two years) and long term. The program goal is to have either a lead test rod (LTR) or lead test assembly (LTA) in a commercial reactor by 2022. In this report, the short term tasks in FY14-15 are defined as Phase 2 of the ATF program, and the long term tasks in FY16-22 are defined as Phase 3 of the ATF program. Rough cost estimates (+50%/-10%) are also provided. It is worth noting that not all necessary activities for a commercial application are included in the report. These activities are mainly vendor specific and will be included in the Phase 3 of the ATF program. More specific activities that are not included in this report are listed below:

1. Transient testing (Pellet Cladding Interaction (PCI), Rod Injection Accident (RIA))
2. Solubility in water of irradiated fuel
3. Seismic testing
4. Lead rods in a commercial reactor, and the pertinent PIE program
5. Neutronic codes
6. Choice of fiber, its desired properties, and the issue of lubrication/slippage vs. pseudo-ductility
7. NRC Licensing

The research and development program required to develop the technology to qualify and commercialize the Westinghouse Electric Company LLC's Accident Tolerant Fuel (ATF) is outlined in Appendix 2 of this report. The research and development work leading to a lead test rod (LTR) or lead test assembly (LTA) during phases 2 and 3, includes the following areas:

1. Bench scale fuel development including UN and U_3Si_2 fuel powder production from UF_6, U_3Si_2 and UN-U_3Si_2 fuel pellet fabrication, and N15 enrichment.
2. Bench and pilot scale SiC ceramic matrix composite (CMC) and coated zirconium alloy tube development including 3 ft long and full length tubes with hermetic end plugs.
3. Design work needed for integrating burnable absorbers and reactivity controls.
4. Long term test reactor rodlet irradiation and post irradiation examination (PIE).

5. Other R&D work including code and standard development, quality assurance program development, detailed core design, and operational analysis.

R&D scope and highlights are summarized as follows:

1. Bench scale production process development is required for both fuel and cladding prior to test reactor irradiation because the irradiation data will be used to acquire exemptions for LTRs/LTAs under 10CFR50 and for initial testing and future licensing of ATF for region reloads in commercial reactors.
2. Numerous potential heavy metal fluorite chemical processing routes are available for conversion of UF_6 to UN, and there is a potential process to convert UF_6 to UF_4 to U_3Si_2 using a modified process defined in a US patent (US 5,901,338).
3. A ZrB_2 Integral Fuel Burnable Absorber (IFBA) is most likely to be used in PWR fuel as the coating layer for U_3Si_2 or U_3Si_2-UN fuels. Coating thickness will be larger than for current UO_2 fuel because of the higher heavy metal loading for the new fuels. Coating of the ATF fuels with ZrB_2 must be demonstrated. A combination of ZrB_2 coating and Gd neutron absorbers should be used for BWR fuel because BWR requires higher neutron adsorption abilities than PWR.
4. Development of computer models for the ATF is needed in the following areas: fuel rod performance, thermal hydraulics, transient analysis, and reactor physics.
5. Laser Isotope Separation (LIS) is concluded to be an economic and technically feasible approach for industrial scale production of N15 isotopes with a minimal environmental impact.

2.3 Licensing Path for ATF

As part of the development of a credible technical concept for new, advanced light water reactor (LWR) fuels with enhanced accident tolerance, a licensing strategy is required. Currently there is no comprehensive plan available for the licensing of non UO_2/Zr alloy nuclear fuels and cladding. The work presented here outlines a strategy for overcoming the hurdles associated with the licensing of a new advanced fuel and cladding composed of materials other than zirconium-based alloys and uranium-oxide (UO_2) fuel in the United States. Modifications to the current regulatory bases, establishing new acceptance criteria, and confirmatory testing will be required for ATF commercialization. This work addresses the modifications that will be required and identifies the regulatory risks associated with this project. This work focuses solely on the United States' licensing environment and does not address challenges that might exist in other countries wishing to implement ATF in the future.

Details of the strategy required to license and commercialize the Westinghouse Electric Company LLC's Accident Tolerant Fuel (ATF) are provided in Appendix 3. The licensing work associated with full region implementation of ATF includes the following areas:

1. In-pile and out-of pile testing
2. Code development and code updates
3. Exemption Requests from current regulations governing fuel cladding and pellet materials
4. Topical report submittals to the NRC for review and approval
5. Rulemaking to relax current requirements within the regulations that would prevent the
6. implementation of ATF in a full core configuration

Projected costs associated with this project account for all of the following:

1. Testing
2. Code development and code updates
3. Engineering work associated with writing the topical reports and responding to RAIs
4. NRC fees associated with the review topicals and work to support defense of approvals to the Advisory Committee on Reactor Safeguards (ACRS)

The costs associated with the licensing of ATF provided in this report do not account for activities associated with rulemaking. In total, the cost associated with the aforementioned activities is approximately $75 million over the course of 19 years. The cost and associated timeframe is based on a lead test rod (LTR) load date of 2022 with full batch implementation occurring in the 2034 timeframe. Licensing of ATF is feasible. While there are significant challenges to overcome, based on past and ongoing licensing activities associated with fuel changes, these challenges can be overcome. Overcoming these challenges to meet the aggressive schedule outlined here will require successful coordination between industry and the NRC.

2.4 Business Case Development for ATF

The current Zr/UO_2 fuel system provides adequate safety for all design basis events. Therefore, a new fuel that is more accident tolerant must provide an adequate business case for the utilities to buy it as well as for the fuel vendors to develop it. With a time to market of between 15 and 20 years, the high risk of technical failure due to unforeseen technical and licensing issues, and high development costs, generating returns on investment to justify the costs and risks is difficult. Therefore, any fuel system that is developed must provide significant operating cost improvements as well as safety improvements if accident tolerant fuel products are to be commercially successful. The detailed analysis presented in Appendix 4 determines the potential business case for the four ATF options being proposed by the Westinghouse team. This analysis developed costs for:

1. Research and development
2. Testing and licensing
3. Manufacturing development and installation
4. Manufacturing for fuel and cladding
5. Utility implementation costs

The results of fuel cycle economic studies were combined with these costs to develop a discounted rate of return on investment (ROI or ROR) analysis for both the fuel vendor and the utility.

Finally, other business issues were considered including:

1. Effect on current business
2. Supply chain considerations
3. Risks and their mitigation

This analysis for the commercialization of ATF was carried out for two fuel pellet options (waterproofed $U^{15}N$ and U_3Si_2) and the two cladding options (SiC composites and zirconium alloys with surface treatments to retard their corrosion under operating conditions and oxidation under accident conditions). This resulted in four potential fuel/cladding combinations:

1. Waterproofed $U^{15}N$ fuel with SiC cladding
2. Waterproofed $U^{15}N$ fuel with treated Zr alloy cladding
3. U_3Si_2 fuel with SiC cladding
4. U_3Si_2 fuel with treated Zr alloy cladding

The following approach was used in this return on investment analysis:

1. The development, testing, licensing and manufacturing costs for each fuel and cladding option were estimated.
2. The value of each fuel and cladding combination was estimated from both the utility and the fuel vendor's point of view.
3. Based on an assumed Department of Energy financial assistance schedule of 80% funding for work up to and including test reactor work and 50% on the lead test rod and assembly work, the ROI for the vendor was made and the benefit to the utility customers was estimated.

A preliminary, best estimate of the discounted rate of return on investment (the rate of return over and above the assumed 8% cost of capital) is between 4% and 14% assuming the same US fuel demand Westinghouse supplies today (1500 metric tons U/year). This discounted return rises to between 9% and 19% if the current worldwide demand that Westinghouse supplies is used (2600 metric tons U per year). The financial model, while explicit and detailed, contains highly uncertain cost inputs and program risks. Thus, the deterministic results should be considered preliminary estimates with a high degree of uncertainty. Although many areas will need additional scrutiny and precision over time, these preliminary estimates were generated as a means to baseline the results based upon current best estimates.

These returns assume that the Westinghouse transition to ATF is 100% in 2032 and utility implementation occurs over 4.5 years (3, 18 month cycles). Westinghouse is assumed to reduce the price of fuel during the 4.5 year utility transition period to produce a positive return on the utility's investment, given 20 years of operation using ATF. Therefore, in addition to the non-financial benefits, the current positive return of the best estimate and the significant upside for the vendor and utilities suggest that this is an investment that is attractive from a financial standpoint.

If SiC thickness can be lowered to approximately the current Zr wall thickness, then fuel cost savings will result that will be attractive to utilities. Combining SiC with high density, high conductivity fuel such as U_3Si_2 or $U^{15}N$, not only increases the safety analysis margin but also significantly improves fuel cycle economics, which is necessary to ensure utility acceptance.

The main risk issues are identified to be the length (>15 years) of the development and licensing periods, the consistency of funding, the large investment required (>$450M), and the ability to meet the

long term technical goals. The vast majority of the technical risk is during the initial research stage up to and including the lead test rod.

2.5 U_3Si_2 Powder Manufacture and Pelleting

The primary uranium compound used in nuclear fuel worldwide is uranium dioxide (UO_2). However, alternative uranium compounds, such as uranium silicides, exists whose properties make them a potential alternative to UO_2 in nuclear fuel. In this work, samples of high density (>94% theoretical density) uranium silicide (U_3Si_2) have been fabricated by powder metallurgy techniques. The developed fabrication techniques were used to create samples that are currently undergoing irradiation testing in the Idaho National Laboratory (INL) Advanced Test Reactor (ATR). Post irradiation examination of these samples will provide important information on the performance of U_3Si_2 under typical LWR conditions.

Uranium and silicon form several different stoichiometric compounds including USi_2, USi (or $U_{34}S_{34.5}$), U_3Si_2, U_3Si. The uranium density and thermophysical properties of high uranium content uranium silicides (U_3Si_2 and U_3Si) make them an attractive material from both an economic and safety perspective as a replacement for UO_2. Experience from research reactor fuel work indicates U_3Si swells too much under irradiation for use as a nuclear fuel; additionally it disassociates into U_3Si_2 and solid solution U above 900°C which is below some expected temperatures in uranium silicide fueled pins. Fortunately U_3Si_2 has a very promising record under irradiation in research reactor fuels and maintains several advantageous properties over UO_2. There are approximately 17% more uranium atoms in a set volume of U_3Si_2 than there are in the same volume of UO_2 given a constant percentage of theoretical density for both samples. This superior uranium loading has the potential to either extend cycle length in LWRs or reduce enrichment both of which are economically beneficial. The lower melting temperature of U_3Si_2 is off-set by its much higher thermal conductivity that drastically drops the anticipated centerline temperature in a fuel pin compared to UO_2 fueled pins. This has significant positive impacts on fuel pin performance in a variety of reactor accident conditions.

The work detailed in Appendix 5 and summarized here is focused on producing uranium silicide (U_3Si_2) pellets by conventional powder metallurgy with a density greater than 94% of the theoretical density of U_3Si_2. This work has produced a process to consistently produce pellets with the desired density through careful optimization of the process. To this end, high phase purity U_3Si_2 has been successfully produced. Milling of the U_3Si_2 has been optimized. Results are presented from sintering studies and microstructural examinations that illustrate the need for a finely ground reproducible particle size distribution in the source powder. The density produced by the optimized process is of 11.57 g/cm3 or 94.7% theoretical density. The optimized process was used to produce more samples for physical property characterization and for the samples being irradiated in the Advanced Test Reactor.

2.6 UN/U_3Si_2 Composite Pellets Manufacture

The use of uranium nitride and uranium sesquisiliside as a composite fuel is motivated by the higher thermal conductivity and higher density both compounds possess. However, there have been documented reports of uranium nitride corrosion with water; uranium sesquisilicide (U_3Si_2) has been combined with the UN to provide a protective barrier. To achieve water resistance a continuous U_3Si_2

phase was desired. Several sesquisilicide fractions were tested to reach these goals. A sesquisilicide content between 25 and 32 mass % achieved the highest densities in these tests.

In this feasibility study several UN-U_3Si_2 sample composites were prepared via liquid phase sintering. Two sources of UN powder were used. The first was UN derived by carbothermic reduction of UO2 which was supplied by LANL. The second was in the form of spherical particles generated using gelation which was supplied by General Atomics. To obtain 95% theoretical densities required extended sintering time and post processing to remove surface voids, or an alternate processing method. Composite accident-tolerant fuel samples had a uranium loading improvement greater than 30% with respect to UO_2 in some cases (Table 1). Details of this work are presented in Appendix 6.

Table 1: Composite pellet densities and uranium content

UN particle	U_3Si_2 Concentration (mass %)	Dwell time (hours)	Density (g/cm^3)	% Theoretical Density	U increase density over UO_2
LANL UN	35	3	12.6	93%	28%
LANL UN	30	3	12.9	94%	31%
GA Sphere	25	3	12.0	87%	22%
GA Sphere	25	1	12.5	91%	27%

2.7 Zirconium Coating Development, Testing and Results

Coatings of MAX phase (Ti2AlC) and NanoSteel SHS 9172® an iron-based-alloy were evaluated for enhancing the oxidation resistance of zirconium-alloy fuel cladding in both normal and beyond design-based operating conditions. High Velocity Oxy Fuel (HVOF) thermal spray and cold spray deposition technologies were investigated for the deposition of coatings. Neutronic analysis using the elemental compositions of the coating materials showed that the coating thicknesses should be less than 30μm to avoid an economic penalty due to excess neutron absorption, although in this preliminary study thicker coatings were used. The MAX phase coatings used in this study were 70-90 μm in thickness. Initial sample screening was performed in a static autoclave steam environment at 427°C and 103 bar. The coatings made by HVOF de-bonded from the zirconium-alloy substrate after these tests, while cold spray deposited coatings were stable. High temperature steam autoclave testing at 1200°C showed that the Nanosteel coating provided little protection for the zirconium. The Ti_2AlC coating did not provide the desired improvements due to un-optimized microstructure and high porosity. Follow-on work utilized HVOF deposition to apply ~ 100 μm Ti_2AlC coatings on zirconium substrates with machined grooves. This resulted in reduced oxidation kinetics via the formation of an Al_2O_3 oxygen diffusion barrier layer once exposed to the steam environment. These results suggested that a critical combination of coating microstructure, thickness, and density is required for the formation of the protective Al_2O_3 layer. This was confirmed by steam testing at 1200°C of near-theoretical density bulk Ti_2AlC samples where low oxidation rates were observed due to the formation of protective Al_2O_3 layer on the surface. Details of this work are presented in Appendix 7.

2.8 SiC composite Cladding Development

Silicon carbide (SiC) structures composed of a combination of ceramic materials including monolithic SiC, pyrocarbon, and SiC-SiC composite layers were evaluated as an accident tolerant fuel cladding. Stress analysis and modeling of the complex behavior of cladding structures was used to investigate performance under beginning of life (BOL), peak power, and end-of-life (EOL) conditions. Planar and tubular cladding samples were fabricated for characterization of permeability and mechanical and thermal properties, and results were used as material property inputs to the design calculations. Performance was also evaluated after subjecting samples to corrosion attack and mechanical and thermal loads. A detailed description of this work is presented in Appendix 8.

To be viable, the cladding must meet a range of specifications established by Westinghouse and must also have acceptable economics. Material and fabrication costs, as well as production scalability were also considered when evaluating potential cladding designs. Ultimately, a cladding design composed of an inner composite layer and outer monolithic layer was determined to provide the best probability of survival and fabrication of these structures to meet a range of dimensional specifications was demonstrated.

The cladding simulation showed that stresses caused by irradiation-induced swelling are larger and oppose stresses caused by thermal expansion under temperature gradients. Reactor shutdown stresses are most severe, when compressive coolant pressure and opposing thermal expansion stresses caused by thermal gradients are removed. The simulation also included a more accurate representation of the pseudo-ductile behavior of the SiC-SiC composite layers. Cladding designs with an inner composite and outer monolith are predicted to offer the highest probability of survival, as the irradiation-induced swelling puts the outer monolithic layer in compression, making fracture unlikely. Fully composite and inner monolithic designs were not predicted to have high probability of survival. The predicted survival probability is sensitive to material properties, and further refinement of fiber architecture and processing parameters could lead to denser composites with improved strength and thermal conductivity, further reducing likelihood of failure.

SiC-based cladding tubes were fabricated in lengths up to 3’ while meeting diameter and wall thickness requirements. Straightness, outer surface roughness, and thickness and outer diameter variation tolerances were achieved, and the fabricated tubes showed good infiltration and over-coating uniformity over the length.

Mechanical and thermal properties, as well as permeability and corrosion response were evaluated. A balanced fiber structure, providing roughly equal hoop and axial strengths, appears to be most suitable for ATF cladding applications and meets requirements to contain internal pressurization. SiC-SiC tubes and SiC-SiC tubes sealed with an endplug can retain hermeticity after mechanical and thermal cycling, and also showed no reduction in performance at LWR-relevant temperatures compared to room temperature. Autoclave exposure of SiC-SiC to high temperatures and pressures showed improved mass change behavior compared to Zircaloy. Mechanical testing of sealed tubes via endplug push-out testing

showed significant joint strength retention after exposure to steam at 1400°C. Mass loss data for SiC-SiC tubes irradiated in PWR water chemistry in the MITR was roughly comparable to previous irradiation data in the literature. Amongst the tube and sealed tube samples, those receiving an additional SiC coating had a reduced mass loss rate, showing a potential route towards better corrosion resistance.

2.9 SiC In-reactor Testing

Appendix 9 presents the irradiation and initial post-irradiation examination (PIE) of SiC/SiC composite tubing manufactured by General Atomics under the Westinghouse-led accident tolerant fuel development project. This tubing is a candidate material for LWR fuel cladding and was exposed in the MITR water loop under conditions closely resembling those that would be encountered in a commercial PWR, including temperature, coolant chemistry, neutron flux and spectrum and gamma irradiation intensity. The irradiation of these samples was performed in a water loop installed in the MITR 6 MW research reactor. The samples are contained within an autoclave in the core region of the reactor.

The corrosion results of this test are shown in Table 2. These corrosion rates were higher than expected and approaches to reduce this corrosion are being pursued in the next phase of reactor testing.

Table 2: In-Reactor Corrosion Results for SiC cladding

Sample Type	Loss After 154 Days	Loss After 291 Days
GA-1	6%	28%
GA-2	8%	7%
GA-3	5%	8%
GA-4	7%	

2.10 SiC High Temperature Oxidation Tests

In this work, five different series of Silicon Carbide (SiC) SiC/SiC ceramic matrix composite (CMC) cladding architectures are assessed under simulated loss-of-coolant accident (LOCA) conditions (Appendix 10). The five series are denominated WEC[2]01 196, WEC01 198, WEC01 200, GAOE[3] and GACE[4]. For each series, sample performance is assessed under high temperature steam oxidation (oxidation at 1,400°C for 48 hours under a steam flow rate of 6 g/min) and thermal shock (quenching from 1,200°C into 100°C and 90°C water). Finally, the strength and ductility of the samples were evaluated and compared against control samples. Performance is quantified by a regimen of weight measurement, optical analysis, scanning electron microscopy (SEM) analysis, energy dispersive spectroscopy (EDS) analysis and mechanical strength analysis (yield stress, failure stresses, elastic moduli, and failure strain).

[2] WEC: Westinghouse Electric Company
[3] GAOE: General Atomics Open Ended
[4] GACE: General Atomics Closed One End

The conclusions from this study are as follows:

1. The thermal shock was observed to only have a small impact on the mechanical and microstructural characteristics of all samples. Strength testing revealed that the failure stresses of the cladding samples was scattered but was not significantly influenced by thermal shock. Furthermore, SEM analysis failed to detect microcracks or other signs of material degradation following thermal shock. Overall, multilayer SiC composite cladding was observed to be resilient to thermal shock.
2. High temperature steam oxidation led to silica buildup in the inner voids of the CMC layer of all samples resulting in a net weight gain of the samples and in the embrittlement of the SiC/SiC CMC region. For all oxidized Westinghouse samples, sudden and catastrophic failure was observed as the CMC layer failed immediately upon inner monolith failure. Post oxidation, those samples showed a reduction in strength from 250 MPa to 180 MPa while the absence of pseudo-ductility resulted in the failure strain dropping from 0.3% to 0.03%. For the GA samples, failure stress fell from 580 MPa as-received to 230 MPa post oxidation, and these samples also experienced a ten times reduction in strain at failure. SiC/SiC composites achieved much better performance than typical Zr or steel claddings as the oxidative embrittlement was non-frangible in nature thereby maintaining a coolable geometry after failure. Additionally, zirconium alloys are nearly completely consumed after 15 minutes at 1200°C and here we are comparing to SiC that has seen 1400°C for 48 hours.
3. The GAOE series (composed of a CMC layer with thin 200 μm outer monolith layer) offered the best performance with a failure hoop stress reaching 600 MPa as-received and higher than 200 MPa after oxidation.
4. The three Westinghouse series (with an inner monolith/CMC/outer EBC) all behaved in a similar way with an inner monolith failure hoop stress reaching 250 MPa as-received. However, the CMC layers behaved differently. Series 196 and 200 exhibited pseudo ductility while monolith and CMC layers of series 198 failed simultaneously in a brittle manner. It cannot be correlated to the weaving pattern since series 198 and 200 have a similar weaving pattern (three tows) while series 196 is made of two tows.
5. Endplug joining appears as a possible limitation. Endplug joint burst strength was estimated by uniaxial loading to approximately 30 MPa as-received. The GACE-B endplug sample/architecture performed poorly compared to the GACE-A. The GACE-B endplug strength drops after quenching (by more than 50%) and less severely after oxidation (by 25%). While the GACE-A endplug strength was largely unaffected. It appears as though fiber weave/architecture could play a role in this trend. Looking at the typical 14 MPa plenum pressure limit for a LWR, the SiC monolithic endplug joint withstanding 30 MPa seems satisfactory. However, plenum pressure could be much higher with SiC cladding as the absence of creep closing the fuel-cladding gap, the radial swelling of SiC and its low thermal conductivity will raise the plenum temperature, and hence the pressure.

A limited number of samples, one or two per each test condition, were tested in this work. Accordingly, it is strongly suggested that more samples be tested to strengthen these conclusions. Also, differences in sample fabrication could also be influencing the results.

2.11 Oxidation Tests on UN, U_3Si_2 and UO_2

Pellets and powders of UO_2, UN, and U_3Si_2 the were tested by Westinghouse (Appendix 12) and Los Alamos National Laboratory (Appendix 11) using differential scanning calorimetry to determine what their steam and 20% oxygen corrosion temperatures were as compared to UO_2. Results from this work are presented in Table 3 and can be summarized as follows:

- The oxidation of U_3Si_2 and UN to U_3O_8 occurs by a single step reaction compared to the previously determined 2 step oxidation reaction of UO_2.
- The Westinghouse results of the temperature of oxidation reaction initiation (Tox, i) for these 3 U bearing fuel compounds in powder form can be ranked as follows.
  - Tox, i (20% O_2 in He) = UO_2 < UN < U_3Si_2
  - Tox, i (steam) = UN < U_3Si_2
- The LANL results of the temperature of oxidation reaction initiation (Tox, i) for these 3 U bearing fuel compounds in pellet form can be ranked as follows.
  - Tox, i (synthetic air) = U_3Si_2< UN< UO_2
- The oxidation reaction enthalpy for these 3 U bearing fuel compounds can be ranked as follows.
  - RXN enthalpy (syn. air) = UO_2 << UN < U_3Si_2
- U_3Si_2 and UN when compared to UO_2 are on order of magnitude more reactive during oxidation and the proper precautions should be taken during the processing and handling of U_3Si_2 and UN.

As of now, there is no good explanation for the difference in order between the pellet and powder samples. All of the samples originated from the same two laboratories (INL and LANL) except for the Westinghouse UO_2 powder and pellet samples which originated from the Westinghouse facility in Columbia SC.

Table 3: Initial Oxidation Temperatures of UO_2, UN, and U_3Si_2

Fuel Compound	LANL - Pellets in Synthetic Air (°C)	Westinghouse - Powder in 20% O_2/80% He (°C)	Westinghouse - Powder in Steam (°C)
U_3Si_2	270	351	429
UN	320	253	351
UO_2	390	164/348 (two step reaction)	
UO_2		453 (pellet)	

3. Work Products

3.1 Publication List

The results of the work performed as part of this contract have been published in a series of respected widely available journals and conferences. The references are as follows:

Second Special Journal of Nuclear Materials issue on accident tolerant fuels for LWRs, edited by P. Xu , E. Lahoda and L. Hallstadius, Introduction page 666:

1. Characterization of SiC – SiC composites for accident tolerant fuel cladding, C.P. Deck, G.M. Jacobsen, J. Sheeder, O. Gutierrez, J. Zhang, J. Stone, H.E. Khalifa and C.A. Back, page 667.
2. Stress analysis and probabilistic assessment of multi-layer SiC-based accident tolerant nuclear fuel cladding, J.G. Stone, R. Schleicher, C.P. Deck, G.M. Jacobsen, H.E. Khalifa and C.A. Back, page 682.
3. Experimental study of thermo-mechanical behavior of SiC composite tubing under high temperature gradient using solid surrogate, L. Alva, K. Shapovalov, G.M. Jacobsen, C.A. Back and X. Huang, page 698.
4. Cold spray deposition of Ti_2AlC coatings for improved nuclear fuel cladding, B.R. Maier, B.L. Garcia-Diaz, B. Hauch, L.C. Olson, R.L. Sindelar and K. Sridharan, page 712.
5. Evaluation of the interfacial shear strength and residual stress of TiAlN coating on ZIRLO ™ fuel cladding using a modified shearlag model approach, Y. Liu, I. Bhamji, P.J. Withers, D.E. Wolfe, A.T. Motta and M. Preuss, page 718.
6. Uranium silicide pellet fabrication by powder metallurgy for accident tolerant fuel evaluation and irradiation, J.M. Harp, P.A. Lessing and R.E. Hoggan, page 728.
7. Structural stability and fission product behaviour in U_3Si, S.C. Middleburgh, P.A. Burr, D.J.M. King, L. Edwards, G.R. Lumpkin and R.W. Grimes, page 739.
8. Synthesis and sintering of UN-UO_2 fuel composites, B.J. Jaques, J. Watkins, J.R. Croteau, G.A. Alanko, B. Tyburska-Püschel, M. Meyer, P. Xu, E.J. Lahoda and D.P. Butt, page 745.

Other papers that have been published include:

1. Ed Lahoda, Lars Hallstadius, Frank Boylan and Sumit Ray, "What Should Be the Objective of Accident Tolerant Fuel?" Paper #10231 NFSM, Reno Nevada, June 17, 2014.
2. Lars Hallstadius, Steven Johnson, Ed Lahoda, "Cladding for high performance fuel," Progress in Nuclear Energy 57 (2012), pages 71-76.
3. Lars Hallstadius, "A Simplified Accident Scenario," OECD-NEA Expert Group Meeting, Paris, March 3-5 2015.
4. S.C. Johnson, H. Patts, and D.E. Schuler, "Mechanical Behavior of SiCf/SiC CMC Tubes Relative to Nuclear Fuel Cladding," Proceedings of ICAPP 2014, Charlotte, USA, April 6-9, 2014, Paper 14348.
5. Lars Hallstadius, Ed Lahoda and Peng Xu, "Accident Tolerant Fuel (ATF)," Jahrestagung Kerntechnik, Frankfurt, 6-8 May, 2014.
6. Abdellatif M. Yacout, Michael Pellin, Sumit Bhattacharya and Edward Lahoda, "Advanced Synthesis for Enhanced Accident Tolerance of LWR Cladding Materials," Proceedings of ICAPP 2015, Nice, France, May 03-06, 2015, Paper 15511.
7. S. Ray, P. Xu, E. Lahoda, L. Hallstadius, F. Boylan, and S. Johnson, "Westinghouse Accident Tolerant Fuel Program - Current Results & Future Plans," TopFuel 2015, Zurich Switzerland.
8. S. Ray, S. Johnson and E. Lahoda, "Preliminary Assessment of the Performance of SiC Based Accident Tolerant Fuel in Commercial LWR Systems," TopFuel 2013, Charlotte, NC, paper 8490.
9. Peng Xu1, Ed Lahoda, Lars Hallstadius, Sumit Ray, Andy Nelson and Sean McDeavitt, "Development of Nitride Fuel for LWR Applications," EMRS, 2013.

10. Sumit Ray, Ed Lahoda, Peng Xu, Steve Johnson, Frank Boylan, Jason Mazzoccoli and Lars Hallstadius, "Progress on the Westinghouse Accident Tolerant Fuel Program," Proceedings of WRFPM 2014 (TopFuel 2014), Sendai, Japan, Sep. 14-17, 2014, Paper No. 100131.
11. Christina A. Back, Edward Lahoda, Robert Schleicher, Christian P. Deck, Hesham E. Khalifa, George M. Jacobsen, Josh G. Stone and Oscar Gutierrez, "SiC-SiC Composite Fuel Cladding for Light Water Reactors," Proceedings of WRFPM 2014 (TopFuel 2014), Sendai, Japan, Sep. 14-17, 2014, Paper No. 100159.
12. Peng Xu, Jason Mazzoccoli, and Ed Lahoda, "Accident Tolerant Fuel Cladding for LWRs," NuMAT 2014.

3.2 Patent Applications List

The list of patent applications submitted as part of this program is listed below in Table 4 below.

Table 4: List of Patents Submitted as Pert of ATF Program

Patent Disclosure Title	Status	Patent Application No.	Published No.	Patent No.
High Temperature Strength, Corrosion Resistant, Accident Tolerant Nuclear Fuel Assembly Grid	Pending	14/046,012	2015/0098546	
A Kinetically Applied Gradated Zr-Al-C Ceramic Or Ti-Al-C Ceramic Or Amorphous Or Semi-Amorphous Stainless Steel With Nuclear Grade Zirconium Alloy Metal Structure	Pending	14/205,799		
Double-Sealed Fuel Rod End Plug For Ceramic-Containing Cladding	Pending	14/205,823		
Manufacture Of SiC Reinforced Zr Nuclear Fuel Cladding Using An Intermediate Coating Layer Of Al2O3	Pending	14/205,967		
Deposition Of Integrated Protective Material Into Zirconium Cladding For Nuclear Reactors By High-Velocity Thermal Application	Issued and filed in EU	13/670,808 Application Number 13876570.6-1556 PCT/US20130 71151	2014/0126683	8,971,476
INL developed the technology and Westinghouse is paying to have this patent filed and assigned to Westinghouse	Pending	Filed USPO 14/746,279 June 22, 2015		

3.3 CARAT Network

Westinghouse has instituted and supported the formation of the "Collaboration for Advanced Research on Accident Tolerant Fuel" (CARAT) network which is complementary to the Westinghouse-led (DOE supported) ATF program. The objective of this program is to provide a framework for performing research oriented work in support of the industrially oriented Westinghouse ATF program. The Westinghouse role in CARAT is to coordinate research topics, provide samples and materials, and

provide a venue for the presentation of results, both in CARAT meetings and as an organizer of sections in journals. All the research is self-funded.

Since CARAT was established in 2012, there have been three annual meetings. The first was in Charlotte NC and served as the organizing meeting. The second was held at Manchester University in the UK. The third meeting (in 2015) was broken up into two sessions. The first was held in July at the Westinghouse Columbia Fuel Fabrication Facility and was centered on pellet work. The second was at Paul Scherer Institute in Switzerland and was centered on cladding. The current list of CARAT members is:

1. Argonne National Laboratory
2. Idaho National Laboratory
3. Los Alamos National Laboratory
4. Brookhaven National Laboratory
5. Oak Ridge National Laboratory
6. Texas A&M University
7. Massachusetts Institute of Technology
8. University of Wisconsin
9. University of South Carolina
10. University of Tennessee
11. Boise State University
12. University of Illinois
13. Ceramic Tubular Products
14. Edison Welding Institute
15. Georgia Institute of Technology
16. University of Virginia
17. Toshiba (Japan)
18. National Nuclear Laboratory (UK)
19. University of Manchester (UK)
20. Imperial College (London, UK)
21. University of Pretoria (South Africa)
22. ANSTO (Australia)
23. Uppsala University (Sweden)
24. Royal Institute of Technology (Sweden)
25. Chalmers University (Sweden)
26. Paul Scherrer Institute (Switzerland)
27. Halden project (Norway, OECD) (N)
28. University of Cambridge
29. University of Manchester
30. Vattenfall
31. Coventry University
32. Hanyang University
33. KU Leuven (Katholieke Universiteit Leuven)

34. Sandvik
35. SCK•CEN (Belgian Nuclear Research Centre)
36. Sheffield University
37. Summerstrand Campus South

3.4 Deliverables

All deliverables for this program have been delivered.

Table 5: Program Deliverables

Milestone	Anticipated Completion	Actual Completion
Develop a credible technical concept describing how Westinghouse proposes to commercialize ATF for Generation II LWRs (Task 1 Report)	2013-01-31	2013-01-31
Describe the Research & Development needed to fully qualify an ATF LTA/LTR by 2022 (Task 2 Report)	2013-05-31	2013-05-30
Document and propose a clear path and plan for regulatory approval of the ATF concept (Task 3 Report)	2013-10-14	2013-09-30
Develop a preliminary business plan that describes the investment and infrastructure needed to produce ATF on a commercial scale (Task 4 Report)	2013-10-14	2013-10-03
Interim Report	2013-10-14	2013-10-03

4. Conclusions and Recommendations

4.1 Conclusions

The following conclusions were reached based on this study:

1. Government investment in the research and development phases of the ATF program is required for there to be a reasonable ROI for the fuel vendors as well as a reduction of risk to a level appropriate for industry. The vast majority of the technical risk is at the research and development stage (<20% of the total cost). Government investment at the 80% level is appropriate at this stage due to the high technical risk involved. Industry pays >83% of the total cost of the program through commercialization for the SiC cladding options.
2. Absent U235 enrichments greater than 5%, the use of higher density pellets for higher U235 loadings dramatically increases the economic attractiveness of ATF. U_3Si_2 offers ~17% gain in U235 density, increased thermal conductivity minimal increases in production equipment, and an increase in the margin to centerline melting during transients. UN (when mixed with U_3Si_2 as a protection against water oxidation) offers ~30% gain in U235 content, high melting point and a very high thermal conductivity which provides a large increase in the margin to centerline melting during

transients. It requires N15 enrichment and treatment to be oxidation resistant to reactor coolant. Additional effort is required for UN and U_3Si_2 to determine if there are swelling issues since the current data is extrapolated from reactor data at temperatures and burnups that are significantly different from those likely to be experienced in commercial fuel service. If testing indicates that the swelling is an issue, then additional work on pellet additives or manufacturing conditions will be needed.

3. Based on preliminary calculations, the coated Zr alloy options offer modest ATF gains (~200°C) before large scale melting of the core begins in beyond design basis events such as long term station blackout. However, it does not prevent the contamination of the PWR primary loop or the BWR balance of plant (BOP) since ballooning and bursting will occur at a relatively modest 800°C to 900°C [5]. This would likely lead to loss of the powerplant due to extensive equipment contamination and dramatically increases the chance of contamination leaving the site boundary. There are reasonable economic opportunities for the fuel vendors with discounted RORs of ~10% to 19% when paired with higher density pellets. They also present the least development risk because the basis for the cladding is still Zr alloy and the required development costs are the lowest.
4. Based on preliminary calculations, SiC offers the most ATF margin (500°C to 800°C) and protection from likely protection from many beyond design basis events such as long term station blackout. SiC technology therefore presents the most likely means of preventing loss of the entire powerplant as well as spread of fission products beyond the site boundary. SiC cladding has reasonable discounted RORs of between 4% and 11% when paired with high density pellets. This option presents the most development risk as well as the highest capital investment requirements. Note that much of the capital requirement is due to the fact that an acceptable cladding design has yet to be decided upon and the design of the manufacturing facilities has not been developed. In addition, since the behavior of the SiC/pellet system while in the reactor is unknown, very conservative fuel rod design constraints were imposed resulting in a large initial pellet-cladding gap which severely penalizes the ATF economics. The thickness of the SiC cladding wall has a large effect on fuel cycle economics. Further developmental efforts to reduce the cladding thickness to levels approaching current Zr alloy cladding wall thickness will provide further fuel cycle value benefits.
5. There are no showstoppers to licensing of accident tolerant fuel technology with the NRC. This is not to say that there are not considerable obstacles to overcome in establishing a licensing basis for ATF. However, there do not appear to be any issues that cannot be overcome.
6. There are no showstoppers to implementation of accident tolerant fuel technology when considering the supply chain, power plant, fabrication and enrichment suppliers.
7. Fuel vendors do not currently have the technical and manufacturing background in SiC, coatings or ^{15}N enrichment. This technology must be developed soon to allow time to internalize it and to provide background for licensing.
8. The annual investment needs for furthering any of these technologies will be in the $10M to $50M per year range for the fuel vendors and in the $10M to $20M per year range for governmental support.
9. Government and industry will have to support significant efforts in setting standards for any of the cladding or fuel options since these options are not currently in use by the industry. The same is

true for the Nuclear Regulatory Commission which must license these new fuels since all current regulations are oriented toward UO_2/Zr fuel.

10. The major risks involved in developing an ATF stem from the fact that none of the technologies being considered have a very significant technological background in the nuclear industry and the costs and time involved in overcoming this gap in knowledge are very high. Options with smaller knowledge gaps (such as stainless steel cladding or Mo cladding) do not offer significant economic gains (and sometimes losses) as compared to the high risk ATF options to justify the time and cost of undergoing even a moderate development program.
11. The utilities will likely be able to utilize the performance gains from ATF to help recapture the costs involved in implementing ATF. Some financial assistance from the fuel vendors may be required to produce a positive NPV during the transition period.
12. Corrosion of SiC composites in a reactor environment is a major issue that needs to be overcome. Autoclave testing did not indicate any significant corrosion issue so that the mechanism for added corrosion must be associated with the radiation environment. Furthermore, since previous testing has indicated that high density, monolithic SiC has a very low corrosion rate, the poor corrosion behavior of the composites is associated with the conditions of deposition which form less corrosion resistant SiC deposits.
13. SiC composites provide significant gains in strength and durability in high temperature steam (>1200°C) beyond design basis accidents as compared to the current Zr and to coated Zr systems. While there is some loss of strength, the SiC composites continue to act as composite structures (they do not shatter). Long term maintenance of the fission product boundary up to 1500°C to 1600°C appears to be possible. At >1600°C, the strength of the SiC composites will likely begin to rapidly decay but some boundary will still exist for a significant time.
14. A process was developed to manufacture U_3Si_2 pellets that consistently were >94% theoretical density.
15. A process was developed to manufacture 30% U_3Si_2/70% UN pellets that consistently were >94% theoretical density. The U_3Si_2 was uniformly distributed around the UN grains so would appear to provide significant waterproofing of the UN.
16. Oxidation tests of the fuel pellets and powders in steam and synthetic air indicate that UN and U_3Si_2 have lower oxidation reaction initiation temperatures than UO_2 and further oxidation studies in with cladding is required to determine if they are low enough to exclude them from consideration.

4.2 Recommendations

Based on these conclusions, Westinghouse makes the following recommendations:

1. Government funding of the high risk research stage for ATF development must continue for ATF to be economically and risk attractive to the fuel vendors. This funding should continue up to and including the lead test rod phase of the program. After a successful implementation of lead test rods, fuel vendors and utilities will have enough confidence in the technical and financial maturity of ATF to fund the industrial development and application.
2. Irradiation of the U_3Si_2 and UN with SiC and treated Zr cladding is required to determine the performance aspects of the fuel and cladding individually as well as a fuel system. Key issues are swelling of the fuel and interactions between the fuel and cladding, especially SiC, and SiC behavior in reactor environments.
3. A significant SiC cladding design, testing and verification effort is immediately required to determine the optimum design. This needs to be followed up with a detailed manufacturing analysis to determine if SiC cladding can offer enough benefit to justify the development effort and be economically competitive with current UO_2/Zr fuel option. Dry in-reactor testing that combine radiation exposure with a significant thermal flux is required to verify the modeling effort that is the basis of the current SiC composite design. In coolant reactor testing that combines the effects of radiolysis and corrosion are also needed.
4. Without a pellet with significantly higher density and thermal conductivity than UO_2, none of the ATF cladding offerings makes economic sense. Therefore a robust high density pellet program is needed if any of the ATF claddings are to be pursued.
5. Additional research to reduce the sensitivity of U_3Si_2 and UN to air oxidation is needed to eliminate the need to manufacture these compounds, powders and pellets in inerted glove boxes.
6. Additional research to reduce the sensitivity of U_3Si_2 and UN to water and steam oxidation is needed to reduce the reaction rate in the event of a leaker.
7. Development work to allow manufacture of UN and U_3Si_2 directly from UF_6 or UF_4 is needed to reduce the cost of manufacture. However, the current methods utilizing uranium and silicon metal for U_3Si_2 and carbothermic reduction of UO_2 for UN can still make these fuels relatively inexpensively.
8. Low cost methods for enriching ^{15}N from natural N_2 are required.

4. References

1. Ed Lahoda, Lars Hallstadius, Frank Boylan and Sumit Ray, “What Should Be the Objective of Accident Tolerant Fuel?” Paper #10231 NFSM, Reno Nevada, June 17, 2014.
2. ASTM International standard C776-06, “Standard Specification for Sintered Uranium Dioxide Pellets” (2011) pp.1-4.
3. Westinghouse Electric Company, LLC, Nuclear Fuel, Product Specification PDPELE02, rev.3, 2007.
4. Westinghouse Electric Company, LLC, Nuclear Fuel, Enriched Fuel Pellet drawing PELE100, rev.14, 2012.
5. NUCLEAR ENERGY AGENCY OECD, Nuclear Fuel Behaviour in Loss-of-coolant Accident (LOCA) Conditions, State-of-the-art Report, page 54, OECD 2009 NEA No. 6846.

5. Acronyms

ACRS:	Advisory Committee on Reactor Safeguards
ADU:	ammonium diuranate
AFD:	axial flux difference
AOO:	anticipated operational occurrences
AOR:	analysis of record
ASI:	axial shape index
ASTM:	ASTM International, formerly known as the American Society for Testing and Materials
ATF:	accident tolerant fuel
ATWS:	anticipated transient without scram
BDBA:	beyond design basis accident
BOC:	beginning of cycle
BOL:	beginning of life
BU:	burn up
BWR:	boiling water reactor
°C:	degrees Celsius
Ca:	calcium
CaF_2:	calcium fluoride
CFR:	Code of Federal Regulations
CHF:	critical heat flux
CILC:	crud induced localized corrosion
CIPS:	crud induced power shift
CMC:	ceramic matrix composite
CO^2:	carbon dioxide
CSR:	contractile strain ratio
CVCS:	chemical volume control system
CVD	chemical vapor deposition
CVI:	chemical vapor infiltration
DBA:	design basis accident
DOE:	U.S. Department of Energy
DNB:	departure from nucleate boiling
DNB:	deviation from nucleate boiling
DNBR:	deviation from nucleate boiling ratio
EBC:	environmental barrier coating
ECCS:	emergency core cooling system
EDS:	electron dispersive spectroscopy
EFPD:	effective full power day
EOC:	end of cycle
EOL:	end of life
FA:	fuel assembly
FAI:	Fauske & Associates, LLC
FCC:	fuel cycle cost
FCEP:	fuel checklist evaluation process
FdH:	enthalpy rise hot channel factor
FEM:	finite element method
Fq:	peak heat flux hot channel factor

FSAR:	Final Safety Analysis Report
FW:	feedwater
Fz:	axial peaking factor
GDC:	General Design Criteria
H/U:	hydrogen to uranium ratio
H_2:	hydrogen
H_2O:	water
HCN:	hydrogen cyanide
HF:	hydrogen fluoride
HFP:	hot full power
HM:	heavy metal
H/HM:	hydrogen to heavy metal ratio
HVOF:	high-velocity oxygenated fuel
HZP:	hot zero power
ID:	inner diameter
IFBA:	integral fuel burnable absorber
INL:	Idaho National Laboratory
K:	thousand
Kg:	kilogram
LANL:	Los Alamos National Laboratory
LIS:	laser isotope separation
LOCA:	loss of coolant accident
LTR:	lead test rod
LTA:	lead test assembly
LUA:	lead use assembly
LWR:	light water reactor
M:	millions
MAAP:	Modular Accident and Analysis Program
MDNBR:	minimum departure from nucleate boiling ratio
MSLB:	main steam line break
MSS:	main steam system
MTC:	moderator temperature coefficient
MTU:	metric tons uranium
MWD:	mega-watt days
MWe:	megawatt electric
MWhre:	megawatt hour electric
MWt:	megawatt thermal
N_2:	nitrogen
N15 or ^{15}N:	15 isotope of nitrogen
NH_4OH:	ammonium hydroxide
NH_4NO_3:	ammonium nitrate
NRC:	Nuclear Regulatory Commission
NS:	stainless steel alloy
NUREG:	Nuclear Regulations
O_2:	oxygen
OD:	outer diameter
OFA:	optimized fuel assembly
PIE:	post irradiation examination

PCI: pellet clad interaction
PCMI: pellet clad mechanical interaction
PCT: peak cladding temperature
PQD: post-quench ductility
PRZ: pressurizer
PVD: physical vapor deposition
PWR: Pressurized water reactor
RCCA: rod cluster control assembly
RCP: reactor coolant pump
RCS: reactor cooling system
RFA: robust fuel assembly
RG: Regulatory Guidelines
RIA: reactivity initiated accident
ROI: return on investment in %
ROR: rate of return in %
SBO: station blackout event
SEM: scanning electron microscope
SG: steam generator
Si: silicon
SiC/SiC CMC: silicon carbide fiber/Silicon carbide matrix ceramic matrix composite
SL: safety limit
SNC: Southern Nuclear Operating Company
SRP: Standard Review Plan
SWU: separative work unit
TAMU: Texas A&M University
TH: thermal hydraulic
Ti_2AlC: titanium aluminum carbide, i.e. Max or MAX Phase
TMI-2: Three Mile Island Unit 2
TS: technical specifications
U: uranium
U235 or ^{235}U: isotope 235 of uranium
UC: uranium carbide
UO_2: uranium dioxide
UO_2F_2: uranium fluoride
$UO_2(NH_4)_2$: ammonium diuranate
$UO_2(NO_3)_2$-$6H_2O$: uranium nitrate hexahydrate
U_3O_8: uranium oxide
UF_6: uranium hexafluoride
UN: uranium nitride
US: United States
U_3Si_2: uranium silicide
w/o: weight percent
wppm: parts-per-million by weight
yr: year
Zr: zirconium
3-D: three dimensional
TH: thermal hydraulic

6. Appendices

Appendix 1 - Development of LWR Fuels with Enhanced Accident Tolerance; Task 1 - Technical Concept Description

Appendix 2 - Development of LWR Fuels with Enhanced Accident Tolerance; Task 2 – Description of Research & Development Required to Qualify the Technical Concept

Appendix 3 - Development of LWR Fuels with Enhanced Accident Tolerance; Task 3: Licensing Plan for Accident Tolerant Fuel

Appendix 4 - Development of LWR Fuels with Enhanced Accident Tolerance; Task 4 – Preliminary Business Plan

Appendix 5 – U_3Si_2 Powder Manufacture and Pelleting

Appendix 6 – UN/U_3Si_2 Composite Pellets Manufacture

Appendix 7 – Zirconium Coating Development, Testing and Results

Appendix 8 – SiC composite Cladding Development

Appendix 9 – SiC In-reactor Testing

Appendix 10 – SiC High Temperature Oxidation Tests

Appendix 11 – Oxidation Tests on U_3Si_2, UN and UO_2 Pellets in Synthetic Air

Appendix 12 – Oxidation Tests on U_3Si_2, UN and UO_2 Powders in 20% O_2/80% He and Steam

Award Number DE-NE0000566

Development of LWR Fuels with Enhanced Accident Tolerance
Task 1 - Technical Concept Description

RT-TR-13-2
January 31, 2013

Westinghouse Electric Company LLC
1000 Cranberry Woods Drive
Cranberry Woods, PA 16066

Principal Investigator: Dr. Edward J. Lahoda
Project Manager: Frank A. Boylan

Team Members
Westinghouse Electric Company LLC
General Atomics
Idaho National Laboratory
Massachusetts Institute of Technology
Texas A&M University
Los Alamos National Laboratory
Edison Welding Institute
Southern Nuclear Operating Company

Executive Summary

As an approach to developing a credible technical concept for new, advanced LWR fuels with enhanced accident tolerance, an analysis was performed of areas critical to the development and potential commercialization of cladding and fuel. This analysis includes the following.

- Discussion of potential NRC requirements for advanced fuel and cladding;
- A proposed specification for U_3Si_2 and U_3Si_2 – UN advanced non-oxide fuels, SiC_f/SiC ceramic matrix composite cladding, and coated Zr base alloy cladding;
- Discussion of the architecture of proposed advanced fuel pellets and cladding;
- Preliminary analysis of the performance of an advanced fuel design including
  - neutronic and economic analysis
  - fuel rod performance analysis
  - thermal hydraulic analysis
  - safety analysis including design basis and beyond design basis accidents
  - shipping, handling, storage, and operational analysis
- Discussion of fabrication methods, potential external providers of materials or processes, and the supply chain for advanced LWR fuel.

This analysis generally provides an overview of the required information and experimental data for commercial implementation of a new LWR cladding and fuel. Specific highlights of this analysis are summarized as follows.

- Calculations indicate replacing the current Zr/UO_2 fuel system with a SiC CMC cladding and high density fuel would result in up to 8.8% fuel cycle cost savings.
- The use of SiC CMC or coated Zr cladding with both U_3Si_2 and UN would provide significantly better safety performance during station blackout or anticipated transients without scram events. The safety performance of advanced fuel during other fuel rod failure mechanisms or transient events appears mixed during this preliminary analysis. For many of these failure mechanism and transient events, additional data during normal fissile operation is required to better characterize the safety performance of this new cladding and fuel.
- Preliminary fuel rod performance calculations indicate use of UN fuel with SiC CMC or coated Zr cladding would allow for an increase in fuel loading compared to current Zr/UO_2 fuel. Use of U_3Si_2 with SiC CMC or coated Zr cladding would cause a decrease in fuel loading compared to current Zr/UO_2 fuel. However, the results for U_3Si_2 are based on very limited fuel swelling data and additional experimental data is required to more accurately predict fuel rod performance using U_3Si_2.
- Preliminary thermal hydraulic performance analysis indicates a significant benefit is obtained by using UN/SiC CMC fuel compared to current Zr/UO_2 fuel when measured as margin from fuel melting. U_3Si_2/SiC CMC fuel would result in a small penalty at low temperatures and a benefit at high temperatures in margin from fuel melting. When using coated Zr cladding, both U_3Si_2 and UN provide a significant benefit in margin from fuel melting.
- Methods to synthesize U_3Si_2 and UN from enriched UF_6 feedstock presently do not exist and need to be developed if either of these fuels is to be fabricated on a commercial manufacturing scale. Once synthesized into powder, both fuels could be fabricated into pellet form using conventional ceramic press and sinter processing. While SiC CMC tubes have been experimentally fabricated into 3 ft. length tubes, significant development is required to fabricate 14 ft. length tubes on a commercial manufacturing scale. Coating deposition processing methods are mature. However, application to Zr

substrates specifically for nuclear application is new and will require development for thin wall Zr tube application. The current nuclear fuel supply chain is specifically for Zr/UO_2 fuel. Transitioning to a new advanced fuel will require significant development of new supply chain, specifically for SiC CMC cladding, of the required nuclear industry quality, safety, and scale.

- Because all current licensing and regulatory requirements for nuclear fuel are based on the Zr/UO_2 fuel system, changing to an advanced cladding and fuel would require each fuel design requirement be redefined with new calculated/experimentally determined values and analytical modeling results.
- Detailed values to be included in a specification for non-oxide fuel, SiC CMC or coated Zr cladding require experimental determination and mostly depend on the fuel design of the specific fuel fabricator.

Table of Contents

List of Tables

List of Figures

Task 1.1: Propose Potential NRC Requirements for an Advanced Fuel and Cladding

The licensing of new Zr base metallic nuclear fuel cladding has previously been accomplished, for example for alloys such as M5™ and ZIRLO® using criteria and test methods established for Zircaloy-2 and -4 cladding. However, a new advanced fuel and cladding composed of materials other than Zr base alloys and UO_2 fuel offer many potential advantages and challenges specifically with respect to regulatory licensing. An advanced cladding and fuel, composed of either SiC/SiC CMC or coated Zr alloy cladding, and U_3Si_2 or U_3Si_2 + UN fuel, have many potential advantages compared to the current Zr/UO_2 fuel system. Some of these potential advantages can be summarized as follows:

cladding

- increased fuel rod failure temperature, resistance to thermal cycling and irradiation induced degradation,
- decreased thermal neutron cross section for SiC/SiC CMC cladding
- increased resistance to expansion and warping,
- increased thermal conductivity, and
- lower rate of oxidation.

fuel

- increased U loading providing increased ^{235}U content at 5 % enrichment,
- increased thermal conductivity resulting in lower fuel temperatures,
- opportunity for extended fuel cycles due to higher energy content of fuel without higher enrichment cost.

While all of the listed potential advantages of a new advanced fuel could benefit commercial nuclear power generation, application of a new LWR cladding and fuel will require regulatory modifications. Application of a cladding and fuel that is significantly different from the current Zr/UO_2 fuel system will require modification to the current regulatory bases, establishing new acceptance criteria, and confirmatory testing. Current nuclear power plant licensing requirements are detailed in Part 50 of Title 10 of the Code of Federal Regulations (10 CFR). Additionally, guidelines for evaluating the licensing bases, for example for new fuel, against 10 CFR are provided by the NRC. The effort to apply an advanced LWR cladding and fuel will require significant analysis and testing to license this fuel to the satisfaction of the NRC. A discussion of potential new requirements and criteria for the licensing of advanced cladding and fuel is presented here.

subtask 1.1.1: Current Licensing Requirements

All current licensing requirements are for the Zr/UO_2 fuel system. Generally, with these requirements, a SiC/SiC CMC or coated Zr alloy cladding and high density fuel would be required to meet the same standards. This advanced fuel system should exceed these standards, but it is unclear how exceeding these standards would be interpreted for licensing. The following describes several key aspects of the current licensing requirements.

a. 10 CFR Part 50, section 46

   Section 46 requires that "zircaloy or ZIRLO cladding" be provided with an emergency core cooling system (ECCS) designed to uphold the criteria presented in paragraph b. The 5 criteria in paragraph b are:

   I. that coolable geometry must be maintained,
   II. that long-term cooling to remove decay heat must be possible,
   III. that the cladding must maintain a temperature below 2200°F,
   IV. that the calculated total oxidation of the cladding shall not exceed 17% of the total cladding thickness before oxidation, and

V. the maximum H_2 generated must remain below 1% of the theoretical amount of H_2 produced from the metal water reaction.

b. 10 CFR Part 100
This regulation requires analyses to be performed to ensure that during a postulated accident the dosage to those outside the exclusion zone will be within regulatory limits.

c. 10 CFR Part 50, Appendix A
The general design criteria for the fuel design states that the fuel design must remain intact during all normal operations and anticipated operational occurrences (AOOs).

d. 10 CFR Part 50, Appendix K
Appendix K gives the allowable means to calculate the emergency core cooling system (ECCS) needed during a loss of coolant accident (LOCA).

subtask 1.1.2: Current Licensing Guidelines

The Standard Review Plan (SRP) in NUREG-0800 sections 4.2 to 4.4 are review guidelines used by the NRC when licensing fuel system designs, nuclear designs, and thermal and hydraulic designs for nuclear power plants. These guidelines detail what analyses and documents are required when licensing a new fuel.

subtask 1.1.3: Requirements for New Fuel Systems Design

To license a new fuel system design, nuclear design, and/or thermal hydraulic design, the following are specific details of required information. This required information is taken directly from sections 4.2 to 4.4 of the SRP in NUREG-0800.

a. Section 4.2 – Fuel System Designs
    1. Design Basis - determines the limiting values of parameters to ensure any beyond design damage is maintained at acceptable levels.
    2. Description and Design Drawings - product specifications of the fuel system.
    3. Design Evaluation - ensures the Design Bases are met during normal operation, AOOs, and any postulated accidents
    4. Testing, Inspection, and Surveillance Plans - ensures that before, during, and after irradiation all evaluation, drawing, and design basis requirements are met.

b. Section 4.3 – Nuclear Designs
    1. Confirms that the design basis is established.
    2. Core Power Distribution
    3. Reactivity Coefficients - generally the amount that the reactivity will change for a given change in a parameter, such as moderator temperature, system pressure, etc.
    4. Reactivity Control Requirements and Provisions
    5. Control Rod Patterns
    6. Criticality of Fuel Assemblies
    7. Nuclear Analytical Methods
    8. Reactor Pressure Vessel Irradiation

c. Section 4.4 – Thermal Hydraulic Designs
    1. Computer calculations to validate reactor analyses.
    2. Experimental data to verify the processes and phenomena applied to the reactor design.

The list of fuel system, nuclear, and thermal hydraulic design requirements was created for the current Zr/UO_2 fuel system. A change from the current system to a SiC/SiC CMC or coated Zr alloy cladding and non-UO_2 fuel would require each design requirement be redefined with new calculated or experimentally determined values and analytical modeling results to determine if

the current design requirements are met. Clearly this is a large undertaking and will require a sustained effort over an extended period of time.

Potential fuel system licensing changes to 10CFR Part 50 in applying a SiC/SiC CMC or coated Zr alloy cladding and non-UO_2 fuel are offered as follows. This list of potential changes is not intended to be fully comprehensive.

1. Integrity of advanced cladding during normal operation and AOOs.
2. Thermal hydraulic behavior of advanced cladding during normal operation and AOOs.
3. Mechanical behavior of advanced cladding and high density fuel during normal operation and AOOs.
4. High density fuel swelling and fission gas release during normal operation and AAOs.
5. The water solubility of proposed high density fuel.
6. Advanced cladding failure criteria.
7. Verified and validated fuel performance, transient, and LOCA analysis computer codes.
8. An experimentally determined property and behavior database capable of accurately predicting advanced cladding and high density fuel behavior during normal operation and AOOs.
9. Any change in the expected radioactivity of a new fuel system and coolant.
10. Performance of the new fuel type in long term spent fuel and dry cask storage.

Additionally, the effect of a new fuel system on licensing of the fuel assembly structural components, in example grids, also needs to be considered. The following licensing requirements for the fuel assembly with an advanced cladding and non-UO_2 fuel should be reviewed for licensing changes.

- Seismic forces on the fuel assembly, reactor internals, and reactor supports
- Hydraulic lift forces on fuel assembly
- Thermal hydraulic behavior of fuel assembly
- Growth of the fuel assembly during operation
- Any impact on control rod drop times
- Criticality safety during storage and operation

Lastly, consideration should be given to the effect of an advanced fuel system on the licensing of other areas of a nuclear power plant such as the following.

- Fuel and core performance analysis and models
- Plant safety analysis
- Fuel storage and transport
- Plant operation
- Site environmental impact
- Offsite radiation levels

Table 1.1.1 presents a summary of current understanding of the effect of a SiC/SiC CMC or coated Zr alloy cladding and high density fuel on certain aspects of new fuel licensing.

Licensing Aspect	SiC/SiC CMC + High Density Fuel	Coated Zr + High Density Fuel
cladding integrity during normal and AOO	No effect due to advanced fuel stability with increased temperature.	Unknown due to lack of performance data on coated cladding during LWR operation.
thermal hydraulic behavior of cladding	Modification of licensing due to effect of CMC clad surface roughness on T/H behavior and SiC heat transfer properties.	No licensing effect due to similar surface roughness of coated Zr compared to current Zr alloy clad.
integrity of cladding during LOCA	Minimal effect on licensing proposed due to increased temperature capability of CMC clad. Data required for support.	Minimal effect on licensing proposed due to increased temperature capability of coated Zr clad. Data required for support.
LTR/LTA exemption requirements	Irradiation data for CMC cladding and the high density fuel required.	Irradiation data for coated Zr and high density fuel required.
seismic response of fuel assembly	No effect simply due to choice of materials. Required values may be changed due to modification in density, mass, overall volume, and mechanical properties.	
fuel centerline melt during normal operation, AOOs, and LOCA	No effect due to higher thermal margin of high density fuel compared to UO_2. Could impact reactivity insertion accidents limits due to surface melting occurring at lower energy in hot zero power rod ejection accident.	
fuel burnup limit	Unknown effect on current burnup limit of 62 GWd/MTU for Zr alloy/UO_2 fuel system. Experimental burnup and fuel behavior data will be required to establish a burnup limit.	
fuel response during severe accidents	Proposed positive effect as advanced fuel system should be more tolerant of severe accident conditions compared to current Zr alloy/UO_2 fuel system. Experimental data will be required to support licensing.	
fuel performance, transient, and LOCA analysis codes	Significant effect on licensing as current analytical codes will require revision based on the irradiation performance data.	
fuel pellet solubility in coolant	No effect simply due to choice of materials. Required values may be changed due to modification in density, mass, and overall volume.	

Table 1.1.1. Summary of effect of advanced fuel on certain aspects of fuel licensing.

Task 1.2: Propose Specifications for an Advanced Fuel and Cladding

subtask 1.2.1: Proposed Advanced Fuel Specification

For currently used UO_2 fuel, specifications for powder, pellet, and pellet drawings already exist. (1,2,3) These specifications and drawings have been highly successful in commercial LWR fuel fabrication for many years. Thus, the current UO_2 specifications and drawings will generally be used as a guide in developing proposed specifications for an advanced fuel.

A specification for both uranium silicide (U_3Si_2) and U_3Si_2 doped uranium nitride (U_3Si_2 - UN) fuel pellets should include the following requirements.

- *Enrichment and Isotopic Content:*
  Enrichment for an advanced fuel will be assumed to not exceed the current NRC license limit content of 5 wt.% ^{235}U. The exact fuel pellet enrichment, typically below 5 wt.%, is determined from neutronic calculations based on the loading of the specific reactor core

and is specified in the enriched fuel pellet drawing. Therefore, the exact advanced fuel pellet enrichment cannot be defined in a proposed specification.

Isotopic content shall be measured for ^{234}U, ^{235}U, ^{236}U, and ^{238}U isotopes.

- *U Content, U to Si/N Ratio, and U_3Si_2 Content in U_3Si_2 - UN:*
  For U_3Si_2, this stoichiometric compound has a composition of 92.7 wt. % U, 7.3 wt. % Si, and a U/Si ratio of 1.50:1.00. (4) For UN, this phase is nearly stoichiometric exhibiting ~1 at.% composition range. The composition of stoichiometric UN is 94.4 wt. % U, 5.6 wt. % N, and a U/N ratio of 1.00:1.00. (5)

  For U_3Si_2, any variation in composition will result in other phases or compounds (for example U_3Si) being present. It is proposed that a U content of 92.7 wt.% or greater and a U/Si ratio of 1.50 + .03/- .00 be initially specified. For UN, increases in U content up to ~0.3 wt.% will retain the UN phase, but increases beyond this will result in free U. Therefore, it is proposed that a U content of 94.4 wt.% + .30/- .00 and a U/Si ratio of 1.00 + .02/- .00 be initially specified. Refinement of these composition specifications will require fuel powder and pellet fabrication trials, and experiments determining the effect of fuel pellet composition on in-reactor fissile behavior.

  The content of U_3Si_2 in U_3Si_2 – UN is at present unknown. While it is assumed that less than 10 wt.% U_3Si_2 will be used in approaches at waterproofing UN, approximate amounts of U_3Si_2 in this method are unknown and will not be proposed here.

- *Impurity Content:*
  Impurities in commercial LWR fuel are specified primarily for 2 reasons:
  1. neutronic – Elements that have relatively large parasitic cross sections are undesirable because they decrease the efficiency of the nuclear fission reaction.
  2. chemical – Elements that could have undesirable interaction or chemical reactions with the fuel or fuel rod material are undesirable.

  Many neutronic and chemical impurity elements to be identified in an advanced fuel specification have already been detailed in both public and Westinghouse proprietary specifications for the UO_2/Zr alloy fuel system. (1,2) Thus, based generally on these specifications, impurity content for an advanced fuel is offered as follows in Table 1.2.1.

  In table 1.2.1, B, Cd, Co, Dy, Er, Eu, Gd, In, Sm, and V are included for their neutronic cross section or neutronic activation properties. C, Cl, F, N, and O are chosen for their potential chemical reactivity properties where specified N would only apply to U_3Si_2 fuel. A more accurate impurity specification for an advanced fuel will greatly depend on the method used to synthesize the fuel material from UF_6 feed stock material and the nuances of the fuel fabrication facility, such as what absorber materials are also fabricated in such a facility. Thus the specified impurity content presented in table 1.2.1 should be taken as preliminary.

- *Total H_2 Content:*
  Total H_2 content in current UO_2 fuels is limited to an approximate maximum of 1 ppm. This is due to the need to limit the amount of H_2 potentially absorbed by the Zr alloy cladding from the fuel pellet and subsequent formation of undesirable metal hydrides in the clad tube. For an advanced fuel consisting of U_3Si_2 or U_3Si_2 – UN fuel in a SiC or coated Zr cladding, it is not clear what effect H_2 would have on either the fuel or

cladding. As example, SiC is inert to H containing acids such as HF or HCl. (6) In a fuel, H_2 could combine with O_2 to form H_2O (g) leading to possible bubble or void formation in a sintered fuel pellet. Thus, future experimental work will be required to more accurately determine the effect of H_2 on these advanced fuel materials and a preliminary total H_2 content of 10 ppm is proposed.

- *Pellet Density:*
  Similar to enrichment, pellet density is specified by the utility or reactor operator and is detailed in the enriched fuel pellet drawing. Current sintered UO_2 pellet densities range from approximately 94 to 98% of the theoretical density of UO_2, 10.96 gm/cm^3. As a preliminary specification this range shall be specified.

- *Thermal Stability or Densification Testing:*
  Thermal stability testing is an NRC required test used to evaluate the possible increase in new fuel pellet density when subject to LWR fission conditions. Most lots of fabricated UO_2 fuel pellets are required to be subjected to a specific time at temperature to measure any increase in pellet density caused by additional sintering. While no values of pellet density increase are proposed here, thermal stability testing is included in this specification because this test will most likely be required of any new advanced fuel.

- *Pellet Grain Size:*
  For a new advanced fuel, the grain size of the sintered polycrystalline fuel pellet should be measured. The grain size of currently used UO_2 fuel pellets is measured generally following ASTM E112 and a range of 5 to 25 μm specified. (7,2) A specified grain size range for either a U_3Si_2 or U_3Si_2 – UN fuel pellet cannot be presented at this time and experiments determining mean grain size ranges for these 2 fuel materials should be performed.

A drawing for fuel pellets of either U_3Si_2 or U_3Si_2 - UN should include the following information.

- *Pellet Outer Diameter:*
  Fuel pellet outer diameter (OD) presently varies from approximately 7.75 to 9.75 mm depending on the fuel design. For an advanced fuel pellet drawing, a pellet OD of 8 to 9 mm is preliminarily specified.

- *Pellet Length:*
  Fuel pellet length presently varies from approximately 9.25 to 11.5 mm depending on the fuel design. For an advanced fuel pellet drawing, a pellet length of 10 to 11 mm is preliminarily specified.

- *Pellet Surface Roughness:*
  Fuel pellet surface roughness is presently specified at approximately 100 μin. Generally, there is no reason to change the surface roughness of an advanced fuel pellet, so a pellet surface roughness of 100 μin is preliminarily specified.

Based on fuel pellet design, other possible pellet features could be specified in an advanced fuel pellet drawing. These features could include:

- dimensions of a chamfer on the circumferential edge of the pellet
- dimensions of a dish on the ends of the solid cylindrical pellet
- other fuel design or fuel vendor specific features

A summary of the features to be included in a proposed advanced fuel specification are presented in Table 1.2.2.

element	max. concentration (μgm/gm U)	element	max. concentration (μgm/gm U)
B	**2**	**F**	**15**
C	**1000**	**Gd**	**2**
Cd	**3**	**In**	**10**
Cl	**50**	**N**	**75**
Co	**10**	**O**	**2000**
Dy	**2**	**Sm**	**5**
Er	**25**	**V**	**3**
Eu	**2**		

Table 1.2.1. Elemental impurity content for a proposed advanced fuel specification.

Specification Requirement	Value Measured	Specific Value (if possible)
enrichment	wt. % ^{235}U	< 5 wt. %, +/- 0.05
isotopes	^{234}U, ^{235}U, ^{236}U, and ^{238}U	wt. %
U – Si content **U - N content**	wt. %	92.7 wt.% U or greater 94.4 wt.% U + .30/- .00
U/Si ratio **U/N ratio**	dimensionless	1.50 + .03/- .00 1.00 + .02/- .00
impurity content	μgm/gm U	see Table 1
total H_2 content	ppm	~10 ppm
pellet density	% theoretical density of UO_2, 10.96 gm/cm^3	94 to 98 %
thermal stability	% increase in pellet density, based on the theoretical density of UO_2	-
grain size	mean grain size, μm	-
Drawing Information	**Value Measured**	**Specific Value (if possible)**
outer diameter	mm	8 to 9
length	mm	10 to 11
surface roughness	μin	~100

Table 1.2.2. Features to be included in a proposed advanced fuel specification.

subtask 1.2.2: Proposed SiC/SiC CMC Cladding Specification

As with currently used UO_2 fuel pellets, specifications and drawings for Zr alloy fuel cladding tubes already exist. (8,9,10) Again, these specifications and drawings have been highly successful in commercial LWR fuel fabrication for many years. Thus, the current Zr alloy fuel tube specifications and drawings will generally be used as a guide in developing proposed specifications for a silicon carbide/silicon carbide ceramic matrix composite (SiC/SiC CMC) fuel tube.

A specification for a SiC/SiC CMC fuel tube should preliminarily include the following requirements.

- *Cladding Architecture and Fabrication:*
  The CMC architecture and required fabrication methods are critical in producing a mechanically acceptable, hermetic fuel tube. Presently, various tube constructions (thin monolith tube surrounded by thick composite for example) and CMC architectures are under evaluation using modeling and experimental methods. One or more specific CMC constructions or architectures have not yet been specified. Therefore, a proposed SiC/SiC CMC fuel tube specification should include specific CMC architecture details, but none are presently available.

  Fabrication of a SiC/SiC CMC fuel tube is presently proposed to be performed by chemical vapor deposition/infiltration (CVD/CVI) densification methods. In this method, SiC fiber tows are wound around a mandrel or inner tube in the desired architecture, a thin C interfacial layer is CVD onto the SiC fiber, and subsequent CVD/CVI of SiC vapor is deposited into/onto the wound fiber to as high a CMC density as possible. A specification for SiC/SiC CMC fuel tubes should include critical fabrication process details such as mass of fiber per tube, fiber C coating thickness, and mass of SiC CV deposited and infiltrated. For a proposed SiC/SiC CMC fuel tube specification, only a value of 0.05 – 0.15 μm fiber C coating thickness can be specified here.

- *Composition:*
  The composition of a CMC fuel tube should include value ranges for each constituent of the composite, in this case the SiC fiber, the C interfacial coating, the CVD/CVI SiC, and the bulk composite. SiC fiber is a purchased CMC constituent so the composition can be copied from the providers' analysis, such as 1.05:1.00 C/Si atomic ratio. Other composite constituents can be preliminarily specified here but experience in CMC fabrication and resulting compositions will be needed to more accurately specify desired composition ranges in the future. For nuclear applications of SiC/SiC CMCs, it is well known that high purity, stoichiometric SiC is required. (6) Preliminarily, compositions can be specified as follows;
    C interfacial coating: 99.95 wt.% C min.
    CVD/CVI SiC: 1.05:1.00 C/Si atomic ratio
    bulk SiC/SiC CMC: 1.05:1.00 C/Si atomic ratio, 30.97 wt.% C and 68.13 wt.% Si
    crystalline SiC, no amorphous content allowed

- *Impurity Content:*
  As stated above, high purity stoichiometric SiC is required for nuclear applications of SiC/SiC CMCs and this includes very low non-Si/C impurity concentrations in each constituent of the composite and the finished bulk composite. Oxygen is known to be the primary impurity in high purity stoichiometric SiC fibers. For interfacial C coating, it will also be assumed that O_2 is the primary impurity. Due to the use of various reactant gases, such as methyltrichlorosilane (CH_3SiCl_3), in CVD/CVI processes, H and Cl are known impurities in CVD/CVI SiC. B impurity content should be determined in the bulk CMC due to its neutron absorbing properties. As with specified composition ranges of the SiC/SiC CMC, experience in CMC fabrication and resulting impurity content will be needed to more accurately specify desired impurity content ranges in the future. Preliminary impurity contents in the constituent and bulk composite SiC/SiC CMC can be specified as follows:

SiC fibers: 0.2 wt.% O_2 max.
C interfacial coating: 0.4 wt.% O_2 max.
CVD/CVI SiC: 150 ppm H_2 and Cl_2 max.
bulk SiC/SiC CMC: 2 ppm B max., 0.2 wt.% O_2 max., 200 ppm H_2 and Cl_2 max.

- *Cladding Structure:*
  Specific structural features of the SiC/SiC CMC fuel tube are critical in assuring that the composite exhibits the desired structural integrity and mechanical behavior. Structural features such as percent porosity, volume of SiC fiber in the composite, bulk composite density, and composite microstructure in both transverse and longitudinal orientations should be specified. All of these features directly depend on the chosen CMC architecture which is presently undetermined. Values of these structural features have been determined from recent experimental SiC/SiC CMC tube fabrication and preliminary specification ranges can be specified as follows;
  SiC/SiC CMC porosity: less than 15% by volume
  bulk composite density: 2.65 gm/cm^3 min.
  fiber volume: vol. %, depends on architecture
  composite microstructure: in cross section, requires experimentally developed microstructural standard

- *Mechanical Properties:*
  Like SiC/SiC CMC fuel tube structural features, SiC/SiC CMC fuel tube mechanical properties are a critical property in specifying CMC fuel cladding. Because this advanced fuel cladding is a ceramic composite, mechanical properties characteristic of technical ceramics must now be specified and determined compared to conventional cladding fabricated from metallic Zr alloys. Mechanical properties such as flexure strength, flexure strain or displacement in flex, flexure or elastic modulus, and hardness should be specified. The mechanical properties specified directly depend on the chosen CMC architecture which is presently undetermined. Values of some mechanical properties have been determined from recent experimental SiC/SiC CMC tube fabrication and preliminary specification ranges can be proposed as follows:
  ultimate flexure strength: 300 – 450 MPa in 4-point bend
  ultimate flexure strain or displacement: 1.00 – 1.25% strain in 4-point bend
  flexure modulus: 400 – 500 GPa in 4-point bend
  bulk hardness: ~20 GPa

- *Hermeticity:*
  SiC/SiC CMC fuel tubes must be gas tight under positive pressures. This hermeticity property ensures that the cylindrical walls of the CMC have been fabricated such that they maintain initial fresh fuel pressurization and retain subsequent gaseous fission products generated during the life of the fuel rod. A test to measure and then specify the CMC fuel rod hermeticity will need to be developed. For this proposed specification, CMC fuel tube gas tightness can only be included and no values of hermeticity identified.

- *Corrosion Resistance:*
  Presently Zr alloy fuel tubes are specified for corrosion property evaluation in a high temperature steam autoclave. (8,11) The mass gain and appearance of the metal fuel tube sample is evaluated after a specified time at temperature and pressure. SiC is known to have a significantly lower oxidation rate in steam than Zr and the mass gain at the current specification temperatures and pressures would be very small. The corrosion

behavior of SiC/SiC CMC fuel tubes should be measured before reactor insertion, but the present evaluation specifications are insufficient. Therefore, corrosion resistance shall be specified in this proposed specification, but no further details presented.

- *Cladding Tube Surface Roughness and Defects:*
  Similar to corrosion resistance, present Zr alloy fuel tubes are specified for OD and inner diameter (ID) surface roughness, and surface and internal defects. For SiC/SiC CMC fuel tubes, desired values of surface and internal tube roughness are presently not known. Additionally, the size and area density of surface and internal defects is unknown. Therefore, surface roughness and defects shall be included in this proposed specification but no further details presented at this time.

A drawing for SiC/SiC CMC fuel tubes should include the following information.

- *Cladding Inner Diameter, Outer Diameter, and Concentricity:*
  A proposed SiC/SiC CMC fuel cladding inner and outer diameter, and the OD/ID concentricity are presently unknown. From table 2, a proposed advanced fuel pellet OD of 8 to 9 mm is proposed. For a presently used UO_2/Zr alloy fuel rod (14 x 14 OFA for example) the difference in pellet OD and fuel tube ID is approximately 0.09 mm. Interaction of an advanced fuel pellet and SiC/SiC CMC fuel cladding is presently unknown and must be determined. Therefore, a CMC fuel cladding ID of 8.2 to 9.2 mm is proposed, which results in an approximate 0.1 mm gap between the pellet OD and clad ID. The behavior of an advanced fuel pellet and SiC/SiC CMC fuel cladding (growth, shrinkage, etc.) needs to be determined before these values can be more confidently specified.

  A SiC/SiC CMC fuel cladding outer diameter and concentricity depend greatly on CMC architecture and fabrication methods. For example, Westinghouse-fabricated experimental SiC/SiC CMC tubes with 3 and 6 layers of composite over a thin wall tube have OD values ranging from 11.3 to 13.4 mm, wall thickness of 1.45 to 2.56 mm, and ID-to-OD concentricity ranging from 0.0641 to 0.2776. In comparison, currently used ZIRLO® fuel tubes have OD values ranging from 9.144 to 10.719 mm and wall thickness of 0.526 to 0.572 mm. As stated previously, CMC architecture for a SiC/SiC CMC fuel tube is unidentified. Therefore, specified ranges of SiC/SiC CMC tube OD and concentricity will not be presented here.

- *Cladding Tube Length:*
  Currently used ZIRLO® fuel tubes have length of approximately 385 cm. Therefore, for a proposed SiC/SiC CMC fuel cladding a similar value can be preliminarily specified here.

- *Cladding Tube Surface Roughness:*
  Currently used ZIRLO® fuel tubes have specified ID and OD surface roughness of 50 and 32 μin respectively. These values are specified for the desired heat transfer, crud deposition, fabricability, and other reasons. For a proposed SiC/SiC CMC fuel cladding, the ID roughness can preliminarily be specified as approximately the same for heat transfer purposes. The OD surface roughness will depend more on desired heat transfer and what surface roughness values are possible in CMC fabrication. Therefore, no OD surface roughness for a proposed SiC/SiC CMC fuel tube will be offered at this time.

A summary of the features to be included in a proposed SiC/SiC CMC fuel clad specification is presented in Table 1.2.3.

Specification Requirement	Value Measured	Specific Value (if possible)
architecture	description	-
fabrication	SiC fiber mass (gm) C coating thick. (μm) SiC CVD/CVI mass (gm)	- 0.05 – 0.15 -
composition	SiC fiber C:Si ratio interfacial coating C wt.% SiC CVD/CVI C:Si ratio SiC CMC C/Si wt. % crystal structure	1.05:1.00 99.95 1.05:1.00 30.97/68.13 no amorphous content
impurity content	SiC fiber O_2 wt.% interfacial coating O_2 wt.% SiC CVD/CVI H_2,Cl_2 ppm SiC CMC B,H_2,Cl2 ppm/O_2, wt. %	0.2 max. 0.4 max. 150 2, 200, 200/0.2 max.
structure	CMC porosity, vol. % bulk CMC density, gm/cm^3 fiber volume, vol. % microstructure	<15 2.65 min. - -
mechanical properties	flex strength, MPa flex strain, % flex modulus, GPa. Vickers hardness, GPa	300-450 1-1.25 400-500 ~20
hermeticity	CMC tube gas tightness	-
corrosion resistance	SiC/SiC CMC mass change, mg/dm^2	-
roughness & defects	external/internal roughness, μin surface and internal defects, #/mm^2	- -
Drawing Information	**Value Measured**	**Specific Value (if possible)**
inner diameter	mm	8.2 to 9.2
outer diameter	mm	-
concentricity	-	-
length	cm	~385
surface roughness	ID μin OD μin	~50 -

Table 1.2.3. Features to be included in a proposed SiC/SiC CMC fuel cladding specification.

subtask 1.2.3: Proposed Coated Zr Cladding Specification

Coating the entire outer circumference of a Zr alloy fuel tube has never been attempted before. Developing a preliminary specification for such a composite structure is approached here by combining the desired features of both the coating and the underlying substrate (i.e.; Zr alloy fuel tube) using the current fuel tube specification and drawing as a general guide. (8,9)

A specification for a coated Zr alloy fuel tube should preliminarily include the following requirements.

- *Coating and Deposition Method:*
  The type or chemistry of the applied coating and the method of coating application should be specified. For this work, two coatings are being investigated, a Ti_2AlC composition known as a MAX phase material and an amorphous stainless steel termed NanoSteel™. Since these coatings are in experimental evaluation, they cannot be

specified at this time. Also, because the deposition method has not been defined, no further details are provided for this preliminary specification.

For coatings applied to a Zr alloy fuel tube substrate, assuring that the temperature of coating application is low is critical. Extended exposure of the Zr tube substrate to elevated temperatures is unacceptable due to possible undesired Zr phase transformations (α to β for example) or recrystallization processes. While no maximum process temperature is specified here, future determination of a maximum exposure temperature during coating deposition is required.

- *Coating Composition:*
  The major composition constituents of a coating to be applied to a Zr alloy fuel tube substrate should be specified. As stated above, a Ti_2AlC composition known as a MAX phase material and an amorphous stainless steel termed NanoSteel™ are currently under investigation. Again, these coatings are in experimental evaluation and cannot be specified at this time.

- *Substrate Composition:*
  The substrate of a coated Zr cladding is of course a typical Zr alloy used for current LWR fuel tubes like ZIRLO®. The major composition constituents of ZIRLO® are detailed in the current fuel tube specification for this material. (8) These constituents are presented as follows:
  Nb: 0.8 – 1.2 wt.%
  Sn: 0.8 – 1.1 wt.%
  Fe: 0.09 – 0.13 wt.%
  O_2: 0.105 – 0.145 wt.%
  Zr: balance

- *Coating and Substrate Impurity Content:*
  Impurity content of a coated Zr fuel tube should be specified for both the coating and the Zr tube substrate. Because the coating is presently unidentified, specific impurities cannot be detailed at this time. Typical impurities such as O_2, C, and B should be included in a specification depending on the coating composition. Impurity content for ZIRLO® is clearly called out in the ZIRLO® specification. (8) These 25 impurities are not repeated here and details can be found in this specification.

- *Coated Zr Cladding Structure:*
  Specific structural features of a coated Zr fuel tube are critical in assuring the coated tube exhibits the desired structural integrity and in-reactor performance. Structural features such as coating density, percent porosity in coating, porosity distribution and morphology, coating microstructure, and coating/substrate interface condition should be specified and determined using conventional metallographic and microscopy techniques. Specific values of these features depend on the coating and application method, and will not be offered here.

  The structure specification of the Zr fuel tube substrate should be as detailed in the ZIRLO® specification. (8) Specifically, the internal hydride orientation of the substrate should be determined.

- *Mechanical Properties:*
  As with the structure specification of coated cladding, the specified mechanical properties of a coated Zr clad should be detailed for the coating and the substrate. For the coating, the bond strength of the coating to the substrate and the coating hardness should be specified. Because the coating has not yet been detailed, values for bond strength and hardness are not offered here.

  For the substrate Zr tube, tensile properties and contractile strain ration (CSR) should be specified, both as outlined in the current ZIRLO® specification. (8)

- *Corrosion Resistance:*
  As discussed previously, currently used Zr alloy fuel tubes corrosion properties are specified in response to a high temperature steam autoclave. (8,11) Mass gain and appearance of the fuel tube sample are evaluated after a specified time at temperature and pressure. For a coated fuel tube, this experimental corrosion evaluation appears sufficient if the uncoated portion of the fuel tube is isolated from the corrosive environment. No specific mass gain or appearance values can be offered here due to lack of a specific coating and preliminary corrosion behavior of this coated cladding.

- *Cladding Tube Surface Roughness and Defects:*
  The OD and ID surface roughness and surface and internal defects are specified for currently used Zr alloy fuel tubes. For a coated fuel tube, an OD and ID surface roughness should be specified. An ID roughness the same as the current ZIRLO® specification of ~50 μin is proposed here. However, no OD roughness will be offered both for the Zr fuel tube substrate or the applied coating. For the Zr substrate, surface roughness should be specified as required by the chosen coating deposition process. The specified applied coating surface roughness will depend on both the deposition method and the chosen coating. The size and area density of surface and internal defects is presently unknown. Therefore, surface and internal defect determination shall be included in this proposed specification but no further details can be presented at this time.

A drawing for coated Zr alloy fuel tubes should include the following information.

- *Cladding Inner Diameter, Outer Diameter, Coating Thickness, and Concentricity:*
  For a coated fuel tube, proposed ID values should be similar to those presented for a SiC/SiC CMC shown in Table 1.2.3, 8.2 to 9.2 mm. A proposed OD would be the thickness of a typical ZIRLO® tube plus the thickness of the applied coating. Depending on the deposition method used, a coating thickness of approximately 1 to 25 μm is possible. Therefore, for a ZIRLO® tube wall thickness of 0.5258 mm, a coated fuel tube OD of approximately 9.3 to 10.3 mm is proposed.

  A proposed OD/ID concentricity for coated Zr fuel tubes is presently unknown. Because the applied coating thickness and the uniformity of this thickness are unknown, no OD/ID concentricity is offered here for a coated Zr fuel tube.

- *Cladding Tube Length:*
  Currently used ZIRLO® fuel tubes have length of approximately 385 cm. Therefore, for a proposed coated Zr fuel cladding a similar value can be preliminarily specified here.

- *Cladding Tube Surface Roughness:*
  As proposed above, the ID roughness of a coated fuel tube should be the same as the current ZIRLO® specification of ~50 μin. Also as proposed above, because the surface roughness of the deposited coating is unknown, no OD roughness specification will be offered here.

A summary of the features to be included in a proposed coated Zr alloy fuel tube specification is presented in Table 1.2.4.

Specification Requirement	Value Measured	Specific Value (if possible)
coating and deposition method	coating description deposition description	- -
coating composition	major constituents, wt.%	-
substrate composition	Nb wt.% Sn wt.% Fe wt.% O_2 wt.% Zr wt.%	0.80 – 1.20 0.80 – 1.10 0.09 – 0.13 0.105 – 0.145 balance
coating and substrate impurity content	coating O_2 wt.%/pp C B substrate ppm max. see reference (8)	- - - -
coating structure **substrate structure**	density, gm/cm^3 porosity, vol. % porosity dist./morph. microstructure hydride orientation	- - - - -
mechanical properties – coating **substrate**	 bond strength hardness, HVN yield strength, MPa ultimate strength, MPa elongation, % contractile strain ratio (CSR)	 - - 531-690 710 min. 12 min. 1.2 – 2.25
corrosion resistance	mass change, mg/dm^2 appearance	- -
roughness & defects	OD roughness, μin ID roughness, μin surface and internal defects, #/mm^2	- ~50
Drawing Information	**Value Measured**	**Specific Value (if possible)**
inner diameter	mm	8.2 - 9.2
outer diameter	mm	9.3 – 10.3
coating thickness	mm	0.00003 – 0.0006
concentricity	-	-
length	cm	~385
surface roughness	ID μin OD μin	~50 -

Table 1.2.4. Features to be included in a proposed coated Zr fuel cladding specification.

Task 1.3: Description of Architecture of Advanced Fuel and Cladding

Improved performance of nuclear fuel during severe accidents requires cladding with resistance to much higher temperatures in a steam environment than can be handled by the current Zr alloy clad system. Improving the economic performance in the current and future light water reactor fleet in order to provide an economic incentive to use this new fuel requires new fuel pellets with both a higher ^{235}U fuel density and higher thermal conductivity than provided by the current UO_2 fuel pellet. These are the primary requirements for an economically successful accident-tolerant fuel. These and other important parameters that must be considered are discussed below.

subtask 1.3.1: Advanced Fuel Architecture
Based mainly on several years of internal Westinghouse analysis and complimented with input from recent DOE review, the following are properties for consideration of an advanced fuel. (13,14)

- Increased heavy metal (HM) density
- Reduced absorption cross-section
- Increased thermal conductivity
- High melting temperature
- Low reactivity with water
- Phase stability during operation
- Fission product retention and low swelling during irradiation
- Chemical compatibility with cladding
- Ease of pellet fabrication
- Acceptable chemical toxicity
- Reprocessability

The advanced fuel HM content should be greater than current UO_2, ideally within the regulatory limit of 5% ^{235}U to allow for higher energy density fuel and potential longer fuel cycles. The parasitic absorption cross-section of an advanced fuel should be less than current UO_2, resulting in improved neutron economy. An advanced fuel should possess higher thermal conductivity and equal or higher melting temperature compared to current UO_2 fuel. Both increased thermal conductivity and melting temperature will result in increased fuel safety, such as an increase in the margin from fuel melting. An advanced fuel should be equal to or better than current UO_2 fuel in reactivity with water (i.e., coolant) and the phases present in the sintered fuel pellet should be stable under the irradiation and temperatures experienced during normal fuel operation. The fission products and swelling due to irradiation of an advanced fuel should be of similar or lower behavior to current UO_2 fuel. The selected advanced fuel should not react with the selected advanced cladding and the creep rate of the advanced fuel should be predictable and amenable with the selected advanced cladding. Finally, a new advanced LWR fuel should be easily processed into pellet form, by press and sinter methods for example, should not be excessively toxic to allow for mass production processing, and should be capable of being reprocessed into subsequently useful or inert forms for eventual disposal. Clearly this is a long list of desired properties in a new advanced fuel. Attaining a majority of these desired properties is the challenge in selecting an advanced fuel that could replace and improve upon UO_2.

These desired properties and an economic analysis were used to evaluate potential advanced fuels. (13,15) This analysis indicated that the best choice for an advanced fuel is UN, where N is

enriched in the ^{15}N isotope resulting in $U^{15}N$. $U^{15}N$ has higher HM density and thermal conductivity than UO_2, a similar melting temperature to UO_2, lower parasitic neutron absorption than UO_2, and can be processed into pellet form with conventional press and sinter methods. However, UN does require enrichment in ^{15}N to make this fuel economically viable in LWR application. Additionally, UN reacts with LWR coolants at normal operating temperatures faster than UO_2. Both of these technical issues need to be solved before $U^{15}N$ can be applied as an advanced fuel in LWRs. U_3Si_2 is selected as the second most desirable advanced fuel from the above mentioned analyses. U_3Si_2 has a higher HM density and thermal conductivity than UO_2, is waterproof in typical LWR coolant, and is slightly lower in parasitic neutron cross section compared to UO_2. U_3Si_2 does have a lower meting temperature than UO_2. However, possible melting of U_3Si_2 and the interaction of U_3Si_2 (l) and SiC or Zr has not been studied. It is possible that, unlike UO_2 (l) which forms a low melting compound on reaction with Zr and quickly fails the cladding, melting of U_3Si_2 could be tolerated during accident scenarios. Melting of U_3Si_2 and interaction with SiC and Zr cladding materials requires investigation.

subtask 1.3.2: Advanced Cladding Architecture

Nuclear fuel cladding functions as the primary fission product barrier in the reactor core. Properties for consideration when developing an advanced cladding should include the following.

- Maintenance of a coolable geometry
- Containment of gaseous fission products
- Low parasitic neutron absorption cross-section
- Reduced reaction kinetics during design basis and beyond design basis accidents
- Improved corrosion resistance during irradiation
- Acceptable thermal conductivity
- Improved erosion resistance
- Fabricable into long, thin-walled tube geometry

As mentioned in section 1.3.1 for advanced fuel development, these desired advanced cladding properties were determined based on both Westinghouse analysis and input from a recent DOE review. (13,14) These analyses resulted in two candidates for advanced cladding.

- SiC fiber - SiC matrix ceramic matrix composites (SiC_f/SiC CMC). A long, thin-walled fuel tube constructed of a SiC_f/SiC CMC can have several different composite constructions. For example, Westinghouse has been pursuing a composite construction consisting of a monolithic SiC thin wall tube surrounded by a SiC_f/SiC CMC consisting of SiC_f of specific fiber architecture and a matrix of chemical vapor infiltrated/deposited SiC. SiC exhibits a very high sublimation temperature, high strength up to temperatures greater than 2000°C, low absorption cross-section compared to current Zr base alloys, and excellent corrosion resistance in high temperature steam. While SiC exhibits the large majority of the desired properties, it has never been fabricated into an approximate 4 m long, thin walled CMC tube.
- Coated Zr base alloy tubes. Currently used Zr base alloy cladding performs acceptably under well defined operating conditions. However, when exposed to design basis and beyond design basis accidents, current Zr base alloys rapidly degrade. For this work, currently used Zr base alloy tubes would be coated with a thin layer of either an amorphous stainless steel or a Ti_2AlC compound. For this advanced cladding, the strength and melting temperature of the cladding is determined by the Zr alloy substrate, while the corrosion and erosion resistance is determined by the coating. Because the coating is less than 100 μm thick, there will be relatively little increase to the absorption cross-section of the Zr alloy substrate. Critical issues of this advanced cladding concept are the application of the

coating and the subsequent performance of the coating/substrate system in LWR coolant. Zr metal requires coating application at low temperature using a nonviolent process. Additionally, O_2 should be excluded from the substrate surface and application process during coating deposition to minimize premature Zr oxide formation and possible coating spalling.

To better understand the response of advanced cladding to core uncovery accidents, Westinghouse in collaboration with Fauske & Associates (FAI) performed modeling using the Modular Accident and Analysis Program (MAAP) software. (16) As a base case model, the Three Mile Island Unit 2 (TMI-2) core uncovery accident was modeled with both a Zr base alloy and SiC as cladding materials. Figure 1.3.1 below presents a result of this modeling showing that, for the TMI-2 accident, a SiC clad core could have survived as a coolable geometry reaching a peak temperature of approximately 1200°C. Additionally, modeling of an extended station blackout event (SBO) was performed as an approach to determine how an advanced cladding would respond to an accident similar to what occurred at the Fukushima Daiichi nuclear power plant in Japan in March 2011. An extended SBO does not allow creep rupture and therefore breach of the reactor cooling system (RCS) to occur during the accident. In this modeling approach, the material of the fuel assemblies are exposed to core uncovery conditions for an extended period of time without allowing failure of other reactor systems.

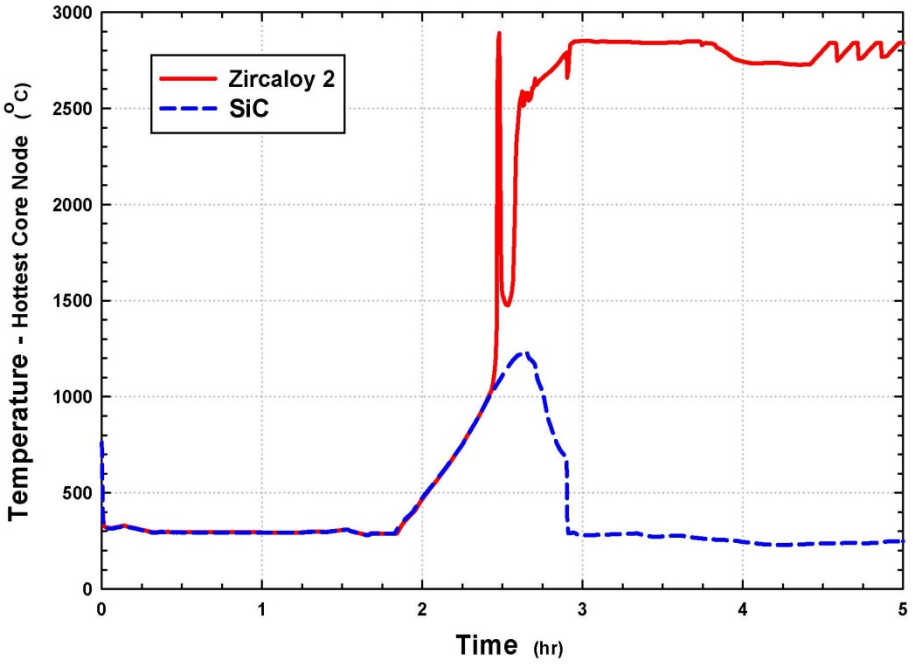

Figure 1.3.1. Temperature of Zr and SiC cladding in the hottest core node during a modeled TMI-2 accident scenario.

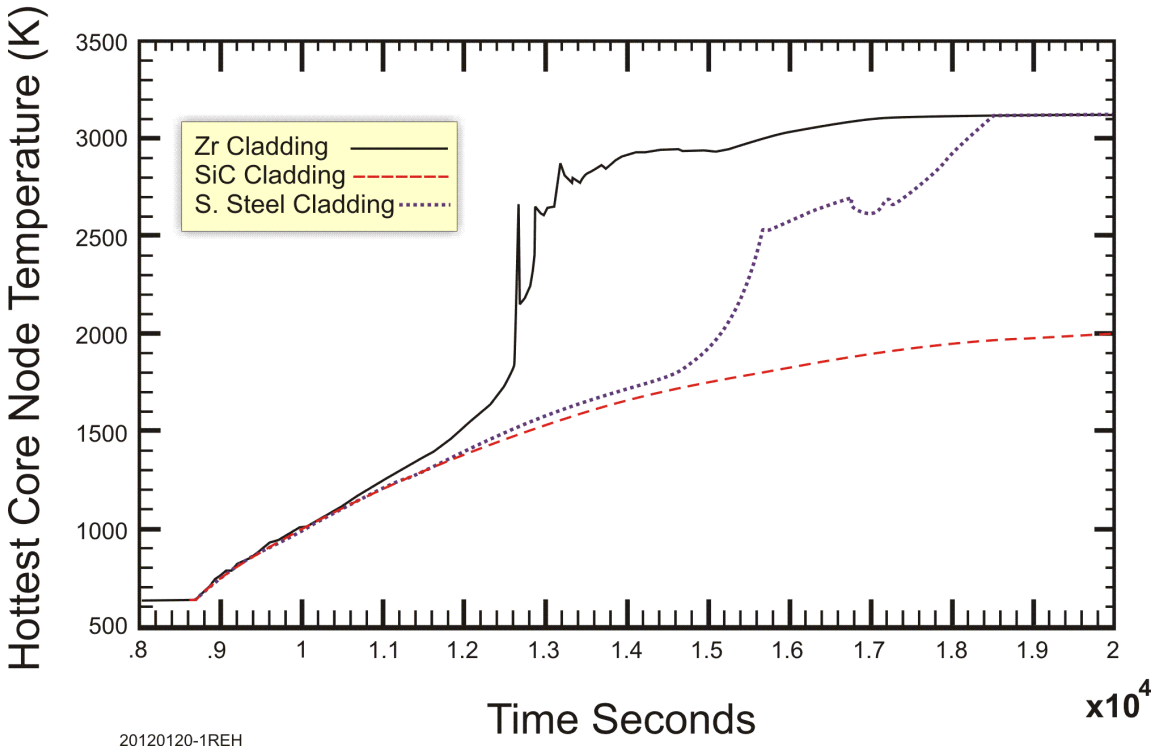

Figure 1.3.2. Temperature of Zr, SiC, and stainless steel cladding in the hottest core node during a modeled station blackout accident scenario.

Figure 1.3.2 presents a result of the extended SBO model showing that SiC cladding could have survived a SBO accident in a coolable geometry reaching a peak temperature of approximately 1727°C. Clearly these modeling results indicate the potential of advanced cladding such as SiC_f/SiC CMC to survive both design basis and beyond design basis core uncovery accidents compared to currently used Zr base alloy cladding.

While coated Zr base alloy tubes would still not likely survive a SBO accident, they would likely provide additional reactor operator reaction time to perform ameliorative efforts. For shorter-timed events such as at TMI-2, treated Zr tubes may have been sufficient to prevent the large scale damage that TMI-2 suffered.

subtask 1.3.3: Fuel Assembly Components other than Fuel and Cladding
Fuel assembly components other than cladding and fuel in a PWR such as the top and bottom nozzles, the assembly skeleton, the support grids, and the mixing grids and their reactions during accidents need to be considered. For a BWR, these components also include the water channel. These component materials experience similar operational conditions as the cladding except they are at lower temperature due to the distance from fissioning fuel.

Components such as the top and bottom nozzles are positioned out of the power generating neutron cloud and can readily be made of many high-temperature, corrosion-resistance materials such as Zr and Ni base alloys. Support grid, mixing grid, water channel, and assembly skeleton materials could be made of low absorption cross-section, corrosion-resistant materials such as SiC or coated Zr alloys. While work to date has focused on cladding and fuel materials,

there clearly is an opportunity to apply more advanced materials such as SiC_f/SiC CMCs and coated Zr alloys to other fuel assembly components.

subtask 1.3.4: Summary of Architecture of Advanced Fuel and Cladding
The advanced fuel and cladding architecture offered by Westinghouse can be summarized as follows.

Assembly Geometry: Square assembly lattice and pitch composed of solid cylindrical fuel pellets in thin walled cladding tubes.
Fuel: Solid cylindrical pellets of U_3Si_2 and $U^{15}N$ treated to be waterproof under conventional PWR operating conditions.
Cladding: SiC_f/SiC CMC fabricated as thin walled cladding tubes and current Zr base alloy cladding tubes coated with thin layers of corrosion and wear resistant materials.
Fuel Assembly Components other than Fuel and Cladding: Application of SiC_f/SiC CMC and coated Zr base alloys where applicable.

Task 1.4: Analysis of the Performance of an Advanced Fuel

subtask 1.4.1: Neutronic and Preliminary Economic Analysis
Neutronic Considerations
The neutronic characteristics of U_3Si_2 and UN are similar to UO_2 fuel with some differences mainly related to the different cross-sections of the binding elements and the higher densities of both U_3Si_2 and UN. The macroscopic absorption cross-section of natural N (practically ^{14}N), Si, O, and ^{15}N are shown in Figure 1.4.1, together with the normalized neutron flux per unit energy. Table 1.4.1 presents the 2-group macroscopic cross-sections collapsed using the fine-energy flux as weight. It can be seen that natural N leads to significant parasitic captures, predominantly as a result of ^{14}N (n,p) ^{14}C reactions. The resulting reactivity penalty exceeds 5,000 pcm which leads to unacceptable degradation in neutron economy and production of radiotoxic ^{14}C. This disadvantage of UN fuel can be mitigated by enriching N in ^{15}N which has exceptionally low cross-sections. Table 1.4.1 shows that 95% ^{15}N in UN will practically have the same 2-group absorption cross-sections as Si in U_3Si_2 leading to acceptable neutron economy. High enrichments of N in ^{15}N appear to be a requirement to reap the potential improvement in fuel cycle cost (FCC) performance of UN compared to UO_2 fuel. For convenience, unless otherwise indicated, when referring to UN in the remainder of this section, it will be implied that N is 95% enriched in ^{15}N.

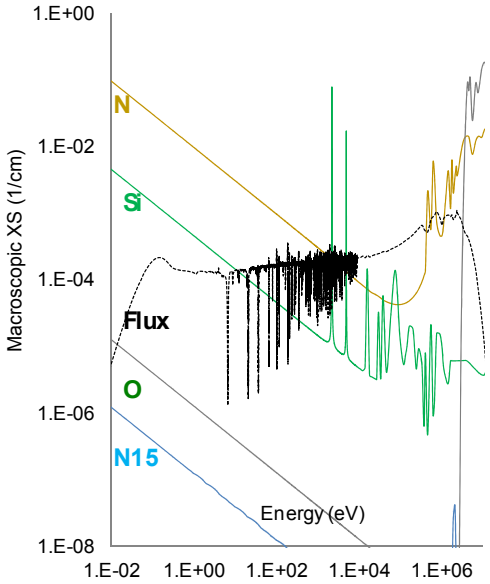

Figure 1.4.1. Macroscopic absorption cross-sections of N, Si, O and ^{15}N.

The higher density of U_3Si_2 and UN compared to UO_2 results in a reduction in neutron moderation from the lower hydrogen to heavy metal (H/HM) ratios. Therefore, the spectrum of both U_3Si_2 and UN is harder, meaning there is a higher neutron population at higher energies relatively to the UO_2 fuel spectrum, as presented in Figure 1.4.2. The spectral ratio, defined as the flux above and below 0.625 eV, is approximately 13, 11 and 9 respectively for fresh UN, U_3Si_2 and UO_2 in a typical 17x17 lattice. As the fuel is irradiated, the spectrum becomes harder for all fuels as a result of thermal captures in fission products and in-bred Pu, and the spectral differences among all fuels are reduced.

Macroscopic Absorption Cross-Sections	**O in UO_2**	**Si in U_3Si_2**	**Natural N UN**	**95% ^{15}N-UN**
Group 1 (> 0.625 eV)	1.80E-04	1.15E-04	2.19E-03	1.12E-04
Group 2 (< 0.625 eV)	4.15E-06	1.33E-03	2.75E-02	1.39E-03
Microscopic XS at 0.025 eV	2.02E-04	1.70E-01	2.02E+00	1.01E-01

Table 1.4.1. Macroscopic absorption cross-sections for various binding elements.

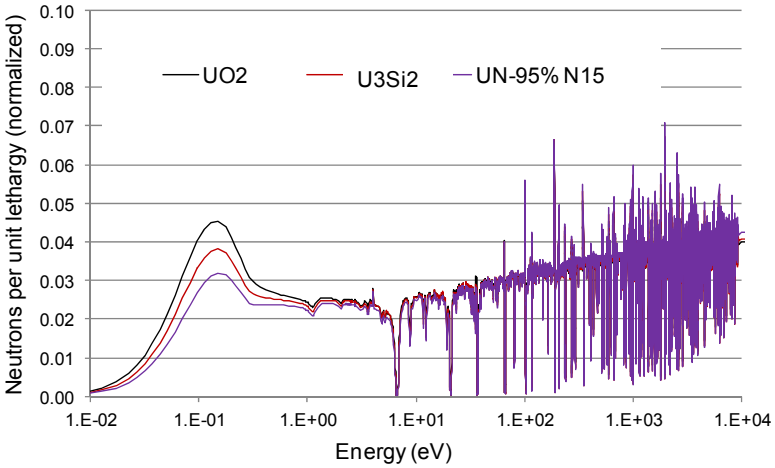

Figure 1.4.2 Neutron spectrum for various fuels.

The harder spectrum of U_3Si_2 and UN has two reactivity effects. First the fissile cross-sections are decreased and therefore, so is the instantaneous reactivity. Second the ^{238}U to Pu conversion is increased due to the higher epithermal captures in ^{238}U, which slows down the reactivity loss as the fuel is burned. The net effect on reactivity depends on the fuel discharge burn-up (BU); for instance 5% ^{235}U UN fuel in a standard 17x17 lattice is initially less reactive than UO_2 fuel of the same enrichment and lattice conditions, but as the two fuels are burned the reactivity in UN fuel becomes larger than UO_2 fuel at BU greater than 50 GWd/tHM in this specific case. If a smaller UN pellet/cladding diameter is adopted, then the loss in H/HM compared to UO_2 is partially compensated, which leads to initial reactivity gains but eventual loss from the reduced Pu generation. In addition, a smaller pellet reduces the HM content of the fuel, which is not desirable from a FCC perspective. The optimum tradeoff in the size of UN and U_3Si_2 fuel pellets will be established in future work. The preliminary studies performed indicate that for typical core designs with <5% ^{235}U enrichment a reduction of the UN pellet diameter with respect to standard UO_2 fuel is beneficial to the economic performance. U_3Si_2 has intermediate spectrum between UO_2 and UN and the optimum pellet size will likely be intermediate between UO_2 and UN.

The higher density of U_3Si_2 and UN is particularly relevant to economic performance. Higher density means higher ^{235}U content than in UO_2 fuel, thereby allowing for a similar enrichment with a decrease in the number of fresh assemblies utilized in a core reload. A reduction in the number of assemblies used results in significant improvements in fuel utilization and potential FCC savings. In addition, the improved thermal performance of U_3Si_2 and UN compared to UO_2 fuel allows implementation of a SiC cladding, which besides the expected operational and safety benefits, also offers superior neutron economy and further FCC savings relative to Zr-based claddings. The cross-sections of Zr and SiC presented in Figure 1.4.3 display similar thermal cross-sections but much lower epithermal cross-sections for SiC vs. Zr. The FCC performance of the various options is discussed in a subsequent section reporting the preliminary economic analysis.

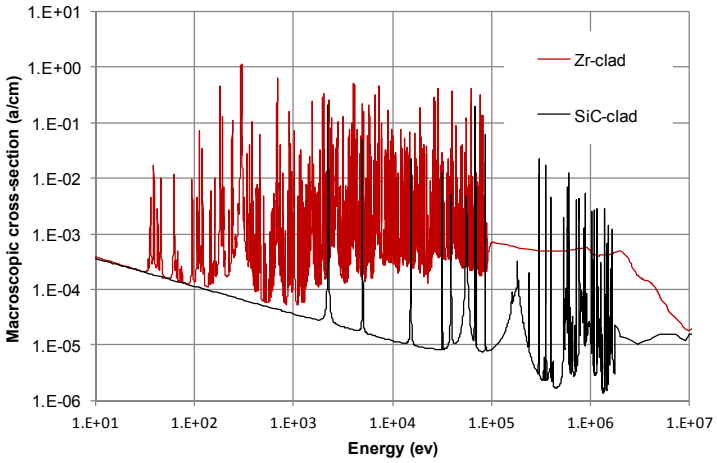

Figure 1.4.3. Macroscopic cross-sections of Zr and SiC cladding.

Impact on Core Design and Reactivity Feedbacks

As a result of the harder spectrum of the proposed fuels, some reduction in the worth of thermal absorbers should be anticipated for U_3Si_2 and UN cores. To avoid excessive soluble B concentrations in the coolant, the loading of burnable absorbers will need to be increased to account for the higher fissile loading of U_3Si_2 and UN fuels and for extended reactivity control. The Westinghouse Integral Fuel Burnable Absorber (IFBA), consisting of a thin ^{10}B enriched ZrB_2 coating on the fuel pellet outer surface, has been used in the preliminary core design calculations presented here. Due to complete depletion of its ^{10}B content during irradiation and no displacement of U from the pellet, IFBA results in optimum economic performance. However, if used alone, the relatively high IFBA loading required for U_3Si_2 and UN fueled cores may lead to excessive rod pressurization from the He released in the ^{10}B (n, α) ^{7}Li reaction. A combination of fuel burnable absorbers will probably be required in U_3Si_2 and UN fueled cores for acceptable fuel rod performance.

The reactivity feedback of U_3Si_2 and UN fuel will in part depend on the final fuel design and core configuration adopted. However, the fuel Doppler coefficient is anticipated to be negative and similar to UO_2 fuel. A slightly less negative Doppler is possible due to the impact of different fuel binding elements (N and Si vs. O) and harder spectrum (fewer absorptions for a given increase in fuel temperature). A compensating effect will occur as a result of the expected lower operating temperatures of U_3Si_2 and UN (the Doppler coefficient becomes less negative as temperature increases). The moderator temperature coefficient depends on the lattice and soluble B content, but for similar conditions and within a reasonable range of variation it is anticipated to be more negative for U_3Si_2 and UN than UO_2. This behavior is the result of the harder spectrum and the larger fraction of burned fuel assemblies anticipated in U_3Si_2 or UN cores compared to UO_2 cores. The power defect is expected to be less negative for U_3Si_2 and UN, with lower reactivity swing when going from Hot Zero Power (HZP) to Hot Full Power (HFP) conditions, and vice versa. The power coefficient is also expected to be less negative for U_3Si_2 and UN compared to UO_2.

These general trends are confirmed in preliminary 3-D core calculations performed using the Westinghouse in-house PWR core physics package for a typical 4-loop 1112 MWe nuclear plant operating on 18-month refueling intervals at the equilibrium cycle. (17,18) The calculated Doppler Temperature Coefficient for U_3Si_2 and UN fueled cores is presented in Figure 1.4.4 and is negative across the power range, and slightly higher than UO_2. The Hot Full Power Moderator

Temperature Coefficient presented in Figure 1.4.5 is more negative for U_3Si_2 and UN compared to UO_2, and has a similar decreasing trend from Beginning of Cycle (BOC) to End of Cycle (EOC).

In light of the basic underlying physics and preliminary core evaluations performed, U_3Si_2 or UN fueled cores appear feasible and viable. A confirmatory full suite of safety analysis evaluations will be performed in the future as experimental data and insights in fuel behavior are gathered and an optimum design can be determined.

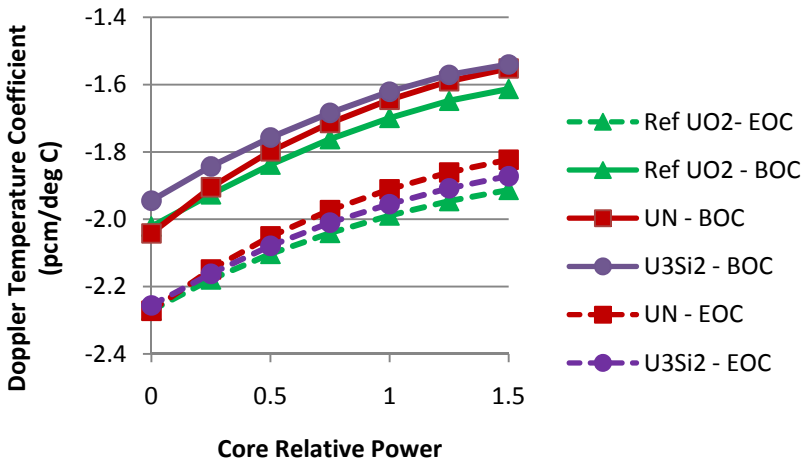

Figure 1.4.4. Doppler temperature coefficient (pcm/°C) plotted against core relative power. Here the reactivity difference is expressed in pcm, defined as $10^5 * \ln(k_2/k_1)$, where k_2 and k_1 are the final and initial reactivity.

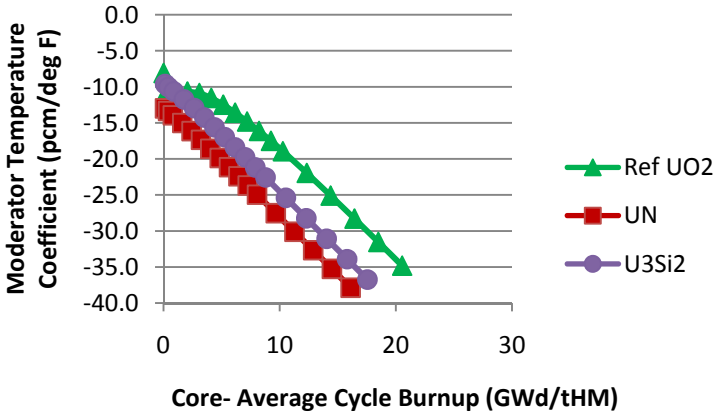

Figure 1.4.5. Moderator temperature coefficient (pcm/°F) plotted against core relative power.

Economic Performance

The economic performance of U_3Si_2 and UN fuel has been assessed using 3-D core calculations performed with the Westinghouse in-house PWR core physics package. (17,18) A

typical 4-loop, 1112 MWe, 193 assembly core operating on 18-month refueling intervals at the equilibrium cycle has been used for the analysis. Various reloading schemes and IFBA loading representative of actual core operation have been applied. The impact of reducing fuel pellet/cladding outer diameter of U_3Si_2 and UN fuel to increase the coolant area and mitigate the H/HM reduction has been assessed. The performance of UO_2 fuel with ^{235}U enrichment greater than 5% has also been assessed.

Fuel cycle neutronic and cost calculations were performed based on fuel procurement and associated financial charges with assumptions presented in Table 1.4.2, and results presented in Table 1.4.3. The reference calculation is for UO_2 fuel with 80 feed assemblies, Zr alloy cladding, ^{235}U enrichment less than 5%, and peak fuel rod BU less than 62 GWd/tHM. These calculations indicate the following:

1. Although UN requires ^{15}N enrichment, its potential economic performance is the best of the fuels analyzed. Even with the 5% ^{235}U enrichment limit, UN fuel with SiC cladding shows a nearly 9 % FCC savings with respect to current UO_2 fuel, with approximately 2% FCC savings coming from the SiC cladding. Based on preliminary engineering analysis by Westinghouse, $1,000/Kg for enriched ^{15}N and same fabrication cost as UO_2 fuel have been assumed for this analysis. The breakeven cost of ^{15}N for this option is approximately $5,000/Kg.
2. U_3Si_2 fuel offers significant FCC savings, up to 7.5 % including approximately 2% from SiC cladding assuming the same manufacturing cost for UO_2 fuel. While the maximum savings could be lower than for UN, U_3Si_2 does not require ^{15}N enrichment and waterproofing. However, its melting point is significantly lower than UN, 1662°C compared to 2600 °C respectively.
3. SiC cladding shows FCC savings in excess of $50,000 per feed assembly when compared to Zr alloy cladding due to fewer parasitic neutron captures in SiC and the resulting reduced ^{235}U enrichment requirements. A SiC cladding is also an enabling technology for higher fuel utilization by allowing higher fuel exposure than the current limits.
4. Although current Zr alloy cladding is at the licensable exposure limit for UO_2 at 5% enrichment, coatings that allow longer Zr cladding exposure times in combination with greater than 5% ^{235}U enrichments may allow for higher discharge BU. The ensuing FCC improvements would be limited to approximately 3%, less than 40 cents/MWhe compared to the reference.

A breakdown of the savings into the various FCC components is presented in Figure 1.4.6. All alternatives to the current UO_2 fuel feature reduced U ore requirements, resulting in reduced conversion and fabrication costs, reduced spent fuel disposal costs due to lower feed assemblies and rate of discharge, and higher in-core carrying charges due to the longer in-core fuel residence time. UO_2 with greater than 5% ^{235}U enrichment features higher enrichments costs while U_3Si_2 and UN offer savings also in this area. Note that lower savings for UN are the result of including the cost of ^{15}N enrichment at an assumed $ 1,000/kg.

Item	Value	Timing (month)
U_3O_8 price ($/lb)	69	-18.0
conversion price ($/kgU)	12	-14.0
SWU price ($/kg-SWU)	162	-6.0
fabrication ($/kgU)	200	-9.1
pre-operational interest (%/yr)	6.0%	
spent fuel cooling time (month)	120	
spent fuel disposal charge ($/MWHre)	1	
spent fuel dry storage charge ($/FA)	50,000	
cycle length (month)	18	
effective full power days (day)	510	
rated thermal power (MWt)	3,587	
rated net electric output (MWe)	1,112	
inflation rate	2.0%	
return on fuel investment (%/yr)	8.0%	
U conversion loss (%)	0.0%	
tails enrichment (w/o)	0.3%	
natural enrichment (w/o)	0.71%	
95% N-15 enrichment cost ($/kg)	1,000	

Table 1.4.2. Assumptions used to evaluate neutronics and economics of the proposed ATF.
Note: SWU – Separative Work Unit; MWt – megawatt thermal; MWe – megawatt electric; FA – fuel assembly

Fuel Type	Cladding Type	Feed Assemblies	Average ^{235}U Enrichment	Cost ($/MWhe)	Savings (%)
UN	SiC	52	4.78	9.80	8.8
U_3Si_2	SiC	60	4.72	9.93	7.5
UO_2	Zr	60	5.70	10.37	3.4
UO_2	Zr	80	4.55	10.74	Ref

Table 1.4.3. Economic results.
Note: Feed Assemblies are the number of fresh assemblies per reload out of 193 total core assemblies.

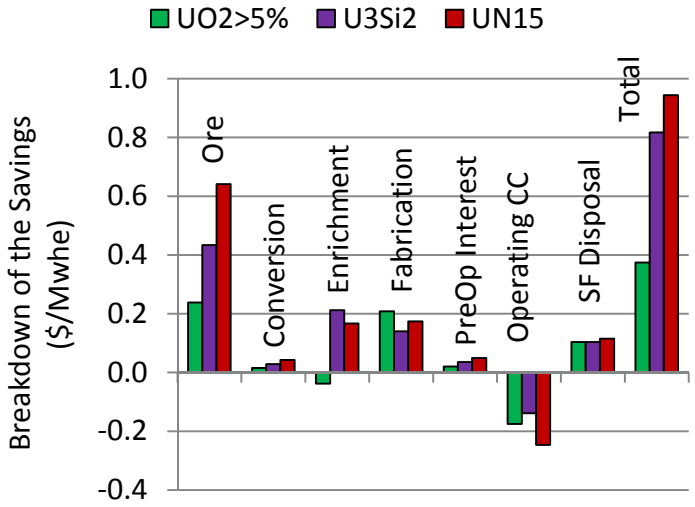

Figure 1.4.6. Breakdown of fuel cycle cost saving plotted as $/MWhe vs. Ref. UO_2 core.

subtask 1.4.2: Fuel Rod Performance of an Advanced Fuel Design
Analysis method and constraints applied
A preliminary evaluation was performed to assess the impact of some basic fuel rod performance constraints on the geometry of an advanced fuel assembly. In this preliminary study it was decided to consider the reference robust fuel assembly (RFA) design and to estimate whether the injection of various fuel-clad material combinations would predict the need to change this geometry in order to meet these constraints. The performance constraints used in this study are:

1. Fuel centerline temperature should remain below melting at a conservatively high linear power of 20 kW/ft.
2. To prevent strain-induced cladding failure, clad tensile strain at end-of-life[1] (EOL) should remain below 2% for coated Zr and below 0.1% for SiC cladding.
3. For SiC cladding, the proposed multilayer structure of the composite requires the cladding to be thicker than a conventional Zr alloy clad. The cladding thickness is estimated to be 0.041 in. for SiC cladding and 0.022 in. for conventional Zircaloy cladding and coated Zr base alloy cladding.

The rationales behind the choice of the strain limits are different for the two cladding materials. For coated Zr, the 2% strain limit results from the following three considerations.

1. conventional Zircaloy has been demonstrated to resist short term strain (i.e. that experienced during hotcell tests) above 2%,
2. conventional Zircaloy resistance to long term strain typical of reactor operation is higher than that to short term strain experienced during hotcell testing, and
3. because of its relatively small thickness, the presence of a coating is not expected to affect the capability of coated Zr to resist strain.

For SiC cladding a 0.1% strain limit was chosen. Due to uncertainty in the irradiation effect on mechanical properties, the dependence of mechanical properties on the SiC composite and

[1] This tensile strain is defined as 100(EOL diameter-minimum OD)/minimum OD, where the minimum diameter is over the rod life, and a burnup of 75 GWD/mtU is assumed for EOL.

manufacture process, this relatively conservative low value was selected. This preliminary strain limit value will be evaluated later in the project.

Fuel rod sizing results

Table 1.4.4 shows the fuel rod geometries resulting from application of the above mentioned constraints and the resulting fuel loading. Fuel loading is an indicator of the economic performance of the proposed fuel designs. Higher fuel loading results in longer fuel cycles and/or lower required fuel enrichment. From table 1.4.4 it can be deduced that;

- UN-fueled geometries are similar to current fuel design geometries. Specifically, the fuel geometry using coated Zr has the same dimensions as the reference design. The fuel geometry using SiC cladding requires thicker cladding due to the limits of SiC CMC fabrication and a larger pellet-clad gap due to the conservative clad strain limit value applied.
- Use of UN fuel results in a significant increase in fuel loading for both cladding materials. Specifically, use of coated Zr cladding with UN results in a 41% increase in fuel loading while use of SiC cladding with UN results in a 15% increase in fuel loading, both relative to the Zr alloy clad/UO_2 fuel reference case.
- U_3Si_2 fueled geometries require a very wide pellet-clad gap to accommodate the expected high swelling of this fuel and avoid exceeding the clad strain limit. (19) This large pellet-clad gap results in fuel temperatures that would lead to fuel melting at approximately normal operating conditions. Additionally, an excessively large pellet-clad gap leads to potential asymmetry of the pellet with respect to the clad. This asymmetry can result in non-uniform circumferential heat transfer across the gap and localized hot spots, and an additional source of uncertainty in heat transfer calculations which reduce fuel temperature prediction accuracy. To avoid these problems, the thermal resistance within the fuel rod should be decreased, possibly by replacing He with a liquid metal (LM) as gap filling material. This concept is discussed below.
- Due to a predicted large pellet-clad gap, use of U_3Si_2 results in a reduction in fuel loading of approximately -13% for coated Zr cladding and approximately -30% for SiC cladding. This results in a significant penalty to fuel cycle economics.

		Cladding/Fuel Material Combinations				
		Reference (UO_2/Zircaloy)	**Coated Zr**		**SiC**	
			UN	U_3Si_2	UN	U_3Si_2
Geometry	Fuel cladding OD, in.	0.374	0.374	0.374	0.382	0.382
	Fuel cladding ID, in.	0.329	0.329	0.329	0.300	0.300
	Clad thickness, in.	0.0225	0.0225	0.0225	0.0410	0.0410
	Pellet OD, in.	0.3225	0.3225	0.2770	0.2910	0.2460
	Pellet-clad gap, in. *(filling material)*	0.00325 *(He)*	0.00325 *(He)*	0.026 *(LM)*	0.0045 *(He)*	0.027 *(LM)*
Performance indicator: fuel loading						
Fuel loading per assembly (assuming 95% TD)	Total, kg	530	692	435	562	343
	HM, kg	464	653	403	531	318
	HM variation, %	0	+41	-13	+15	-31

Table 1.4.4. Assembly geometries resulting from application of fuel rod performance constraints.

While the above results apply to fresh fuel, it should be understood that the difference in thermal and mechanical performance of different designs increases as the fuel is burned. Based on this preliminary fuel rod performance analysis, the following comments are offered.

Zr cladding compared to SiC cladding

SiC does not creep below 1300°C. (20) This is an advantage since it delays Pellet Clad Mechanical Interaction (PCMI). However, this is also a disadvantage since it delays the reduction in thermal resistance occurring from gap closure. The larger pellet-clad gap combined with the low thermal conductivity of irradiated SiC results in higher fuel temperatures.

Coated Zr cladding with UN (or U_3Si_2) compared to Zr cladding with UO_2

Coated Zr cladding is expected to creep at the same rate as typical Zr cladding due to a minimal mechanical effect of the thin coating. However, clad transient strains are expected to be much lower due to the high thermal conductivity of the proposed fuel materials, and similar fuel expansion coefficient.

Considerations on the feasibility of liquid metal bonding

As mentioned above, the swelling behavior assumed in this analysis for U_3Si_2 does not allow a safe margin from fuel melting unless the fuel rod thermal resistance is reduced. A possible technique to achieve this, as well as to eliminate the issues related to the non-concentricity of the pellet with respect to the clad, is the use of a high-conductivity filling for the rods, in place of conventional helium gas. A possible candidate is the low melting eutectic Pb-Sn-Bi, which has already been extensively investigated as bonding material for LWR rods. (21,22,23) This eutectic, which melts at 120°C and has a thermal conductivity approximately 100 times higher than helium, does not react with water and UO_2 and was demonstrated to react with Zircaloy cladding forming a thin $ZrSn_2$ that passivates the cladding from further attack. (21,22,23) No information is available about its chemical compatibility with SiC or non-UO_2 fuels. Wongsawaeng and Olander successfully developed a fabrication technique shown to work on a full-size fuel element that, they claimed, should fit well with existing manufacturing lines. (21) They also claimed that the improvement in performance over helium-bonded fuel elements appeared to outweigh any disadvantages and the higher fabrication cost of the liquid-metal bonded rods. While, performance-wise, this is true, liquid metal escaping from the rods as a consequence of a clad failure would imply a much greater effort to clean the RCS with respect to using a gas to bond the rods. Since the objective of this study is to develop fuel rods whose reliability is equal or greater than that of typical rods, the possibility of clad failure cannot be excluded a priori and the phenomena subsequent to clad failure should be the subject of a thorough investigation. At the same time, however, U_3Si_2 cannot be ruled out based on this eventuality since there is significant uncertainty on the magnitude of the property at the root of this problem, i.e. irradiation-induced swelling. In fact, swelling data used for this analysis are based on irradiation tests performed at the Oak Ridge Research Reactor in the 80s' of U_3Si_2 dispersed in Al at 45-59 vol.% loading. (19) Aluminum, which was originally added to silicide fuels to improve corrosion resistance, has a deleterious effect on the swelling behavior of uranium silicide compounds, and therefore it is reasonable that the swelling of pure U_3Si_2 is lower than the value assumed in this analysis. (24)

subtask 1.4.3: Thermal Hydraulics of an Advanced Fuel Design

A preliminary evaluation was performed on the effect of the proposed fuel/cladding material combinations on fuel assembly thermal hydraulic (TH) performance. This evaluation includes the following sections.

1.4.3.1 - Analysis Approach and Constraints Used:
1.4.3.2 - Performance Indicators
1.4.3.3 - Analysis Results and Observations

1.4.3.1 - Analysis Approach and Constraints Used

The preliminary evaluation of the TH performance of various fuel/cladding combinations during steady-state operation was determined by modeling PWR cores with these materials. Typically,

the best practice in designing a high performance core involves performing a geometry optimization over wide ranges of assembly lattice parameters, i.e. fuel rod diameter and rod-to-rod distance, for both square and triangular lattices. For this preliminary evaluation, the same fuel assembly geometry was first used for modeling all the fuel-cladding combinations, specifically a 17×17 robust fuel assembly (RFA) design with helium-bonded fuel rods (Case 1). Then, the TH analysis was performed on the designs obtained in subtask 1.4.2, which resulted from the application of some key fuel rod performance constraints. As explained in subtask 1.4.2, these constraints are as follows.

1. Fuel centerline temperature should remain below the fuel melting temperature at a linear power of 20 kW/ft.
2. Clad strain at end-of-life (EOL, ~75 GWD/ton) should remain below 2% for coated Zr and 0.1% for SiC to prevent strain induced clad failure.
3. Cladding wall thickness used is estimated to be 0.022 in. for Zr alloy and 0.041 in. for SiC cladding.

By applying these fuel rod performance constraints, more applicable designs are developed within the conventional 17x17 RFA fuel assembly geometry.

The reactor operating conditions selected are summarized in Table 1.4.5. These conditions are the design values typically used for Zr/UO_2 fuel system cores and therefore are not best estimates for nominal operation. In addition to the reference power distribution presented in Table 1.4.5, the alternative fuel/cladding combinations were also analyzed using the enthalpy rise hot channel factor (FdH) increased by 15% in order to account for the possibility of not being able to achieve the same low peaking of typical UO_2 fuel.

Parameter	Value	Reference
plant type	-	typical Westinghouse 4-loop
core power, MWt	3459	Table 1 of (25)
core operating pressure, psi	2240	(26)
core inlet temperature, °C	287.9	(26)
core flow rate excluding bypass, kg/s	16395	calculated from minimum measured flow rate (379100 gpm) and best estimate bypass flow fraction (0.086), from Section 7.3.8.2 of (26)
hot assembly flow distribution factor	0.95	section 1.6.5.2.4 of (28)
hot assembly peaking factor	1.5506	design value (1.482, from Figure B-2 of (28)) increased to comply with RFA-2 specific FdH
enthalpy rise hot channel factor (FdH)	1.6218	recommended FdH for RFA-2 (1.59,(25)), accounting for 1.02 tilt factor (27)
axial peaking factor (Fz) & axial power shape	1.55 (chopped cosine)	assumed
peak heat flux hot channel factor (Fq)	2.5138	calculated as FdH · Fz
pellet-clad gap conductance, W/m^2 K	He-bonded: $5682 \cdot t_{ref}/t$	1000 Btu/hr ft^2 F (5682 W/m^2 K) scaled based on gap width t (t_{ref}=0.00325 in.)
	LM-bonded: 35/t	Pb-Sn-Bi eutectic thermal conductivity (35 W/m K,(29)) divided by gap width

Table 1.4.5. Operating conditions selected for preliminary thermal hydraulic assessment.

1.4.3.2 - Performance Indicators

To assess the TH performance modeling results, the following 6 performance indicators are applied for all modeling in this subtask.

1. Heavy metal loading per fuel assembly,
2. Maximum fuel temperature,
3. Maximum fuel average temperature across the pellet radius,
4. Maximum temperatures on the inner and outer surfaces of the cladding,
5. Minimum Departure from Nucleate Boiling Ratio (MDNBR), and
6. Core pressure drop.

The heavy metal loading indicator has primarily economic implications in that higher HM loading can result in a longer fuel cycle and/or lower required enrichment. The other 5 performance indicators have primarily safety implications. The maximum fuel temperature needs to guarantee a margin below the fuel melting temperature sufficient to allow operational flexibility and to accommodate transients. The maximum fuel average temperature affects the amount of fission gas released during operation as well as irradiation induced swelling of the fuel pellet. The maximum cladding temperatures will affect the mechanical properties of the cladding material, especially the temperature of the outer surface and the kinetics of any temperature-affected reaction between the cladding material and the coolant.

MDNBR is monitored to allow for sufficient margin from critical heat flux (CHF) conditions. Two key aspects of MDNBR as a performance indicator are as follows.

- Due to the degradation in mechanical properties with increasing temperature of Zr base alloys, operation with rods in DNB is unacceptable using Zr alloy and coated Zr alloy cladding since clad failure will occur. However, the high temperature capabilities of SiC make reaching CHF conditions less of a concern and operation of fuel in DNB may be possible without resulting in cladding failure. Thus it is possible that SiC may have significant safety and performance advantages compared to conventional Zr alloy cladding and should be further investigated.
- The surface wettability of the cladding material is known to affect CHF and is different for Zr alloy, coated Zr alloy, and SiC cladding. For this preliminary effort, the effect of surface wettability on CHF is conservatively[2] neglected. Due to this and that constant operating conditions and fuel assembly geometry are used for all fuel/cladding combinations examined in Case 1, the calculated MDNBR is the same for all fuel/cladding combinations. Thus, MDNBR is not a useful performance indicator for the fuel designs modeled in Case 1.

Core pressure drop provides an indication of the effect that variations in assembly lattice geometry (fuel rod diameter in this analysis) would have on the coolant flow rate, since the flow provided by the reactor coolant pumps (RCPs) decreases as the hydraulic resistance increases.

1.4.3.3 - Analysis Results and Observations

Results for Case 1 modeling are summarized in Table 1.4.6. Here, modeled cases 1a, 1b, and 1c use progressively higher peak linear power (q'_{max}). The calculated results are highlighted compared to the reference design (Zr/UO_2) using the following cell coloration scheme.

[2] Coated Zr and composite SiC are expected to have a CHF at least equal to that of conventional (uncoated) Zr, if not higher. The higher porosity characterizing both the protective layer deposited on Zr and, eventually, the SiC composite structure, are expected to yield a higher nucleation site density, whose enhancement is known to benefit CHF.

no highlight – similar performance to Zr/UO_2
green highlight – significantly better performance than Zr/UO_2
yellow highlight – slightly worse performance than Zr/UO_2
red highlight – significantly worse performance than Zr/UO_2

Results of Case 1 modeling shown in Table 1.4.6 can be summarized as follows.

- Use of U_3Si_2 and UN results in significantly higher HM loadings compared to the Zr/UO_2 reference design. U_3Si_2 increases HM content by 18% and UN by 41%. These values are determined assuming 95% of theoretical density for all fuels.
- U_3Si_2 has a similar margin to melting compared to UO_2 whereas UN has a much higher margin. For U_3Si_2, this is due to the lower melting point and higher thermal conductivity of this fuel compared to UO_2. Additionally, because the thermal conductivity of U_3Si_2 increases with temperature, the margin to melting of U_3Si_2 becomes larger than UO_2 as peak linear power and fuel temperature increase from Case 1a to Case 1c. For UN, the higher margin to melt in all cases is due to the relatively very high melting temperature and thermal conductivity of UN compared to UO_2.
- The temperature of the cladding is independent of the type of fuel used and dependent on the thermal conductivity of the cladding material. Therefore, this temperature is 200°C higher than the reference design only when using SiC as cladding material as shown in table 1.4.6. The thermal conductivity of SiC is lower than Zr and is independent of temperature, as shown in Figure 1.4.7 for a 1 dpa radiation damage, which is expected to be reached after 4-5 months of irradiation (30).
- Core pressure drop is effectively equivalent for all designs due to the fixed assembly geometry and coolant flow.

			Cladding and Fuel Materials			
		Reference (Zr/UO_2)	SiC		Coated Zr	
			U_3Si_2	UN	U_3Si_2	UN
Fuel loading per assembly	total, kg	530	590	692	590	692
	HM, kg	464	546	653	546	653
	HM variation (% compared to reference)	0	+18	+41	+18	+41
Case 1a: design conditions (q'_{max}=14.2 kW/ft)	maximum fuel centerline T, °C	2058	1066	1041	908	872
	margin from fuel melting T, °C	782	599	1722	757	1890
	maximum fuel average T, °C	1342	979	966	812	793
	hot spot cladding T (inside/outside), °C	402/348	579/348	579/348	402/348	402/348
	MDNBR[a]	2.769	2.769	2.769	2.769	2.769
	core pressure drop, psi	29.1	29.1	29.1	29.1	29.1
Case 1b: +15% in FdH for ATF fuel-clad combinations (q'_{max}=16.3 kW/ft)	maximum fuel centerline T, °C	-	1155	1127	973	937
	margin from fuel melting T, °C	-	510	1635	692	1825
	maximum fuel average T, °C	-	1058	1045	869	850
	hot spot cladding T (inside/outside), °C	-	610/348	610/348	409/348	409/348
	MDNBR[a]	-	2.307	2.307	2.307	2.307
	core pressure drop, psi		29.2	29.2	29.2	29.2
Case 1c: (q'_{max}=20 kW/ft)	maximum fuel centerline T, °C	2720	1374	1329	1125	1088
	margin from fuel melting T, °C	120	291	1433	540	1674
	maximum fuel average T, °C	1832	1251	1230	1001	982
	hot spot cladding T (inside/outside), °C	427/350	682/350	682/350	427/350	427/350
	MDNBR[a]	1.385	1.385	1.385	1.385	1.385
	core pressure drop, psi	29.6	29.6	29.6	29.6	29.6

Table 1.4.6. Performance of various fuel-clad material combinations when loaded in a reference assembly geometry (Rod OD=0.374", clad thickness= 0.0225"; pellet OD=0.3225", He-bonded rods).
[a] The Westinghouse WRB-2M correlation is used to compute CHF.

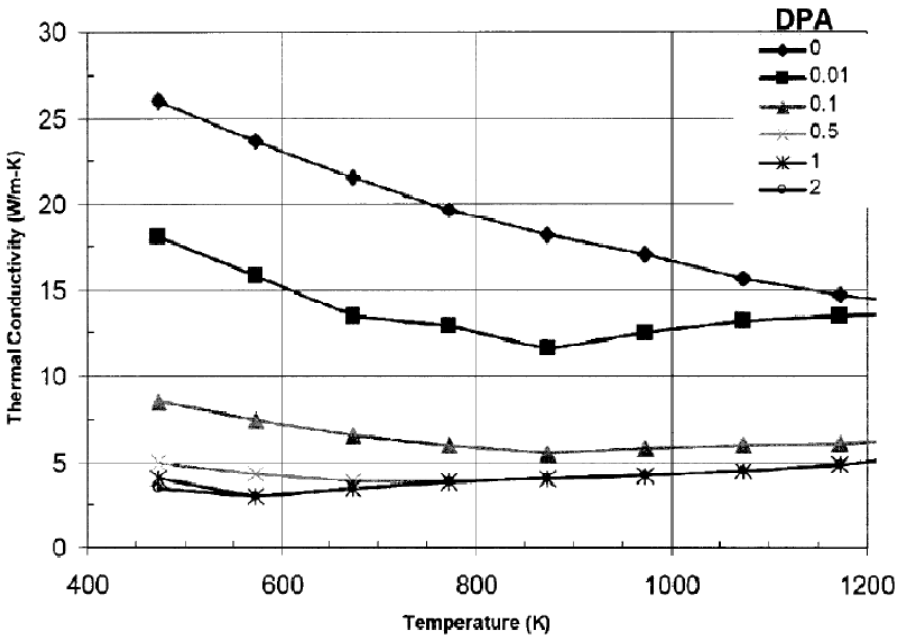

Figure 1.4.7. Variation of thermal conductivity with temperature and irradiation for SiC composite (High-Nicalon Type S with CVI SiC from (31) and originally in (32)).

Results for Case 2 modeling are presented in Table 1.4.7 and again Case 2a, 2b, and 2c only differ in the peak linear power used in the analysis. These results can be summarized as follows.

- With the exception of the Zr/UN- design, application of fuel performance constraints results in a reduction of HM loading. This is due to the need for a larger pellet-clad gap and larger clad thickness for SiC. For U_3Si_2, HM loading decreases to -31% for SiC cladding and -13% for coated Zr alloy cladding, both compared to the Zr/UO_2 design. For UN, HM loading decreases to 15% for SiC cladding and remains the same at 41% for coated Zr alloy cladding, again both compared to the Zr/UO_2 design. This reduction in HM loading penalizes fuel cycle economics particularly for U_3Si_2 fuel.
- U_3Si_2 shows a slightly higher margin to melting than UO_2. However, this is due to using a LM bonding material since the use of He would have resulted in no margin to melting at the design conditions of Case 2a.
- UN shows significant margin to melting ranging from approximately 600 to 1500°C greater than that for UO_2. For UN, He was used as the bonding material due to the calculated smaller pellet-clad gap.
- Due to the increase in fuel rod outer diameter when using SiC cladding, heat transfer area and coolant velocity both increase and MDNBR increases approximately 3%. However, core pressure drop increased approximately 7% in designs employing SiC, due to the tighter lattice resulting from the larger fuel rod diameter.

		Cladding and Fuel Materials				
		Reference (Zr/UO_2)	**SiC**		**Coated Zr**	
			U_3Si_2	UN	U_3Si_2	UN
geometry	fuel cladding OD, in	0.374	0.382	0.382	0.374	0.374
	fuel cladding ID, in	0.329	0.300	0.300	0.329	0.329
	clad thickness, in	0.0225	0.041	0.041	0.0225	0.0225
	pellet OD, in	0.3225	0.246	0.291	0.277	0.3225
	pellet-clad gap, in. (filling material)	0.00325 (He)	0.027 (LM)	0.0045 (He)	0.026 (LM)	0.00325 (He)
Performance Indicator: fuel loading						
fuel loading per assembly	total, kg	530	343	562	435	692
	HM, kg	464	318	531	403	653
	HM variation (% compare to reference)	0	-31	+15	-13	+41
Performance Indicator: temperature and MDNBR						
Case 2a: design conditions (q'_{max}=14.2 kW/ft)	maximum fuel centerline T, °C	2058	1010	1396	678	872
	margin from fuel melting T, °C	782	655	1366	987	1890
	maximum fuel average T, °C	1342	920	1328	562	793
	hot spot cladding T (inside/outside), °C	402/348	783/348	783/348	402/348	402/348
	MDNBR[a]	2.769	2.858	2.858	2.769	2.769
	core pressure drop, psi	29.1	31.2	31.2	29.1	29.1
Case 2b: +15% in FdH for ATF fuel-clad combinations (q'_{max}=16.3 kW/ft)	maximum fuel centerline T, °C	-	1089	1529	715	937
	margin from fuel melting T, °C	-	576	1233	950	1825
	maximum fuel average T, °C	-	991	1454	588	850
	hot spot cladding T (inside/outside), °C	-	840/348	840/348	409/348	409/348
	MDNBR[a]	-	2.385	2.385	2.307	2.307
	core pressure drop, psi	-	31.3	31.3	29.2	29.2
Case 2c: (q'_{max}=20 kW/ft)	maximum fuel centerline T, °C	2720	1284	1851	801	1088
	margin from fuel melting T, °C	120	381	911	864	1674
	maximum fuel average T, °C	1832	1162	1755	647	982
	hot spot cladding T (inside/outside), °C	427/350	975/350	975/350	427/350	427/350
	MDNBR[a]	1.385	1.431	1.431	1.385	1.385
	core pressure drop, psi	29.6	31.8	31.8	29.6	29.6

Table 1.4.7. Performance of assembly designs satisfying fuel rod design constraints.
[a] The Westinghouse WRB-2M correlation is used to compute CHF.

subtask 1.4.4: Safety, Design Basis, and Beyond Design Basis Accident Analysis of an Advanced Fuel

The safety related performance of a PWR core during normal operation, anticipated transients, and beyond design basis accidents (BDBAs) is typically assessed through extensive analysis

requiring comprehensive knowledge of all in-core components. Presently, this level of knowledge of cladding and fuel components is incomplete because information such as in-core material performance is unknown. However, a preliminary study of the safety performance of an advanced fuel design can be performed by using currently available material properties and making a relative comparison to current materials and components. Through this approach, engineering judgment can be used to perform this analysis and draw conclusions about materials and the reactor response during transients.

This engineering judgment analysis can be performed using two bases for the analysis.

1. Analysis based on the fuel rod damage mechanism.
2. Analysis based on the type of transient.

These analyses are presented in Sections 1.4.4.1 and 1.4.4.2, respectively.

1.4.4.1 - Preliminary Advanced Fuel Safety Analysis based on Fuel Rod Damage Mechanism

This analysis is performed by surveying typical damage mechanisms considered in reactor analysis and determining if the properties of the new cladding and fuel materials will protect against these mechanisms. Damage mechanisms considered in reactor analysis can be classified into three major categories. (28)

- Category I: Mechanisms potentially resulting in "fuel system damage", i.e. either fuel rod failure, deviation of fuel rod dimensions beyond tolerance margins, or reduction of functional capabilities below those assumed in safety analyses. These mechanisms apply to normal operation and anticipated operational occurrences (AOOs).
- Category II: Mechanisms potentially resulting in fuel rod failure which apply to normal operation, AOOs, and postulated accidents.
- Category III: Mechanisms resulting in loss of coolability, i.e. the fuel assembly does not retain its rod bundle geometric configuration with adequate coolant channels to permit heat removal. These mechanisms apply to postulated accidents.

Specific fuel rod damage mechanisms belonging to each of these three categories are presented in column two of Table 1.4.8. For each failure mechanism category and fuel rod damage mechanism, Table 1.4.8 presents the relative performance of the selected fuel rod and fuel materials with respect to the current Zr/UO_2 fuel system. A coloring scheme is used to identify the damage mechanisms in which the new materials are expected to perform definitely better (green) or definitely worse (red) than current materials. Light blue is used to identify fuel rod damage mechanisms requiring further experimental or computational investigation. For some fuel rod damage mechanisms, table information is supplemented with additional information identified by capital letters inside table cells correlated to the lettered paragraphs following the table.

Failure Mechanism Categories	Fuel Rod Damage Mechanisms	Fuel Rod & Fuel Materials			
		SiC CMC (to Zr)	**Coated Zr** (to Zr)	**U_3Si_2** (to UO_2)	**UN** (to UO_2)
Category I: *fuel system damage* (normal operation & AOOs)	clad design stress	BETTER at high T, to be determined at normal operation (F)	SAME	WORSE Higher fuel swelling	
	clad design strain		SAME	WORSE Higher fuel swelling	
	clad fatigue		SAME	WORSE Higher fuel swelling	
	clad fretting wear	Unknown for SiC CMC; limited data for SiC (C)	SAME for bulk material, but coating adhesion may be challenged	No effect	
	oxidation & crud buildup	BETTER (E)	BETTER (testing under irradiation required)	No effect	
	rod bow	BETTER (D)	Same	No effect	
	axial growth	BETTER (D)	Same	No effect	
	internal pressure	BETTER at high T, to be determined at normal operation (F)	No effect	Unknown wider gap for swelling reduces pressure, burnable poisons still unknown	
	assembly liftoff	WORSE (SiC lighter than Zr), but not a concern	Same	BETTER heavier fuel	
Category II: *fuel rod failure* (normal operation, AOOs, postulated accidents)	clad hydriding	BETTER (less corrosion, less H)	BETTER (less corrosion, less H)	No effect	
	clad collapse into gap - fuel densification	Somewhat BETTER (limited clad creep (A)	Same	Somewhat BETTER due to higher fuel swelling	
	clad overheat by CHF	BETTER: minimal concern due to limited mechanical property degradation with T (F)	Same	No effect	No effect
	fuel overheat	WORSE due to low clad thermal conductivity and low creep (B)	Same	Somewhat BETTER due to higher thermal conductivity BUT lower melting T	BETTER due to higher thermal conductivity and similar melting T
	pellet-clad interaction	BETTER (A)	Same	WORSE due to higher fuel swelling	
	fuel rod fracturing by external loads - core/plate motion	BETTER at high T, undetermined during normal operation (F)	Same	No effect	No effect

Category III: fuel rod failure and loss of *fuel coolability* (postulated accidents)	Fragmentation of cladding (during LOCA)	BETTER due to low degradation of mechanical properties with T (F)	BETTER due to expected lower corrosion	No effect	No effect
	expulsion of fuel upon RIA	BETTER due to low degradation of mechanical properties with T (F)	Same	Probably WORSE: similar Doppler coefficient at nominal conditions, but lower Doppler-induced reactivity suppression during transients due to higher thermal conductivity & higher fuel swelling	
	Clad ballooning and flow blockage during LOCA	BETTER due to low degradation of mechanical properties with T (F)	Same	BETTER: lower fuel stored energy due to lower initial T	BETTER: lower fuel stored energy due to lower initial T
	fuel assembly structural damage from external forces	BETTER due to low degradation of mechanical properties with T (F)	Same	No effect	No effect

Table 1.4.8. Expected relative performance of advanced fuel materials based on fuel rod damage mechanisms.

The letter scheme indicated in Table 1.4.8 refers to the following additional information.

A. Unlike Zircaloy, SiC does not creep up to 1300°C making PCMI less likely to occur under similar conditions of fuel geometry, fuel type, and irradiation level. (34) This is an advantage because it results in reduced stress in the cladding, but also a disadvantage because lack of creep defers the reduction in thermal resistance that occurs from gap closure. The combination of low thermal conductivity of irradiated SiC and lack of gap closure results in higher fuel temperatures when using SiC based cladding. Additionally, the lack of creep in SiC requires an increased pellet-clad gap in the as fabricated condition.

B. Carpenter states that "*SiC cladding performance may be limited unless cladding/fuel conductivity or gap conductance is improved*". (34) This is due to two factors:
    1. SiC experiences a significant degradation in thermal conductivity upon irradiation;
    2. SiC does not creep at temperatures below 1300°C.

   The reduction in thermal resistance that normally accompanies pellet-clad gap closure is deferred when using SiC base cladding. According to data from Youngblood (and reported by Carpenter), Hi-Nicalon Type-S SiC composite experiences a reduction in thermal conductivity to a saturation value of approximately 4 W/m K after 0.5 to1 dpa of irradiation from an unirradiated value of 23 W/m K. (32,31) For a typical PWR or BWR, the time required to accumulate 1 dpa of radiation damage is approximately 4 to 5 months of operation at full power. (30)

C. There is no data in the open literature on SiC composite wear or fretting but some data does exist for solid SiC. SiC wears, but the extent of wear is significantly reduced when water is present because it acts as lubricant. (34)

D. SiC CMC tubes have been experimentally verified to grow axially under irradiation to saturation values of 0.2 to 0.7% ($\Delta L/L$) after 240 EFPD of operation. (34) These values are consistent with data for solid SiC of 1.7% volume increase corresponding to 0.57% length increase. (38) Radial growth data for SiC ranges from 0.5 to 3% ($\Delta D/D$). Significant data scatter exists for both axial and radial growth of SiC.

E. Monolithic and composite SiC exposed to steam up to 1200^{o}C exhibits oxidation kinetics 2 to 3 orders of magnitude slower than Zircaloy-2 and Zircaloy-4. (39,40) Carpenter also exposed SiC to steam in irradiation. (34) These tests showed that SiC exposed to steam at 300°C exhibited similar low oxidation kinetics without and with irradiation. Instead, SiC composites showed a reduction in oxidation resistance upon irradiation and specifically an increase in oxidation-induced weight change by 5-15 times with respect to that of unirradiated samples for EBC coated composites, and by 10-25 times for those without this coating. In spite of this, the recession rates of the best performing composite tubes were below 3 μm/month which for a 100 μm EBC layer would guarantee protection for approximately 30 months, i.e. much longer than the assembly expected residence time. Lastly, the oxidation rates of uncoated and coated SiC composites showed no dependence on exposure duration from 100 to 500 days exposure, as a demonstration of the saturation effect already noticed for other properties of SiC (e.g. thermal conductivity). This would advantage SiC over Zr based alloys for extended burnup applications since the property degradation for the latter does not reach saturation but monotonically increases with fluence. These preliminary results strongly imply that SiC composite both with and without EBC's offer significant advantage over currently used Zr alloys in high temperature steam oxidation.

F. SiC is a material capable of maintaining room temperature mechanical properties to very high temperatures. In example, the tensile fracture stress of SiC is 300 MPa at 300 and 1000°C. (41) However, the mechanical properties of SiC composites are dependent on the composite

architecture and construction. Even though the composite architecture for fuel cladding tubes has not been finalized, it can be stated that SiC CMC fuel cladding will have greater mechanical stability at elevated temperatures than currently used Zr base alloys.

1.4.4.2 - Preliminary Advanced Fuel Safety Analysis Based on Event Type

For a safety analysis based on event type, events are divided into two categories which are subdivided into specific event groups as presented in Table 1.4.9. Each event group comprises several specific events, which are typically analyzed for licensing purposes and whose results are presented in the Safety Analysis Report of any PWR plant in the US. These specific events are listed in the second column of Table 1.4.9. The analysis of each event requires input parameters, such as fuel and cladding thermophysical properties, reactivity coefficients, or geometric characteristics of RCS components and has the ultimate goal to determine if specific safety acceptance criteria are met. Many of these input parameters are directly or indirectly dependent on the fuel and cladding materials. The effect that advanced fuel and cladding materials have on the reactor safety analysis can therefore be estimated by determining whether changes in those input parameters are beneficial or detrimental in meeting the acceptance criteria. This assessment is presented in Table 1.4.10 which for each event presents the following information:

- Category of event consistent with the frequency based classification developed by the American Nuclear Society in 1973. (42)
  - Condition I: normal operation and AOOs;
  - Condition II: faults of moderate frequency;
  - Condition III: infrequent faults;
  - Condition IV: limiting faults.

- Expected Impact of ATF on Analysis – specifically the fuel and cladding materials of ATF with impact ranked as Significant, Moderate, Minor, or None.

- Current Acceptance Criteria for each event.

- Expected Performance in meeting current Acceptance Criteria of each proposed cladding and fuel material. The performance of these materials is rated as Better, Worse, or Unknown with respect to the currently used Zr/UO_2 fuel system and the same coloring scheme as in Table 1.4.8 is used.

- Notes for discussion of the performance rating of the cladding and fuel materials for each event group analyzed. These notes are identified by capital letters which coincide to descriptive paragraphs following Table 1.4.10.

The acceptance criteria presented in Table 1.4.10 are those used in the analysis of the current UO_2/Zr fuel system. Implementation of new cladding and fuel materials may not only change these criteria, but may also introduce new safety acceptance criteria. Therefore, some level of uncertainty exists in the performance rating presented in the table.

Event Category	Event Group
Anticipated Transients	Reactor Cooling System (RCS) overcooling events
	RCS overheating events
	Reactivity insertion events
	Increase in RCS inventory events
	Decrease in RCS inventory events
	Fuel handling accident
Beyond Design Basis Accidents (BDBAs)	Anticipated Transients Without Scram (ATWSs)
	Station blackout event

Table 1.4.9. Event categories and groups for preliminary safety analysis based on event type.

					Expected performance in meeting current acceptance criteria				Note
	Transient	**Category**	**Expected impact of ATF on analysis**	**Current acceptance criteria** (for conventional PWR)	**SiC CMC** (to Zr)	**Coated Zr** (to Zr)	**U_3Si_2** (to UO_2)	**UN** (to UO_2)	
RCS overcooling events	HZP steamline break & HFP steamline break	IV	Moderate/ Significant	MDNBR & no fuel melting	BETTER	~SAME	WORSE	WORSE	(A)
	increase in FW flow/ decrease in FW enthalpy	II	Minor/Moderate	MDNBR & no fuel melting	BETTER	~SAME	WORSE	WORSE	
	increase in steam flow/ excessive load increase	II	Minor	MDNBR	BETTER	~SAME	WORSE	WORSE	
	inadvertent opening of SG relief/safety valve	II	Minor	MDNBR	BETTER	~SAME	WORSE	WORSE	
RCS overheating events	RCP shaft seizure or RCP shaft break	IV	Moderate/ Significant	RCS overpressure, PCT, fraction of rods in DNB	Unknown	~SAME	Unknown	Unknown	(B)
	complete loss of forced reactor coolant flow	III	Minor/Moderate	MDNBR	BETTER	~SAME	Unknown	Unknown	
	partial loss of forced reactor coolant flow	II	Minor/Moderate	MDNBR	BETTER	~SAME	Unknown	Unknown	
	loss of external electrical load, condenser vacuum, and turbine trip	II	Minor	MDNBR, RCS overpressure, MSS overpressure	BETTER	~SAME	BETTER	BETTER	
	loss of normal FW flow	II	Minor	preclude PRZ overfill	~SAME	~SAME	BETTER but likely unchanged		
	loss of non-emergency AC power to station auxiliaries	II	Minor	preclude PRZ overfill	~SAME	~SAME	BETTER but likely unchanged		
	FW system pipe break	IV	Minor	prevent hot leg saturation	~SAME	~SAME	BETTER	BETTER	
Reactivity insertion events	spectrum of RCCA ejection accidents	IV	Significant	fuel pellet enthalpy < 200 cal/gm; fuel melting < 10% of pellet cross section; Zr-H_2O reaction < 16%	BETTER	~SAME	WORSE	WORSE	(C)
	uncontrolled RCCA bank withdrawal from subcritical or low power startup	II	Moderate/ Significant	MDNBR & no fuel melting	BETTER	~SAME	WORSE	WORSE	
	dropped RCCA	III	Moderate	MDNBR & no fuel melting	BETTER	~SAME	Unknown	Unknown	(D)
	uncontrolled RCCA bank withdrawal at power	II	Minor	MDNBR, no fuel melting, RCS overpressure	BETTER	~SAME	WORSE	WORSE	(C)
	CVCS malfunction resulting in B dilution	II	Minor	operator action time to preclude criticality	~SAME	~SAME	~SAME	~SAME	(E)

					Expected performance in meeting current acceptance criteria				Note
	Transient	**Category**	**Expected impact of ATF on analysis**	**Current acceptance criteria** (for conventional PWR)	**SiC CMC** (to Zr)	**Coated Zr** (to Zr)	**U_3Si_2** (to UO_2)	**UN** (to UO_2)	
RCS inventory increase	inadvertent operation of ECCS at power	II	Minor	operator action time to preclude pressurizer overfill	~SAME	~SAME	~SAME	~SAME	(F)
	CVCS malfunction increasing RCS inventory	II	Minor	operator action time to preclude pressurizer overfill	~SAME	~SAME	~SAME	~SAME	
RCS inventory decrease	large break LOCA	IV	Significant	cladding oxidation	Unknown	BETTER	Unknown	Unknown	(G)
	steam generator tube rupture	IV	Minor	Dose to the secondary side	~SAME	~SAME	~SAME	~SAME	(H)
	inadvertent opening of a PRZ safety/relief valve	II	Minor	MDNBR and pressurizer overfill	BETTER	~SAME	~SAME	~SAME	(I)
Misc	fuel handling accident	IV	Minor/ Moderate	dose	no effect (failure of all rods assumed)		WORSE	WORSE	(J)
BDBAs	station blackout	N/A	Moderate/ Significant		BETTER	BETTER	BETTER	BETTER	(K)
	anticipated transients without scrams (ATWS)	N/A	Minor/ Moderate	RCS overpressure	BETTER	BETTER	BETTER	BETTER	

Table 1.4.10. Expected performance in meeting accepted criteria of advanced fuel materials in event based safety analysis

A. These events, typically bounded by the steamline break, cause an overcooling of the RCS. Because of the negative MTC, these events result in an insertion of positive reactivity which, depending on the initial reactor condition, cause an increase in nuclear power or a return to power. In both cases, negative reactivity is subsequently inserted through the Doppler feedback integrated over the fuel temperature rise, which is lower for fuels having high thermal conductivity. For these events, the performance of U_3Si_2 and UN are expected to be worse than for UO_2 for three reasons:
    1. an expected smaller Doppler integrated feedback,
    2. the more negative MTC, and
    3. the lower initial stored energy in the fuel for events starting at power.

    These events are analyzed using a minimum fuel temperature to reduce the fuel stored energy (and consequently the heat transferred to the coolant) and thus maximize the RCS cool down and resultant positive reactivity insertion.

    For events starting at power, the temperature of U_3Si_2 and UN will be lower due to higher thermal conductivity, resulting in less heat transferred to the RCS and a more severe overcooling of the RCS. Combined with the more negative MTC and smaller Doppler integrated feedback for U_3Si_2 and UN, these fuels will be penalized compared to UO_2, because of a larger cool down reactivity insertion and lower Doppler-induced power reduction. For events starting at zero power, the performance of U_3Si_2 and UN is expected to improve slightly, since the penalty associated with the lower stored energy is not applicable. However, performance is expected to still be worse than UO_2, since the more negative MTC and the lower integrated Doppler feedback still apply.

B. For RCS overheating events, the RCS overheats due to a reduction in primary coolant flow or a reduction in heat removal capability by the secondary side. Depending on the specific event transient, the safety acceptance criteria are related to RCS expansion through heating of the coolant, DNB, and peak cladding temperature. The performance of U_3Si_2 and UN compared to UO_2 depends primarily on a tradeoff between three aspects:
    1. the lower initial fuel stored energy of U_3Si_2 and UN,
    2. the more negative MTC of U_3Si_2 and UN, and
    3. the higher thermal conductivity of U_3Si_2 and UN.

    The first two aspects help satisfy the safety criteria used for RCS overheating events, while the higher thermal conductivity is detrimental since it results in a faster heat transfer to the coolant (and therefore a faster RCS expansion) and in a smaller Doppler feedback due to the smaller fuel temperature rise. For rapid event transients such as RCP shaft seizure or complete loss of forced reactor coolant flow, these three aspects are equivalent and it is not possible to estimate whether U_3Si_2 or UN will perform better or worse than UO_2. For slower event transients such as the loss of normal feedwater flow, the lower stored energy in U_3Si_2 and UN will dominate compared to faster heat transfer to the RCS and the performance of U_3Si_2 and UN are expected to be better than UO_2.

C. For reactivity insertion events, the integrated Doppler feedback functions to terminate the event by inserting negative reactivity. For these events, U_3Si_2 and UN are penalized compared to UO_2 due to their slightly less negative Doppler temperature coefficient and their much higher thermal conductivity. These fuel properties result in lower fuel temperature increase due to the initial reactivity insertion and therefore less negative Doppler integrated effect to terminate the event. Because the melting temperature of U_3Si_2 is more than 1000°C lower than UO_2 and UN, fuel pellet centerline melting could be a problem for U_3Si_2 during reactivity insertion events. Additionally, for events such as rod ejection accidents, the mechanical behavior of the proposed fuel rod and fuel materials will need to be experimentally verified to determine the impact on fuel assembly coolability.

D. In the analysis of an RCCA drop event, a power overshoot is postulated to occur as a consequence of the reactor control system trying to rebalance core power. The nuclear power evolution in the fuel assemblies subjected to this overshoot depends on the Doppler feedback, as well as on rod shadowing factors that must be considered due to the dropped rod interfering with the ability of the detectors to correctly measure the power response as the control system pulls some rods out. For U_3Si_2 and UN, they begin the transient at a lower temperature and their integrated Doppler feedback will be lower due to their higher thermal conductivity. Due to these two properties and the uncertainty in power redistribution during this transient, it is not possible to estimate whether U_3Si_2 or UN will perform better or worse than UO_2.

E. Because the neutron spectrum of U_3Si_2 and UN is likely to be harder, the B worth is expected to be lower compared to UO_2. Additionally for U_3Si_2 and UN, the degree of B dilution resulting from injecting the same amount of CVCS coolant into the RCS should also be lower due to the higher B concentration needed to compensate for the lower B worth. However, the difference in B worth is generally small and the overall performance of U_3Si_2 and UN compared to UO_2 for B dilution events is expected to be the same.

F. For RCS inventory increase events, fuel has little impact on the event progressions.

G. Large break (LB) LOCA considerations for the proposed cladding and fuel materials are presented below.
    - SiC cladding: Compared to currently used Zr base alloy cladding, SiC cladding exhibits far superior high temperature steam oxidation resistance with minimal generation of H_2 from the oxidation reaction. This property alone should allow SiC cladding to exhibit superior performance compared to Zr cladding during LB LOCA conditions. However, the high stiffness and low fracture toughness of SiC could also reduce this material's durability during LB LOCA conditions. Further investigation is required to more accurately determine the relative behavior of SiC cladding compared to Zr cladding during LOCA conditions.
    - Coated Zr cladding: A coating applied to the outer diameter of currently used Zr alloy cladding tubes should offer significant improvement of cladding corrosion resistance during LOCA events. However experimental data is needed to better quantify the corrosion behavior of a coated cladding as well as the adhesion of the protective layer during LOCA events.
    - U_3Si_2 and UN: The maximum cladding temperature reached during the blowdown phase of a LB LOCA is likely to be lower with U_3Si_2 and UN with respect to UO_2. This is because during this initial phase of the LB LOCA transient, a very rapid and almost adiabatic heat redistribution inside the fuel rod occurs, which results in cladding overheating proportional to the energy stored in the fuel during normal operation, which is lower for U_3Si_2 and UN due to their higher thermal conductivity. However, for U_3Si_2 potentially higher fuel swelling could require a large pellet-cladding gap resulting in an increase in fuel stored energy. The margin in blowdown cladding temperature from the UO_2 case could therefore be lower for U_3Si_2 than for UN.

H. In a steam generator tube rupture event, radioactive primary coolant enters the secondary side resulting in contamination. Although U_3Si_2 and UN are expected to be operated up to a higher burnup than UO_2, thus resulting in larger gaseous fission product inventory inside the assemblies, the nominal level of contamination of the primary coolant is not expected to differ significantly.

I. An event involving the opening of a pressurizer valve is typically non-limiting for DNBR, i.e. it does not result in DNBR values close to the limit imposed on this parameter, and would be expected to be non-limiting for whatever fuel integrity criterion replaces DNBR, if any. Also, the time to pressurizer overfill, which needs to be long enough to allow sufficient steam condensation by the pressurizer spray system and therefore to limit RCS pressure, in this event has a weak dependence on the fuel characteristics, and would not be expected to change significantly upon transition to the new fuels.

J. For a fuel handling accident, the amount and type of gaseous radionuclides released determine the dose-related consequences of such an event. Even if the type of radionuclides generated and released are the same, U_3Si_2 and UN are expected to be discharged at higher burnup compared to the current UO_2/Zr fuel system. Thus for a given fuel assembly geometry, the amount of gaseous radionuclides contained in the assembly and potentially released during this event should be greater.

K. ATWS could be any event in the table, however analyzed assuming no reactor scram. ATWS events are generally analyzed near beginning of cycle (BOC) conditions since the most limiting conditions occur with the least negative MTC. Preliminary assessment of the effect of advanced cladding and fuel materials on reactivity coefficients indicate the MTC will be more negative than the value for UO_2/Zr fuel system, which is therefore expected to benefit the safety performance of the advanced materials for ATWS events. Also, due to the higher temperature capabilities and significantly reduced steam oxidation kinetics of SiC and coated Zr cladding, the proposed cladding should perform much better than the current UO_2/Zr fuel system during a station blackout event. However the timing of various events during a BDBA will be important and could dictate the performance improvement of the proposed cladding and fuel during such a transient.

subtask 1.4.5: Shipping, Handling, Storage, and Operation Analysis of an Advanced Fuel Design

SiC has a density of 3.21 g/cm^3 which is 51% lower than currently used Zr-base alloys. Due to the significantly lower density of SiC shipping requirements for an assembly of ATF will be different than current requirements. The high density fuels U_3Si_2 or $U^{15}N$ are 11% and 30% more dense than UO_2, so the impact of fuel weight gain on shipping should also be evaluated. For example the shipping container would require redesign to carry an assembly of SiC cladding containing high density fuel pellets. Additionally, the NRC will require testing of a newly designed shipping container to evaluate the response during transportation. Since the mass of an ATF assembly will be different from current Zr/UO_2 fuel assemblies, the plenum spring inside the fuel stack would also require redesign to ensure no loads greater than 4 times the acceleration due to gravity (4g) are placed on the fuel assembly during transport. The fuel loading and shipping should also be evaluated for the coated Zr cladding because the coating material will alter the properties of the cladding and its surface.

The transportation and storage of spent ATF assemblies presents a unique challenge to both commercial utilities and the NRC. Nuclear utilities require reasonable expectations that spent ATF assemblies can be disposed of using spent fuel pools, dry storage casks, and at a permanent site if designated in the future. The NRC currently does not have any documentation in place to support the handling and disposal of ATF assemblies. This will need to be addressed in the future. It is highly probable that changes in the regulatory acceptance criteria for transportation and storage of ATF assemblies in spent fuel pools or permanent sites will be required. The decision should be made with adequate fuel performance and irradiation data before and after discharge for the SiC cladding and high density fuel. Specifically, the acceptance criteria for disposal will require chemical, mechanical, and nuclear properties of fresh and spent ATF.

It is anticipated that the operational margins and limits will be different for ATF compared to the Zr/UO_2 fuel system due to the changes in materials properties such as thermal conductivity, strength, fissile material density, and response to irradiation. It is proposed that the following preliminary operational analysis be performed for ATF during the feasibility assessment stage:

- The startup ramp rate limits and maximum linear heating rate limits at normal conditions. The startup ramp rate limits are intended to mitigate the effects of fuel/clad mechanical interaction (PCMI). The PCMI and PCI are related to fuel properties and irradiation performance, and thus the PCI and PCMI risk assessment should be performed for ATF.
- Effect of local power changes on fuel integrity and safety.
  It is known that sudden axial power changes increase the risk of a fuel failure related to PCI. In order to limit local power changes, limits on axial flux difference (AFD) and axial shape index (ASI) may need to be evaluated for ATF.
- Effect of crud deposition on the fuel corrosion and operation.
  It is known that crud deposition adversely effects fuel operation. Some of the known effects are crud induced power shift (CIPS) and crud-induced localized corrosion (CILC). For the coated Zr cladding and SiC cladding, crud formation and deposition may be different from the current Zr base alloy cladding and are worthy of attention in this study.

subtask 1.4.6: Potential for Higher Burnup and Power Upgrades of an Advanced Fuel Design
The potential to increase the current regulated burnup limit of 62 GWd/MTU for the Zr/UO_2 fuel system by application of a new cladding material such as SiC in combination with a higher density fuel is a significant opportunity for the commercial nuclear power industry. SiC is known to be more resistant to irradiation and corrosion than Zr and therefore could be used in commercial PWR's to higher burnups. With application of high density fuel, such as U_3Si_2 or U_3Si_2 – UN, containing greater ^{235}U content, exceeding the current burnup limit is possible. Additionally, due to the higher ^{235}U content of high density fuels, it is offered that burnup could now be quantified in MWd/assembly or MWd/rod. For the current Zr/UO_2 fuel system, the maximum burnup in this unit is approximately 36000 MWd/assembly or 124 MWd/rod. To operate SiC cladding with high density fuel to higher burnups, experimentally determined irradiation data will be required to obtain regulatory approval. The irradiation performance data should include fission gas release, rod internal pressure, characteristics of the pellet structure and rim region, pellet volumetric swelling, fuel thermal conductivity degradation, and pellet cladding interaction (PCI) all at the desired burnup. Additionally, cladding mechanical properties at the desired burnup should be experimentally determined. This data should be sufficient to prove that all fuel storage and safety requirements are satisfied. For power upgrades, similar irradiation data is required and could be obtained from research reactor tests.

Task 1.5: Describe Fabrication Methods, Materials/Process Providers, and the Supply Chain Impact on Current Nuclear Fuel Supply

subtask 1.5.1: Advanced Fuel Fabrication Methods
For the currently used UO_2 fuel/Zr alloy cladding system, both the fuel and cladding fabrication methods are very mature, having been used and refined over 30 years. A large change to this LWR fuel manufacturing process could present a significant challenge in the development and insertion of accident-tolerant fuel. The methods used to fabricate new advanced fuel, SiC/SiC CMC cladding, and coated Zr alloy cladding will be discussed for each fuel and cladding material or material system including relevant contrast to the currently used fabrication methods.

U_3Si_2 Advanced Fuel:
The fabrication method for any LWR fuel requires a feed stock of ^{235}U containing material, a method of converting this enriched feed stock into processable enriched material (enriched UO_2 powder as example), and lastly a process for forming a high density, solid cylindrical enriched fuel pellet.

Enriched Uranium Hexafloride (UF_6, l) is the commercially accepted feed stock material used in fissile nuclear fuel fabrication. The technical, safety, transportation, and regulatory infrastructure for commercial use of UF_6 is well established. Therefore for these and other reasons, UF_6 (l) should be used as feed stock for fabrication of U_3Si_2 and U_3Si_2 – UN advanced fuels. One currently used method to synthesize UO_2 powder from UF_6 is a 3 step process involving hydrolysis of UF_6 to UO_2F_2 (Uranyl Fluoride), precipitation of $(NH_4)_2U_2O_7$ (Ammonium Uranium Oxide) from UO_2F_2 using NH_4OH (Ammonium Hydroxide), and then calcination of $(NH_4)_2U_2O_7$ into UO_2. It is presently not clear what specific chemical synthesis route should be used to produce enriched U_3Si_2 powder. However, enriched UF_6 should be used as feed stock material. The chemical synthesis of enriched U_3Si_2 powder from UF_6 is a process that requires laboratory and pilot scale research to progress the use of U_3Si_2 as an advanced fuel.

Once U_3Si_2 powder has been synthesized, conventional powder processing methods such as grinding, milling, sizing, mixing, and blending can be used to produce a powder particle morphology and size distribution tailored for compaction. These powder processing methods are similar to currently used methods for UO_2 and are technically mature. However the specific details of processing U_3Si_2 into a compressible powder would need to be experimentally determined. Additionally, during powder processing any additives for assisting the compaction process can be blended into the powder.

The U_3Si_2 powder of desired morphology and size distribution would then be consolidated into a high density pellet using conventional closed die compaction and sintering processes. Powder compaction should be performed with currently used multi-station rotary compaction presses. These presses are capable of producing large numbers of green pellets in short periods of time (~300/min.) and represent a mature compaction technology. Sintering should be performed with currently used multi-zone, controlled atmosphere belt furnaces. Removal of additives should be performed in a separate zone to avoid contamination during subsequent sintering. Sintering would then be performed in the desired controlled atmosphere to achieve the required sinter density, prevent alternate phase formation, and minimize interstitial (C, O_2, H_2, etc.) contamination. While the press and sinter processing of ceramic powders represents a mature technology, the specific details of compaction and sintering of U_3Si_2 powder would need to be experimentally determined.

Lastly, for development, debugging, and application of press and sinter processing of U_3Si_2 powder, computer models of the compaction and sintering processes should be developed. Because press and sinter processing of fuel pellets is such a highly repetitive and quality sensitive fabrication method, accurate process computer models would greatly benefit the debugging of process problems and development or refinement of the process. Some compaction and sintering models do exist; however models more specific to ceramic fuel processing and U_3Si_2 powder would need to be developed.

U_3Si_2 – UN Advanced Fuel:
Like U_3Si_2 fuel fabrication, U_3Si_2 – UN fuel fabrication should use enriched UF_6 as feed stock material for the synthesis of UN powder. Also as with U_3Si_2, no mature, large scale process for the synthesis of UN powder from enriched UF_6 feed stock presently exists. Several concepts for synthesis of UN have been experimentally investigated as follows:

- direct nitriding of U metal,
- nitridation by arc melting of U metal in N_2 (g),
- hydriding pure U metal prior to nitriding, and
- carbothermic reduction of UO_2 prior to nitridation. (42)

From the above mentioned experimental methods, only carbothermic reduction of UO_2 powder prior to nitridation would directly use UF_6 as feed stock for the synthesis of UO_2. Clearly, significant research and development is required before choosing a method for large volume synthesis of UN powder.

Additionally, it has been shown that enrichment of the ^{15}N isotope in UN is required for UN to economically function as a LWR fuel. (43) Presently, a commercial method for ^{15}N enrichment for use in synthesizing $U^{15}N$ does not exist. Westinghouse has surveyed potential methods for ^{15}N isotope enrichment and the laser isotope separation method appears to hold promise. (44) However, only limited experimental work on ^{15}N enrichment towards the fabrication of a fissile $U^{15}N$ LWR fuel has occurred. As with a method for large volume synthesis of UN powder, creating a large volume method for enriching ^{15}N will require significant research and development.

Assuming that large volumes of UN powder enriched in the ^{15}N isotope can be synthesized, the processing of $U_3Si_2 – U^{15}N$ powder into high density enriched fuel pellets is very similar to the processing for U_3Si_2. Powder processing to produce a $U_3Si_2 – U^{15}N$ powder tailored for compaction including blending of the desired amount of U_3Si_2 powder, compaction of $U_3Si_2 – U^{15}N$ powder into green pellets using closed die compaction methods, and thermal additive removal and sintering into high density pellets can all be accomplished using technically mature processing methods. As with U_3Si_2, the specific processing would need to be experimentally determined. Specific to fabricating a $U_3Si_2 – U^{15}N$ pellet, compaction and sintering of this mixture of 2 different powders would need to be experimentally determined.

Lastly, as with the development of a U_3Si_2 fuel pellet, computer models of the compaction and sintering processes used to fabricate a $U_3Si_2 – U^{15}N$ fuel pellet should be developed. Models such as these would prove very beneficial in the long term fabrication and quality control of manufacturing an advanced nuclear fuel pellet.

SiC/SiC CMC Cladding:
Ceramic matrix composite fabrication methods represent a reasonably mature technology. However, the fabrication of SiC/SiC CMC's in approximate 14 ft. long, thin walled tube length has not been performed. Therefore, in general, large volume fabrication of SiC/SiC CMC fuel tubes is feasible but specific details of different steps in assembling a composite thin wall tube require investigation. The methods to fabricate a SiC/SiC CMC thin wall fuel tube will be discussed relative to the different features of the fuel tube, specifically the inner hermetic seal tube, the overlying SiC fiber winding, C interface layer deposition, and SiC CVD/CVI densification of the composite. This discussion assumes the desired CMC architecture has been decided upon. Additionally, Westinghouse has had 3 ft. SiC/SiC CMC experimental fuel tubes fabricated and the results of this effort will be offered in the following discussion.

The inner wall of a SiC/SiC CMC fuel tube adjacent to fuel pellets must be dimensionally accurate and hermetic. Two fabrication methods to create a gas tight inner tube of SiC are chemical vapor deposition of a tube of desired thickness on a friable mandrel and extrusion of a plastic, binder containing SiC mass and subsequent sintering into a thin walled tube. CVD fabrication of a thin wall SiC tube would require equipment capable of producing approximate 14 ft. long tubes and a CVD reactor capable of accurately controlling deposit chemistry, thickness, and roughness. The mandrel the SiC is deposited on must be removable by thermal or chemical

means, and could be used as support for subsequent fiber winding and CVD/CVI of the CMC fuel tube and removed later. Extrusion of plasticized SiC requires the ability to form a dimensionally accurate thin wall tube of approximate 14 ft. length and subsequent decanting and sintering to near theoretical density. Westinghouse has had 3 ft. long thin wall SiC tubes experimentally fabricated by the plastic SiC extrusion method as shown in Figure 1.5.1. These tubes had measured wall thickness of approximately 0.35 in. and ID-to-OD concentricity of 0.07. While encouraging, further development is required to fabricate 14 ft. long thin wall tubes by the plastic SiC extrusion method. For both CVD and plastic extrusion methods, the processing parameters required to fabricate the desired thin wall, 14 ft. long SiC tube requires experimental determination.

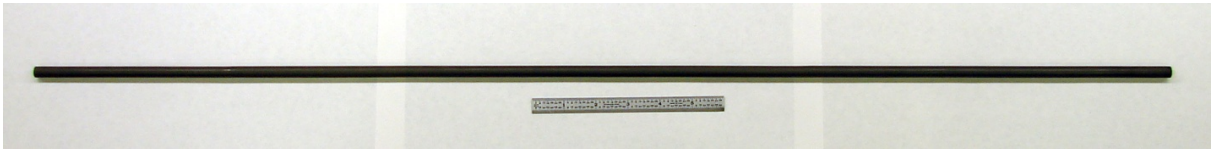

Figure 1.5.1. 3 ft. long thin wall SiC tube fabricated by extrusion of plasticized SiC.

SiC fiber winding to the desired composite architecture can be performed using conventional composite fiber braiding methods as currently used for carbon fiber composites. SiC fiber would be braided in the desired architecture on top of the hermetic, inner thin wall SiC tube. The thin wall tube could be supported during braiding using the deposition mandrel used in the CVD deposition method or a metallic structural mandrel inserted into the extruded thin wall tube. Westinghouse has had 3 ft. long SiC CMC tubes experimentally braided as shown in Figure 1.5.2. Braiding of these tubes was performed on top of a mandrel inserted into an extruded thin wall tube. While these results are encouraging, further development is required to fabricate 13 ft. long braided SiC tubes and determining specific fiber braiding processing details requires experimental work.

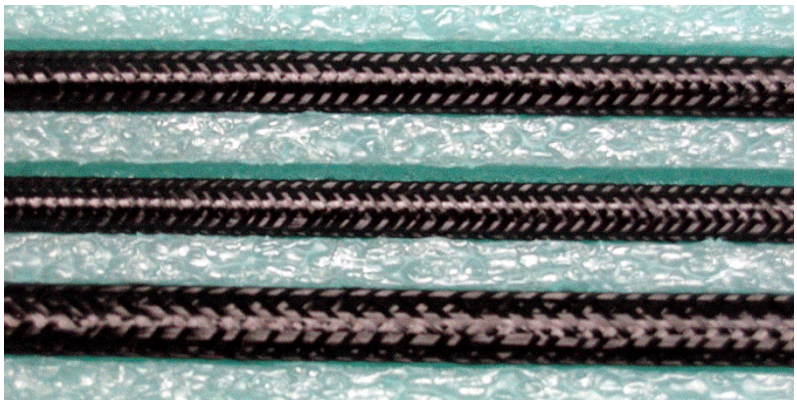

Figure 1.5.2. 3 ft. long tube samples of braided SiC fiber on top of an extruded thin wall SiC tube.

Deposition of a C interface layer on top of the braided SiC fiber can be performed using conventional vapor deposition techniques. This process could be performed in a CVD chamber prior to SiC CVD/CVI for process efficiency. During Westinghouse's fabrication of 3 ft. long SiC/SiC CMC experimental tubes, the C interface layer was deposited to an average thickness of 15 μm Again, specific processing details of C interface layer deposition requires experimental determination.

Lastly, densification of a SiC/SiC CMC by CVI of SiC into the braiding and subsequent CVD of SiC on top of the composite should be performed using technically mature chemical vapor methods. This process for SiC CVD/CVI densification requires a CVD reactor capable of accurately controlling deposit chemistry, thickness, and outer surface roughness. A significant challenge in CVD/CVI densification is attaining a structurally significant high density, approximately 95% or greater. Various efforts have been attempted to attain high densities in SiC/SiC CMC's with limited results. (45) The Westinghouse effort to fabricate 3 ft. long SiC/SiC CMC experimental tubes resulted in densities between 70.8 to 89.5% as shown in Figure 1.5.3. Attaining higher densities in SiC/SiC CMC fuel tubes will be a significant challenge. Again, processing details of CVD/CVI SiC densification will require experimental determination.

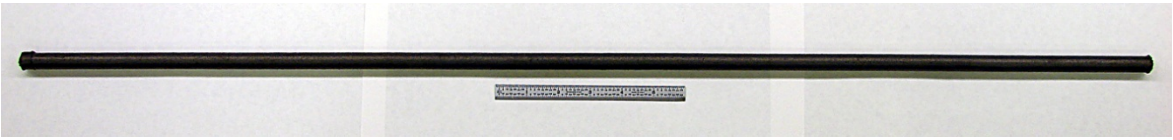

Figure 1.5.3. 3 ft. long SiC/SiC CMC experimental tube.

Coated Zr Alloy Cladding:
Applying a coating to the full length of an approximate 14 ft. long fuel has not been attempted before. Many processing and technical challenges exist in attempting to coat a full length fuel tube including what type of coating to apply, what method to apply the coating, how to process a full length fuel tube, and what is the irradiation response of substrate/coating in LWR conditions. Here critical aspects of fabricating a coated full length fuel tube will be discussed.

The substrate for all coating application should be the typical Zr alloy cladding tube as presented in subtask 1.2.2. (8,9) In using currently accepted and applied materials as a substrate, only the coating and any effect on the substrate during coating application need be considered in developing, experimentally verifying, and licensing a substrate/coating system. This could make the effort in implementing a coated fuel cladding for LWR application easier.

Surface preparation in any overlay coating process is critical for coating adhesion and subsequent coating performance. Substrate preparation for coating depends entirely on the coating method applied. For example, coating/substrate bonding in processes like cold spray or plasma spray is primarily or entirely mechanical. Here the substrate must be roughened usually using grit blasting. Careful consideration must be made as to how a fuel tube substrate is roughened, how rough the fuel tube substrate is to be made, and any effects the roughening process will have on the fuel tubes subsequent performance. Cleanliness of the substrate is also critical for coating adhesion and subsequent performance, and also depends on the coating method. For example, physical vapor deposition (PVD) methods require a clean substrate for coating application in an ultra-high vacuum and could require energetic particle sputter cleaning. For the plasma spray coating process, the substrate is cleaned with a general solvent like methyl alcohol before coating application. Specific details of Zr alloy tube substrate pre-coating preparation and cleaning will require experimental determination after the coating and coating deposition method are chosen.

The method of coating application used to coat fuel cladding for LWR application is equally important as the material coated. Presently several different coating application processes are being investigated; however, a specific coating process has not been chosen. Three candidate processes, plasma spray, cold spray, and PVD, are presently under investigation for coating application onto a Zr alloy tube substrate. Plasma spray involves passing powder of the desired coating through a small plasma to partially liquefy the powder particles and then propel them onto the substrate. Cold spray accelerates coating powder particles to near the speed of sound

and propels them onto the substrate. Here the powder particles deform and mechanically bond to the substrate in the solid state. Lastly, the PVD process involves generating a vapor cloud of the coating material and depositing it onto the substrate line of site. The entire PVD process is performed in a vacuum chamber at a partial pressure. Each coating process has advantages and disadvantages, and experimental trials are required to determine which process to select for coating deposition onto a Zr alloy fuel tube. Once a coating and coating process have been selected, coating processing parameters would be experimentally determined.

For application of a coating onto a 14 ft. long Zr alloy fuel tube, the ability to coat the entire fuel tube, the uniformity of the coating thickness and structure/properties along the tube length, and the effect the coating process has on the fuel tube are critical aspects determining the success of coating application. To coat a 14 ft. long substrate, the coating process must be extremely stable and controllable including motion of substrate or coating source and flow of coating powder onto the substrate. The applied coating must be uniform in deposit thickness and structure and properties along the entire 14 ft. length. Additionally, the coating process must have minimal effect on the Zr alloy fuel tube substrate. Specifically, Zr alloy cladding is sensitive to temperature and a maximum temperature attained during the coating process (400^{o}C for example) must not be exceeded.

subtask 1.5.2: Advanced Fuel Materials and Process Providers
Fabrication of a new advanced LWR fuel requires adequate availability of fuel and cladding materials, and fabrication process providers as needed. The availability of these materials and processes are discussed here.

Fuel materials and processes:
To fabricate U_3Si_2 or $U_3Si_2 – U^{15}N$ fuel, feed stock material enriched in ^{235}U and ^{15}N are required. The presently available source of enriched ^{235}U is UF_6, which is the feed stock for all current UO_2 LWR fuel fabrication. If large volume processes for the synthesis of U_3Si_2 or $U^{15}N$ powder from enriched UF_6 feed stock material can be developed, then the required materials for these advanced LWR fuel are currently available. However, if a ^{235}U feed stock other than UF_6 is required, than a source for this feed stock will need to be developed. Presently there is no large volume source of ^{15}N available, so a ^{15}N feed stock source will require development.

Presently all fabrication of enriched LWR fuel pellets occurs at different LWR fuel vendor sites. Due to the regulatory, licensing, safety, and security requirements involved in nuclear fuel fabrication, all processing of UF_6 into UO_2 is performed internally by fuel vendors. It is a reasonable assumption that future advanced fuel fabrication will also be captively performed by fuel vendors due to various requirements. Therefore no process providers will be required for fabrication of new advanced fuels. Adequate enriched fuel processing capabilities presently exist at all domestic fuel vendors.

SiC/SiC CMC Cladding Materials and Processing:
The SiC/SiC CMC fuel cladding design discussed in subtask 1.2.2 is composed of a sintered SiC thin wall inner tube, stoichiometric SiC fibers, and a CVD/CVI SiC composite matrix. The availability of these materials and processes to fabricate the CMC fuel tube are discussed here.

Sintered SiC in a variety of purity, density, and forms is presently available from several for-profit, domestic companies. For application to a SiC/SiC CMC fuel tube, a thin wall tube 14 ft. in length is required. Westinghouse worked with a domestic company to fabricate 3 ft. long thin wall sintered SiC tubes for use in fabricating experimental SiC/SiC CMC fuel tubes as shown in figure 1.5.1. Therefore it can be generally stated that the materials and processes currently exist to fabricate this component of a SiC/SiC CMC fuel tube assuming this component is purchased from a supplier. However, for large volume manufacturing of LWR SiC/SiC CMC fuel tubes, the

capacity to produce the required number and length of thin wall SiC tubes would need to be developed.

Presently the SiC fiber used for nuclear grade SiC/SiC CMC fuel tubes is stoichiometric, β-SiC fiber of very low O_2 content. The desired commercial fiber trade name Hi-NICALON™ type S, is exclusively fabricated by in Japan, and distributed in the United States by a domestic company. Therefore, no domestic supply of SiC fiber for fabricating nuclear grade SiC/SiC CMC fuel tubes currently exists. For large volume manufacture of SiC/SiC CMC fuel tubes to supply domestic nuclear fuel, a United States based source of nuclear grade SiC fiber should be developed. The braiding process used for SiC fiber composites is exactly the same as required for C fiber composites and significant volume for braided C fiber polymer matrix composites has been recently developed domestically. Therefore, processing capabilities of SiC fibers for SiC/SiC CMC fabrication already exists domestically but additional capacity should be developed for large volume SiC/SiC CMC fuel tube manufacture.

The final process for fabricating SiC/SiC CMC fuel tubes is SiC CVD/CVI of the composite matrix. Presently this is performed in batch process vapor deposition reactors. Processing capability for CVD/CVI of SiC currently exists domestically from several for-profit companies. However, the largest CVD reactor available domestically is 4 ft. in length. Therefore, processing capabilities for CVD/CVI of SiC already exists domestically but additional supplier capacity to 14 ft. lengths should be developed for large volume SiC/SiC CMC fuel tube manufacturing. Additionally for higher throughput and greater processing reproducibility, a continuous CVD/CVI process would be desirable and should be investigated further.

Coated Zr Alloy Cladding Materials and Processing:
Fabricating a coated Zr alloy fuel tube will require adequate supplies of coating material or powder of the material to be coated, and processing capabilities to apply a coating to a 14 ft. long Zr alloy fuel tube. The availability of these materials and processes for coated Zr alloy fuel tube fabrication are discussed here.

Coating of a Zr alloy fuel tube could occur by spray application of powder materials or PVD deposition of material from a solid sputter target. For both types of processes it is assumed that the starting material will be powder of the desired coating composition. For PVD deposition, the coating sputter target would be fabricated by consolidating powder into a solid target using a process like hot pressing. For spray deposition, powder of the desired composition, particle morphology, and size distribution for the chosen coating process would be required. Westinghouse would purchase this powder or consolidated sputter targets and sources of large volumes of powder for coating deposition or sputter target fabrication would have to be developed.

The coating deposition process chosen would largely determine the available coating capacity for application to large numbers of 14 ft. long tubes. For PVD coating methods, either a chamber capable of holding 14 ft. long tubes or a vacuum feed through mechanism capable of continuously feeding a tube into a chamber for coating would need to be developed. For spray deposition coating methods, commercially available coating equipment is available. An environmentally controlled cubicle capable of holding 14 ft. long tubes and methods for manipulating the spray device or tube would both need to be developed. However, both of these developments are feasible. At this time, it is not clear if Westinghouse would perform fuel tube coating internally or contract coating to a supplier.

subtask 1.5.3: An Advanced Fuel Supply Chain
Presently, the supply of commercial nuclear fuel is a mature, somewhat captive process. Fuel feed stock is enriched UF_6 supplied by a single blended commercial/federal source. Processing

of UF_6 into UO_2 pellets is performed captively by different fuel vendors, such as Westinghouse. Zr alloy fuel tube fabrication is either a captive process or purchased from specific Zr alloy tube fabricators. For example, for PWR fuel tubes Westinghouse performs all aspects of fuel tube fabrication including Zr synthesis, alloy melting and refinement, and tube pilgering. Fuel tubes of other Zr alloys, such as BWR fuel tubes, are purchased from specific domestic and foreign suppliers. Clearly the supply chain for the current UO_2/Zr alloy nuclear fuel system is well established in scale, cost, safety, and quality.

Transitioning to an advanced commercial nuclear fuel other than the current UO_2/Zr alloy nuclear fuel system would require development of an almost entirely new supply chain. Generally, the current UO_2/Zr alloy fuel supply chain can be divided into 2 areas; enriched fuel and cladding tubes. For enriched fuel, if enriched UF_6 can be used as fuel fabrication feed stock, then this supply chain could remain unchanged. However, if the synthesis of U_3Si_2 or U_3Si_2 – $U^{15}N$ could not be performed from enriched UF_6, then an entirely new supply mechanism of enriched feed stock would need to be developed. For $U^{15}N$, a supply of ^{15}N would need to be developed. For advanced fuel cladding supply, there presently exist sources of sintered SiC thin walled tubes, SiC fiber, and CVD/CVI SiC deposition services. These supply sources presently service the aerospace industry, so they would require development to nuclear industry quality, safety, and scale for fuel tube supply. The present source of SiC fiber is exclusively a single Japanese company, so it would be beneficial to develop domestic sources of nuclear quality SiC fiber.

Recently, the aerospace industry has developed significant interest in SiC/SiC CMCs for application in gas turbine engines. Through this interest it is very possible that the supply of materials and processing services required for SiC/SiC CMC fabrication could be further developed. This synergistic development would directly benefit nuclear application of SiC/SiC CMCs, although specific nuclear quality and safety aspects of this supply chain would still require development. For fuel vendors, a choice would exist to either purchase SiC/SiC CMC tube components (sintered SiC thin wall tubes, SiC fiber, and CVD/CVI SiC processing) and assemble the cladding tube in-house or purchase the fully assembled cladding tube from an external vendor.

References

1. ASTM International standard C776-06, “Standard Specification for Sintered Uranium Dioxide Pellets” (2011) pp.1-4.
2. Westinghouse Electric Company, LLC, Nuclear Fuel, Product Specification PDPELE02, rev. 3, 2007.
3. Westinghouse Electric Company, LLC, Nuclear Fuel, Enriched Fuel Pellet drawing PELE100, rev.14, 2012.
4. Okamoto, H., “Si-U Phase Diagram”, Binary Alloy Phase Diagrams, 1990, pp. 3374-3375.
5. Okamoto, H., “N-U (Nitrogen – Uranium)”, J. Phase Equilib., Vol. 18, 1997, p. 107.
6. Snead, LL, et. al., “Handbook of SiC properties for performance modeling”, J. Nuc. Mater., V371 (2007) pp. 329-377.
7. ASTM International standard E112-10, “Standard Test Methods for Determining Average Grain Size” (2010) pp.1-26.
8. Westinghouse Electric Company, LLC, Nuclear Fuel, Material Specification MATBZL00, rev. 19, 2007.
9. Westinghouse Electric Company, LLC, Nuclear Fuel, Fuel Rod Tube drawing TBFR100, rev.70, 2011.
10. ASTM International standard B811-02, “Standard Specification for Wrought Zirconium Alloy Seamless Tubes for Nuclear Reactor Fuel Cladding” (2007) pp.1-16.
11. ASTM International standard G2/G2M-06, “Standard Test Method for Corrosion Testing of Products of Zirconium, Hafnium, and Their Alloys in Water at 680^{o}F [360^{o}C] or in Steam at 750^{o}F [400^{o}C]” (2011) pp.1-8.
13. S. Ray, E. Lahoda and F. Franceschini, Assessment of Different Materials for Meeting the Requirement of Future Fuel Designs, Reactor Fuel Performance Meeting, Paper # A0115, Manchester, UK, Sept. 2-6, 2012.
14. Enhanced Accident Tolerant LWR Fuels National Metrics Workshop, US Department of Energy – Office of Nuclear Energy sponsor, October 10-11, 2012, Germantown, MD.
15. E.J. Lahoda and F. Franceschini, Task Order #5: Advanced Fuels for Future Light Water Reactors, Subtask 2: Advanced Fuel Concepts, US DOE contract RT-TR-11-12, September 15, 2011.
16. Johnson, S.C. *et. al.*, “Severe Accident Modeling of a PWR Core with Different Cladding Materials”, paper 12175, Proceedings of ICAPP’12 (June 2012) pp. 1-9.
17. M. Ouisloumen et al., “PARAGON: The New Westinghouse Assembly Lattice Code”, *ANS Int. Mtg. on Mathematical Methods for Nuclear Applications*, Salt Lake City, Utah, USA (2001).
18. Y. S. Liu et al., “ANC: A Westinghouse Advanced Nodal Computer Code”, *WCAP-10966-A,* Westinghouse Electric Company, September (1986).
19. IAEA-TECDOC-643, Research reactor core conversion guidebook – Volume 4: Fuels (Appendices I-K).
20. Carpenter, D.M., An assessment of Silicon Carbide as a cladding material for Light Water Reactors. PhD thesis. Massachusetts Institute of Technology. October 2010.
21. Wongsawaeng, D., Olander, D., 2007. Liquid-metal bond for LWR fuel rods. Nuclear Technology, Vol. 159.
22. Wongsawaeng, D., Olander, D., 2004. Effect of replacing helium with a liquid metal in the fuel cladding gap on fission gas release. Nuclear Technology, Vol. 146, 211-220.
23. Wright, R.F., Tulenko, J.S., Schoessow, G.J., 1996. Thermal bonding of Light Water Reactor fuel using non alkaline liquid-metal alloy. Nuclear Technology, Vol. 115, 281-292.
24. Finlay, M.R., Hofman, G.L., Snelgrove, J.L., Irradiation behavior of uranium silicide compounds. Journal of Nuclear Materials 325 (2004) 118-128.
25. CN-WA09-9. Watts Bar Unit 1 Cycle 9 T/H Design Initialization.
26. CN-WA10-026. T/H RSAC Confirmation for Watts Bar Unit 1 Cycle 10.

27. Thermal-Hydraulic Design Procedure Manual, Revision 30.
28. WCAP-8054-P-A. Application of the THINC-IV Program to PWR Design.
29. Garkisch, H.D., Petrovic, B., Reference Data and Constraints for Uranium-Zirconium-Hydride and Uranium-Thorium Hydride Fuels for Light Water Reactors. Westinghouse Electric Company LLC, Rev.6, March 9, 2003.
30. Heinisch, H.L., et al., Displacement damage in silicon carbide irradiated in fission reactors. Journal of Nuclear Materials, 327 (2004) 175-181.
31. Carpenter, D.M., Assessment of innovative fuel designs for high performance Light Water Reactors. B.S. and M.S. thesis. Massachusetts Institute of Technology, 2006.
32. Youngblood, G.E., presented at the 6th IEA SiC/SiC workshop. Boston, June 10-11, 2004.
33. WCAP-12488-A, Westinghouse Fuel Criteria Evaluation Process. October 1994.
34. Carpenter, D.M., An assessment of Silicon Carbide as a cladding material for Light Water Reactors. PhD thesis. Massachusetts Institute of Technology. October 2010.
35. Youngblood, G.E., presented at the 6th IEA SiC/SiC workshop. Boston, June 10-11, 2004.
36. Carpenter, D.M., Assessment of innovative fuel designs for high performance Light Water Reactors. B.S. and M.S. thesis. Massachusetts Institute of Technology, 2006.
37. Heinisch, H.L., et al., Displacement damage in silicon carbide irradiated in fission reactors. Journal of Nuclear Materials, 327 (2004) 175-181.
38. Snead, L.L., et al., Handbook of SiC properties for fuel performance modeling. Journal of Nuclear Materials, 371 (2007) 329-377.
39. Cheng, T., et al., Oxidation of fuel cladding candidate materials in steam environments at high temperature and pressure. Journal of Nuclear Materials 427 (2012) 396-400.
40. Terrani, K.A., et al., High temperature oxidation of silicon carbide and advanced iron-based alloys in steam-hydrogen environments. TopFuel 2012. Manchester, United Kingdom, 2012.
41. Cheng, B., Fuel behavior in severe accidents and Mo-alloy based cladding designs to improve accident tolerance. Top Fuel 2012. Manchester, United Kingdom, 2012.
42. American Nuclear Society 18.2-1973, “Nuclear Safety Criteria for the Design of Stationary Pressurized Water Reactor Plants”.
43. Butt, D.B., “Synthesis and Optimization of the Sintering of Actinide Nitrides”, Annual Progress Report for award DE-FC07-05ID14650, Boise State University (March 2009) pp.1-92.
44. Franceschini, F. and Lahoda, E.J., “Advanced Fuel Developments to Improve Fuel Cycle Cost in PWR” Proceedings of GLOBAL 2011, Makuhari, Japan, paper 464820 (December 2011), pp.1-8.
45. Xu, P., “Water Corrosion Resistance of UN and Development of ^{15}N isotope Separation Technology”, MFRD-11-153 (October 2011) pp. 1-18.
46. Jaglin, D. *et. al.*, “Microwave Heated Chemical Vapor Infiltration: Densification Mechanism of SiC_f/SiC Composites”, J. Am. Ceram. Soc., vol. 89, n9 (2006) pp. 2710-2717.

Appendix A List of Acronyms

AFD:	axial flux difference
AOO:	anticipated operational occurrences
ASI:	axial shape index
ASTM:	ASTM International, formerly known as the American Society for Testing and Materials
ATWS:	anticipated transient without scram
BDBA:	beyond design basis accident
BOC:	beginning of cycle
BU:	burn up
BWR:	boiling water reactor
CHF:	critical heat flux
CILC:	crud induced localized corrosion
CIPS:	crud induced power shift
CMC:	ceramic matrix composite
CSR:	contractile strain ratio
CVCS:	chemical volume control system
CVD/CVI:	chemical vapor deposition/chemical vapor infiltration
DNB:	deviation from nucleate boiling
DNBR:	deviation from nucleate boiling ratio
EBC:	environmental barrier coating
ECCS:	emergency core cooling system
EFPD:	effective full power day
EOC:	end of cycle
EOL:	end of life
FA:	fuel assembly
FAI:	Fauske & Associates, LLC
FCC:	fuel cycle cost
FdH:	enthalpy rise hot channel factor
Fq:	peak heat flux hot channel factor
FW:	feedwater
Fz:	axial peaking factor
HFP:	hot full power
HM:	heavy metal
H/HM:	Hydrogen to heavy metal ratio
HZP:	hot zero power
ID:	inner diameter
IFBA:	integral fuel burnable absorber
LOCA:	loss of coolant accident
LTR/LTA:	lead test rod/lead test assembly
LWR:	light water reactor
MAAP:	Modular Accident and Analysis Program
MDNBR:	minimum departure from nucleate boiling ratio
MSLB:	main steam line break
MSS:	main steam system
MTC:	moderator temperature coefficient
MWe:	megawatt electric
MWt:	megawatt thermal
NRC:	Nuclear Regulatory Commission
OD:	outer diameter
PCI:	pellet clad interaction

PCMI: pellet clad mechanical interaction
PCT: peak cladding temperature
PRZ: pressurizer
PVD: physical vapor deposition
PWR: pressurized water reactor
RCCA: rod cluster control assembly
RCP: reactor coolant pump
RCS: reactor cooling system
RFA: robust fuel assembly
RIA: reactivity initiated accident
SBO: station blackout event
SG: steam generator
SiC/SiC CMC: Silicon Carbide fiber/Silicon Carbide matrix ceramic matrix composite
SRP: Standard Review Plan
SWU: separate work unit
TH: thermal hydraulic
TMI-2: Three Mile Island Unit 2
UF_6: Uranium Hexafluoride
UN: Uranium Nitride
U_3Si_2: uranium Silicide
10CFR: Part 50 of Title 10 of the Code of Federal Regulation

ZIRLO® is a trademark or registered trademark of Westinghouse Electric Company LLC, its affiliates and/or its subsidiaries in the United States of America and may be registered in other countries throughout the world. All rights reserved. Unauthorized use is strictly prohibited. Other names may be trademarks of their respective owners.

Award Number DE-NE0000566

Development of LWR Fuels with Enhanced Accident Tolerance
Task 2 – Description of Research & Development Required to Qualify the Technical Concept

RT-TR-13-8
May 31, 2013

Westinghouse Electric Company LLC
1000 Cranberry Woods Drive
Cranberry Woods, PA 16066

Principal Investigator: Dr. Edward J. Lahoda
Project Manager: Frank A. Boylan
Author: Peng Xu

Team Members

Westinghouse Electric Company LLC
General Atomics
Idaho National Laboratory
Massachusetts Institute of Technology
Texas A&M University
Los Alamos National Laboratory
Edison Welding Institute
Southern Nuclear Operating Company

Table of Contents

Executive Summary

The program required to develop the technology to qualify and commercialize the Westinghouse Electric Company LLC's Accident Tolerant Fuel (ATF) is outlined in this report. An analysis was performed as part of Task 1 of the ATF program to identify areas critical to the development and potential commercialization of ATF [36]. The analysis performed during Task 1 included discussion of potential NRC requirements for ATF, proposed specifications and architectures of the fuel and cladding, as well as preliminary analysis of the ATF performance and accident tolerant features. This report, Task 2 of the ATF program, outlines the research and development (R&D) work required to implement the ATF fuel and cladding concepts in commercial reactors. The research and development work leading to a lead test rod (LTR) or lead test assembly (LTA) during phases 2 and 3, includes the following areas:

- Bench scale fuel development including UN and U_3Si_2 fuel powder production from UF_6, U_3Si_2 and UN-U_3Si_2 fuel pellet fabrication, and N15 enrichment.
- Bench and pilot scale SiC ceramic matrix composite (CMC) and coated zirconium alloy tube development including 3 ft long and full length tubes with hermetic end plugs.
- Design work needed for integrating burnable absorbers and reactivity controls.
- Long term test reactor rodlet irradiation and post irradiation examination (PIE).
- Other R&D work including code and standard development, quality assurance program development, detailed core design, and operational analysis.

R&D scope and highlights are summarized as follows:

- Bench scale production process development is required for both fuel and cladding prior to test reactor irradiation because the irradiation data will be used to acquire exemptions for LTRs/LTAs under 10CFR50 and for initial testing and future licensing of ATF for region reloads in commercial reactors.
- Numerous potential heavy metal fluorite chemical processing routes are available for conversion of UF_6 to UN, and there is a potential process to convert UF_6 to UF_4 to U_3Si_2 using a modified process defined in a US patent (US 5,901,338).
- A ZrB_2 Integral Fuel Burnable Absorber (IFBA) is most likely to be used in PWR fuel as the coating layer for U_3Si_2 or U_3Si_2-UN fuels. Coating thickness will be larger than for current UO_2 fuel because of the higher heavy metal loading for the new fuels. Coating of the ATF fuels with ZrB_2 must be demonstrated. A combination of ZrB_2 coating and Gd neutron absorbers should be used for BWR fuel because BWR requires higher neutron adsorption abilities than PWR.
- Development of computer models for the ATF is needed in the following areas: fuel rod performance, thermal hydraulics, transient analysis, and reactor physics.
- Laser Isotope Separation (LIS) is concluded to be an economic and technically feasible approach for industrial scale production of N15 isotopes with a minimal environmental impact.

Acknowledgment: This material is based upon work supported by the Department of Energy under Award Number DE-NE0000566.

Disclaimer: This report was prepared as an account of work sponsored by an agency of the United States Government. Neither the United States Government nor any agency thereof, nor any of their employees, makes any warranty, express or implied, or assumes any legal liability or responsibility for the accuracy, completeness, or usefulness of any information, apparatus, product, or process disclosed, or represents that its use would not infringe privately owned

rights. Reference herein to any specific commercial product, process, or service by trade name, trademark, manufacturer, or otherwise does not necessarily constitute or imply its endorsement, recommendation, or favoring by the United States Government or any agency thereof. The views and opinions of authors expressed herein do not necessarily state or reflect those of the United States Government or any agency thereof.

Introduction

During Task 1 of the DOE award DE-NE0000566, the Westinghouse-led ATF team described the Westinghouse team's ATF concept and enumerated areas that required further research and development [36]. This report, performed as Task 2 of this program, describes the R&D needed to fully qualify and commercialize this ATF concept. This includes the development and testing needed in the short term (two years) and long term. The program goal is to have either a LTR or LTA in a commercial reactor by 2022. In this report, the short term tasks in FY14-15 are defined as phase 2 of the ATF program, and the long term tasks in FY16-22 are defined as phase 3 of the ATF program. Rough cost estimates (+50%/-10%) are also provided. It is worth noting that not all necessary activities for a commercial application are included in the report. These activities are mainly vendor specific and will be included in the Phase 3 of the ATF program. More specific activities that are not included in this report are listed below:

- Transient testing (Pellet Cladding Interaction (PCI), Rod Injection Accident (RIA))
- Solubility in water of irradiated fuel
- Seismic testing
- Lead rods in a commercial reactor, and the pertinent PIE program
- Neutronic codes
- Choice of fiber, its desired properties, and the issue of lubrication/slippage vs. pseudo-ductility
- NRC Licensing

Task 2.1. Cladding Bench Scale Development (Phase 2)

The development of ATF cladding will be performed in several length or volume scales to ensure fabrication efficiency and necessary validation of process scale-up to full-size coated Zirc cladding as well as SiC cladding. Bench scale development will be performed to confirm fabrication methods such as SiC fiber winding in CMC fabrication and coating deposition method. Generally bench scale development efforts in ATF cladding samples involve 3 ft in length and tens of 1 ft length. These intermediate length ATF samples would then be used for cladding characterization, cladding property determination, and insertion into test reactor experiments. Here, the specific research and development to be performed for bench scale development of ATF cladding is discussed in detail.

For bench scale ATF cladding development, the following fabrication process research will be performed:

- SiC CMC processing using the chosen CMC fiber architectures including fiber tow winding and chemical vapor deposition/chemical vapor infiltration (CVD/CVI) of SiC.
- Post SiC CMC fabrication processing of cladding tubes such as outer diameter (OD) surface finishing.
- OD coating of Zr alloy cladding tubes.
- Post coating processing of coated tubes such as OD surface finishing.
- Sealing or end plug bonding of coated Zr alloy cladding tubes.
- ATF cladding characterization and property determination.

Subtask 2.1.1. Coated Zr Alloy Tube Processing Bench Scale Development (Phase 2)

Thermal spray coatings are widely deployed across many industrial applications to protect critical components from wear, oxidation, and high temperatures. Perhaps the most dramatic example of thermal spray coatings impact is in gas turbines where a composite metal and ceramic thermal barrier coating allows nickel alloy components to operate with hot gas streams well above their melting temperature. This is made possible by understanding of the materials precursors, thermal spray processing, and failure mechanisms of the deposited coatings.

Coatings made of the MAX phase compounds like Ti_2AlC and Iron based amorphous alloys like Nanosteel® can be applied to cladding surface using the cold spray technology and high velocity oxy-fuel process (HVOF), a thermal spray technology. In order to design the coatings with anticipated performance under normal operation and accident conditions, a deeper understanding of the coating microstructure and failure mechanisms will be necessary. Knowledge on how powder morphology and processing steps affect the morphology of the final coating will be helpful for moving toward a tailored coating design. Another important step is to analyze the microstructural origins of coating failure under different conditions. If the failure mechanisms can be better understood from microstructure analysis, then the coating parameters can be tuned and the coating processes such as surface preparation and post coating finishing can be better designed to ameliorate failure initiators. The final step is to evaluate the irradiation effects on coating integrity and performance.

Bench scale development of coated Zr alloy cladding tubes includes precoating surface preparation and coating application processing. Precoating surface preparation includes any required surface roughening, such as grit blasting, to insure adequate mechanical adhesion of the coating to the Zr alloy tube substrate. Also, the substrate tube must be cleaned of any surface contamination or surface roughening debris prior to coating application. Repeatable surface preparation processes will be developed during bench scale work to ensure consistent coating adhesion to the Zr tube substrate.

Using the chosen coating, coating application process development will be performed during bench scale development. Coating method parameters such as powder feed rate, torch transverse and substrate rotation rates, and other specific coating method parameters will be determined to achieve the desired coating deposition rate, coating thickness, and a uniform coating thickness over the surface area coated. Additionally, the desired coating microstructure and as-deposited coating surface roughness will be developed. Processing methods will be developed that have minimal effect on the Zr tube substrate.

Subtask 2.1.2. SiC CMC Processing Bench Scale Development (Phase 2)

SiC CMC bench scale development will refine the composite fabrication processing methods for subsequent scale up to pilot volumes and lengths. Specific research to be performed includes SiC fiber tow winding for repeatable placement of fiber tows, uniform infiltration/deposition of SiC vapor for high density composite matrix fabrication, and removal of any tube support mandrel from the fabricated CMC tube. SiC fiber winding and CVI/CVD SiC deposition should produce a CMC tube of the desired wall thickness and desired CMC microstructure. Specifically, the CMC microstructure will be characterized by the desired volume, distribution, and morphology of matrix porosity within the CMC wall thickness. Processing to the desired CMC microstructure is critical for development of a thin wall CMC tube exhibiting the required mechanical and thermal properties.

Additionally, depending on the CMC design chosen, a removable or friable mandrel may be used in fabrication of the SiC CMC. This mandrel must be removed and the inner diameter (ID) of the SiC CMC cladding tube must be of the required dimension and tolerance. Fabrication of a

dimensionally accurate CMC cladding tube ID is critical for beginning of life pellet-clad gap determination. Methods to remove this mandrel from the fabricated CMC tube and inspection of the tube ID will be researched during bench scale development.

The bench scale development plan is described more in details in the following five categories of activities with numbered tasks in each.

A. Scale up
- A1. Perform baseline stress analysis with structural /statistical analyses to show that rod design meets service requirements for normal operating loads.
- A2. Demonstrate scalability of cladding for 3 ft to 14 ft while maintaining specifications on fiber architecture and matrix uniformity.
- A3. Demonstrate scalability with respect to meeting specifications on wall thicknesses, fiber volume, porosity, interface layers, and material composition.
- A4. Demonstrate scalability with respect to tolerances on joint material composition, thickness, strength and hermeticity.
- A5. Demonstrate that tolerances on fabricated rod straightness, thickness, and hermeticity are met for intermediate 3-ft length with techniques that scale to 14 ft tubes.
- A6. Refinement of finite element methods (FEM) modeling with fabricated material data to show that rods meet service requirements for normal and abnormal operating loads.

B. New process or hardware development
- B1. Develop cost-effective mandrel removal from long tubes.
- B2. Develop equipment to perform localized joining without the need for putting the entire fuel rod into a furnace for final sealing.
- B3. Develop process for sealing fuel rod with fuel and inert gas with specified gas pressure.
- B4. Demonstrate process for polishing the outer surface to specifications.
- B5. Develop process for meeting internal surface roughness specifications to be compatible with fuel loading processes.
- B6. Develop non-destructive characterization techniques to examine integrity of joint and cladding.

C. Extension to operating and accident conditions
- C1. Experimental and analytical investigation of fatigue, fretting wear, impact, and vibrations performed on 3-ft rod and analysis extending to full-sized rod.
- C2. Perform thermal shock experiment with analysis to full-sized rod for quenching accident.
- C3. Generate data for developing model of pellet-cladding mechanical interactions.
- C4. Generate data for development of model of pellet-cladding chemical interactions.

D. Manufacturing development
- D1. Explore new potential fabrication for large volume, low-cost domestic production of SiC fiber.
- D2. Develop conceptual design and layout for large volume cladding production.
- D3. Generate data for integration of SiC-SiC rod into fuel assemblies and possible SiC-SiC LWR infrastructure components.

E. Quality assurance needed for licensing
- E1. Provide data for development of ANSI and other standards for licensing of fuel.

The strategy for the Phase 2 is to focus on translating what is learned on planar and other more fundamental studies to cylindrical geometries specific to LWR fuel rods (A, B), evaluate and meet necessary tolerances for component performance (C), and address manufacturing and licensing aspects (D,E). Thus, the R&D plan involves continued refinement of cladding processes and models to hone performance characteristics and robustness of the cladding.

The focus for the work will be less on material properties such as 4-point bend tests or material strength, and more on relevant quantifiable cylindrical measurements such as pressure testing, tube flexure, outer and inner surface roughness, Charpy testing on tubes, and fatigue.

An important aspect of the scale-up will examine LWR component characteristics, such as straightness of the rod, hermiticity, and thickness over long length on an intermediate sized tube (task A5). In order to perform some of the work in category B, details such as the internal gas pressure and all internal parts (fuel, plenum details, etc.) will need to be specified in order to move beyond the present schematic of how to make the final endcap seal on the fuel rod. In addition, the internal surface roughness, which will depend on how the fuel is loaded into the rod, must also be specified.

Concerning the extension to characterize cladding in service (C), operating and accident conditions will need to be better defined. These details will also be needed for the FEM modeling that supports the scale-up experimental work (A1, A6).

Subtask 2.1.3. Post ATF Cladding Fabrication Processing (Phase 2)

For both SiC CMC and coated Zr alloy ATF cladding, specific post coating processing will be developed during bench scale work. Cladding OD surface processing to attain the desired OD, OD tolerance, and surface roughness will be developed for both CMC and coated cladding. Additionally, methods to determine dimensions such as OD, ID, OD/ID concentricity, and tube straightness of ATF cladding will be developed.

Methods to seal and/or join the fuel tube end plug to the different ATF claddings will be developed during bench scale development. For SiC CMC cladding, sealing must demonstrate that the current SiC-to-SiC bonding method is robust and does not leak gaseous fission products. For coated Zr alloy cladding, sealing could involve joining of Zr-to-Zr if the ends of the Zr cladding tubes are not fully coated. For both ATF claddings discussed here, methods to both seal the cladding tube and fill the cladding tube with a positive pressure of inert gas will be developed. Sealed and positive pressure inert gas filled short length tubes are required for test reactor irradiation of ATF cladding concepts both without and with fuel.

Subtask 2.1.4. Characterization and Property Determination of ATF Cladding Tubes (Phase 2)

During bench scale development, significant characterization and property determination of both SiC CMC and coated Zr alloy cladding will be performed. Performing thorough and detailed characterization and property determination at this stage of development will allow for understanding the effects processing has on the resultant microstructure and properties. This processing – property relationship is extremely important in developing robust processes to fabricate desired properties and thin walled tube structures. For SiC CMC cladding, the microstructure of the CMC will be thoroughly characterized including SiC fibers, fiber/matrix interface, and the SiC matrix. Additionally, the porosity in the CMC will be characterized for pore size, morphology, and distribution in the SiC matrix. SiC CMC tube properties such as CMC density, CMC mechanical properties, CMC thermal conductivity, hermeticity of the CMC tube, bulk chemistry (i.e.; Si and C), and impurity chemistry will also be determined.

For coated Zr alloy cladding, the microstructure of the applied coating and the Zr alloy substrate/coating interface will be thoroughly characterized. Coating density, coating bond or adhesion strength, and coating bulk chemistry and impurity content will all be determined. It is

assumed that the Zr alloy tube substrate maintains hermetic integrity during processing so coated cladding tube hermeticity determination is not required.

Task 2.2. Fuel Bench Scale Development (Phase 2 and 3)

Subtask 2.2.1. Synthesis of UN from UF_6 (Phase 2)

Synthesis of uranium nitride (UN) from uranium hexafluoride (UF_6) and subsequent ceramic processing of the resultant product using available industrial infrastructure are major concerns that must be addressed before any proposed composite nitride system may be considered for use as a commercial reactor fuel. While this work has received limited historical attention, the typically envisioned applications of nitride fuels made identification of solutions to these problems less consequential. The core sizes and the required loadings were far smaller than the output demanded of commercial light water reactor (LWR) fuel, and as such allowed consideration of laboratory scale fabrication pathways. Furthermore, use of a nitride as a minor actinide bearing fuel or plutonium burner would require glovebox fabrication, and thus eliminate many of the concerns brought about by handling in air.

The required research and development can be divided into three primary areas.

Subtask 2.2.1.1. Demonstration of Heavy Metal Fluorite Chemistry

Numerous potential heavy metal fluorite chemical processing routes are available for conversion of UF_6 to UN. Evaluation and optimization of these processes must be performed with respect to four aspects. First, UN product purity (principally in terms of oxygen and carbon) must be maintained below acceptable levels. Initial fabrication of UN for this study focused on limiting carbon at 1000 wppm and oxygen at 5000 wppm, but these criteria may be adjusted based upon ongoing experimental efforts.

The presence of U_2N_3 in the produced uranium nitride material is highly undesirable and would require subsequent high temperature heat treatment of the powder. While this would be possible, it would represent a non-trivial addition to the fabrication process and complication in terms of both processing time and expense.

The characteristics of the UN powder must be evaluated with regard to the planned subsequent processes. For use in this proposal as currently envisioned, a fairly coarse powder will be required. Secondary powder coarsening steps could be performed but not without added complexity and expense. It is not anticipated that the particle character will greatly affect the silicide coating process or end product, but this will require verification. The product's geometric characteristics (e.g. size distribution, surface area) are likely to greatly impact final processing of the material into pellet geometry. Powders produced using various synthesis routes can be conditioned with minimal time or complication (although inert atmospheres would be required for UN), but the degree to which a given feedstock can be improved is typically limited if its initial character is poor. Sintering studies both in the as-synthesized and as-coated condition can be readily performed in conjunction with evaluation of final microstructures to evaluate the above.

Finally, the chemical processes explored above must be considered in terms of their industrial feasibility. Chemical byproducts of an UF_6 to UN conversion process are not likely to provide a significant challenge for a fuel fabrication facility already deploying UF_6 to UO_2 synthesis via ammonium di-uranate (ADU) or dry conversion processes, but this must be evaluated within the specifics of any proposed conversion pathway. Industrial process considerations (e.g. footprint,

energy requirements, reaction efficiency) must also be evaluated with direction from fuel vendors.

The proposed research path forward is summarized in the following paragraphs.

The proposed research within this area consists of a three-tier research effort. Initially, a white paper will be prepared by Los Alamos National Laboratory (LANL) heavy metal fluorite chemists to evaluate the feasibility of both demonstrated (e.g. Czerwinski, et al. [21, 30-35]) and other proposed methods for the preparation of UN from uranium fluorides. The referenced technique was developed in collaboration with researchers at the Seaborg Institute at LANL who will be contributing to this effort for both nitride synthesis as well as exploration of UF_6 conversion to other actinide compounds of interest. Routes identified as the most promising will be investigated using 'shielded' UF_6 in existing laboratory space authorized for this work. 'Shielded' UF_6 are well-defined uranium fluoride molecules that have several direct uranium fluoride bonds and strongly bonded inert organics. The resulting molecule is fully capable of undergoing any chemical process applicable to native UF_6, but with far less reactivity and associated hazards. This approach provides a means to rapidly evaluate candidate chemical processes.

The second phase would consist of a scale up to full UF_6 synthesis. Again, minimal differences are anticipated transitioning a demonstrated technique from shielded UF_6 to unmodified UF_6, but full synthesis is necessary for production of initial UN feedstock. Two facilities are currently available at LANL for UF_6 synthesis, but it is currently unclear whether the existing laboratories are well suited to this work or whether it would be preferable to dedicate a new laboratory to this work given the low capital costs of such a transition.

The final component is judging the product of the proposed methods according to the powder character as described above. Standard powder evaluation methods (e.g. particle size analysis, surface area analysis, electron microscopy) will be used to document the geometric character of the material. X-ray diffraction will be used to probe phase content, and combustion spectroscopic analysis will be performed to monitor oxygen and carbon content. Pressing and sintering studies will then be employed (both in the as-produced and as-coated condition) in order to evaluate potential processing challenges resulting from a specific synthesis route. Should concerns be evident in the results of initial fabrication studies, standard meshing and milling methods will be explored in order to attempt improvement.

Synthesis routes found to be the most promising will be analyzed with industrial partners in order to identify any concerns of the process itself.

Subtask 2.2.1.2. Open Air / Modified Open Air Processing

Use of existing fuel fabrication facilities will likely require handling of the produced powders in open air. While it is probable that silicide coating would occur in relatively short order following synthesis of the nitride, exposure of the nitride to air may occur during transportation, storage, or if the silicide coating process is either incomplete or flawed. Uranium nitride's affinity for oxidation is well known; initial UN powder fabrication performed during Phase 1 of this study encountered significant oxidation of powder surfaces during even brief exposure to uncontrolled atmosphere. Any reaction must be mitigated should residual oxygen or oxide content be found a critical factor in fuel performance.

A possible solution would be processing in inert atmospheres. However, this is highly undesirable as it would require extensive modification to the fabrication plant. An alternative may be performing specific processes where UN may be exposed to air under flowing nitrogen to desensitize the UN to oxygen exposure and allow for free release into the fabrication facility.

The proposed research path forward is summarized in the following paragraphs.

Consideration of any mitigation method or modification to the fabrication process first requires understanding of the extent of the problem. The effect of residual oxide on fuel performance would not be suitable for study without test irradiations executed with controlled oxide content. Such data is unlikely to be available near-term. However, relatively straightforward experimental analyses are possible at minimal expense to evaluate this degree of the problem.

Thermogravimetric analysis performed for ~hundreds of hours in air at slightly elevated temperatures (e.g. 50, 100°C) will reveal the relevant surface oxidation kinetics at temperatures above those expected during storage in air. Higher temperatures could also be readily incorporated should a specific process elevate the temperatures prior to silicide coating. X-ray diffraction or neutron diffraction could also be utilized to evaluate the effects of nitride powder aging in air. Neutron diffraction in particular could be very valuable to identify the specific kinetics of UO_2 and U_3O_8 formation on UN powders. The Lujan Center at LANL offers access to such facilities via user proposals and has been utilized by team members with great success previously. It is anticipated that such a study could be executed at no cost to this proposal.

Results of the above analysis will then be compiled and analyzed in order to determine if a significant concern will exist, following which mitigation options will be discussed with industrial partners.

Subtask 2.2.1.3. Scrap Recycle Research

Handling and processing losses are inevitable during industrial pellet fabrication. Means to recycle this scrap with known isotopics are therefore vital for evaluation of any proposed commercial fuel using current infrastructure. A composite system such as a coated nitride presents challenges in this respect.

While it should be noted that this area requires further research, at present it will be delayed until precise synthesis routes and fabrication pathways are identified.

Subtask 2.2.2. U_3Si_2 Fuel Bench Scale Development (Phase 2)

It has been shown that the U_3Si_2 powder can be produced at laboratory scale with high purity (>98%) and various particle sizes from submicron to microns. The largest issue is to find an economical method which can be adopted for mass production of U_3Si_2 powder. Pellet making is a lesser issue, where several methods could prove acceptable.

Subtask 2.2.2.1 Synthesis of U_3Si_2 from Enriched UF_6

One synthesis method can be adopted by modifying a process patented by William T. Nachtrab. The patent number is US 5,901,338 and the title of the patent is “Method for Producing Uranium Oxide and Silicon Tetrafluoride from Uranium Tetrafluoride, Silicon, and a gaseous oxide”. The processing can be described in the following steps. First UF_6 is reduced by UF_4 using hydrogen. Then the UF_4 (green salt) would be mixed with the appropriate/stoichiometric amount of fine Si metal and heated to produce U_3Si_2 powder. The process from the Nachtrab’s patent is shown in Figure 1. The process is modified by elimination of addition of metal oxides and oxygen.

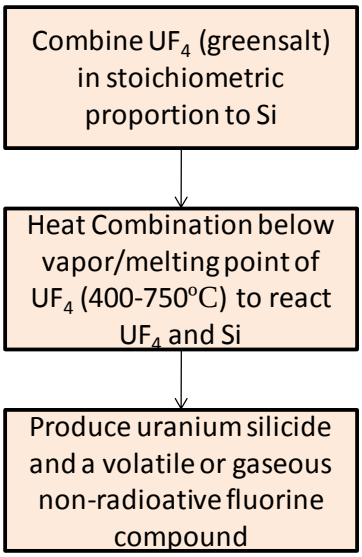

Figure 1. Flow diagram for production of U_3Si_2 from UF_4

The team members have contacted the patent author Dr. Bill Nachtrab (wnachtrab@supercon-wire.com) who is interested in the U_3Si_2 production process and expressed a willingness to participate as a part-time "consultant" to Westinghouse. Dr. Nachtrab has extensive experience in converting depleted uranium fluorides into uranium metal and other products. He was the Research Director of Starmet Metals (formerly Nuclear Metals).

Subtask 2.2.2.2 Large Scale Production of Enriched U_3Si_2 Pellets

Two methods seem to be appropriate to produce enriched U_3Si_2 fuel pellets. One is the widely used method of a high-speed rotary press using metal double-acting punches and metal die body. The second method, Dry Bag Isostatic Pressing [14], provides for high production rates (used for spark plug insulator production) with the added advantage of applying homogeneous stresses to produce homogeneously strained green pellets. The pellets can also be fabricated to a variety of heights (including very long pellets – if desired). This method is described in detail in reference 14 and a patent application [15]. In addition, casting methods will also be explored as an alternative process to pelletization.

Subtask 2.2.3. UN- U_3Si_2 Fuel Bench Scale Development (Phase 2)

In the current two year project plan, Texas A&M University (TAMU) is focused on demonstrating the fabricability the UN-U_3Si_2 pellets for initial behavior tests and process variable determination. At the end of this initial phase, the nominal process variables for fabrication will have been demonstrated and at least ten 10g pellets will have been manufactured and subjected to various characterization studies at TAMU and various partner facilities.

The next phase of bench scale development studies will include process and pellet optimization studies as well as continued behavior assessments and will require a fresh supply of nitride and silicide powders. In short, the topics to address include the most effective volume fraction for waterproof pellet performance while optimizing mechanical stability (no slumping), nitride encapsulation, and thermal properties. The work will include generating a significant number of fuel pellet samples (w/ depleted uranium) to generate a database with at least 2 samples per data point to explore the impact of U_3Si_2 volume fraction and possible binders. Characterization methods will include microscopy and thermal diffusivity measurements as well as other performance tests performed at partner facilities.

With respect to process scale-up issues, consideration must begin immediately regarding the unique processing requirements for this fuel system and how they might need to be customized for large scale commercial fabrication. The powders being handled are pyrophoric and air sensitive, so handling methods need to be developed that may be implemented in an inert atmosphere facility. In addition, the powders need to be generated and handled in this facility, so equipment needs, and practical powder properties need to be identified. TAMU may contribute to this activity by investigating the flowability of the UN and U_3Si_2 powders in the TAMU glovebox facilities, evaluating options to improve green pellet stability during pressing (e.g., binders, pressures, and die methods).

Subtask 2.2.4. N15 Enrichment (Phase 3)

UN fuel offers advantages over UO_2 in terms of higher U density and higher thermal conductivity. One requirement for the use of UN is that >90% ^{15}N be used instead of natural N which consists of 99.636% ^{14}N to minimize parasitic neutron losses and ^{14}C production. Estimates for producing >90% ^{15}N using centrifuge technology are about $35,000/kg. This high cost is due to the low throughput of the centrifuge process, low selectivity per stage and the low molecular weight of nitrogen. Westinghouse has explored alternative technologies and estimated the costs associated with different separation schemes and determined that LIS methods were likely to be the most economically competitive (see Table 1).

Table 1. Comparison of Capital and Production Costs for ^{15}N Isotope Separation Technologies

Method	Capital Cost (Million$)	Production Cost ($/kg 90--99% ^{15}N)
Laser Isotope Separation (LIS) [1,2]	300 to 400	500 to 1000
Chemical Exchange [3-12]	>500	1500 to 2000
Ion Exchange [13]	>500	~1600

Based on this study, Westinghouse experimentally explored several laser based ^{15}N isotope separation technologies at the molecular bench scale to verify the separation factors that could be obtained (β from 50 to 100, where β is used to denote the dissociation yield, namely the fraction of molecules dissociated in the irradiated volume per laser pulse.). The LIS approach that was identified serves as the basis for describing the bench, pilot and full scale development programs that follow.

The next stage of development consists of bench scale tests where ~1 gram per day of >90% ^{15}N can be produced. This stage of development serves to support the design of the reaction chamber as well as establish the mass and energy balance for the process. Based on the work performed at this stage, a firm design for the pilot scale can be established along with relatively firm estimates of capital and operating costs. The estimated time for this stage of development is shown in Table 2.

Table 2. Time Estimates for a Gram/Day Bench Scale LIS Process for ^{15}N Separation

Task	Time (Months)

Design of process	2
Acquisition of equipment	12
Construction	12
Startup	6
Testing	6
Analysis	2
Totals	40

Task 2.3. Burnable Absorber and Reactivity Control (Phase 2)

Burnable absorbers (BA) are routinely used for reactivity control in commercial LWRs. The most common BAs currently employed include: ZrB_2 (IFBA), a thin coating deposited on the surface of the pellet; gadolinium or erbium in the form of Gadolinia or Erbia, Gd_2O_3 or Er_2O_3, which are mixed with UO_2 within the pellet; various boron-bearing inserts such as B_4C which are inserted in the guide thimble positions of assemblies without control rods and typically extracted after one irradiation cycle.

Due to the higher per volume ^{235}U loading of high density fuels compared to UO_2 fuel of comparable enrichment, increased loading of BAs for reactivity control is anticipated once high density fuels will be commercially deployed. IFBA is the preferred solution because of the favorable neutronic properties of ^{10}B: it depletes completely before discharge and, unlike other options, it does not lead to a reactivity penalty nor does it displace U from the fuel matrix. These characteristics contribute to its superior economic performance. In addition, the current process for depositing IFBA on the UO_2 pellet is expected to be applicable to U_3Si_2 and UN.

However, the higher U loading of the new fuels and the longer irradiation cycles may entail higher IFBA loading than those in typical UO_2 cores. This higher IFBA loading may be problematic from the following standpoints: it could lead to unfavorable depletion characteristics and high peaking factors; the higher ^{10}B content could cause excessive rod pressurization from the Helium generated in ^{10}B neutron captures and higher fission gas release from the longer irradiation periods; ^{10}B axial relocation could exacerbate power shifts and axial offset anomalies.

For the above reasons a combination of two BAs, IFBA and either gadolinium or erbium or a boron-bearing insert such as the Westinghouse Wet Annular Burnable Absorber (WABA) may be desirable but this needs to be ascertained with detailed core physics and fuel rod performance analyses. Also Gd_2O_3 or Er_2O_3 may be chemically incompatible with U_3Si_2 and UN and alternative compounds or processes could be required for incorporating Gd or Er with the new fuels.

Therefore, the following R&D activities are envisioned:

RD need#1: Core Physics and Fuel Rod Performance Analyses to Determine Optimum Burnable Absorber Selection

Detailed core physics and rod performance analyses will be undertaken to ascertain whether IFBA, alone or in combination with WABA, is an adequate BA choice for U_3Si_2 or UN cores. A

representative PWR core operating on an 18 or 24-month cycle can be chosen for the analyses. A critical input that needs consideration is the fission gas release from U_3Si_2 or UN as well as the gap required to accommodate the swelling from these two fuels. The feedback from the irradiation campaign is likely to be required to complement the sparse data available from the literature [22, 23] for final licensing.

RD need #2: Development of BA compounds and/or Improved Deposition Techniques for Incorporation in U_3Si_2 *and UN*

If additional or alternative BAs to IFBA and WABAs are required for implementation of the new fuels then proper compounds, likely GdN or ErN, that can be incorporated in UN and $GdSi_2$ [24] or Er_3Si_5 [25], that can be incorporated in U_3Si_2, or deposited on their surface must be explored. The basis of choice will be the exploration of potential low melting eutectic compounds that could be formed when mixed in with either UN or U_3Si_2 respectively, or the efficacy of surface application methods such as hot spray, cold spray or plasma arc deposition for depositing these compounds or other boron containing compounds (such as ZrB_2 or UB_4) on the surface of the pellets. While surface deposition is preferred for easier logistics in the manufacturing process, the applied surface coatings may not have the required structural integrity and adhesion. The required characteristics can only be determined through experimental work.

Task 2.4. Rodlet Irradiation Testing and PIE (Phase 2 and 3)

Irradiation testing, post irradiation examination (PIE), and detailed analysis of irradiated cladding and fuel materials are required for further development of the proposed ATF cladding and fuel concepts. For the ATF concept proposed here, limited irradiation and analysis has been performed of SiC CMC material and no irradiation and analysis has been performed of coated Zr alloy cladding materials [26]. Uranium Silicide (U_3Si_2) has been irradiated previously in composite form (U_3Si_2 + Al) [27, 28]. U_3Si_2 doped UN (U_3Si_2 - UN) has never been irradiated under any power generating reactor condition. Thus significant irradiation and PIE experimental work is required to progress the proposed ATF concept towards LWR application.

Because of the significant irradiation and PIE work required to progress this ATF concept, it is proposed that irradiation and PIE experimental work be performed in two stages. Initially, proof of concept irradiation and PIE will be performed of these cladding and fuel materials using LWR irradiation conditions. After proof of concept irradiation and PIE, experiments designed to produce data required for fuel performance models and fuel licensing will be performed. Through this two-stage approach to irradiation and PIE, it is possible that down selection of the proposed ATF concepts could occur based on the irradiation performance of the proposed cladding and fuel materials.

Subtask 2.4.1. Proof of Concept Irradiation and PIE of Proposed ATF (Phase 2 and 3)

For proof of concept irradiation, it is proposed that unfueled, 6 inch length ATF cladding tube samples, sealed on the ends and pressurized with an inert gas, be placed in a water-moderated and cooled test reactor and irradiated. The experimental irradiation conditions will be an accelerated LWR fluence with an approximate 200% increase in linear power (~15 kw/ft). A target final fuel burnup of 60 GWd/MTU is proposed and cladding tube samples will be removed for PIE after an equivalent 20, 40, and 60 GWd/MTU fuel burnup. PIE of unfueled 6 inch length cladding samples will include visual examination, length and diameter dimension measurement, cladding strength determination, cladding burst testing, and cladding material analysis using scanning electron microscopy (SEM), optical microscopy (OM), or other techniques. Irradiation

conditions and target fuel burnup exposure will be the same for both SiC CMC and coated Zr alloy cladding tube samples.

The proposed ATF fuels, U_3Si_2 and U_3Si_2 – UN, will also be irradiated for fuel behavior proof of concept evaluation. Pellets of U_3Si_2 and U_3Si_2 – UN will be placed in 6 inch length Zr alloy cladding rodlets, sealed on the ends and pressurized with an inert gas, and irradiated in a water-moderated and cooled test reactor. Similar to ATF cladding proof of concept irradiation, ATF fuel proof of concept irradiation will be conducted using accelerated LWR fluence experimental conditions with an approximate 200% increase in nominal linear power (~15 kw/ft). ATF fuel pellets will be irradiated to a target final fuel burnup of 60 GWd/MTU and fuel pellet samples removed for PIE at 20, 40, and 60 GWd/MTU fuel burnup. PIE of ATF fuel pellet samples will include dimension measurement and pellet swelling, solid and gaseous fission product determination, fuel chemical analysis, ceramography for microstructure analysis including pore size and distribution, phase determination and microcomposition analysis.

Lastly, irradiation experiments of ATF fuel in ATF cladding will be performed for proof of concept. The specific combination or combinations of ATF fuel and cladding to be irradiated are not specified at this time, but can be determined later based on results of the separate ATF cladding and fuel irradiation experiments. As with separate ATF fuel and cladding experiments, ATF fuel pellets will be placed in 3 ft length ATF cladding rodlets, sealed on the ends and pressurized with an inert gas, and irradiated in a water-moderated and cooled test reactor. Irradiation will be conducted using typical LWR fluence conditions with an approximate 10% increase in linear power. ATF fuel plus cladding rodlets will be irradiated to a target final fuel burnup of 60 GWd/MTU and fueled rodlets removed for PIE at 20, 40, and 60 GWd/MTU fuel burnup. Specifically, this experiment will be highly instrumented with measurement of fuel temperature, cladding temperature, fuel rod pressure, fuel stack extension, and cladding extension performed throughout the experiment [29]. PIE of ATF rodlets will include all analysis discussed for separate ATF fuel and ATF cladding irradiation experiments and analysis of fuel pellet/cladding interaction.

The above detailed ATF fuel and ATF cladding irradiation tests will require significant time to achieve up to 60 GWd/MTU fuel burnup. To decrease the time to achieve this irradiation, fuel enriched to higher than 5 weight percent ^{235}U will be used. The exact fuel enrichment required to achieve 60 GWd/MTU burnup in a reasonable period of time will be calculated during irradiation experiment design. Fuel enrichments up to 20 wt. % ^{235}U are possible for proof of concept irradiation experiments.

A summary of the proposed proof of concept irradiation experiments for ATF fuel and cladding are summarized below in Table 3.

Table 3. Summary of proposed ATF cladding and ATF fuel proof of concept irradiation experiments

ATF Cladding/ Fuel Samples	Irradiation Condition	Target Burnup (GWd/MTU)	Sample Extract Burnup (GWd/MTU)	Desired PIE
SiC CMC/unfueled	LWR + 10% linear power	60	20, 40, 60	dimensions, strength, burst, structure analysis
coated Zr/unfueled	LWR + 10% linear power	60	20, 40, 60	dimensions, strength, burst, structure analysis

Zr alloy/U_3Si_2	LWR + 10% linear power	60	20, 40, 60	dimensions/swelling, fission products, chemistry, phases, microchemistry, microstructure
Zr alloy/U_3Si_2 – UN	LWR + 10% linear power	60	20, 40, 60	dimensions/swelling, fission products, chemistry, phases, microchemistry, microstructure
SiC CMC/ ATF fuel	LWR + 10% linear power	60	20, 40, 60	all clad and fuel PIE, instrumented experiment clad and fuel
coated Zr/ ATF fuel	LWR + 10% linear power	60	20, 40, 60	all clad and fuel PIE, instrumented experiment clad and fuel

Subtask 2.4.2. Fuel Performance Modeling and Licensing Irradiation of Proposed ATF (Phase 3)

After completing ATF cladding and fuel proof of concept irradiation experiments, additional irradiation experiments will be performed to generate data required for fuel performance models and licensing of accident tolerant fuel. These experiments could also be performed using fueled rodlets in a test reactor. While the data required will be determined in the future based on the specific fuel performance model(s) used and the specific licensing requirements requested by the Nuclear Regulatory Commission (NRC), the following is proposed as required data for both fuel performance models and licensing purposes.

Cladding models and licensing data include:

- irradiation creep of cladding as a function of irradiation
- irradiation growth of cladding as a function of irradiation
- the limit of ductility or equivalent mechanical property for fresh and high burnup fuel cladding conditions
- cladding corrosion in typical LWR coolant chemistry and fluence
- a LOCA type test for fresh and high burnup fuel cladding conditions

Fuel models and licensing data include

- fuel shrinkage and/or swelling as a function of irradiation
- fuel gaseous and solid fission product generation determination
- fuel gaseous and solid fission product production as a function of irradiation

The above data will require specific irradiation experiments. For example, for cladding creep and growth, a fueled rodlet of the desired ATF cladding with ATF fuel will be irradiated in a water-moderated and cooled test reactor using typical LWR fluence conditions to the desired fuel burnup. The fueled rodlet will be instrumented to measure in-situ ATF cladding creep and growth. The collected data will then be used to develop a mechanistic model of the irradiation-induced ATF cladding creep and growth, used to predict cladding creep and growth under different fuel operating conditions, and satisfy NRC regulatory requirements.

The required fuel performance model data will be determined after the specific fuel performance model has been chosen. The required licensing data will be determined after discussions with and specific requests from the NRC.

Task 2.5. Other R&D Needs (Phases 2 and 3)

Subtask 2.5.1. Pilot Scale Development and Testing for SiC and Coated Zr Alloy Cladding (Phase 3)

Pilot scale development of SiC CMC tube cladding will function as a continuation of bench scale development described in previous tasks. For pilot scale development however, the result of this effort will be hundreds of full length ATF fuel cladding tubes suitable for insertion into commercial nuclear reactors as LTRs and LTAs. More specific in migration from bench scale development is that pilot scale development will result in cladding tubes that are fabricated using CMC architectures and coatings to cladding specifications that are representative of licensable LWR fuel cladding. The data collected during LTR/LTA operation experience and subsequent pool side measurements and hot cell PIEs will be used for subsequent licensing of ATF cladding.

Subtask 2.5.1.1. General Design/Architecture of Pilot Scale Fabricated ATF Cladding

Based on results from bench scale development and subsequent properties determined, one or two designs or architectures of ATF cladding will be selected for full length cladding tube fabrication. The architecture features to be chosen during pilot scale work will include the following:

- outer diameter of cladding
- inner diameter and wall thickness of cladding
- length of cladding

For SiC CMC ATF cladding, architecture or design features will include the following:

- solid inner SiC tube covered by SiC CMC cladding design or single SiC CMC tube cladding design
- SiC fiber winding architecture including number of layers of wound fiber
- SiC infiltration and deposition details
- roughness of CMC OD surface

For coated Zr alloy tube ATF cladding, architecture or design features will include the following:

- coating material
- thickness of coated layer
- roughness of coated OD surface

Subtask 2.5.1.2. Coated Zr Alloy Tube Cladding Pilot Scale Development

Similar to pilot scale SiC CMC cladding development, pilot efforts to develop coated Zr alloy tube cladding will work to perfect coating application onto full length ATF cladding tubes. Specific pilot scale coated cladding tube development efforts will include the following.

- precoating tube surface preparation

- application of the selected coatings onto the OD of a full length Zr alloy cladding tube of ~3.85 m length
- coating application to the desired thickness on the full length Zr alloy cladding tube

The coating processes under consideration, such as the HVOF, and cold spray are relatively mature. Thus the application of a coating onto a 3.85 m long thin walled Zr alloy tube will mainly depend on the coating processing parameters selected. Therefore, pilot scale coated cladding development could be easier than for SiC CMC clad development. Similar to SiC CMC cladding development, coated cladding development will require an extremely stable coating processes to fabricate uniform coatings of the desired dimensions and properties over a 3.85 m length tube. Again, in-situ analysis and analysis based control of the coating process will be required for reproducible fabrication.

Subtask 2.5.1.3. SiC CMC Cladding Pilot Scale Development

Based on the chosen CMC designs or architectures, pilot scale development of SiC CMC cladding will work to perfect fabrication of this design/architecture into full length ATF cladding tubes. Specific pilot scale development efforts will include the following:

- fabrication of solid inner SiC tubes to ~3.85 m cladding length and tube dimensions, if the inner tube plus CMC design is chosen
- SiC fiber tow winding to the chosen architecture and number of layers over the full cladding length
- chemical vapor deposition and infiltration of SiC over the full cladding length to form the CMC of specified density

Pilot scale development of solid SiC inner tube, SiC fiber winding, and SiC CVD/CVI to form an approximate 3.85 m length CMC cladding tube will be extremely challenging. Specifically, developing and stabilizing these 3 processes to fabricate full length CMC tubes of desired dimensions and properties over a length of approximately 3.85 m reproducibly has never been done. In-situ analysis and analysis based control of these processes will be required to reproducibly fabricate the desired CMC tubes with length over ~3.85 m.

Subtask 2.5.1.4. Post ATF Cladding Fabrication Processing

For both SiC CMC and coated Zr alloy tube ATF claddings, post fabrication processing would include OD surface processing to the desired roughness and tube sealing by end plug attachment. For SiC CMC cladding, the OD surface would be an undulating roughness due to the millimeter deep hills/valleys of the coated SiC fiber tows. This very large roughness must be reduced to some value more appropriate to the desired thermal hydraulic (TH) behavior of fuel cladding in commercial LWR's. For coated cladding, conventional surface grinding of the coated tube OD surface should suffice to generate the TH required roughness.

Again for both SiC CMC and coated Zr alloy tube ATF claddings, tube sealing by end plug attachment processing is required. At this time, it is envisioned that end plugs of materials similar to mating cladding material be placed into the ends of cladding tubes and then joined to the cladding tubes. For fueled tube fabrication, the end plug joining will be conducted with a positive pressure of inert gas in the fuel tubes. The specific joining process is presently under development. Results of this pilot scale development will be a reproducible joining process that can easily be scaled up to larger production volumes.

Subtask 2.5.1.5. Characterization, Property Determination, and Quality Control of ATF Cladding Tubes

For ATF cladding fabricated during pilot scale development, the characterization, property determination, and quality inspection of these tubes will be sufficient to allow for future placement in a commercial LWR as LTR/LTAs. This investigation of fabricated ATF cladding will be thorough and detailed, and sufficient to provide the information required by the NRC prior to region loading.

For coated Zr alloy tubes fabricated during pilot scale development, the following characterization, property determination, and quality inspections will be performed.

Characterization

- dimensional inspection including OD, ID, OD/ID concentricity, length, and straightness over entire length
- coating microstructure and substrate/coating interface characterization
- coating density
- coating chemistry including impurities and neutron absorbers
- OD surface roughness

Property determination

- bond strength of coating on Zr alloy substrate

Quality inspection

- tube hermeticity
- non-destructive inspection of coating and substrate/coating interface for internal defects
- visual inspection

Similarly, for SiC cladding fabricated during pilot scale development the following characterization, property determination, and quality inspections will be performed.

Characterization

- dimensional inspection including OD, ID, OD/ID concentricity, length, and straightness over entire length
- microstructure
- density
- chemistry including impurity and neutron absorber contents
- OD surface roughness

Property determination

- mechanical properties
- thermal conductivity

Quality inspection

- tube hermeticity
- non-destructive inspection of tubes for internal defects
- visual inspection of tubes.

The different characterization, property determination, and quality inspections of pilot scale fabricated ATF cladding will be capable of being scaled to production volumes of ATF cladding.

Subtask 2.5.2. Production Scale Development and Testing for SiC Cladding (Phase 3)

Production scale development of SiC CMC and coated Zr alloy tube cladding will serve as the final development step to production scale fabrication of ATF cladding. Production scale development will function as continuation of bench scale and pilot scale development described in previous tasks. The result of production scale ATF cladding development will be upwards of thousands of ATF cladding tubes suitable for fulfilling region reload contracts. At the conclusion of this development work, it is projected that ATF cladding will be licensed for domestic commercial LWR use by the NRC.

Subtask 2.5.2.1. Production Scale Fabrication of ATF Cladding

Production scale development of ATF cladding, either SiC CMC or coated Zr alloy tubes, should simply function to increase in fabrication scale the work performed in the pilot scale development. Here the cladding CMC designs and architectures, coatings deposited, and processes used to fabricate CMC and coated cladding are unchanged, but the fabrication volume capabilities of these processes are increased to full production levels. While specific work to be performed in this subtask is difficult to detail at this time, general areas of effort can be summarized as follows:

- production volume capability determination of CMC fabrication and coating deposition processes, and required equipment
- optimization of CMC fabrication and coating deposition processes
- SiC CMC and coated Zr alloy tube fabrication process flow and optimization

Subtask 2.5.2.2. Production Scale Quality Control of ATF Cladding

Nuclear fuel components, specifically fuel cladding for this subtask, are required to be of the highest quality and contain no defects and are in compliance with 10CFR50 Appendix B, Quality Assurance Criteria for Nuclear Power Plants and Fuel Reprocessing Plants. The obligation for zero defects requires stringent quality control methods that increase the number of acceptable components to a maximum and do not allow any defective components or foreign materials into the final product. This stringent requirement requires development of specific quality control inspection methods and these methods will be developed in this subtask. Possible quality control development work to be performed in this subtask is as follows:

- nondestructive evaluation of ATF cladding tubes *before* fuel loading
- automated visual inspection of ATF cladding tubes
- statistical determination of the number of ATF cladding tube inspection samples fabricated from destructive evaluation; i.e.; sectioning of a cladding tube
- automated hermiticity testing of ATF cladding tubes
- nondestructive evaluation of ATF cladding tubes *after* fuel loading

Subtask 2.5.3. Additional R&D Supporting Codes and Standards Development (Phase 2)

The codes typically used for the analysis of existing LWRs contain models and assumptions that are often applicable to UO_2 fuel and Zr-based cladding only. Some R&D is needed to generate models/databases to be implemented in these codes, so that they can be used to predict the reactor behavior when the fuel is U_3Si_2 or UN and the cladding material is SiC or coated Zircaloy. The following list summarizes key R&D activities that are needed to achieve this objective, categorized based on the type of code in which such models/databases need to be implemented. While not necessary for scoping calculations, it is recognized that the current

tools are not licensed for the ATF fuels, and a licensing effort will be accounted for in the future if the ATF fuels will be deployed on industrial scale.

Subtask 2.5.3.1. Fuel Rod Performance Codes

R&D need #1: development of irradiation-induced fuel swelling models of U_3Si_2 and UN. Limited data is available on the irradiation-induced swelling of U_3Si_2 and UN. For U_3Si_2, available swelling data is either at high burnup (70≤BU≤170 GWD/MTU) but low temperature (<100°C) or at high temperature (~1000°C) but low burnup (<10 GWD/MTU) [16, 17]. For UN, swelling has been correlated with temperature and burnup, with ±25% accuracy in the ranges 1200≤T≤1600 K and 10<BU<45 GWD/MTU for the fuel volume-averaged temperature and burnup, respectively [19]. R&D is needed to collect new data points, and to use them to develop swelling models to be implemented into fuel performance codes.

R&D need #2: development of correlations for fuel and cladding irradiation-induced thermal property degradation. R&D is needed to assess the dependency of some key material properties on burnup. Of particular importance is the fuel melting temperature, especially for U_3Si_2 due to its low melting point in unirradiated conditions, and the thermal conductivity of U_3Si_2 and UN, as well as SiC. While testing is needed for U_3Si_2 and UN, since no experimental data exists either on melting temperature or thermal conductivity degradation with burnup, for SiC composites some data on thermal conductivity degradation already exists (e.g. [19]).

R&D need #3: development of mechanical performance models for SiC composites. Modeling cladding performance during normal operation and transients requires knowledge of the mechanical properties of SiC composites under irradiation. These properties are known to be dependent upon the composite type, the extent of irradiation, and are often anisotropic. R&D is needed to assess these dependencies and to develop a model which is able to predict them.

Subtask 2.5.3.2. Thermal Hydraulic Codes

Development of a DNB correlation for SiC composite cladding is needed for PWR applications. For BWR, the equivalent of DNB is called dry-out. Typical DNB correlations used for LWR analysis do not explicitly account for cladding surface effects and their development was based on experimental data collected using metal cladding. The known dependence of DNB on surface wettability, combined with the fact that SiC composites are not homogeneous but made with fibers, require assessing whether typical DNB correlations are applicable to SiC cladding.

Subtask 2.5.3.3. Transient Analysis Codes

R&D need #1: development of models for predicting the behavior of SiC and coated zircaloy cladding materials during loss of core cooling events. Knowledge of cladding oxidation rate, corrosion-induced cladding fragmentation, hydrogen generation rate, as well as high temperature mechanical behavior, is needed to predict the fuel rod performance during Design Basis Accidents (DBAs) and BDBA: Beyond Design Basis Accidents (BDBAs), and to select appropriate safety limits (e.g. peak cladding temperature during LOCA, peak cladding temperature during Locked Rotor). For both SiC composite and coated zircaloy, the existing information is not complete, so either testing or collection of available data is required. The ultimate objective would be development of models and their implementation in codes.

R&D need #2: development of models for predicting the behavior of U_3Si_2/UN-fueled, SiC/Zircaloy-clad rods during Reactivity Initiated Accidents (RIAs). During some RIAs, such as Control Rod Ejection, the fuel rod experiences an almost instantaneous, power pulse-induced deposition of a significant amount of energy, which may lead to its failure. Fuel rod thermo-

mechanical models developed from data collected during slower heating transients are likely not applicable, and new testing is needed to understand the behavior of the new materials during power surges. The ultimate objectives would be to a) develop models able to accurately predict the energy deposition, and b) to determine the maximum energy deposition that can be tolerated without experiencing rod failure. For typical UO_2/Zr rods, this limit is typically set to 280cal/g.

Subtask 2.5.3.4. Reactor Physics Codes

R&D need #1: in order to properly capture feedback effects, nuclear data (cross sections) for new cladding and fuel materials need to be made available.

R&D need #2: Changes may be required to correctly handle the presence of resonant isotopes in the cladding, or the coating of the cladding if present. A validation of such changes and overall capabilities of the physics tools with regards to the simulation of the ATF fuels will also be undertaken. This will include numerical benchmarks against stochastic codes and comparison against experiments, when available.

Subtask 2.5.3.5. Multiple Code Applications

Development of an appropriate decay heat curve is needed. The American National Standard (ANS) decay heat models that are typically used for UO_2 fuel (e.g., ANS 1979, [20]) need to be reviewed to determine if they are still applicable to U_3Si_2 and UN. The decay heat model could be affected by the harder spectrum which leads to higher U238->Pu239 conversion. Also, the energy deposition could be different.

Subtask 2.5.4. Pilot Scale Development and Testing for Fuel and N15 (Phase 3)

LIS processes are limited in throughput by the size of the available lasers. The process for separating ^{15}N isotopes uses two colors of lasers, one for activation and one for separation. The separation laser is by far the largest and so controls the size of the module. For this work, a 1000 beam watt pulsed CO_2 laser is used as the basis for separation because of its low cost and high efficiency. The pilot scale isotope separation process is based on one module (Figure 2) utilizing a 1000 beam watt CO_2 laser with a small activation laser. The objectives of the pilot scale development program are:

- Verify expected ^{15}N yields and heads/tails ^{15}N ratio based on the photo reaction.
- Determine the meantime between maintenance outages required for the CO_2 and activation lasers.
- Evaluate the efficiency of the process for recovering the product ^{15}N from the output stream.
- Determine the compressor power and maintenance needs.
- Determine the operability of the equipment and overall separation module.

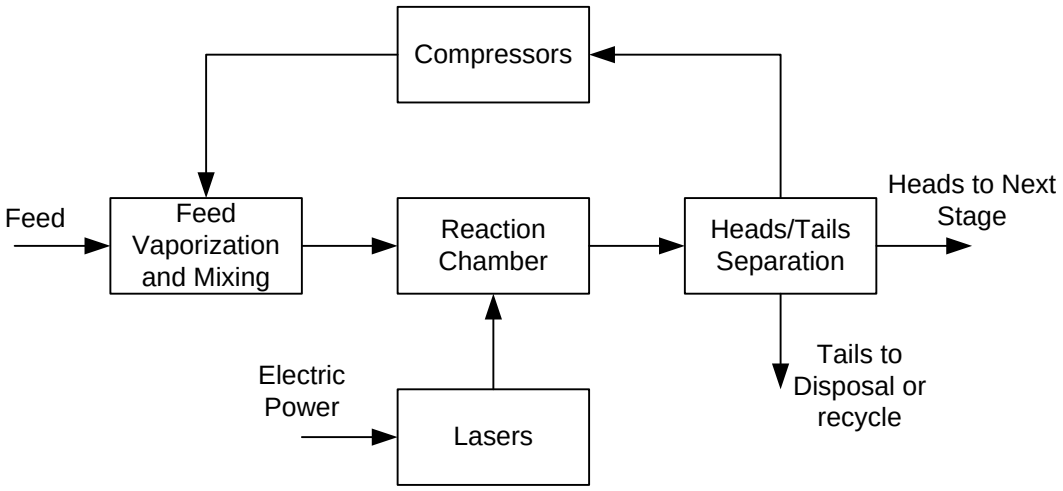

Figure 2. Laser Isotope Separation Stage (Note: Heads is enriched in ^{15}N and tails are depleted in ^{15}N)

This program is expected to take about 4 years to complete. During the first year, the system would be designed and the parts ordered. During year 2, the module would be assembled and started. Long term testing would then be carried out in years 3 and 4 with a final report produced at the end of year 4.

Subtask 2.5.5. Production Scale Development and Testing for Fuel and N15 (Phase 3)

Scale-up of the ^{15}N production facility from pilot to full scale is relatively straightforward since the full scale facility consists of multiple pilot scale units. Other than a multiple of pilot scale laser separation units, the main change will be in the feed, product and waste handling systems which need to operate at maximum efficiency in order to minimize feed and product losses. Ideally, the full scale plant would be tied into an industrial chemical facility that produces the feedstock required by the separation facility and can act as a user of the tails from the separation plant. Examples of such chemical plants for feeding nitrogen into a ^{15}N separation plant (with the feedstock/tails material) would be ammonia (NH_3), nitric acid (NO or NO_2), methylamines (CH_3NH_2, $CH_2(NH_2)_2$), and cyanides (HCN), among others. If the tails from the isotope separation plant is the same as the feed or one of the feeds to the chemical plant, then the tails can be absorbed into the normal production stream of the chemical plant where the isotopics do not matter and there is no disposal issue.

The major development effort for scale-up to full production will be centered on designing and testing any equipment required for feed and tails handling. This will be a minimal cost since laboratory scale testing can be used to determine separation factors for distillation, molecular sieves and other separations devices. This effort is split into 4 phases over a two year period. During phase 1, the design of the feed, heads and tails systems will be developed and uncertainties identified. During phase 2, equipment for testing will be acquired and assembled. This equipment will then be operated and data acquired as needed. During Phase 4, the design will be finalized.

Conclusions and Recommendations

In conclusion, R&D is needed in various areas defined above as an expansion to the phase 1 project and a necessary step to qualify the ATF for use as a LTR/LTA in a commercial reactor.

As a continuation to the phase 1 project and recommendation to move forward, a phase 2 project that encompasses the R&D areas defined in this report and also listed in Table 4 is proposed for FY14-15, and the estimated R&D cost is summarized in Table 4.

Table 4. Summary of Tasks in Phase 2 and Estimated Cost for Each Task

Phase 2 R&D in FY14-15	
Task	**Estimated Cost ($)**
Manufacturing Development	9,800,000
Preparation for test reactor irradiation in FY16-22 (assumed to be in ATR water loop; SiC and coated Zr; UN+U_3Si_2 and U_3Si_2)	7,500,000
Continuation of Phase 1 Testing	5,800,000
Project Management	2,700,000
Total Cost in Proposed Phase 2 Project	25,800,000

References

1. Dcunha, R., et al., *The Nu-2 Band of (NH3)-N-15.* Journal of Molecular Spectroscopy, 1985. **111**(2): p. 352-360.
2. Apatin, V.M., et al., *Laser Separation of Nitrogen Isotopes by the IR Plus UV Dissociation of Ammonia Molecules.* Quantum Electronics, 2008. **38**(8): p. 775-782.
3. Spindel, W. and T.I. Taylor, *Separation of Nitrogen Isotopes by Chemical Exchange between NO and HNO3*. Vol. 23. 1955: AIP. 981-982.
4. Spindel, W. and T.I. Taylor, *Preparation of 99.8% Nitrogen-15 by Chemical Exchange.* The Journal of Chemical Physics, 1956. **24**(3): p. 626-627.
5. Brown, L.L. and G.M. Begun, *Nitrogen Isotopic Fractionation between Nitric Acid and the Oxides of Nitrogen.* The Journal of Chemical Physics, 1959. **30**(5): p. 1206-1209.
6. Kauder, L.N., T.I. Taylor, and W. Spindel, *Isotope Enrichment Factors for Nitrogen-15 in the Nitric Oxide-Nitric Acid Exchange System.* The Journal of Chemical Physics, 1959. **31**(1): p. 232-235.
7. Monse, E.U., et al., *Enrichment of Nitrogen-15 by Chemical Exchange of NO with Liquid N_2O_3.* The Journal of Chemical Physics, 1960. **32**(5): p. 1557-1566.
8. Semiokhin, I., *Chemical Methods of Stable Isotope Separation.* Journal of Radioanalytical and Nuclear Chemistry, 1996. **205**(2): p. 201-213.
9. Axente, D., M. Abrudean, and A. Bâldea, *Nitrogen Isotope Exchange between Nitric Oxide and Nitric Acid.* Journal of Radioanalytical and Nuclear Chemistry, 1996. **207**(1): p. 163-170.
10. Akhtar, M.J., D. Axente, and F.T. Bonner, *Nitrogen Isotope Exchange between Nitric and Nitrous Acids*. Vol. 71. 1979: AIP. 3570-3572.
11. Axente, D., et al., *The Kinetics of the $^{15}N/^{14}N$ Isotopic Exchange between Nitric Oxide and Nitric Acid.* Journal of Radioanalytical and Nuclear Chemistry, 1976. **30**(1): p. 233-244.
12. Gverdtsiteli, I.G., et al., *An Automatic Cascade Device for Producing Highly Concentrated Heavy Nitrogen Isotope.* Atomic Energy, 1962. **10**(5): p. 475-481.
13. Ding, X.-C., et al., *High Enrichment of 15n Isotope by Ion Exchange for Nitride Fuel Development.* Progress in Nuclear Energy, 2008. **50**(2-6): p. 504-509.
14. "Dry bag isostatic pressing for improved green strength of surrogate nuclear fuel pellets", G.W. Egeland, L.D. Zuck, W.R. Cannon, P.A. Lessing, and P.G. Medvedev, Journal of Nuclear Materials, **406**(2), Nov. 15, 2010**,** 205-211
15. "Methods of Forming Nuclear Fuel Pellets, and Nuclear Fuel Pellets and Structures formed by Such Methods", P.A. Lessing, U.S. Patent Application, Docket No. 2930-9318US (BA-367)
16. IAEA-TECDOC-643, Research reactor core conversion guidebook – Volume 4: Fuels (Appendices I-K).
17. Shimizu, H., The properties and irradiation behavior of U_3Si_2. NAA-SR-10621, Atomics International. July 25, 1965.
18. Ross, B. S., El-Genk, M., Uranium nitride fuel swelling correlation. Journal of Nuclear Materials, 170 (1990) 169-177.
19. Stempien, J.D., 2011. Behavior of Triplex Silicon Carbide Fuel Cladding Designs tested under simulated PWR conditions. MS thesis. Massachusetts Institute of Technology.
20. American National Standard Decay Heat Power in Light Water Reactors, ANSI/ANS-5.1-1979.
21. G. W. Chinthaka Silva, P. F. Weck, E. Kim, C. B. Yeamans, G. S. Cerefice, A. P. Sattelberger, and K. R. Czerwinski, "Crystal and Electronic Structures of Neptunium Nitrides Synthesized Using a Fluoride Route," *J. Am. Chem. Soc.* **2012**, *134*, 3111-3119.

22. Shimizu, H., The properties and irradiation behavior of U_3Si_2. NAA-SR-10621, Atomics International. July 25, 1965.
23. Matthews, R.B., Irradiation performance of irradiated fuels. Specialist conference on space nuclear power and propulsion technologies – materials and fuels. Podolsk-Moscow, Russia. September 21-24, 1993.
24. A. B. Gokhale and G. J. Abbaschian, The Gd-Si (Gadolinium-Silicon) System, Bulletin of Alloy Phase Diagrams, October 1988, Volume 9, Issue 5, pp 574-578.
25. S. P. Luzan, et. al., Phase Equilibria in the Erbium-Silicon System, Powder Metallurgy and Metal Ceramics, Vol. 36, Nos. 1-2, 1997.
26. L.L. Snead *et. al.*, Fusion Materials – Semi Annual Report, DOE-ER-301.22 (2002) pp.49-57.
27. IAEA-TECDOC-643, “Research Reactor Core Conversion Guidebook, Volume 4: Fuels”, International Atomic Energy Agency, Vienna, Austria (1992) pp. 1-547.
28. H. Shimizu, “The Properties and Irradiation Behavior of U_3Si_2”, NAA-SR-10621, Atomics International (1965) pp. 1-44.
29. R. Van Nieuwenhove, “Design report for the IFA-740 Westinghouse Irradiation Test on the fuel performance of U_3Si_2”, FC-Note 2074 (10 February 2010).
30. F. Poineau, G. W. C. Silva, C. B. Yeamans, G. S. Cerefice, A. P. Sattelberger, K. R. Czerwinski, "X-ray Absorption Fine Structure Spectroscopic Study of Uranium Nitrides," *J. Radioanal. Nucl. Chem.* 2012, ***292***, 898-994.
31. G. W. C. Silva, C. B. Yeamans, P. F. Weck, J. D. Hunn, G. S. Cerefice, A. P. Sattelberger, and K. R. Czerwinski, "Synthesis and Characterization of $Th_2N_2(NH)$ Isomorphous to Th_2N_3," *Inorg. Chem.* 2012, ***51***, 3332-3340.
32. G. W. C. Silva, C. B. Yeamans, A. P. Sattelberger, T. Hartmann, G. S. Cerefice, and K. R. Czerwinski, "Reaction Sequence and Kinetics of Uranium Nitride Decomposition," Inorg. Chem. 2009, **48**, 10635-10642.
33. G. W. C. Silva, C. B. Yeamans, G. S. Cerefice, K. R. Czerwinski, and A. P. Sattelberger, "Synthesis and Characterization of $(NH_4)_4ThF_8$ and ThNF," *Inorg. Chem.* 2009, ***48***, 5736-5746.
34. G. W. C. Silva, C. B. Yeamans, L. Ma, G. S. Cerefice, K. R. Czerwinski, and A. P. Sattelberger, "Microscopic Characterization of Uranium Nitrides Synthesized by Oxidative Ammonolysis of Uranium Tetrafluoride, " *Inorg. Chem.* 2009, ***48***, 5736-5746.
35. C. B. Yeamans, G. W. C. Silva, G. S. Cerefice, K. R. Czerwinski, T. Hartmann, A. K. Burrell, and A. P. Sattelberger, "Oxidative Ammonolysis of Uranium(IV) Fluorides to Uranium(VI) Nitride, " *J. Nucl. Mat.* 2008, ***374***, 75-78.
36. Development of LWR Fuels with Enhanced Accident Tolerance, Task 1 - Technical Concept Description, Award Number DE-NE0000566, January 31, 2013.

Appendix A List of Acronyms

AFD:	axial flux difference
AOO:	anticipated operational occurrences
ASI:	axial shape index
ASTM:	ASTM International, formerly known as the American Society for Testing and Materials
ATWS:	anticipated transient without scram
BDBA:	beyond design basis accident
BOC:	beginning of cycle
BU:	burn up
BWR:	boiling water reactor
CHF:	critical heat flux
CILC:	crud induced localized corrosion
CIPS:	crud induced power shift
CMC:	ceramic matrix composite
CSR:	contractile strain ratio
CVCS:	chemical volume control system
CVD/CVI:	chemical vapor deposition/chemical vapor infiltration
DBA:	design basis accident
DNB:	deviation from nucleate boiling
DNBR:	deviation from nucleate boiling ratio
EBC:	environmental barrier coating
ECCS:	emergency core cooling system
EFPD:	effective full power day
EOC:	end of cycle
EOL:	end of life
FA:	fuel assembly
FAI:	Fauske & Associates, LLC
FCC:	fuel cycle cost
FdH:	enthalpy rise hot channel factor
FEM:	finite element method
Fq:	peak heat flux hot channel factor
FW:	feedwater
Fz:	axial peaking factor
HFP:	hot full power
HM:	heavy metal
H/HM:	Hydrogen to heavy metal ratio
HZP:	hot zero power
ID:	inner diameter
IFBA:	integral fuel burnable absorber
LANL:	Los Alamos National Laboratory
LIS:	laser isotope separation
LOCA:	loss of coolant accident
LTR/LTA:	lead test rod/lead test assembly
LWR:	light water reactor
MAAP:	Modular Accident and Analysis Program
MDNBR:	minimum departure from nucleate boiling ratio
MSLB:	main steam line break
MSS:	main steam system
MTC:	moderator temperature coefficient

MWe:	megawatt electric
MWt:	megawatt thermal
NRC:	Nuclear Regulatory Commission
OD:	outer diameter
PIE:	post irradiation examination
PCI:	pellet clad interaction
PCMI:	pellet clad mechanical interaction
PCT:	peak cladding temperature
PRZ:	pressurizer
PVD:	physical vapor deposition
PWR:	pressurized water reactor
RCCA:	rod cluster control assembly
RCP:	reactor coolant pump
RCS:	reactor cooling system
RFA:	robust fuel assembly
RIA:	reactivity initiated accident
SBO:	station blackout event
SG:	steam generator
SiC/SiC CMC:	Silicon Carbide fiber/Silicon Carbide matrix ceramic matrix composite
SRP:	Standard Review Plan
SWU:	separate work unit
TAMU:	Texas A&M University
TH:	thermal hydraulic
TMI-2:	Three Mile Island Unit 2
UF_6:	Uranium Hexafluoride
UN:	Uranium Nitride
U_3Si_2:	Uranium Silicide
10CFR50:	Part 50 of Title 10 of the Code of Federal Regulation

Award Number DE-NE0000566

Development of LWR Fuels with Enhanced Accident Tolerance
Task 3: Licensing Plan for Accident Tolerant Fuel

RT-TR-13-19
September 30, 2013

Westinghouse Electric Company LLC
1000 Cranberry Woods Drive
Cranberry Woods, PA 16066

Principal Investigator: Dr. Edward J. Lahoda
Project Manager: Frank A. Boylan
Author: Nicole T. Brichacek

Southern Nuclear Company
42 Inverness Center Parkway
Birmingham, AL 35242
Authors: Ronald G. Cocherell and Ryan M. Joyce

Team Members

Edison Welding Institute
General Atomics
Idaho National Laboratory
Los Alamos National Laboratory
Massachusetts Institute of Technology
Southern Nuclear Company
Texas A&M University
University of Wisconsin
Westinghouse Electric Company LLC

TABLE OF CONTENTS

EXECUTIVE SUMMARY

The strategy required to license and commercialize the Westinghouse Electric Company LLC's Accident Tolerant Fuel (ATF) is outlined in this report. This strategy focuses on licensing and commercialization in the United States. However, similar challenges may exist in other countries. Licensing challenges outside of the United States are not considered as part of this report. An analysis was performed as part of Task 1 of the ATF program to identify areas critical to the development and potential commercialization of ATF [1]. The analysis performed during Task 1 included discussion of potential Nuclear Regulatory Commission (NRC) requirements for ATF, proposed specifications and architectures of the fuel and cladding, as well as preliminary analysis of the ATF performance and accident tolerant features. Task 2 of the ATF program outlined the research and development (R&D) work required to implement the ATF fuel and cladding concepts in commercial reactors [2]. This report, Task 3 of the ATF program, outlines the licensing actions and timeline associated with implementation of ATF at commercial reactors. The licensing work associated with full region implementation of ATF includes the following areas:

- In-pile and out-of pile testing
- Code development and code updates
- Exemption Requests from current regulations governing fuel cladding and pellet materials
- Topical report submittals to the NRC for review and approval
- Rulemaking to relax current requirements within the regulations that would prevent the implementation of ATF in a full core configuration

Projected costs associated with this project account for all of the following:

- Testing
- Code development and code updates
- Engineering work associated with writing the topical reports and responding to RAIs
- NRC fees associated with the review topicals and work to support defense of approvals to the Advisory Committee on Reactor Safeguards (ACRS)

The costs associated with the licensing of ATF provided in this report do not account for activities associated with rulemaking. In total, the cost associated with the aforementioned activities is approximately $75 million over the course of 21 years. The cost and associated timeframe is based on a lead test rod (LTR) load date of 2022 with full batch implementation occurring in the 2034 timeframe.

Licensing of ATF is feasible. While there are significant challenges to overcome, based on past and on-going licensing activities associated with fuel changes, these challenges can be overcome. Overcoming these challenges to meet the aggressive schedule outlined here will require successful coordination between industry and the NRC.

Acknowledgment: This material is based upon work supported by the Department of Energy under Award Number DE-NE0000566.

Disclaimer: This report was prepared as an account of work sponsored by an agency of the United States Government. Neither the United States Government nor any agency thereof, nor any of their employees, makes any warranty, express or implied, or assumes any legal liability or responsibility for the accuracy, completeness, or usefulness of any information, apparatus, product, or process disclosed, or represents that its use would not infringe privately owned rights. Reference herein to any specific commercial product, process, or service by trade name, trademark, manufacturer, or otherwise does not necessarily constitute or imply its endorsement, recommendation, or favoring by the United States Government or any agency thereof. The views and opinions of authors expressed herein do not necessarily state or reflect those of the United States Government or any agency thereof.

1 INTRODUCTION

As part of the development of a credible technical concept for new, advanced light water reactor (LWR) fuels with enhanced accident tolerance, a licensing strategy is required. Currently there is no comprehensive plan available for the licensing of non UO_2/Zr alloy nuclear fuels and cladding. This document outlines the strategy for overcoming the hurdles associated with the licensing of a new advanced fuel and cladding composed of materials other than zirconium-based alloys and uranium-oxide (UO_2) fuel in the United States. There are many operating advantages and safety extensions associated with the advanced ATF concepts. Modifications to the current regulatory bases, establishing new acceptance criteria, and confirmatory testing are required to unlock these considerable advantages. The contents of this report address these modifications that will be required and identify the regulatory risks associated with this project. This report focuses solely on the United States' licensing environment and does not address challenges that might exist in other countries wishing to implement ATF in the future.

Implementation of these ATF designs will occur through four major phases. Phase 0 consists of the pre-work required prior to loading of LTRs into commercial reactor cores. The licensing process and key tasks associated with Phase 0 are discussed in Section 4. Key tasks associated with Phase 1, the LTR phase of the program, are outlined in Section 5. Section 6 covers licensing actions required as part of LTA implementation slated to occur during Phase 2. Testing, inspections and examinations expected to occur during Phases 0 through 2 are also discussed within each respective section. Phase 3 is discussed in Section 7 and focuses on the NRC submittal required by vendors and utilities for use of ATF in full region implementation. Additionally, Phase 3 focuses on the regulatory modifications such as rulemaking that should occur prior to full batch reloads.

In order to license and obtain approval for ATF in full regions, proper scheduling must occur to align with the regulatory timeframes associated with regulation modifications. Section 8 contains a preliminary licensing schedule for the tasks required to obtain NRC approval for ATF designs. The projected cost estimate of such work is presented in Section 9.

The licensing strategy documented herein is based on similar, successful licensing of new cladding material. However, similar programs utilized zirconium-based cladding and therefore did not require as many regulatory actions. There are a number of risks associated with the introduction of ATF, as discussed in Section 3, but the advantages of ATF counterbalance the risks associated with its licensing and final implementation.

2 BACKGROUND

2.1 CURRENT FUEL DESIGNS

The fuel currently used in commercial nuclear reactors consists of UO_2 fuel pellets stacked inside of a zirconium-based cladding tube. These tubes are then bundled into square arrays held in place by support and mixing grids, also made of zirconium-based alloys, to form a full assembly. The following sections provide additional details on the design of the pellets, rods and fuel assemblies currently in use.

2.1.1 UO_2 Fuel Pellets

Fuel pellets used in today's fuel designs are made of uranium dioxide enriched in U-235. Currently the maximum enrichment limit for commercial light water reactor fuel is 5 wt% U-235. These pellets are cylindrical in shape and made of a ceramic to mitigate the effects of the high temperature environment of the fuel rod and reactor core. While the ceramic pellets have high heat tolerance to melting, these pellets are prone to swelling and expansion. To account for this, pellets are dished and chamfered to ensure uniform swelling and densification during irradiation. After the UO_2 is properly enriched and formed into cylindrical pellets, the pellets are stacked on top of each other into a hollow tube made of a zirconium-based alloy to form a fuel rod.

2.1.2 Fuel Rods

Fuel rods are cylindrical tubes, which are sealed at both ends and contain the fuel pellets. The tubing is made from a zirconium-based alloy to maximize heat transfer while minimizing neutron absorption. Its main purpose is to keep the fuel pellets and fission gases that result from nuclear fission contained within the rod and to maintain a coolable geometry in case of a design basis accident such as a loss of coolant accident (LOCA).

The major components inside of the zirconium-based cladding of the fuel rod are the enriched fuel pellets, the plenum, and helium gas. The fuel pellets contain the fissile material needed to maintain the nuclear chain reaction used in commercial nuclear power plants to heat the water and eventually produce steam and electricity. Above the stack of fuel pellets is the plenum, which contains a plenum spring. This spring holds the pellets down during transport and handling and provides support as the pellets expand. Additionally the plenum provides an area inside the hermetically sealed tube to hold fission gases released during reactor operation. Lastly, the fuel rod is backfilled with helium gas. Helium gas improves heat conduction out of the fuel pellet and into the cladding across the pellet-cladding gap.

2.1.3 Fuel Assemblies

After the fuel pellets are loaded into the fuel rod, the rods are placed into an array to form a fuel assembly. These arrays can vary in size from 14x14 lattices to 17x17 lattices. The arrays are held in place with the support of grids placed incrementally over the height of the assembly. In addition to providing support for the fuel rods, these grids also provide mixing around the fuel rods to increase cooling capability and limit the potential for the rods to go into departure from nuclear boiling (DNB). Within the array of fuel rods are guide tubes, which provide support to the fuel assembly and maintain an opening for

control rods to insert during accidents and reactor shutdowns. The number of guide tubes ranges from 5 to 25 depending on the fuel design type and lattice array. Fuel rods and guide tubes sit on a component referred to as the bottom nozzle and sit beneath the top nozzle. The top and bottom nozzles are attached to the guide tubes and form the fuel assembly skeleton, which also plays a large role in the structural integrity of the assembly. The assemblies are loaded into the reactor core and used to produce the energy required by the Rankine cycle to create electricity. Current burnup limits for the highest duty fuel rods in a standard fuel assembly is between 60,000 and 62,000 MWD/MTU (megawatt days/metric ton uranium).

2.2 ACCIDENT TOLERANT FUEL DESIGN

There are two main differences between the current fuel designs described in Section 2.1 and ATF, both of which stem from material differences. These differences exist in the form of modifications to materials used in cladding and fuel pellet composition. With the exception of the material used in these two components, all of the features of ATF remain consistent with those of fuel currently in use. If in the future a higher burnup or higher enrichment limit is requested, additional licensing work will be required.

2.2.1 Accident Tolerant Fuel Cladding

Currently two different cladding types are being investigated for use in ATF designs: SiC_f/SiC_m Ceramic Matrix Composite (CMC) and Zr alloy coated cladding.

SiC_f/SiC_m CMC cladding consists of SiC fiber reinforced SiC composites; a two or three-layer tube of high purity beta or alpha phase stoichiometric silicon carbide covered by a central composite layer of continuous beta phase stoichiometric silicon carbide fibers infiltrated with beta phase SiC and, in the case of three layers, an outer protective layer of fine grained beta phase silicon carbide. Zr alloy coated cladding investigations currently consist of evaluating the performance of two separate coatings: Ti_2AlC known as MAX Phase, and an amorphous stainless steel known as NanoSteel^{TM}. The coatings consist of fine particles of the coating materials that are sprayed onto the outside surface of the zirconium alloy rod at high velocity to form a 10 to 20 micron thick layer.

2.2.2 Accident Tolerant Fuel Pellets

Similar to the cladding, there are two different pellet types currently under investigation for use in ATF:

1. UN pellets which have been waterproofed by the addition of U_3Si_2 or UO_2 using N enriched to >90% ^{15}N.
2. U_3Si_2 pellets.

3 LICENSING ENVIRONMENT

To be in compliance from a licensing point of view, licensees must meet the requirements of a number of NRC rules and regulations governing the design and implementation of fuel used in commercial power reactors. These rules are documents in Title 10 of the Code of Federal Regulations (10 CFR). Title 10 specifically deals with the Energy sector. In addition to the requirements captured in the 10 CFRs, a number of other recommended guidelines are captured in Nuclear Regulations (NUREG). The main NUREG of interest for fuel designs is NUREG-0800, Sections 4.2-4.4. The NRC also issues documents referred to as Regulatory Guides (RG), which help to provide additional guidance on what needs to be included in documents seeking NRC review and approval. Currently there are two draft RGs that have the potential to impact this program. The requirements of each of these regulations and guidance documents are captured in the following sections. These regulations explicitly deal with the properties and failure mechanisms associated with zirconium-based cladding and therefore may not be applicable to the higher performing ATF in the future.

Additionally, each utility wishing to implement ATF will need to review the plant licensing basis for the facility to see if additional requirements must be addressed. Utilities should review plant Technical Specifications (TS) as well as the Final Safety Analysis Report (FSAR), at a minimum, for each unit wishing to use ATF and take the actions necessary to update these accordingly.

3.1 CODE OF FEDERAL REGULATIONS, TITLE 10

3.1.1 10 CFR Part 100

This regulation requires analyses to be performed to ensure that during a postulated accident the dosage to those outside the exclusion zone will be within regulatory limits. Specifically, reactors are currently licensed such that no persons outside of the exclusion zone will receive a dose greater than 1500 mREM during a postulated accident.

3.1.2 10 CFR Part 50.44

10 CFR 50.44 requires that the amount of combustible gas present in a containment structure be limited and monitored to ensure that the structural integrity of the containment is maintained. Under accident conditions with Zr clad fuels, the gas of main concern is hydrogen (H_2) that is released as part of the high temperature zirconium/water reaction.

3.1.3 10 CFR Part 50.46

This regulation governs the Emergency Core Cooling System (ECCS) design requirements in the event of a loss of coolant accident (LOCA). Based on the requirements of this regulation, there are five main design requirements for nuclear fuel used in commercial reactors, as specified in part c of the regulation:

1. The maximum fuel cladding temperature cannot exceed 2200°F.
2. The local cladding oxidation shall not exceed 17% of the total cladding thickness before oxidation. This assumes zirconium is converted to ZrO_2 locally on the cladding wall.

3. The maximum hydrogen generated shall not exceed 1% of the theoretical amount of hydrogen that could be generated during a steam-zirconium reaction in which all of the cladding surrounding the fuel pellets was to react excluding the cladding around the plenum volume.
4. Changes to core geometry shall not affect the ability to cool the core.
5. Long-term cooling of the core will be such that the fuel temperature will be maintained at an acceptably low value and decay heat will be removed for the duration of time required by the long-lived radioactivity remaining in the core.

3.1.4 10 CFR Part 50 Appendix A

10 CFR Part 50, Appendix A contains all of the General Design Criteria (GDC). GDCs are the minimum requirements that need to be met. The GDCs that are specifically applicable to fuel design are GDC 10-13, 20, and 25-28. These GDCs collectively hold that the fuel design criteria remain intact during all normal operations and anticipated operational occurrences (AOOs). Additionally, these design criteria are contained within the licensing basis of most reactors, as they are typically included in Chapter 3 of the plant FSAR. The following criteria are taken directly from 10 CFR Appendix A.

GDC 10 – Reactor Design

The reactor core and associated coolant, control, and protection systems shall be designed with appropriate margin to assure that specified acceptable fuel design limits are not exceeded during any condition of normal operation, including the effects of anticipated operational occurrences.

GDC 11 – Reactor Inherent Protection

The reactor core and associated coolant systems shall be designed so that in the power operating range the net effect of the prompt inherent nuclear feedback characteristics tends to compensate for a rapid increase in reactivity. (This is negative feedback on a power transient).

GDC 12 – Suppression of Reactor Power Oscillations

The reactor core and associated coolant, control, and protection systems shall be designed to assure that power oscillations which can result in conditions exceeding specified acceptable fuel design limits are not possible or can be reliably and readily detected and suppressed.

GDC 13 – Instrumentation and Control

Instrumentation shall be provided to monitor variables and systems over their anticipated ranges for normal operation, for anticipated operational occurrences, and for accident conditions as appropriate to assure adequate safety, including those variables and systems that can affect the fission process, the integrity of the reactor core, the reactor coolant pressure boundary, and the containment and its associated systems. Appropriate controls shall be provided to maintain these variables and systems within prescribed operating ranges.

GDC 20 – Protection System Functions

The protection system shall be designed (1) to initiate automatically the operation of appropriate systems including the reactivity control systems, to assure that specified acceptable fuel design limits are not

exceeded as a result of anticipated operational occurrences and (2) to sense accident conditions and to initiate the operation of systems and components important to safety.

GDC 25 – Protection System Requirements for Reactivity Control Malfunctions

The protection system shall be designed to assure that specified acceptable fuel design limits are not exceeded for any single malfunction of the reactivity control systems, such as accidental withdrawal (not ejection or dropout) of control rods.

GDC 26 – Reactivity Control System Redundancy and Capability

Two independent reactivity control systems of different design principles shall be provided. One of the systems shall use control rods, preferably including a positive means for inserting the rods, and shall be capable of reliably controlling reactivity changes to assure that under conditions of normal operation, including anticipated operational occurrences, and with appropriate margin for malfunctions such as stuck rods, specified acceptable fuel design limits are not exceeded. The second reactivity control system shall be capable of reliably controlling the rate of reactivity changes resulting from planned, normal power changes (including xenon burnout) to assure acceptable fuel design limits are not exceeded. One of the systems shall be capable of holding the reactor core subcritical under cold conditions.

GDC 27 – Combined Reactivity Control and Systems Capability

The reactivity control systems shall be designed to have a combined capability, in conjunction with poison addition by the emergency core cooling system, of reliably controlling reactivity changes to assure that under postulated accident conditions and with appropriate margin for stuck rods the capability to cool the core is maintained.

GDC 28 – Reactivity Limits

The reactivity control systems shall be designed with appropriate limits on the potential amount and rate of reactivity increase to assure that the effects of postulated reactivity accidents can neither (1) result in damage to the reactor coolant pressure boundary greater than limited local yielding nor (2) sufficiently disturb the core, its support structures or other reactor pressure vessel internals to impair significantly the capability to cool the core. These postulated reactivity accidents shall include consideration of rod ejection (unless prevented by positive means), rod dropout, steam line rupture, changes in reactor coolant temperature and pressure, and cold water addition.

3.1.5 10 CFR Part 50, Appendix K

Appendix K gives the allowable means to calculate emergency core cooling system (ECCS) needs due to a loss of coolant accident (LOCA). This Appendix lists the applicable methods and equations that are available for use to calculate the ECCS needs during a LOCA without further review by the NRC.

3.2 REGULATORY GUIDES

Regulatory Guides (RG) are used to give instruction to calculations and analyses of specific areas for nuclear power licensing, i.e. plume models for reactivity release. The RG is NRC approved methodology

that is meant as a guideline. These guidelines are meant to help facilitate the licensing process by increasing efficiencies when dealing with common calculations and common problems or questions that arise during licensing.

Currently one main RG, NUREG-0800, is of interest to the fuel design used in commercial reactors. Sections 4.2 through 4.4 of the Standard Review Plan (SRP) are a guideline for review by the NRC when licensing fuel system design, nuclear design, and thermal and hydraulic design. From these sections the needed documentation and analyses can be ascertained. These documents and analyses ensure that the requirements of the codes of federal regulations are followed when licensing a new fuel, cladding, or geometry.

These sections of the SRP are also directly reflected in Chapter 4 of most plant FSARs and therefore create a portion of the licensing basis for the operating fleet, and should be followed whenever possible. Deviation from the guidance is allowed, provided adequate justification for alternate methods is presented to and accepted by the NRC.

3.2.1 NUREG-0800, Section 4.2, "Fuel Systems Design"

Fuel system design is divided into four sections. These four sections are "Design Basis", "Descriptions and Design Drawings", "Design Evaluations", and "Testing, Inspection and Surveillance Plans." The first, "Design Basis", is used when determining the limiting values for important parameters so that damage is limited to acceptable levels. The second, "Descriptions and Design Drawings", is used when reviewing fuel systems and places an emphasis on product specifications. The third, "Design Evaluation" is used to evaluate and ensure that "Design Bases" are met during normal operation, AOOs, and postulated accidents. Finally, "Testing, Inspection, and Surveillance Plans", ensures that before, during and after irradiation, all requirements that have been set forth in the previous three areas have been and will continue to be met.

3.2.2 NUREG-0800, Section 4.3, "Nuclear Design"

The nuclear design is used to develop many of the analyses performed on the core where core performance analyses are concerned. This section is used to confirm the design bases established by the GDC are met. Specifically the neutronics are important here. From this section the core power distribution, reactivity coefficients, control requirements, rod patterns and reactivity worths, criticality, and pressure vessel irradiation can be determined. Finally the analytical methods used to determine many of the above criteria are addressed.

3.2.3 NUREG-0800, Section 4.4, "Thermal and Hydraulic Design"

The thermal and hydraulic (T&H) design section is used to determine the computer calculations that are needed to substantiate reactor analyses. Furthermore, the correlation of experimental data and verification of process and phenomena applied to reactor design are also included. This section is not as in depth as SRP 4.2 but is useful when determining the T&H portion of the licensing approach.

3.3 DRAFT REGULATORY GUIDES

3.3.1 DG-1261, "Conducting Periodic Testing for Breakaway Oxidation Behavior"

This draft RG deals with the testing required with respect to "breakaway oxidation" as it relates to the provisions of 10 CFR 50.46c. Because of the current fuel design, this document predominantly focuses on zirconium-based cladding and the requirements associated with it. However, similar requirements may be imposed on ATF cladding.

3.3.2 DG-1262, "Testing for Postquench Ductility"

This draft RG describes an approved technique for measuring ductile-to-brittle transition for a zirconium-based cladding material, as required by 10 CFR 50.46c. Postquench Ductility (PQD) predominantly focuses on zirconium cladding; however similar requirements may be required for ATF fuel as part of the licensing process.

Additional discussion regarding the implementation of the requirements of these draft RGs can be found in Section 4.1.

3.4 REGULATORY RISKS

Currently many unresolved regulatory risks exist that could have a significant impact on the licensing strategy associated with ATF. These risks fall into two categories; the first being regulation based and the second being process based.

3.4.1 Regulation Based Risks

The NRC is currently going through the rulemaking process for new requirements related to the requirements documents in 10 CFR 50.46. This new "LOCA Rule" will inevitably change the amount of oxidation allowed during long-term core cooling that occurs following a LOCA. While ATF shows significantly less oxidation, the resolution of this rulemaking could have a major impact on the marketability and need for ATF. Prolonged rulemaking could also potentially delay the approval of ATF designs, because the final rule could introduce additional changes that challenge the proposed ATF cladding concept.

In addition to the rulemaking associated with 10 CFR 50.46 that is currently underway, new reactivity initiated accident (RIA) limits are also being proposed by the NRC. This new rule limits the amount of hydrogen pick-up to limit the loss of ductility on the fuel. While this shouldn't impact the ATF process for SiC_f/SiC_m cladding, rulemaking resolution now could impact the future rulemaking required to implement ATF using coated Zr with respect to cladding ductility.

3.4.2 Process Based Risks

Licensing of a new fuel design cannot occur in a vacuum. Instead, the entire fuel process must be evaluated, considered and licensed accordingly. Therefore, risks exist with the activities associated with transportation and long and short term storage of the ATF. Recent experiences and communications with

the NRC have revealed that new fuel products and designs will have to be flexible enough to address a variety of backend of the fuel cycle options. While these issues are currently beyond the scope of this document, the risks need to be considered moving forward. Note however, that if ATF can be shown to behave as well as or better than current Zr/UO_2 fuels in terms of physical properties and reaction with environmental conditions, then this risk may be minimized. In addition, just about any version of ATF that increases performance also dramatically reduces the amount of spent fuel that is discharged per kilowatt of electricity produced.

A large number of Westinghouse topical reports will need to be resubmitted and reviewed. However, due to the long timeline needed for testing, analysis and reporting, any schedule risk due to implementation of a "Prioritization Process" by the NRC for review of the topical reports can be minimized if topical reports are resubmitted in parallel with the testing when possible.

3.5 FUTURE REGULATORY ACTIONS

Prior to full scale implementation of ATF, changes to a number of regulations will be required. While Phase 1 and 2 can be completed with the use of exemption requests, to move towards a more efficient loading process and implementation plan, rulemaking will be needed to remove the references to "zirconium-based" cladding and UO_2 pellets. In particular, rulemaking will be required to modify the requirements contained in 10 CFR 50.46 and 10 CFR 50, Appendix K. Additionally, the specified acceptable fuel design limits (SAFDLs) may also need to be modified, resulting in the need for a modification to GDC 10.

10 CFR 50.46

10 CFR 50.46 specifically calls out Zircaloy and ZIRLO® cladding in the regulation. In order to extend this regulation to other cladding types, such as those being proposed for use in ATF, rulemaking will need to occur to remove this specificity.

10 CFR Part 50, Appendix K

This regulation takes into account the impact of both UO_2 and zirconium-based cladding alloys on LOCA analysis and requirements. In order to extend applicability of this regulation to the fuel and cladding types under development for use in ATF, rulemaking will need to occur.

The rulemaking process can be quite lengthy and therefore must be accounted for in the overall licensing schedule. After rulemaking begins, the public has 75-90 days to comment on the proposed rule and/or rule change. Once public comments are received, the NRC reviews the comments and makes appropriate changes. Depending on the magnitude of the change, an additional public comment period may occur. After all comments have been resolved, the rule is sent for final approval and publication. The rule usually becomes effective 30 days after publication in the Federal Register. While the process can take as little as 6 months, it can also take a number of years before the rule is finalized.

ZIRLO® is a trademark or registered trademark of Westinghouse Electric Company LLC, its Affiliates and/or its Subsidiaries in the United States of America and may be registered in other countries throughout the world. All rights reserved. Unauthorized use is strictly prohibited. Other names may be trademarks of their respective owners.

4 PHASE 0 – PRE – LEAD TEST ROD ACTIVITIES

Prior to the loading of rods or assemblies into a commercial reactor, a large amount of development work and testing must take place. Results from the testing provide the necessary data for claiming safe operation is achievable in a commercial reactor and that no substantial safety hazards will be introduced.

4.1 PROTOTYPE TESTING

Before loading ATF into any type of reactor, samples of the materials must be tested to obtain out-of-pile data that is needed to support the licensing requirements for new fuel and new cladding. In addition to the current types of data required for new fuel component material such as creep, growth and oxidation, two new draft RGs have been released with additional testing protocol and requirements.

DG-1261 discusses the need for periodic testing requirements for breakaway oxidation. Details are given regarding the types of testing that should be conducted as well as the appropriate way in which results should be reported to the NRC. Appendices to this RG contain procedures for testing zirconium-based alloys. While the CMC cladding may not be subject to these testing requirements, the Zr-coated cladding may be subject to the procedures contained within.

DG-1262 discusses testing requirements for PQD utilizing ring-compression testing for zirconium-based cladding. Similar to the applicability of DG-1261, the requirements of this RG may not include CMC cladding, Zr-coated cladding may be subject to the procedure and requirements identified within the document.

Similar growth and expansion testing will need to be conducted on the fuel pellet prototypes as well. These tests will need to confirm that pellet swelling is limited to a value that will not result in fuel failures from cracking, pellet-cladding interaction (PCI) or other contact related failure mechanisms.

4.2 TEST REACTOR IRRADIATION

ATF will most likely have significantly different operational properties from the current UO_2/Zr fuel types in use today. As such, significant basic data on ATF material properties in operating reactor environments will be required to support the analysis and model development required to license ATF.

Similar to the approach used on **Optimized ZIRLO™** High Performance Fuel Cladding Material, irradiation testing should occur on both fueled and unfueled rodlets. Irradiation of unfueled rods will provide the unconstrained growth and creep data that will be needed for future licensing actions as well as help to understand the characteristics of the ATF materials. Additionally, these tests will ensure the structural integrity and corrosion characteristics associated with irradiation environments.

Fueled rodlets should contain both types of pellets proposed for ATF as well as the standard UO_2 pellets to use as a control. This will provide preliminary data on the pellet behavior as well as provide for a

Optimized ZIRLO™ is a trademark or registered trademark of Westinghouse Electric Company LLC, its Affiliates and/or its Subsidiaries in the United States of America and may be registered in other countries throughout the world. All rights reserved. Unauthorized use is strictly prohibited. Other names may be trademarks of their respective owners.

comparative evaluation to be performed. In order to show the safety benefit of ATF, this type of data will need to be provided to the NRC prior to loading into a reactor core.

Upon completion of the test reactor program, preliminary results can be used to justify the safe operation of lead test rods, which will be required as part of the exemption requests needed in Phase 1.

In addition to irradiation testing of the materials, DNB testing and seismic testing will be needed to show there are no adverse consequences to nuclear safety by the introduction of these rods. While it is still uncertain, a new DNB correlation may be required based on grid design and fuel rod surface modifications. In order to develop this correlation prior to LTR and LTA loading, DNB and flow testing will need to be carried out on prototype rods and assemblies. Seismic testing will be needed as well to show that the rods can withstand the forces imposed during a Safe Shutdown Earthquake (SSE) or Seismic LOCA event.

In all of the Phase 0 testing, the fuel and cladding that is tested should be made using the processes and designs that will be used to make the final commercial product. Otherwise, the data developed from test reactors can be questioned as to its applicability to the final commercial product.

4.3 CODES AND MODEL ANALYSIS

Results from the prototype testing will be used to update current design codes and models so that the new fuel properties can be calculated and analyzed before LTR implementation. The new fuel and cladding will have different operational properties that must be accounted for in the standard fuel assembly. This will require new fuel and cladding, models and analyses.

For currently used LWR fuel, the codes (i.e. software) used to model fuel performance, fuel design, and fuel safety are intended for use with and for licensing of the Zr/UO_2 fuel system. Generally, for implementation of ATF, similar performance, design, and safety models will be required to test and license this fuel. Because the thermo-physical properties and possibly the fissile response of ATF are different and better than the Zr/UO_2 fuel system, the codes and the standards used will require significant modification or new code development. Code modification and/or new code development will require very large labor and financial investments, as captured in the cost estimates in Section 9.

Westinghouse uses many software products to model nuclear fuel in steady state and transient behavior. Some of the software applied by Westinghouse for fuel performance, design, and safety are presented in Table 1.

Table 1. Fuel performance, design, and safety codes currently used by Westinghouse.

Presently used codes	***purpose***	***ATF applicability***	***comments***
fuel performance			
PAD	single fuel rod performance	probable; requires appropriate material data	used for licensing, primary fuel performance code
STAV	single fuel rod performance	possible	used for US BWR licensing, has PWR fuel modeling capability
FRAPCON	single fuel rod performance	possible	not used for licensing, NRC audit code
Enigma	single fuel rod performance	possible	used for PWR licensing in UK
High Duty Drive	core wide fuel rod performance	possible	not used for licensing, used for corrosion calculations
VIPRE	fuel thermal hydraulics	possible, requires appropriate material data such as fuel thermal conductivity	used for licensing; EPRI code licensed by Westinghouse
STAR-CCM+	computational fluid dynamics	probable; requires appropriate material data	nonconfigurable code
ANSYS	finite element analysis with many applications	probable; requires appropriate material data	used for stress calculations, configurable code
fuel design			
ANC	neutronics core design	probable; requires appropriate material data	used for licensing, primary Westinghouse core design code
STAR-CCM+	computational fluid dynamics	probable; requires appropriate material data	nonconfigurable commercial code
ANSYS	finite element analysis with many applications	probable; requires appropriate material data	configurable commercial code
fuel safety			
ANC	version of ANC used in evaluating transients such as RIA	probable, requires appropriate material data	used for licensing
RELAP5	thermal hydraulic safety	probable; requires appropriate material data	commercial code
ASTRUM	Automated Statistical Treatment of Uncertainty Method, used for realistic large-break LOCA evaluation methodology	probable; requires appropriate material data	used for licensing

4.3.1 Fuel Performance Code Updates

For steady state fuel performance, Westinghouse applies the internally developed PAD code for NRC fuel licensing. PAD is a single fuel rod performance code incorporating different fuel behavior models such as cladding corrosion, cladding creep, fuel pellet swelling, fuel fission gas release, and many others. For test reactor experiments and subsequent licensing of ATF, the models comprising PAD and the data used to develop these models will require redevelopment. Table 2 offers a preliminary compilation of steady state cladding and fuel performance data required for redevelopment of various PAD models.

Table 2. Steady state cladding and fuel performance data required for applying the fuel performance code PAD to ATF

cladding data	**associated PAD model**	**fuel data**	**associated PAD model**
cladding corrosion rate	corrosion	fuel densification	pellet – clad interaction
cladding creep rate	creep	fuel swelling	pellet – clad interaction and clad strain
cladding creep rate	pellet – clad interaction	fuel fission gas release	rod internal pressure
cladding irradiation damage	mechanical property change	fuel temperature	fuel melt and feedback to core physics code
cladding elongation	dimensional change	fuel rod length	fuel assembly sizing

For the development and subsequent licensing of ATF, NRC accepted fuel performance, design, and safety codes should be applied whenever possible. If required, FRAPCON modifications can be supplied to the NRC to enable NRC audit calculations of ATF designs.

Other fuel performance codes are used for modeling specific fuel performance phenomena. For example, STAR-CCM+ is used to model the T&H performance of fuel. Generally this code is not used for NRC licensing of fuel. However, this code is extremely useful in developing and predicting the T&H behavior of ATF cladding and fuel. For application of this code, data such as cladding surface roughness and thermal conductivity of both fuel and cladding is required.

4.3.2 Nuclear Design Codes

Similar to PAD, ANC is the Westinghouse internally developed steady state code used for neutronics design in NRC licensing of nuclear fuel. For application to ATF, ANC will require data detailing the neutronics behavior of the ATF fuel used. For application of ANC to ATF fuels, known cross-sections for U, Si and N can be used. For UN, using the desired enrichment in the ^{15}N isotope will also be required. There should be cross-sections for Si and N available that are then included in the code input. The main objective would be optimization of the ^{15}N enrichment.

4.3.3 Fuel and Mechanical Design Codes

STAR-CCM+ and ANSYS are both commercially available software with many applications in fuel design. Some of these applications include coolant fluid flow, fuel heat transfer, mechanical or structural fuel assembly design, fuel assembly component design, and fuel rod mechanical behavior. STAR-CCM+ is nonconfigurable software making it limited in applications such as repeatable design calculations. However, STAR-CCM+ is very useful in predicting the behavior of designs or design modifications making it very useful for reducing the number of experiments required to confirm design behavior. ANSYS is a configurable code and allows for the development of repeatable fuel behavior routines. In this way ANSYS is more useful in developing designs for licensing in that various design behaviors (i.e.; mechanical, thermal, etc.) can be evaluated using verified behavior routines. Much of the data required for application of this software is the same as that presented in Table 2.

4.3.4 Safety-Related Codes

The fuel safety-related codes applied by Westinghouse include ANC, RELAP5, and ASTRUM. These codes are used to model various fuel safety transients such as RIA, DNB, and LOCA. For application of these codes to ATF during safety transients, significant amounts of ATF data during these postulated accidents are required. As an example, the thermal conductivity of both ATF cladding and fuel are required to model an RIA. To model ATF during DNB, again thermal conductivity and various surface properties of ATF cladding are required. Significant effort and funding will be required to collect the required ATF safety behavior data and then modify the different fuel safety codes.

Once the new models have been completed, they will need to be resubmitted to the NRC for evaluation and acceptance, as will be discussed in Phase 3.

Preliminary data from the test reactor can be used to perform necessary analyses for LTR and LTA implementation during Phases 1 and 2.

4.4 MANUFACTURABILITY

The manufacturing challenges for CMC tubing associated with tube length and cladding thickness will be addressed before LTR or LTA implementation. Fuel fabrication facilities will also need to install and qualify equipment to process the new fuel pellet. Because of the licensing requirements of Part 72 facilities, additional licensing may be required for manufacture of U_3Si_2 and U_3Si_2-doped pellets. However these fuel facility licensing issues are beyond the scope of this licensing strategy and will be handled at a later time.

5 PHASE 1 – LEAD TEST ROD ACTIVITIES

5.1 EXEMPTION REQUESTS

The number of LTRs per core will be approximately 30 rods distributed among four assemblies, which is well within the "limited number" listed in most plant TS. Because regulations governing fuel design and analysis are all written in terms of zirconium-based cladding and UO_2 fuel pellets, utilities wishing to implement LTRs in the reactor core will need to file exemption requests with the NRC prior to fuel load and start up. Ideally, at least two plants would operate with a limited number of LTRs. Utilities interested in participating will need to confirm that the plant specific TS allow for LTAs and lead use assemblies (LUAs) in non-limiting locations.

Interested utilities will need to file exemptions from at least 10 CFR 50.46 and potentially Appendix K, depending on the LOCA Analysis of Record (AOR). Other exemption requests may be required to address the departure from UO_2 fuel pellets. These exemption requests will need to be filed at least two years prior to LTR loading. Two years is approximately the average time it takes the NRC to review and approve and exemption requests. Adequate data must exist from Phase 0 to provide support and justification for safe operation of the reactor with ATF LTRs.

5.2 INSPECTION AND TESTING

Upon receiving NRC approval for implementation of LTRs in the core, the reactor will operate as it normally would during any cycle. During the refueling outage, preliminary inspections will be carried out on the LTRs in the form of Post Irradiation Exams (PIEs). These tests will consist of both visual inspections and measurements. PIEs will continue to occur during refueling outages to collect necessary irradiation data from the LTRs.

When the assembly containing the LTRs reaches its design limit, the LTRs will be sent for hotcell examination to obtain additional, more detailed data regarding the performance of ATF under reactor conditions. Data should be taken from more than one LTR to account for process or product variability, meaning that at least two hotcell evaluations should be conducted on LTRs from at least two different reactor cores.

Preliminary data obtained from the LTR phase will be used to move forward into the LTA phase, Phase 2. In order to minimize the delay in submitting the LTA exemption request, intermediate PIEs will be carried out after each of the cycles. This will provide data that can be used to prepare the LTA exemption request and perhaps serve as a basis for the early submission of an exemption request if the early PIE data indicates performance as the design intends. This approach implies the use of the largest number of LTRs as is feasible to provide a sufficient number of LTRs that reach full burnup.

Data obtained during this phase of the process will also go into the code development required to support Phase 2. Additional data will continue to be obtained to further refine the models and data used in code development.

6 PHASE 2 – LEAD TEST ASSEMBLY ACTIVITIES

6.1 EXEMPTION REQUESTS

Similar to the LTR process, exemption requests from NRC regulations regarding cladding and fuel pellet material will be required during the LTA phase. As with the LTRs, these exemption requests will need to be filed 2 years in advance of LTA load. Data collected from the preliminary LTR PIE exams and the prototype testing will be used to justify loading of LTAs into reactor cores. LTAs should be loaded into non-limiting locations of the reactor core so as to not violate plant Technical Specification (TS). Additionally, LTAs should be irradiated in more than one reactor if possible. Utilities interested in loading ATF LTAs will need to confirm that this is allowable per plant specific TS.

6.2 ENGINEERING REPORT

To facilitate the licensing activities and engineering work required of the utility, Westinghouse will provide an LTA Engineering Report. This report covers the technical justification for analysis and evaluations carried out in support of reload calculations related to the LTAs. The LTA report also discusses how regulatory requirements continue to be met even with the presence of LTAs in the core. This document is not meant to be a licensing report sent to the NRC, but is instead intended to provide input for the licensing actions that are required of the utility.

In order to provide the technical justification, sufficient code development work will have to be completed prior to and during Phase 2 to ensure codes and models appropriately reflect the behavior of ATF in reactor conditions. Code modifications completed during this phase will ultimately go to support the submittal of licensing topical reports in Phase 3 of the process.

6.3 INSPECTION AND TESTING

As with the LTRs, a number of inspections, examinations and testing will be conducted on the LTAs in the reactor core. PIE exams will be carried out after each cycle of operation to capture both visual and measurement data.

After reaching the peak rod licensed burnup limit of 62,000 MWD/MTU, LTAs will be sent for hotcell examination to obtain additional, more detailed data regarding the performance of ATF under reactor conditions. Data should be taken from more than one LTA to account for process or product variability, meaning that at least two hotcell evaluations should be conducted on LTAs from at least two different reactor cores.

Data collected from post irradiation inspection and testing will be used to update the analysis codes and methods and for input into the fuel mechanical design topical report, which will be finalized as part of Phase 3. As with the LTRs, in order to minimize the delay in submitting the fuel mechanical design topical report, intermediate PIEs will be carried out after each of the cycles. This will provide data that can be used to prepare the topical report and perhaps serve as a basis for the early submission if the early PIE data indicates performance as the design intends. This approach implies the use of the largest number of LTAs (up to 8 per unit) as is feasible to provide a sufficient number of LTAs that reach full burnup.

7 PHASE 3 – TOPICAL REPORT UPDATES AND SUBMITTALS

Currently all Westinghouse safety analysis and core design codes are written to address UO_2 fuel pellets in a zirconium-based cladding material. To continue to accurately analyze and predict behavior of fuel in reactor, these codes will need to be updated to reflect the change in material properties and behaviors associated with ATF.

7.1 SAFETY ANALYSIS AND CORE DESIGN CODES

Because all operating reactor fuel is currently based on the UO_2/Zr design, all Westinghouse analysis codes are currently designed to only handle this combination of fuel components. In order to move to the full implementation phase, these codes and their associated manuals will need to be updated so that the irradiation behavior of ATF is accurately modeled in safety calculations, as discussed in Section 4.3. As part of this phase, all safety analysis code updates will need to be finalized to confirm they accurately capture the impact of the new fuel. Additionally, the topical reports submitted to the NRC for approval of these codes will also need to be updated to reflect this change. These updated codes and reports will then need to be resubmitted to the NRC for review and approval to extend applicability to ATF fuel and its properties.

7.2 FUEL MECHANICAL DESIGN REPORT

Westinghouse typically uses the Fuel Checklist Evaluation Process (FCEP) to make fuel modifications under 50.59 for minor changes to approved fuel designs. However, the change to ATF will require the submittal of a topical report containing a large amount of design and test data before full region implementation begins. This report will contain all of the design specifications and drawings as well as the structural analyses performed as part of the testing process in the previous 3 phases. Upon approval of this report and all of the safety analysis code reports, utilities will be able to load ATF in full regions.

8 LICENSING STRATEGY TIMELINE

The proposed Licensing strategy is presented in Table 3. This timeline is based on a LTR load date of 2022.

Table 3. Proposed Timeline for ATF Licensing Activities

Phase	Action	Date
Phase 0	Out-of-Pile and In-Pile Testing	2013
	In-Pile Test Reactor Testing of Short Prototype	2016
	In-Pile Hotcell Exam	2018
	Code Development and Updates	2018
Phase 1	Submit Exemption Request for LTR	2020
	Load LTR into core	2022
	First PIE Exam on LTR	2023
	Code Development and Updates	2023
	Submit Exemption Request for LTA	2023
	Second PIE Exam on LTR	2025
Phase 2	Code Development and Updates	2025
	Load first LTA into core	2025
	Third PIE Exam on LTR	2027
	First PIE Exam on LTA	2027
	Second PIE Exam on LTA	2029
	First Hotcell Exam on LTR	2030
	Code Development and Report Writing	2025
Phase 3	Third PIE Exam on LTA	2031
	Submit Reports to NRC	2027
	Petition for Rulemaking	2030
	NRC Approves Topicals	2032
	Rulemaking Complete	2034
	Full Region Implementation Begins	2034

9 COST ESTIMATE

The cost estimates provided in this section are based on a preliminary look into the licensing requirements and associated fees. Anytime there are regulators, lawyers and interveners involved or potentially involved, the costs are very difficult to predict.

This cost analysis assumes a simple topical report will cost $70,000 to review and a complex topical will cost $1,500,000 to review. Additionally, this cost estimate assumes the average engineering cost per engineer is $200/hour.

Based on these assumptions, Table 4 provides an estimate of the total cost to license an ATF fuel product.

Table 4. Cost estimate for Licensing of ATF fuel product

Activity	**Dates**	**Cost**
In-Pile and Out-of-Pile Testing	2013-2018	$25,000,000
Code Development and Updates	2016-2030	$20,000,000
LTR Exemption Request Submittal and Review	2020-2022	$1,000,000
LTA Exemption Request Submittal and Review	2023-2025	$1,000,000
Topical Report Writing	2025-2030	$6,500,000
NRC Review	2027-2032	$20,500,000
Full Region Exemption Request	2030-2032	$1,000,000
	Total	$75,000,000

The NRC Review entry in the table accounts for both NRC Review fees associated with reviewing the topical and the engineering effort associated with responding to any RAIs received as part of the process. Additionally, this $20.5 million includes fees that would be incurred as part of ACRS reviews.

Cost estimates provided in Table 4 address activities from the beginning of test reactor tests all the way through to full region implementation. However, the costs associated with Rulemaking are not included since this could vary greatly and is difficult to predict. Additionally, the total presented in Table 4 does not account for initial research and development work completed to-date.

10 REFERENCES

1. RT-TR-13-2, Development of LWR Fuels with Enhanced Accident Tolerance, Task 1 - Technical Concept Description, Award Number DE-NE0000566, January 31, 2013.

2. RT-TR-13-8, Development of LWR Fuels with Enhanced Accident Tolerance, Task 2 – Description of Research and Development Required to Qualify the Technical Concept, May 31, 2013.

APPENDIX A: LIST OF ACRONYMS

ACRS	Advisory Committee on Reactor Safeguards
AOO	Anticipated Operational Occurrence
AOR	Analysis of Record
ATF	Accident Tolerant Fuel
CFR	Code of Federal Regulations
CMC	Ceramic Matrix Composite
DG	Draft Regulatory Guide
DNB	Departure from Nucleate Boiling
ECCS	Emergency Core Cooling System
FCEP	Fuel Checklist Evaluation Process
FSAR	Final Safety Analysis Report
GDC	General Design Criteria
LOCA	Loss of Coolant Accident
LTA	Lead Test Assembly
LTR	Lead Test Rod
LUA	Lead Use Assembly
LWR	Light Water Reactor
MAX	Max Phase Material
mREM	Mille Roentgen Equivalent Man
MWD/MTU	Megawatt days/Metric Ton Uranium
NRC	Nuclear Regulatory Commission
NUREG	Nuclear Regulation
PIE	Post Irradiation Exams
PQD	Postquench Ductility
RG	Regulatory Guide
RIA	Reactivity Initiated Accident
SAFDLs	Specified Acceptable Fuel Design Limits
SiC	Silicon Carbide
SRP	Standard Review Plan
SSE	Safe Shutdown Earthquake
T&H	Thermal and Hydraulic
TS	Technical Specifications
US	United States

Award Number DE-NE0000566
Development of LWR Fuels with Enhanced Accident Tolerance
Task 4 – Preliminary Business Plan

RT-TR-13-20

October 2, 2013

Principal Investigator: Edward J. Lahoda

Project Manager: Frank A. Boylan

Westinghouse Electric Company LLC
1000 Cranberry Woods Drive
Cranberry Woods, PA 16066

Authors: Frank Boylan, Fausto Franceschini

Steve Johnson, Edward Lahoda, Jeffrey Secker, Peng Xu

General Atomics
3550 General Atomics Crt.
P.O. Box 85608
San Diego, CA 92121

Authors: Dr. Christina Back and Robert Schleicher

Southern Nuclear Company
42 Inverness Center Parkway
Birmingham, AL 35242

Authors: Ronald G. Cocherell and John Williams

Team Members

Edison Welding Institute
General Atomics
Idaho National Laboratory
Los Alamos National Laboratory
Massachusetts Institute of Technology
Southern Nuclear Company
Texas A&M University
University of Wisconsin
Westinghouse Electric Company LLC

Table of Contents

LIST OF TABLES

1. Executive Summary

A preliminary business plan for multiple fuel and cladding candidates for the Enhanced Accident Tolerant Fuel (ATF) program was developed. The fuel pellet options included waterproofed $U^{15}N$ and U_3Si_2 and the cladding options SiC composites and zirconium alloys with surface treatments. This preliminary evaluation indicated that SiC cladding can provide 500°C to 800°C and the zirconium alloys with surface treatments can provide approximately 200°C to 400°C additional margin during beyond design basis accidents though the development risks and investment costs are higher for the SiC cladding.

A preliminary, best estimate of the discounted rate of return on investment (the rate of return over and above the assumed 8% cost of capital) is between 4% and 14% assuming the same US fuel demand Westinghouse supplies today (1500 metric tons U/year). This discounted return rises to between 9% and 19% if the current worldwide demand that Westinghouse supplies is used (2600 metric tons U per year). The financial model, while explicit and detailed, contains highly uncertain cost inputs and program risks. Thus, the deterministic results should be considered preliminary estimates with a high degree of uncertainty. Although many areas will need additional scrutiny and precision over time, these preliminary estimates were generated as a means to baseline the results based upon current best estimates.

These returns assume that the Westinghouse transition to ATF is 100% in 2032 and utility implementation occurs over 4.5 years (3, 18 month cycles). Westinghouse is assumed to reduce the price of fuel during the 4.5 year utility transition period to produce a positive return on the utility's investment, given 20 years of operation using ATF. Therefore, in addition to the non-financial benefits, the current positive return of the best estimate and the significant upside for the vendor and utilities suggest that this is an investment that is attractive from a financial standpoint.

If SiC thickness can be lowered to approximately the current Zr wall thickness, then fuel cost savings will result that will be attractive to utilities. Combining SiC with high density, high conductivity fuel such as U_3Si_2 or $U^{15}N$, not only increases the safety analysis margin but also significantly improves fuel cycle economics, which is necessary to ensure utility acceptance.

The main risk issues are identified to be the length (>15 years) of the development and licensing periods, the consistency of funding, the large investment required (>$450M), and the ability to meet the long term technical goals. The vast majority of the technical risk is during the initial research stage. The research stage is <10% of the total cost and currently is mainly (80%) funded by the government. Industry pays >66% of the total cost of the program through to commercialization.

Acknowledgment: This material is based upon work supported by the Department of Energy under Award Number DE-NE0000566.

Disclaimer: This report was prepared as an account of work sponsored by an agency of the United States Government. Neither the United States Government nor any agency thereof, nor any of their employees, makes any warranty, express or implied, or assumes any legal liability or responsibility for the accuracy, completeness, or usefulness of any information, apparatus, product, or process disclosed, or represents that its use would not infringe privately owned rights. Reference herein to any specific commercial product, process, or service by trade name, trademark, manufacturer, or otherwise does not necessarily constitute or imply its endorsement, recommendation, or favoring by the United States Government or any agency thereof. The views and opinions of authors expressed herein do not necessarily state or reflect those of the United States Government or any agency thereof.

2. Introduction

The severe nuclear accident at Fukushima Daiichi in March 2011 and the Three Mile Island accident in 1979 imply that severe nuclear accidents may occur at higher frequencies than previously predicted, and that the financial liabilities of such accidents can cripple a utility. These accidents have provided the current impetus to the fuel vendors to pursue new fuel materials that provide significant increases in the time for the reactor operator to respond to unforeseen events before significant releases of fuel materials occur. However, with a time to market of between 15 and 20 years, the high risk of technical failure due to unforeseen technical and licensing issues, and high development costs, generating returns on investment to justify the costs and risks is difficult. Therefore, any fuel system that is developed must provide significant operating cost improvements as well as safety improvements if accident tolerant fuel (ATF) products are to be commercially successful. The objective of this report is to determine the potential business case for the four ATF options being proposed by the Westinghouse team. This analysis developed costs for:

1. Research and development
2. Testing and licensing
3. Manufacturing development and installation
4. Manufacturing for fuel and cladding
5. Utility implementation costs

The results of fuel cycle economic studies were combined with these costs to develop a discounted rate of return on investment (ROI or ROR) analysis for both the fuel vendor and the utility.

Finally, other business issues were considered including:

1. Effect on current business
2. Supply chain considerations
3. Risks and their mitigation

This analysis for the commercialization of ATF was carried out for two fuel pellet options (waterproofed $U^{15}N$ and U_3Si_2) and the two cladding options (SiC composites and zirconium alloys with surface treatments to retard their corrosion under operating conditions and oxidation under accident conditions). This resulted in four potential fuel/cladding combinations:

1. Waterproofed $U^{15}N$ fuel with SiC cladding
2. Waterproofed $U^{15}N$ fuel with treated Zr alloy cladding
3. U_3Si_2 fuel with SiC cladding
4. U_3Si_2 fuel with treated Zr alloy cladding

The following approach was used in this return on investment analysis:

1. The development, testing, licensing and manufacturing costs for each fuel and cladding option were estimated.
2. The value of each fuel and cladding combination was estimated from both the utility and the fuel vendor's point of view.

3. Based on an assumed Department of Energy financial assistance schedule of 80% funding for work up to and including test reactor work and 50% on the lead test rod and assembly work, the ROI for the vendor was made and the benefit to the utility customers was estimated.

3. Economic Considerations

The economic analysis performed for this study results in a discounted rate of return on investment (ROI) analysis for the various ATF options from the vendors' perspective. In order to carry out the vendor portion of this analysis, estimates of the various capital and operating costs were made. Capital costs were for research and development (Section 3.1), licensing (Section 3.2) and new manufacturing facilities (Section 3.4). Cost incurred as part of the Lead Test Rod (LTR), Lead Test Assembly (LTA) and Region reloads are addressed in Section 3.3. Operating costs that were estimated were for the fuel pellet (Section 3.5), the cladding (Section 3.6). A similar effort was made for the utility (Section 3.8). Fuel cycle economics were analyzed (Section 3.7). This is followed by the calculation of the ROI for the vendor in Section 3.9.

3.1. Research and Development Costs

The research and development effort for ATF is carried out in three phases. During the first phase, options for the fuel pellet and the cladding are built and tested to determine whether or not they can achieve the desired performance characteristics. For example, UN fuel reacts with water at reactor operating temperatures (300°C to 350°C). Part of the development program is to develop and test various options for making a UN pellet (waterproof $U^{15}N$) that would not react with water at reactor operating conditions. Another issue is to determine if there is a cost effective means for producing N enriched with 99% N15. Phase 1 has been on-going since October 2013 and is scheduled to end in 2014.

Once options have been defined in Phase 1, they are tested in reactor for fuel and cladding and in oxidation and mechanical testing for the cladding during Phase 2. This testing is scheduled to continue until about 2016.

Finally, in order to generate the data required to obtain license exemptions for lead test rod (LTR) testing during the licensing phase and to convince commercial reactor operators that the LTR is safe to put into their reactor, a test reactor program with fuel rodlets ~6 inches to 12 inches in length is carried out over about a 6 year period. This time period assumes three 18 month cycles with about 1.5 years at the end to perform post irradiation examinations. Current schedules estimate the time for Phase 3 as between 2016 and 2022.

The costs and times for the three development phases are summarized in Table 3.1 for each of the four options being considered. For purposes of the final ROI analysis, Phases 1 to 3 and the N15 development costs are assumed to be funded 20% by the fuel vendor and 80% with federal assistance. The background for these numbers is provided in the Task 2 report (1).

	Dates	SiC+U15N ($M)	SiC+U3Si2 ($M)	Treated Zr+U15N ($M)	Treated Zr+U3Si2 ($M)
Phase 1 Deveolpment + Phase 2 Testing	to 2016	$ 31.6	$ 31.6	$ 31.6	$ 31.6
Phase 3 Test Reactor	2016 to 2020	$ 6.0	$ 6.0	$ 6.0	$ 6.0
Phase 3 PIEs	2018 to 2022	$ 6.0	$ 6.0	$ 6.0	$ 6.0
N15 Development Costs	2018 to 2022	$ 4.6	$ -	$ 4.6	$ -
Total		$ 48.2	$ 43.6	$ 48.2	$ 43.6

Table 3.1 – Estimated Costs for Research and Development

3.2. Licensing Costs

The licensing times and costs for ATF were developed based on the input from the licensing report from Task 3 of this contract. The licensing task is broken into three phases. The first phase (Lead Test Rods, LTR) develops, designs, produces and tests up to about 30 rods in each of two commercial reactors. This phase will use the data developed as part of Phase 3 (test reactor) of the Research and Development program to generate the license exemptions required to put a new fuel in a commercial reactor. This phase will take about 6 years to complete and can slightly overlap the trailing and leading phases. The 30 LTRs will be withdrawn in three 18 month stages over the 4.5 year period that they are in the reactor and subjected to post irradiation examinations (PIEs).

The Lead Test Assembly (LTA) phase follows the LTR phase. During this phase, topical reports on a variety of issues need to be generated based on data from the test reactor and LTR stages of development and submitted to the NRC for approval. After NRC approval, up to about 4 LTAs will be inserted into at least two commercial reactors. This phase will take about 6 years to complete and can slightly overlap the trailing and leading phases. The 4 LTRs will be withdrawn in three 18 month stages over the 4.5 year period that they are in the reactor and subjected to PIEs. The data from this phase will be used to verify the data used to generate the topical for the LTAs and will provide the basis for full commercial implementation.

The final stage of licensing implementation is when regions (about one half to one third of the reactor core) are introduced in commercial operation. Implementation would be done one region at a time. This phase will take about 6 years to complete and can slightly overlap the LTA phase. Samples will be obtained from each region after 18 months in the reactor to verify performance predictions until the entire reactor is operating with ATF fuel after about a 4.5 year period.

Parallel to the LTR stage, the exposed rodlets from the Phase 3 development program will undergo transient testing to evaluate their performance in accident conditions. Transient tests will be carried out in either Halden or in specialized reactors such as the TREAT reactor at the Idaho National Laboratory (INL). Typically, these transient tests consist either of steady ramp tests or stepwise ramp tests until failure of the exposed fuel rods occurs.

The costs and times for the three licensing phases are summarized in Table 3.2. These costs are approximately the same for each of the 4 options being considered. Note that the testing required for licensing is included in the costs listed for the Phase 1, 2 and 3 programs as well as the LTR and LTA programs. This approach is aggressive since it assumes that each phase of the program overlaps with the previous one. For instance, fuel normally stays in the reactor for three 18 month cycles. A normal development schedule would provide for three, 18 month cycles plus the time for cool-down, shipping and post irradiation examination (PIE) (about 7 years total). This schedule assumes, for instance, that the fuel is exposed for 1 full lead test rod (LTR) cycle plus the time for cool-down, shipment and PIE for a total of about 4 years before the lead test assembly (LTA) phase is started. The fuel in the LTR phase continues on for two more exposure cycles and the PIE while the LTA is proceeding. The assumption is that if the fuel goes through one full cycle without performance issues, it will also perform successfully for three cycles. If the fuel in the LTR cycle begins to show unexpected degradation in the second or third cycles, then the LTA would also have to be pulled at the point in the cycle that the LTR began its degradation. The risk is that the cost and time expended in putting in the LTA will now have been wasted since the LTR had shown that this approach was untenable.

Activity	Dates	Cost
Code Development and Updates	2016-2030	$ 20,000,000
LTR Exemption Request Submittal and Review	2020-2022	$ 1,000,000
LTA Exemption Request Submittal and Review	2023-2025	$ 1,000,000
Topical Report Writing	2025-2030	$ 6,500,000
NRC Review	2027-2032	$ 20,500,000
Full Region Exemption Request	2028-2032	$ 1,000,000
	Total	$ 50,000,000

Table 3.2 – Estimated Costs for Licensing

However, the use of an aggressive approach is required since the alternative is to use a strictly series approach where each phase of the program is successfully completed before the next phase begins. While having less incremental financial risk, this approach would lengthen the already long (~24 year) implementation time to at least 36 years. Since the value of the final product is discounted with time, this further time extension further reduces the potential for obtaining an economically viable ATF product.

As with the timeline, these cost estimates are aggressive in that there is no rework assumed. That is, outside of the development phase where multiple approaches are assumed to be tried, the option that is chosen to go forward to the LTR stage and beyond is assumed to succeed. Government assistance at the 50% level is assumed for all licensing efforts during the LTR and LTA stages except for the full region exemption activity.

3.3. Lead Test Rod and Assembly and Regions Development Costs

During the LTR and LTA and the regions stages of development, costs are incurred for the manufacture, installation and evaluation of the test articles, design and planning. These costs extend over a 14 year period from the research and development stage until introduction of the new fuel is complete. The costs and time estimates for this stage are shown in Table 3.3. Note that the licensing costs are shown here as well as in Section 3.2 but are not double counted in the economic analysis. During the LTR and LTA stages, government assistance is assumed at the 50% level. No government assistance is assumed during the regions time period.

Development and Testing	Dates	SiC+U15N ($M)	SiC+U3Si2 ($M)	Treated Zr+U15N ($M)	Treated Zr+U3Si2 ($M)
LTR	**2020 to 2026**				
Development		$ 10.0	$ 10.0	$ 10.0	$ 10.0
VIPER Tests		$ 0.5	$ 0.5	$ 0.5	$ 0.5
Licensing		$ 6.0	$ 6.0	$ 6.0	$ 6.0
LTR Tests		$ 15.0	$ 15.0	$ 15.0	$ 15.0
PIE		$ 19.5	$ 19.5	$ 19.5	$ 19.5
Severe accident test		$ 46.1	$ 46.1	$ 46.1	$ 46.1
Total LTR		$ 97.1	$ 97.1	$ 97.1	$ 97.1
LTA	**2024 to 2030**				
Development		$ 24.2	$ 24.2	$ 24.2	$ 24.2
VIPER tests		$ 0.5	$ 0.5	$ 0.5	$ 0.5
Licensing		$ 6.0	$ 6.0	$ 6.0	$ 6.0
LTA tests		$ 15.0	$ 15.0	$ 15.0	$ 15.0
Total LTA		$ 45.7	$ 45.7	$ 45.7	$ 45.7
Full-region	**2028 to 2034**				
Development		$ 15.0	$ 15.0	$ 15.0	$ 15.0
Licensing		$ 28.0	$ 28.0	$ 28.0	$ 28.0
Total Regions		$ 43.0	$ 43.0	$ 43.0	$ 43.0

Table 3.3 – Estimated LTR, LTA and Region Development Costs

3.4. Manufacturing Development and Installation Costs

This phase begins during the LTA stage and continues until commercial deployment is complete. During this time, any development needs, including pilot plant testing that is required to manufacture the ATF product, are performed. After any development work, full scale manufacturing facilities are brought on-line to support the regions phase of commercialization.

Capital cost estimates were based on studies by Westinghouse manufacturing for similar projects. So for instance, the UN conversion capital costs were based on studies for new UO_2 conversion lines (assumed to be twice the cost, one for conversion of UF_6 to UO_2 and the second for UO_2 to UN), and treated Zr alloy coated tubes were based on coating applications to pellets (same technology with a different target). This approach is justified by the observation that while the chemistry of the ATF components will be different from the current components, the manufacturing operations will be similar. The chemistry differences are made up in the manufacturing cost calculation. For UN there is the additional cost of the N15 enrichment facility. The prototype and capital costs were based on previous work performed by Westinghouse on N15 enrichment.

The SiC prototype and manufacturing facility costs were based on estimates by General Atomics (GA). The prototype costs were assumed to be one module of the final production facility. The time and costs for manufacturing implementation are shown in Table 3.4 for each of the 4 options being considered. These costs are conservative and are highly dependent on the final design of the SiC structure. For instance, this cost estimate is based on a four layer design consisting of two solid layers deposited using chemical vapor deposition and two composite layers consisting of wound fibers densified by chemical vapor infiltration (CVI). An alternate design using an extruded solid layer with one composite layer consisting of wound fibers densified by CVI would likely be less capital intensive.

Development and Testing	Dates	SiC+U15N ($M)	SiC+U3Si2 ($M)	Treated Zr+U15N ($M)	Treated Zr+U3Si2 ($M)
Prototype Scale	2026 to 2028				
Fuel		$ 5	$ 5	$ 5	$ 5
Coated Zr Cladding				$ 5	$ 5
SiC		$ 28	$ 28		
Total		$ 33	$ 33	$ 10	$ 10
N15 Prototype	2022 to 2028	$ 22		$ 22	
Production Scale	2028 to 2034				
Fuel		$ 150	$ 150	$ 150	$ 150
N15		$ 205		$ 205	
Coated Zr Cladding				$ 20	$ 20
SiC		$ 504	$ 504		
Total		$ 859	$ 654	$ 375	$ 170
Total Production + Prototype		$ 914	$ 687	$ 407	$ 180

Table 3.4 – Estimated Capital Costs for Manufacturing

3.5. Manufacturing Cost Estimate for Fuel

The current fuel manufacturing operations for all commercial vendors is based on making UO_2 from either UF_6 (uranium hexafluoride) or $UO_2(NO_3)_2$-$6H_2O$ (uranyl nitrate hexahydrate or UNH). It is important to note that these manufacturing operations allow vendors to blend down

impurities, blend for achieving powder properties such as powder density and BET, as well as blend for achieving the exact enrichment. Any new manufacturing process must be able to allow these same operations. The steps in the all dry process for UF_6 feed are:

$UF_6 + 2H_2O(g) \Rightarrow UO_2F_2 + 4HF$

$UO_2F_2 + H_2 \Rightarrow UO_2 + 2HF$

For UNH feed a wet process such as the Ammonium Diuranate (ADU) process is used. The reaction steps are:

$UO_2(NO_3)_2\text{-}6H_2O + 4NH_4OH \Rightarrow UO_2(NH_4)_2 + 8H_2O + 2NH_4NO_3 + O_2$

$UO_2(NH_4)_2 + H_2 \Rightarrow UO_2 + N_2 + 5H_2$

For U_3Si_2, the current manufacturing technique used to make test reactor fuel is to strike an arc between Si and U metal electrodes to form the U_3Si_2 powder. The disadvantages of this approach are the relatively large grains of powder that would need to be milled down as well as the need to make U metal which entails a relatively complicated manufacturing process in itself. As of yet, there are no other manufacturing processes available that do not use U and Si metal as the starting point. While other processes can be envisioned, this cost analysis will assume that the current manufacturing process will be used. The steps in this process are as follows:

$UF_6 + H_2 \Rightarrow UF_4 + 2HF$

$UF_4 + 2Ca \Rightarrow U + 2CaF_2$

$U_3 + Si_2 \Rightarrow U_3Si_2$

The current process for manufacturing UN in any large scale is to reduce UO_2 to make uranium carbide and then to nitride the carbide with nitrogen. These process steps are then (from the UF_6 feed):

$UF_6 + 2H_2O(g) \Rightarrow UO_2F_2 + 4HF$

$UO_2F_2 + H_2 \Rightarrow UO_2 + 2HF$

$UO_2 + 2.5C \Rightarrow UC + 0.5CO_2 + . CO$

$UC + N_2 + .5H_2 \Rightarrow UN + HCN$

Current manufacturing costs for UO_2 are estimated at about \$10/kgU per process step. Therefore the added cost for U_3Si_2 is about \$10/kgU and for UN is about \$20/kgU. The cost for producing nitrogen enriched to 99% N15 is estimated at about \$1130/kg N using the laser isotope separation methods developed by Westinghouse for N15 enrichment.

3.6. Manufacturing Cost Estimate for Cladding

The target SiC cladding manufacturing costs for an extruded monolithic tube wound with SiC fiber and then densified using CVI'd SiC are estimated to add about $38/rod (see Table 3.5 – current cost is ~$90 to $95/rod) above current Zr alloy rod costs for an expected wall thickness of 1.04mm based on current designs. An estimate for stoichiometric, crystalline, low oxygen, beta phase SiC fibers to be produced at the 90 metric tons/year level in 20 years is about $1.10/gram compared to the current $10/gram. This reduction assumes a 1000 fold scale-up in manufacturing levels and more cost effective manufacturing techniques. The estimate for the winding/CVI of the SiC cladding was based on the cost of performing these operations on a small scale (90 feet were wrapped and CVI'd with 693 grams of fiber and CVI deposited SiC) and using an assumed scaling exponent of 0.40 to get the cost of manufacturing for ~10 million feet per year which equates to about 90,791 kg/yr of fiber and 99,532 kg/yr of CVI'd SiC. The scaling equation was:

$$\text{Future Cost (\$/gm)} = \$158/\text{gm} * ((693/1000)/(90791+99532))^{0.40} = \$1.05/\text{gm}$$

The cost for the extruded monolithic tube for large production levels was estimated by a current manufacturer as about $1/ft or about $0.08/gm. Installing plugs on each end of the SiC rod was assumed to cost $10/plug or $20/rod.

Note that the above calculation is a target value for the cost of SiC cladding. General Atomics estimated the cost for SiC cladding using their 4 layer approach is higher and achieving the target costs for SiC will be difficult. After the final SiC cladding design is reached, a detailed engineering study will be required to design a process that makes the SiC cladding in a cost effective manner.

The added costs for coated Zr alloy rods would be about $13/rod for the Ti_2AlC coating based on the application of cold spray technology. This cost is based on estimates using cold spray to apply coatings to pellets.

	Current Zr Alloy Dimensions	Expected SiC Dimensions	
Total Wall thickness	0.572	1.041	mm
Monolith	0.381	0.381	mm
Composite	0.191	0.660	mm
OD	9.50	9.50	mm
ID	8.93	8.46	mm
Density of SiC	3.16	3.16	gm/cm^3
Volume % of Fiber	40%	40%	
Volume % of CVI	45%	45%	
Weight of Fiber	1.07	3.61	gm/30 cm
Weight of CVI	1.21	4.10	gm/30 cm
Weight of Monolith	5.17	4.90	gm/30 cm
Total Weight of SiC	7.45	12.6	gm/30 cm
Cost of SiC Fiber	$ 0.50	$ 1.10	/gm
Cost of SiC CVI and Winding	$ 0.73	$ 1.05	/gm
Cost of SiC Monolith	$ 0.13	$ 0.08	/gm
Endplug	$ 10.00	$ 10.00	/plug
Length of Rod	388	388	cm
Weight of each rod	96	163	gm
Cost of SiC Fiber	$ 7	$ 51	/rod
Cost of SiC CVI and Winding	$ 11	$ 56	/rod
Cost of SiC Monolith	$ 9	$ 5	/rod
Endplug	$ 20	$ 20	/rod
Total Target SiC Cladding Cost	$ 47	$ 132	/rod

Table 3.5 – Target Costs for SiC Cladding Manufacture

3.7. Fuel Cycle Economics

The value of ATF was evaluated from the point of view of the fuel vendor. The fuel designs were analyzed with 3-D core calculations and ensuing economic analysis via fuel cycle cost calculations to determine their economic viability using the assumptions in Table 3.6. The Westinghouse in-house core physics package has been employed for the neutronic simulations. Various reloading schemes and burnable absorber loadings representative of actual core operation have been employed to establish the optimum configuration for each option analyzed.

Item	Value
U_3O_8 Price ($/Lb)	55.00
Conversion Price ($/KgUnat)	12.00
SWU Price ($/Kg-SWU)	142.00
Base Fabrication Price ($/kgU)	275.00
N15 Price ($/Kg)	1120.24
Tails Assay (w/o)	0.3
Pre-Operational Interest (%/Yr)	6.0
Conversion and Fabrication Loss (%)	0.0
Spent Fuel Cooling Time (Months)	120
Spent Fuel Disposal Charge ($/$MWHr_e$)	1.00
Spent Fuel Dry Storage Charge ($/FA)	50,000.00
Cycle Length (Months)	18
Rated Thermal Power (MW_{th})	3,587.0
Rated Net Electric Output (MW_e)	1,112.0
Inflation Rate (%)	2.0
Return on Fuel Investment (%/yr)	8.0

Table 3.6 – Assumptions Used in the Core Economics Study

Self generating equilibrium cycle fuel management cases have been developed to compare the economic performance of the various fuel and cladding options. A reference UO_2/Zr case was developed for an uprated four loop core (1,112 MWe) using the Westinghouse 17x17 RFA fuel design. This design uses a pellet outside diameter (OD) of 0.3225", a cladding OD of 0.3740", and a cladding thickness of 0.0225" (22.5 mils). This case loads 76 assemblies using 1.5X ZrB_2 as the burnable absorber. The fuel uses 8 inch annular axial blankets at 3.2 w/o (weight percent) U235 on the top and bottom of the fuel stack. The central 128" fuel-stack is enriched to 4.87 w/o U235 to achieve an 18 month cycle at 510 EFPD (effective full power days) with no coast-down. The ZrB_2 IFBA (integral fuel burnable absorbers) rods are also 128" long and centered with respect to the fuel stack. All of the accident tolerant cases also use 128" 1.5X ZrB_2 and 8 inch 3.2 w/o U235 annular axial blankets on the top and bottom of the fuel stack.

The SiC cladding thickness requirement has been estimated at 0.030" (30 mils) rather than the current 0.0225" (22.5 mil) cladding thickness used with Zr alloy in RFA fuel. The additional cladding thickness displaces moderator and increases neutron absorption. With U_3Si_2 the increased uranium loading and thicker cladding resulted in a decrease in the H/U ratio, decreasing fuel efficiency. To offset the increase in uranium density, the fuel pellet diameter was reduced. This case uses a pellet OD of 0.3088" and a cladding OD of 0.3750". This resulted in a requirement to load 68 assemblies with a central enrichment of 4.830 w/o. This case was able to achieve fuel costs significantly better than the UO_2/Zr reference case.

UN was then used as the pellet material with the 0.0300" thick SIC cladding. Direct substitution of UN fuel into the RFA pellet geometry would also reduce H/U ratio, offsetting some of the increased reactivity resulting from higher density fuel. To optimize this design, a pellet OD of 0.2900" was used along with a cladding OD of 0.3562". This case required 60 assemblies with a central enrichment of 4.900 w/o. The UN fuel costs were also significantly reduced relative to the reference UO_2/Zr case.

Next the fuel efficiency of the corrosion resistant coating options was explored. These designs will use 0.0225" thick Zr as the cladding material with a thin, 0.0003937" (10 micron) coating in the Zr surfaces. Two different types of coatings were investigated. The first is Ti_2AlC and the other is NanoSteel™,(NanoSteel™ is a register trademark of the NanoSteel Company, Inc.) referred to as NS, is composed primarily of iron and chromium, with additional proprietary alloys. The pellet materials used were UN or U_3Si_2. A reference case using the advanced pellet materials with Zr cladding and no coatings was generated for each pellet material. With the increased density, the pellet OD was reduced. For these cases, the standard Westinghouse 17x17 OFA design was chosen. This fuel rod has a smaller pellet and cladding OD compared to RFA fuel and allows for a more favorable H/U ratio compared to RFA fuel when higher density pellet material is used. Some further improvements in fuel costs could likely be obtained by using even smaller pellets and cladding, but for these cases the OFA 0.3088" pellet OD and 0.3600" cladding OD with 0.0225" thick Zr cladding was used.

The UN/Zr reference case uses 56 feed assemblies with a central enrichment of 4.675 w/o to meet the 510 EFPD energy requirement. The resulting fuel cost is lower than the 76 feed RFA UO_2/Zr reference case. The addition of the thin Ti_2AlC coating also requires 56 feed assemblies with an increased central enrichment of 4.710 w/o. This case was also lower than the reference case, but slightly higher than the UN/Zr case. The use of the NS coating requires 56 feeds with a central enrichment of 4.715 w/o. The resulting fuel costs are lower than the reference case, but slightly higher than the UN/Zr case.

The U_3Si_2/Zr reference case uses 68 feed assemblies with a central enrichment of 4.810 w/o to meet the 510 EFPD energy requirement. The resulting fuel cost is lower than the 76 feed RFA UO_2/Zr reference case. The addition of the thin Ti_2AlC coating also requires 68 feed assemblies with an increased central enrichment of 4.840 w/o. This case has fuel costs lower than the reference case, but also higher than the UN/Zr case. The use of the NS coating requires 68 feeds with a central enrichment of 4.845 w/o. The resulting fuel costs are lower than the reference case, but still higher than the UN/Zr case.

Both the $U^{15}N$ and U_3Si_2 new pellet types provide large economic benefits due to their significantly higher density and thermal conductivity. Additional effort is required to determine if there are swelling issues since the current data is extrapolated from reactor data at temperatures and burnups that are significantly different from those likely to be experienced in commercial fuel service. If testing indicates that the swelling is an issue, then additional work on pellet additives or manufacturing conditions will be needed to overcome this issue.

The thickness of the SiC cladding also has an effect on the fuel economics. Development work to minimize the required thickness will provide significant benefits to the fuel cycle economics.

A summary of the ATF fuel cycle value over that of the UO_2/Zr reference is shown in Table 3.7. Note that the cost adders for SiC and Zr alloy coated cladding and for U_3Si_2 and $U^{15}N$ have already been incorporated into these results.

Fuel	Cladding	Value vs. Zr Alloy-UO2 ($/kgU)
UN	SiC	$251
U3Si2	SiC	$107
UN	Ti2AlC	$238
U3Si2	Ti2AlC	$130
UN	NanoSteel	$152
U3Si2	NanoSteel	$114

Table 3.7 – Estimated Values of Various ATF Fuels and Claddings

3.8. Utility Return on Investment Analysis

Southern Nuclear Operating Company Inc. (SNC) performed an investment analysis from the point of view of the utility. In this analysis, they evaluated their investment in such items as licensing, equipment changes and training along with the cost of the ATF in $/kgU against the value of the ATF.

Southern Nuclear Operating Company Inc. (Southern Nuclear), headquartered in Birmingham, Alabama, operates Southern Company's six nuclear reactors at three locations: the Alvin W. Vogtle Electric Generating Plant near Waynesboro, Georgia; the Edwin I. Hatch Nuclear Plant near Baxley, Georgia; and the Joseph M. Farley Nuclear Plant near Dothan, Alabama.

As part of the Accident Tolerant Fuel project, Southern Nuclear was tasked with a review of the economics of ATF from a utility perspective. Both Alabama Power and Georgia Power are regulated utilities under the oversight of both Federal Energy Regulatory Commission (FERC) and their respective State Public Services Commissions. As part of this task, SNC Nuclear Fuel personnel reviewed the Westinghouse fuel cycles prepared for the ATF project and performed various fuel cycle economic studies of the fuel and cladding types used in the studies

Potential benefits of ATF to the current UO_2/Zr fuel type were identified during the SNC fuel cycle economics review. In general, the economic evaluations indicated the use of a UN pellet in conjunction with continued use of a Zr based cladding material had the largest direct benefit in fuel cost. Use of a uranium silicide pellet with Zr cladding, while not as beneficial as a UN pellet fuel, was still substantially lower in fuel cost compared to the reference UO_2/Zr fuel type. The combination of a UN pellet with SiC cladding was approximately the same fuel cost as the uranium silicide pellet with Zr cladding.

However, as discussed below, fuel cost is only a portion of nuclear power plant operating cost. The benefits due to possible licensing regulatory relief and Risk Informed Engineering (RIE) analyses resulting from the large reduction or elimination of Zr from the core with the use of SiC

cladding material indicates that a UN/SiC combination may have the most total potential economic benefit for a utility.

As regulated utilities, both Georgia Power Company and Alabama Power Company have an obligation to deliver electricity to the ratepayers within the requirements established by federal and state regulators. Regulated utilities are allowed to earn a return on plant capital investments but not on fuel. As a result, focusing only on fuel cycle economics of a regulated utility could result in the selection of the lowest cost fuel evaluated without taking into account the costs of potential impacts on plant capital and operation. This would not be in the best interest of the utility or the customer.

General Design Criteria 1 requires that structures, systems, and components important to safety be designed, fabricated, erected, and tested to quality standards commensurate with the importance of the safety functions to be performed. ATF modeling information provided by Westinghouse to SNC shows that during a postulated station blackout (SBO), similar to the event at the Fukushima Daiichi plant, certain ATF designs show no creep rupture and therefore no breach of the reactor coolant system (RCS) should occur. As a result, ATF could potentially allow certain plant components currently classified as safety-related to be re-classified as non-safety related. The potential benefit to the utility of re-classification could be significant in both licensing and economic benefit of ATF. Reducing the number of safety-related plant systems, components and processes would provide broader options for equipment and vendors with the potential to greatly reduce O&M and plant capital costs over the life of the plant.

ATF could also have a large effect on the risk managed technical specifications (RMTS) calculated risk informed completion time (RICT) if a limiting condition for operation (LCO) is not met. If ATF is shown to withstand more severe accident conditions than current fuel designs, the ATF fuel designs have the potential for significant economic benefit to the nuclear plant operator as well.

The cost benefit of this regulatory relief to the utility and the ratepayers is not easy to estimate but could easily be as high as tens of millions of dollars per year.

As an example, the reactor core safety limits found in Chapter 2 of the FSAR protect the core from departure from nucleate boiling (DNB) and fuel centerline melting. With a higher thermal conductivity and higher cladding operating temperatures, ATF could potentially provide relief to the Safety Limits (SLs) related to fuel centerline melting. If ATF is shown to have a lower propensity for cladding-water reaction, the SLs related to DNB could be relaxed, potentially reducing or eliminating the requirement for certain safety related equipment while increasing operator action times, reducing fuel cost and providing additional plant operating margin.

A specific example of the potential cost benefit for plant capital equipment is the difference in cost of a commercial grade diesel versus a safety-related diesel. Depending upon current market conditions and vendors, safety-related diesel generators are approximately $2.5M/MWe while a commercial diesel generator is approximately $750K/MWe. For a two unit nuclear plant site, assuming 4 diesels rated at approximately 7 MWe each, the capital cost of new safety-related diesels would be approximately $70M, while use of commercial grade diesels would be

about $50M less ($70M versus $21M). No credit was taken in either the utility or vendor economic analyses.

The potential licensing benefits in relaxed Safety Limits and Technical Specifications could have significant beneficial impact on operating cost, capital cost and fuel cost of nuclear units operating with ATF. Nuclear utility staffing and work planning should see benefits due to the potential reduced need for safety related equipment and systems. Operating crews should see benefits with the potential for reduced operator burden. Additionally, ATF could potentially allow certain Technical Specification parameters to be moved out of the Technical Specifications, and into the licensee-controlled technical requirements manual. These cost savings could be substantial ($M's/yr) as well depending on the amount of regulatory relief realized. Intangible benefits associated with the potential to avoid an unplanned shutdown as a result of regulatory relief and favorable RIE analysis with the use of ATF is unknown but should be included since the replacement power cost of an 1150 MWe unit is approximately $1M/day at current low ($35/MWhre) replacement power rates. For this study, the benefits will be assumed to be $5M/yr.

Southern Nuclear performed several different fuel cycle economic analyses of the Westinghouse fuel cycles created for the Reference fuel type (V5 RFA utilizing the current UO_2/Zr pellet/cladding combination) and different combinations of pellet and cladding materials identified as potential Accident Tolerant Fuel. Potential fuel cycle costs benefits (as well as penalties) of ATF to the current UO_2/Zr fuel type were identified during these analyses.

Present worth analyses utilizing the assumptions shown in Table 3.8 and V5RFA fuel type (UO_2/Zr based) as the reference were performed.

Item	Value
Uranium	\$69.00/lb U_3O_8
Conversion	\$12.00/KgU as UF_6
Enrichment	\$162.00/SWU
Tails Assay	0.21
Fabrication	\$250.00/KgU (base) + $ adders for new pellet and cladding as needed
Dry Cask Storage	\$50K/fuel assembly
Escalation	2%/year
In-Core Carrying Cost	14%/year
Present Worth rate	8%/year

Table 3.8 – Assumed Economic Parameters for the SNC ATF Fuel Economics Study

Two different analyses were performed. One was a single equilibrium reload over its entire life (from purchase of initial uranium to discharge and dry cask storage after 5 years of cooling). A second analysis was performed for a reload purchase and cycle of equilibrium operation with total equilibrium core carrying cost and spent fuel loadings included.

The results of both analyses were fairly consistent and provided additional confirmation of the economic evaluation. The results for the equilibrium reload over its entire life are shown below in Table 3.9 for the various fuel types with the V5RFA (UO_2/Zr) fuel type as the reference.

Positive dollar values indicate a Present Worth fuel cost benefit to the reference while a negative value indicates a Present Worth fuel cost penalty compared to the reference. Note that the 30 mil SiC case was estimated by ratios between the Westinghouse 30 mil estimates in Table 3.7 with the SNC 41 mil estimates in Table 3.9 to provide comparisons with the Westinghouse numbers.

Fuel Type	Present Worth Benefit ($M) per reload
UN/Zr	$9.8
UN/30 mil SiC	Estimated $8.8
UN/Zr(Ti2AlC)	$8.3
UN/Zr(NS)	$6.7
U_3Si_2/Zr(Ti2AlC)	$4.7
U_3Si_2/Zr(NS)	$4.5
U_3Si_2/30 mil SiC	Estimated $3.9
U_3Si_2/Zr	$3.9
UN/41 mil SiC	$3.8
V5RFA (UO_2/Zr)	$0.0 (Reference)
UO_2/41 mil SiC	($0.3)
U_3Si_2/41 mil SiC	($2.4)
RFA (UO_2)/41 mil SiC	($15.8)

Table 3.9 – Results for the SNC ATF Fuel Economics Study

The economic analyses were performed on equilibrium fuel cycles and did not include the upfront licensing and transition costs to move to a new fuel type. Licensing and transition costs can be substantial. Since these costs are incurred at the beginning of the switch in fuel type (before any fuel cycle cost benefits are realized) upfront licensing and transition costs are expected to have a large present worth negative impact on the final fuel cycle economics of ATF.

Licensing and safety analysis cost incurred by a utility as part of the transition to a new fuel type utilizing the current pellet and cladding materials can easily exceed $20M. It is expected that transitioning to a new pellet type and a new cladding material will be substantially more. For this preliminary study, the utility licensing and safety analysis costs were assumed to be 2x that for current fuel changes or $40M. This seems conservative since the vendor costs for a much broader scope of reports is only about $50M. This upfront fuel licensing transition cost would need to be recovered over the remaining life of the nuclear unit. Assuming no plant capital/O&M (operating and maintenance) cost benefits, and only savings from operational simplification of $5M/yr, an inflation rate of 2%/yr, a discount rate of 8%/yr, and a transition period of 4.5 years (3, 18 month cycles), the fuel discount per reload during this transition to generate a $0 net present value (NPV) over at least a 20 year remaining life span is $1.3M per reload or about $41/kgU. If a plant has only 10 operating years left, the required payment to get an NPV of $0 would be an unacceptable $303/kgU. The switch to ATF should be much easier to justify on an economic basis for the next generation of light water reactors or if the licenses for the current generation of reactors is extended to 80 years. This preliminary estimate shows a positive return to utilities given they have ~20 years to recapture the benefit on their investment.

3.9. Vendor Return on Investment Analysis

A vendor oriented discounted cash flow analysis was performed to determine a discounted rate of return as a function of the type of ATF and the fraction of value claimed by the vendor. For this analysis, the amount of research and development support provided by the US Department of Energy (DOE) was 80% for research oriented tasks and 50% for development tasks. The cost inputs used in this discounted return on investment analysis are summarized in Table 3.10.

Development Program ($M)					
	Dates	**SiC+U15N**	**SiC+U3Si2**	**Treated Zr+U15N**	**Treated Zr+U3Si2**
Phase 1 Development + Phase 2 Testing	to 2016	$ 31.6	$ 31.6	$ 31.6	$ 31.6
Phase 3 Test Reactor	2016 to 2020	$ 6.0	$ 6.0	$ 6.0	$ 6.0
Phase 3 PIEs	2018 to 2022	$ 6.0	$ 6.0	$ 6.0	$ 6.0
N15 Development Costs	2018 to 2022	$ 4.6	$ -	$ 4.6	$ -
Total		$ 48.2	$ 43.6	$ 48.2	$ 43.6
Code Development	2016 to 2022	$ 10.0	$ 10.0	$ 10.0	$ 10.0
Total		$ 58.2	$ 53.6	$ 58.2	$ 53.6
% Industry Investment		20%	20%	20%	20%
Licensing and Development Program ($M)					
LTR	2020 to 2026	$ 97	$ 97	$ 97	$ 97
LTA	2024 to 2030	$ 46	$ 46	$ 46	$ 46
Full-region	2028 to 2034	$ 43	$ 43	$ 43	$ 43
Total		$ 186	$ 186	$ 186	$ 186
% Industry Investment		50%	50%	50%	50%
Capital Investment ($M)					
Pilot Scale Development Costs (Less N15 costs)	2026 to 2028	$ 33	$ 33	$ 10	$ 10
N15 Pilot Plant Costs	2022 to 2028	$ 22	$ -	$ 22	$ -
Total Pilot Scale		$ 55	$ 33	$ 32	$ 10
SiCar Full Scale Manufacturing Plant	2028 to 2034	$ 504	$ 504		
Full Scale 15N manufacturing	2028 to 2034	$ 205		$ 205	
Fuel Production	2028 to 2034	$ 150	$ 150	$ 150	$ 150
Coated Zr Alloy	2028 to 2034			$ 20	$ 20
Total Full Scale		$ 859	$ 654	$ 375	$ 170

Table 3.10 – Summary of Investment Costs and Times for ATF

The calculations were done in an Excel spreadsheet using the Internal Rate of Return (IRR) function. The general formula used for each cash flow line was:

$CF_i = [\{ \Sigma - CO_i * IFR\} + S_i * V_i \}] (1+Ri)^{(i-1)}/(1+Rc)^{(i-1)}$ for I = 1 to DT+10, DT+20, and DT+30

Where:

CF = cash flow for year i in dollars

CO_i = capital costs for year I in dollars

IFR = percent of industry funding for total in percent. For research activities that are supported by the DOE, industry pays 20% of the costs while for development activities that are supported by the DOE industry pays 50%.

S_i = sales of fuel in kilograms U/year

V_i = net value of fuel (total value – manufacturing costs – utility payments during the first 5 years) in dollars

R_i = rate of inflation as a fraction

R_c = rate for capital as a fraction

i = numeral year from start of program (1, 2, 3 … years from 2012)

DT = development time in years

The discounted rate of return calculations were run for the development time (22 years for 2012 to 2034) and for 10, 20 and 30 years of sales (2034 to 244, 254, 2064). That is, the cash flow for each year was first discounted for the Westinghouse cost of capital (8%) and then the ROR was calculated from this cash flow. The annual fuel sales were assumed to be 1.5×10^6 kg U per year (the current Westinghouse US production rate) and 2.6×10^6 kg U per year (the current Westinghouse worldwide production rate). The results of these discounted ROR calculations are shown in Table 3.11. Undiscounted values would have approximately 8% added to each of these results.

Fuel Option	SiC+U15N	SiC+U3Si2	Treated Zr+U15N	Treated Zr+U3Si2
Rate of Return for Invested Capital	8%	8%	8%	8%
Inflation Rate	2%	2%	2%	2%
	1500 Metric Tons U			
10 Year Discounted Rate of Return	8%	0%	13%	10%
20 Year Discounted Rate of Return	11%	4%	14%	12%
30 Year Discounted Rate of Return	11%	5%	14%	12%
	2600 Metric Tons U			
10 Year Discounted Rate of Return	14%	6%	18%	14%
20 Year Discounted Rate of Return	16%	9%	19%	15%
30 Year Discounted Rate of Return	16%	9%	19%	16%

Table 3.11 – Discounted RORs for the Various ATF Options as a Function of Sales Years and Sales

The total estimated investment required by the fuel vendor and the DOE for the various ATF options are shown in Table 3.12. These calculations indicate that bringing various ATF options to market will require at least $419 million up to about $1158 million dollars (2013 constant dollars). Of this total, industry would pay anywhere from 66% to 86% of the total including commercialization efforts.

	SiC+U15N ($M)	SiC+U3Si2 ($M)	Treated Zr+U15N ($M)	Treated Zr+U3Si2 ($M)
Total Cost	$ 1,158	$ 926	$ 651	$ 419
DOE Support	$ 167	$ 152	$ 155	$ 141
Industry Funding	$ 991	$ 774	$ 496	$ 279

Table 3.12 – Total Investment for the Various ATF Options in 2013 Constant Dollars

This analysis indicates that significant governmental assistance during the research and development phases of the ATF program is needed for the fuel vendors to achieve reasonable returns on investment. This assumes that, based on the conclusion from Section 3.8 that the utility can recover their costs for conversion from their outage savings with the remaining value of the fuel being realized by the vendor. Finally, the length of time that the fuel is on the market beyond 20 years does not significantly affect the discounted return on investment for any of the ATF choices.

4. Other Business Considerations

Systems and business considerations other than return on investment are considered in this chapter. Included are:

- Supply chain, power plant, fabrication and enrichment supplier considerations

- Effect on current business
- Expected market
- Resource needs both monetary and technical
- The ability of the current organizations and support activities (for instance, standards groups and the NRC) to support ATF
- Major risks and their mitigation

4.1. System Effects

The effects of the various ATF options on the supply chain, fuel fabrication plant, power plant and used fuel handling systems were considered and compared to the reference design (cylindrical UO_2 pellets with zirconium-based cladding) in the following categories:

- Summary of fabrication and quality assurance processes relative to current LWR fuel
- Anticipated impact on LWR system design
- Estimate of required ^{235}U enrichment
- Anticipated impact on the life cycle cost of future LWRs, including:
    a. Plant construction
    b. Plant operations
    c. Wet storage of used fuel
- Anticipated impact on the quantity of used fuel
- A cost/benefit analysis including positive and negative impacts on the cost of:
    a. Enrichment
    b. Fuel fabrication
    c. Transportation
    d. Dry storage of used fuel

The result of this analysis is presented in Table 4.1. The following observations result from this analysis:

- All fuel options are manufacturable in current facilities with modifications on the order of $100 million to $200 million being required. Additional facilities will be required for SiC (up to $500M) and coated tubing manufacture (about $20M and for N15 enrichment (about $200M).
- The UN/SiC option would support a maximum uprate of up to 30% by removal of the DNB restrictions and by the availability of the added U235. U_3Si_2/SiC would support a maximum uprate of up to 15% limited by the availability of the added U235 and removal of the DNB limit. In both cases, the added thermal conductivity of the fuels supports the maximum uprates.
- The UN/SiC and U_3Si_2/SiC offer some potential for simplification in the power plant safety systems. With the new passive plants such as the AP1000®[1] Pressurized Water Reactor (PWR), these safety advantages may not be needed, but the ATF will still offer large

[1] AP1000 is a trademark or registered trademark of Westinghouse Electric Company LLC, its Affiliates and/or its Subsidiaries in the United States of America and may be registered in other countries throughout the world. All rights reserved. Unauthorized use is strictly prohibited. Other names may be trademarks of their respective owners.

economic benefits. It is expected that a significant number of the current reactors will continue to operate for an additional 20 to 40 years past the current license extensions. These reactors would benefit from both the economic and safety aspects of ATF. In addition, the safety benefits of ATF may provide added margins that will help get license extensions for the current reactor fleet.

- There are no major impacts to wet storage, transportation, dry storage and reprocessing technologies for any of the used fuels considered.
- Advanced fuels offer significant potential for a reduction of up to ~20% in the amount of irradiated fuel assemblies.

Category	U3Si2 fuel @5% U235 enrichment	$U^{15}N$ fuel @5% U235 enrichment	SiC Cladding	Ti2AlC or NS on Zr cladding
Fabrication and Quality Assurance Processes Relative to UO_2/Zr Fuel	Added step UF6 to UF4 and UF4 to U3Si2 conversion All other steps same as UO2	Added steps UO2 to UN conversion Requires N15 isotope production All other steps same as UO2	Requires different manufacturing system than for Zr tubing Requires different endplug joining technique than current welding Requires different statistics and modeling than current Zr tubing	Added coating process for Zr alloys All other processes the same
Anticipated Impact on LWR System Design	Allow uprated cores (30%) giving smaller reactors with increased maneuverability and accident forgiveness	Allow uprated cores (30%) giving smaller reactors with increased maneuverability and accident forgiveness	Allow 50% uprated cores for current reactors with increased maneuverability Fuel temperature margin increased ~800C Reduced number of safety systems	Fuel temperature margin increased ~200C Reduced number of safety systems
Maximum U235 Enrichment	~5% optimum	~5% optimum	8 to 9% optimum for UO2; resistance to radiation allows increased burnup	8 to 9% optimum for UO2; resistance to radiation allows increased burnup; higher enrichment for UO2 may be required due to higher parasitic neutron absorption
Fuel Power Density Uprate Capability	~30% due to increased thermal conductivity, removal of DNB limit and added U235	~15% due to increased thermal conductivity, removal of the DNB limit and added U235	30% (Removes DNB margin limits to increase energy density of core)	0%
Plant Construction Savings	None	None	May reduce requirements for safety systems for old style plants but will not have a significant effect on new passive (**AP1000**) plants	May reduce requirements for safety systems for old style plants but will not have a significant effect on new passive (**AP1000**) plants
Wet Storage Issues For Used Fuel	No effect on storage time but higher thermal output from used fuel due to higher U235 density	No effect on storage time but higher thermal output from used fuel due to higher U235 density	With SiC cladding, longer times in spent fuel pool will be acceptable.	With sprayed coatings, longer times in spent fuel pool will probably be acceptable.
Quantity of used fuel	~20% reduction (80 assemblies for UO2 to 64 assemblies for UN)	~10% reduction (80 assemblies for UO2 to 72 assemblies for U3Si2)	No effect	No effect
Enrichment	No effect	No effect	No effect except if used with UO2	No effect
Fabrication Cost Changes	Increased by ~$20/kgU	Increased ~$10/kgU	Increased by ~$38/rod	Increase by ~$10/rod
Transportation Cost per Assembly	Slight increase in cost due to increased weight (~20%) but number of assemblies the same per cask.	Slight increase in cost due to increased weight (~10%) but number of assemblies the same per cask.	$0 (but slightly lower weight per cask)	No effect
Dry Storage Issues of Used Fuel	No effect	No effect	No effect	No effect

Table 4.1 – ATF System Effects

4.2. Effect on Current Business

The major effect on current business would be the need to replace or augment the fuel powder production process and the fuel cladding manufacture process. Since the fuel powder would likely be made starting from UF_6 feed, the current manufacturers would continue to produce the fuel powder and pellets. If coated Zr alloy cladding is used, the current manufacturers would still also produce the Zr alloy fuel cladding and then coat the cladding by adding another production step. In the case of SiC composite cladding, since this material is outside the current realm of their production knowledge, the current fuel producers could easily move the production of this product to outside suppliers. Of course these suppliers would also have to develop their own quality control measures to meet the standards of the nuclear industry, but this could likely be done with some help from the current fuel vendors. This approach would also decrease the capital investment required from the vendors though their costs may increase since an outside vendor would likely require a much larger return on investment than the current nuclear fuel industry to supply what is a specialty item. Finally, if UN fuel is used, a N15 enrichment plant will be required. This would be the single largest capital investment. Again, this feedstock would likely be supplied by an outside vendor due to the lack of knowledge in this area by current fuel vendors. The technology required to economically separate N15 is likely to be laser isotope separation. This technology is not present among current enrichment vendors though in the future, General Electric may be in a position to use this technology based on their current uranium separation work.

There will be a large reduction in the number of assemblies that would be required for each customer. While the uranium conversion area (UF_6 to either UN or U_3Si_2) would be the same, the higher density of the products would mean that a fewer number of assemblies will be needed for each reload. In order to achieve a reasonable return on invested capital, the fuel vendor that markets an ATF will have to capture enough added market share to either maintain or increase the current production rates.

4.3. Expected Market

At this time, it is expected that low natural gas prices are expected for the next 20 to 50 years\ and very few additional nuclear plants may be built and in fact, some are likely to be abandoned. This could change if a large export market for natural gas develops or if a carbon tax is imposed on fossil fuel users. More certain is that by 2032, many plants will be into their 40 to 60 year license extension. In order to get a return on their investment, the fuel vendors offering ATF will have to quickly capture the operating plants. In addition, further license extensions may be required to maintain their profitability if a significant number of power plants are shut down. This will aggravate the effect of reduced fuel shipments in terms of assemblies as noted in section 4.3 above.

This effect is compounded by the fact that not all power plants will adopt ATF as soon as it is available. The more likely scenario is that the adoption (and the required power plant investment) will be based on the operating years remaining, the size and health of the plant, and

the willingness of the plants' owners to take the initial risk that is always attendant to the introduction of a very new technology.

4.4. Monetary and Technical Resource Needs

As shown in Table 3.12, industry will need to invest $300 million to $1 billion while DOE will need to invest about $150 million to make ATF a reality. This is a major investment for any vendor as well as for the DOE. This investment averages out to between $15 million to $50 million per year for the fuel vendors and about $15 million to $20 million per year for the DOE. Some of the larger investments for the N15 separation plant or the SiC cladding facility may be able to obtain funding from private sources such as banks if the fuel vendors are willing to negotiate take or pay type contracts with the new suppliers. This puts the initial risk on the suppliers to get their plants up and running and the long term market risk on the fuel vendors. Spinning off these two items from the fuel vendors would reduce their capital needs by about $600 million to $800 million.

This approach would also support the technical needs of the fuel vendors since they do not currently have the manufacturing expertise to support these two areas. The production of SiC cladding will require large investments in the supply chain for SiC precursor chemicals, the production of crystalline phase, low oxygen, stoichiometric fiber, extruded monolithic tubing and chemical vapor infiltration facilities. In order to produce about 3000 tons U/year of nuclear fuel, about 400 to 500 tons per year of precursor materials, 300 tons per year of fiber and 300 to 500 tons per year of monolithic tubes per year will be required. This is about 100 to 1000 times more than the current production rate of any of these materials. However, the high temperature properties of SiC composites with their concurrent advantages make acceptance of SiC composites in such high performance needs as jet engines almost inevitable. It is therefore reasonable to expect that the production facilities for the SiC materials will greatly expand and the costs will rapidly drop.

4.5. Support Activities

Significant support for this program will be required from both government agencies as well as from semi-public agencies. The government will need to significantly upgrade NRC staffing if the licensing tasks are to stay on schedule. In addition, the DOE will need to support timely access to test reactors. The Advanced Test Reactor (ATR) and the MIT Reactor (MITR) are two that will be heavily used as well as potentially the Halden reactor in Norway. Exposure time in these reactors will be needed during the first 10 years of the program for testing options and providing the basis for LTR testing. After the initial testing period, these reactors will be required to perform testing for non-steady state (ramp) testing of the fuel. In addition, specialty facilities such as the TREAT reactor will be required to provide specific testing. Much of the later testing will need to be supported through universities doing basic research work. The time span for this testing will be about 20 years to get the initial products on the market and probably another 20 years to address operating issues as they arise.

Semi-private efforts in code development such as for the American Society for Testing and Materials (ASTM) will also be required to form the basis for standardization of the product design, testing and handling procedures. Support for these programs will be provided by a mix of industry, government and academia with funding mainly from the government and some from industry. A large government component is needed due to the research and development that will be required for characterizing the new fuel and cladding materials.

4.6. Major risks and their mitigation

The major risks for this program are categorized into 5 areas:

- Technical
- Economics
- Market
- Organizational
- Resources

The risks, their likelihood, effect and mitigating factors are shown in Table 4.2. Note that the mitigating factor for each risk is the task that will be performed as a go/no go indicator on a regular basis. If the results of the analysis, test, etc. are negative, then that ATF option or the whole ATF program should be re-evaluated. This approach is taken since the Westinghouse program is based on the assumption that the optimum options have already been chosen and that other options are not economically viable. Westinghouse maintains that without economic viability, ATF will be an unacceptable fuel option for their utility customers. The added safety value of the ATF fuel has already been integrated into the total value of the fuel.

Category	Risk	Liklihood	Effect	Mitigating Action
Technical	UN not waterproofed	moderate	High - unless UO2 is about equal, non-viable fuel	Determine waterproof capability in Phase 1
	N15 Separation not feasible	low	High - non-viable fuel	Performed experimental work to prove concept
	U3Si2 swells too much	moderate	High - non-viable fuel	Determine swelling in Phase 2 ATR testing
	SiC endplug seal not viable	moderate	High - non-viable cladding	Demonstrate endplug seal in Phase 2
	SiC strength not sufficient	moderate	High - non-viable cladding	Demonstrate strength in Phase 1
	Ti2AIC coating too porous	high	High - non-viable cladding	Demonstrate abiltiy to protect Zr in Phase 1
	Nanosteel coating too porous	high	High - non-viable cladding	Demonstrate abiltiy to protect Zr in Phase 1
Economics	UN manufacture >$60/kgU	low	Low - small increase in fuel cost	Already demonstrated production technique - further demonstrations in Phase 2
	U3Si2 manufacture >$40/kgU	low	Low - small increase in fuel cost	Already demonstrated production technique - further demonstrations in Phase 2
	SiC cost >$140/tube	moderate	moderate	Demonstrate cost in Phase 1 or 2
	N15 cost >$1200/kg N15	low	moderate	Previous estimate of cost
Market	>30 powerplants off line by 2032	moderate	high	Follow trend and redo economic study
	Powerplants do not buy ATF	low	high	Follow trend and redo economic study
Organization	Multiple vendors have same ATF keeping profit margin low	moderate	high	Follow trend and redo economic study
	Other entities for N15 and SiC CMCs not found	moderate	moderate	Reduces profit margins to current estimates
Resources	DOE does not have funds to continue ATF program	moderate	high	Leave ATF program
	Vendors do not have funds to continue ATF program	moderate	high	Leave ATF program
	Costs higher than predicted	moderate	high	Follow trend and redo economic study

Table 4.2 – Risks and Mitigating factors

5. Conclusions and Recommendations

The following conclusions were reached based on this study:

1. Government investment in the ATF program is required for there to be a reasonable ROI for the fuel vendors. The vast majority of the technical risk is at the research and development stage (<10% of the total cost). Government investment at the 80% level is appropriate at this stage due to the high technical risk involved. Industry pays >66% of the total cost through commercialization.
2. Absent U235 enrichments greater than 5%, the use of higher density pellets for higher U235 loadings increases the economic attractiveness of ATF. U_3Si_2 offers ~17% gain in U235 density, increased thermal conductivity minimal increases in production equipment and an increase in the margin to centerline melting during transients. UN offers ~40% gain in U235 content, high melting point and a very high thermal conductivity which provides a large increase in the margin to centerline melting during transients. It requires N15 enrichment and treatment to be oxidation resistant to reactor coolant. Additional effort is required for UN and U_3Si_2 to determine if there are swelling issues since the current data is extrapolated from reactor data at temperatures and burnups that are significantly different from those likely to be experienced in commercial fuel service. If testing indicates that the swelling is an issue, then additional work on pellet additives or manufacturing conditions will be needed.
3. Based on preliminary calculations, the treated Zr alloy options offer modest ATF gains (~200°C) but reasonable economic opportunities for the fuel vendors with discounted RORs of ~10% to 19% when paired with higher density pellets. They also present the least development risk because the basis for the cladding is still Zr alloy and the required development costs are the lowest.
4. Based on preliminary calculations, SiC offers the most ATF margin (500°C to 800°C) and reasonable discounted RORs of between 4% and 11% when paired with high density pellets. This option presents the most development risk as well as the highest capital investment requirements. Note that much of the capital requirement is due to the fact that an acceptable cladding design has yet to be decided upon and the design of the manufacturing facilities has not been developed. In addition, since the behavior of the SiC/pellet system while in the reactor is unknown, very conservative fuel rod design constraints were imposed resulting in a large initial pellet-cladding gap which severely penalizes the ATF economics. The thickness of the SiC cladding wall has a large effect on fuel cycle economics. Further developmental efforts to reduce the cladding thickness to levels approaching current Zr alloy cladding wall thickness will provide further fuel cycle value benefits.
5. There are no showstoppers to implementation when considering the supply chain, power plant, fabrication and enrichment supplier.
6. Fuel vendors do not currently have the technical and manufacturing background in SiC, coatings or N15 enrichment.
7. The annual investment needs for furthering any of these technologies will be in the $10M to $50M per year range for the fuel vendors and in the $10M to $20M per year range for governmental support.

8. Government and industry will have to support significant efforts in setting standards for any of the cladding or fuel options since these options are not currently in use by the industry. The same is true for the Nuclear Regulatory Commission which must license these new fuels since all current regulations are oriented toward UO_2/Zr fuel.
9. The major risks involved in developing an ATF stem from the fact that none of the technologies being considered have a very significant technological background in the nuclear industry and the costs and time involved in overcoming this gap in knowledge are very high. Options with smaller knowledge gaps (such as stainless steel cladding) do not offer significant economic gains (and sometimes losses) as compared to the high risk ATF options to justify the time and cost of undergoing even a moderate development program.
10. The utilities will likely be able to utilize the performance gains from ATF to help recapture the costs involved in implementing ATF. Some assistance from the fuel vendors may be required to produce a positive NPV during the transition period.

Based on these conclusions, Westinghouse makes the following recommendations:

1. Government funding of the high risk research stage for ATF development must continue for ATF to be attractive to the fuel vendors risk wise and economically. Refinement of the financial model inputs and program risks should be incrementally refined to support its financial viability. Results of subsequent analysis should be considered against the baseline results in this preliminary estimate.
2. Irradiation of the U_3Si_2 and UN with SiC and treated Zr cladding is required to determine the performance aspects of the fuel and cladding individually as well as a fuel system. Key issues are swelling of the fuel and interactions between the fuel and cladding, especially the SiC.
3. A significant SiC cladding design, testing and verification effort is immediately required to determine the optimum design. This needs to be followed up with a detailed manufacturing analysis to determine if SiC cladding can offer enough benefit to justify the development effort and be economically competitive with current UO_2/Zr fuel option.
4. Without a pellet with significantly higher density and thermal conductivity than UO_2, none of the ATF cladding offerings makes economic sense. Therefore a robust high density pellet program is needed if any of the ATF claddings are to be pursued.

6. References

1. Development of LWR Fuels with Enhanced Accident Tolerance; Task 2 – Description of Research & Development Required to Qualify the Technical Concept, Peng Xu, RT-TR-13-8, May 31, 2013, http://www.westinghousenuclear.com/docs/RT-TR-13-8_2.pdf

7. Acronyms

ASTM:	ASTM International, formerly known as the American Society for Testing and Materials
ATF:	Accident Tolerant Fuel
BET	Brunauer–Emmett–Teller theory (surface area measurement)

°C:	degrees Celsius
Ca:	Calcium
CaF_2:	Calcium fluoride
CMC:	ceramic matrix composite
CO^2:	Carbon dioxide
CVD/CVI:	chemical vapor deposition/chemical vapor infiltration
DBA:	design basis accident
DOE:	US Department of Energy
DNB:	departure from nucleate boiling
EFPD:	effective full power day
FA:	fuel assembly
FSAR:	Final Safety Analysis Report
H/U:	Hydrogen to uranium ratio
H_2:	Hydrogen
H_2O:	Water
HCN:	Hydrogen Cyanide
HF:	Hydrogen Fluoride
ID:	inner diameter
IFBA:	integral fuel burnable absorber
INL:	Idaho National Laboratory
K:	thousand
Kg:	kilogram
LIS:	laser isotope separation
LOCA:	loss of coolant accident
LTR/LTA:	lead test rod/lead test assembly
LWR:	light water reactor
M:	millions
MWe:	megawatt electric
MWhre:	megawatt hour electric
MWt:	megawatt thermal
N_2:	Nitrogen
N15 or ^{15}N:	15 isotope of nitrogen
NH_4OH:	Ammonium hydroxide
NH_4NO_3:	Ammonium nitrate
NRC:	Nuclear Regulatory Commission
NS:	stainless steel alloy
O_2:	Oxygen
OD:	outer diameter
OFA:	Optimized Fuel Assembly
PIE:	post irradiation examination
PCI:	pellet clad interaction
PCMI:	pellet clad mechanical interaction
PWR:	pressurized water reactor
RCS:	reactor cooling system

RFA: robust fuel assembly
RIA: reactivity initiated accident
ROI: return on investment in %
ROR: rate of return in %
SBO: station blackout event
Si: Silicon
SiC/SiC CMC: Silicon Carbide fiber/Silicon Carbide matrix ceramic matrix composite
SL: safety limit
SNC: Southern Nuclear Operating Company
SWU: separative work unit
Ti_2AlC: Titanium aluminum carbide
TMI-2: Three Mile Island Unit 2
U: Uranium
U235: Isotope 235 of uranium
UC: Uranium carbide
UO_2: Uranium dioxide
UO_2F_2: Uranium fluoride
$UO_2(NH_4)_2$: Ammonium diuranate
$UO_2(NO_3)_2$-$6H_2O$: Uranium nitrate hexahydrate
U_3O_8: Uranium oxide
UF_6: Uranium Hexafluoride
UN: Uranium Nitride
US: United States
U_3Si_2: Uranium Silicide
w/o: weight percent
yr: year
Zr: Zirconium
3-D: three dimensional

Uranium Silicide Fabrication for use in LWR Accident Tolerant Fuel

Jason M. Harp, Paul A. Lessing, Rita E. Hoggan

Idaho National Laboratory, PO Box 1625, MS 6188, Idaho Falls, ID 83415-6188 jason.harp@inl.gov

In collaboration with industry, Idaho National Laboratory (INL) is investigating uranium silicide for use in future light water reactor fuels as a more accident resistant alternative to uranium oxide base fuels. This work is part of a larger effort to create accident tolerant fuel forms where changes to the fuel pellets, cladding, and cladding treatment are considered. Specifically this project is focused on producing uranium silicide (U_3Si_2) pellets by conventional powder metallurgy with a density greater than 94% of the theoretical density of U_3Si_2. This work has produced a process to consistently produce pellets with the desired density through careful optimization of the process. To this end, high phase purity U_3Si_2 has been successfully produced. Milling of the U_3Si_2 has been optimized. Results are presented from sintering studies and microstructural examinations that illustrate the need for a finely ground reproducable particle size distribution in the source powder. The density produced by the optimized process is of 11.57 g/cm^3 or 94.7% theoretical density. The optimized process will be used to produce more samples for physical property characterization and an upcoming irradiation in the Advanced Test Reactor.

I. INTRODUCTION

Enhancement of the safety and performance of Light Water Reactors (LWR) remains an active research area. Several accident tolerant fuel concepts are currently being evaluated by industry lead teams in collaboration with national laboratories and universities. This work is part of one such collaboration. The primary uranium compound used in nuclear fuel worldwide is uranium dioxide (UO_2) however alternative uranium compounds, such as uranium silicides, exists whose properties make them a potential alternative to UO_2 in nuclear fuel. In this work, samples of high density (>94% theoretical density) uranium silicide (U_3Si_2) have been fabricated by powder metallurgy techniques. The developed fabrication techniques will be used to create samples for irradiation testing in the Idaho National Laboratory (INL) Advanced Test Reactor (ATR). Post irradiation examination of these samples will provide important information on the performance of U_3Si_2 under typical LWR conditions.

Uranium and silicon form several different stoichiometric compounds including USi_2, USi (or $U_{34}S_{34.5}$), U_3Si_2, U_3Si [1, 2]. The uranium density and thermophysical properties of high uranium content uranium silicides (U_3Si_2 and U_3Si) make them an attractive material from both an economic and safety perspective as a replacement for UO_2. Experience from research reactor fuel work indicates U_3Si swells too much under irradiation for use as a nuclear fuel; additionally it disassociates into U_3Si_2 and solid solution U above 900°C which is below some expected temperatures in uranium silicide fueled pins. Fortunately U_3Si_2 has a very promising record under irradiation in research reactor fuels and maintains several advantageous properties over UO_2. Some of these properties are shown in Table 1. There are approximately 17% more uranium atoms in a set volume of U_3Si_2 than there are in the same volume of UO_2 given a constant percentage of theoretical density for both samples. This superior uranium loading has the potential to either extend cycle length in LWRs or reduce enrichment both of which are economically beneficial. The lower melting temperature of U_3Si_2 is off-set by its

Table 1. Key Properties of UO_2 and U_3Si_2

Property	*UO_2*	*U_3Si_2*
Theoretical Density (g/cm^3)	10.96	12.2
Theoretical Uranium Number Density (atom/cm^3)	2.44×10^{22}	2.86×10^{22}
Thermal Conductivity (W/m·K 400-1200°C)	6 to 2.5	38 to 21 [**Error! Reference source not found.**]
Melting Point	2847	1665

much higher thermal conductivity that drastically drops the anticipated centerline temperature in a fuel pin compared to UO_2 fueled pins. This has significant positive impacts on fuel pin performance in a variety of reactor accident conditions.

II. Uranium Silicide Formulation

The U_3Si_2 formulation process used in this work is described in detail in Reference 3 and summarized here. Uranium silicide is formed from mixing powders of elemental uranium and silicon in near stoichiometric quantities. Uranium powder is created by a hydride / dehydride process, and silicon powder is created by mechanical crushing. The mixture is then pressed into a compact as seen in Fig. 1. The compacts are agglomerated in a furnace at 1450°C, and then sent to an arc melter to completely react the uranium and silicon. In the arc melter, a tungsten electrode passes current through the uranium and silicon sample into a water cooled copper or graphite hearth. The arc melting process is repeated two additional times to ensure complete reaction. This process produces uranium silicide that is more U_3Si_2 phase pure (97% U_3Si_2) than what was typically produced by arc melting bulk uranium and silicon pieces which usually had about 10% U_3Si [1, 4]. An example of the uranium silicide ingot after arc melting is shown in Fig. 2

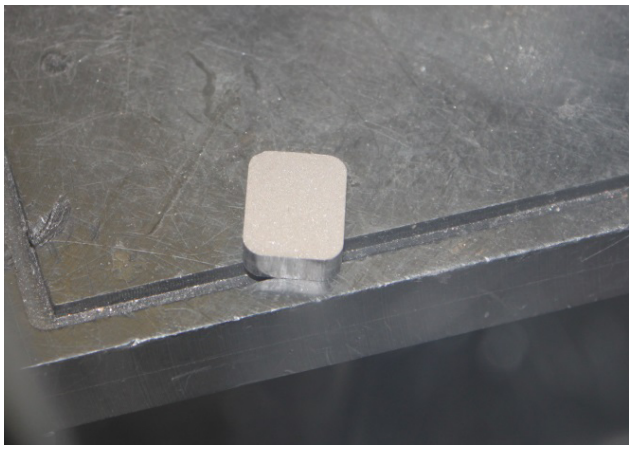

Fig. 1. Uranium and Silicon Compact before Arc Melting

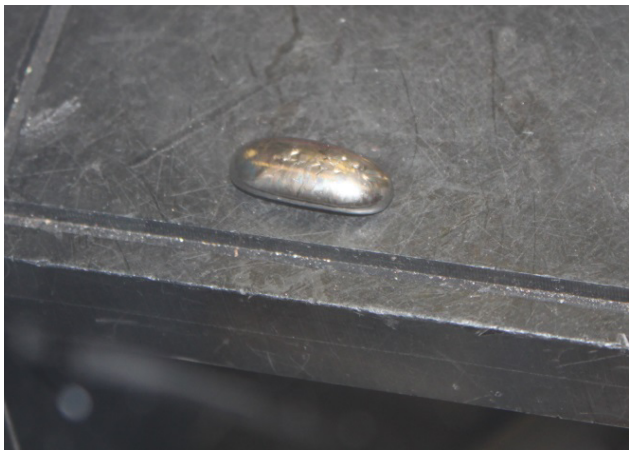

Fig. 2. Uranium Silicide Ingot after Arc Melting

III. Uranium Silicide Pellet Fabrication

Uranium silicide ingots from the arc melter are comminuted into a fine powder before being pressed into a green pellet and subsequently sintered. The comminution process to create a fine sinterable powder has undergone extensive refinement. Uranium silicide presents several challenges to the creation of a fine powder. Most notably, it is highly reactive in oxygen requiring the use of inert atmosphere gloveboxes for the majority of the powder work. The high density of uranium silicide compared to most other common materials complicates the grinding process as ideally grinding media should be at least close in density if not more dense than the material being ground. Additionally, all the precautions associated with handling a radioactive substance must be followed.

III.A. Comminution

Planetary milling was chosen as the means to reduce the arc melted ingots into a fine powder. Before milling the arc melted ingots are manually broken up using a hammer mill. Appropriately sized U_3Si_2 particles are then loaded into a milling jar with along with the milling media. In planetary milling, about 10-20% of the milling jar volume is taken up by the grinding media, and 10-40% of the milling jar volume is taken up by the material being ground. Zirconia grinding media and zirconia lined milling jars were utilized in this work. The density disparity between zirconia and U_3Si_2 is undesirable, but no other higher density ceramic milling media was available. In order to achieve the desired final particle size in this work, it was necessary to progressively reduce the size of the milling media. A single milling step with 10 mm media was initially attempted, but even after switching to a smaller 5 mm grinding media the final particle size was still to coarse for high density sintering. A two step approach was then adopted where material from the hammer mill was initially milled with 5mm media followed by sieving. The fines (<39 μm particle size) were then milled a second time with 1mm milling media. Milling aids may also be added to increase the process efficiency. Initially in this work no milling aids were utilized; however the powder tended to stick to the side of the milling jar preventing further milling. Several lubricants were tried including Oleic acid and several molecular weights of polyethylene glycol (PEG). The best results were found with PEG 3350.

The particle size distributions of the resulting powders from milling were evaluated using a Micromeretics Sedigraph III. This equipment uses sedimentation theory and x-ray attenuation to calculate

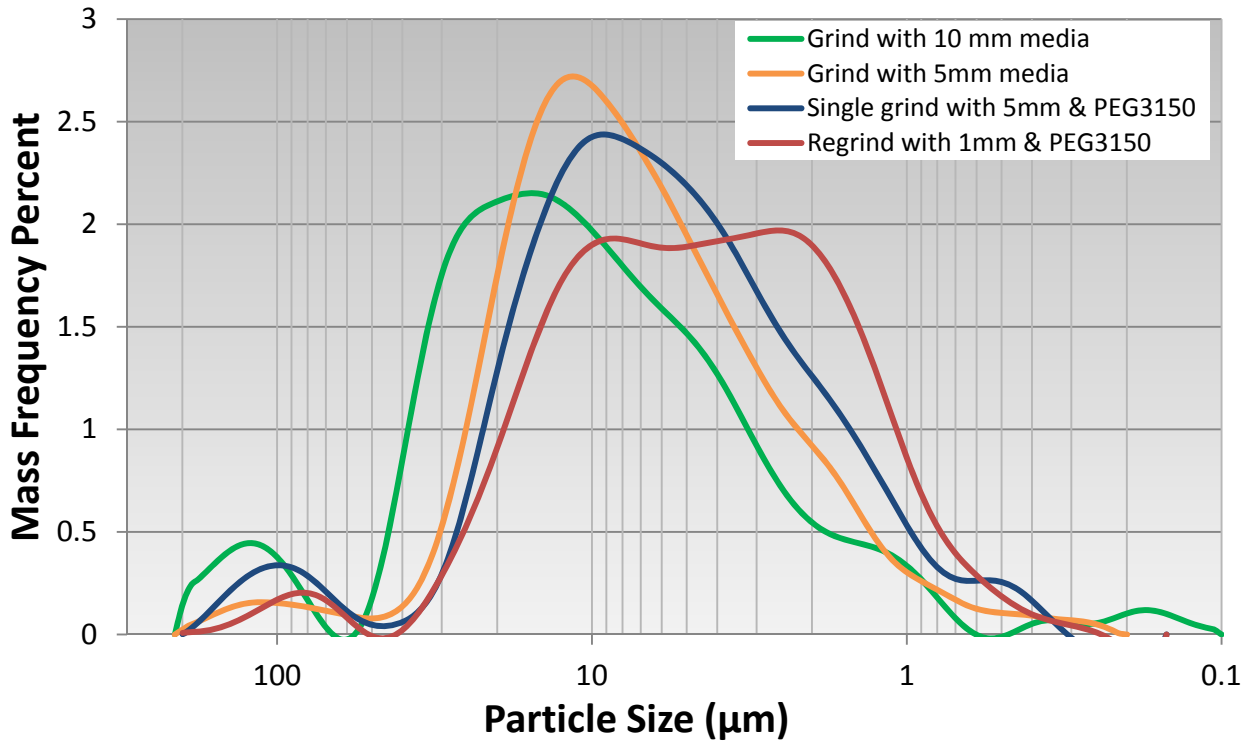

Fig. 3. Particle Size Distribution of U3Si2 from different milling recipes

the mass percent of particles in a sample. In this technique, a sample of powder is mixed with a liquid to create a slurry. The liquid must have a well-known viscosity and often contains a surfactant to keep particles from agglomerating. The slurry is injected into a sample chamber viewed by an x-ray source and allowed to settle. As the larger particles settle to the bottom of the chamber, the x-ray attenuation is decreased. The time required for a particle to settle out of the sample chamber and no longer attenuate x-rays can be related to its Reynolds number which is related to its equivalent diameter.

The curves in Fig. 3 show different particle size distributions attained from different milling parameters. The blips in the curves in the range near 100 µm and below 0.5 µm are statistical anomalies inherent in this particle size distribution technique. In initial studies, 10 mm grinding media were used to comminute the U_3Si_2. Powder from this distribution (shown in green in Fig. 3) did not sinter to high enough densities for this work. To produce a finer particle size distribution smaller grinding media were employed and regrinding was investigated. Without any milling aids, 5 mm milling media were able to drop the median particle size, but high densities could not be consistently achieved with this powder (orange curve in Fig. 3). After further process refinement a two-step milling process was established. Arc melted ingots are crushed by a manual hammer mill and sieved through a <1mm sieve. This powder is mixed with 0.1 weight % PEG3150 and milled with 5 mm media. The resulting powder is sieved through a less than 39 µm sieve (400 mesh). The particle size distribution of this powder is shown by the blue curve in Fig. 3. The sieved powder is then reground with 1mm media to produce a particle size distribution shown by the red curve in Fig. 3. Pellets pressed from this particle size distribution have consistently sintered to high densities and the production of this particle sized distribution has proved to be reproducible by following the same milling parameters on multiple batches of arc melted uranium silicide.

III.B. Pellet Pressing

Forming the fine powder from milling into a green pellet for sintering also required several iterations of development. To produce green pellets, charges of powder are loaded into a lubricated die with two floating punches. The floating punches and die are pressed in a manual press, ejected and then examined before sintering.

Pellets were pressed from a 9.525 mm (0.375 inch) diameter die. Before pressing the die wall was lubricated with zinc sterate. A charge of 4 grams of U_3Si_2 was selected that would create pellets with an aspect ratio of less than one to help facilitate pellet production. Two floating punches provided dual action compaction to the charge when pressure was applied. Pellets were pressed with a pressure ranging from approximately 124 to 248 MPa. Most successful pellets were pressed between 124 to 156 MPa. Pellets pressed at higher pressures tended to delaminate after ejection from the die. Increasing the pressure did not necessarily lead to higher green densities

or green strengths. The best sintering results tended to occur with pellets with a green density between 60 and 65% theoretical density. This was achievable with most powder distributions only using 124 MPa. This is behavior with increasing pressure and optimum green density is consistent with some earlier work reported in literature for uranium silicide [5].

The final powder from the comminution process, shown by the red curve in Fig. 3, was highly suspecatble to delamination and had very low green strength after pressing. This had been observed previously with other milling lubricants as well. It was therefore necessary to burn off the PEG from the powder. This was accomplished by heating the powder under vacuum to 350°C for about 1 hour. Even after the removal of the PEG the powder still needed some additional cohesion to create green pellets. Approximately 0.1 weight percent polyox was added to the powder to act as a binder during pressing. This produced pellets with adequate green strength that were appropriate for sintering.

III.C. Pellet Sintering

Sintering studies on the different powders from milling have been carried out in parallel with the milling and pressing development. Sintering of the U_3Si_2 has been conducted in both Ar with 40 ppm O_2 and under vacuum. After sintering the density of the pellets is measured, and the microstructure of select pellets is examined. The final density of the sintered pellets appears to depend on several parameters including the particle size distribution, pellet green density, the maximum sintering temperature and the time at maximum sintering temperature. Sintering temperatures ranging from 1400°C to 1550°C have been investigated. Sintering times ranging from 2 to 8 hours at maximum temperature have also been investigated. Two step sintering was briefly investigated, but the final density was always similar to simply sintering the pellet for the same time at the maximum sintering temperature. The best sintering results occurred when the pellets were inside at tantalum crucible on a bed of small tantalum pellets. The Ta works as an effective oxygen getter during sintering. Without the Ta pellets, the U_3O_2 pellets tended to stick to the Ta crucibles or Ta foil. The Ta pellets act as a setter sand for the U_3Si_2 pellets decreasing interactions and encouraging U_3Si_2 densification.

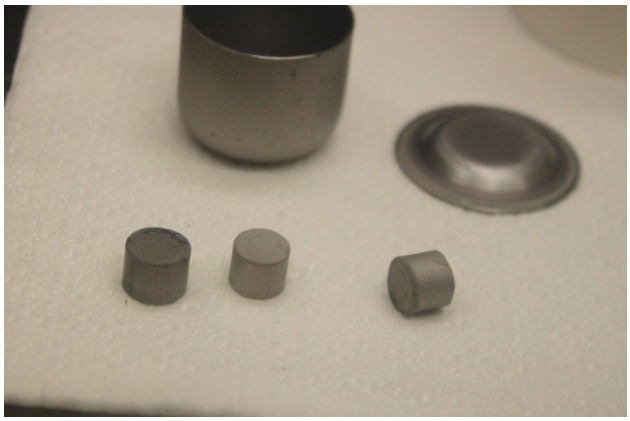

Fig. 4. Typical unsintered U_3Si_2 pellet on left compared to two sintered pellets in center and to the right with Ta crucible in the background

IV. Pellet Characterization

The primary metric for evaluating U_3Si_2 pellets in this work has been density. Additionally, the microstructure of the final product has been evaluated via scanning electron microscope (SEM) examinations and XRD to confirm the phase. The density of the sintered pellets was measured using immersion density following ASTM B962. In this procedure the sample are oil impregnated to fill any porosity left in the sintered pellets. In the future, density will most likely be evaluated by helium pycnometry.

Pellets pressed from the initially milled powder (green curve in Fig. 3) were sintered at several different temperatures and times resulting in a range of densities for the different conditions. Pellets sintered for 1 hour at 1400°C had densities ranging from 86.3 to 89.6 % theoretical density. Pellets sintered at 1450°C for 1 hours had an average density of 92.4 % theoretical density, and pellets sintered at 1450°C for 2 hours had an average density of 93.7 % theoretical density (11.44 g/cm^3). All this sintering was carried out in the Ar atmosphere furnace. This early success established 1450°C and higher as the desired sintering temperature with a time at temperature of 2 hours or longer.

However these densities were short of the programmatic goal of around 95.5% theoretical density and atleast 94% theoretical density. A finer particle size distribution was required. Several pellets were sintered from powder typified by the orange curve in Fig. 3. However without milling aids these powders appear to have had highly variable particle size distributions and consistent densities under similar conditions were difficult to obtain. Some pellets were sintered with densities as high as 94.6 % theoretical density, but the majority of pellets sintered from this powder had theoretical densities ranging from 91 to 93.5% theoretical density. Sintering temperatures of 1450°C and 1500°C were investigated and sintering times ranging from 2 hours to 4 hours were investigated.

After a more consistent powder product was established (powders with a particle size distribution represented by the red curve in Fig. 3), it was possible to consistently produce pellets with a density above 94% theoretical density. This was done both in the Ar furnace and under vacuum using the same sintering parameters. Pellets sintered for 4 hours at 1500°C under Ar had an average theoretical density of 94.7% (11.57 g/cm^3).

These pellets contained polyox, and the PEG from milling had been burned off. Similar pellets with polyox, but still containing PEG from milling sintered nicely as well. However these pellets had lower densities ranging from 92.9 to 94.4 % theoretical density.

Examination of the porosity and mictrostructure of the sintered U_3Si_2 also informed the milling development and also confirmed the sintering was proceeding as planned. XRD examinations of sintered pellets confirmed that the primary phase present in the sintered pellets was U_3Si_2. No secondary silicide phases or uranium oxide phases were observed in the XRD spectra. Additionally SEM examination of the sintered pellets revealed no U_3Si, pure U, pure Si, or UO_x phases in the sintered pellets. SEM did reveal some minor contamination phases from the arc melting process. The amount of porosity in the sintered microstructure followed the density of the pellets as can be seen in Fig. 5, Fig. 6, and Fig. 7. The SEM examination also provided evidence for the need to produce a smaller particle size distribution. In Fig. 8 the grain structure is faintly visible and it is clear that the majority of porosity falls along the grain boundaries and at triple points. Arrows point towards intergranular porosity in the figure. This porosity is difficult to close via thermal diffusion that occurs during conventional sintering. This illustrated the need to produce a finer particle size distribution in milling the help eliminate intergranular porosity.

Themorphysical characterization of sintered U_3Si_2 will subsequently begin as samples of high density pellets are produced. Measurements to determine the thermal conductivity of sintered U_3Si_2 will be performed. Corrosion studies of U_3Si_2 in water and steam will also be performed. Samples will also be produced to study the elastic and creep properties of U_3Si_2. Neutron diffraction may also be considered.

V. Summary

Uranium silicide pellets have been produced by powder metallurgy techniques for as part of an accident tolerant fuel concept. The process to produce these pellets has undergone extensive optimization to produce pellets with a sintered density of greather than 94%

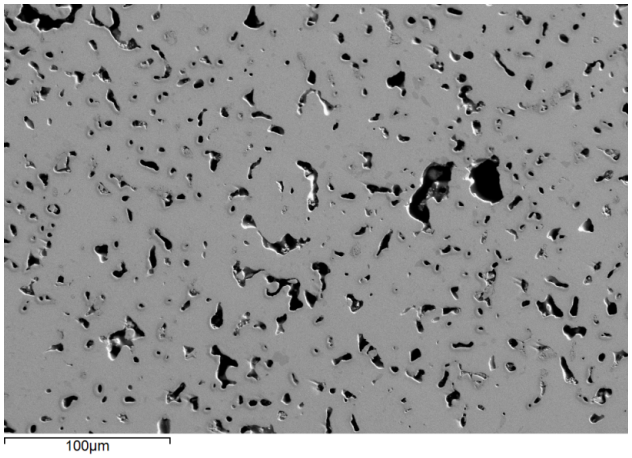

Fig. 5. SEM secondary electron image showing the sintered microstructure of 88.6% theoretical density U_3Si_2

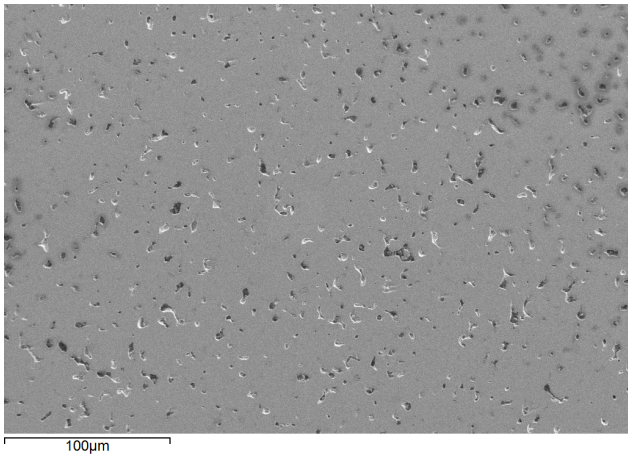

Fig. 6. SEM secondary electron image showing the sintered microstructure of 92.1% theoretical density U_3Si_2

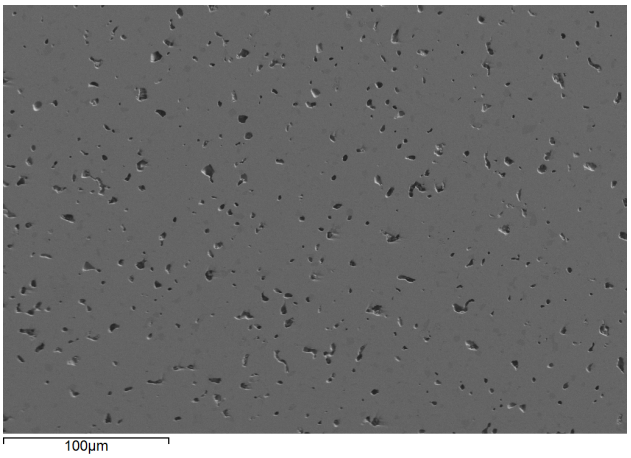

Fig. 7. SEM backsatter electron image showing the sintered microstructure of 92.4% theoretical density U_3Si_2

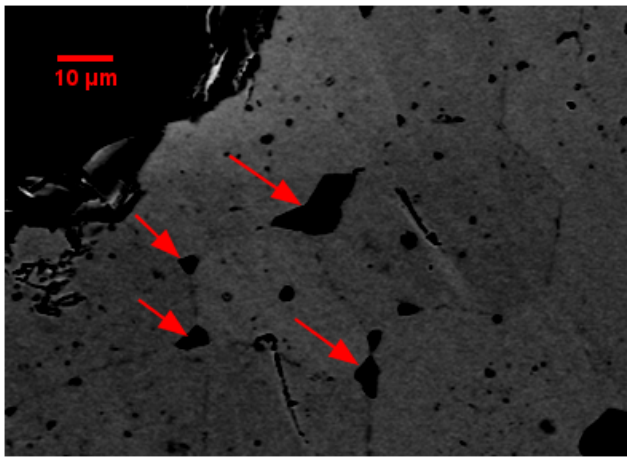

Fig. 8. SEM backsatter electron image showing the location of porosity in U_3Si_2

theoretical density (11.47 g/cm^3). In order to produce pellets of this density, the particle size distribution of the source powder was optimized. Pressing and sintering parameters were also optimized until high denisity pellets could be consistently produced. Work will now begin on producing samples to better characterize the unirradiated properties of U_3Si_2 and samples of enriched uranium silicide will be produced for irradiation testing beginning in the summer of 2014.

ACKNOWLEDGMENTS

This work was supported by the U.S. Department of Energy, Office of Nuclear Energy. This work is also part an collaboration lead by Westinghouse Electric Company comprising several national laboratories, vendors, and universities awarded in response to the DE-FOA-0000712 funding opportunity. The authors would also like to acknowledge the assistance of the support staff associated with the Fuels Applied Science Building at INL

REFERENCES

1. J.L. Snelgrove, R.F. Domgala, et al, "The Use of U_3Si_2 Dispersed in Aluminum in Plate-Type Fuel Elements for Research and Test Reactors," ANL/RERTR/TM--11. Argonne National Lab., IL (United States), 1987.
2. H. Okamoto, Si-U (Silicon-Uranium), Binary Alloy Phase Diagrams, II Ed., Ed. T.B. Massalski, Vol. 3, 1990, p 3374-3375
3. J.M. Harp, P.A. Lessing, B.H. Park, J. Maupin, "Preliminary Investigation of Candidate Materials for Use in Accident Resistant Fuel," Proc. TopFuel 2013, Charlotte, North Carolina, 2013
4. T.C. Wiencek, "Summary report on fuel development and miniplate fabrication for the RERTR program, 1978 to 1990," ANL/RERTR/TM--15. Argonne National Lab., IL (United States), 1995.
5. K.M. Taylor, C.A. Lenie, P.E. Doherty, C.H. McMurtry, "Synthesis and Fabrication of Refractory Uranium Compounds," Fourth Quarterly Report, TID-6591, No. ORO-340. Carborundum Co., Niagara Falls, NY, 1960

Development of an accident-tolerant fuel composite from uranium mononitride (UN) and uranium sesquisilicide (U_3Si_2) to improve thermal conductivity and increase uranium loading.

Luis H. Ortega*, Jordan A. Evans, Sean M. McDeavitt

Fuel Cycle & Materials Laboratory
Texas A&M University Department of Nuclear Engineering
College Station, Texas

Abstract

The processing steps necessary to prepare a potential accident-tolerant fuel composite consisting of uranium mononitride (UN) combined with uranium sesquisilicide (U_3Si_2) are described. Liquid phase sintering, with U_3Si_2 as the liquid phase, combined with UN powder or UN μ-spheres was performed. Various UN to U_3Si_2 ratios resulted in up to 94% theoretically dense pellets. Thermal diffusivity measurements were made from 298 to 578 K, and thermal conductivity calculations were carried out. Composite UN-U_3Si_2 pellets had >30% higher uranium content and approximately double the thermal conductivity than UO_2 at 573 K.

Keywords: accident-tolerant fuels, nuclear fuel, uranium sequisilicide, U_3Si_2, uranium mononitride, UN, high density nuclear fuel

1. Introduction

Uranium dioxide (UO_2) has been the uranium bearing compound of choice for commercial nuclear power generation due to several beneficial properties. These properties include a high melting point, thermal stability, chemical stability, and low swelling under irradiation. These come at the expense of a relatively low thermal conductivity of 7-8 W/m·K at 573 K, which decreases with increased temperature and burn-up [1]. A fuel with a higher thermal conductivity will improve heat removal efficiency, thus lowering centerline temperatures. This will reduce temperatures overall during operation and therefore lessen the severity of thermal gradients within the fuel. This will reduce temperature dependent detrimental effects, such as grain growth, pellet cracking, and fission product transport, which in turn can lead to increased fission gas release. In an accident scenario, these qualities become more important. A high thermal conductivity fuel will reject heat more rapidly and operate at a lower temperature, thus have less stored energy. Higher thermal conductivity can also improve safety margins if the lower operating temperature is enough to compensate for a lower fuel melting point.

The use of uranium mononitride (UN) as a nuclear fuel is desirable due to its high uranium loading and high thermal conductivity, which increases with temperature [2]. The reactivity of UN with water has been a concern in nuclear reactor applications. For this reason, uranium sesquisilicide (U_3Si_2) has been combined with the UN to provide a protective barrier. To achieve water resistance a continuous U_3Si_2 phase was desired. Several sesquisilicide fractions were tested to reach these goals. A sesquisilicide content between 25 and 32 mass % achieved the highest densities in these tests. The U_3Si_2 also has a high thermal conductivity and high uranium density relative to UO_2. A fuel based on U_3Si_2 alone is an option, but the current work is focused on a UN-U_3Si_2 composite.

A fuel composed of UN and U_3Si_2 will significantly improve the fuel's thermal conductivity over UO_2 (Table 1). Another fuel improvement over UO_2 is a higher uranium density and therefore higher fuel loading. For example, an inter-metallic composite with UN combined with 25 mass% U_3Si_2 at 95% of the theoretical density

*Corresponding author telephone: 765-743-5642 fax: 979-845-6443

Email addresses: bertortega@tamu.edu (Luis H. Ortega), jordanevans@tamu.edu (Jordan A. Evans), mcdeavitt@tamu.edu (Sean M. McDeavitt)

will have 33% more uranium than UO_2 per unit volume. This will translate to a 33% increase in the fuel content without increasing the U^{235} enrichment.

2. Materials & Methods

Uranium mononitride (UN) was provided by Los Alamos National Laboratory (LANL) and General Atomics (GA). The UN obtained from LANL was prepared by single pass carbothermic reduction and nitridization, resulting in a carbon content of 836 ppm, Standard Deviation (SD) 19 and an oxygen level of 2228 ppm, SD 232. A portion of the powder was also subsequently sintered at high temperature to reduce the carbon and nitrogen impurities. This resulted in a carbon content of 218 ppm, SD 6.8, and oxygen at 1794, SD 30. The impurity levels for the GA-provided UN μ-spheres, and sesquisilicide were not available at the time of writing.

The LANL UN had been been ground and sieved to produce a 100-200 μm powder. A fraction was prepared at Texas A&M University (TAMU) by partially milling the UN and re-sieving it to obtain a 45-75μm powder. General Atomics provided UN microspheres for testing as well; these were used as-received. The uranium sequisilicide was furnished by Idaho National Laboratory. The U_3Si_2 had been ground and sieved to less than 37 μm in size. A separate fraction of U_3Si_2 was further ground at TAMU with a jet mill (Model 00 Jet-O-Mizer, Fluid Energy) down to ≈10μm. The powders were mixed with Zn-stearate as a binder (<1 mass%). The bimodal mixture was then pressed to form green pellets for sintering. These pellets we prepared in 6mm and 13mm diameter dies. Liquid phase sintering temperatures used were as high as 2073 K with dwell times at the peak temperature of up to 4 hours. The pellet densities were measured using the Archimedes method with ethanol.

2.1. Powder Preparation

Powders were stored inside an argon-filled glove box which was kept below 10 ppmV O_2. Powder weighing and pellet pressing were also carried out inside the glove box. The powder morphology was analyzed by embedding the powders in epoxy and polishing for Scanning Electron Microscopy (SEM). Prior to pelletization the powders were mixed outside of the glove box with a rotary jar mill (CV-80461, U.S. Stoneware) inside of small glass autoclavable bottles (120 ml) with hermetically sealed caps. The bottles were placed inside of a 1 L HDPE bottle to set on top of the rollers for tumbling. The plastic bottle also provided secondary containment. Mixing of the powders was done in two steps to promote an even distribution of binder. Half of the Zn-stearate binder was added to the mononitride alone and mixed for approximately one hour. The sesquisilicide and remaining binder were then added to the mononitride powder mixture (inside the glove box) and mixed for another hour on the rotary mill. The bottle with the mixed powder was then returned to the glove box for pellet pressing. The binder concentration was kept to < 1 mass%. Typically 0.5 mass% was used. When preparing samples with UN μ-spheres, the binder was increased to 0.75 mass% to improve powder adhesion. Even with the increased binder, the UN μ-sphere powders formed fragile pellets which required extra care during handling to avoid crumbling.

2.2. Pellet Preparation

The dies used for green pellet compaction were trapezoidal split sleeve dies from Across International LLC. These simplified the removal of the pellets after pressing. A saturated solution of Zn-stearate in benzene was applied as a die wall lubricant. The die sleeve was assembled, then the bottom core die was dipped in the lubricant solution. The excess lubricant was removed by touching a corner on a flat surface allowing the excess liquid to run off, leaving only a thin film on the core die. The lubricated core die was then fitted into sleeve assembly and pushed to the bottom with the push rod. The solution was allowed to dry. Next, the desired amount of mixed precursor powder was added to the die assembly. Minimal handling of the mixed powder was necessary in order to avoid segregation of larger particles from the fines. Scooping with a spatula diminished the separation to some degree, but separation was not completely avoided. The top core die was coated with the lubricating solution in the same manner as before, then inserted into the die assembly and allowed to slide on top of the powder. The push rod was inserted into the die assembly and pushed down, then the assembly was transferred to a Carver Model C hydraulic press. Pressures applied were from 260 to 700 MPa. The pressure was held for approximately one minute. The pressure was maintained manually during relaxation.

2.3. Sintering

After the pellets were pressed, they were placed on a yttria crucible, which was set in a refractory metal crucible, which was then placed in a large alumina crucible with a heavy lid (Figure 1a). The refractory metal provided a barrier between the yttria and the alumina which have a low temperature eutectic, and the alumina provided a protective enclosure to reduce oxidation of the pellet surface. The alumina crucible had small grooves

Table 1: Properties of uranium compounds

Uranium Compound	Density (g/cm^3)	U content (gU/cm^3)	Melting point (°C)	Thermal conductivity @ 573 K (W/m·K)
UN	14.3	13.55	2850	18
U_3Si_2	12.2	11.31	1662	15
UO_2	10.97	9.66	2865	7

ground onto the edge of the rim to allow a gases to escape. The pellets were sintered in a tungsten element, tungsten shielded, M-5X12 Materials Research Furnace (MRF) with a ultra-high purity argon cover gas (Figure 1b). The samples were exposed to room temperature air briefly when they were transferred from the glove box and placed in the furnace. Once the samples were inside the furnace, the door was immediately closed and placed under vacuum. The furnace was then back-filled with ultra-high purity argon flowing through an oxygen/moisture trap. The argon was vacuumed out and backfilled twice to remove residual moisture and oxygen with the system turbo pump. The sintering temperature profile included a 350°C (623 K) thirty minute hold to remove the Zn-stearate binder, which was ramped at ≈ 17.5°C per minute to 1400°C (1673 K), and then slowed to between 6 and 6.67°C per minute to the final peak dwell temperature. Dwell times tested ranged from 1 to 4 hours. The cool down rates closely mimicked the heating profiles, cooling at 6 to 6.67°C per minute to 1400°C then cooling to room temperature at 17.5°C per minute.

2.4. Microprobe Analysis

To prepare samples for Scanning Electron Microscopy (SEM) and Wavelength Dispersive Spectroscopy (WDS), the pellets were cut with a diamond wafering saw and mounted in epoxy. After setting, the samples were polished with successive grits ending with 3µm diamond paste. Samples were then sputter coated with graphite to make them conductive. System settings were 15kV and 1nA for backscatter and secondary electron imaging, during WDS 15kV and 40nA were used. The samples were analyzed by Dr. Ray Guillemette from the Department of Geology and Geophysics at Texas A&M University on a Cameca SX50 microprobe.

2.5. Thermal Diffusivity

A Netzsch LFA 447 was used to measure the thermal diffusivity of the samples applying the Cape Lehman model with pulse correction [3]. Before introducing the samples to the instrument the samples were flattened with fine sandpaper on plate glass to make the surfaces smooth and parallel to each other. After sanding the samples were weighed and measured with calipers to determine the bulk density. The samples were then coated with a graphite aerosol spray (DGF-123). Each sample was given three light coats of graphite on both sides. Measurements were carried out from 298K-573K at 25 degree increments with 5 shots at each temperature.

The thermal diffusivity (α) was used to calculate the thermal conductivity (κ) according to Equation 1.

$$\kappa = \alpha \cdot C_p \cdot \rho \tag{1}$$

Where:

C_p = specific heat

ρ = density

The specific heat of the composite was calculated by multiplying the mass fraction of the individual components with the corresponding heat capacity correlation, and adding them together. This is assuming no chemical reactions occur. The heat capacity was calculated for the UN from equation 2, where θ is the empirically determined Einstein temperature of UN at 365.7 K [4]. The heat capacity for the U_3Si_2 was calculated according to Equation 3 [5].

$$C_{pUN}(T,\theta) = \Big[51.14 \cdot \frac{\theta}{T} \cdot \frac{e^{\frac{\theta}{T}}}{e^{\frac{\theta}{T}} - 1} + T \cdot 9.491 \cdot 10^{-3} + \frac{2.642 \cdot 10^{11}}{T^2} \cdot e^{-\frac{18081}{T}}\Big] \cdot \frac{1}{0.252036} \tag{2}$$

$$C_{pU_3Si_2} = 199 + 0.104 \cdot (T - 237.15) \tag{3}$$

To assess the calculated thermal conductivity values, theoretical values were created from the individual component thermal conductivities found in literature, then scaled according to mass fraction and added together. The UN thermal conductivity was estimated with Equation 4 [6].

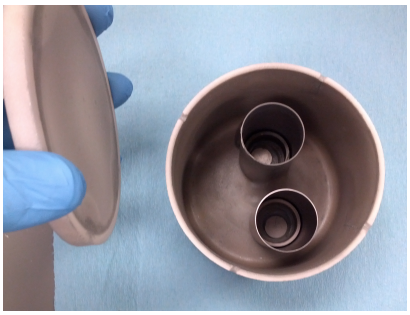

(a) Green pellets inside nested crucibles.

(b) Crucibles inside of furnace before sintering.

Figure 1: Green pellets before sintering (a) samples inside nested crucibles (b) crucibles with lid inside of furnace.

$$\kappa_{UN} = 1.864 \cdot e^{2.14\phi} \cdot T^{0.361} \quad (4)$$

To estimate the thermal conductivity of the U_3Si_2, literature data was converted to Equation 5 [7].

$$\kappa_{U_3Si_2} = (-8.095 \cdot 10^{-6}) \cdot T^2 + (2.594 \cdot 10^2) \cdot T + 2.678 \quad (5)$$

To correlate the measured data with literature values a linear porosity correction was done according to Equation 6 [8].

$$\kappa_s = \frac{\kappa_m}{(1 - \phi)} \quad (6)$$

Where:

κ_s = thermal conductivity of the sample scaled to 0 porosity

κ_m = sample thermal conductivity (porous)

ϕ = porosity

The porosity was estimated with Equation 7.

$$\phi = \frac{V_v}{V_t} = \frac{V_v}{V_s + V_v} = 1 - \frac{TD}{100} \quad (7)$$

Where:

V_v = void volume within the sample

V_t = total volume of the sample

V_s = solid volume

TD = percent theoretical density

3. Results

The LANL UN powder as received was a relatively large particle, approximately 100-200 μm in size with a porous structure (Figure 2). To improve particle mobility during sintering, the LANL UN was ground and sieved to obtain a powder <70 μm in size. The porous nature of the raw powder resulted in rapid size reduction with less than an hour of tumbling with yttria-stabilized zirconia grinding media. The resulting ground powder had a significant fraction of fines (Figure 3).

The mixed powders were pressed into 65 - 70 % TD green pellets with ≈ 300 MPa pressure. Higher pressures were tested but led to fragile pellets which delaminated easily. Pellets prepared from the GA UN μ-spheres were fragile, so additional binder was used to alleviate chipping and crumbling of the green pellets. In general, handling of the unsintered pellets was minimized to avoid these problems. Unsintered pellet densities were only checked when experimental parameters were changed. The green densities were typically 65-70% of the theoretical density.

Several heating profiles were tested. Initial tests done below the melting point of U_3Si_2, up to 1662°C (1935 K), did not result in significant densification. Sintering temperatures were increased to 1700°C (1973 K), thus shifting the sintering into the liquid phase. After transitioning to liquid phase sintering, the jet-milled U_3Si_2 was no longer used. Experiments carried out at temperatures >1700°C exhibited increased interactions with the crucible material and some slumping occurred. For these reasons, and the increased possibility of phase changes, experiments at temperatures greater than 1700°C were subsequently avoided. Sintering at 1700°C for 2 hours was sufficient to consistently approach 90% TD (Figure 4). To increase the product density, longer sintering times

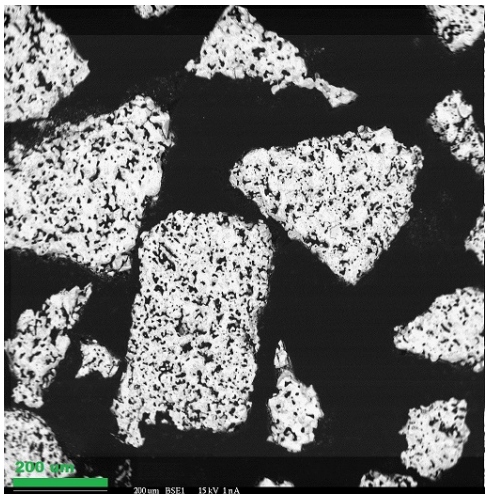

(a) LANL UN Particles

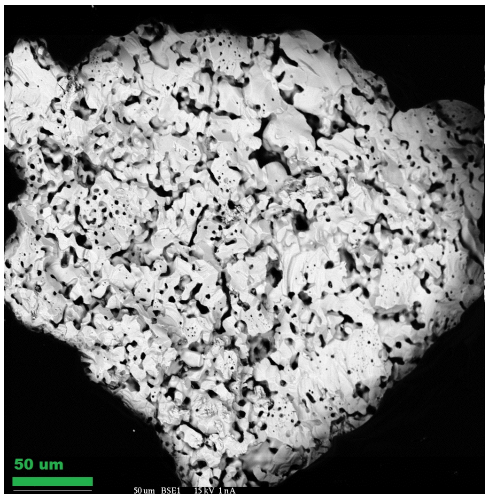

(b) LANL UN particle detail

Figure 2: SEM images of LANL UN powder particles as received.

were tested. The method was marginally effective. The extended sintering resulted in the accumulation of the residual porosity at the top of the sample. Post-sintering grinding with sandpaper was necessary to obtain flat right cylinders. Pellet densities improved after removing surface bubbles. Voids were often exposed after removing the surface defects from the these samples (Figure 5). This method was not reliable, as some sanded sample surfaces did not reveal voids. These voids may have remained deep within the sample, or the bubble-like features were the result of some other yet to be determined phenomena.

Typical sample results are listed in Table 2. The LANL UN, which was ground to <70μm at 35 mass% U_3Si_2 resulted in a density of 12.6 g/cm^3, a theoretical density

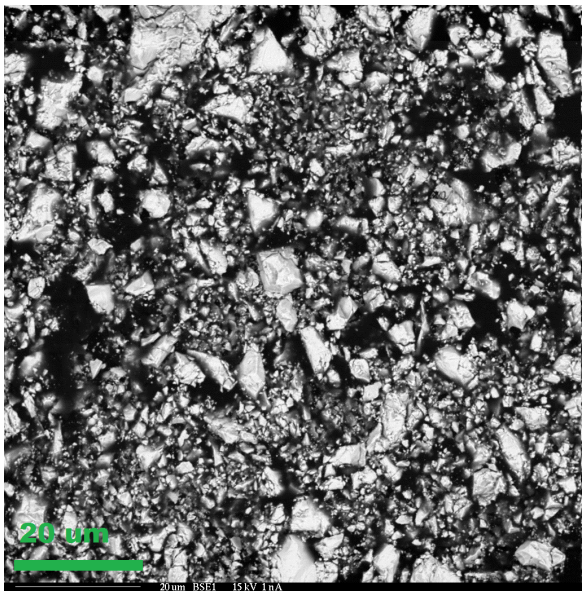

Figure 3: LANL UN after grinding (SEM).

of 93%. Similarly a sesquisilicide concentration of 30 mass% led to a density of 12.9 g/cm^3, a theoretical density of 94%. Samples prepared from the UN μ-spheres were slightly less dense at 12.0 g/cm^3, and 12.5 g/cm^3 with 25 mass% U_3Si_2, theoretical densities of 87% and 91% respectively. Higher mass fractions of sesquisilicide combined with the UN μ-spheres led to severe slumping. Similarly, longer sintering times also led to increased slumping among the samples prepared with the UN μ-spheres. The UN μ-sphere pellets did not exhibit the surface bubbling which occurred with the <70μm UN powder-derived pellets.

3.1. Thermal Properties

The thermal conductivity (κ) of the composite pellets was calculated to be between 6 and 16 W·m^{-1}·K^{-1} from 298K to 573K (Figure 6). After normalizing to 100% TD, the values increased to 7-18 W·m^{-1}·K^{-1} (Figure 7).

4. Discussion

In this feasibility study several UN-U_3Si_2 sample composites were prepared via liquid phase sintering. The steps required to prepare >90% dense experimental fuel forms are described. To obtain 95% theoretical densities requires extended sintering time and post processing to remove surface voids, or an alternate processing method.

Composite accident-tolerant fuel samples had a uranium loading improvement greater than 30% with respect to UO_2 in some cases (Table 2). The thermal

Table 2: Composite pellet densities and uranium content

UN particle	U_3Si_2 conc. (mass %)	Dwell time (hours)	Density (g/cm^3)	Theoretical density	U increase over UO_2
LANL UN	35	3	12.6	93%	28%
LANL UN	30	3	12.9	94%	31%
GA μ-sphere	25	3	12.0	87%	22%
GA μ-sphere	25	1	12.5	91%	27%

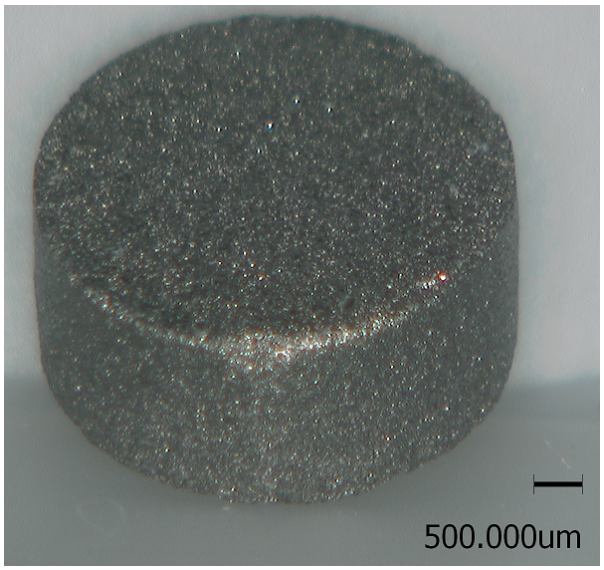

Figure 4: Ground LANL UN 30 mass% U_3Si_2 composite, sintering dwell time of 2 hours ρ=11.9 g/cm^3 (89% TD).

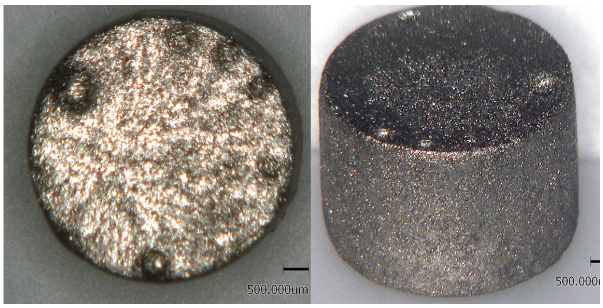

Figure 5: UN 35 mass% U_3Si_2 composite before and after sanding off bubbles revealing voids, 12.62 g/cm^2 93% TD.

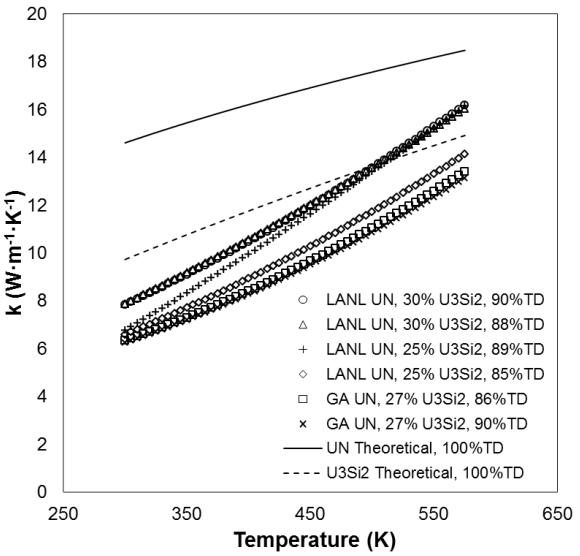

Figure 6: Thermal conductivity of UN-U_3Si_2 composites: ∘ LANL UN 30 mass% U_3Si_2 90% TD, △ LANL UN 30 mass% U_3Si_2 88% TD, + LANL UN 25 mass% U_3Si_2 89% TD, ⋄ LANL UN 25 mass% U_3Si_2 85% TD, □ GA μ-spheres 27 mass% U_3Si_2 86% TD, × GA μ-spheres 27 mass% U_3Si_2 90% TD, interpolated points added for clarity.

conductivity of these composites was found to be double that of UO_2 at 573 K (Table 1 and Figures 6, 7).

The thermal conductivity of fuel forms prepared from UN powders <70 μm in diameter was higher than those prepared from UN μ-spheres. Further study is necessary to ascertain the cause, but one possible reason may be phase separation within the μ-sphere-derived composites. Scanning electron microscopy found voids at the UN-U_3Si_2 interface within these samples (Figure 8). Images of a powder-derived UN composite pellet did not show phase separation (Figure 9).

5. Acknowledgements

We would like to extend special thanks to Ed Lahoda and Peng Xu of Westinghouse Electric Company for the productive conversations while carrying out this work. This material is based upon work supported by the Department of Energy under Award Number DE-NE0000566. Disclaimer: This report was prepared as an account of work sponsored by an agency of the United States Government. Neither the United States Government nor any agency thereof, nor any of their employees, makes any warranty, express or implied, or assumes any legal liability or responsibility for the accuracy, com-

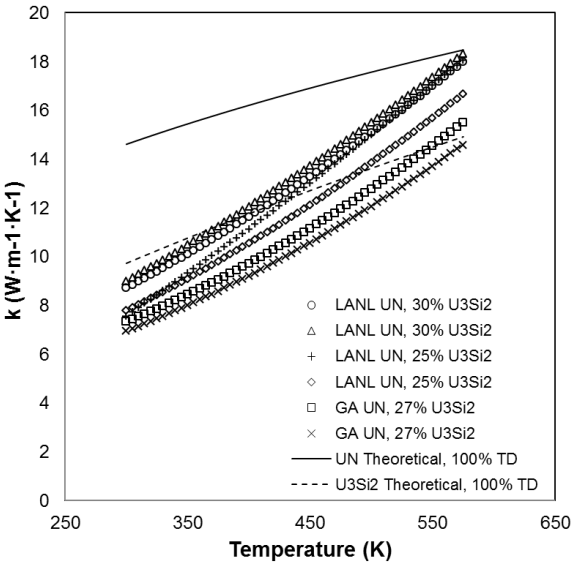

Figure 7: Thermal conductivity of UN-U_3Si_2 composites normalized to 100% density: ∘ LANL UN 30 mass% U_3Si_2, △ LANL UN 30 mass% U_3Si_2, + LANL UN 25 mass% U_3Si_2, ⋄ LANL UN 25 mass% U_3Si_2, □ GA μ-spheres 27 mass% U_3Si_2, × GA μ-spheres 27 mass% U_3Si_2. Interpolated points added for clarity.

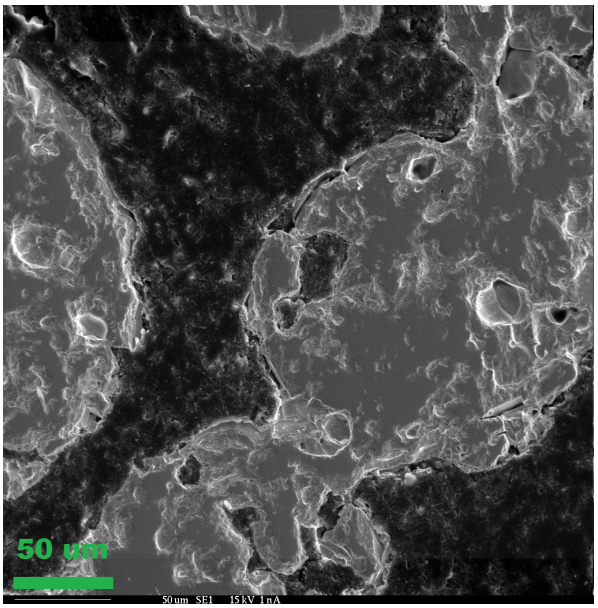

Figure 8: Uranium mononitride-uranium sequisilicide composite composed of GA UN μ-spheres showing possible phase separation.

pleteness, or usefulness of any information, apparatus, product, or process disclosed, or represents that its use would not infringe privately owned rights. Reference herein to any specific commercial product, process, or service by trade name, trademark, manufacturer, or otherwise does not necessarily constitute or imply its endorsement, recommendation, or favoring by the United States Government or any agency thereof. The views and opinions of authors expressed herein do not necessarily state or reflect those of the United States Government or any agency thereof.

References

[1] J. Harding, D. Martin, Journal of Nuclear Materials 166 (1989) 223 – 226.

[2] S. B. Ross, M. S. El-Genk, R. Matthews, Journal of Nuclear Materials 151 (1988) 318 – 326.

[3] J. A. Cape, G. W. Lehman, Journal of Applied Physics 34 (1963).

[4] S. Hayes, J. Thomas, K. Peddicord, Journal of nuclear materials 171 (1990) 300–318.

[5] J. Matos, J. Snelgrove, Research reactor core conversion guidebook, 1992.

[6] S. Hayes, J. Thomas, K. Peddicord, Journal of nuclear materials 171 (1990) 289–299.

[7] H. Shimizu, The properties and irradiation behavior of u3si2, 1965.

[8] J. Francl, W. Kingery, Journal of the American ceramic Society 37 (1954) 99–107.

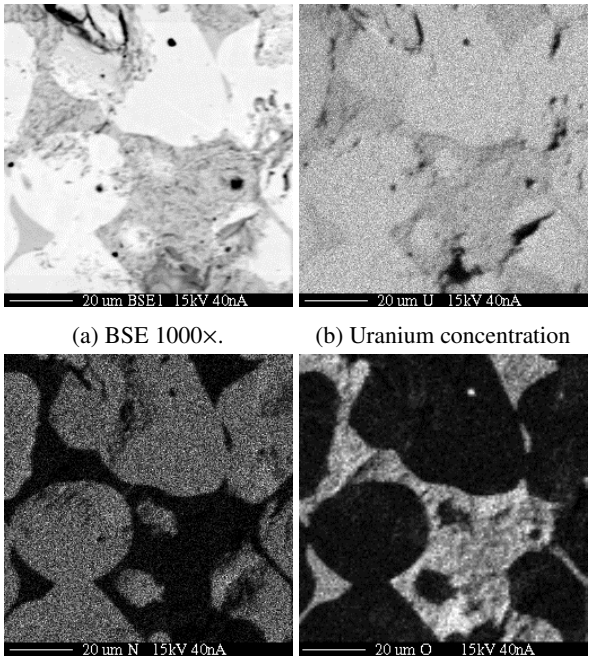

(a) BSE 1000×. (b) Uranium concentration

(c) Nitrogen concentration (d) Oxygen concentration

Figure 9: Composite sample (93% TD) consisting of ground LANL UN and 30 mass% U_3Si_2 with qualitative elemental concentrations, brighter representing a higher concentration of the element specified (a) Backscatter electron image at 1000× (b) Uranium concentration (c) Nitrogen concentration (d) Oxygen concentration.

Evaluation of Coatings for Nuclear Fuel Rods for Improved Accident Tolerance

Frank Boylan[a], Fausto Franceschini[a], Jeffrey R. Secker[a], Ed Lahoda[a], Jason Mazzoccoli[a], Jonna Partezana[a], Peng Xu[a], Sean Gleason[b], Edward Herderick[b] and George Ritter[b], Benjamin Hauch[c]. Ben Maier[c], Kumar Sridharan[c], Tom McKrell[d], Michael Pantano[d], Valentina Avincola[e]

[a]Westinghouse Electric Company LLC, 1000 Westinghouse Drive, Cranberry Township, PA 16066, [b]EWI, 1250 Arthur E. Adams Drive, Columbus, OH 43221, [c]University of Wisconsin, [d]Massachusetts Institute of Technology, [e]Karlsruhe Institute of Technology, Hermann-von-Helmholtz-Platz 1, 76344 Eggenstein-Leopoldshafen, Germany.

Abstract

The Westinghouse-led accident tolerant fuel (ATF) program is evaluating coatings of MAX phase (Ti_2AlC) and NanoSteel SHS 9172® an iron-based-alloy for enhancing the oxidation resistance of zirconium-alloy fuel cladding in both normal and beyond design-based operating conditions. High Velocity Oxy Fuel (HVOF) thermal spray and cold spray deposition technologies were investigated for the deposition of coatings. Neutronic analysis using the elemental compositions of the coating materials showed that the coating thicknesses should be less than 30μm to avoid economic penalty, although in this preliminary study thicker coatings were used. The MAX phase coatings used in this study were 70-90 μm in thickness. Initial sample screening was performed in a static autoclave steam environment at 427°C and 103 bar. The coatings made by HVOF de-bonded from the zirconium-alloy substrate after these tests, while cold spray deposited coatings were stable. High temperature steam autoclave testing at 1200°C showed that the Nanosteel coating provided little protection for the zirconium. The Ti_2AlC coating did not provide the desired improvements due to un-optimized microstructure and high porosity. Follow-on work utilized HVOF deposition to apply ~ 100 μm Ti_2AlC coatings on zirconium substrates with machined grooves. This resulted in reduced oxidation kinetics via the formation of an Al_2O_3 oxygen diffusion barrier layer once exposed to the steam environment. These results suggested that a critical combination of coating microstructure, thickness, and density is required for the formation of the protective Al_2O_3 layer. This was confirmed by steam testing at 1200°C of near-theoretical density bulk Ti_2AlC samples where low oxidation rates were observed due to the formation of protective Al_2O_3 layer on the surface.

Introduction

Westinghouse Electric Company LLC is leading a consortium of industry and universities to explore the use of coatings for zirconium-alloy (Zr-alloy) fuel cladding. The objective of this ongoing study is to increase the accident tolerance of the current fuel cladding designs to beyond design basis accidents, while maintaining or improving oxidation resistance under normal operating conditions. Modeling of accident scenarios in a pressurized water reactor (PWR) where cooling water is not re-introduced to the core after about 400 seconds, shows that the zirconium-alloy cladding will exothermically burn in steam, particularly starting at about 1200°C, as shown in Figure 1 [1]. Once the steam/air exothermic oxidation initiates, destruction

of the core is almost inevitable due to the large amount of chemical energy provided by the zirconium-steam reaction. Additionally, hydrogen is produced as a by-product of this oxidation reaction and has the potential for igniting and causing further damage to containment. Oxidation resistance at normal operating temperatures (300°C to 320°C for PWRs and 250°C to 300°C for BWRs), was also deemed important as it improves cladding performance by way of reduced oxide layer thickness and hydriding of the cladding, thus increasing the allowable fuel burn-up and improved economics [2]. However, in order to have a net benefit, the parasitic neutron absorption as a result of the coating must be to be kept to a minimum either by using coatings composed of low cross-section elements or by keeping the coating thicknesses at low values.

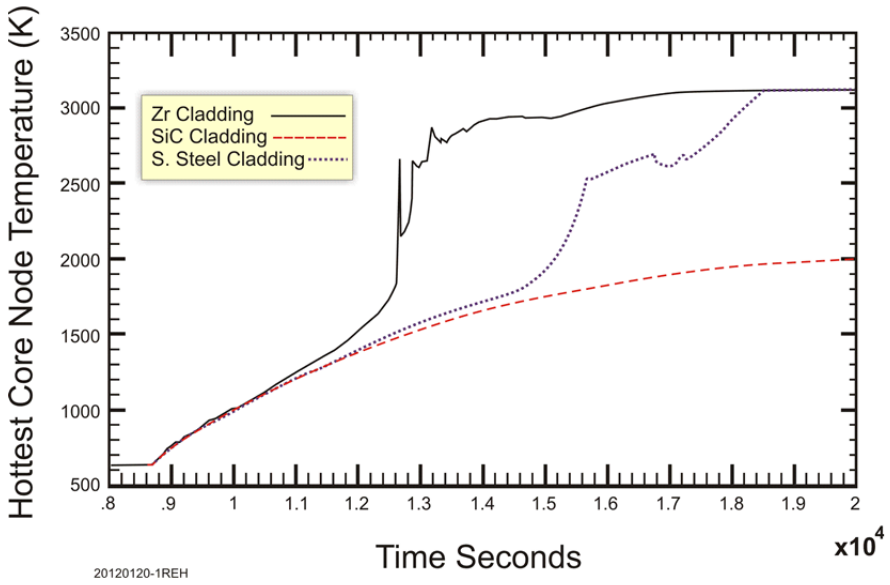

Figure 1. Modeling of beyond design basis accident core temperatures for long term loss of coolant.

Applying an adherent coating to Zr-alloys is challenging since zirconium forms an adherent, dense native oxide layer of zirconium-oxide. While this oxide layer provides zirconium with an effective anti-corrosion barrier in normal operation, it also makes it difficult to apply coatings that will remain adherent over a wide temperature range. Therefore, in the present study high velocity powder spray deposition processes were investigated, which could breach this native oxide layer to form a well-bonded coating.

Experimental

Test Materials and Coatings

In this study, two high velocity powder spray coating technologies, namely High Velocity Oxy Fuel (HVOF) and cold spray technology was investigated. Based on previous evaluations [3] two coating materials were selected:

1. Ti_2AlC MAX Phase – a hard material with good high temperature oxidation resistance in air [3,4,5] and a high melting point, and a coefficient of thermal expansion close to Zr ($8x10^{-6}K^{-1}$

for Ti_2AlC versus $7.2x10^{-6}K^{-1}$ for Zr). The powder particle size of this material was in the range -150/+280 mesh.

2. NanoSteel SHS9172® (NanoSteel) – a commercially available hard coating material that has been developed for high temperature corrosion and wear resistance applications in coal-fired power plants. The powder size for this material was in the range of 15-53 μm [6].

In both cases, no sieving of the powders was performed and the as-received powders were sprayed. The study was performed on Zr-alloy coupons 11 mm x 50-55 mm (width x length) and 0.25-mm thick and contained a 3-mm hole, 6 mm inboard of one end for suspension of samples in the autoclave environments.

Coating Deposition Methods

For HVOF spraying, the samples were grit blasted with 80-grit alumina at 60 psi pressure followed by rinsing with isopropyl alcohol and air drying. A JAFA JP5000 HVOF spray apparatus was used with kerosene fuel to spray the coatings. To promote, the formation a stable protective Al_2O_3 protective layer on the surface [8], select HVOF samples were subjected to a laser surface treatment (in air) using a LaserLine LDF 5.000-30 system using 100 to150W power and multiple passes and a 11 mm x 4 mm integrated focused beam. The HVOF work was performed at the Edison Welding Institute (EWI). The spray conditions employed are summarized in Table 1 below.

Table 1. Spray Parameters Used for EWI HVOF Spraying

Parameter	Nanosteel Coupons	Ti_2AlC Coupons
Barrel Length (m)	0.1016	0.1016
Spray Distance (m)	0.3302	0.3302
Traverse Speed (m/hr)	457.2	457.2
Step Increment (m)	0.00508	0.00508
Number of Passes	1 or 2	2 or 4
Feeder RPM	170	170
Fuel Rate (m^3/hr)	1.181	1.181
Oxygen Rate (SCMH)	52.3862	52.3862
Chamber Pressure (Pa)	634000 – 641000	627000 - 634000

Cold spray deposition was performed at the University of Wisconsin, Madison (UW) using a commercial high pressure 4000-34 Kinetik cold spray system, using the as-received Ti_2AlC MAX phase and Nanosteel powders. MAX phase coatings were deposited at nitrogen gas (propelling gas) preheat temperature (not the particle temperature, which is much lower) and pressure of 790°C/40 bars and 600°C/35 bars while the corresponding conditions for depositing Nanosteel were 790°C/35 bars, and 600°C/35 bars.

High Temperature Oxidation Testing and Analysis

The high temperature autoclave tests in oxidative environments were performed at Westinghouse Electric Company and at MIT. Static steam autoclave tests were performed at 427°C and 1.03×10^7 Pa for up to 57 days exposure. The coated samples were periodically

removed from the autoclave for visual observation and to monitor changes in sample weight. Recorded weight gains from uncoated ZIRLO®[1] (high performance fuel cladding material) samples exposed to identical autoclave conditions from previous experiments was used as a base-line. Weight gain per unit surface area was plotted as a function of autoclave exposure time for each coating type and deposition temperature, and the data was fit to a power law shown in Equation 1, where δ is the weight gain per unit area, K the rate constant, t is the exposure time, and n is the exponent [9].

$$\delta = Kt^n \tag{1}$$

High temperature steam oxidation tests at 1200°C were performed in a facility shown schematically in Figure 2. In this facility, steam is produced in the bottom section of a vertical quartz tube by using a constant heat source to boil water [13]. The samples are suspended in this tube and the steam rises through the tube and exits to the atmosphere at the top. A steam flow rate of 5 g/min was used.

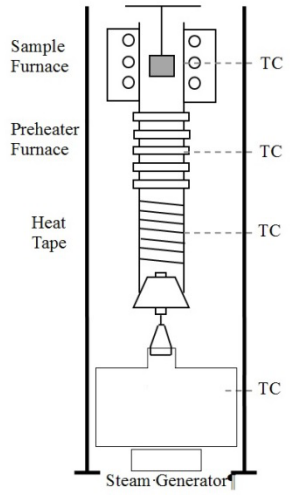

Figure 2. Schematic illustration of the high temperature steam oxidation facility used in this study.

All samples were weighed and photographed prior to and after high temperature oxidation tests. Prior to conducting any tests, samples were photographed, measured, and weighed. Post-test analysis was performed using scanning electron microscopy (SEM) in conjunction with energy dispersive spectroscopy (EDS).

Mechanical Testing

Two types of mechanical tests were performed, namely, rod pull tests and radius bend tests. Rod-pull tests were employed to measure coating adhesion on representative samples before and after the autoclave exposure. Here an 11-mm x 75-mm long aluminum rod was

[1] ZIRLO is a registered trademark of Westinghouse Electric Company LLC, its affiliates and/or its subsidiaries in the United States of America and may be registered in other countries throughout the world. All rights reserved. Unauthorized use is strictly prohibited. Other names may be trademarks.

bonded to the surface of each coated sample using an epoxy adhesive as shown in Figure 3a. The end of the rod was grit blasted prior to bonding. Testing was performed by placing the strip in a fixture and pulling the rod straight up at a velocity of 1.25 mm/min and the force required for failure was recorded. The radius bend tests (Figure 3b) were used as a semi-quantitative measure of coating in-plane strength before and after exposures. Here the samples were bent manually around a radius of 53-mm and held for 10-15 seconds and then allowed to relax naturally. The samples were then examined under for any obvious signs of cracking or delamination.

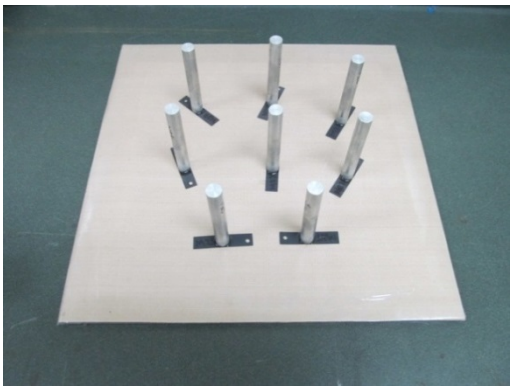

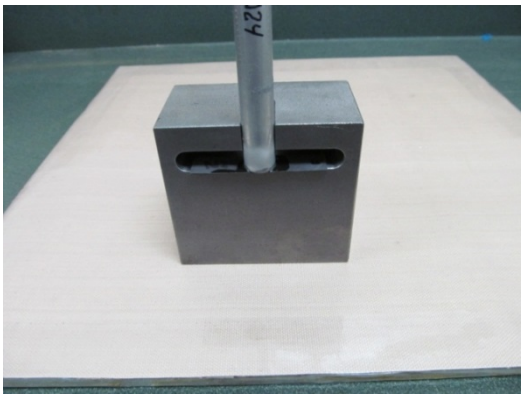

(a) **(b)**

Figure 3. Sample configurations for (a) rod pull tests and (b) radius bend tests.

Results and Discussion

Neutronic Calculations

Neutronic calculations were carried out using the Westinghouse standard production codes (ALPHA/PARAGON/ANC [10, 11]) suitably modified for the two coatings on ZIRLO tubes to determine their effect on the fuel cycle cost. The economic assumptions used in this analysis are shown in Table 2. The number of fuel assemblies and their enrichment for each case was varied until the cost for achieving 510 effective full power days was minimized. In all cases, a 10 micron fully dense layer of either the Ti_2AlC or the NanoSteel coatings was used. The calculations were performed for standard pellet and cladding diameters for Westinghouse 17X17 fuel assemblies. A smaller standard diameter was used for the UN and U_3Si_2 fuel pellets to increase the H/U ratio to be equivalent to the current UO_2/Zr fuel. It was assumed that 99% N-15 with 1% N-14 would be in the UN fuel case.

Table 2. Economic Assumptions Used for Neutronic Calculations

Item	Value
U3O8 Price ($/Lb)	$ 121
Conversion Price ($/KgUn)	$ 12
SWU Price ($/Kg-SWU)	$ 142
N15 Price ($/kgN15)	$ 1,119
Fabrication ($/FA)	$ 138,893
Pre-Operational Interest (%/Yr)	6%
Spent Fuel Cooling Time (Months)	120
Spent Fuel Disposal Charge ($/KgU)	$ -
Spent Fuel Disposal Charge ($/MWHre)	$ 1
Spent Fuel Dry Storage Charge ($/FA)	$ 50,000
Cycle Length (Months)	18
Rated Thermal Power (MWt)	3,587
Rated Net Electric Output (MWe)	1,112
Inflation Rate	2%
Return on Fuel Investment (%/yr)	8%

The results for the neutronic analysis are shown in Table 3. Both the UN and the U_3Si_2 fuels yielded significant cost advantages as compared to the current UO_2 fuel (5.26% and 4.04% respectively). The analysis shows that a 10 micron thick coating of either the Ti_2AlC or the NanoSteel coating reduces this benefit. For the MAX Phase Ti_2AlC coating this reduction is about 12% for the UN and 13% for the U_3Si_2, while for NanoSteel coating, this amounted to a reduction of 14% for the UN and 16% for the U_3Si_2. The use of a 20 micron thick coating would approximately double the loss in benefit. Therefore, in order to keep a reasonable economic gain from the use of these fuels, a maximum coating thickness was estimated to be approximately in the 20-30 microns range. It should be noted here that the goal of this initial study was to conduct a preliminary assessment of coating deposition feasibility and coating performance, and was not targeted at specific thicknesses to maximize neutronic efficiency.

Table 3. Results of Fuel Economics Analysis for Coated ZIRLO Cladding

Fuel	Cladding	Pellet OD (mm)	Clad OD (mm)	Clad Thickness (mm)	Coating Thickness (microns)	H/U Ratio	Effective Full Power Days	Discharge Burnup (MWD/MTU)	Fuel Cycle Costs ($/MWhr)
UO2	ZIRLO	8.19	9.50	0.57	-	3.96	510	53224	9.209
UO2	SiC	8.19	10.44	1.04	-	3.39	510	50573	9.910
U3Si2	SiC	7.70	9.94	1.04	-	3.58	510	54565	9.186
UN99	SiC	7.31	9.55	1.04	-	3.55	510	57354	8.900
UN99	Zr-maxthal	7.84	9.14	0.57	10	3.25	510	56630	8.783
UN99	Zr-nanosteel	7.84	9.14	0.57	10	3.25	510	56630	8.793
U3Si2	Zr-maxthal	7.84	9.14	0.57	10	3.87	510	55561	8.886
U3Si2	Zr-nanosteel	7.84	9.14	0.57	10	3.87	510	55562	8.895
UN99	Zr	7.84	9.14	0.57	-	3.26	510	56631	8.725
U3Si2	Zr	7.84	9.14	0.57	-	3.88	510	55562	8.837

Static Steam Autoclave Test Results

Upon visual inspection of the samples after 3 days autoclave exposure, the HVOF-deposited MAX phase Ti_2AlC coating had delaminated from the surface of the ZIRLO as an intact film, implying oxidation of the underlying substrate/coating interface. The HVOF-deposited NanoSteel coating remained adherent to the substrate, however cracks in the coating were visible. Due to these effects, no meaningful weight data could be collected, and the samples were removed from the autoclave. The evaluation of the cold spray deposited coatings was continued to longer times. Weight changes, standard deviations, and power law-fits of the data recorded for the cold spray-coated samples and the ZIRLO controls are shown in Figure 4.

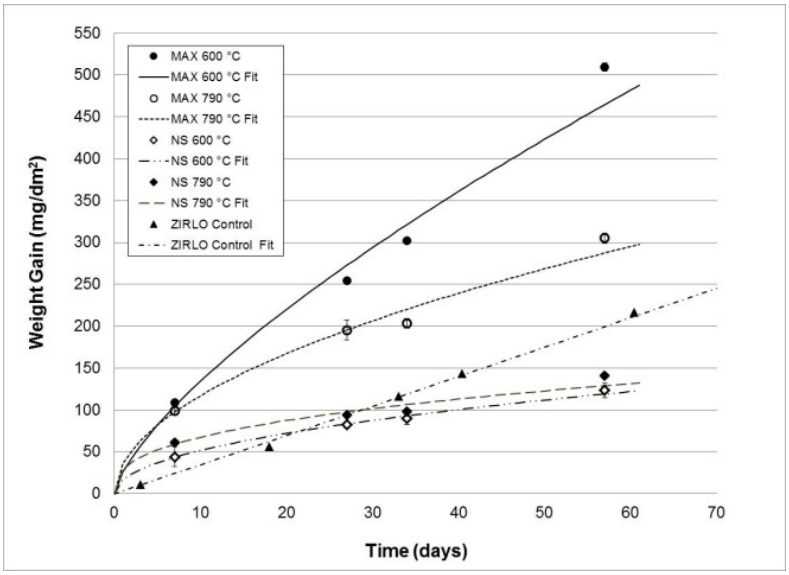

Figure 4. Sample weight gain as a function of autoclave exposure with power law fits for cold-spray samples and the ZIRLO control (note that the temperatures indicated are the gas preheat temperatures).

A series of two sample t-tests were conducted at each exposure time using Minitab statistical software at an alpha level of 0.05 for the coated samples [12]. The MAX phase coatings deposited at gas preheat temperatures of 600°C showed higher weight gains than those deposited at 790°C for all exposure times, due to greater coating densification in the latter case. For exposure durations of less than about 34 days, the NanoSteel coated samples showed statistically significant differences compared to MAX phase coated samples deposited at both preheat temperatures. However, for greater exposure times the data were not significantly different. Overall, it was apparent that the MAX phase coated samples gained more weight than NanoSteel or ZIRLO control samples. The weight gains recorded for NanoSteel coated samples were generally similar regardless of gas preheat temperature and exhibited less weight gain than the ZIRLO controls samples at extended exposure times. It is noted here that the MAX phase coatings in this study were performed under non-optimized conditions. Subsequent studies on cold spray coatings using more optimized parameters have

led to denser coatings with improved performance and these results will be reported in a subsequent paper.

The power law exponent *n* were calculated from data in Figure 4 and summarized in Table 4 along with the R^2 value of the linear fit. An exponent value of 0.33, 0.50, or 1.00, indicates cubic, parabolic, or linear kinetics, respectively.

Table 4. Power law exponent *n* of the cold spray coated samples

Sample Type	Gas Preheat Temperature (°C)	Power Law Exponent n	R^2 of linear fit to determine n
Max Phase	600	0.71	0.98
Max Phase	790	0.52	0.98
NanoSteel	600	0.48	0.99
NanoSteel	790	0.37	0.95
ZIRLO Control	Not Coated	1.00	1.00

The uncoated ZIRLO control samples exhibited linear kinetics suggesting little protection of the alloy from an oxide layer upon exposure to this steam environment. The MAX phase coated samples fabricated with a gas preheat temperature of 600°C exhibit quasi-linear behavior with an exponent of 0.71, suggesting that this coating was not protective to any significant degree. The MAX phase coating deposited with a preheat temperature of 790°C and the NanoSteel coating deposited with a preheat temperature of 600°C both exhibited parabolic kinetics with exponent fits close to 0.50, whereas the NanoSteel coating deposited with a preheat temperature of 790°C had kinetics that approached cubic-type behavior. These data suggest that cold spray coatings (deposited in this study under unoptimized condition) has the potential to provide protection if deposited under more optimized conditions.

Figure 5a and 5b show cross-sectional SEM images of MAX Phase coatings deposited with a gas pre-heat temperatures of 600°C and 790°C, respectively after exposure to steam autoclave tests at 427°C for 57 days. An X-ray map of this region was also collected and shown in Figure 6. The coatings deposited at the gas preheat temperature of 600°C showed porosity and consequently oxygen permeation, as indicated by an approximately 12μm layer of Zr-oxide at the interface between the coating and the substrate (Figure 5a). As a result of oxygen permeation, EDS analyses at various regions within the coating showed different compositions of oxygen. For example, regions 4 and 5 showed compositions consistent with the MAX phase composition while regions 3 and 6 showed considerable oxygen content. The darker areas in the coating represent the oxidized regions. The coatings deposited at the gas preheat temperature of 790°C (Figure 5b) showed significantly superior oxidation resistance, as observed by smaller area of darker regions. Furthermore, the coating was denser and no Zr-oxide layer was present at the interface of the coating and the substrate. Although, oxygen permeation had occurred to some extent in the coating, most of the coating remained unoxidized and provided protection to the underlying Zr-alloy. For example, the lighter regions

marked 3 and 6 were consistent with the composition of MAX phase composition, while the darker regions (points 4 and 5) showed high oxygen content.

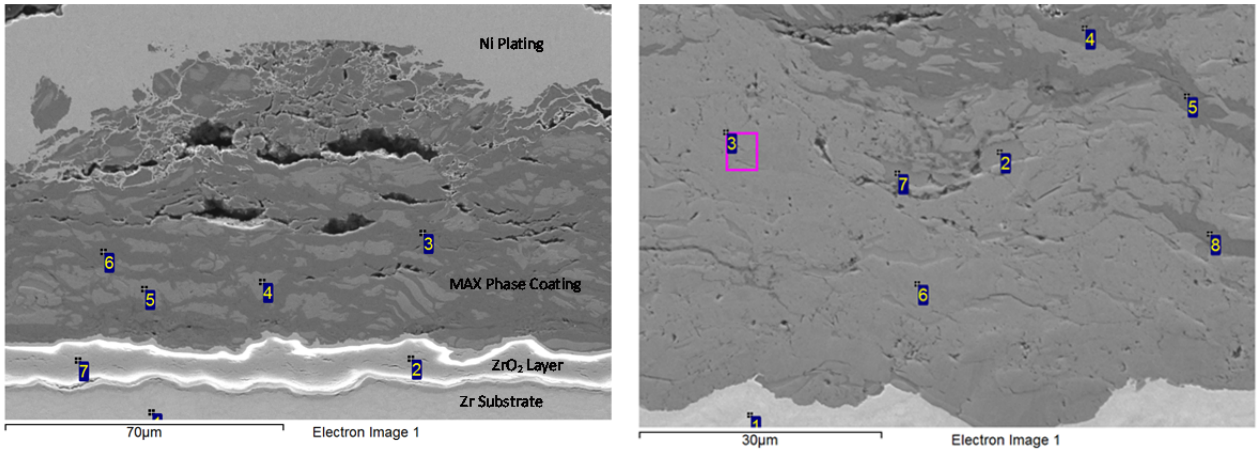

(a) (b)

Figure 5. Cross-sectional SEM images of cold spray MAX phase coating after testing in steam autoclave at 427°C for 57 days: (a) gas preheat temperature of 600°C and (b) gas preheat temperature of 790°C.

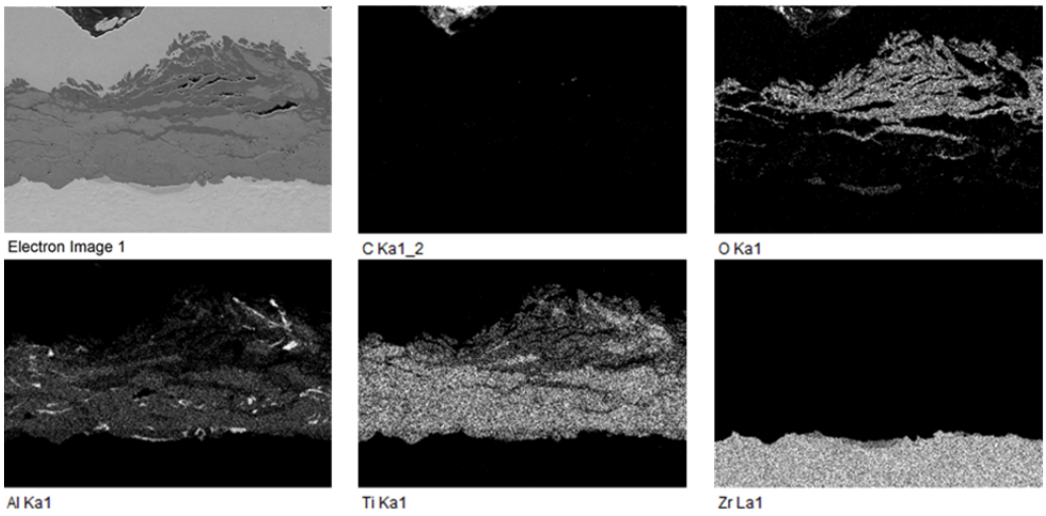

Figure 6. MaxPhase 790°C Deposition Temperature – X-ray Map. The Electron Image (top left) shows the SEM image of the analysis area. The bright regions within each X-ray elemental map show the concentration of that element within the electron image.

Figure 7a and 7b show cross-sectional SEM images of Nanosteel coatings deposited with a gas pre-heat temperature at 600°C and 790°C, after exposure to steam autoclave tests at 427°C for 57 days. Figure 8 is an X-ray map of the **NanoSteel** coatings deposited with a gas pre-heat temperature of 600°C. It is clear that several particles had not fully deformed during the spray process and oxygen permeation had occurred at the particle boundaries. More cracks were observed in the coatings deposited at preheat temperature of 600°C compared to those

deposited at preheat temperature of 790°C. EDS analysis performed at several points showed that the Nanosteel particles themselves were resistant to oxidation, but interfacial regions (for example, points 3 in both micrographs) clearly showed the presence of Zr-oxide.

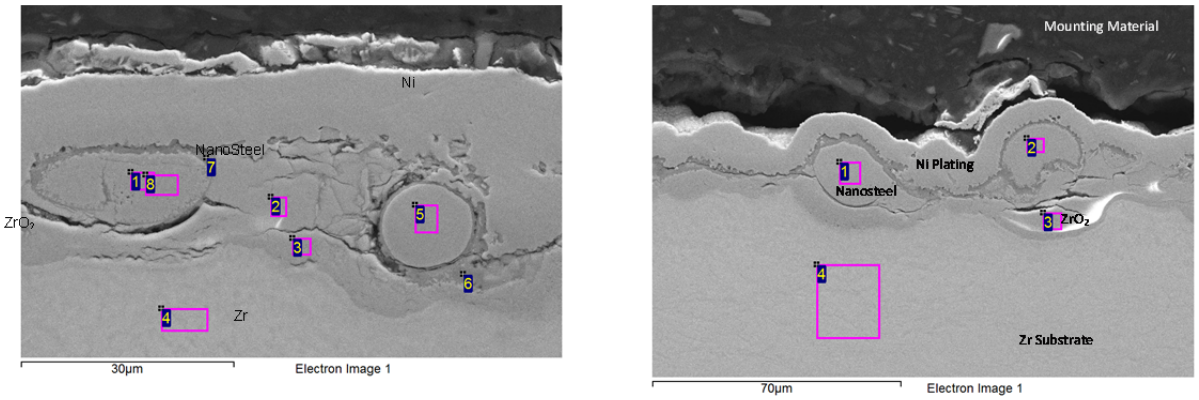

(a) (b)

Figure 7. Cross-sectional SEM images of cold spray Nanosteel coatings after testing in steam autoclave at 427°C for 57 days: (a) gas preheat temperature of 600°C and (b) gas preheat temperature of 790°C.

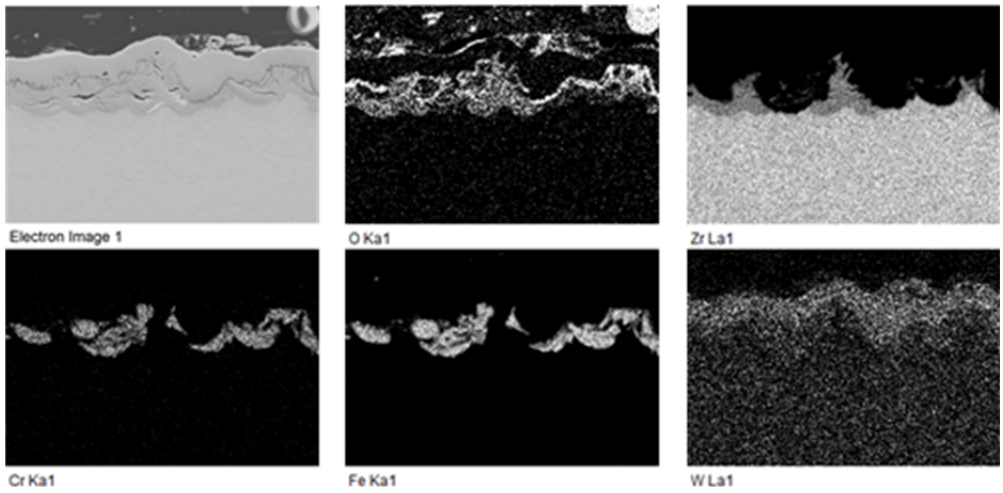

Figure 8. NanoSteel Deposition at a Gas Preheat Temperature of 600°C – X-ray Map

Mechanical Test Results

Table 5 summarizes the results for the rod pull tests before and after steam autoclave tests. Generally, samples that survived did not lose appreciable adhesion to the Zr-substrate with increasing exposure times. Cold-sprayed samples performed for both coating materials performed quite well.

Table 5. A Summary of the Result for Rod Pull Tests

Rod Pulls (lbf)												
	HVOF Process				Cold Spray Process							
	MAX Phase		NanoSteel		MAX Phase				NanoSteel			
Sample	Before	After 30 days	Before	After 30 days	Before	After 30 days (790°C)	After 60 days (790°C)	After 60 days (600°C)	Before	After 30 days (790°C)	After 60 days (790°C)	After 60 days (600°C)
1	396	N/A	98	N/A	458	369	200	227	338	329	276	258
2	258	N/A	236	N/A	409	258	365	343	334	285	271	254
3	391	N/A	418	N/A	307				298	258		
AVE	**348**	**0**	**251**	**0**	**391**	**314**	**282**	**285**	**323**	**291**	**274**	**256**

The results for the bend tests are shown in Table 6. A “P” for pass indicated there were no visible signs of coating cracking or spalling. Curiously, the cold-sprayed MAX Phase showed fairly poor bend resistance prior to exposure. Those cold-sprayed with a gas preheat temperature of 790^{o}C seemed to ‘toughen’ from the exposure. The samples cold-sprayed with a gas preheat temperature of 600^{o}C showed good adhesion, but the metal itself fractured during the bend test.

Table 6. A Summary of the Radius Bend Test Results

Bend Tests (53-mm dia)												
	HVOF				Cold Spray							
	MAX Phase		NanoSteel		MAX Phase				NanoSteel			
Sample	Before	After 30 days	Before	After 30 days	Before	After 30 days (790)	After 60 days (790)	After 60 days (600)	Before	After 30 days (790)	After 60 days (790)	After 60 days (600)
1	P	N/A	P	N/A	F	P	P	Metal Broke	P	P	P	P
2	P	N/A	P	N/A	P	P	P	Metal Broke	P	P	P	P
3	P	N/A	P	N/A	F	P			P	P		

High Temperature (1200^{o}C) Steam Oxidation Results

NanoSteel Coating Test Results

The Nanosteel coated samples (Figure 7a) were tested for exposure duration of up to 18 minutes in 1200^{o}C steam autoclave tests. Upon insertion into the autoclave, a pyrophoric reaction was observed as evidenced qualitatively by a bright orange glow in the quartz tube and the evolution of a lime green smoke from the autoclave system. Additionally, after autoclave testing the samples exhibited a light colored patch on the surface (Figure 7b). The origin of these effects is not known and is currently being investigated. SEM examination indicated that the Nanosteel coating was removed from the Zr-alloy test as a result of either oxidation or the pyrophoric reaction.

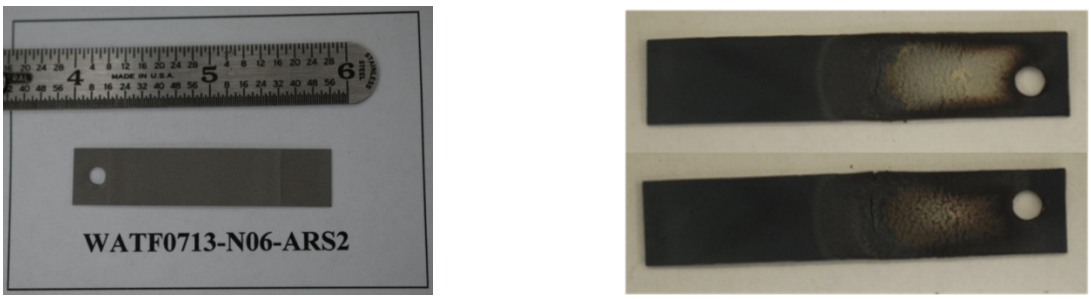

(a) (b)

Figure 7. Photographs of the Nanosteel coated samples: (a) as-coated condition and (b) after steam autoclave tests at 1200°C (a light colored patch was observed on the autoclave tested sample).

Ti_2AlC Test Results

The cold sprayed coated Ti_2AlC sample was tested in 1200°C steam autoclave for exposure duration of 60 minutes. The samples experienced cracking upon removal from the facility, so a reliable weight change measurement could not be performed. All of the samples tested were cross-sectioned and polished for SEM imaging. Under the SEM, it was possible to see the portion of the ZIRLO substrate that had not been oxidized. This value is expressed as "Remaining ZIRLO Thickness". Due to the limited number of samples, one of these (the sample tested for 8 minutes) was not cut and was further oxidized for 22 minutes (30 minutes total). The results showing the weight gain and 'remaining ZIRLO thicknesses are shown in Table 7. Following oxidation, the samples changed from their initial dark gray color to a lighter gray with patches of pale yellow. This yellow color was prevalent along cracks in the surface and the EDS analysis suggested the surface was covered by TiO_2.

Table 7. Normalized Mass Gain and Remaining Zr Thickness After 1200°C Steam Oxidation Test for Cold Sprayed Coating Samples

Test Duration (min)	Norm. Mass Gain (mg/cm^2)	Remaining **ZIRLO** Thickness (μm)
2	6.78	415
8	26.7	N/A
15	34.6	235
15	32.0	233
8+22	39.7	190
60	N/A	114

In addition to the cold sprayed coatings, the HVOF coatings were revisited for 1200°C steam oxidation tests, where two approaches were investigated to improve the coating performance. The first was to use an unfocused laser with a spot size larger than the sample to attempt to pre-oxidize the HVOF deposited Ti_2AlC coating in air. Previous studies have found such a treatment to improve oxidation resistance [8]. Nevertheless, our study showed no oxidation resistance improvement from this laser treatment. The other method involved the deposition of Ti_2AlC coating on substrates milled with thin channels along the length of the substrate on one side prior to coating application. This grooved topography approach was investigated for two samples. The first had channels 160 μm deep and 180 μm wide. These channels were plainly

visible, even after a coating between 70 and 140 µm in thickness had been applied. The second sample had shallower, wider channels 90 µm deep and 240 µm wide. Because of the shallower channel dimensions, the coating appeared more uniform. In Figure 8 the weight change of cold spray samples and grooved samples has been compared to the oxidation data of ZIRLO from the work of Steinbrueck [14]. The lower mass gain for the grooved samples is likely due to the higher coating thickness of ~100 µm.

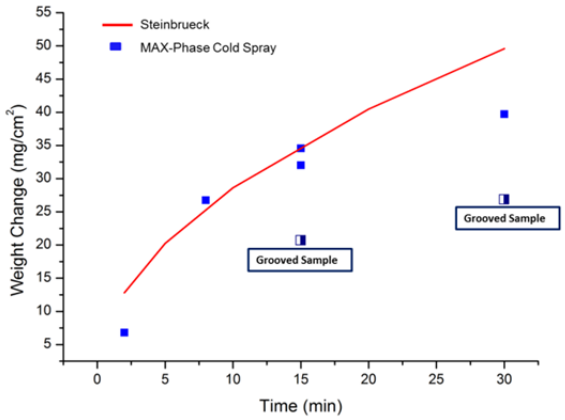

Figure 8. Weight gain results for smooth and grooved MAX phase coated samples and comparison with literature data.

SEM analysis performed on the section of the grooved sample shown in Figure 9 indicates a distinct alumina rich layer (in red), which had likely prevented the underlying Zr-alloy from oxidation.

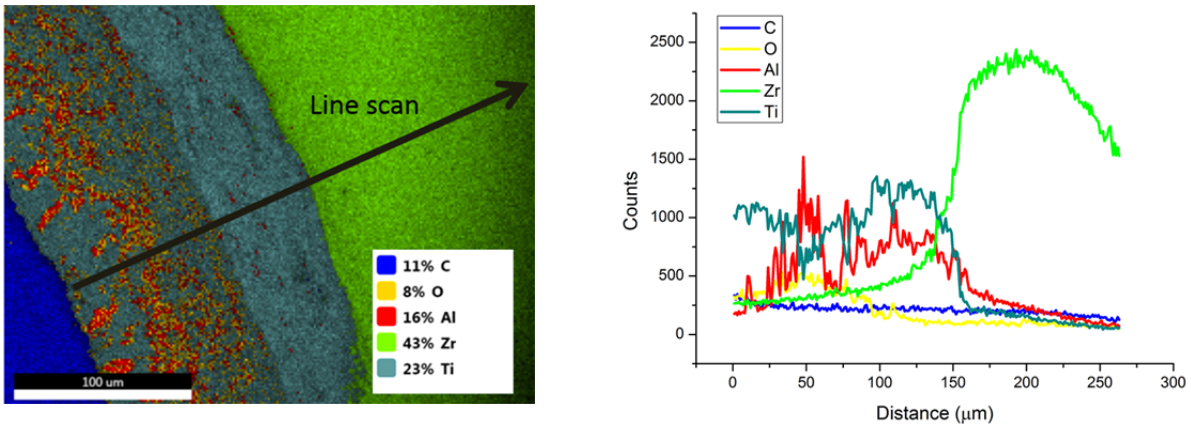

(a) **(b)**

Figure 9. Cross-sectional SEM image of the grooved sample after high temperature autoclave tests at 1200°C and elemental line scan across the oxidized region.

Some of the above results for Ti_2AlC coatings were unexpected in that there is a significant amount of literature that suggests that Ti_2AlC forms a protective Al_2O_3 layer that resists

oxidation at temperatures up to at least 1400°C in air [4,15-16]. Therefore, additional oxidation tests were carried out using bulk disks and pellets of Ti_2AlC. The samples tested include two sets of pellets, made by pressing the Ti_2AlC powder at room temperature. One set was pressed at 50 ksi and the other at 86.6 ksi, giving densities of ~40% and 60% of the theoretical density (4.11 g/cm^3). The third set of tested samples was fully dense discs purchased directly from the company, Sandvik. These samples allowed for investigation of the role of density in the high temperature oxidation process.

As can be seen in Table 8, the fully dense pellet exhibited over an order of magnitude lower weight gain following a short period of oxidation at 1200°C. In this table, an "ECR (Equivalent Cladding Reacted) Thickness" is indicated. This is an estimate of the depth of oxygen penetration into the sample. By assuming all Al and Ti in the near-surface regions covert to Al_2O_3 and TiO_2, respectively and all carbon leaves the sample as a gas, then the amount of material oxidized can be estimated. Using the density of the oxide, this value can be converted to a depth of oxidation. Taking the experimental data collected for the fully dense discs and plotting it against published data from Basu [4] for similar steam oxidation of fully dense Ti_2AlC, good agreement is observed (Figure 10). Therefore, achieving high coating density appears to be critical for achieving good oxidation resistance.

EDS compositional analysis was performed on the fully dense disc samples that had been oxidized for 30 minutes. The resulting line scan, shown in Figure 11 indicates the formation of an Al_2O_3 oxide layer at the surface (and corresponding decrease in Ti) confirming that the formation of alumina layer is necessary for good oxidation. The alumina layer is 4 μm in thickness and agrees well with the ECR thickness predicted for this sample.

Table 8. Normalized Weight Gain of Ti_2AlC Pressed Pellets and Fully Dense Discs Procured from Sandvik Following Steam Oxidation tests at 1200°C

Pellet Formation	Time (min)	Normalized Mass Gain (mg/cm^2)	ECR Thickness (μm)
50 ksi	15	33.9	366
86.6 ksi	15	21.7	156
Fully Dense	30	1.05	2.7
Fully Dense	30	0.63	4.5
Fully Dense	96 hrs	1.85	8.0

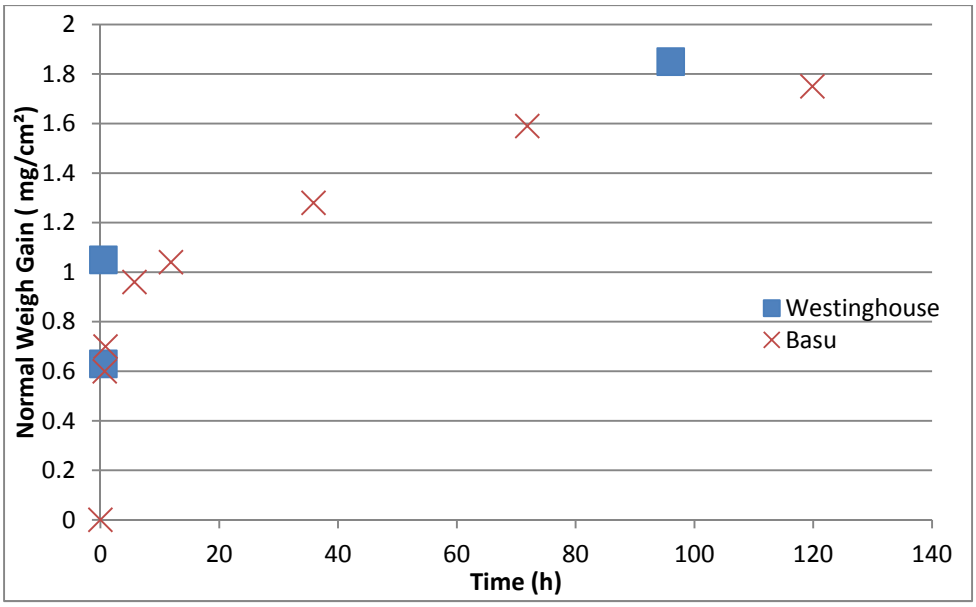

Figure 10. Comparison of normalized weight gain of the fully dense Ti_2AlC discs from 1200°C steam oxidation between this study and literature [4]

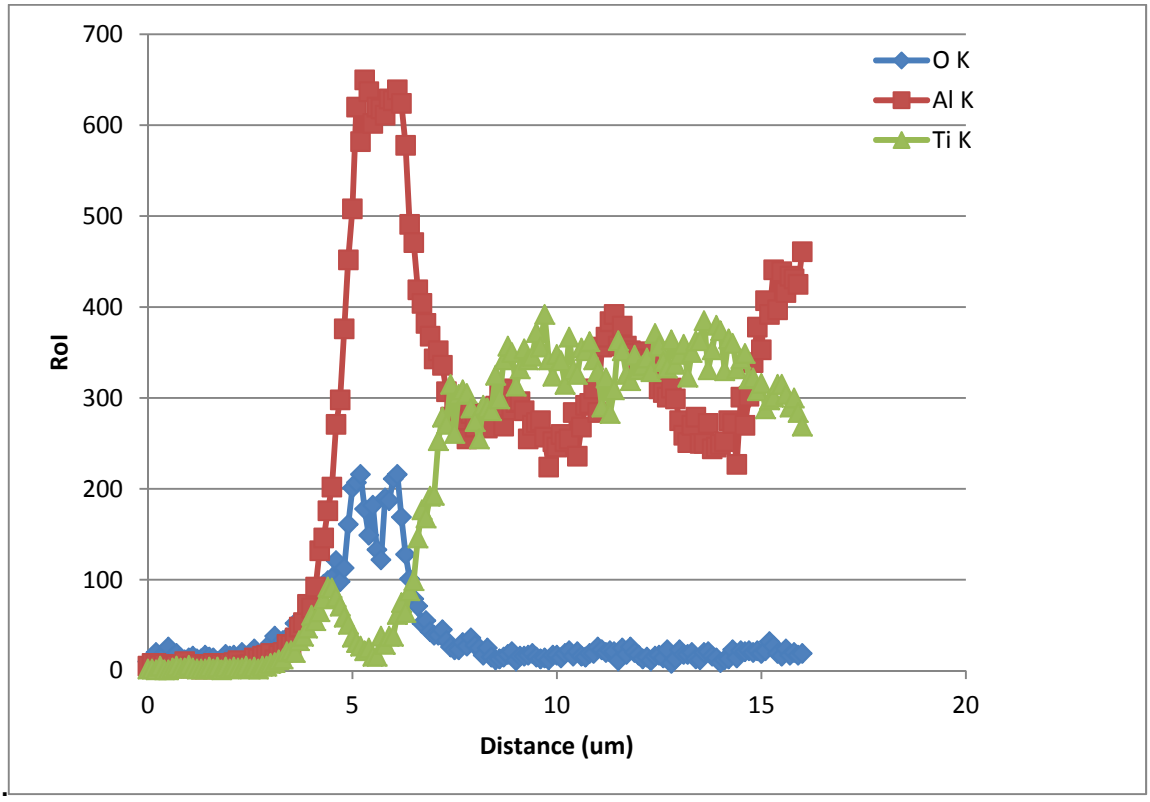

Figure 11. EDS scans of the first 18 microns of the surface of the fully dense sample after steam autoclave tests at 1200°C.

Conclusions

A preliminary evaluation study of Ti_2AlC MAX Phase and NanoSteel coatings deposited by HVOF and cold spray processes has been performed to provide enhanced oxidation resistance for zirconium-alloy fuel cladding. Neutronics calculations taking into account the elemental composition of the coating materials has shown that the coating thickness must be maintained below 30 μm for economic feasibility, although thicker coatings were used for these preliminary evaluations. In pressurized steam autoclave tests performed at 427°C, the HVOF coatings exhibited spallation while the cold spray coatings remained relatively intact. Coatings cold sprayed at gas preheat temperatures of 790°C showed significantly higher oxidation resistance compared to those sprayed with a gas preheat temperature of 600°C, due to increased coating densification. The Nanosteel coatings deposited by the cold spray process showed inadequate plastic deformation of particles, and while they survived the test, oxidation was seen to occur along the inter-particle boundaries. Mechanical testing of the coatings performed before and after 427°C steam autoclave tests showed generally satisfactory results. In high temperature steam oxidation tests performed at 1200°C, the Nanosteel coatings performed poorly and MAX phase Ti_2AlC coatings showed the formation of titania at the surface. Laser surface treatment of HVOF-sprayed Ti_2AlC coatings did not show any improvements in these tests. Tests performed on full density bulk Ti_2AlC MAX phase material showed good oxidation resistance and this was associated with the formation a protective alumina layer on the surface. Future work in MAX phase cold spray coatings will focus on producing higher density coatings that appear to promote the formation of alumina layer on the surface.

2. Acknowledgement

This material is based upon work supported by the Department of Energy under Award Number DE-NE0000566.

This report was prepared as an account of work sponsored by an agency of the United States Government. Neither the United States Government nor any agency thereof, nor any of their employees, makes any warranty, express or implied, or assumes any legal liability or responsibility for the accuracy, completeness, or usefulness of any information, apparatus, product, or process disclosed, or represents that its use would not infringe privately owned rights. Reference herein to any specific commercial product, process, or service by trade name, trademark, manufacturer, or otherwise does not necessarily constitute or imply its endorsement, recommendation, or favoring by the United States Government or any agency thereof. The views and opinions of authors expressed herein do not necessarily state or reflect those of the United States Government or any agency thereof.

3. References

[1] Ed Lahoda, Peng Xu, Sumit Ray and Lars Hallstadius, “Potential Performance Improvements of New Fuels”, The Minerals, Metals and Materials Society, Meeting in Orlando Florida, March 14, 2012.

[2] B. A. Pint, K. A. Terrani, Y. Yamamoto, L. J. Ott and L.L. Snead, “Practical & Scientific Aspects of FeCrAl Oxidation”, Oak Ridge National Laboratory, Fuel Cycle Research and Development, Salt Lake City Utah, August 28, 2013.

[3] S. Ray, E. Lahoda and F. Franceschini, “Assessment of Different Materials for Meeting the Requirement of Future Fuel Designs”, 2012 Reactor Fuel Performance Meeting, Manchester, UK, Sept. 2-6, 2012, Paper # A0115.

[4] S. Basu, N. Obando, A. Gowdy, I. Karaman, and M. Radovica, “Long-Term Oxidation of Ti_2AlC in Air and Water Vapor at 1000–1300◦C Temperature Range”, Journal of The Electrochemical Society, 159 [2] C90-C96 (2012).

[5] H. Zhang, V. Presser, K.G. Nickel, C. Berthold, and Y. Zhou, “Hydrothermal Oxidation Behavior of Bulk Titanium Aluminum Carbide”, J. Am. Ceram. Soc., 94 [10] 3460-3466 (2011).

[6] http://www.NanoSteelco.com/images/uploads/resources/9172_hvof_tech_data.pdf

[7] A.T. Motta, M.J. Gomes DeSilva, A. Yilmazbayhan, R.J. Comstock, Z. Cai, B. Lai, “Microstructural Characterization of Oxides Formed on Model Zr Alloys Using Synchotron Radiation”, Zirconium in the Nuclear Industry:15th International Symposium, ASTM STP 1505, 2009, p. 486.

[8] X. Qian, X. He, Y. Li, and Y. Sun, “Improving the Cyclic-Oxidation Resistance of Ti_3AlC_2 at 550°C and 650°C by Pre-oxidation at 1100°C”, Int. J. Appl. Ceram. Technol., 7 [6] 760–765 (2010)

[9] A.T. Motta, M.J. Gomes DeSilva, A. Yilmazbayhan, R.J. Comstock, Z. Cai, B. Lai, “Microstructural Characterization of Oxides Formed on Model Zr Alloys Using Synchotron Radiation”, Zirconium in the Nuclear Industry:15th International Symposium, ASTM STP 1505, 2009, p. 486.

[10] M. Ouisloumen et al.,“Qualification of the Two-Dimensional Transport Code PARAGON’, WCAP-16045-NP-A, August, 2004.

[11] Y.S. Liu, et al., “ANC: A Westinghouse Advanced Nodal Computer Code”. WCAP-10966-A, Westinghouse Electric Company, Sep. 1986

[12] Minitab 15, Minitab Inc., Quality Plaza, 1829 Pine Hall Road, State College, PA, (2007).

[13] R.P. Arnold , T. McKrell, M.S. Kazimi, “Silicon Carbide Oxidation in High Temperature Steam”, Massachusetts Institute of Technology, Cambridge, MIT-ANP-TR-139. 2011

[14] Steinbrück, M., Vér, N. & Große, M. Oxidation of Advanced Zirconium Cladding Alloys in Steam at Temperatures in the Range of 600–1200°C. *Oxid. Met.* **76,** 215–232 (2011).

[15] Wang, X. H. & Zhou, Y. C. High-Temperature Oxidation Behavior of Ti 2 AlC in Air. **59,** 303–320 (2003).

[16] Sundberg, M., Malmqvist, G., Magnusson, a. & El-Raghy, T. Alumina forming high temperature silicides and carbides. *Ceram. Int.* **30,** 1899–1904 (2004).

GENERAL ATOMICS

October 15, 2015

Edward Lahoda
Westinghouse Electric Company LLC
1332 Beulah Rd
Pittsburgh, PA 15235-5083

Reference: a) DE-FOA-0000712
b) GA Project 30396

Dear Mr. Lahoda:

Enclosed is one copy of the following report to be submitted in accordance with the referenced award.

GA REPORT	TITLE
GA-A28191	**"Westinghouse Accident Tolerant Fuel Phase 1a Project Final Report"**

If you have any questions or comments, please do not hesitate to contact me by telephone at 858.455.2507, at FAX 858.455.3545 or by E-mail at Ziba.Ahkami@ga.com.

Sincerely,

Ziba Ahkami
Contract Administrator

Enclosure: As stated

GA–A28191

WESTINGHOUSE ACCIDENT TOLERANT FUEL PHASE 1A PROJECT

Final Report for the Period November 12, 2012 Through September 7, 2015

by
C.P. DECK

Prepared under
Westinghouse Contract 4500454220

DATE PUBLISHED: SEPTEMBER 2015

DISCLAIMER

This report was prepared as an account of work sponsored by an agency of the United States Government. Neither the United States Government nor any agency thereof, nor any of their employees, makes any warranty, express or implied, or assumes any legal liability or responsibility for the accuracy, completeness, or usefulness of any information, apparatus, product, or process disclosed, or represents that its use would not infringe privately owned rights. Reference herein to any specific commercial product, process, or service by trade name, trademark, manufacturer, or otherwise, does not necessarily constitute or imply its endorsement, recommendation, or favoring by the United States Government or any agency thereof. The views and opinions of authors expressed herein do not necessarily state or reflect those of the United States Government or any agency thereof.

GENERAL ATOMICS

GA–A28191

WESTINGHOUSE ACCIDENT TOLERANT FUEL PHASE 1A PROJECT

Final Report for the Period November 12, 2012 Through September 7, 2015

By
C.P. DECK

Prepared under
Westinghouse Contract 4500454220

GENERAL ATOMICS PROJECT A30396
DATE PUBLISHED: SEPTEMBER 2015

Contents

List of Figures

List of Tables

Executive Summary

In this work, accident tolerant fuel cladding designs for light water reactors were fabricated and tested. The structures evaluated were composed of a combination of ceramic materials including monolithic SiC, pyrocarbon, and SiC-SiC composite layers. Stress analysis and modeling of the complex behavior of cladding structures was used to investigate performance under beginning of life (BOL), peak power, and end-of-life (EOL) conditions. Planar and tubular cladding samples were fabricated for characterization of permeability and mechanical and thermal properties, and results were used as material property inputs to the design calculations. Performance was also evaluated after subjecting samples to corrosion attack and mechanical and thermal loads.

The objective of modeling work and testing was to develop one or more viable ATF SiC cladding options to replace the Zircolay cladding currently used for LWR fuel. To be viable, the cladding must meet a range of specifications established by Westinghouse and must also have acceptable economics. Material and fabrication costs, as well as production scalability were also considered when evaluating potential cladding designs. Ultimately, a cladding design composed of an inner composite layer and outer monolithic layer was determined to provide the best probability of survival and fabrication of these structures to meet a range of dimensional specifications was demonstrated.

The cladding simulation showed that stresses caused by irradiation-induced swelling are larger and oppose stresses caused by thermal expansion under temperature gradients. Reactor shutdown stresses are most severe, when compressive coolant pressure and opposing thermal expansion stresses caused by thermal gradients are removed. The simulation also included a more accurate representation of the pseudo-ductile behavior of the SiC-SiC composite layers. Cladding designs with an inner composite and outer monolith are predicted to offer the highest probability of survival, as the irradiation-induced swelling puts the outer monolithic layer in compression, making fracture unlikely. Fully composite and inner monolithic designs were not predicted to have high probability of survival. The predicted survival probability is sensitive to material properties, and further refinement of fiber architecture and processing parameters could lead to denser composites with improved strength and thermal conductivity, further reducing likelihood of failure.

SiC-based cladding tubes were fabricated in lengths up to 3’ while meeting diameter and wall thickness requirements. Straightness, outer surface roughness, and thickness and outer diameter variation tolerances were achieved, and the fabricated tubes showed good infiltration and over-coating uniformity over the length.

Mechanical and thermal properties, as well as permeability and corrosion response were evaluated. A balanced fiber structure, providing roughly equal hoop and axial strengths, appears to be most suitable for ATF cladding applications and meets requirements to contain internal pressurization. SiC-SiC tubes and SiC-SiC tubes sealed with an endplug can retain hermeticity after mechanical and thermal cycling, and also showed no reduction in performance

at LWR-relevant temperatures compared to room temperature. Autoclave exposure of SiC-SiC to high temperatures and pressures showed improved mass change behavior compared to Zircaloy. Mechanical testing of sealed tubes via endplug push-out testing showed significant joint strength retention after exposure to steam at 1400°C. Mass loss data for SiC-SiC tubes irradiated in PWR water chemistry in the MITR was roughly comparable to previous irradiation data in the literature. Amongst the tube and sealed tube samples, those receiving an additional SiC coating had a reduced mass loss rate, showing a potential route towards better corrosion resistance.

1. Introduction

This document is the final report and constitutes the final deliverable specified in PO 4500454220, based on GA GACP 20003518R1. The sections of this document are identified by the subtask in the statement of work. These subtasks are as follows:

Subtask 1: Design and modeling
Subtask 2: Planar Coupon Testing
Subtask 3: Infiltration Studies of the Composite Layer
Subtask 4: Fabrication of Tube Samples
Subtask 5: Characterization of Tube Samples
Subtask 6: Tubular Samples for Oxidation and Autoclave Testing
Subtask 7: Tubular Samples for Irradiation Testing
Subtask 8: Demonstration of Manufacturability of Extended Length SiC Cladding Tubes
Subtask 9: SiC Joining Tests
Subtask 10: Fabrication of Sealed Rodlets for Oxidation and Irradiation Testing

In this document, the subtasks are not sequentially ordered, and instead, they are ordered to allow for a more logical flow of the information for the reporting. All subtasks were executed and results are summarized. Overall, the methods in the original statement of work were performed as described, with the exception of the permeability, which was adapted to achieve the measurements required.

2. Design and Modeling (Subtask 1)

Detailed modeling was performed to assess the potential performance of different cladding structures. An initial model looked at probabilistic sequential failure of a multi-layered structure composed of alternating SiC and pyrolytic carbon layers. This structure is a potential candidate structure for the hermetic seal coat layer to be included in the overall cladding design. This initial model only considered mechanical loading for a simplified geometry. The second model provided a more detailed analysis of the cladding structure, and considered more realistic loading conditions, including thermal gradients which would be experienced during the fuel life. This model determined stresses arising from thermal expansion, coolant and fission gas pressure, and temperature dependent swelling, and also considered the pseudo-ductile failure process of the composite. The model was used to compare different potential cladding designs by calculating stresses and resulting failure probabilities (determined based on Weibull parameters for the different layers in the cladding).

A computer code has been developed to predict the failure of the cladding due to a multilayer construction. This code accounts for a temperature-dependent swelling of the SiC due to both thermal and neutron irradiation-induced swelling effects. This swelling leads to a large stress gradient which goes from tensile at the inner wall to compressive at the outer wall. The combined results can lead to particularly large stresses at shutdown, as the loss of external pressure eliminates compressive stress, and the cessation of power generation eliminates the temperature-induced stress gradient, which is opposite to the swelling induced one and partially cancels it out. The conditions for beginning-of-life, end-of-life and shutdown were examined. Analysis concluded that an outer monolithic design was the best option because it keeps the monolithic portion under compression.

The model used in this work is derived using the method outlined by Timoshenko and Goodier. It is a one-dimensional axisymmetric model, which is used as an approximation for LWR cladding because the highest stresses in the cladding are at the axial center region where edge effects are negligible. For a one-dimensional axisymmetric model, there are no shear stresses, so only the normal components of Hooke's equations need to be considered. This model accounts for swelling and thermal expansion, and treats the elastic modulus and Poisson's ratio of SiC as constants. These are valid assumptions, as Poisson's ratio changes minimally with temperature and irradiation, and the elastic modulus varies less than 10% over LWR conditions. The effect of irradiation on elastic modulus is also similar for both mSiC and SiC-SiC (Katoh, 2014), so stresses arising due to the difference in elastic modulus will be similar before and after irradiation.

The model requires the temperature and swelling profiles. The temperature profile T(r) is calculated for a hollow cylinder with uniform heat flux using a constant thermal conductivity that is evaluated iteratively to the mean wall temperature. The heating rates were based on values supplied by Westinghouse. The swelling profile S(r) is then obtained based on the temperature profile and the irradiation dose. This approach can be expanded from a single cylinder to a multi-layer cylinder and the following boundary conditions are applied:

1. Radial continuity: The radial displacement at the outer radius of a layer must be equal to the radial displacement of the adjacent layer at the inner edge.

2. Equilibrium condition 1: The radial stress at the outer radius of a layer must be equal to the radial stress of the adjacent layer at the inner edge

3. Equilibrium condition 2: The radial stress at the inner wall of the innermost layer must equal the internal pressure, and the radial stress at the outer wall of the outermost layer must equal the external pressure.

4. Axial continuity: The axial displacement at the outer radius of a layer must be equal to the axial displacement of the adjacent layer at the inner edge

5. Saint-Venant's principle: The sum of the forces resulting from the corrective stress must equal the force required to axially constrain the ends of the tube plus the net

force of pressurization on the end caps of the tube. This should accurately reflect the free end stress distribution far away from the end of the tube

In this model it is assumed that the layers are rigidly bonded to one another. Monolithic CVD SiC and the CVI matrix of SiC-SiC composite are produced in a near identical manner and it is expected that these two materials will bond strongly to each other. Preliminary data gathered at General Atomics on multilayer specimens seems to demonstrate that this is true as no delamination is observed during mechanical testing. This model also does not consider shear stresses. Future analyses should consider the potential consequences of asymmetric loading, especially at the interface of the mSiC and SiC-SiC layers.

To create a simulation of the stress evolution in the cladding throughout the life of the fuel pin, the loading conditions are updated at successive time steps. This also allows for certain thermal and mechanical properties to be updated throughout the simulation period.

Using a closed form solution can be highly advantageous due to its calculation speed. The closed form solution is much less computationally intensive for this problem than a finite element method; the time to compute the solution for a single loading scenario in the finite element analysis program ANSYS can be on the order of minutes, whereas the model outlined here can run hundreds of cases per second in MATLAB. This makes it well-suited for failure probability analysis, where the variability in multiple material strength parameters makes rapid calculation of several thousand individual cases necessary. ANSYS was used to verify the accuracy of the model; the results of the closed for solution agreed with the ANSYS results to within a few percent for both irradiated and unirradiated conditions.

2.1. Loading Conditions

In LWR fuel cycles, fuel assemblies in the core experience varying conditions due to the effects of burn-up, temperature and pressure. The heat generation rate decreases as the fuel burns, and internal pressure builds up due to fission gas release. In addition, the reactor is periodically shutdown and depressurized to introduce new fuel and shuffle existing assemblies. This analysis is modeled after the AP1000, which utilizes 18 month fuel cycles. A given fuel assembly may undergo either two or three fuel cycles before it is retired to a spent fuel storage facility. For this work a full three fuel cycle lifetime is considered.

A conservative estimate is used for linear heating rate by using the value associated with peak operating conditions; it is modeled as decreasing linearly throughout irradiation. Since the peak heating rates are used, the stresses calculated will be higher than what the average cladding tube will experience. Cladding internal pressure and irradiation damage are modeled as increasing linearly. The final operational internal pressure of 20 MPa was chosen as a conservative value, although it is possible to reduce this value by increasing the free volume at the ends of the fuel pins. By examining the conditions throughout the life of the fuel pin, the most strenuous conditions in terms of failure probability can be determined. The loading conditions used in modeling the LWR fuel cycle are given below in Table 1.

Table 1: Loading conditions for LWR fuel cycle

	0-18 months	18-36 months	36-54 months
Linear Heating Rate (kW/m)*	36.1 - 32.7	32.7 - 29.3	29.3 - 25.9
Operating Internal Pressure (MPa)*	1 - 7.33	7.33 - 13.67	13.67 - 20
Shutdown Internal Pressure (MPa)	5.6	11.2	16.8
Irradiation damage (dpa)*	0-2	2-4	4-6
Heat Transfer Coefficient (W/m^2*K)	10,000		
Operating Coolant Temperature (°C)	316		
Operating Coolant Pressure (MPa)	15		
Cladding Shutdown Temperature (°C)	50		

**First value represents condition at the start of the fuel cycle and the second represents the condition at the end. Values are assumed to change linearly over time*

Note that the loading condition assumptions only include a linear heat rate, and fuel pellets are not modeled individually or included. Changes in fuel-cladding gap due to swelling, thermal expansion, and other factors may affect the fuel pellet temperature and gap thermal conductivity. These effects on fuel rod performance must be included in future fuel performance models, but are beyond the scope of this current work, which only focuses on cladding stresses. For cladding stresses (excluding any PCMI or PCCI), the linear heat rate is sufficient.

2.2. Material Properties

SiC has been studied over the past several decades and the properties are available in the literature for both SiC-SiC and mSiC. The model uses a combination of internally generated data and data and correlations published in the literature as input for the material properties. The out-of-pile internal data is consistent with the literature. The most important properties are discussed in further detail in this section, and the rest are summarized in Table 2.

For this analysis, a set of baseline data has been chosen as the composite property input for this model. The fiber architecture should primarily influence the orthotropic stress-strain attributes and thermal conductivity of the material; it may have effects on other properties as well that have yet to be elucidated in the literature. Data for SiC-SiC properties are obtained from nuclear grade composites made with high-purity, near stoichiometric fibers such as the Tyranno-SA3 and Hi-Nicalon Type S fibers.

2.3. Swelling

SiC is undergoing continued irradiation campaigns and data for the irradiation swelling of SiC is available for LWR conditions. For the temperature range of 200-800 °C, swelling is due to the accumulation of Frenkel defects in the crystal lattice. The swelling saturates at a relatively low dose, around 1 or 2 dpa, and the magnitude of the saturation swelling decreases

with the irradiation temperature. Katoh et al give the following differential equation to describe the swelling evolution in SiC from 200 to 800 °C [12]:

$$\frac{dS}{d\gamma} = k(T)\gamma^{-\frac{1}{3}} \exp\left(-\frac{\gamma}{\gamma_0(T)}\right)$$

Where:
S = Volumetric swelling strain, $\Delta V/V_0$
γ = Dose, in dpa
$k(T), \gamma_0(T)$ = Proportionality and time constants, respectively, as functions of temperature

The swelling at each radial point is determined with a uniform radial dose at each time step in conjunction with current temperature profile. Swelling is assumed to equilibrate instantaneously for the given temperature and dose at each time step. Figure 1 shows how swelling varies with dose at different temperatures. The swelling for CVI SiC-SiC and CVD mSiC are taken to be the same in this model, as the reference data suggests there is no significant difference between the two materials. Due to the similarity of the base materials, a substantial difference in swelling behavior is not expected. However, the existing data is limited and based on small individual samples rather than larger multi-layer structures. To account for this uncertainty, the effect of different swelling rates for different materials is examined.

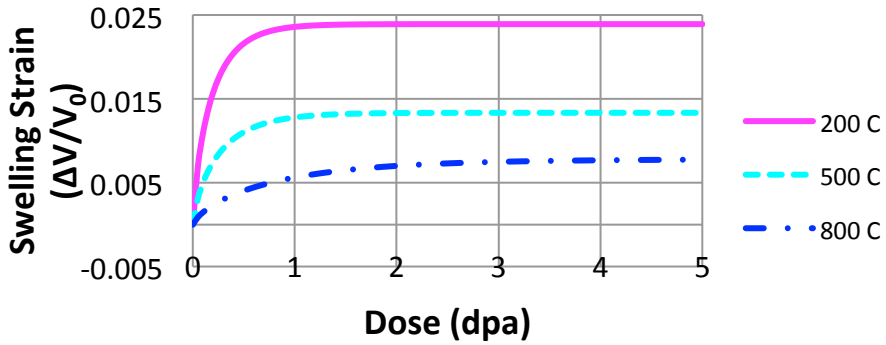

Figure 1: SiC swelling as a function of dose at varying temperatures

2.4. Thermal Conductivity

Thermal conductivity of unirradiated SiC-SiC was modeled using a 4th order polynomial fitted to data shown in Figure 2 for computational purposes. The data was obtained from GA-fabricated planar coupon specimens in the through-thickness direction and is consistent with data gathered by Katoh, also shown for comparison. Monolithic SiC thermal conductivity was based on data for polycrystalline, small grain CVD SiC.

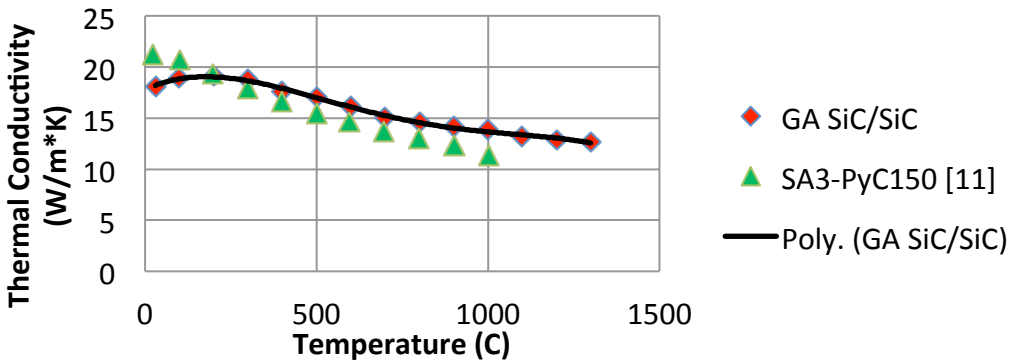

Figure 2: Thermal conductivity of unirradiated SiC-SiC composite up to 1300 °C

The change in SiC thermal conductivity due to irradiation can be understood by examining the components of its thermal resistivity. The thermal resistivity is comprised of two components, the unirradiated resistivity R_0, and the irradiation damage resistivity R_{irr}. This can be represented in equation form by:

$$\frac{1}{k} = R_0 + R_{irr}$$

The unirradiated resistivity is simply the inverse of the unirradiated thermal conductivity. The irradiation resistivity is directly proportional to swelling, and the proportionality constant for SiC-SiC is approximately two and a half times greater than that of mSiC. Since swelling saturates at progressively lower values with increasing temperature, the maximum irradiation resistivity also decreases with increasing temperature.

2.5. Stress-Strain Characteristics

Unlike mSiC, SiC-SiC cannot be treated as a purely linear-elastic material that deforms with a constant elastic modulus until fracture. The interwoven fibers give the composite material improved fracture toughness, allowing it to deform in a pseudo-plastic manner and hence achieve a more "graceful" failure. SiC-SiC typically exhibits an initial linear-elastic region up to the initiation of matrix cracking, followed by a secondary, non-linear region associated with continued matrix cracking and fiber sliding. This stress-strain behavior of SiC-SiC must be taken into account.

In order to more accurately model SiC-SiC, a modified stress-strain curve is implemented to calculate the composite stress-strain behavior. The curve consists of two lines, shown in Figure 3. The first is a proportional region, which begins at the origin and goes up to the proportional limit, given by (ε_p, σ_p). σ_p is referred to as the proportional limit stress (PLS). The second line, the non-proportional region, extends from the proportional limit to the ultimate tensile limit, (ε_u, σ_u). σ_u is referred to as the ultimate tensile stress (UTS). Since the calculation relies on linear elastic behavior, the stress-strain curve is used to generate an effective elastic modulus to approximate the correct stress-strain behavior where the true elastic limit is exceeded. This effective modulus is the slope of the line drawn from the origin to any point on the non-proportional region of the stress-strain curve. The effective modulus is determined by

iterating on the elastic modulus used for the given loading conditions until the maximum stress in the composite and effective modulus are consistent with the given stress-strain curve.

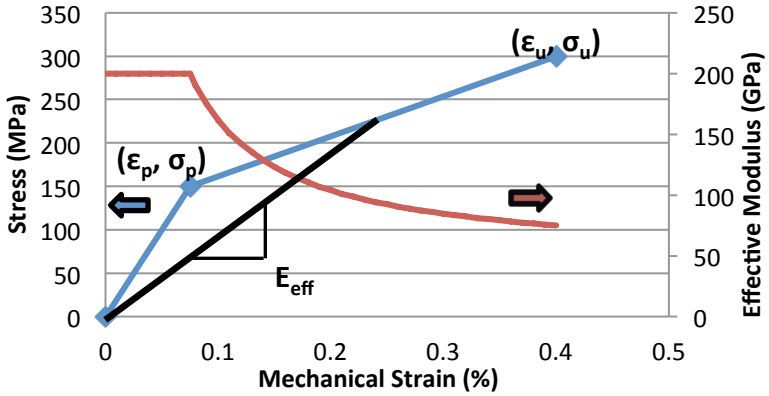

Figure 3: Example of stress-strain model for composite SiC-SiC

Physically, when the PLS is exceeded, the composite undergoes matrix cracking. These cracks affect the stress-strain behavior, even if the load drops below the initial PLS. These changes to the elastic modulus and PLS reflect the increased compliance caused by matrix cracking in SiC-SiC, even with loads that previously would have fallen within the elastic limit. The effect of this more realistic consideration of the composite behavior is shown in Figure 4, where the composite behavior with a modified effective modulus predicts lower overall stresses as some of the loads are transferred from the cracked region of the composite.

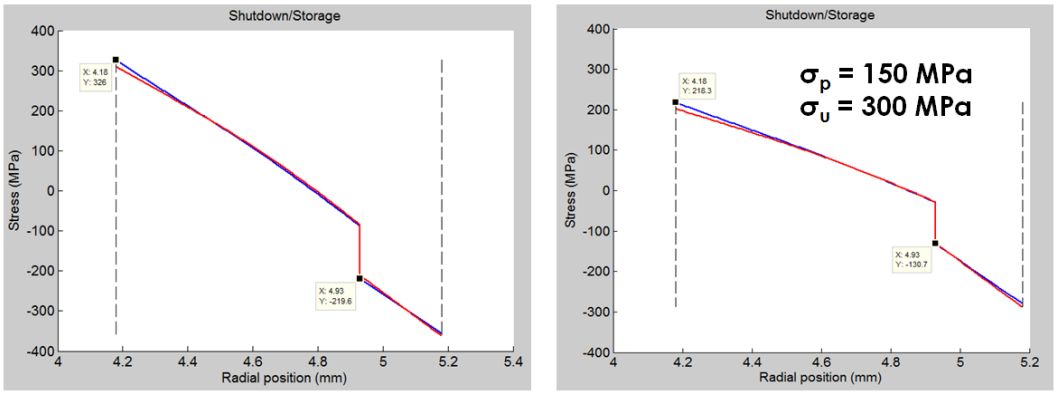

Purely Elastic Model **Modified Effective Modulus Model**

Figure 4: Stress at shutdown with the elastic model and the modified effective modulus model.

Previous studies indicate that the stress-strain curve effectively remains constant for temperature and irradiation conditions in LWRs. Lipetzky et al. concluded that temperature does not have a significant effect on the stress-strain behavior up to 1000 °C. Katoh et al. showed that irradiation does not affect the composite's UTS, and the effect on the PLS is within the statistical error bar.

2.6. Material Property Summary

A summary of the material properties used in this work for both SiC-SiC composite and monolithic SiC is given in Table 2. Note that the CTE equation is for the instantaneous form, and this must be converted into a secant CTE to be used in the model.

Table 2: Material Property Input Models

	SiC-SiC	mSiC
Elastic modulus	E = 296 GPa	E = 460 GPa
Poisson's ratio	ν = 0.18	ν = 0.21
Thermal conductivity (Unirradiated)	$k(T) = -1.71 * 10^{-11}T^4 + 7.35 * 10^{-8}T^3 - 1.10 * 10^{-4}T^2 + 0.061T + 7.97 \left(\frac{W}{m * K}\right)$	$k(T) = -3.70 * 10^{-8}T^3 + 1.54 * 10^{-4}T^2 - 0.214T + 153.1 \left(\frac{W}{m * K}\right)$
Thermal resistivity from irradiaton	$R_{irr} = 15.11 * S \left(\frac{W}{m * K}\right)^{-1}$	$R_{irr} = 6.08 * S \left(\frac{W}{m * K}\right)^{-1}$
Instantaneous CTE	$\alpha(T) = 3.83 * 10^{-9}T^3 - 1.22 * 10^{-5}T^2 + 0.0144T - 0.777 \left(\frac{10^{-6}}{K}\right)$	$\alpha(T) = 3.83 * 10^{-9}T^3 - 1.22 * 10^{-5}T^2 + 0.0144T - 0.777 \left(\frac{10^{-6}}{K}\right)$
Swelling	$\frac{dS}{d\gamma} = k(T)\gamma^{-\frac{1}{3}} \exp\left(-\frac{\gamma}{\gamma_0(T)}\right)$	$\frac{dS}{d\gamma} = k(T)\gamma^{-\frac{1}{3}} \exp\left(-\frac{\gamma}{\gamma_0(T)}\right)$

2.7. Cladding Designs

Three representative cladding concepts for current LWRs were analyzed. These concepts are depicted in Figure 5, and their geometries are summarized in Table 3. The first is 0.58 mm thick tube consisting of pure composite. The pure composite tube has the same dimensions as the zirconium alloy tubes currently used in LWRs. The other two concepts are monolith/composite two-layer designs; one with the monolith on the inner surface, and one with the monolith on the outer surface. The total wall thickness for the two-layer concepts was chosen to be 1 mm. This thickness, driven by current manufacturing considerations, was selected to allow for a sufficient fiber volume fraction in the SiC-SiC and thus ensure composite behavior. Each concept was examined in the same manner.

For all three concepts, it is assumed that the internal pressure acts on the inner wall of the cladding. For cases with composite inner layers, porosity contained within the composite may be subject to pressurization, potentially changing the loading distribution. This potential effect has been discussed previously [28], however given the high density of nuclear grade composites we believe that the impact on the stress distribution would be minimal.

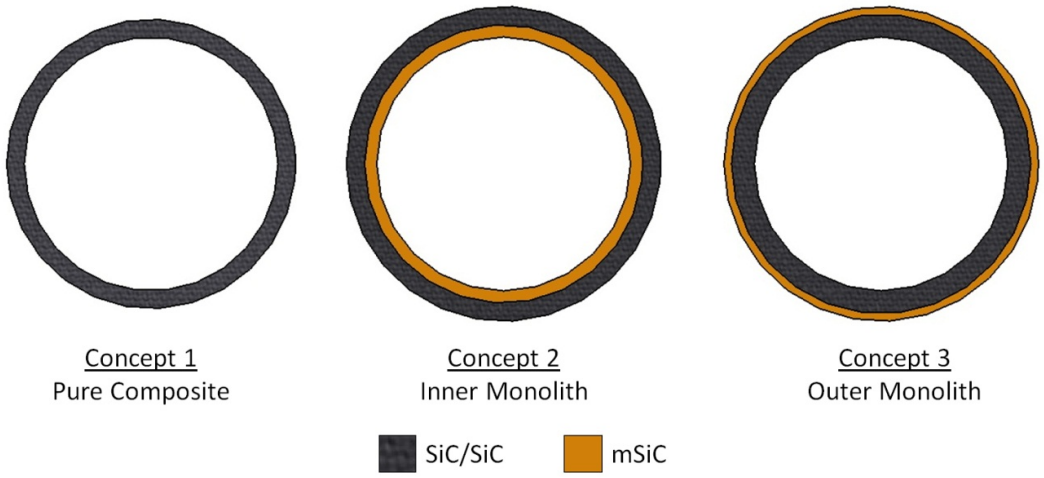

Figure 5: SiC Cladding concepts evaluated in this work

Table 3: Geometry of SiC-based cladding concepts

Concept	Inner Diameter (mm)	SiC-SiC layer thickness (mm)	mSiC layer thickness (mm)
1. Pure composite	8.36	0.58	N/A
2. Inner monolith	8.36	0.60	0.40
3. Outer monolith	8.36	0.75	0.25

2.8. Analysis of cladding design concepts

The cladding concepts were analyzed for the entire LWR fuel lifetime. As outlined earlier, this is composed of three 18 month operating periods, along with their following shutdowns, which are referred to as fuel cycles 1, 2 and 3 sequentially. The maximum stress in each layer is tracked throughout the fuel lifetime. The radial stresses are ignored in computing the maximum layer stress, as they are mostly compressive and are small in magnitude compared to the axial and hoop stresses. In addition to the maximum layer stresses, the stress profiles are examined at three critical points within each fuel cycle. The first is the beginning of life, when the reactor has just started and linear heating rate is highest. This is followed by end of life, the point right before the reactor is shutoff and the fuel has accumulated the maximum radiation dose for the cycle. The final critical point is the shutdown/storage state, where power generation is negligible and the coolant has been depressurized. All three concepts are examined in this matter.

In order to model SiC cladding behavior, mean stress-strain properties for SiC-SiC are used as input. While there is a large database of planar SiC-SiC stress-strain properties in the literature, differences in stress-strain properties resulting from fiber architecture, tube vs planar geometry, and fabrication parameters suggest it is important that this data come from representative material that will be used in reactor. In order to provide highest quality model

input, stress-strain properties were taken from GA fabricated nuclear grade SiC-SiC tubes of dimensions relevant to LWR cladding geometry. This data is taken from expanding plug and c-ring tensile hoop strength tests of tubular SiC-SiC samples, described more fully in Jacobsen et. al., as well as results presented in section 5.1. For the purposes of the model, test data presented in Jacobsen et. al. and further expanded upon here in Table 4, will be used for the model input, but it should be noted that repeat testing on follow up batches of material with the same fiber architecture have yielded data typically within +/- 10% of values reported here. Other reports in the literature for hoop strength of SiC-SiC tubes measured in expanding plug tests give similar ultimate strength values.

Table 4: Mean stress-strain properties measured on pure SiC-SiC tubes

Proportional Limit Stress (MPa)	Strain at PLS (%)	PLS Weibull Modulus	Elastic Modulus	Ultimate Tensile Strength	Strain at UTS (%)	UTS Weibull Modulus
163	0.056	10.5	296	404	0.494	6.8

2.9. Concept 1 - Pure composite tube

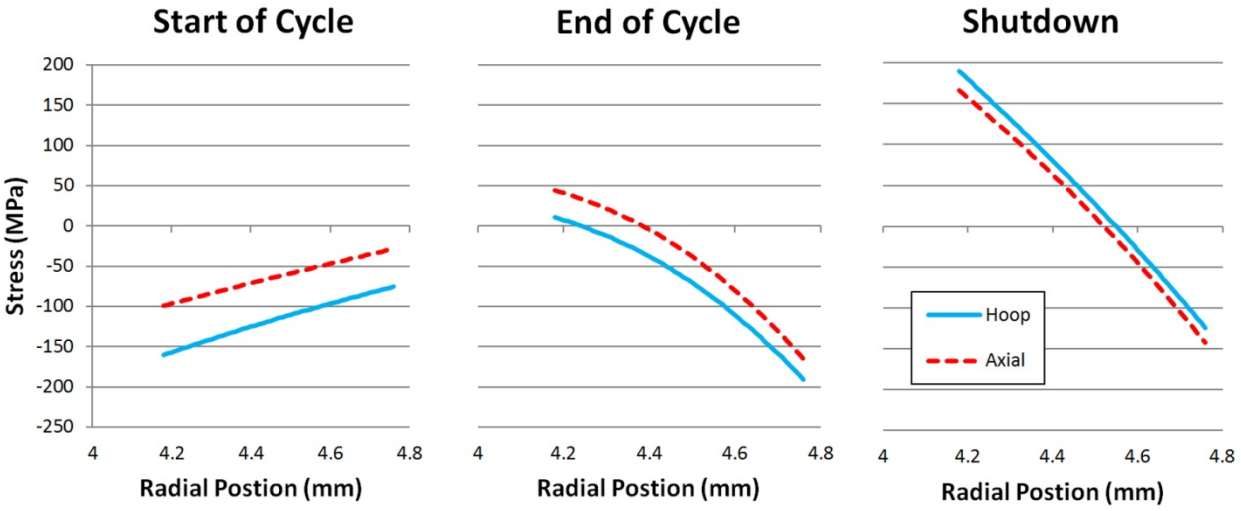

Figure 6: Concept 1 (pure composite): Stress profiles during the first LWR fuel cycle

Figure 6 depicts the stress profiles across the pure composite cladding for the critical points throughout the first fuel cycle. At the start of the first fuel cycle, no swelling has occurred, so the only stresses present are due to the temperature and pressure gradients. The temperature gradient puts a compressive stress on the inner wall of the cladding and a tensile stress on the outer wall, while the net external pressure from the coolant exerts a compressive stress across the entire profile. At the beginning of the first fuel cycle, this external pressure applies larger stresses than the thermal gradient, which keeps the cladding in compression throughout its thickness.

At the end of the first cycle, the cladding has received a substantial dose of radiation, causing differential swelling between the relatively cooler outer wall and hotter inner wall. The differential swelling has the opposite effect of the temperature gradient on the cladding stress; it exerts tension on the inner wall and compression on the outer wall. The stresses are dominated by irradiation swelling and the slope of the stress profile flips. This effect is magnified by the decrease in thermal conductivity of the SiC-SiC due to irradiation damage, which increases the temperature gradient almost threefold and results in greater differential swelling. This is illustrated in Figure 7, which shows the temperature profile for the pure composite concept and the beginning and end of the first fuel cycle. Additionally, fission gas release increases the internal pressure, lowering the net external compression of coolant. The combination of increased internal pressure and swelling stresses result in a small tensile stress on inner wall of the cladding. The differences in the stress profile between the beginning and end of the first fuel cycle show the effect of temperature dependent swelling, as demonstrated previously by Ben Belgacem et al, whose results show good agreement to the ones presented here.

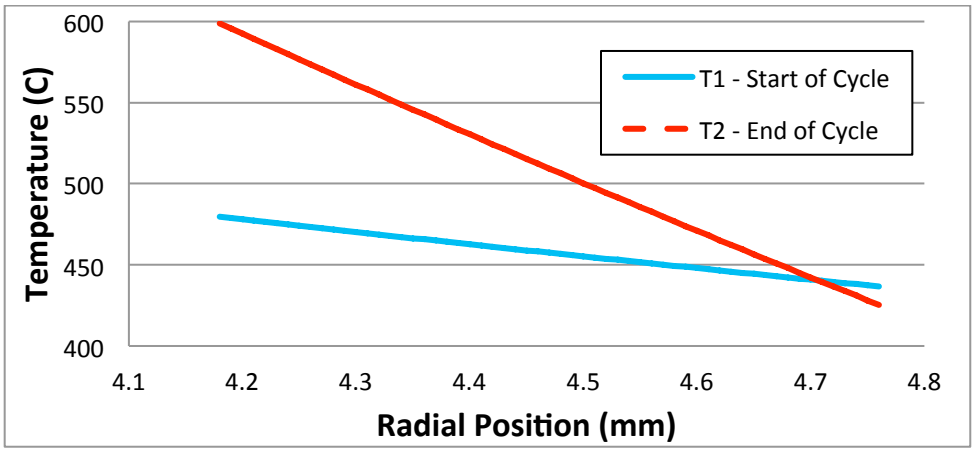

Figure 7: Temperature profiles for concept 1 (pure composite) at start and end of first fuel cycle

The final critical stress state shown in Figure 6 is for reactor shutdown conditions. At this point, the coolant has been depressurized and the nuclear reaction has ceased, resulting in a negligible temperature gradient. These changes lead to a substantial increase in tensile stress within the cladding; the maximum stress jumps from 60 MPa prior to shutdown to almost 200 MPa afterwards. The assumed PLS is 163 MPa, so upon shutdown after the first cycle the composite undergoes significant matrix cracking and starts to exhibit pseudo-plastic behavior.

To help understand the cause of this stress increase at shutdown, Figure 8 compares the individual contributions of mechanical, thermal and swelling forces at the end of the first fuel cycle and during the following shutdown. The temperature and swelling gradients have opposite loading effects and the resulting stresses partially cancel each other out during operation, with the stronger effect of the swelling gradient dominating. When the reactor is shut off and the temperature gradient disappears. However, the accumulated swelling strain remains, subjecting the cladding to the full stress loading of the differential swelling. The mechanical loading also shifts from compressive to tensile with coolant depressurization. However, the mechanical stresses from internal pressurization are small relative to the swelling

stresses. Note that the swelling stress drops due to the stress exceeding the proportional limit, decreasing the effective modulus. Despite this reduction, the swelling stress still far exceeds the mechanical stress and is the primary reason for cladding failure.

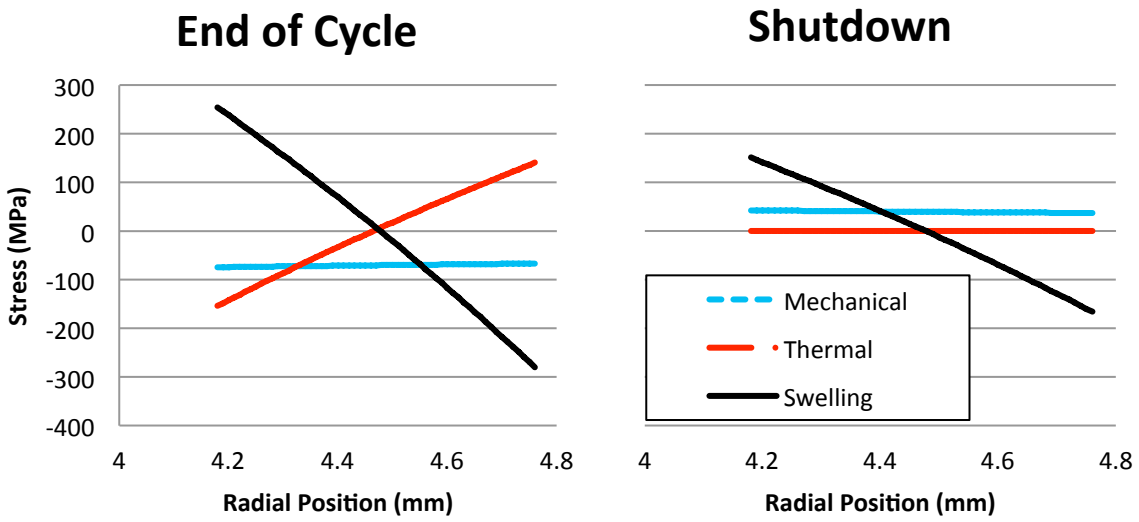

Figure 8: Concept 1 (pure composite): Stress components at end of first fuel cycle

In the second and third fuel cycles, the change in the cladding stress profile from start to end of operation is very small. The irradiation effects of swelling and decreased thermal conductivity in the SiC-SiC material effectively saturate after the first cycle, and the effects of increasing internal pressure and falling linear heat rate are minor relative to the stress shifts of the first fuel cycle. The stress profile at any time during operation for the latter two cycles appears similar to stress profile at the end of the first cycle. Likewise, the stress profiles for the shutdown states in the latter cycles are similar to the stress profile for the first shutdown, with small increases in the magnitude of the tensile loading from internal pressure buildup.

Figure 9 shows the max stress on the cladding over the LWR fuel cycle. This clearly demonstrates that for all three cycle the worst loading case occurs at shutdown. Once the stresses at shutdown exceed the PLS, some pseudo-plastic behavior is observed. The loading conditions used at the end of one cycle and the beginning of the subsequent cycle are identical. However, Fig. 7 clearly shows a drop in stress upon resuming operation after the shutdowns in cycles 1 and 2 relative to the stresses before shutdowns. This stress drop is a result of the decrease in effective elastic modulus that accompanies stress exceeding the linear-elastic regime during shutdown, which decreases the stresses from swelling and thermal loading. The maximum stress occurs at the final shutdown following the third fuel cycle, where internal pressure is highest.

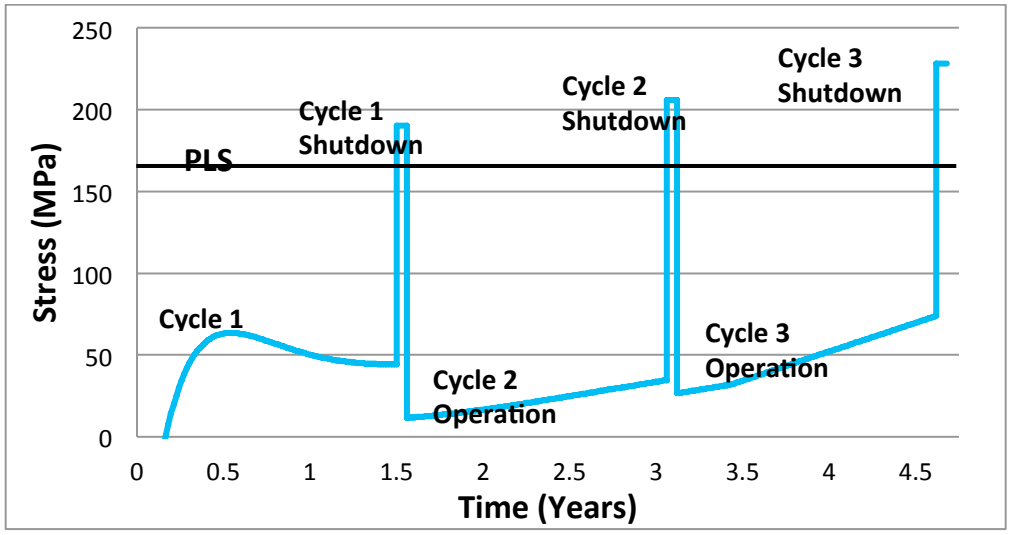

Figure 9: Concept 1 (pure composite): Maximum cladding stress over LWR fuel cycle

2.10. Concept 2 - Inner mSiC, Outer SiC-SiC

Figure 10 shows the stress profiles for the inner monolith concept over the first LWR fuel cycle. The inner monolith concept, often referred to as a "duplex" design, has been examined in other studies. They have been considered attractive because they could be manufactured by laying SiC fiber over an extruded mSiC tube. The profiles are similar to the pure composite tube, although there are two notable differences. First, the overall thickness of the tube has increased, which increases the stresses due to the temperature and swelling gradients, but decreases the stresses from internal gas pressure. Second, while the monolithic material has a higher elastic modulus than the composite, it has a much higher thermal conductivity, reducing the temperature gradient and resulting swelling gradient in the monolithic layer. These two factors result in the slope of the stress profile being lower in the monolith, despite the higher elastic modulus.

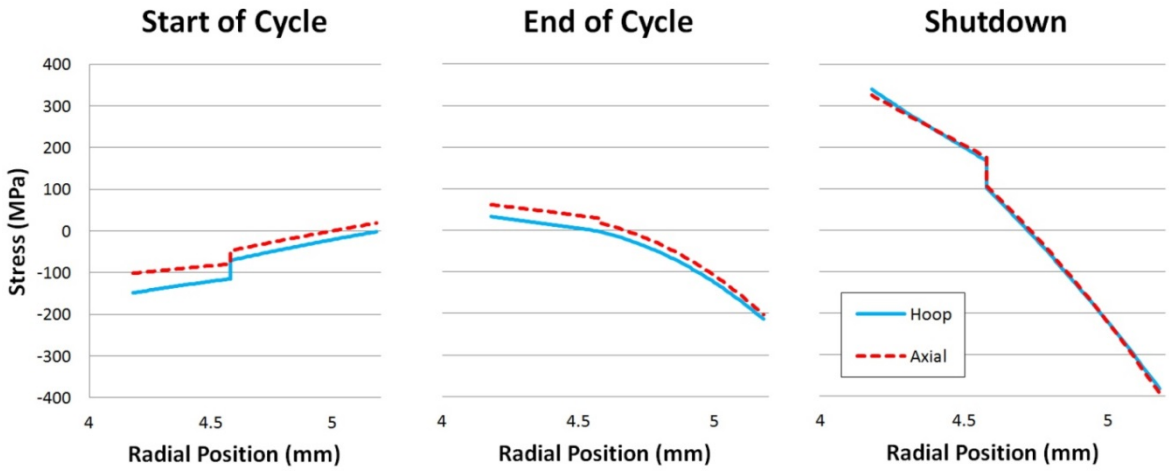

Figure 10: Cladding concept 2 (inner monolith): Stress profiles during first LWR fuel cycle

Figure 11 shows the maximum stresses in both composite and monolith layers over the complete LWR fuel cycle. Like the pure composite case, tensile loading is greatest during the

shutdown condition for all cycles. The magnitude of the maximum tensile stress at shutdown is almost 80% greater than in the pure composite concept. This is partly because of the increased wall thickness of the inner monolith concept, but also because the mSiC layer cannot deform in the same pseudo-plastic manner as the SiC-SiC.

The inner monolith cladding concept must depend on the composite to remain impermeable. However, the high tensile stresses at shutdown would lead to a high probability of exceeding both the monolith fracture strength and composite PLS.

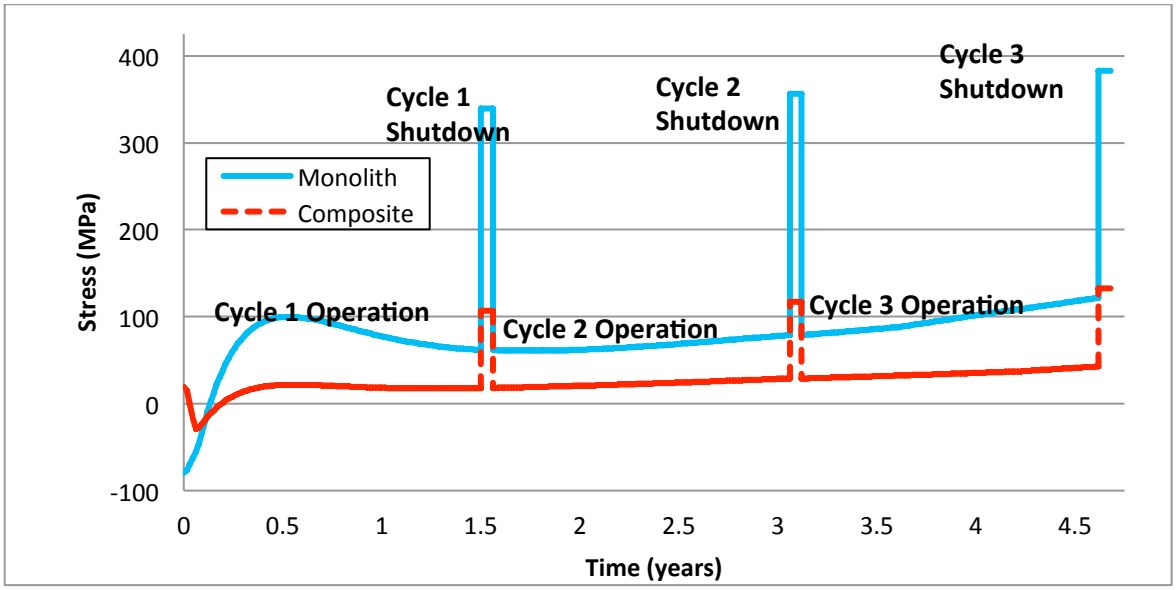

Figure 11: Concept 2 (inner monolith): Maximum cladding stress over LWR fuel cycle

2.11. Concept 3 – Inner SiC-SiC, Outer mSiC

The outer monolith concept has been overlooked because of the obvious stresses caused by thermal gradients. In the absence of swelling, thermal gradients and internal pressure will result in increased tension on the outer wall of the cladding, leading to increased failure probability of the outer monolithic layer. For example, in Fig. 12 the outer wall is much closer to being in tension in the stress profile at the start of the first fuel cycle where no irradiation-induced swelling has occurred.

Without swelling, the accumulation of fission gases and falling thermal conductivity would cause increasing tensile stresses in the mSiC layer. However, with irradiation-induced swelling, the outer layer quickly goes into compression. Since this swelling remains after shutdown, the outer layer remains in compression during shutdown, as seen in the stress profiles of Figure 12.

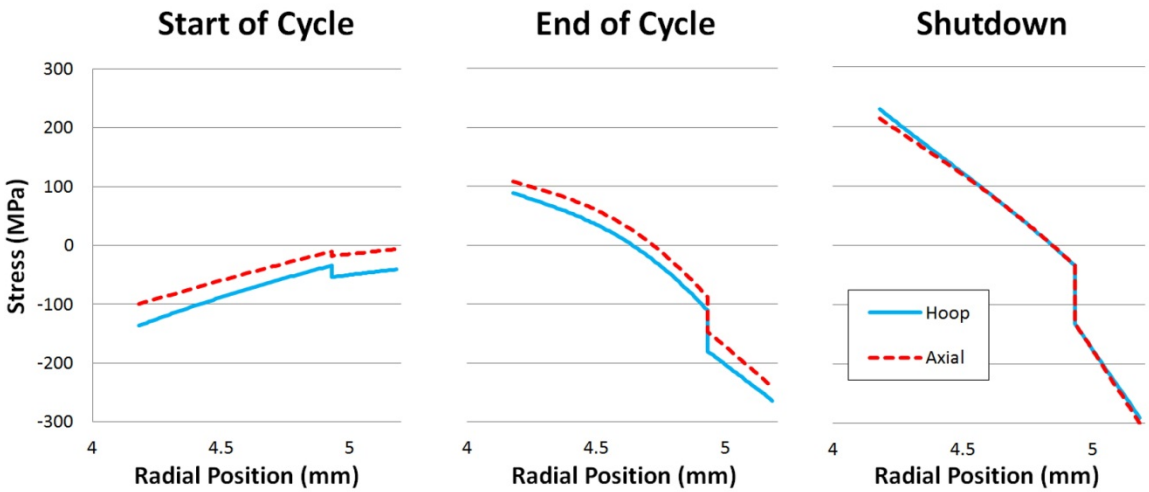

Figure 12: Concept 3 (outer monolith): Stress profiles during first LWR fuel cycle

The swelling gradient also puts a large tensile stress on the SiC-SiC layer, particularly at shutdown. At shutdown, the composite exceeds its PLS (163 MPa) and is no longer in the linear-elastic behavior region. This means the SiC-SiC is now deforming more per unit stress, which keeps the composite from exceeding the UTS. The increased compliance of the SiC-SiC also increases the tensile loading on the mSiC layer from internal pressurization. Despite this additional loading, the swelling gradient keeps the outer monolith in compression.

Due to the tensile loading from the first core shutdown, the composite is permanently altered by exceeding its proportional limit. Matrix cracking increases the compliance of the material, which is manifested in the model by a reduced effective elastic modulus. The increased compliance effectively reduces the thermal and swelling gradient induced stresses in the composite layer. Figure 13 compares the hoop stress at the end of operation in cycle 1 to the hoop stress at beginning of operation in cycle 2. These scenarios have identical loading conditions; the resulting stress profiles are different due the reduction in effective modulus after the first shutdown, which decreases the tensile load on the composite layer while increasing the tensile loading on the monolith.

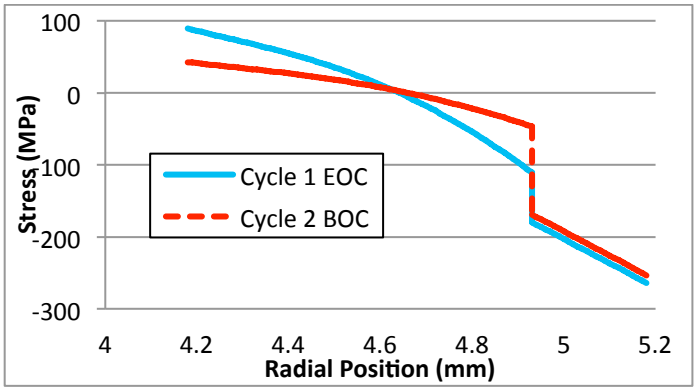

Figure 13: Concept 3 (outer monolith): Hoop stresses for end cycle 1 and beginning of cycle 2

Figure 14 shows the maximum strength on both composite and monolith layers over the life of the fuel rod for the outer monolith concept. Initially, the maximum stress curves diverge

as swelling accumulates. After 6 months, the stress magnitudes peak locally and start to converge. This corresponds with the peak differential swelling, as the saturation dose is larger for the hotter SiC material. Once swelling has saturated, the stresses gradually slope upward with the build-up of internal pressure from fission gases, with sharp, brief tensile spikes due to reactor shutdown. The maximum stresses in the composite throughout the fuel life are similar to the thinner pure composite concept and much lower than the tensile stresses on the inner monolith concept, with the SiC-SiC remaining below its UTS. The mSiC layer remains in compression throughout the fuel life. This compression in the monolith makes the PLS of the composite less critical, as the mSiC will remain impermeable. With relatively low stresses on each layer, the outer monolith concept has a low failure probability.

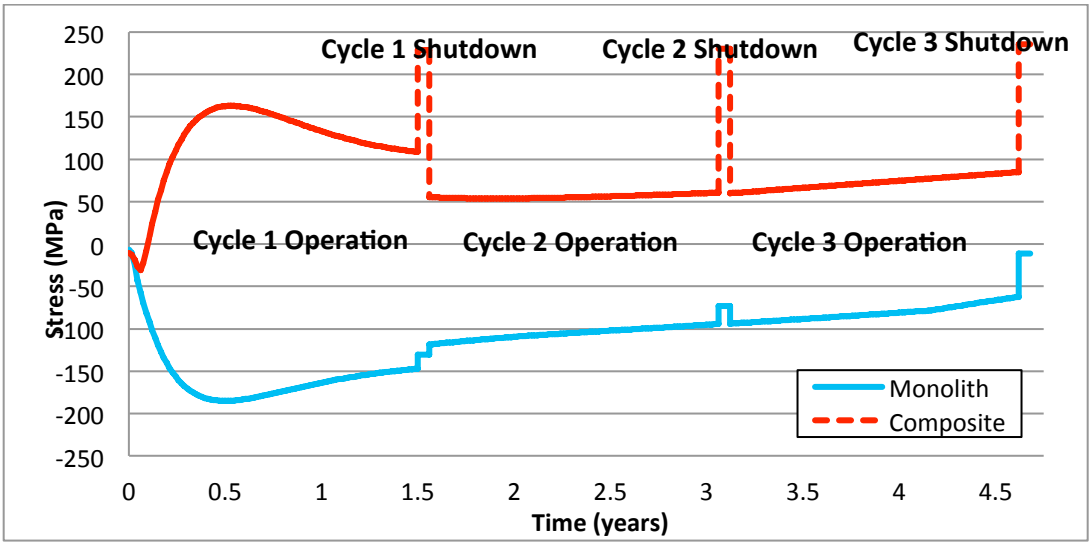

Figure 14: Concept 3 (outer monolith): Maximum cladding stress over LWR fuel cycle

2.12. Sensitivity to Material Properties

Given the statistical variances in the measurements of material properties, it is important to examine the possible outcomes if properties change significantly. Data in the literature for thermal conductivity, swelling, and coefficient of thermal expansion were examined to determine realistic ranges that would cause the highest stresses. Based on the largest deviations observed in the literature, the input to the model for this worst-case scenario was modified to decrease thermal conductivity by 20% and increase swelling by 25%. While studies indicate that thermal expansion for SiC-SiC and mSiC are equal, the variation in data allows for a mismatch in composite and monolith CTEs. This possibility is modeled by increasing the CTE of SiC-SiC 15% while leaving the mSiC CTE unchanged. The reference temperature for thermal expansion was chosen as 1000 °C, which is within the range of typical manufacturing temperatures used in the chemical vapor deposition processes. The modified results for the worst-case scenario were computed for the outer monolith concept. Figure 15 compares this worst-case stress profile to the nominal one for the end of operation in cycle 1, and Figure 16 compares those same cases for the shutdown after cycle 1. In both cases, the hoop and axial stresses are similar and follow the same trends, with the axial stress being higher during operation and the hoop stress higher during shutdown. As such, Figure 15 shows the axial stresses and Fig. 16 shows the hoop stresses.

The worst-case results show an increase of approximately 40% in the tensile stress on the inner wall. The largest stress increase is due to the CTE mismatch, which widens the stress discontinuity at the boundary between the SiC-SiC and mSiC layers. The stress increases in the composite layer due to greater swelling and lower thermal conductivity are partially negated due to pseudo-plastic deformation. The swelling and thermal conductivity effects are more pronounced in the increased stress gradient in the mSiC layer. In both loading scenarios, the stress in the composite layer remains below its nominal UTS.

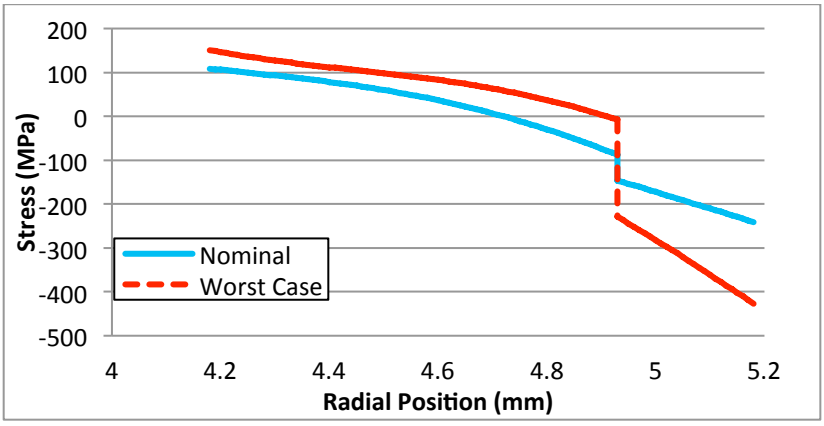

Figure 15: Axial stress profile of outer monolith concept at end of cycle 1 operation for nominal and worst-case material properties

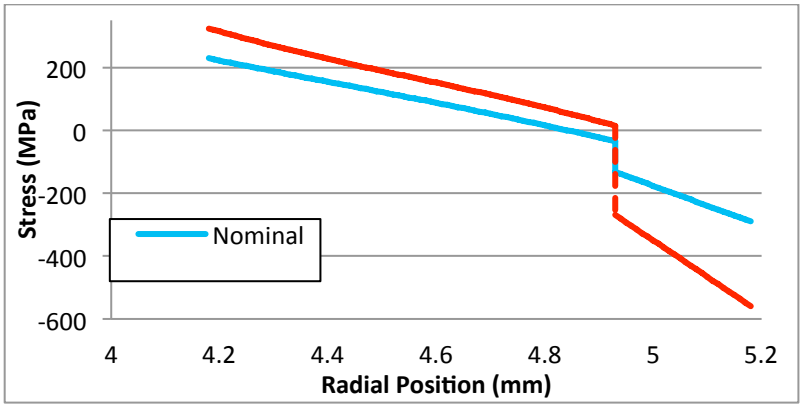

Figure 16: Hoop stress profile of outer monolith concept at shutdown following cycle 1 for nominal and worst-case material properties

To examine the uncertainty associated with mSiC and SiC-SiC irradiation swelling rates, the end-of-life stress conditions for cycle 1 were evaluated for the outer monolith concept using modified swelling inputs. The radial profile of the hoop stress in the assumed uniform swelling was compared to a case where the swelling was 25% greater in the monolith, and a case where the swelling was 25% greater in the composite, as shown if Figure 17. The differential swelling between the two layers greatly increased the discontinuity at the interface boundary, resulting in the material with greater swelling in compression and the material with lesser swelling in tension. In these cases, temperature dependent irradiation swelling dwarfs the other loading effects and the resulting clad stresses are largely dictated by the differential

swelling between materials rather than the relative location of individual layers. These results are similar to those of Shirvan and Lee and highlight the need for accurate swelling data.

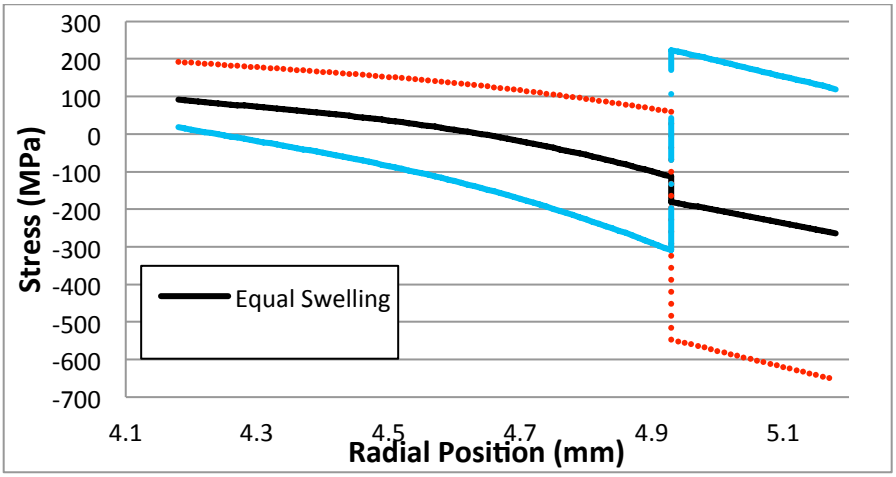

Figure 17: Hoop stress profile of outer monolith concept at end of cycle 1 operation for different swelling conditions

2.13. Failure Criteria for Probabilistic Assessment

In LWRs the function of the cladding is to maintain the core geometry and prevent the release of fission products into the primary coolant. Monolithic SiC has been examined in ceramic claddings to provide the latter function, and is considered to remain impermeable until it reaches its fracture stress. However, in this assessment, mSiC is not depended on to maintain core integrity on its own due to its brittle nature. For multi-layer cladding, if the composite layer exceeds its UTS, it is considered failed even if the monolith is below its fracture stress. The fracture stress of mSiC has been studied in the literature and is dependent on underlying random flaw populations. The variation in fracture stress is commonly modeled with a Weibull distribution.

The failure criteria for composite SiC-SiC are more difficult to define. As noted earlier, SiC-SiC initially deforms elastically until it reaches its proportional limit. After the proportional limit is exceeded, SiC-SiC can continue to deform in a pseudo-plastic manner until the UTS is reached. SiC-SiC is considered capable of maintaining core geometry up to its UTS. To address the impermeability of SiC-SiC, two cases were examined. In the first, SiC-SiC is considered impermeable up to the PLS, where matrix cracking occurs. This represents the best case scenario with regard to SiC-SiC impermeability. In the second case, SiC-SiC is treated as having inherent porosity and is always considered to permeable, the opposite extreme of the first case. This second case, in which impermeability is provided by an mSiC layer, is more representative of an engineered SiC-based cladding design. Such concepts would be designed to allow the stresses in the composite to exceed the PLS, provided they remain below the UTS, and position mSiC layers to minimize their exposure to tensile stresses.

Due to the failure mechanisms based on random underlying flaw populations associated with ceramics and ceramic composites, the stress-strain curves of SiC-SiC require a statistical approach to accurately model the cladding behavior. While underlying flaws in the

microstructure of SiC-SiC do not cause catastrophic failure as in mSiC, they do affect the shape of the stress-strain curve.

2.14. Probabilistic Modeling of the Stress-Strain Curve

Probabilistic modeling requires examination of the construction of the stress-strain curve, which is defined by two points that can be further broken out into four variables: the proportional limit stress σ_p, the strain at the proportional limit stress ε_p, the ultimate tensile stress σ_u, and the strain at the ultimate tensile stress ε_u. Due to the nature of ceramics, a statistical approach must be used. There is assumed to be little correlation between values for the PLS, UTS, strain at the PLS, and strain at the UTS. This is supported by experimental observations on planar samples (section 4.1), and tubular samples (section 5.1).

Using a statistical approach to construct the stress-strain curve requires care in choosing the distribution of the variables. Based on the consistency observed in the experimental data, the elastic modulus is assumed to be constant, providing a linear relation for stress and strain at the proportional limit. The variation in the stress-strain curve is then accounted for by three distributed variables. These are the PLS (σ_p), the difference in stress between the PLS and UTS (σ_{u-p}), and the difference in strain between the PLS and UTS (ε_{u-p}). Both σ_p and σ_{u-p} are modeled with a Weibull distribution, which is consistent for SiC-SiC throughout the literature, as summarized by Katoh. However, distribution properties regarding strain in SiC-SiC are not typically calculated in literature. With no precedent, three different distributions were examined for ε_{u-p}: Weibull, normal, and log-normal. From this examination, the log-normal distribution was found to fit the data best and therefore was used in failure probability calculations. Figure 18 illustrates how the various components are assumed to be distributed. Due to the low correlation between variables shown above, for modeling purposes the distributions are assumed to be independent of each other.

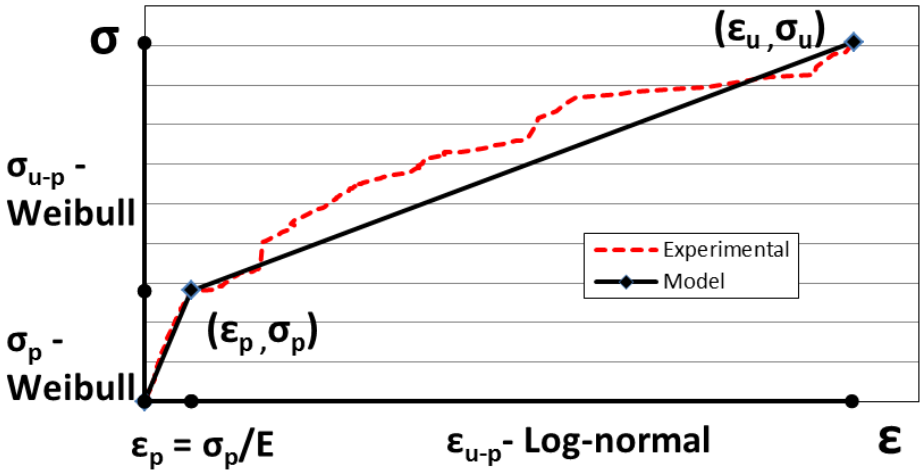

Figure 18: Components and distribution types for simplified stress-strain curve

It is important to note that using a distribution to describe the strain and stress differences from the PLS to the UTS requires a full set of stress-strain curves for each specimen tested. If the PLS and UTS are examined independently, their respective probability density function curves will overlap as shown in Figure 19, resulting in a statistically significant

fraction of cases where the UTS is lower than the PLS. This non-physical result would invalidate the probability calculation.

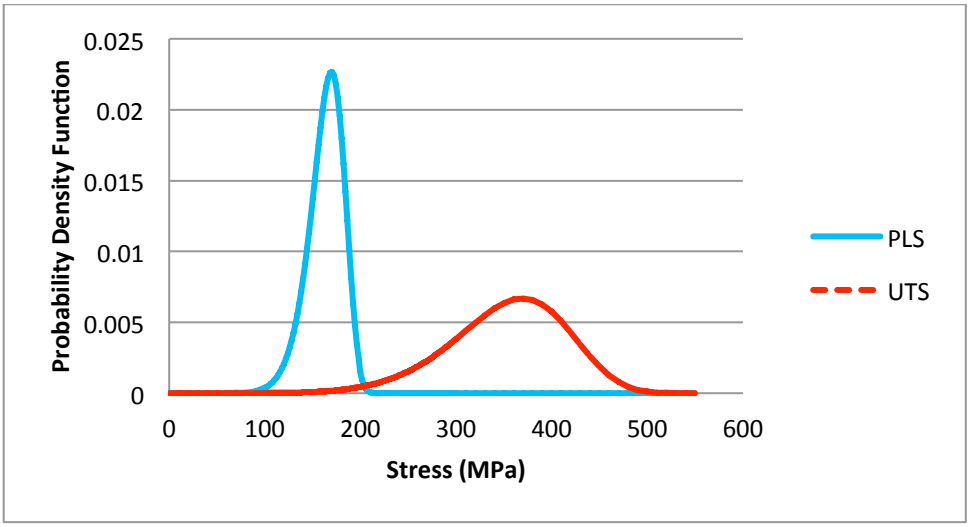

Figure 19: Probability density functions of PLS and UTS examined independently

The data for the composite variables was taken from testing of tubular material discussed in section 5. The distribution parameters used for the three composite stress-strain curve variables are given in Table 5. These values were taken from experimental data (section 5.1). Additionally, Table 5 contains the distribution parameters used for the monolith fracture stress. There are several studies that have examined the effect of irradiation on the fracture stress distribution of mSiC. While the distribution parameters vary widely from test to test, all of them show that irradiation reduces the Weibull modulus, typically by 30-40% and increases or has no effect on the Weibull characteristic stress. The values used in this work are based on data from internal pressurization tests of irradiated CVD mSiC. The distribution parameters for these tests had significantly lower Weibull moduli when compared to some of the flexural tests, and provide a conservative result for the failure probability calculation.

Table 5: Distribution parameters for SiC materials

Property	Symbol	Distribution Type	Distribution Parameters
SiC-SiC PLS [27]	σ_p	Weibull	m = 10.5, σ_0 = 171 MPa
SiC-SiC difference between UTS and PLS [27]	σ_{u-p}	Weibull	m = 4.1, σ_0 = 211 MPa
SiC-SiC difference between strain at UTS and strain at PLS [27]	ε_{u-p}	Log-normal	$\mu_{\ln(\varepsilon)}$ = -5.49, $\sigma_{\ln(\varepsilon)}$ = 0.287
mSiC fracture stress [16]	$\sigma_{f,m}$	Weibull	m = 4.5, σ_0 = 370 MPa

It should be noted that no normalization against volume or surface area was performed for either material. Although there is a well-established relationship that characteristic fracture stress of monolithic ceramics should decrease as test specimen size increases, as detailed in ASTM C1683, there has yet to be a comprehensive size versus strength study for monolithic

SiC in the literature, and the limited data that is present often shows considerable uncertainty. For instance, Byun et al studied the effects of volume and surface area on internal pressurization tests for two sets of tubes, both made from CVD SiC. In this test, the larger SiC specimens reported a higher mean fracture stress than the smaller ones, the opposite of what would be expected. Additionally, the Weibull moduli for the different SiC samples differed by a factor of two, despite using identical material. This indicates a large degree of variability based on material and test parameters, which was likely exacerbated by the relatively small size of the tubes used in that study. As such, a volume- or surface-based Weibull approach to mSiC is not easily definable, and therefore the simpler version of the Weibull probability equation is used. While outside the scope of this work, further study is required to determine these effects, and based off similar monolithic ceramic behavior, it would be reasonable to assume that the characteristic stress used for mSiC in larger components would ultimately be size dependent.

2.15. Failure Probability Calculation

With the distribution parameters determined and assuming the variable distributions are independent, the overall failure probability can be calculated by integrating over the probability density functions.

$$P_{f,total} = \int_{\sigma_{u-p}=0}^{\infty} \int_{\varepsilon_{u-p}=0}^{\infty} \int_{\sigma_p=0}^{\infty} P_f\left(\sigma_p, \varepsilon_{u-p}, \sigma_{u-p}\right) pdf(\sigma_p)\, pdf\left(\varepsilon_{u-p}\right) pdf\left(\sigma_{u-p}\right) d\sigma_p d\varepsilon_{u-p} d\sigma_{u-}$$

Where:

$P_{f,total}$ = Overall failure probability of individual cladding tube

$pdf(x)$ = The probability density function of variable x

σ_p = Composite proportional limit stress

ε_{u-p} = Difference between strain in composite at UTS and strain in composite at PLS

σ_{u-p} = Difference in composite UTS and composite PLS

$P_f\left(\sigma_p, \varepsilon_{u-p}, \sigma_{u-p}\right)$ = Failure probability of a tube for the given stress-strain variables

The individual tube failure probability function is a piece-wise function that accounts for the maximum stress on each layer. If the stress on the composite exceeds the UTS, then the cladding is considered failed. If the stress on the composite remains below the UTS, then the cladding maintains its structural integrity but must still remain impermeable to fission products. If the composite is considered permeable, the failure probability becomes dependent on the fracture stress of the monolith. If the composite is considered impermeable under its PLS, the maximum composite stress is considered before calculating monolith fracture probability. The equation for the individual tube failure probability is given as:

$$P_f(\sigma_p, \varepsilon_{u-p}, \sigma_{u-p}) = \begin{cases} \sigma_{max,c}(\sigma_p, \varepsilon_{u-p}, \sigma_{u-p}) > \sigma_u, & 1 \\ \sigma_{max,c}(\sigma_p, \varepsilon_{u-p}, \sigma_{u-p}) < \sigma_p, & 0 \quad (optional) \\ otherwise, & 1 - \exp\left[-\left(\frac{\sigma_{max,m}(\sigma_p, \varepsilon_{u-p}, \sigma_{u-p})}{\sigma_0}\right)^m\right] \end{cases}$$

Where:
$\sigma_{max,c}$ = Maximum stress on the composite layer as a function of stress-strain curve variables
$\sigma_{max,m}$ = Maximum stress on the monolithic layer as a function of stress-strain curve variables
σ_0 = Weibull characteristic stress for monolith fracture stress
m = Weibull modulus stress for monolith fracture stress

Since the stress profile depends on the input stress-strain properties, the failure probability is calculated with a numerical approximation. The loading conditions used correspond to the shutdown condition after the third and final fuel cycle. This is the highest stress shutdown condition due to the build-up of fission gases within the cladding tube. The results for all three cladding concepts are shown below in Table 6.

Table 6: Overall failure probability of SiC-based cladding concepts

Concept	SiC-SiC impermeable under PLS	SiC-SiC permeable
1 - Pure composite SiC-SiC	1.00	1.00
2 - Inner Monolith	$7.56*10^{-2}$	0.693
3 - Outer Monolith	$5.28*10^{-5}$	$5.28*10^{-5}$

These results indicate that the cladding concept with the lowest failure rate for use in SiC-based LWR fuel is the outer monolith concept. The stresses from swelling during shutdown are too high for a pure composite tube, which will exceed its PLS, or an inner mSiC layer, which has a high fracture probability under such tensile loading and leaves the cladding dependent on the composite to remain impermeable. However, a composite tube with a monolithic outer layer allows the SiC-SiC to deform sufficiently upon exceeding its PLS and avoid failure by transferring load to the outer mSiC, which is in compression from the irradiation-induced swelling. Using properties consistent with the current understanding of SiC materials, the calculation shows that the failure probability of the outer monolith concept would be at least three orders of magnitude better than the inner monolith concept, and less than two orders of magnitude away from the nominal failure probability of current LWR cladding.

2.16. Failure Probability Sensitivity Analysis

To determine the effects of variation in distribution parameters, a sensitivity study was performed. The outer monolith concept was examined in this study, assuming the composite material to always be permeable. Failure probability sensitivity was tested by adjusting a single parameter up or down by 10% in an attempt to isolate its effect. Parameters tested include stress-strain curve distribution parameters, material properties, and wall thickness.

Distribution parameters tested include the shape and scale factors (m and σ_0 respectively) for the Weibull distributions of PLS (σ_p), difference in PLS and UTS (σ_{u-p}), and mSiC fracture stress ($\sigma_{f,m}$), and the underlying sample mean and standard deviation for the log-normal distribution of difference in strain at PLS and UTS (ε_{u-p}). For the log-normal distribution, the variation was carried out by scaling based on the underlying sample mean and standard deviation as modifying the mean of logarithms would create larger than intended changes. The results of this sensitivity study for the distribution parameters are shown in Figure 20.

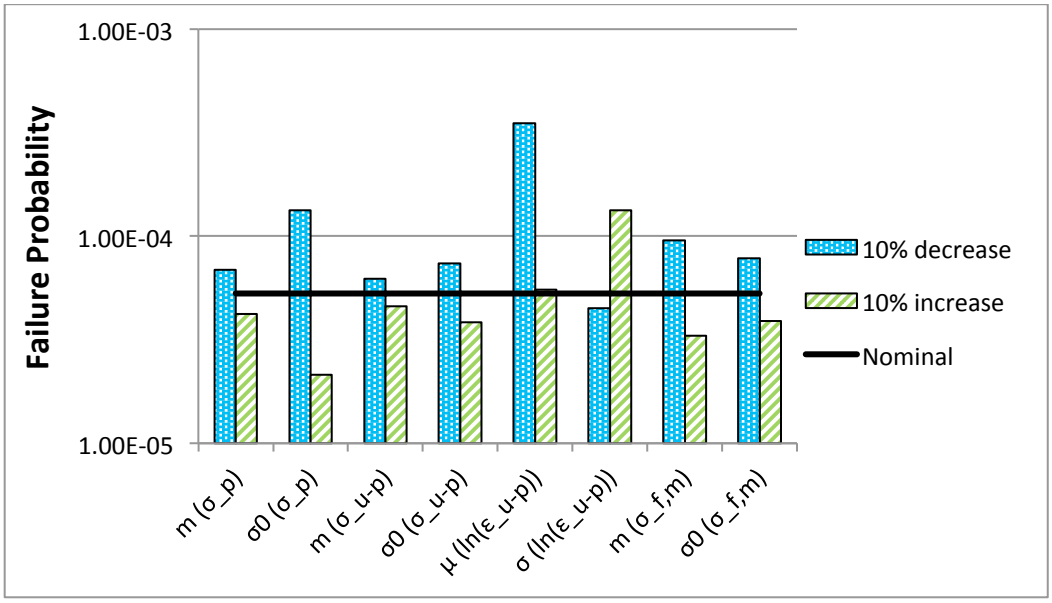

Figure 20: Failure probability sensitivity to stress-strain distribution parameters

The results show several interesting trends. For the Weibull distribution of PLS, the failure probability is more sensitive to the scale factor compared to the other Weibull distributions evaluated. This is due the relatively larger shape factor for the PLS distribution. The larger shape factor cause the distribution to center more narrowly around the mean, making outliers more unlikely as the deviation from the mean grows. As such, changes is the scale factor of the PLS, make a statistically large difference in the magnitude of outlier needed to cause a failure. In contrast, the failure probability is relatively insensitive to the shape parameter, as it is already relatively large, and 10% fluctuations have a lesser impact on the distribution.

Using the same reasoning, the failure probability was more sensitive to the shape factor for the monolith fracture stress distribution. Since the nominal value for the fracture stress shape factor is lower than that of the composite PLS, 10% changes have a large effect in determining the number of distant, low strength outliers. With regard to the scale factor, mSiC layers in the outer monolith concept are unlikely to reach large tensile stresses due to the compressive swelling effects on the outer layer, making failure probability less sensitive to fluctuations of the mean around 300 MPa.

Compared to the PLS scale factor and mSiC fracture shape factor, the failure probability shows much lower sensitivity to both distribution variables for the difference in UTS

and PLS. Two different factors account for this observation. The first is that the UTS is the sum of the PLS and difference in UTS and PLS, and the latter distribution is much more scattered. This means that changes to the PLS scale factor dominate over changes to the difference in UTS and PLS. The second is that for the outer monolith concept, the failure is much more dependent on the monolith layer. After exceeding its PLS, the SiC-SiC stress is much less sensitive to additional incremental strain. However, incremental loading continues to have a more pronounced effect on the mSiC. Therefore, the SiC-SiC is unlikely to exceed its UTS, while at the same time the monolith already exists in a state of compression.

While the difference in stress between the UTS and PLS has a relatively small effect on failure probability, the opposite is true for difference in strain between these two points. A 10% decrease in the underlying sample mean caused a larger increase in failure probability than adjusting any of the other parameters by the same amount. This is again due to the post-PLS behavior of the outer monolith concept, as specimens with limited capability to deform in the composite layer will exceed the UTS of the tensioned inner portion before sufficient load can be shifted to the compressed outer monolith layer. Interestingly, increasing the underlying sample mean slightly increased the failure probability as specimens with highly compliant composite layers transferred excessive load to the monolith. This implies that there may be a design range of post-PLS strain that minimizes failure probability. Variation of underlying sample standard deviation in the strain difference displayed a clearer trend, with failure probability increasing along with the variance. This is logical, as reduced variation decreases the likelihood of a low strain outlier. It should be noted that the strain distribution, while clearly important, cannot be used in a one-to-one comparison with the other Weibull distributions. As Fig. 22 shows, the Weibull distributions show near-linear correlation between the failure probability and distribution parameters on the logarithmic chart, whereas the strain distribution does not.

In addition to the distribution parameters, the irradiation swelling (S), thermal conductivity (k) and composite elastic modulus (E_c) were also examined for failure probability sensitivity, along with the overall wall thickness (t_{wall}). In testing the wall thickness, the layer proportions were kept the same, but the tube outer diameter was varied. Results for wall thickness variations obtained by using a fixed outer diameter and varying the inner diameter were not calculated, but the trend is expected to be similar to the case shown. The results are presented in Figure 21. Calculations on thermal expansion were also performed, but due to the negligible temperature gradient at shutdown, its effect is insignificant.

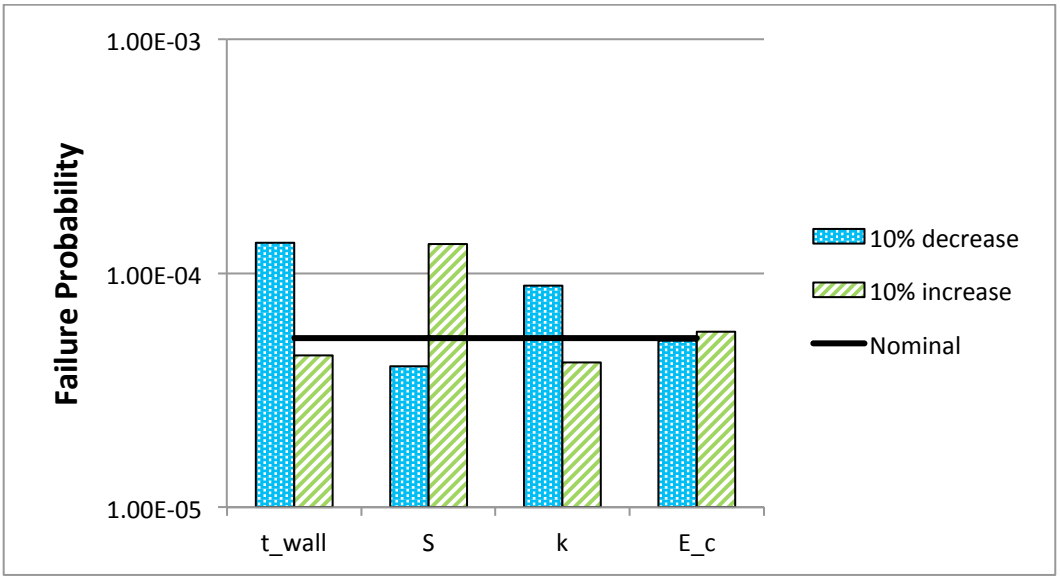

Figure 21: Failure probability sensitivity to wall thickness and material properties

Of the material properties tested, the composite elastic modulus seems to have the least effect, as failure probability for the outer monolith concept is largely dictated by the post-PLS mechanical behavior. Swelling and thermal conductivity show very similar effects as they both affect the cladding stress profile in the same way, albeit in opposite directions. Manipulating swelling directly changes the swelling stresses, whereas changes to thermal conductivity change the temperature gradient, which in turn changes the swelling gradient at shutdown.

Finally, the failure probability shows an inverse correlation with the wall thickness. This is perhaps counterintuitive, given that the temperature dependent, irradiation induced swelling gradient leads to the largest stresses and a larger wall thickness will increase this gradient. However, this swelling gradient is compressive for the outer mSiC layer, and the gradient induced composite stresses are reduced past the PLS due to its pseudo-plastic behavior. Thus, the dominant effect of decreasing wall thickness is that the mechanical stresses due to internal pressurization increases and becomes a more dominant loading factor. This means the monolith is more likely to enter a tensile stress state and leads to additional likelihood of failure. To illustrate this point, using the nominal values for the stress-strain curve given in Table 4, the maximum monolith layer stresses in the 0.9 mm and 1.1 mm thick variations of the outer monolith are 19.4 and 4.7 MPa respectively.

2.17. Monte Carlo modeling of multi-layered structures

Additional modeling was performed to predict the behavior of multiple monolithic SiC layers separated by compliant layers (pyrolytic carbon). Four-point bend experiments on planar multilayers have shown that an initial crack does not propagate through all the multilayers immediately, and instead deflects along the thin carbon layers (Figure 22). This suggests that thin alternating layers of pyrolytic carbon may serve as a crack arresting layer and enable a multilayer to withstand greater deflection than a single monolithic layer without fully failing and losing hermeticity.

Figure 22: Four-point bend sample showing multilayer specimen with upper layers remaining intact while lower layers fractured.

The stress strain behavior in experiments is qualitatively similar to an analytic Monte-Carlo multilayer model (Figure 23).

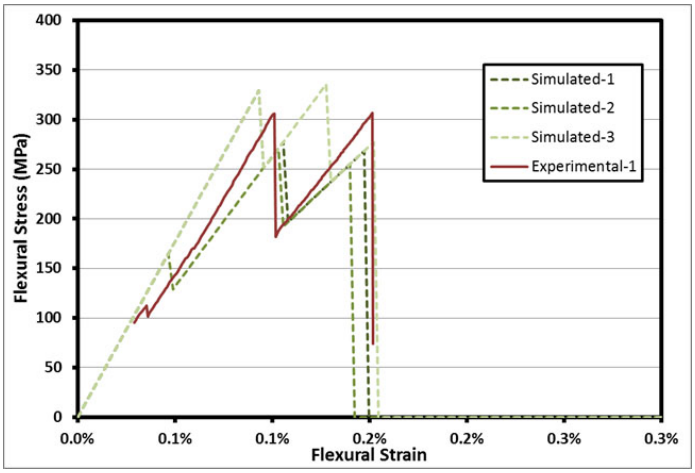

Figure 23: Experimental data compared to multi-layer Monte-Carlo model.

3. Fabrication of Material (Subtasks 3, 4, 6, 7, 8, 10)

As part of the development effort of SiC-SiC based accident tolerant fuel cladding, samples were fabricated with a range of designs and lengths. In some cases these variations were used to assess relationships between structure and performance, and in other cases these variations were included to accommodate specific characterization or experimental requirements. Additional samples were made and tested to build a statistically significant data set of material properties relating to SiC-tubing performance. This section provides an overview of the fabrication of tube material for deliverables during this project, and also provides results for the assessment of manufacturability and scale-up of these SiC-SiC cladding tube structures, including consideration of cladding dimensional tolerances and specifications.

3.1. Fabrication of Multi-layer Tube Samples

In this work, chemical vapor infiltration was used to fabricate SiC-based cladding tubes at approximate LWR cladding diameters and in lengths up to three feet. Prototypical cladding architectures were produced representing several concepts proposed for SiC-based accident tolerant cladding structures, including structures containing an outer monolithic SiC layer and structures containing an inner monolithic SiC layer, as well as structures composed entirely of SiC-SiC composite. Composite samples were reinforced with stoichiometric SiC fiber (Hi-Nicalon type-S fiber, NGS Advanced Fiber Co.).

Those tubes containing an inner monolithic layer incorporated a thin-walled (~450μm wall thickness) extruded and sintered SiC Hexoloy tube (St. Gobain Ceramic Materials). Compared to CVD SiC, Hexoloy has similar unirradiated material properties but contains sintering aids and has slightly lower density and purity. Reinforcing fiber was then formed around this inner monolith as a second layer. The as-received monolithic Hexoloy SE tubes and examples of these tubes wrapped with reinforcing fiber are shown in Figure 24.

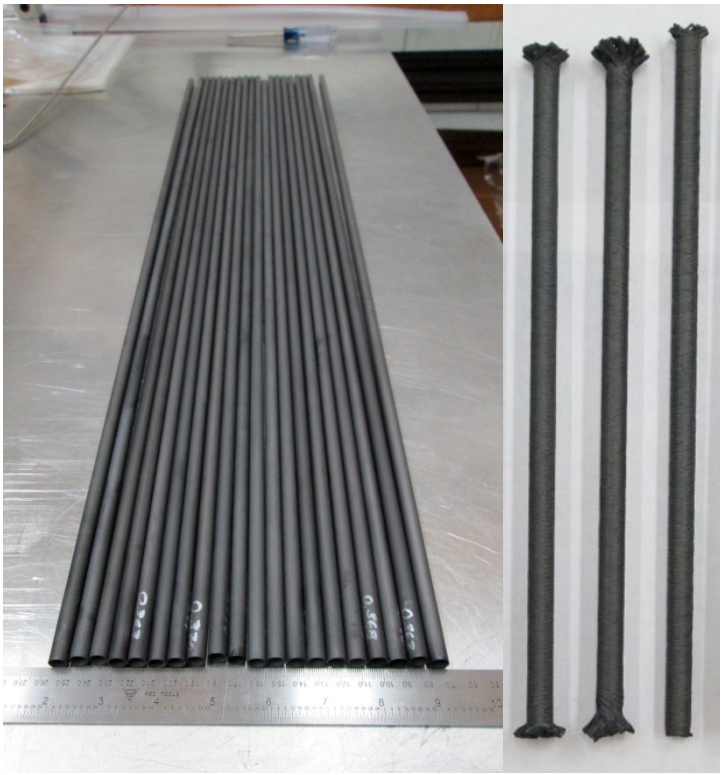

Figure 24: (left) as-received thin-walled Hexoloy SiC tubing, (right) inner monolith structure following fiber preforming and initial infiltration

The other tube structures (tubes composed of only SiC-SiC composite and those with an inner composite layer and an outer monolith layer) were formed by placing fiber around a mandrel to define the tube inner diameter. Graphite was commonly used as the mandrel material, and the mandrel was later removed as part of the overall fabrication process. With graphite mandrels, this was accomplished by burning out the graphite in a furnace in air.

Fiber orientation was varied by adjusting the number of fiber tows used and the angle relative to the tube axis, and for this work, preforms were produced containing different ratios of fiber in the hoop and axial directions, ranging from 1.65:1 (hoop biased) to 0.64:1 (axially biased, meaning the fiber component in the axial direction was ~50% more than the fiber component in the hoop directions).

A pyrolytic carbon interphase coating of ~150nm was deposited via the chemical vapor decomposition of methane or acetylene, and the matrix was then deposited and densified through the chemical vapor infiltration of methyltrichlorosilane (CH_3SiCl_3) to a final relative density of approximately 80-85%. Micrographs taken of a cross section of infiltrated composite show the fiber tows and the thin pyrolytic carbon interphase layer around each fiber (Figure 25).

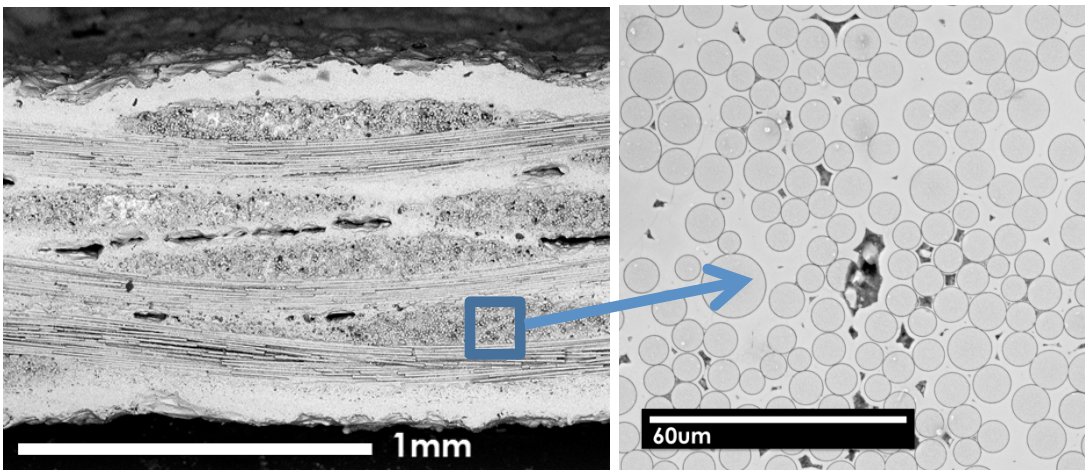

Figure 25: (left) cross section showing full width of a SiC-SiC composite panel, (right) magnified view showing matrix infiltration around fibers and pyrolytic carbon interphase layer

The composite densification step represented the final processing step for those tubes composed of all composite and those containing a SiC inner monolith. For those tubes containing an outer monolith, additional SiC was deposited to form a dense outer SiC coating. Final tube wall thicknesses varied depending on the structure. For the two layer structures, those with an inner monolithic layer contained between 30-35% monolithic material through the wall thickness, and those with an outer monolithic layer contained between 10-30% monolithic material. The minimum thickness of monolithic material for the inner monolith structures was governed by the minimum obtainable thickness of the extruded Hexoloy SE tube material, which was ~350μm. For those structures with an outer monolith, the minimum thickness could be a thin as possible (determined as a function of the CVD over-coating deposition duration), but realistically in this work a minimum thickness of ~100μm was required to obtain a hermetic structure. Examples of cross-section of the outer and inner monolith layer structures are shown in Figure 26.

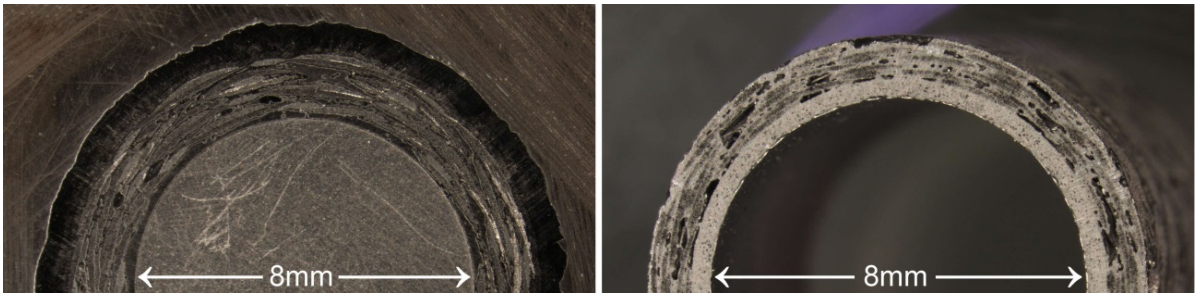

Figure 26: (left) cross-section of example of outer monolith structure, (right) cross section of example of inner monolith structure

3.2. Infiltration Studies of the Composite Layer

In the fabrication of SiC-SiC tubes, the chemical vapor infiltration of the SiC matrix needs to be carefully controlled to provide a high density composite which meets the application requirements while making the infiltration processing step as time efficient as possible. The resulting composite must also be high purity, stoichiometric SiC, to ensure good performance under irradiation.

Previous work had considered modifications to the chemical vapor infiltration process to reduce the overall fabrication time for planar composite samples. Initial infiltration occurred under conditions to provide a slower reaction rate, allowing precursors to diffuse into fiber tows and react and deposit matrix material between individual fibers. Eventually these infiltration pathways will close, and the fiber tows will become closed off. At this point, the remaining porosity is larger scale, and the diffusion pathway to reach this porosity is not as tortuous. By increasing the SiC deposition reaction rate at this point during the infiltration, the densification of the remaining porosity can occur more rapidly, and the overall infiltration time can be reduced. These previous results provided an improved infiltration process which reduced the overall infiltration processing time by roughly 25% while achieving comparable material performance.

In this current work, the same approach was applied to a tubular sample geometry. The fixtures required to process tubular samples differ from those used for planar samples, and as a consequence, the modified infiltration used for a planar sample may vary from that which is best for a tubular sample. In addition, as the cladding requirements became more well-defined, the fiber architecture was modified to provide a reduced overall cladding wall thickness. Tubes with a balanced fiber architecture (designed to provide nearly equal strengths in the axial and hoop directions were fabricated with the baseline infiltration process, and then this infiltration was altered to reduce the overall processing time. In addition to modifying the infiltration conditions and durations, the fiber architecture was adjusted to reduce the overall thickness from ~1mm down to 0.75mm. Through these adjustments, a significant time savings was achieved, reducing the infiltration duration by over 40% compared to the original baseline case. This was accomplished while producing tubular samples which also had improved mechanical performance compared to the baseline case (Figure 27).

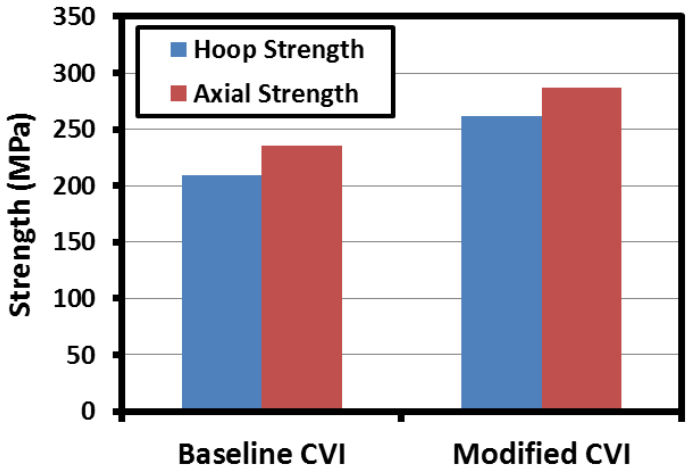

Figure 27: Measured hoop and axial strengths for tubes fabricated using a baseline CVI process and an optimized CVI process

Several other matrix infiltration techniques were considered, but ultimately determined not as viable as chemical vapor infiltration. A liquid phase deposition route which involved liquid methyltrichlorosilane was considered to be too hazardous at an production scale, given the corrosive and pyrophoric nature of methyltrichlorosilane. When using this precursor with a vapor phase process, the concentrations are lower and the potential hazards more easily controlled. A hybrid CVI/PIP process was also considered; however, the finely structured SiC material (nano-grained and nano-porous) is extremely difficult to infiltrate to high density. Initial scoping trials indicated that dense CVI infiltration could only penetrate and densify PIP-based SiC material within roughly 100μm of the surface, making this hybrid approach unsuitable for infiltration of a structure with a ~700-800μm wall thickness.

Finally, additional studies were performed to improve the infiltration conditions associated with maintaining uniformity during part scale-up. Different reaction parameters were varied to reduce the variation observed in the deposition rate as a function of axial position along the length of the furnace. This optimization was performed for both SiC deposition and pyrolytic carbon deposition. After a series of iterations, the variation in the SiC deposition rate over the length of the three foot furnace was reduced by roughly half compared to the starting condition. An even larger improvement was obtained in the deposition variation of the pyrolytic carbon layer used for the fiber interphase, where the variation was reduced by over an order of magnitude compared to the baseline case. Results for quantification of the uniformity obtained in longer, 3' tube parts are provided in section 3.10.

3.3. Tubular Samples for Oxidation and Autoclave Testing

A set of tube samples was fabricated and delivered to Westinghouse and MIT where they were subjected to oxidation and corrosion testing. An additional set of tubes which were sealed at one end with a SiC endplug and a SiC-based joint were also fabricated and provided to MIT for additional oxidation testing. The first set of tubes consisted of a fiber braided architecture with a highly biased 3.0:1 ratio of fiber in the hoop to axial direction, and six tubes of ~1" length were supplied to WEC, and three tubes of ~2" length were supplied to MIT. All

tubes had a ~2.5mm holes drilled in one end to facilitate hanging the samples during testing, and the tubes received a CVD SIC overcoat following the final cutting and drilling to overcoat all exposed edges. These specimens are shown in Figure 28.

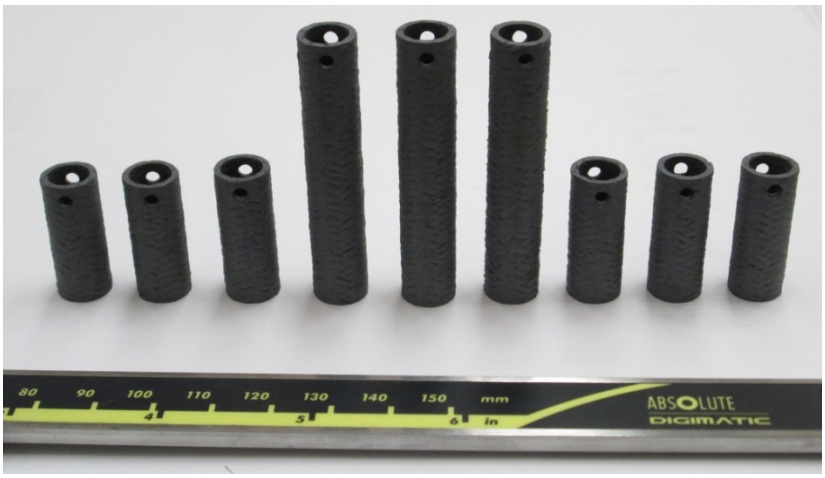

Figure 28: Set of open ended tubes for autoclave and oxidation/quench testing

The second set of tubes were provided to MIT for oxidation and quench testing, and consisted of eight samples, each sealed at one end by a SiC endplug joined using the GA-proprietary SiC-based joining method. This approach produces a high purity, fully crystalline β-SiC joint, and a scarf joint geometry was used (truncated cone endplug shape). The endplugs were fabricated by hot pressing SiC nanopowders using transient eutectic phase processing approach. These corrosion test specimens were nominally 26 mm long. For mounting, holes were drilled through the composite tube wall on the open end. This set was composed of five samples with a hoop-bias fiber structure (1.65:1 hoop to axial fiber ratio), and three samples with an axial bias (0.64:1 hoop to axial fiber ratio). These sealed tube samples received an additional CVD SiC overcoat after the endplug joining process prior to delivery, and the final samples are shown in Figure 29.

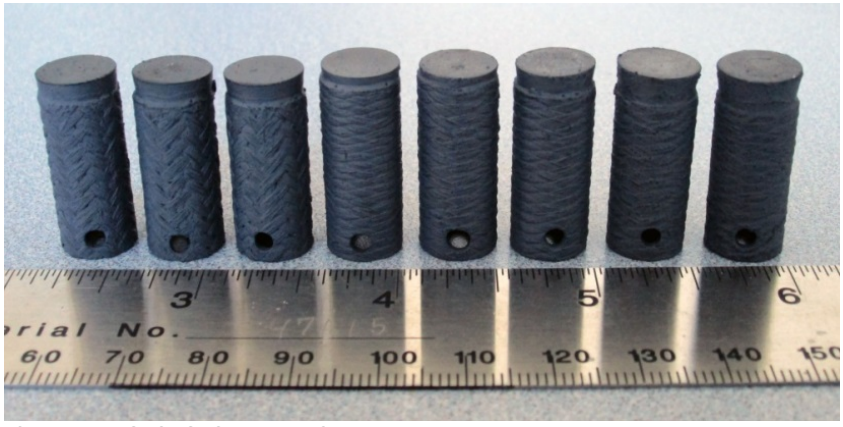

Figure 29: Set of sealed SiC-SiC tubes for oxidation and quench testing at MIT

3.4. Tubular Samples for Irradiation Testing

A total of twenty eight tube samples were fabricated for irradiation testing in the MITR. These consisted of four sets. Three composite-based sets were composed of eight samples

each, and one control set was composed of four monolith-only samples. Each composite set varied in tube structure (layers and fiber architecture), and there were also some variations in outer SiC coating applied within each set. All specimens were scanned using XCT prior to shipment, and careful dimensional and mass measurements were taken.

The first set of tubes consisted of a fiber braided architecture with a 1.3:1 ratio of fiber in the hoop to axial direction. The outer diameter was polished and then overcoated with CVD SiC to a final diameter of ~10.2mm and wall thickness of 1.57mm. Specimens GA1-2, 3, and 4 received an additional layer of CVD SiC coating. X-ray tomographic scans were taken of all specimens. These specimens are shown in Figure 30.

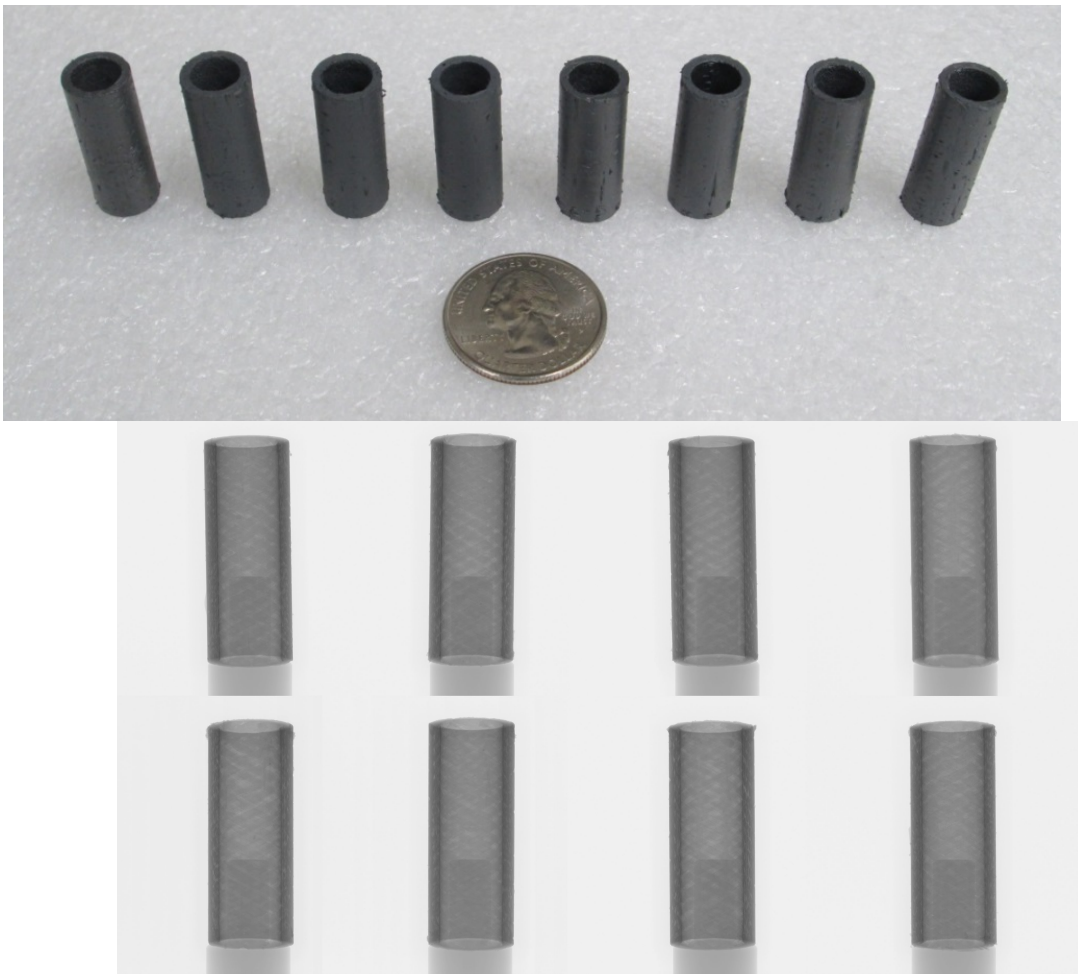

Figure 30: Photo and XCT scans of the first set of open ended tubes delivered for irradiation in MITR

The second set of tubes consisted of a fiber braided architecture with a 1.65:1 ratio of fiber in the hoop to axial direction. The outer diameter was left in the as-fabricated condition (unpolished) and overcoated with CVD SiC to a final diameter of ~10.6mm and wall thickness of 1.51mm. All of the GA2 specimens received the same additional CVD SiC over-coating as specimens GA1-2, 3, and 4. X-ray tomographic scans were taken of all specimens. These specimens are shown in Figure 31.

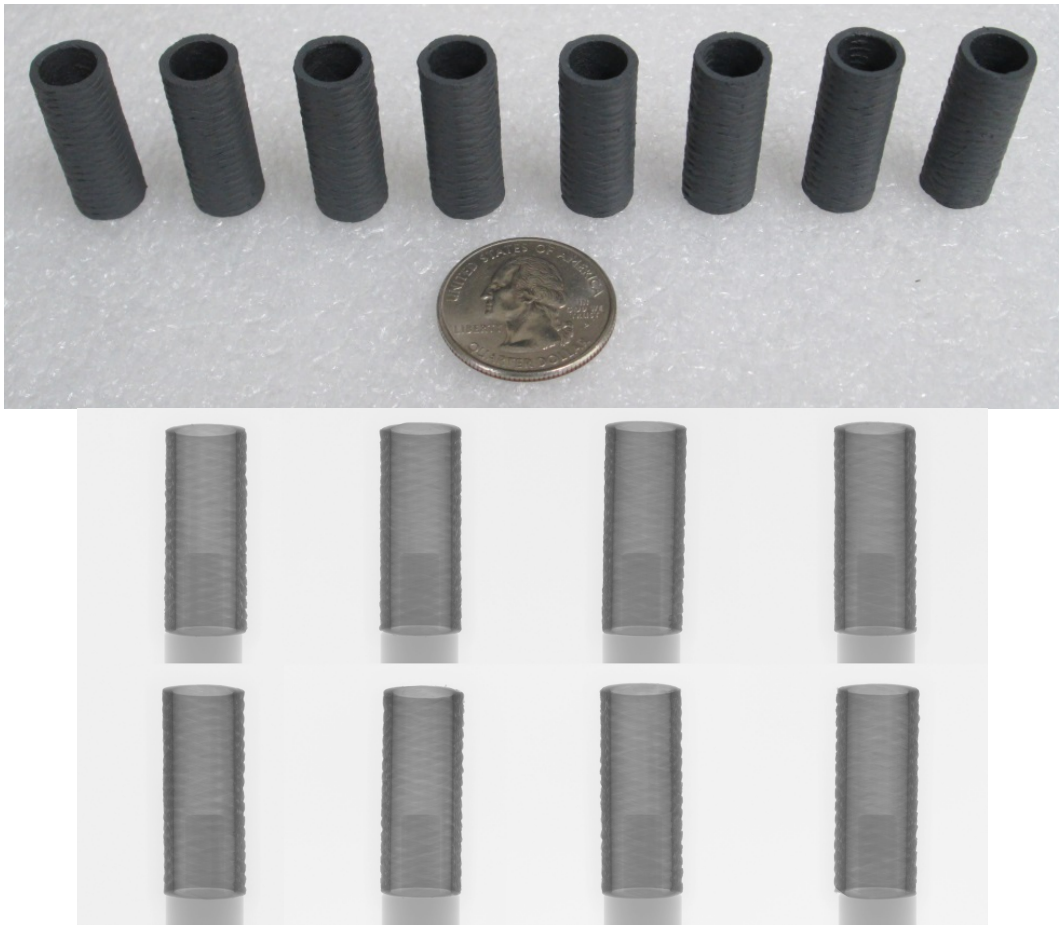

Figure 31: Photo and XCT scans of the second set of open ended tubes delivered for irradiation in MITR

The third set of tubes consisted of a fiber braided architecture with a 0.64:1 ratio of fiber in the hoop to axial direction. This composite layer surrounded an inner SiC monolith made of Hexoloy SE with a thickness of ~0.45mm. The outer diameter was polished and then overcoated with CVD SiC to a final diameter of ~11.2mm with a wall thickness of 1.49mm. While the wall thicknesses of all samples in this experiment was approximately equal (~1.5mm), the larger diameter of the Hexoloy SE tube resulted in a larger overall diameter for the GA3 specimens. The GA3-8 specimen received the same additional CVD SiC over-coating as specimens GA1-2, 3, and 4 and the GA2 specimens. X-ray tomographic scans were taken of all specimens. These specimens are shown in Figure 32.

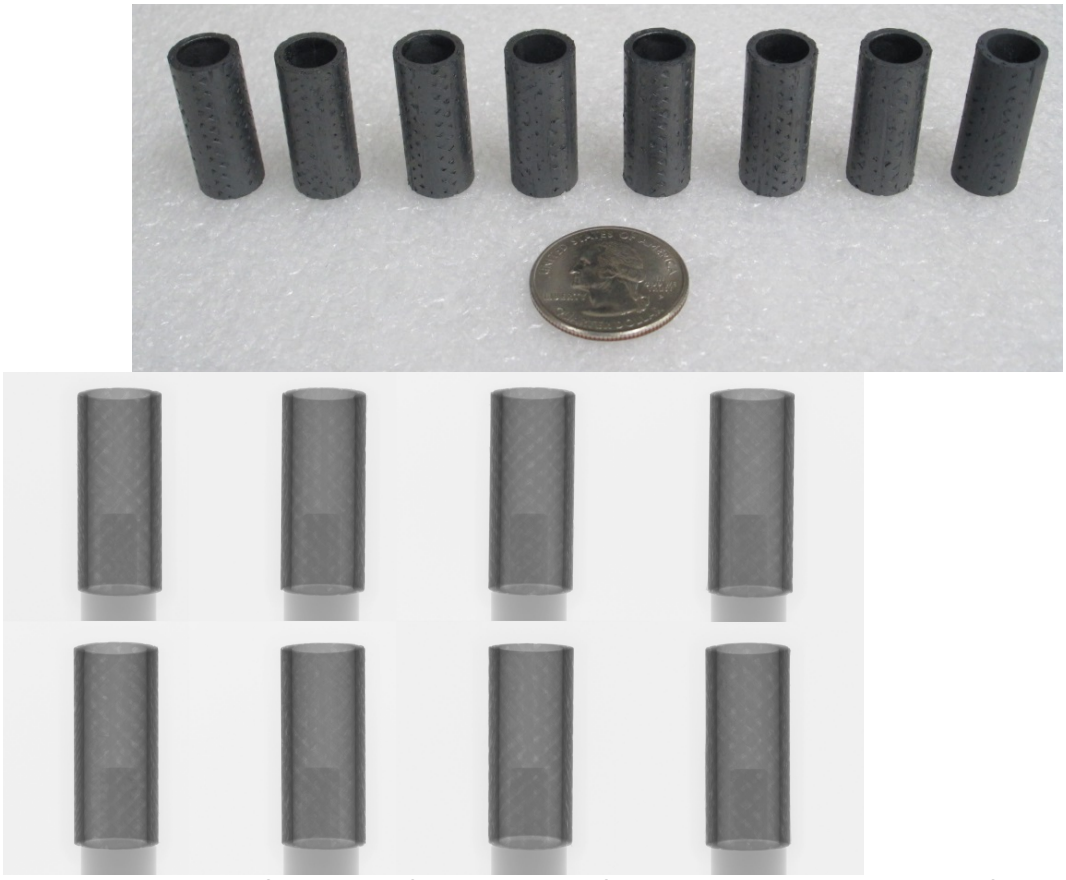

Figure 32: Photo and XCT scans of the third set of open ended tubes delivered for irradiation in MITR

The fourth and final set of tubes consisted of a thin walled Hexoloy SE tube coated with CVD SiC to be used as control samples. These were supplied in the as-fabricated condition, with no additional machining or polishing, with an outer diameter of ~9.6mm and wall thickness of 0.66mm. These specimens are shown in Figure 33. X-ray tomographic scans were taken of all specimens, and images from these scans are also shown in Figure 33.

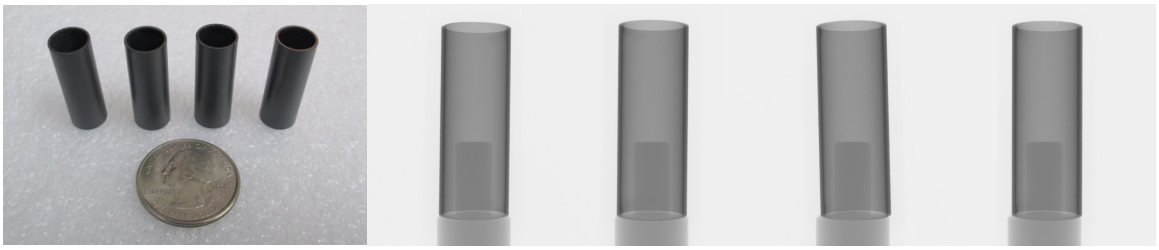

Figure 33: Set of monolithic SiC control samples for irradiation at MITR

3.5. Fabrication of Sealed Rodlets for Oxidation and Irradiation Testing

General Atomics delivered eight sealed rodlet specimens to MIT for irradiation in MITR (Figure 34). Each of the specimens were joined with one endplug using GA's proprietary high purity, fully crystalline β-SiC joint material. The endplugs were fabricated by hot pressing SiC nanopowders using transient eutectic phase processing approach. This process results in monolithic β-SiC material with density >3 g/cm^3. All specimens have a scarf joint geometry,

meaning the endplug is a truncated cone, and the ID of the composite tube has been machined to have a mating surface. Prior work by GA established that the scarf joint gives the best combination of mechanical and permeability performance.

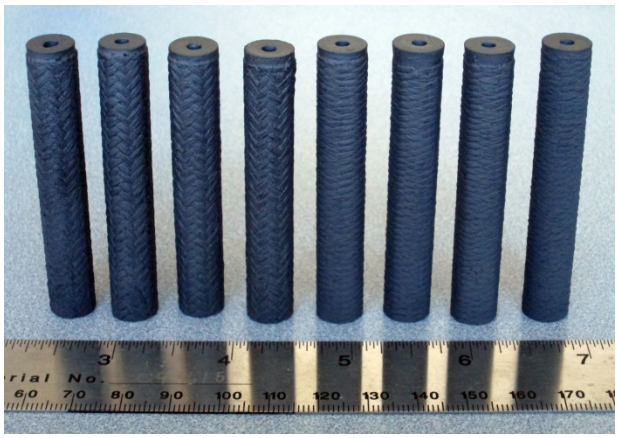

Figure 34: Eight tube joint specimens delivered for irradiation in MITR

The irradiation specimens were nominally 64 mm long and had special endplugs that were fabricated with a blind hole ~ 3mm deep on the outer circular face (Figure 35). To achieve this, GA modified its endplug mold and changed some processing steps to reduce stress cracking. The modified endplug was needed to enable mounting of the joints for adequate exposure in the MIT reactor in a secure way.

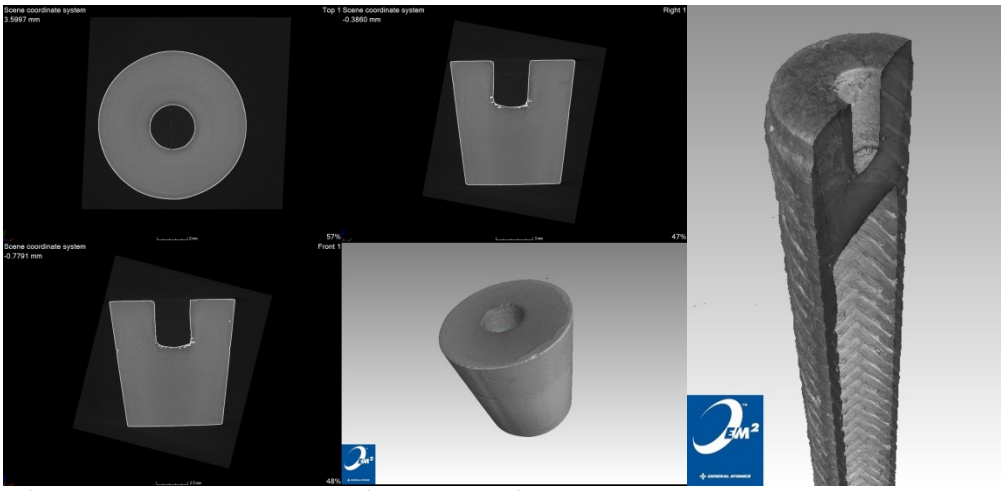

Figure 35: XCT scans showing detail of blind hole feature incorporated into the sealed irradiation samples

Prior to delivery, XCT scans were taken of all test specimens. VolumeGraphics analysis software provides a powerful tool for investigation and visualization of the cladding and endplug. Scans of the delivered specimens are shown in Figure 36. The data from these scans will be used for analysis following the irradiation and corrosion campaigns to correlate specimen performance with microstructural features in each specimen.

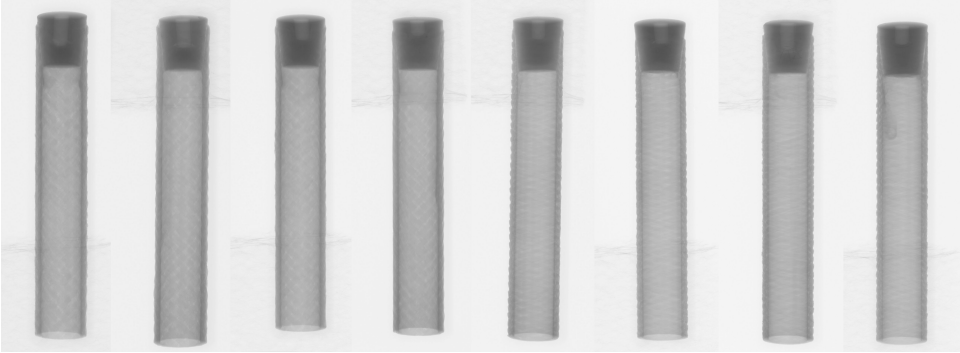

Figure 36: XCT scans of tube joint irradiation specimens

Samples delivered for the oxidation and irradiation tests had varying fabrication parameters and structures, and these differences are summarized in Table 7. These parameters were varied in order to obtain a range of irradiation and oxidation performance data.

Table 7: Fiber architecture and surface coatings for closed ends tubes used in irradiation corrosion tests

Sample #'s	Hoop:Axial Fiber	Surface Coating
GA1-TCJ-I-1,2	0.64 : 1	CVD SiC
GA1-TCJ-I-3,4	0.64 : 1	SiC particles + CVD SiC
GA1-TCJ-I-5,6,7,8	1.65 : 1	CVD SiC

3.6. Manufacturability of Extended Length SiC Cladding Tubes

The manufacturability of extended length SiC-SiC tubes was demonstrated at an intermediate size by scaling from lengths of 12" up to lengths of up to 36". In this process, uniformity and dimensional tolerances were assessed for these longer length tubes, and compared to requirements for LWR cladding. Demonstration of scale-up must be evaluated at all steps of the fabrication process. For the first step of the fabrication process (fiber preforming), capital equipment purchases by General Atomics done outside the scope of the DOE/Westinghouse-funded ATF contract have provided fiber preforming capability up to full, 14' LWR cladding lengths. Currently mandrels have been fabricated in 3' lengths, and linked together for extended length braiding. Repeatability and consistency in the fiber preforming has been evaluated and variability along the length is small, with fiber angle and positioning repeatable within a few percent (for example, tow angle is repeatable within ±2°). No major scale-up challenges are anticipated in scaling up the mandrel and fiber preforming lengths, although straightness will need to be carefully monitored (see section 3.9). To speed through-put, the fiber preforming step could also converted (with equipment modifications) to a continuous processing step, rather than a batch step (where each length is done individually).

Following fiber preforming, the fiber must be infiltrated with a SiC matrix to form a strong, dense SiC-SiC composite. During the course of this cladding development project, General Atomics invested its own funding to upgrade the furnace used for this infiltration step, to accommodate larger parts. Currently tube lengths up to 36" can be processed in this

furnace, which provides a very controlled, uniform temperature profile. Future equipment upgrades will be needed to accommodate and fabricate full-size cladding tubes (up to 14' long). In addition, while this larger furnace has been currently used to infiltrate batches of up to ten parts at once, other infiltration furnaces at General Atomics have been used to investigate the possibility of producing parts in even larger batches. To date, batches of material to produce over 250 parts have been processed simultaneously. Fabrication uniformity is very important to achieve for both scale-up of the lengths of parts being made, and scale-up of the number of parts produced concurrently in a batch. While additional refinement is anticipated for the transition form 3' lengths up to 14' lengths, current technology is able to produce 3' parts with very good uniformity for both the infiltration and for SiC over-coating (see section 3.10). Examples of some of the ~3' tubes fabricated by General Atomics during the course of this work are shown in Figure 37.

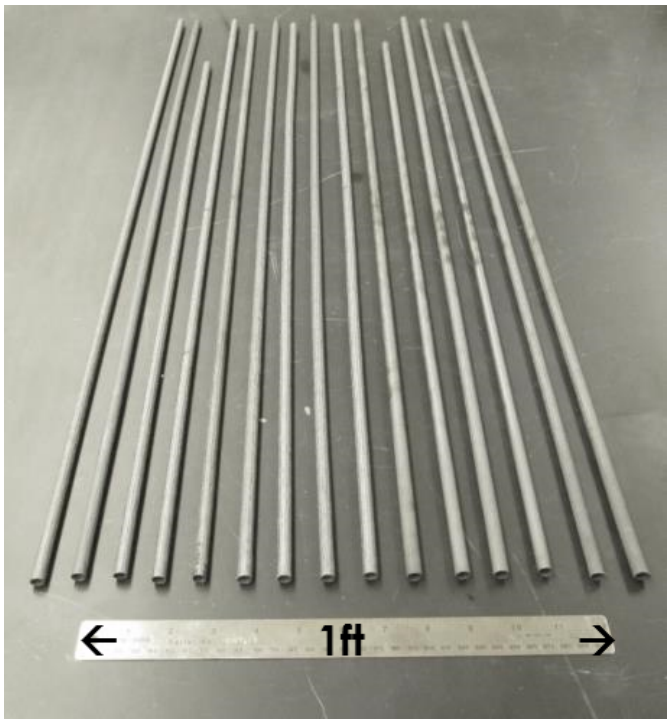

Figure 37: Set of ~3' long SiC-SiC tubes produced during this project

Following infiltration, the cladding tubes may need to undergo additional surface finishing and smoothing steps (depending on final cladding roughness specification). In this current work, smoothing was only demonstrated on small lengths of tubes. However, equipment is commercially available which could be used to provide a controlled surface finish and obtain the desired target outer diameter along a full length part. The machining approach envisioned would involve a centerless grinder with a long support stand and automatic feeder to quickly and continuously process parts in series.

After cladding tube fabrication, the ends of the tubes need to be sealed. One end would be sealed initially, and that tube, following QC checks and loading with fuel pellets, would then have the final end sealed and be pressurized to complete the fuel rod fabrication. Like the infiltration process, the high-purity, fully-SiC joining method developed previously by General

Atomics would be suited for batch processing. With proper equipment, this processing step has potential to produce many hundreds of joints in a single batch. Furthermore, because the joint is only a small region of the longer overall rod, uniformity is anticipated to be very good. General Atomics has continued to independently refine and improve the joining process, and the joints are now more repeatable, with minimal voids compared to earlier techniques.

In order to demonstrate that cladding tubes can meet dimensional requirements, accurate means of measuring uniformity, roughness, roundness, and straightness/cylindricity must be utilized. Currently, there are a range of tools available to obtain these dimensional tolerance values, including microscopy, coordinate measuring machine (CMM), micrometers, height gauges, and stylus profilometers. X-ray computed tomography can be used to generate a high resolution 3D reconstruction of a part, and it is possible to extract a range of dimensional measurements from a single XCT scan. This would be the final QC step for the tubes, and current capabilities limit part length to 3' for x-ray tomography imaging. However, equipment is available which could facilitate use of this technique and accommodate full size parts (14' long).

In these studies, portions of several SiC-SiC tube samples were scanned using x-ray tomography, and then reconstructed for analysis. Dimensional measurements were obtained from x-ray computed tomography (XCT) using a Nikon XT H 225 X-Ray Computed Tomography unit equipped with a Perkin Elmer 1620 CS3 detector. Due to the high aspect ratio of the SiC-cladding tubes being examined, scans were performed at different resolutions and magnifications depending on the dimensional tolerance being evaluated. Volume Graphics "VGStudio Max" was used for analysis of the resulting image volumes. For roughness measurements, smaller regions were scanned at higher resolution and roughness values were obtained directly from these volumes without further processing. For larger scale measurements (straightness, cylindricity) over the full tube length (~0.9m), separate volumes had to be aligned, stitched, and combined into one larger volume comprising the entire tube. To assist in the alignment process, there must be recognizable features in adjacent scan volumes that can be oriented and merged. The use of appropriate alignment features is particularly important when the volumes to be merged have similar, repeating features which cannot be easily distinguished between volumes.

To serve as an alignment aid in this work, small additional portions of SiC-SiC tubes were attached to the sides of the longer tube being scanned at three intervals along the length. The exact nature of these additional alignment aids is not critical, as long as they are sized so that they have features which can easily be oriented between scans, can be fully included in adjacent scans, and have similar densities to the SiC-SiC tubes being scanned so as to not cause contrast issues in the XCT. The configuration of one of these alignment aids relative to the SiC-SiC tube is shown in Figure 38(a), along with the four individual scanned volumes and the full stitched and reconstructed 0.9m long SiC-SiC tube [Figure 38(c)].

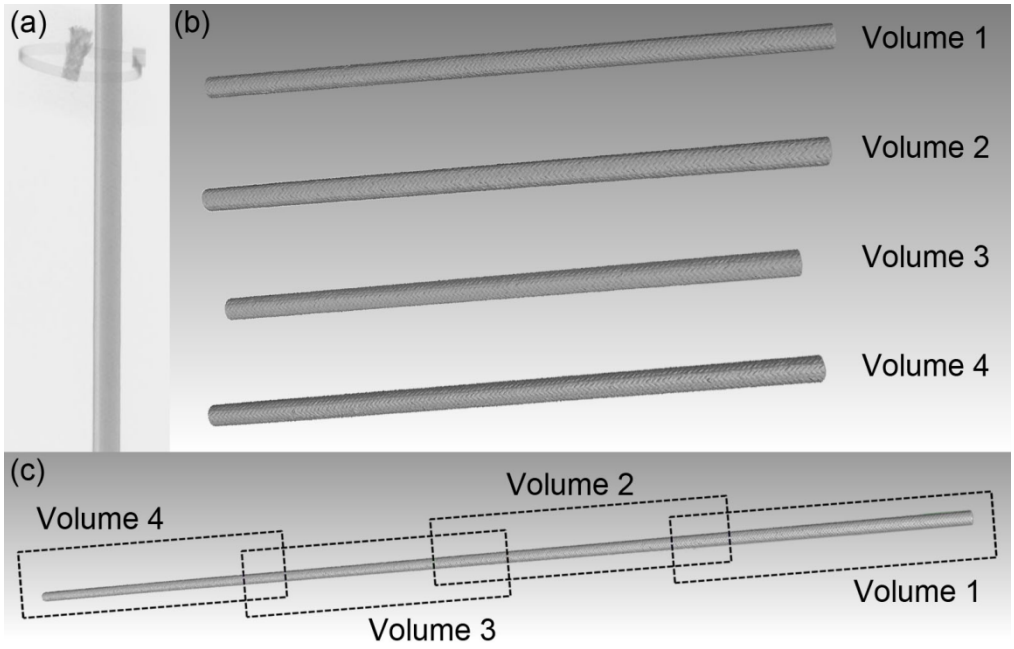

Figure 38: (a) reference feature to aid volume alignment, (b) individual scanned volumes, each ~25cm long, and (c) full reconstructed and stitched volume of entire 0.9m long SiC-SiC tube

3.7. Roughness

Surface roughness measurements were obtained from both line scans from XCT-reconstructed volumes, and from stylus profilometer scans. Two tube samples were examined: one as-fabricated SiC-SiC composite tube and a second tube, which had undergone additional processing steps (mechanical smoothing following by additional SiC deposition) to reduce the surface roughness.

The as-fabricated tube shows significant surface texture resulting from the underlying fiber tow architecture, as seen in a representative photo of starting fiber structure prior to infiltration (Figure 39). Note that it is not feasible to obtain line scans from both the XCT and profilometer on the exact same line, as orientation and identification of the regions is extremely challenging. However, multiple scans were obtained for each approach, and average roughness for the overall tube can be obtained. Representative surface profiles from both the XCT reconstruction and the stylus profilometer are shown in Figure 39 and are qualitatively similar.

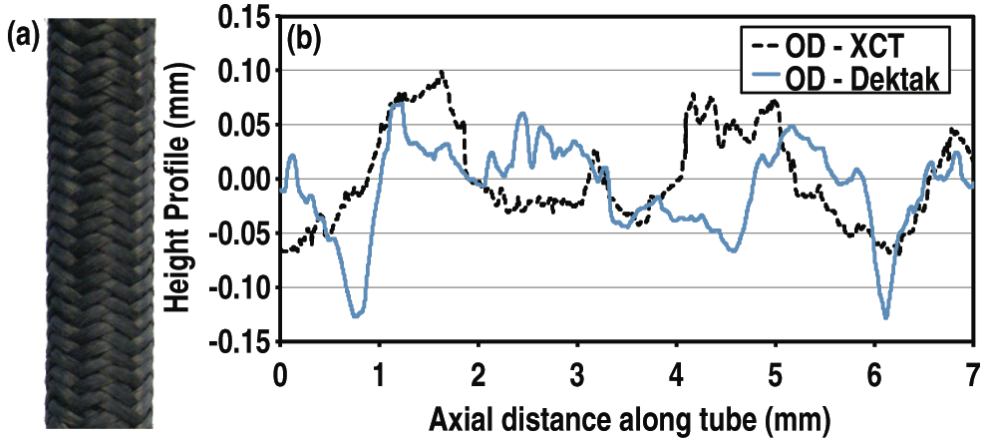

Figure 39: (a) Photo of representative fiber structure prior to infiltration, and (b) Representative surface height profiles obtained from an as-fabricated tube using both XCT reconstruction and stylus profilometer.

Roughness values obtained from the XCT reconstruction and the profilometer are given in Table 8 and show good agreement. The height of the individual reinforcing SiC fiber tows is in the range of ~200μm – 300μm, and the fiber architecture and regions where tows overlap contribute to the surface undulations in the as-fabricated tube. Therefore, it is an expected result that the peak-valley roughness measurement obtained is very similar to the thickness of the individual fiber tows.

Table 8: Roughness values for the outer surface of an as-fabricated SiC-SiC tube, taken from a 7mm long axial line profile

Roughness	XCT result	Profilometer result
$R_{average}$	37.3 μm	32.7 μm
R_{rms}	43.8 μm	42.4 μm
$R_{peak\text{-}valley}$	169.2 μm	197.4 μm

The large peak-valley roughness (as well as average and rms roughness values) in the as-fabricated tube is not expected to be sufficient for a nuclear fuel cladding application. Excessive roughness on the cladding inner surface will lead to variations in the gap between the fuel and cladding and can result in non-uniform temperature gradients, causing additional stresses in the cladding. In addition, although high surface roughness on the outside surface of the cladding may provide some benefits to heat transfer due to turbulent mixing, this roughness will increase the coolant pressure drop through the core.

It is therefore necessary to produce and be able to characterize cladding tubes with controllable roughness on both the inner and outer surfaces. Several methods can be used to achieve controlled surface roughness, such as polishing or grinding, and in this work a tube which had been subjected to mechanical smoothing following by subsequent deposition of additional silicon carbide was examined (Figure 40). The amount of smoothing required will depend on the as-fabricated surface roughness, but typically 100-150μm of material is removed measured from the highest points on the outer surface. Silicon carbide can then be

deposited via CVI to bring the tube back to a diameter specification or to form a structure with an outer monolithic layer. This additional SiC deposition may also repair minor damage incurred during machining by coating any grinding induced micro-cracking or exposed carbon interphase layers with an oxidation-resistant SiC layer.

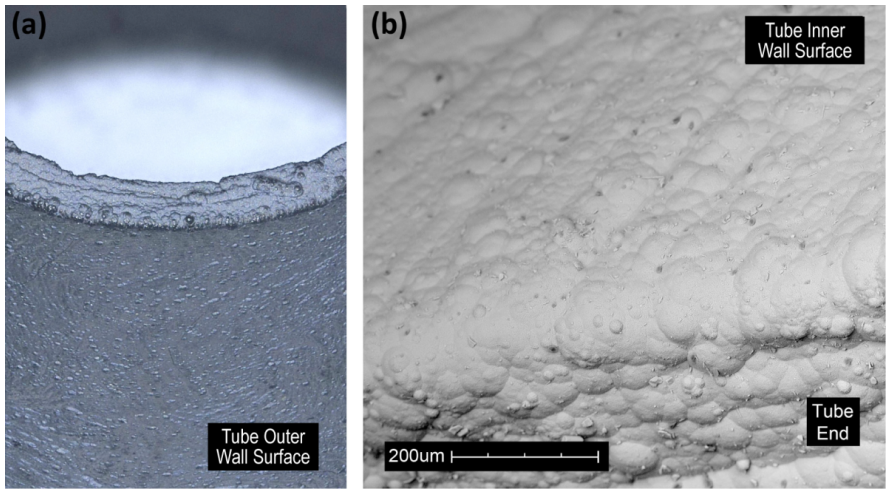

Figure 40: Optical image of the smoothed SiC-SiC tube outer wall surface, wall thickness is ~0.75mm, SEM image of smoothed SiC-SiC tube inner surface showing small-scale texture.

As with the as-fabricated SiC-SiC tube, roughness values were obtained from both XCT reconstructions and stylus profilometry, and representative surface profiles for the inner and outer surfaces are shown in Figure 41.

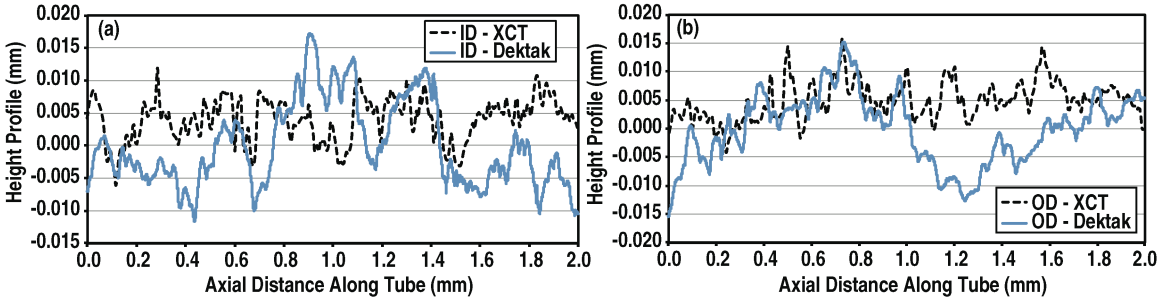

Figure 41: Representative surface profiles for smoothed SiC-SiC tube inner surface, and outer surface, taken from both XCT and Profilometer measurements.

Average, root-mean-square, and peak-valley roughness are tabulated in Table 9, and represent a significant (~5-10x) reduction in roughness for this smoothed tube compared to the as-fabricated SiC-SiC tube. While roughness specifications for SiC-based fuel cladding has not yet been defined, these values are close to the current specification for Zircaloy cladding tubes, and further improvement could be obtained through additional refinements to processing methods. Roughness values for the inner and outer surfaces are comparable. Standard deviations were obtained from roughness values from 2mm long line scans taken from six different areas on the tube sample. For these smoother profiles, the XCT roughness values are approximately half those of the stylus profilometry results.

Table 9: Roughness values for smoothed SiC-SiC tube obtained using XCT reconstructions and stylus profilometry, taken from 2mm long axial line profiles

Roughness	XCT result	XCT Std. Dev.	Profilometer result	Profilometer Std. Dev.
Inner - $R_{average}$	2.6 μm	0.3 μm	6.4 μm	2.2 μm
Inner - R_{rms}	3.2 μm	0.2 μm	7.9 μm	2.7 μm
Inner - $R_{peak\text{-}valley}$	16.6 μm	1.7 μm	37.6 μm	13.1 μm
Outer - $R_{average}$	2.6 μm	0.5 μm	6.1 μm	1.8 μm
Outer - R_{rms}	3.2 μm	0.6 μm	7.7 μm	2.3 μm
Outer - $R_{peak\text{-}valley}$	16.2 μm	3.1 μm	38.1 μm	10.3 μm

While the use of x-ray computed tomography allows for rapid measurement of roughness over a large area of a sample surface (via multiple profile scans), as well as roughness assessment in arbitrary directions (not limited to axial), these results show limitations of the XCT approach based on the scan resolution. For samples with larger surface roughness (the as-fabricated tubes), the XCT roughness results agree well with the reference measurement (the stylus profilometer value). For smoother samples, the scan resolution used for the XCT scans in this work was not sufficient to provide the same roughness detail as the profilometer scan, and underestimated the actual sample roughness. For these smoother SiC-SiC tubes (Ra ≈ 5μm), a higher magnification XCT scan should be used, with a resolution of ~1μm or better. X-ray tomography of SiC-SiC composites has been reported in the literature with sub-μm resolution. With this improved resolution and modification to the XCT scan parameters and volume reconstruction, this technique could be used to rapidly assess SiC-based nuclear cladding tubes.

Careful polishing, with increasingly fine polishing media, coupled with additional SiC deposition via CVD can produce a sample surface with a near mirror surface (Figure 42). White light interferometry was used to measure surface roughness of this mirror polished sample. Averaged over six scans (each of a ~1mm^2 area), the average roughness was 36nm, the root-mean-square roughness was 47nm, and the average maximum peak-to-valley roughness was 724nm. This smoothness is far beyond what would be needed for an LWR cladding application, but demonstrates that with careful polishing, controlled roughness can be achieved to target values over a wide range (from 10's to 100's of μm in the as-fabricated condition, down to 100's of nm when carefully polished).

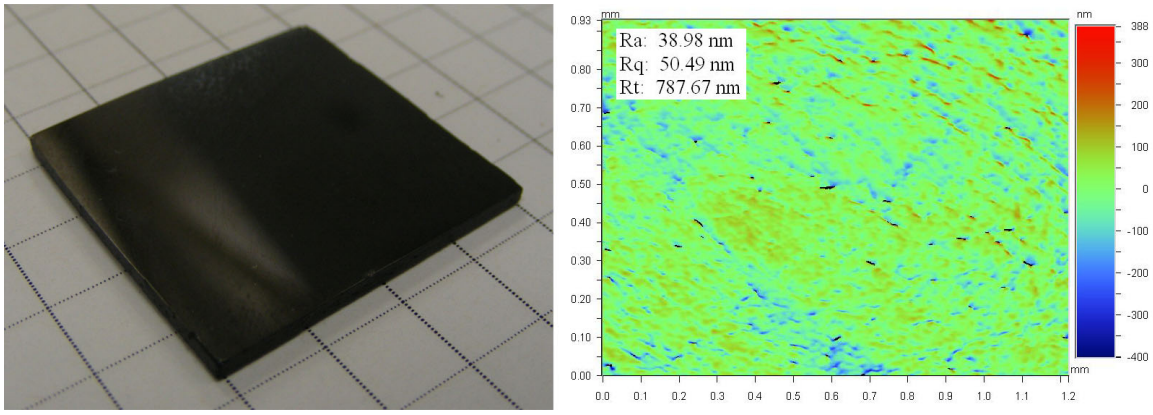

Figure 42: (left) Photo of mirror-polished SiC-SiC plate, (right) white light interferometry scan of surface roughness of polished plate

3.8. Roundness and Diameter Control

Roundness was measured by fitting circles to either the inner or outer diameter of the XCT tube volume. Each fit circle utilized 5000 evenly spaced points and a Gaussian least squares method to determine the circle diameter. The roundness was then determined using the maximum inscribed and minimum circumscribed circles based on the locations of the 5000 points fit to the circle (Figure 43). This approach was used to measure roundness (and corresponding tube radii values) at 11 evenly spaced points along the axis of the stitched XCT 3D reconstruction of the entire 0.9m tube. The average outer radius based on these 11 measurements was 4.56mm (standard deviation of 0.02mm), and roundness was 242μm (standard deviation of 22μm). Roundness values and tube radius values along the tube length are plotted in Figure 43.

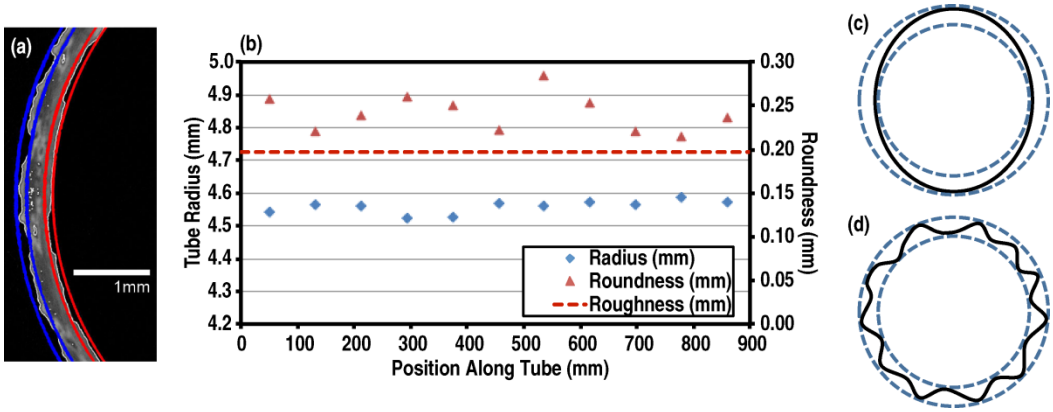

Figure 43: (a) Image demonstrating surface roughness contribution to outer (blue), and inner (red) roundness calculation, (b) Outer radius and outer surface roundness values measured along length of 0.9mm SiC-SiC tube, along with typical as-fabricated composites

The roundness values represent a significant deviation from circularity and exceed the roundness specification of ±25μm; however, this is a consequence of the large surface roughness of the as-fabricated tubes, which for these measurements had not undergone additional processing steps to reduce roughness. Since the roundness measurement is a function of the highest and lowest points along a cylindrical cross section, the unevenness

caused by the underlying fiber tow structure leads to the large measured roundness values. For tubes such as those measured in this work with high roughness, the contributions of ovality and roughness to the overall roundness value cannot be isolated [Figure 43(c), (d)].

The mechanical polishing and smoothing techniques used to control surface roughness can also be used to obtain precise, repeatable diameter control of finished tubes. A set of polished tubes were fabricated (Figure 44), and then scanned using x-ray tomography to generate volume representations of the tubes.

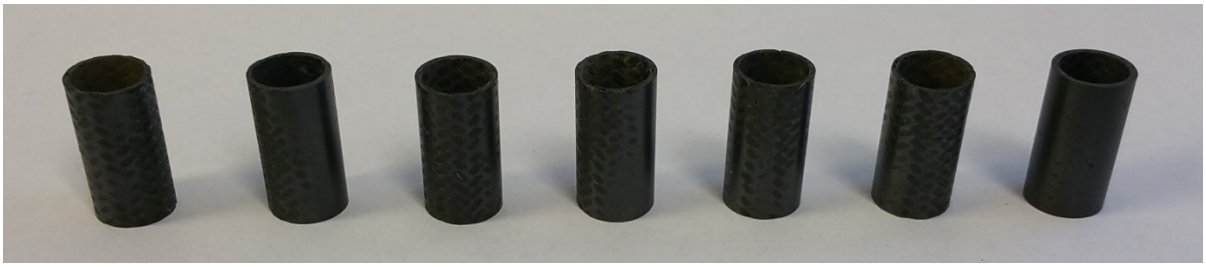

Figure 44: Seven polished tube samples prepared for analysis of roundness and wall thickness variation

Through polishing these tubes samples, the roughness which prevents a good roundness measurement is also eliminated. From these samples, outer diameter roundness values can be obtained which reflect the actual tube roundness. These values can be obtained directly from x-ray tomographic scans, which allows for rapid sampling of many points on the tube surface. The cross-sections at which roundness values were obtained were selected randomly, and the roundness determination was done using a procedure developed to eliminate potential operator bias when obtaining a dimensional value. XCT reconstructions of three of the tubes imaged are shown in Figure 45.

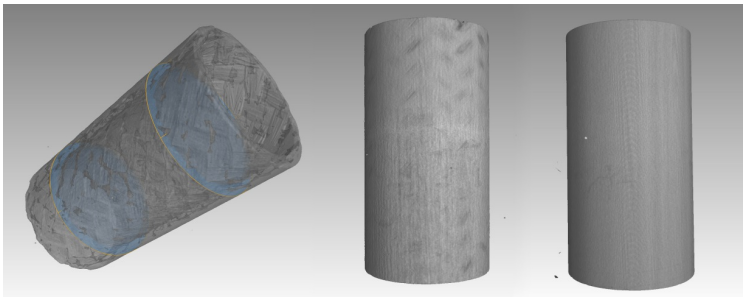

Figure 45: XCT reconstructions of three polished tubes used for roundness and wall thickness variation calculations

For all-composite tubes, roundness values for all measurements were <100μm, with the exception of one measurement on one sample where some of the as-fabricated roughness remained due to insufficient polishing. Excluding that specimen, average roundness for all-composite tubes was 61μm, with a standard deviation of 13μm. Another sample, containing an outer monolith is shown on the right of Figure 45 and was also characterized. Average roundness for this outer monolith sample was 39μm, with a standard deviation of 18μm, an

improvement of roughly 35% compared to the all-composite tubes. Cylindricity values can also be obtained from these polished specimens, and an average value of roughly 0.26mm was obtained for the all-composite tubes. Finally, diameter tolerances and uniformity can also be obtained from these same scans. The standard deviation of the diameter across the set was 32μm.

The deviation in the outer and inner radius values for the scanned tubes is another approach to give an indication of the variation in the diameters. At nine randomly selected cross sections across three different samples, comparisons were made between the actual tube surface and an idealized, best-fit circle at each axial height position. Roughly 125 points were measured at each of the nine cross sections, and the standard deviation between the actual surface position and a perfectly circular position was obtained. For these polished tubes, a better surface finish was obtained on the outer surface, and this led to an improved diameter deviation measurement (20μm average standard deviation in diameter measurements taken from nine different fit locations on three different specimens). The inner surface polishing was not as deep, and as a result, there was some residual surface roughness in these parts which contributed to a larger variation in the inner diameters. The average standard deviation for nine inner diameter measurements was 89μm.

Wall thickness deviation can also be obtained from the XCT reconstructions. Cylinders were fit to the tube surface (similar to the approach used for roundness determination), and the center point of circles fit at different axial positions was determined. The distance between the center of the best-fit ID circle and the center of the best-fit OD circle gives an approximation of the maximum variation in wall thickness for that axial position along the tube. The XCT analysis software can also directly supply a histogram of the wall thickness for a tube sample. For the measurements taken on selected circular cross-sections over three tubes, the average wall thickness variation (measured by the center-to-center spacing between circles defining the inner and outer diameter) was 47μm (standard deviation 22μm). This was for samples with an average wall thickness of 628μm (standard deviation 27μm). Using the built-in histogram wall thickness analysis, the wall thickness variation for an outer monolith tube is shown in Figure 46.

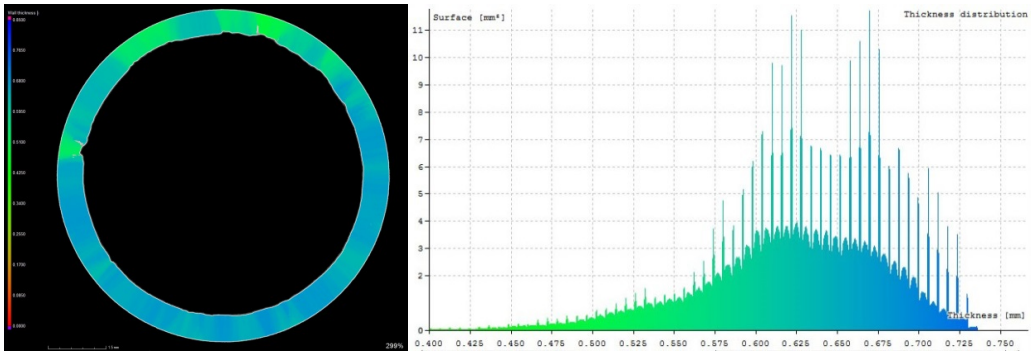

Figure 46: (left) XCT cross section of an outer monolith tube, (right) histogram showing wall thickness variation around tube circumference

3.9. Straightness and Cylindricity

Straightness and cylindricity are very important for fuel cladding applications, as deviations from straightness can lead to non-uniform spacing between tubes in a tightly packed fuel assembly [39], causing variations in heat transfer, increases stresses, and potential bowing.

For tubular structures, straightness measurements assess the maximum deviation of the tube surface from a straight reference line aligned along the tube axial direction. Although only straightness and roundness (or ovality) may be required specifications for a cladding tube, cylindricity measurements combine an assessment of both the tube straightness and the tube roundness into a single measurement, as deviations from both straightness and circularity contribute to the overall cylindricity value. Cylindricity measurements may be easily obtained through analysis of reconstructed XCT volumes, and this provides a single value to assess the tube geometry.

Cylindricity was measured by fitting cylinders to the exterior of the measured tube, and this was performed for each of the four ~25cm long XCT volumes, as well as the stitched full length tube. The same 0.9m long as-fabricated SiC-SiC tube shown in Figure 38 was used for this cylindricity measurement. The fitting process involved a user manually selecting a large number of randomly chosen points on the surface to be fit (either the inner or outer surface of the tube; for the following results the outer surface was used). 5000 evenly spaced points were automatically fit to the surface of the tube to envelope the manually selected points and a perfect cylinder was fit to these automatically selected points using a Gaussian least squared fit method. These points were used to obtain the cylinder diameter, and the cylindricity was also determined by finding the maximum inscribed and minimum circumscribed circles based on the fit to the cylinder. The scan size selected for these measurements gave a resolution for the cylindricity measurements of 127μm, and this represented a balance between the scan resolution and number of scans necessary to encompass the full tube length.

Cylindricity results were first obtained for the individual scanned volumes (each approximately 25cm long). The cylindricity for these volumes averaged 399μm (standard

deviation of 49μm), with an average outer radius of 4.56mm (standard deviation of 0.019mm). The stitched and merged volume representing the entire 0.9m long tube was then analyzed, and the fit process (initiated by user-selected surface points) was repeated eight times. Average tube outer radius for the entire length was almost identical to the average radius for the individual sections at 4.57mm (compared to 4.56mm), and there was essentially no variation between each of the eight individual fits that were analyzed (standard deviation of the radius for these eight different fits was 0.001mm). The average cylindricity for these eight different fits of the merged volume was 774μm, with a standard deviation of 30μm between the different fits. This indicated that while there is a manual aspect to the fitting process (the user selection of surface points which forms the basis for the fit), the potential error introduced by this selection is small (standard deviation is only ~4% of the average cylindricity value).

For the SiC-SiC tubes analyzed in this work, even though the surface roughness of the as-fabricated tubes contributed to a large roundness deviation value, the overall cylindricity still had a significant component due to straightness deviations. Assuming the straightness deviation is the main contribution to the 774μm average cylindricity value over the 0.9m long tube, this would correspond to a straightness deviation of ~3.1mm over a full ~4m long fuel rod. However, the straightness tolerance for nuclear fuel cladding tubes is large relative to the roundness requirements.

The increase in the cylindricity obtained from the individual and stitched XCT reconstructions (average cylindricity of 399μm for the individual volumes compared to 774μm for the merged volume) could arise from two different sources. One cause of this would be an actual increase in the straightness deviation for the longer tube compared to the 25cm individual segments scans. If there was a larger straightness deviation in the overall length of tube that was being missed by analyzing individual 25cm long scans, then it would be expected that the straightness value would increase with increasing tube length, and correspondingly, decrease with tube length being analyzed was decreased.

Alternately, there could be errors associated with the stitching process, which result in misalignment and introduce straightness deviations, which are an artifact of the stitching process rather than present in the actual tube.

To assess the relative contribution of each of these potential issues to the cylindricity value obtained from the stitched 0.9m tube volume, a coordinate measuring machine (CMM) was used to evaluate the cylindricity of the same tube. This measuring approach offers improved resolution compared to the XCT scans (12.7μm in the X, Y, and Z directions), and can measure the entire 0.9m length of the tube at once. In these CMM measurements, five points encompassing 180° were taken around the circumference of the tube at each of 25 different circumferences, evenly spaced along the tube axis. Although CMMs can be operated automatically to gather thousands of data points, in this work data points were manually obtained, and the limited number of points may introduce some sampling error. The cylindricity value obtained from this measurement was 472μm. This CMM cylindricity value is similar to the cylindricity values obtained from the individual (25cm long) XCT volumes (399μm), but smaller than the cylindricity in the merged XCT volume (774μm). The difference between the merged

XCT volume and the CMM measurement (~300μm) is large compared to the variation between different cylindricity values for the merged XCT volume (30μm deviation between different user fits). This suggests the difference in cylindricity in the merged XCT volume compared to the CMM value could be due to stitching and alignment errors in the XCT analysis software or a consequence of sampling from the CMM. A summary of the cylindricity values obtained in this work from different scan lengths and measurement methods is given in Table 10.

Table 10: Average Cylindricity or straightness values obtained for different scan lengths and measurements techniques.

Measurement (number)	Average Cylindricity (Std. Dev.)
XCT – 0.25m length (four different scans)	399μm (49μm)
XCT – ~0.9m stitched length (one volume, eight fits)	774μm (30μm)
CMM – ~0.9m Length (single measurement)	472μm (N/A)
Height Gauge – ~0.9m length (nine separate tubes)	863μm (453μm)

The cylindricity for either an all SiC-SiC composite tube or a composite tube with an outer monolithic layer will depend on the straightness obtained in the underlying composite, and would be defined near the start of processing (absent any mechanical grinding or polishing steps at the end of fabrication). The cylindricity value reported above therefore gives a good approximation of the straightness that could be currently obtained for these structures. For a tube structure composed of an inner monolith surrounded by an outer composite layer, the straightness would instead be strongly influenced by the straightness of the underlying monolithic tube. To investigate this, the cylindricity of an extruded, ~0.9m long, thin-walled (~400-500μm wall thickness) Hexoloy tube was measured using the CMM. This was the same material used in the inner monolith structures shown in Figure 2(c).The cylindricity for this part was 267μm, or slightly more than half that of the as-fabricated SiC-SiC tube. As the surface roughness of this Hexoloy tube is far smoother than that of the as-fabricated composite tube, there is a significant roughness contribution (~200μm, see Table 1) to the cylindricity in the all composite tube that is absent in the Hexoloy cylindricity. In addition, for the inner monolith structure, the roughness caused by the fiber architecture would still be present in the overlaying composite layer, so the 267μm cylindricity measured for the Hexoloy tube should represent a best-case cylindricity for a tube with an inner monolith structure, and the final cylindricity may be comparable to that of the all-composite or outer monolith tube.

One additional method was used as a rapid assessment of tube straightness. A vertical height gauge was used to find the highest point along the length of a tube while the tube ends rested on a flat granite surface. While this method provided a quick measurement, the practical accuracy of this approach relied on a visual assessment to ensure the highest point on the tube was being measured. As such, while the resolution of the vertical height gauge was 10μm,

the accuracy of this measurement method was subject to more user error than both the XCT and CMM cylindricity measurement methods. Furthermore, as this method only measured the highest point on the tube, it provides a straightness measurement, rather than a cylindricity measurement (cylindricity would incorporate both straightness and roundness assessments, and with only the highest point sampled, the vertical height gauge does not measure the roundness contribution to the cylindricity). However, this height gauge measurement was still used to evaluate the straightness distribution across a range of tubes produced using nominally the same fabrication method. All tubes were ~0.9m long, and across the nine tubes, the average straightness was 863µm, and the standard deviation between all samples was 453µm. This set of measurements is shown in Figure 47. The current cladding straightness requirement is 0.25mm per 300mm length (which translates to 0.833mm/m), and the tube measured using the XCT and CMM methods, and approximately half the tubes measured by the height gauge method meet the specification (three of the tubes measured using the height gauge exceed the requirement, and two are within 3%). With production scale-up and increased automation in the fabrication process, repeatability is expected to improve and result in a higher yield of tubes meeting this specification.

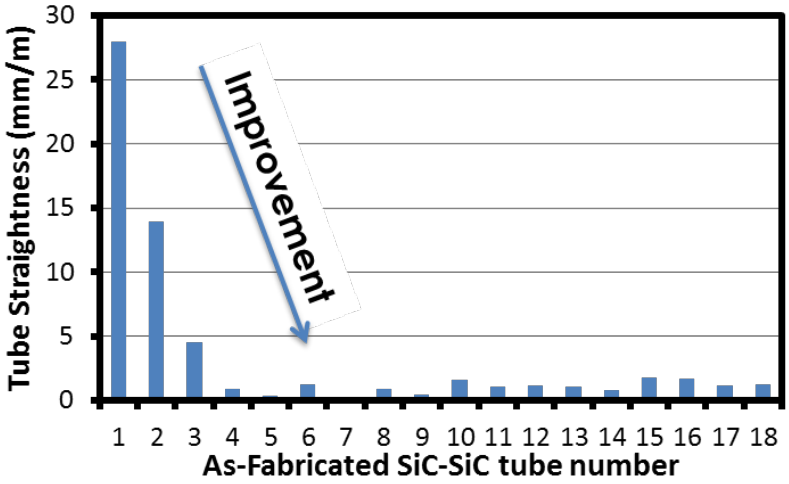

Figure 47: Straightness measurements obtained using a vertical height gauge for a set of nine tubes fabricated using the same fabrication approach.

3.10. Infiltration and Overcoat Uniformity

In addition to meeting dimensional tolerances in the production of long SiC-SiC tube for fuel cladding applications, it is also essential that the material performance is uniform along the tube length, and meets mechanical, thermal, and permeability requirements. Fiber structures and orientations can be maintained with good consistency for long tubes; however, the infiltration of these fibers can vary as a function of length during the chemical vapor infiltration process. The completeness of infiltration is a function of the temperature, pressure, and local precursor concentrations during infiltration, and all these parameters, as well as byproduct concentrations, can vary throughout the infiltration chamber, both spatially and temporally. During the infiltration process, a deposition gradient develops from the outside of the composite to the center, and this will result in the gradual formation of a dense SiC layer on the outer surface of the composite. The uniformity of the infiltration can be assessed by measuring

properties or porosity as a function of position along the length of the tube, or as a coarse approximation, the thickness of this outer SiC layer can be used as a gauge of the infiltration uniformity. This approximation assumes that if the deposition of SiC on the outer composite surface is uniform, then the interior infiltration will likely be similar. While not as accurate as direct comparison of mechanical and thermal performance at different points along the tube length, or density measurements, the variation in the SiC coating thickness as a function of length can provide important feedback on the uniformity of the infiltration process.

Measurements of uniformity along the length of a representative tube were performed using two approaches. First, XCT scans were taken at approximately 10cm intervals along the length, starting at one end and continuing to the center of the tube. A representative volume of the tube was analyzed at each interval and total material volume as well as total internal pore volume was measured. Note that with the resolution used for these scans (17μm), extremely small pores between fibers and inside tows are not resolved, and therefore not included in the porosity values obtained. As such, these values may slightly underestimate the actual total sample porosity. However, a significant variation in this underestimation as a function of position is not expected, and these XCT scans should give a good indication of uniformity. The porosity fraction was calculated from these measurements, and is plotted as a function of position along the tube length in Figure 48. The second approach utilized the overcoat thickness approximation, and measurements of overcoat and variations in thickness (normalized to the average thickness) were obtained and are also shown in Figure 48. This data only represents half the distance along the tube length (from one end to the center); however through periodic rotation of the tube during fabrication it is expected that any thickness variation is symmetric from each tube end. These initial results show that the porosity ranges between 5% and 8% along the tube length, and the coating thickness variation is 5% or less. In addition, no clear trend of varying porosity or overcoat thickness is observed as a function of position. A complete assessment of the density, mechanical, and thermal properties along the tube length would provide a more complete data set, however, these results suggest that good tube axial uniformity is being achieved, and these measurement approaches can provide feedback on uniformity in a much shorter timeframe.

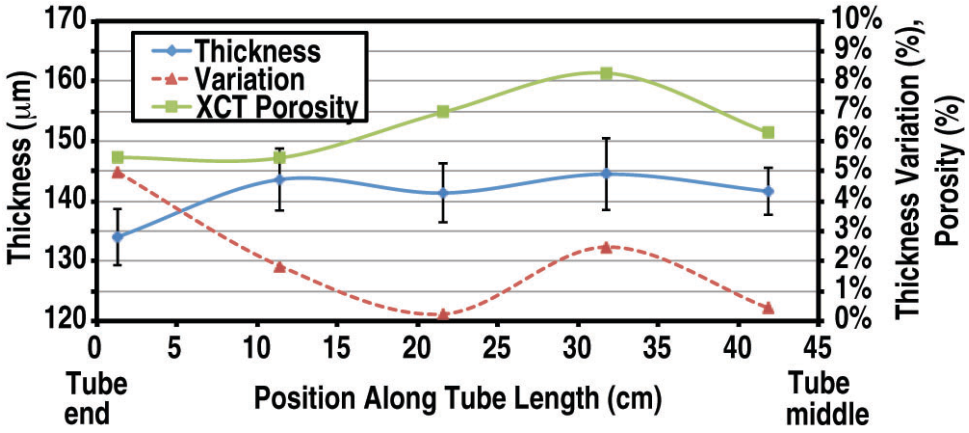

Figure 48: SiC overcoat thickness and variation in overcoat thickness (normalized to the overcoat thickness) and fraction porosity as a function of axial distance along tube length. Error bars represent standard deviation in thickness measurements

4. Planar Coupon Characterization (Subtask 2)

Planar SiC-SiC coupons were fabricated and tested for mechanical and thermal properties, hermetic performance, and corrosion resistance. Mechanical characterization included flexure testing and impact testing; thermal characterization included measurements of thermal diffusivity and specific heat, and hermeticity was measured using a helium leak detector with very high sensitivity. This task included analysis of a large set of planar flexure specimen results to provide a statistically representative data set for SiC-SiC material.

4.1. Mechanical Characterization

Mechanical properties were measured on SiC-SiC panels using flexure and impact testing. Several SiC-SiC panels were fabricated as part of this work, although efforts quickly transitioned into fabrication and characterization of tube geometry samples. However, in addition to the fabrication of several planar samples, characterization and analysis was performed on a number of previously-fabricated panel specimens to provide a larger and more statistically robust sample set. These additional panels included panels with variations in fiber volume fraction, infiltration speed, and fiber interphase, and additional parameters involved in the specimen preparation were also investigated. Tests were performed on either an Instron 5969 or Instron 5982 Universal Mechanical Tester. Flexure testing of planar samples followed ASTM 1341C 1 (using a 16mm support span in the 4 point-1/4 point configuration), with a nominal specimen size of 1mm thick by 3mm wide by 26mm long. The specimens were tested in the as-fabricated condition, without additional surface preparation or polishing, and actual dimensions of each specimen were measured prior to testing. A double ball interface micrometer was used to find the minimum thickness within the load span.

In this work, a large set of SiC-SiC flexure bar specimens (271 total) were tested to build a more statistically significant population of composite mechanical properties. Specimens were taken from a number of panels, which varied slightly in the pyrolytic carbon interphase used (ranging from ~110-220nm thick), but were all densified using the same CVI process to nominally the same relative density. Values for composite flexural modulus, proportional limit

stress (PLS), flexural strength, and strain at flexural strength were obtained for each specimen according to ASTM C1341. Mechanical properties were similar across all panels, and the distribution of modulus, PLS, flexural strength, and strain at the flexural strength values within the specimens from each panel was broader than the range of characteristic values across different panels. Representative stress-strain curves for these flexure tests are shown in Figure 49.

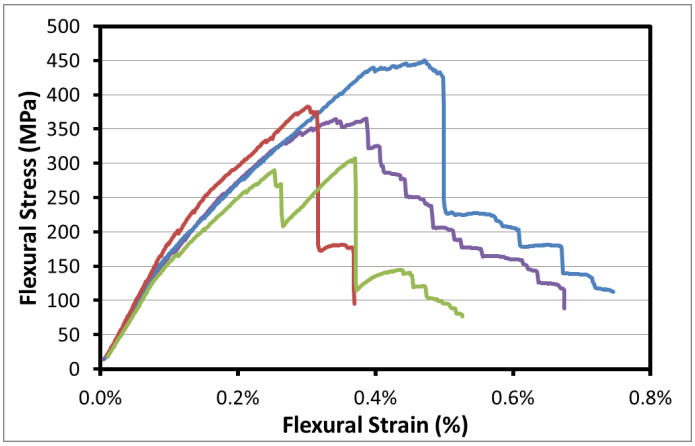

Figure 49: Representative stress-strain curves for planar SiC-SiC four-point bend test

From the set of 271 bend bar specimens, those tests considered to be valid based on the ASTM criteria were then analyzed using the Weibull analysis method explained in ASTM C1239-07. The Weibull modulus and characteristic value were obtained by iteratively solving using the maximum likelihood estimators approach.

In fiber reinforced composites fabricated via chemical vapor infiltration, the shape and location of the porosity is highly dependent on the reinforcing fiber architecture. Voids both within tows and between adjacent tows tend to have a high aspect ratio, and run parallel to fiber tows. Due to the regular, repeating structure of the fiber reinforcement, voids within the composite will also have a periodic occurrence, and because of this, changes in the specimen size will have a minimal impact on the location and sizes of voids (assuming the fiber architecture remains constant, which is true for all specimens examined in this work). As a result, no volume dependence has been included in the calculation of Weibull values for these composite specimens. Weibull modulus and characteristic value results for this data set are listed in Table 11.

Table 11: Weibull Modulus and Characteristic values for flexure specimen data (censored according to ASTM C1239-07)

Property	Weibull Modulus	Characteristic Value
Flexural Modulus	4.40	184 GPa
Flexural Strength	4.41	425 MPa
PLS	3.69	163 MPa
Strain at Flexural Strength	3.63	0.51%
Flexural strength - PLS	2.78	294 MPa

Reports in the literature have suggested that statistics for mechanical properties of ceramic matrix composites may be better described using normal or log-normal distributions, so the data was also fit to these distributions to compare to the Weibull statistical analysis. Results for these fits for the Flexural modulus data values are shown in Figure 50. For the flexural modulus, the quality of the fits of the data to normal and log-normal distributions was slightly better than the fit to a Weibull distribution. The normal and log-normal fits were very similar, and this held true for the other properties analyzed as well.

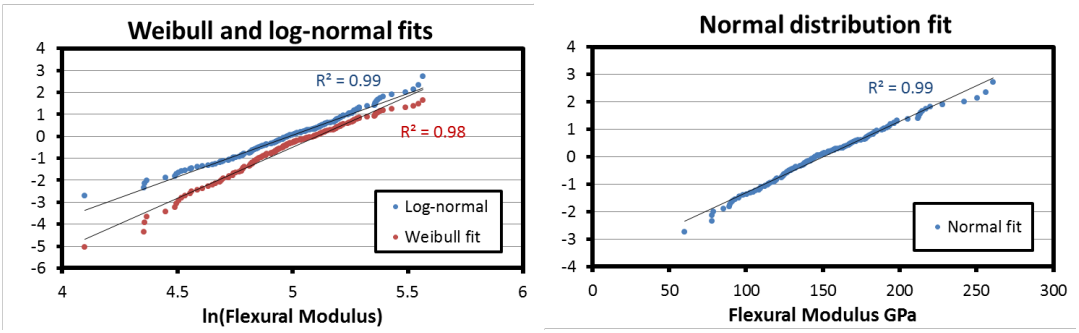

Figure 50: Flexural Modulus data fit to Weibull, log-normal, and normal distributions

Log-normal and Weibull fits were also obtained for the flexural strength, PLS, strain at flexural strength, and differences between the flexural strength and PLS. In general, the three distributions all provided approximately the same quality of fit for the flexural modulus, flexural strength, and the difference between the flexural strength and PLS value for the data. For the PLS and strain at flexural strength, the log-normal distribution provided the best fit to the data.

The distribution of the range of measured property values has important implications in the design and design requirements for the use of these SiC-SiC composite materials in cladding and other applications requiring a very low failure rate. When fit to a log-normal distribution, the predicted range of values for a given property is narrower than that predicted by a Weibull fit for the same values. This difference becomes very apparent when looking at property values with a very low frequency of occurrence, and these rare values must be considered when the application has a target failure rate in the ppm level.

Elevated temperature testing of planar samples was planned as part of this subtask; however, tubular material was available at the time elevated temperature testing was ready to begin, so all elevated temperature testing of SiC-SiC material was performed on more representative tubular geometries. These results are provided in section 5.1.

Charpy impact testing was performed on a small subset of previously fabricated planar material to assess the correlation between sample density and energy absorbed during impact events. The ASTM E23 standard was followed and twenty two specimens were tested with a range of specimen widths and specimen densities. The impact specimens were not notched, and tests were conducted at room temperature. The hammer angle was ~150° to produce an impact speed of ~3.5 m/s. The initial impact testing was performed to see if there was an effect of the specimen thickness on the results. Specimens were cut with a nominal width of either 5mm or 10mm from the same composite panel. Impact energy (in kJ/m^2) for both widths was

essentially the same, at 6.07 (1.1 standard deviation) for the 5mm specimens, and 6.20 (1.0 standard deviation) for the 10mm specimens. These results are shown in Figure 51. A second sent of experiments were performed to assess the effect of sample density on impact energy. Specimens were cut to a 10mm width from two panels, one with a relative density of 76%, and one with a relative density of 82%. Here an 8.7% increase in composite density resulted in a 16.5% increase in impact energy, as shown in Figure 51.

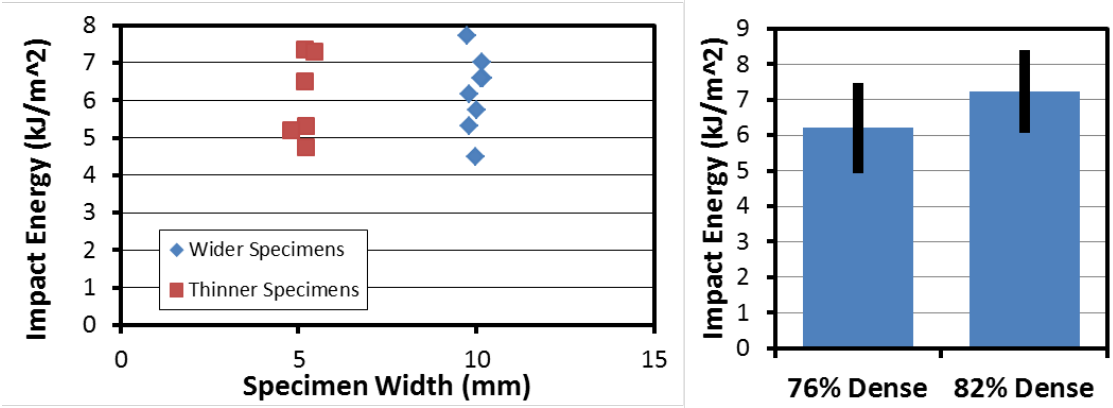

Figure 51: Impact energy as a function of specimen width and density (Charpy impact test)

4.2. Thermal Characterization

In addition to providing mechanical strength and containment of the fuel, any nuclear fuel cladding material must also serve to allow heat transfer from the fuel through the cladding and to the coolant. In this role, a high thermal conductivity is essential. The thermal conductivity of unirradiated silicon carbide is high (over 400 W/m-K for high purity, dense monolithic SiC), and SiC-SiC composites, while lower than monolithic SiC, also exhibit a relatively high thermal conductivity (~25 W/m-K at room temperature, compared to Zircaloy at ~14 W/m-K). However, the thermal conductivity of SiC and SiC-SiC composites drops considerably with irradiation, due to irradiation-induced defect accumulation which increases phonon scattering, reducing thermal conductivity. This reduction saturates after 1-2 dpa, and is dependent on the irradiation temperature and is inversely proportional to the swelling, and can reduce the thermal conductivity of monolithic SiC down to 10-20 W/m-K, and SiC-SiC down to 1-10 W/m-K (with a strong dependence on the irradiation temperature and composite structure and composition).

The thermal conductivity of fuel cladding materials must be high enough to transfer sufficient heat from the fuel to the coolant and maintain the fuel centerline at below the melting temperature. Due to the large irradiation-induced changes in the thermal conductivity of SiC, the effects of the composite structure must be evaluated for the thermal performance, in addition to the mechanical performance. Composite density has a significant effect on the material thermal conductivity, which is calculated as a function of the density, and this has already been demonstrated in previous studies and was not repeated. Higher density composites also provide higher thermal diffusivity values. In addition to density, other microstructural features can influence thermal properties, and a series of panels were fabricated with varying fiber interphase coatings. Thermal diffusivity and specific heat were measured as a function of temperature, and these values, combined with the measured

composite density, were used to calculate the thermal conductivity for each sample. In each case, multiple thermal diffusivity specimens were measured from each sample, to provide more representative results. A representative specific heat curve and the calculated thermal conductivity as a function of fiber coating and temperature are shown in Figure 52. Thermal diffusivity was measured using a NETZSCH LFA LFA 427 laser flash analyzer, following the approach introduced by Parker et al, and with modifications for sample geometry according to Zhang et al. The sample size was kept constant at 10 mm x 10 mm to fit into the specimen holder for the analyzer. Thermal diffusivity was measured at 25°C, 300°C, and 800°C, and three measurements were taken at each temperature.

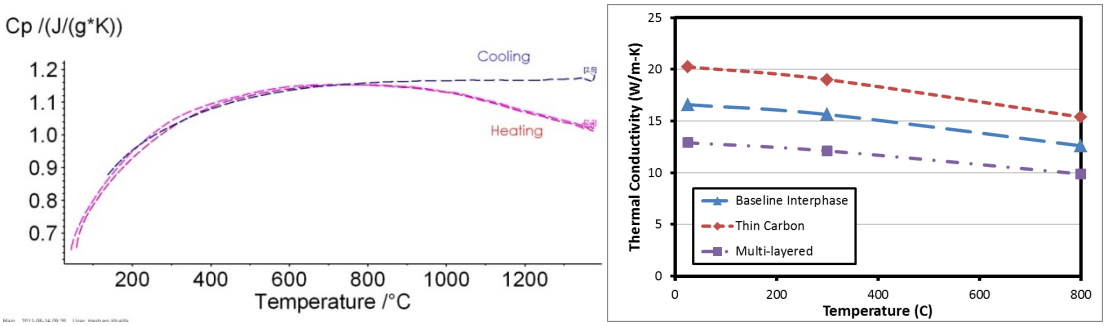

Figure 52: A representative specific heat curve, and calculated thermal conductivity values as a function of interphase type and temperature

4.3. Permeability

Permeability is a critical property of any fuel cladding tube, and must be accurately characterized. However, the extremely low permeability requirements result in challenges in the fixture design, and require highly sensitive permeability measurement equipment. Initial planning had considered the use of a tritium permeation test rig available at GA, but there were limitations associated with use of this equipment, including sample size and geometry and a restriction of testing to a single hood where this equipment was already installed.

Upon further consideration of the permeability requirements, a mass spectrometer helium leak detector was identified which could provide the needed sensitivity while offering a much more versatile test capability. This approach facilitated the testing of planar, tubular, joint, and endplug samples, and could also accommodate sample tests at elevated temperatures. This test rig offered both high sensitivity and low baseline reading of 1 E -12 atm cc/sec. The setup is primarily composed of a helium source, a tube furnace, a low and high pressure chamber, a specimen holder, a mass spectrometer leak detector (VS MD30 from Agilent), and a roughing pump (Figure 53). The selection of the leak testing method used to evaluate the fixtures and specimens was obtained from ASTM E432-91 (2011).

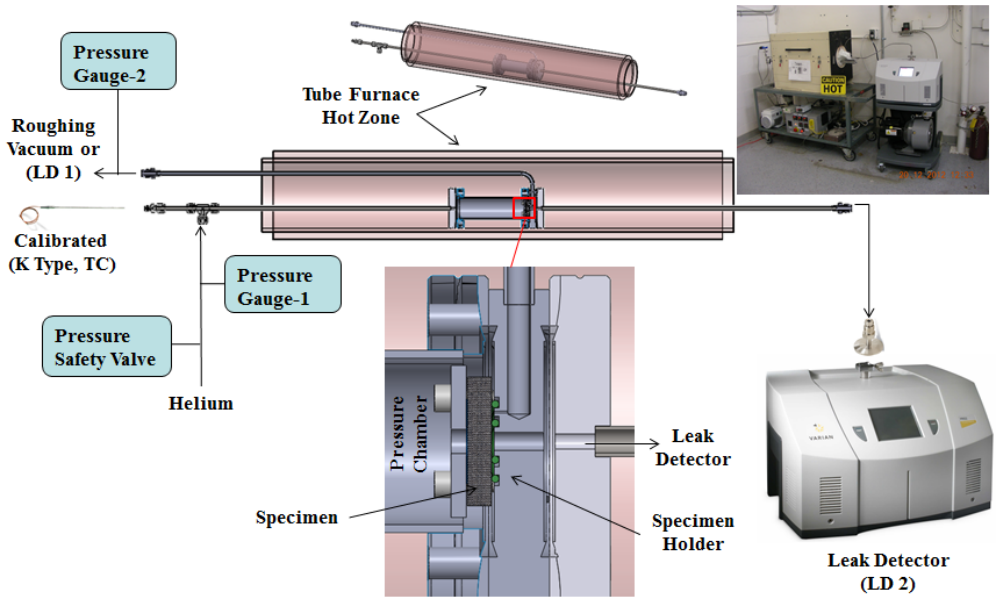

Figure 53: Permeability test setup schematic.

In order to evaluate the leak rate performance of different structures, materials, and cladding designs, a leak rate requirement had to be established. The maximum leak rate for an as-manufactured LWR fuel rod is 1.0E-6 atm cc/sec when pressurized with helium to 1.7 MPa (250 psi) at room temperature. Leak rates for small planar and tubular specimens have been allocated by extrapolating the fuel rod leak requirement using a linear pressure and area ratio. The summary is given in Table 12. For a tubular specimen, the given joint leak rate represents the allocation for one cylindrical joint that has a 50μm axial length between the tube and end plug.

Table 12: Helium Leak Rate Allocation Summary for Small Specimens

Specimen Configuration	Specimen	Sealing Dimensions	Leak Rate (atm cc/sec)*
Planar	Cladding	6 mm diameter	1.4 E-11
	Joint	50µm gap by 6 mm long	6.0 E-10
Tubular	Cladding	9.5 mm dia, 51 mm L	7.3E-10
	Joint	50µm	2.9E-9

*Test pressure differential of 1 atm.

Initial work focused on identifying a suitable method for sealing the sample against the fixture, to ensure that any helium leak measured was coming through the sample and not through the fixture or joint. For this work a surrogate stainless steel plate was used as a sample along with a monolithic Hexoloy SA silicon carbide plate, and a SiC-SiC composite plate. Figure 54 shows the stainless steel surrogate plate attached to the fixture using epoxy, as well

as a representative leak measurement result. In the leak test measurement, there is some lag time between the introduction of helium (indicated on the plot), and the rise in the leak rate of helium through to the detector. The helium leak rate typically rises and then levels off at a steady state, which is take to be the leak rate for the sample. Studies have been performed over a range of peak-to-valley surface roughness from 2.5 to 150μm. Depending on the method of seating the sample in the test fixture, all surface finishes are able form a seal with vacuum-compatible epoxy for room temperature tests.

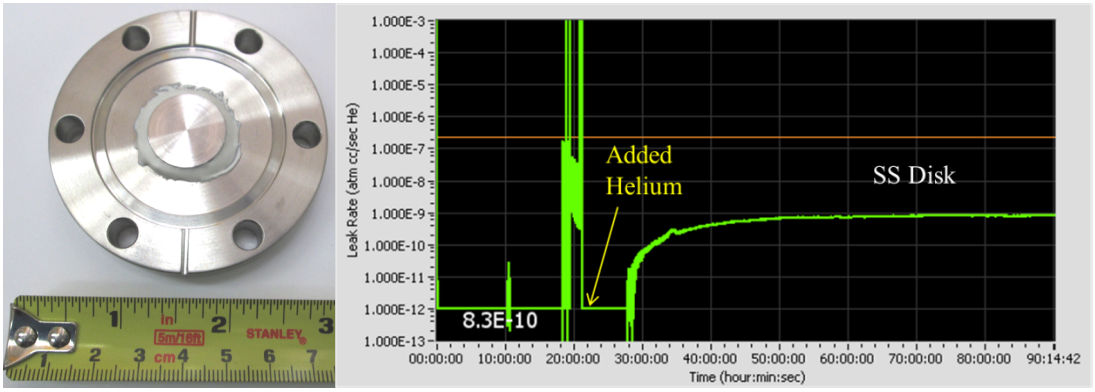

Figure 54: Baseline leak rate measurement for stainless steel disc with an epoxy seal

Leak rate results for the material evaluated with the epoxy seal are listed in Table 13. The leak rates varied between the samples, and were not consistent with the anticipated relative leak rates expected between the different samples (where the fully dense stainless steel and the monolithic Hexoloy material would be expected to have a lower leak rate than the composite). It was determined that leakage through the epoxy made a significant contribution to the measure leak rate, and that variations in the application of the epoxy were causing the differences in the measurements, rather than variations between samples. The best epoxy (Epotek H74) has a steady state leak rate of 2.6E-10 atm cc/sec at room temperature and won't meet the requirement allocation for a small planar specimen; therefore, a new specimen holder approach is required.

Table 13: Summary of steady state leak rates observed for different sealing configurations

Sample	Joint	Steady State Leak
Stainless Steel	Epoxy	8.3×10^{-10} atm cc/sec
Hexoloy SA SiC	Epoxy	9.2×10^{-10} atm cc/sec
SiC-SiC composite	Epoxy	5.7×10^{-10} atm cc/sec
Monolithic SiC	Single O-ring	$\sim 2 \times 10^{-6}$ atm cc/sec
Monolithic SiC	Double O-ring	$<1 \times 10^{-12}$ atm cc/sec

An alternate sealing approach offering a lower baseline measurement was needed in order to obtain an accurate leak measurement through the actual sample. This is also necessary for temperatures up to 300 ° C where the epoxy bond starts to fail and an alternate fixture design is needed to meet LWR requirements.

For this, an O-ring approach was developed. While this method did not have the forgiveness of the epoxy approach in terms of sealing against rough surfaces, this approach

(with some modification) did allow for an extremely tight seal with a baseline leak rate below the detection limit of the equipment. Leak rates measured through a monolithic SiC sample with a single O-ring were not sufficient, and were higher than those measured using the epoxy seal. However, a double O-ring configuration provided an extremely low leak rate, below the baseline measurement capability of the leak detector. The leak rate plot is shown in Figure 55. In testing this O-ring configuration, the test fixture was heated incrementally to 100°C, 200°C, and 300°C, and as expected, with increasing temperature a corresponding increase in the helium leak rate was observed. However, after cooling, the leak rate measurement returned to the baseline below the detection limit of the equipment, indicating the O-rings remained intact and undamaged. The specimen holder is limited to the low E-9 atm cc/sec range at 300C. Compared to the single o-ring configuration, the double o-ring arrangement offers approximately five orders of magnitude improvement for each temperature step of 100, 200 and 300C.

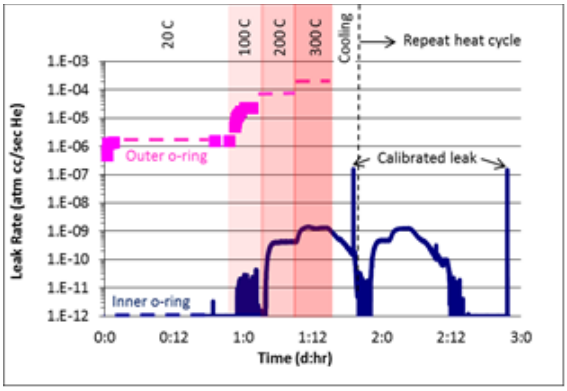

Figure 55: Comparison of single and double o-ring leak rates

The planar double o-ring configuration can successfully seal on a maximum peak to valley roughness of 55μm. In order to meet the surface finish requirement, a planar SiC CMC composite was polished down on only one side in three steps. After the third polishing step was completed, an overcoat had to be applied to make the SiC CMC impermeable. Figure 56 has the surface profilometry results, where Rt is the peak to valley surface roughness.

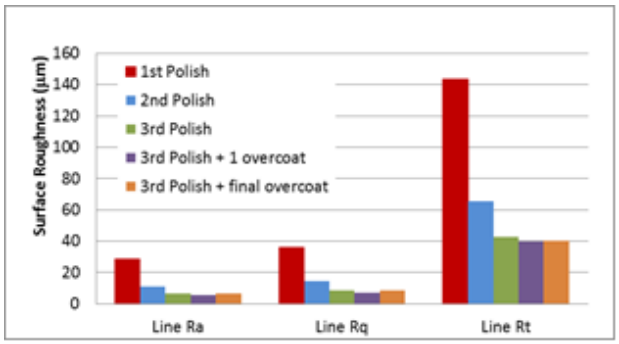

Figure 56: Surface profilometry results

The specimen experienced leak measurements (>1E-4 atm cc/sec) for the first, second and third polishes. It was determined that a ~100μm thick mSiC overcoat layer was required in

order for the specimen to become impermeable (Figure 57). It had a permeability <1E-12 atm cc/sec at RT and 1 atm pressure differential, satisfying its leak rate allocation.

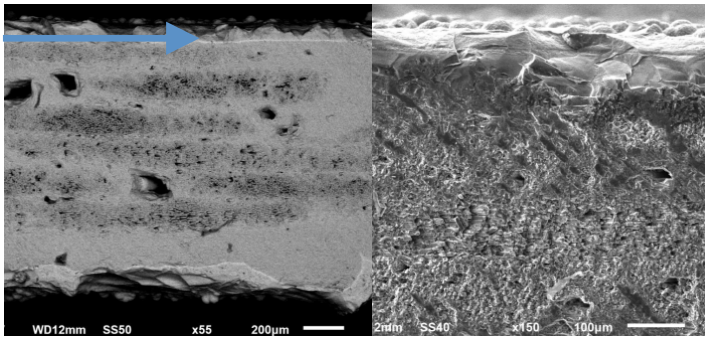

Figure 57: Section view for the overcoated SiC CMC specimen (top side was polished and then overcoated)

After the third polish and final overcoat leak test was performed, the specimen was subjected to a four point bending stress test. The polished layer was oriented in tension and the thicker unpolished layer under compression. A stress of ~70 MPa (Figure 58) was imposed on the specimen resulting in a small leak in the E-11 atm cc/sec range. The specimen was the subjected to a second four point bend test of ~100 MPa resulting in a gross leak.

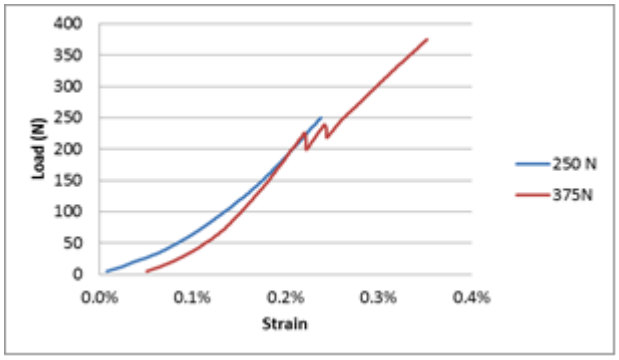

Figure 58: Loading plot for planar SiC CMC

All hermeticity is lost between 70 and 100 MPa. This result is comparable to the 80MPa upper limit value presented by Sabiego et al. for a tubular SiC CMC under tension. Careful placement of the impermeable thin mSiC barrier along the cladding thickness will be required in the final configuration to minimize its tensile stress level during normal operation, accident and end of life conditions.

4.4. Autoclave corrosion test results

A set of six planar SiC-SiC composite samples were fabricated for autoclave testing at Westinghouse. These were approximately 10mm wide, 20mm long, and 1.1 to 1.4mm thick, with a small (2.5mm diameter) hole drilled near one end to facilitate supporting the samples during the test. Four of the samples received an additional SiC coating after the hole was drilled and they were cut to size; two received a thinner coating and two received a thicker coating. The two remaining samples received no additional coating. Also included were an

additional monolithic SiC sample as a control and Zircaloy plate samples for comparison with current LWR cladding material. The samples are listed in Table 14.

Table 14: Summary of samples included in autoclave corrosion testing

Sample	Type	Overcoat	L (mm)	W (mm)	T (mm)	Mass (g)
GA-1	SiC-SiC	Thick	20.29	10.24	1.45	0.58
GA-2	SiC-SiC	Thin	20.05	10.34	1.35	0.57
GA-3	SiC-SiC	None	20.19	10.20	1.46	0.57
GA-4	SiC-SiC	Thick	20.26	10.01	1.68	0.69
GA-5	SiC-SiC	Thin	20.27	10.24	1.61	0.70
GA-6	SiC-SiC	None	20.18	10.11	1.65	0.64
GA-7	Mono SiC	None	20.02	9.99	1.14	0.71
T860-1	Zircaloy	None	27.69	25.91	0.47	2.19
T860-2	Zircaloy	None	27.95	25.46	0.44	2.16
T860-3	Zircaloy	None	27.67	25.59	0.47	2.15

The samples spent up to 57 days in an autoclave at 800°F and 1500 psia, with periodic readings taken at 7, 27, and 34 days. In general, the monolithic SiC saw essentially no change, the overcoated SiC-SiC saw a slight mass gain, the uncoated SiC-SiC experienced a slight mass loss, and the Zircaloy saw the largest change, with increasing mass. The weight change, normalized to sample area, is shown in Figure 59.

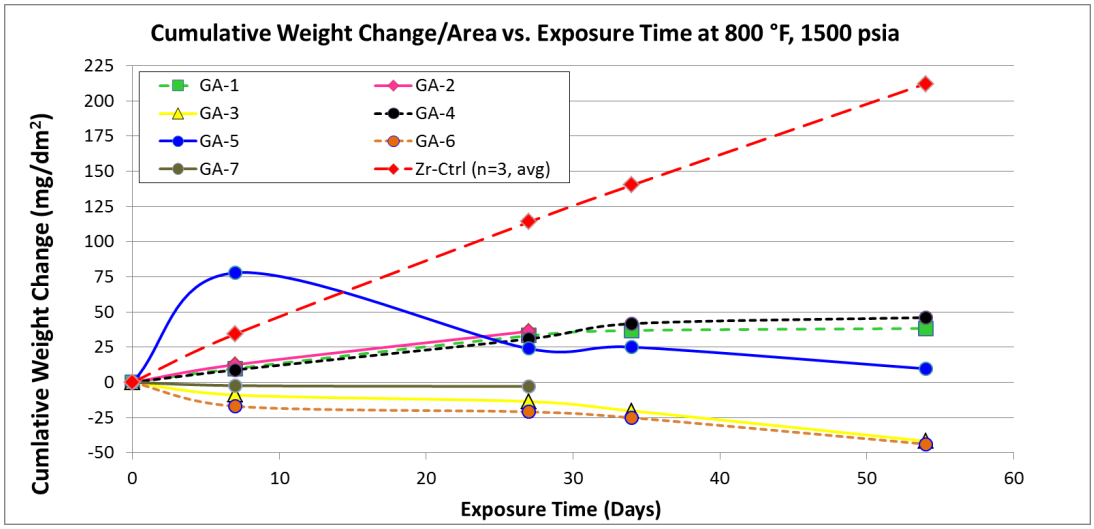

Figure 59: Cumulative mass change for SiC-SiC samples exposed to autoclave testing

One of the SiC-SiC samples (GA-5) experienced an anomalously large weight gain after the first exposure (after 7 days), and then the weight dropped with additional exposure. After excluding this sample, there was no significant difference in mass change behavior between the samples which received the thicker vs. the thinner over-coating.

The mass change can also be plotted as a percentage change normalized to a one month exposure time, and these results are shown in Figure 60. For clarity, results from the overcoated samples (GA-1, -2, -4) were averaged together, and results from the uncoated samples (GA-3, -6) are also averaged together.

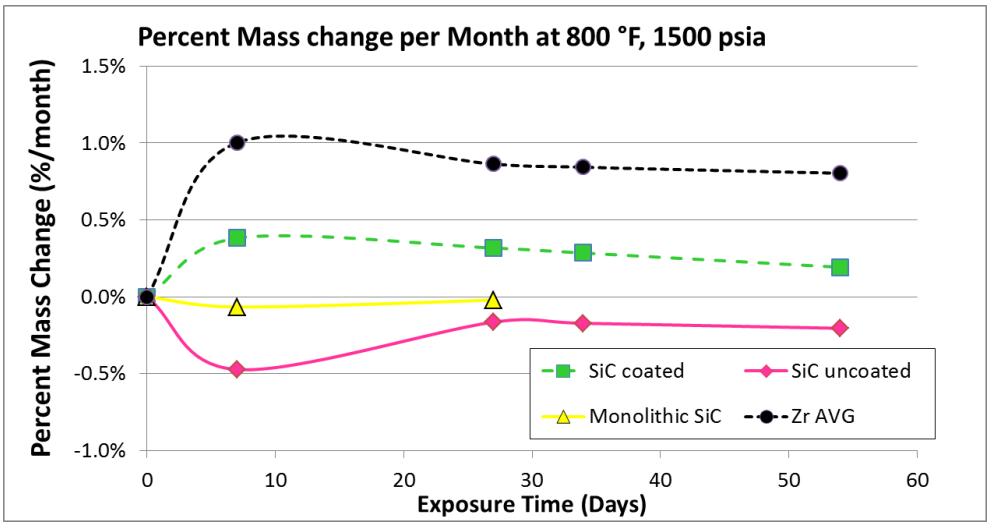

Figure 60: percent mass change per month observed for SiC-SiC samples exposed to autoclave testing

For all samples, the rate of mass changes was highest after the initial exposure, and then decreased with additional exposure time. The mass change of Zircaloy (~1%/month) was approximately three times higher than that of the coated SiC-SiC samples (~0.3%/month).

Optical microscopy and SEM was used to characterize the samples after exposure. The SiC-SiC samples showed some discoloration, and this was observed on both coated and uncoated samples. Small particulates and other debris were also observed on the surfaces of the samples. Representative optical images of the samples surfaces after exposure are shown in Figure 61.

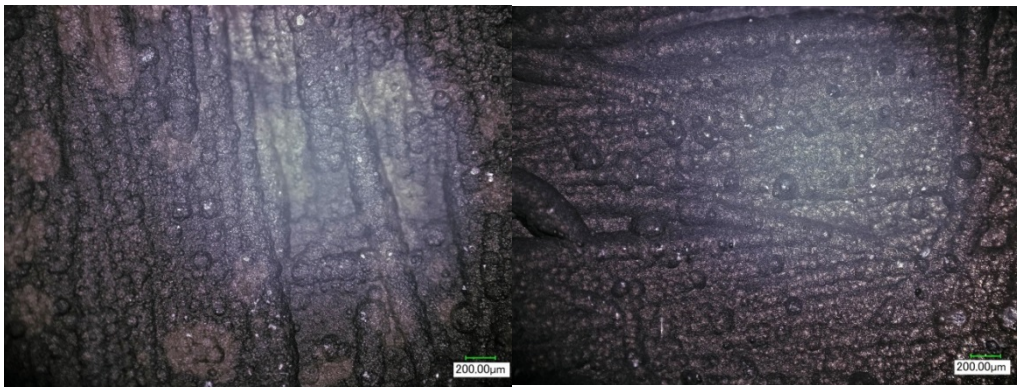

Figure 61: Surface discoloration observed for SiC-SiC samples exposed to autoclave testing

The uncoated samples showed evidence of chipping and material loss at the cut edges which was not observed on the coated samples. Examples of this chipping are shown in Figure 62, and this material loss could explain the reduction of mass that was observed for these

samples during the autoclave exposure (the mass loss was a results of actual chipping away pieces of material, rather than accelerated corrosion and dissolution of material).

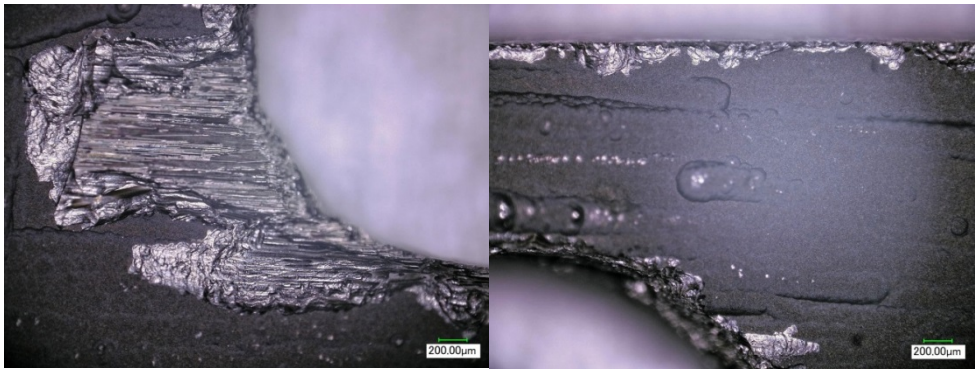

Figure 62: Chipping observed at cut edges for uncoated SiC-SIC tubes exposed to autoclave testing

SEM analysis was also performed, and EDS was used to identify the particulates observed on the sample surfaces. The particulate material included carbon deposits, salt deposits, and metal deposits (likely arising from the Zircaloy material being tested concurrently). Results of this EDS analysis are shown in Figure 63.

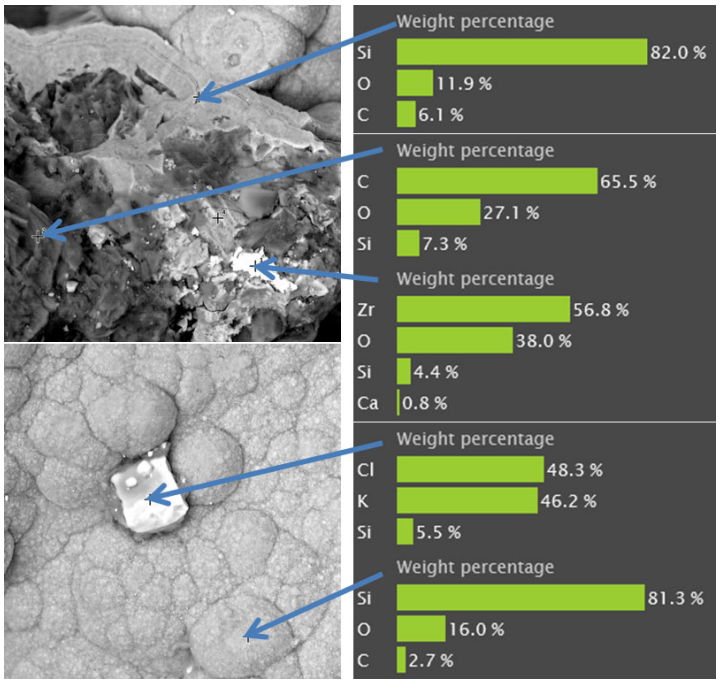

Figure 63: Composition analysis of particulates observed on SiC-SiC samples following autoclave testing (EDS data from SEM)

5. Cladding Tube Characterization (Subtask 5)

Fabrication of a range of candidate structures for SiC-based fuel cladding was demonstrated, and samples were produced and characterized. Internal pressurization was

applied via expanding plug tests, and external pressurization was simulated using C-ring compression tests. Hermeticity was measured using a helium leak detector, and thermal conductivity was measured using laser flash analysis. For these ceramic composite materials, the investigation includes analysis of micro-cracking, and effects of stress applications on the hermeticity. To further this investigation, complimentary characterization techniques, including acoustic emission detection and digital image correlation were also used, through collaboration with the University of South Carolina. These results helped establish the relationship between small scale cracking events which occur before the PLS, tube structures, and impermeable behavior.

5.1. SiC-SiC Tube Mechanical Performance

Hoop strengths of tubular samples were measured using expanding plug and C-ring testing, and monotonic axial tensile testing was used to obtain axial strength. Expanding plug testing followed procedures described in the literature, and used a polyurethane plug with 95 durometer hardness and specimens of approximately 25mm length. Strain was monitored during testing. The C-ring test procedure is described by Jacobsen et al, and follows similar guidelines to those established for monolithic ceramics in ASTM C1323. For the C-ring test a thin ring, approximately 1-2 times the wall thickness, is cut from the tube and a small gap, no bigger than ¼ of the circumference, is cut into the ring to yield a C-shaped specimen. Uniaxial load, 90º from the gap, is applied to the specimen until failure, Figure 64a. The specimen experiences a mixed mode stress state as a result of the applied load where the outer portion of the specimen is in tension and the inner portion is in compression. The maximum tensile stress is experienced at the outer surface of the specimen. Most testing was performed on tubes sized for LWR cladding applications (~7.5-8.0mm inner diameter), although some larger samples (inner diameter ~19mm, fabricated using the same approach) were also measured. Specimen rings were cut to 2-3 mm thicknesses and subsequently polished. Between five and ten specimens were typically measured from each tube sample.

In expanding plug testing, an internal pressurization is applied to the test specimen through the use of axially applied load to a polyurethane plug. The plug is compressed axially using two push rods, causing radial displacement of the plug and a tensile force on the inside wall of the composite, Figure 64b. This plug is made of a material with an ideal Poisson's ratio that allows axial load to be properly transmitted to hoop stress with little or no axial stress applied. Reported stresses are calculated at the OD of the cladding using thick walled cylinder theory.

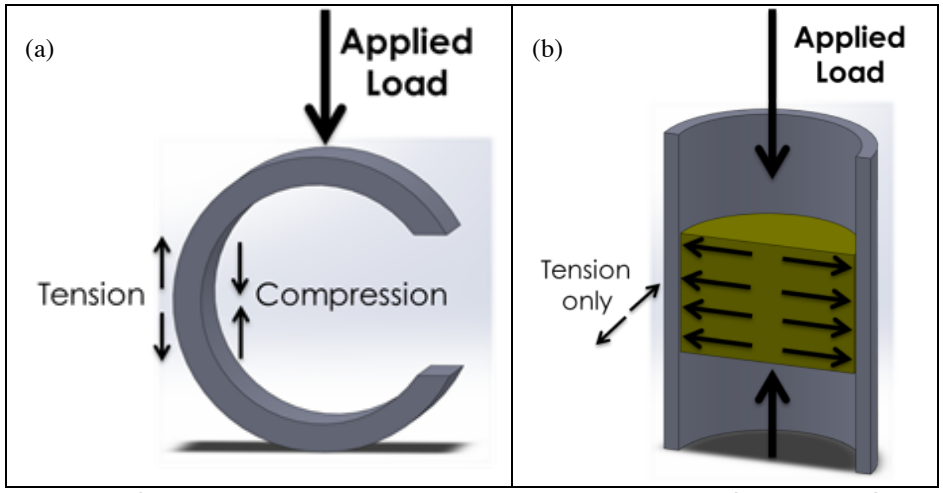

Figure 64: Direction of applied load and resulting stress distribution for the (a) C-ring test and (b) expanding plug test.

Axial tensile testing was performed according to ASTM C1773. Specimens of between 100-120mm length were epoxied at the ID and OD into a passive gripping fixture, leaving a 50mm gauge section. A U-Joint helped ensure proper alignment, which was measured using 4 or 8 strain gauges mounted in 90 degree intervals.

Nuclear grade GA fabricated SiC-SiC$_f$ tubes were used for mechanical testing of composite properties. Data for monolithic SiC obtained from Hexoloy is also presented as a control. Composites and monolithic were fabricated with a wall thickness of 1-1.5 mm. The composite material was fabricated specifically for use in validation of fabrication techniques and to demonstrate the benefits of a tubular composite material like increased fracture toughness and graceful failure. It is important to note that this material is not a multilayered SiC based cladding and it does not contain an inner monolithic layer, but is rather a composite only specimen. A summary of the mechanical data obtained is given in Table 15.

Table 15: Mechanical characteristics of composite in hoop direction

Test	Average Hoop UTS (MPa)	Standard Dev (MPa)	Strain at Failure (m/m)	PLS (MPa)	Elastic Modulus (GPa)	Weibull Modulus	Characteristic Strength (MPa)
C-Ring	419	54	N/A	N/A	N/A	8.9	451
Expanding Plug	418	33	.0046	182	282	11.3	448

Typical engineering stress versus displacement plots for C-ring measurements on monolithic and composite materials can be seen in Figure 65. For the Hexoloy SE tubing average C-ring ultimate tensile strength (UTS) of 300 MPa was obtained. Brittle failure was observed and specimens typically broke into several pieces. For the composite materials, improved strength and toughness is observed as evidence by the larger area under the stress-displacement plot. Average UTS for the SiC-SiC$_f$ is 419 MPa. For this plot, an initial linear elastic region is observed followed by nonlinear behavior due the initiation and propagation of matrix cracking. Post test fracture analysis demonstrates crack deflection behavior is

occurring, Figure 66. The test was typically stopped at a drop of 50% of peak load, however the composite retained ability to carry load past this point and was fully intact as a single piece.

Hexoloy

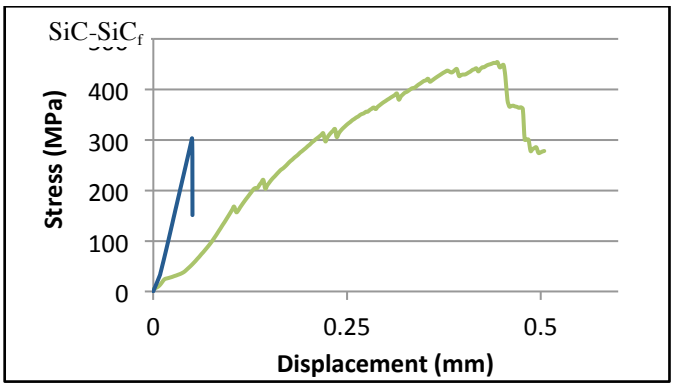

Figure 65: Engineering stress vs displacement for C-ring test.

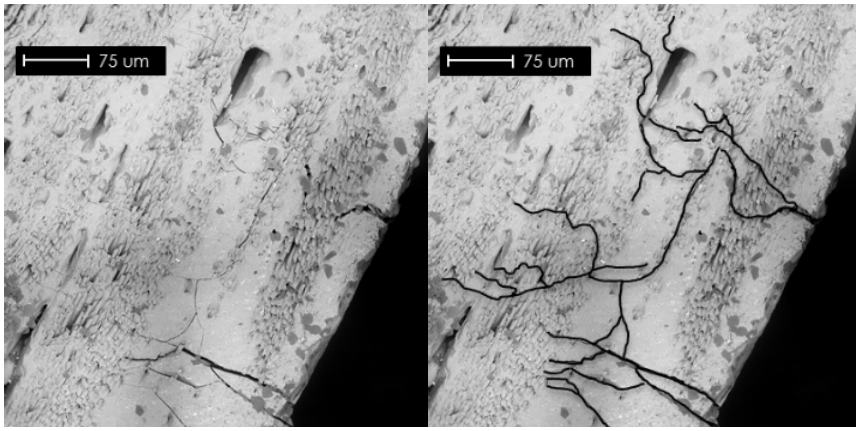

Figure 66: (a) Original cross section SEM view of a C-ring specimen at location of fracture (b) Location of major cracking has been drawn in using black lines to make more visible.

Stress versus strain plots for select expanding plug measurements on monolithic and composite materials can be seen in Figure 67. For the Hexoloy SE tubing average expanding plug ultimate tensile strength of 281 MPa was obtained. Linear elastic behavior was observed for the entire test duration and an elastic modulus of 412 GPa was obtained. Brittle failure was observed with specimens violently breaking into multiple pieces. For the composite materials, improved strength and toughness is clearly observed. Average UTS for the LWR SiC-SiC_f is 418 MPa and average proportional limit stress (PLS) is 182 MPa. The PLS is similar to what is seen in planar composites which are typically in the range of 150-200 MPa. Like the C-ring test, the engineering stress/strain plot exhibits an initial linear region until the onset of matrix cracking occurs and non-linearity due to fiber loading and crack deflection begins. Post-test fracture analysis shows the presence of fiber pullout from the matrix, Figure 67. Fiber pull out is due to weak bonding interface between matrix and fiber and is one of the primary indicators of ideal composite behavior. The expanding plug causes a breach of the composite at the end of test condition, but the composite retains its shape and remains in a single piece and can carry small amounts of residual load.

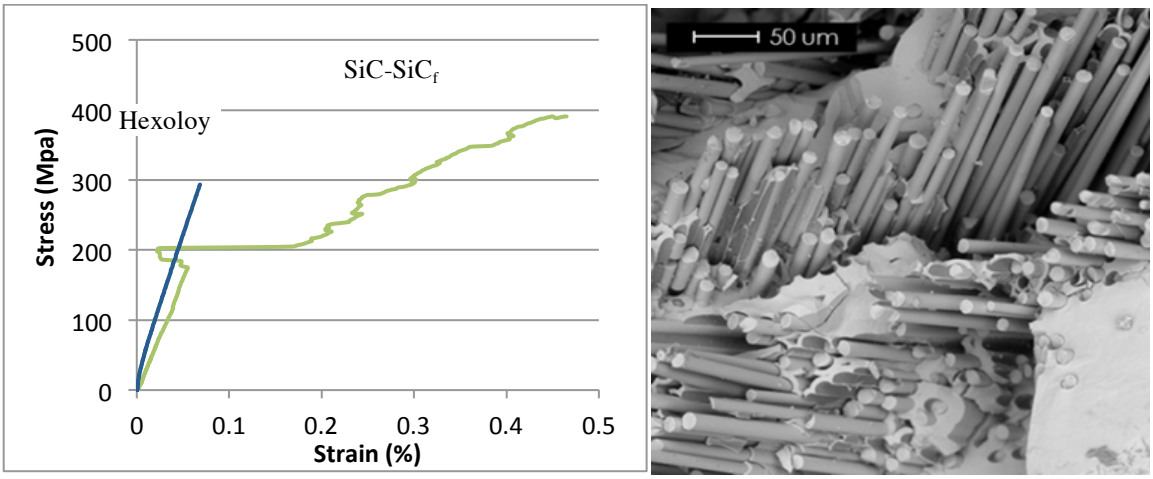

Figure 67: Engineering stress vs strain for expanding plug test and post-test fracture analysis showing fiber pull out

Two parameter Weibull analysis was used for statistical analysis of the hoops tensile strength test data. A Weibull plot of porbability versus strength can be seen in

Figure 68 for the C-Ring test. A Weibull modulus of 8.9 and a charecteristic strength of 451 MPa was obtained for the C-Ring test and a Weibull modulus of 11.3 and 448 was obtained for the expanding plug test. Weibull modulii for the tubular composites are within or better than the typical values for planar flexural specimens of 6-10 (Snead, 2007). Weibull plots for the PLS, UTS, and the difference between the UTS and PLS are shown in Figure 69.

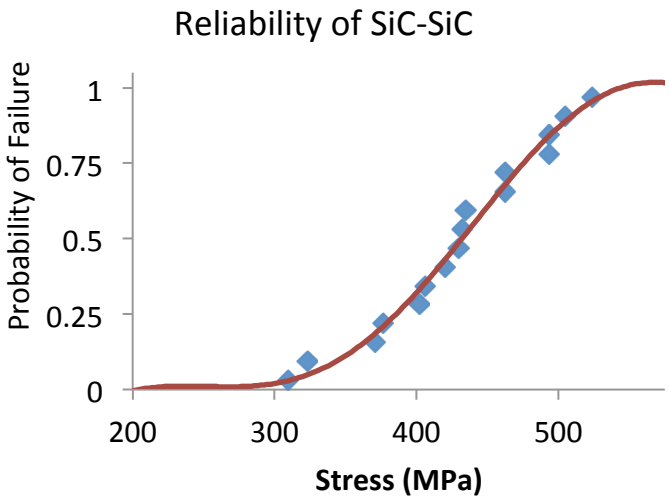

Figure 68: Weibull probability plot for ceramic composite.

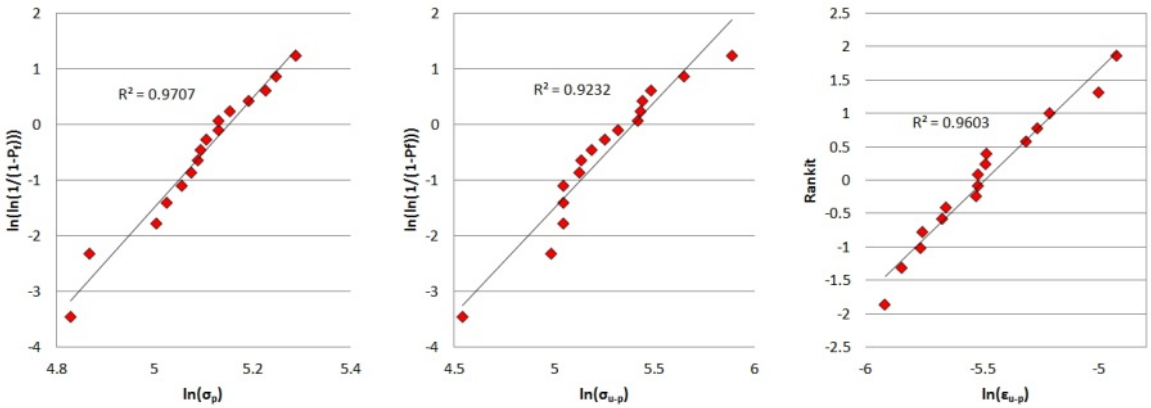

Figure 69: Probability plots for SiC-SiC stress-strain distribution variables, from left to right; PLS, difference between UTS and PLS, difference between strain at UTS and strain PLS.

In order to verify test methodology for measuring of the axial tensile strength of composite tubes, monolithic SiC and alumina rods with well-known tensile strengths were tested following the methodology in ASTM C1773. Strain was monitored during testing to ensure bending moment was below 10% during testing. An adhesive based approach was used for gripping of tubes. Using this methodology, results were found to be within 10% of the reported strengths in the literature, well within the typical strength distribution seen in ceramics.

Testing on SiC-SiC composite tubes have given average axial strengths of 235 MPa, with strain at failure in the 3000-4000 με range, Figure 70. The elastic modulus is typically 200-225 GPa. While UTS and PLS is somewhat lower in the axial direction than observed for the hoop direction; the fiber preform could be adjusted to increase strength in the axial direction, if necessary. Continued mechanical testing is being performed to fully characterize surrogate materials that were used in deliverable specimens.

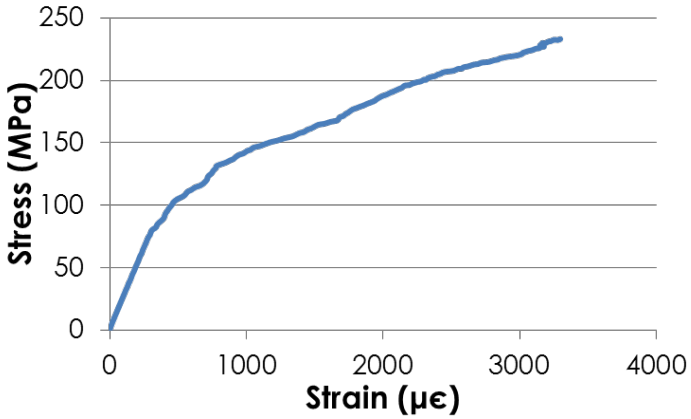

Figure 70: Representative axial tensile stress-strain curve

Hoop and axial strength measurements were obtained for tubes fabricated with a range of reinforcing fiber geometries. In a fuel cladding application, the cladding strength in the hoop and axial directions must be balanced to meet cladding performance requirements. Modeling of stresses on fuel cladding over the life of a fuel rod has shown that the peak axial and hoop

stresses are similar [6]. Stresses during operation can be caused by a number of sources, including stresses due to thermal gradients, swelling, fission gas build-up, coolant pressure, and pellet-cladding interactions. The architecture of the reinforcing fibers in the SiC-SiC composite play an important role in the relative cladding strengths in the hoop and axial directions, and SiC-SiC tube samples with different fiber structures were fabricated to investigate this effect.

An initial screening of effects of fiber structure on mechanical properties focused on hoop strength measurements with a set of SiC-SiC tubes with a higher ratio of fiber reinforcement in the hoop direction compared to the axial direction. Results are given in Table 16, and several important trends are observed.

Table 16: Comparison of UTS and Weibull properties for hoop strength measurements of different tube samples

Fiber Structure (Hoop:Axial fiber ratio)	Average UTS (MPa)	Standard Deviation (MPa)	Weibull Characteristic Strength (MPa)	Weibull Modulus	Notes
1.65 : 1	544	55	561	11.2	Baseline
1.65 : 1	419	54	451	8.9	Reduced CVI time
1.65 : 1	475	70	520	7.6	Reduced CVI time
1.35 : 1	317	73	296	5.0	Lower fiber Vf
1.35 : 1	474	92	472	6.8	Higher fiber Vf
3.0 : 1	338	72	381	5.1	Alternate fiber structure

A correlation is observed with increasing strength with increased infiltration time. For this set of samples, the infiltration conditions were kept constant, and with optimization of the CVI process, high strengths can be achieved with shorter overall infiltration times. In general, the samples with a higher percentage of fiber in the hoop direction showed higher hoop strength. Fiber volume fraction is very important to the overall performance and the ultimate strength, and reductions in fiber volume fraction led to decreased overall density, increased porosity and significantly lower strengths. Finally, two distinct approaches to the fiber preforming were investigated, and the alternate approach, despite having the highest ratio of fibers in the hoop direction showed some of the lowest hoop strengths.

For a more detailed investigation incorporating axial strength measurements in addition to hoop strength measurements, four different fiber architectures were tested, with different ratios between the fiber components in the hoop and axial directions. The ratios ranged from strongly hoop-biased to strongly axially-biased; these ratios and the resulting strength values are given in Table 17. Hoop strengths were measured using the C-ring test procedure [3], and axial strengths were obtained with an axial tensile test. Table 17: Hoop and Axial Strengths measured from SiC-SiC tubes with different reinforcing fiber architectures.

Fiber Architecture	Hoop UTS (C-ring)	Axial PLS (uniax. tens.)	Axial UTS (uniax. tens.)	Hoop:Axial Fiber Ratio	Hoop:Axial Strength Ratio
Strong hoop bias	482 MPa	59 MPa	95 MPa	1.65 : 1	5.1 : 1
Hoop-biased	331 MPa	47 MPa	93 MPa	1.3 : 1	3.56 : 1
Axial-biased	209 MPa	71 MPa	236 MPa	1 : 1.5	1 : 1.13
Strong axial bias	93 MPa	125 MPa	371 MPa	1 : 3	1 : 4.3

The axial and hoop strength results were then plotted against the ratio of fiber reinforcement parallel to and perpendicular to the direction of the strength measurement (Figure 71). For the axial strength measurements, the PLS was plotted along with the ultimate tensile strength.

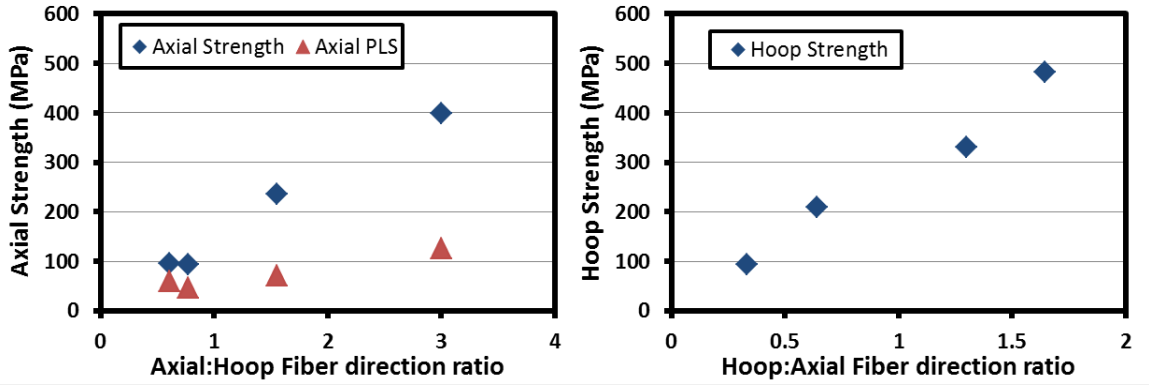

Figure 71: Axial (left) and Hoop (right) strengths plotted against ratio of fiber reinforcement parallel to and perpendicular to the direction of strength measurement

A strong correlation was expected between the amount of fiber aligned towards the loading direction and the strength of the composite in that direction, and this was observed in all the hoop strength measurements and almost all of the axial strength measurements. The trend in axial PLS values also correlated very well with the trend in axial tensile strengths. In general, hoop strengths tended to be higher than axial strengths for a given ratio of reinforcing fiber in the loading direction. The hoop strength was also observed to be more sensitive than the axial strength to a change in the fiber direction ratio, and with a given increase in the directional fiber reinforcement, a larger increase in hoop strength was observed than in axial strength.

For structures which showed the lowest axial strength (those with a strong hoop bias and the highest hoop strengths), further reductions in the axial fiber reinforcement did not appear to reduce the axial properties below approximately 50-60 MPa PLS and 90-100 MPa UTS. At these low values, it is probable that the strength is largely governed by the SiC composite matrix, and the amount of reinforcing fiber aligned in the loading direction is small enough that a variation in the angle of the fiber no longer has a large contribution to the strength. For the set of structures examined, the hoop strength continued to increase or decrease with increasing or decreasing amounts of fiber in the loading direction, and did not plateau at either high or low values. However, this effect could be a consequence of the limited range of structures examined in this work, and it is likely that fiber architectures with more

extreme hoop-axial fiber ratios would reach limitations in further increases or decreases in hoop or axial strengths. Changes in fiber architecture can also influence the relative fiber and matrix volume fractions as well as the size, shape, and orientation of the voids, so extrapolating the trends observed in this work to vastly different fiber architectures would be challenging. For fiber reinforced ceramic composites in nuclear cladding applications, the fiber architecture must be carefully selected to balance hoop and axial strengths and meet operation requirements.

Elevated temperature testing was also performed on SiC-SiC tube samples. In this work C-ring specimens were used, and mechanical performance at 300°C was compared to performance at room temperature. Specimens were heated in air and allowed to stabilize at the test temperature, and taken from the same tube sample as the room temperature test specimens. The results show essentially no change in strength at 300°C compared to room temperature. Average failure strength was 473 MPa at room temperature and 485 MPa at 300°C, although the standard deviation of the data at 300°C was higher than that measured at room temperature. The failure strengths for the different C-ring specimens are plotted in Figure 72. For both test conditions, the samples showed composite-like behavior and graceful failure.

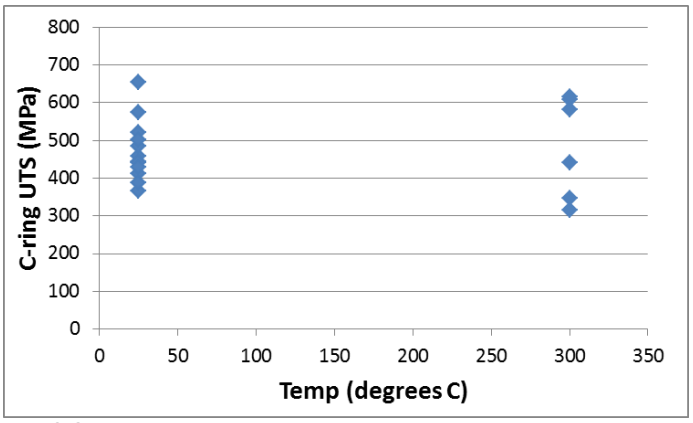

Figure 72: Comparison of C-ring hoop strength measurements at room temperature and at 300°C

One approach being investigated to improve permeability performance of SiC-based cladding is through the use of a multi-layered structure in which a monolithic layer of SiC is placed either on the outside or inside of the composite, or both. The monolithic SiC offers improved oxidation resistance compared to SiC-SiC composites, and, provided it remains uncracked, can provide hermeticity, while the composite layer provides increased strength and toughness to the cladding. As fission gas must be contained throughout the fuel life, it is important for the monolithic layer to remain intact through normal operating conditions. Ongoing modeling efforts are exploring how to optimally position this monolithic layer to best accommodate expected stresses during reactor operation.

Multi-layered tubes have been tested with either an inner or outer monolithic layer to investigate the effects of this multi-layered structure on mechanical performance. During mechanical testing, this multi-layered structure remained intact, and delamination between layers was not observed. Additional tubes composed solely of SiC-SiC composite with the same fiber architecture but lacking a monolithic SiC layer were processed in identical

conditions and tested for comparative purposes. Fully monolithic tubes were not tested in this work, but as a reference, CVD SiC has a modulus of ~460 GPa and strength ranging from 200 MPa to 500 MPa, and sintered Hexoloy SiC has a reported flexural strength of 280 MPa and modulus of 420 MPa at room temperature. Hoop strength results for both multi-layered and all-composite tubes are presented in Table 18. Weibull analysis was performed on the C-ring results, and Weibull moduli are also reported in Table 18. For these tests, ten specimens were tested for the inner monolith structure and the corresponding all-composite structure as well as the outer monolith structure. Weibull modulus values for these samples range from 4.6 to 7.9. Only five specimens were tested from the all-composite structure corresponding to the outer monolith structure, and it is believed that this smaller specimen set is the reason this sample had a higher Weibull modulus, of 12.1. These values are similar to those reported in the literature for SiC-SiC composites (between 3.7 and 11.0). For the inner monolith and corresponding all-composite samples, the reinforcing fiber architecture used is the same as the axial biased architecture used previously. The outside monolith and their corresponding all-composite tubes were larger than typical LWR cladding diameters (~19mm inner diameter); however, the fabrication process for these tubes was essentially identical to that for the smaller tubes, the fiber structure was representative, and similar results would be expected for an LWR-sized tube. The fiber architecture for the outer monolith and corresponding all-composite structures was hoop-biased. Due to the differences in reinforcing fiber architecture, comparisons between the strength values of the overall inner and outer monolith structures cannot be made; in this work these strength values should only be compared with their corresponding all-composite tube samples.

In the case of the multi-layered materials both C-ring data and expanding plug data are provided due to the non-uniformity of the tube, which can cause greater deviations from hoop UTS in the c-ring test. For the expanding plug test, stresses at both the OD and ID are calculated and reported, but this calculation assumes a uniform material (rather than multi-layered). The differences in elastic modulus and Poison's ratio between composite and monolithic cause different stress profiles between the layers and as such the reported values should be treated as approximations only. In particular, when compared to a uniform material approximation, actual stresses in the monolithic layer would be higher than those in the composite layer, due to the higher modulus of the monolith. More detailed FEM analysis would be needed to provide a more accurate calculation of the stress distribution through these layered cladding structures.

For the case of the inside monolith, the UTS as measured by C-ring testing is slightly lower than the corresponding composite only UTS. The PLS of 140 MPa, located at the inner diameter, corresponds to the cracking of the inner monolith layer. Stress versus displacement for the C-ring test for these specimens can be seen in Figure 73(a). The C-ring test puts the OD of the composite in tension and the ID in compression and as such it is both expected and experimentally observed that the stress-displacement behavior for the inner monolith specimen is very similar to the composite only, as the tensile stress is being primarily applied at the composite layer in both cases. While the overall shape and UTS are very similar, a higher displacement at UTS is observed on average for the all composite specimen. This suggests

that the addition of the monolith causes some loss of toughness in the specimens due to reduced fiber fraction, but further experiments are needed to verify this.

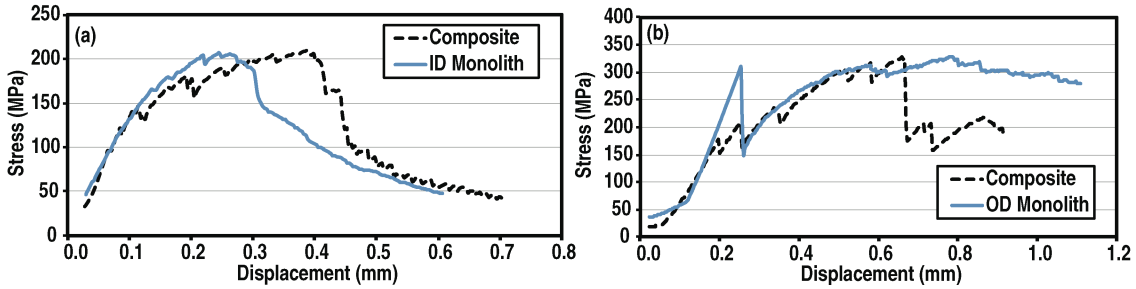

Figure 73: (a) Representative hoop stress versus displacement as measured with the C-ring test for inner monolith material and corresponding composite only, (b) Representative hoop stress versus displacement as measured with the C-ring test for outer monolith material and corresponding composite

For the outside monolith structure, the UTS is closer to the corresponding composite-only specimen suggesting that the application of the outside monolith has little effect on the composite layer itself and once the monolith layer is breached it behaves similarly to a composite only specimen. This observation is supported by C-ring testing seen in Figure 73(b). For the outside monolith specimen an initial linear elastic region is observed as the monolith layer is loaded to failure. Once the monolith layer has failed the load redistributes onto the composite and the stress-displacement behavior becomes very similar to that observed for the composite-only specimen. For both the outer monolith and inner monolith specimens, there is significant additional load-carrying capacity after the PLS is reached, and composite behavior is observed.

Strain was measured through use of strain gauges on the OD of the composite, and the stress versus strain plots for the expanding plug testing performed on the multi-layered tubes can be seen in Figure 74. Of particular interest in these plots is the shape of the stress strain plot at, and just following, the PLS.

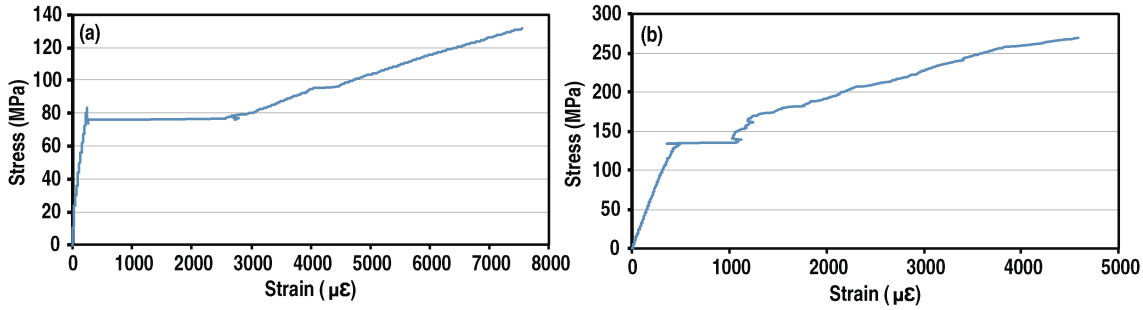

Figure 74: (a) Representative hoop stress versus strain as measured with expanding plug test for inner monolith material, (b) Representative hoop stress versus strain as measured with expanding plug test for outer monolith material.

The PLS can be determined at both the outer and inner surfaces of the tube (these are listed in Table 18), and despite the dissimilarity in PLS values seen in the plots due to the

difference in location of the monolith (inner versus outer), in both cases the monolith fails at approximately 130-140 MPa. Once the monolith fails, a rapid redistribution of the strain in the system takes place due to a significant reduction in the ability of the monolith to carry stress/strain. The effect is particularly noticeable in the case of the inner monolith structure where a large jump in strain is observed at the OD of the composite once cracking in the inner monolith occurred. As stress is highest at this inner surface, this means a larger redistribution must take place. This data highlights the advantage of using a monolith on the outside for the simple case of internal pressurization of a tube.

Table 18: Mechanical data for hoop direction properties for two different multi-layered architectures and corresponding composite only tubes (Standard deviation given in parentheses)

Architecture	UTS C-Ring (MPa)	Weibull Modulus	PLS -Expanding Plug (MPa)		UTS -Expanding Plug (MPa)		Modulus - Expanding Plug (GPa)
Inside Monolith	174 (28)	7.0	OD= 92 (6)	ID= 140 (7)	OD= 152 (8)	ID= 231 (9)	278 (20)
Composite	209 (24)	7.9	N/A		N/A		N/A
Outside Monolith	311 (59)	4.6	OD=129 (10)	ID=158 (12)	OD=271 (2)	ID=332 (3)	288 (13)
Composite	304 (14)	12.1	N/A		N/A		N/A

For SiC-based accident tolerant fuel under operating conditions, the actual stress distribution would be much more complicated due to thermal gradients and irradiation induced swelling. As a consequence, no definitive conclusions can be drawn from this data alone, and a more comprehensive assessment of these complex conditions is needed. However, the C-ring and expanding plug test methods used here can still provide valuable basic strength information, to help evaluate all-composite structures and more complex multi-layered cladding designs.

The measured mechanical properties of the SiC-based tubular structures were evaluated to determine if correlations existed between different properties. As with the similar analysis performed on the planar composite samples, no strong correlation was observed between different mechanical properties (Figure 75).

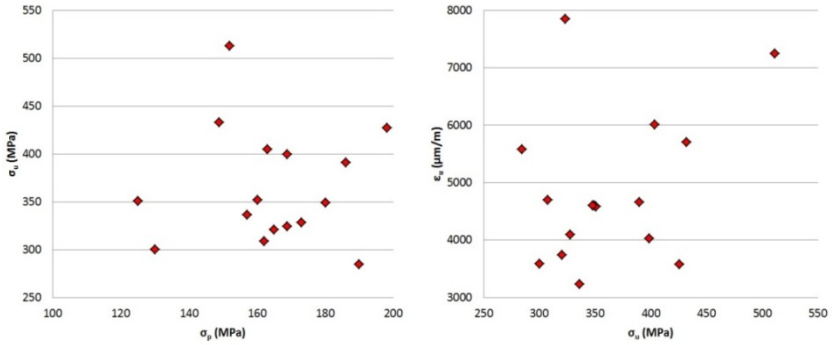

Figure 75: Scatter plot of PLS vs. UTS (left) and UTS vs. strain at UTS (right)

Experiments have been performed to understand the signal and threshold of acoustical emission test sensitivity. A series samples were used to debug the system. The procedure now established indicates that acoustical emission signals are found to start at > 130 MPa , which is about 80% of the proportional limit stress, consistent with expectations. Figure 76 shows the a graph of the capability established up to 14,000 psi. This has now been extended to ~ 20,000 and is able to follow the sample all the way to failure.

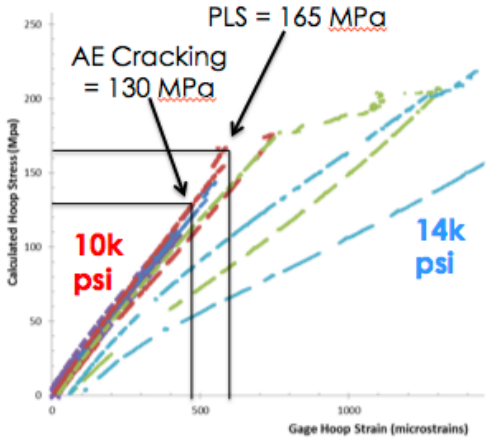

Figure 76: Stress-strain curves derived from acoustical emission and strain gauges, respectively

In addition, the hydrostatic pressure burst capability has been shown to have a good correlation with the cumulative acoustical energy signal. This pressure test rig uses a piston-type hydraulic pressure generator to pressurize oil inside flexible rubber tubing that is placed inside of the SiC-SIC tube. It can accommodate specimens from a few to 30 centimeters in length. The hydrostatic hoop strain measurements show clean signals returning to the baseline as the composite is loaded with successively higher pressures. This data is shown in Figure 77.

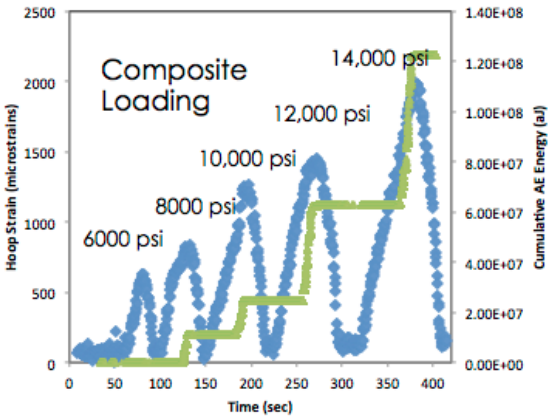

Figure 77: Plot showing successive loading of a sample as measured by digital image correlation (blue), and cumulative acoustical emission (green).

The high pressure burst test rig has been fully developed and uses a piston-type hydraulic pressure generator to create internal pressure via hydraulic oil inside a flexible rubber tubing. It can reliably measure specimens as small as one inch to minimize material needs and thus facilitates sufficient numbers for statistics. Measurements of proportional limit stress, hoop stress and stress versus strain from this setup are consistent with expanding plug measurements and provide more confidence in the values since this is an independent setup. Digital image correlation used in conjunction with the test rig allows for non-contact measurements of the outer surface strain. Refinement of the analysis has yielded better data by optimizing the exposure times, increasing the pressure more slowly and applying filtering. Simultaneous strain gauge measurements track well with the DIC measurements. Depending on the sample, the microstrains measured are 2000-4000, with an error on the order of 150. This work has been performed with University of South Carolina.

5.2. SiC-SiC tube thermal characterization

Whether cladding designs have the monolithic layer on the inside or outside, it is important to characterize the dependence of the thermal conductivity on this parameter. Experiments have been performed on all-composite tubes as well as tubes with varying monolithic layers. These include tubes with a 150 to 300μm SiC overcoat and tubes composed of a composite layer surrounding a 400 to 500μm hexoloy inner tube. Measurements are performed on a laser flash system with a split cladding tube, meaning the tube is cut in half with each tube specimen providing samples having a hemispherical cross section. The measurement is performed in the same way as for a planar sample, with an application of a geometric correction factor to account for tube curvature. This factor has already been established through experiments with surrogate materials, and details have been published by Zhang et al.

Thermal conductivity values for as-fabricated, all-composite tubes varied as a function of density, infiltration time, and fiber structure. There is a general trend of increasing thermal conductivity with increasing density. Increasing density is obtained through increased infiltration time (assuming constant infiltration conditions are used), so infiltration time also correlates with increasing conductivity. However, optimized infiltration can reduce infiltration time while still

achieving sufficient density for mechanical and thermal performance. A plot of thermal conductivity at room temperature as a function of tube density is given in Figure 78 for some tubes examined in this work.

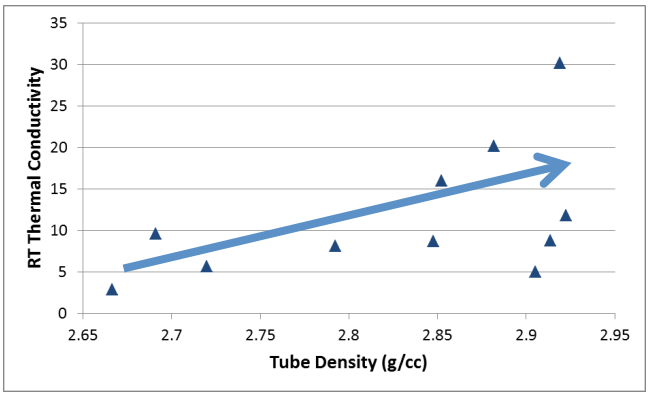

Figure 78: Thermal conductivity plotted against tube density, showing trend of increasing conductivity with density

For multi-layered tubes (those with a monolithic layer on either the inside or outside of the tube), thermal conductivity values were measured to assess the impact of the monolithic layer on the thermal conductivity. Tube samples were measured before and after the application of a monolithic SiC over-coating. As with the fiber architecture comparison, thermal conductivity values have been normalized to density to isolate the over-coating effect. The monolithic SiC coating resulted in an increase in thermal conductivity of roughly 40%, and these results are shown in Figure 79.

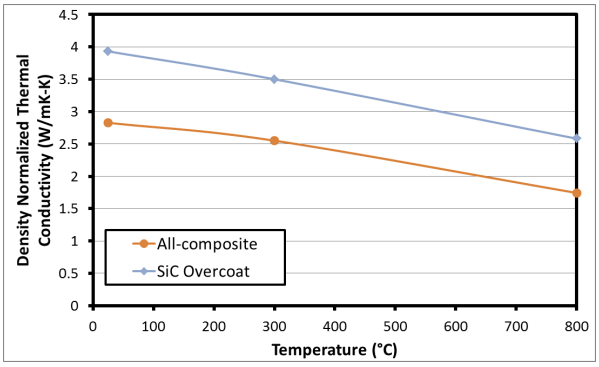

Figure 79: Thermal conductivity comparison between an all-composite tube and one with an outer SiC overcoat

An even larger change in thermal conductivity was observed for samples with a thick inner monolith layer structure compared to a fully-ceramic composite. For these samples, the total thickness was ~1.5 mm, and thermal conductivity was again normalized to density. Two different versions of the inner monolith sample were fabricated; in one the inner monolith represented roughly 30% of the total wall thickness, and in the other the inner monolith represented a larger fraction of the overall thickness, roughly 35%. Results are shown in Figure 80. The fact that the inner monolith duplex structure has higher conductivity is consistent with

the fact that monolithic SiC has a significantly higher thermal conductivity than SiC-SiC composite (roughly seven times higher when comparing Hexoloy SE to a CVI SiC-SiC composite). With increasing volume fraction of monolithic SiC through the wall thickness the thermal conductivity increases, even when normalized to samples density.

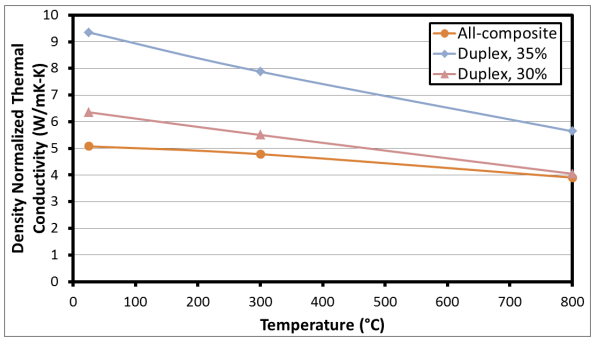

Figure 80: Thermal conductivity for all-composite versus duplex tubes.

5.3. SiC-SiC tube permeability measurements

The holder for tubular specimens is similar in principle to the planar specimen holder. The tube nominal outside diameter is 9.5 mm and lengths up to 0.75 meter (30in) long can be accommodated. The planar and tubular specimen holders are interchangeable and utilize the same setup described for planar specimens.

The tubular specimen holder was characterized with both a smooth and a sand blasted solid stainless steel (SS) rod. The sand blasted SS rod simulated the surface finish of a polished SiC CMC tube. The surface finish results are displayed in Figure 81. The surface profilometry of the as-is SS is very smooth (<1μm Ra). The polished SiC CMC and the sand blasted SS solid rod have comparable surface finishes.

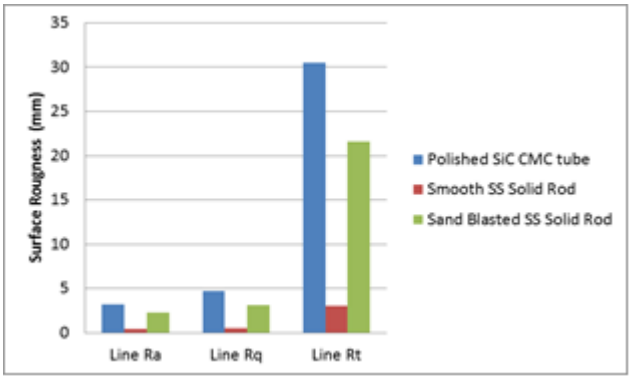

Figure 81: Surface profilometry for tubular setup

As expected, the surface finish has a significant impact on the permeability through the o-ring sealing section. The double o-ring seal over the smooth SS solid rod has the lowest leak rate results of <1.0E-12 atm cc/sec from room temperature (RT) to 300C. The tests were run for at least 70 hrs at RT and 1 atm ΔP without experiencing helium break through the o-rings.

The specimen was subjected to an additional 114 hrs at RT and 11 atm ΔP without helium breakthrough. The specimen was leak tested at 300C under 1 and 10 atm ΔP without helium breakthrough during 24 hrs for each test. A RT leak test was performed on the cladding portion of a SiC CMC tube specimen (Figure 82). One end of the SiC CMC tube was sealed with a SS impermeable plate plus Epotek H74 epoxy. A baseline test with a mSiC tube (Hexoloy from Saint-Gobain) was also obtained.

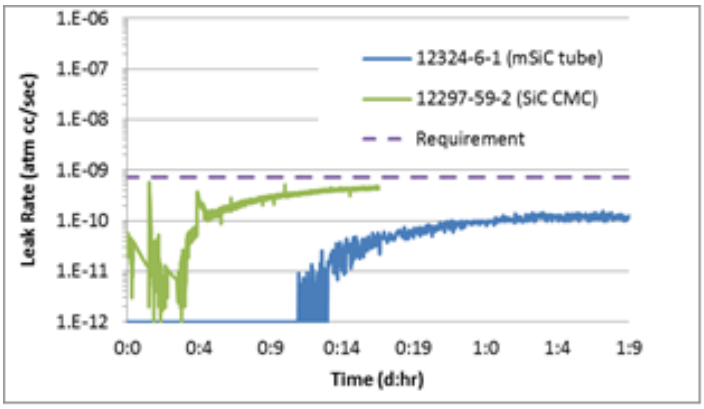

Figure 82: Leak rate comparison of a mSiC and a SiC CMC specimen at RT

A separate high temperature test was conducted on a sand blasted SS rod and a polished over coated SiC CMC tube resulting with similar leak rates in the E-9 atm cc/sec range at 300C. This value represents the upper limit for the double o-ring seal under this surface roughness condition at high temperature. The overcoated SiC CMC tube had a CVD joint on one end.

Tube specimens were fabricated for additional testing of incremental stress applications followed by permeability measurements. These specimens were composed of a composite tube roughly 5 inches long and 10.8mm outer diameter. The wall thickness was ~1.35mm, and consisted of a ~1.0mm thick composite layer, with a thin inner monolith (~100μm thick), and a thicker outer CVD SiC monolith (~250μm thick). Cross-section images of this specimen are shown in

Figure 83.

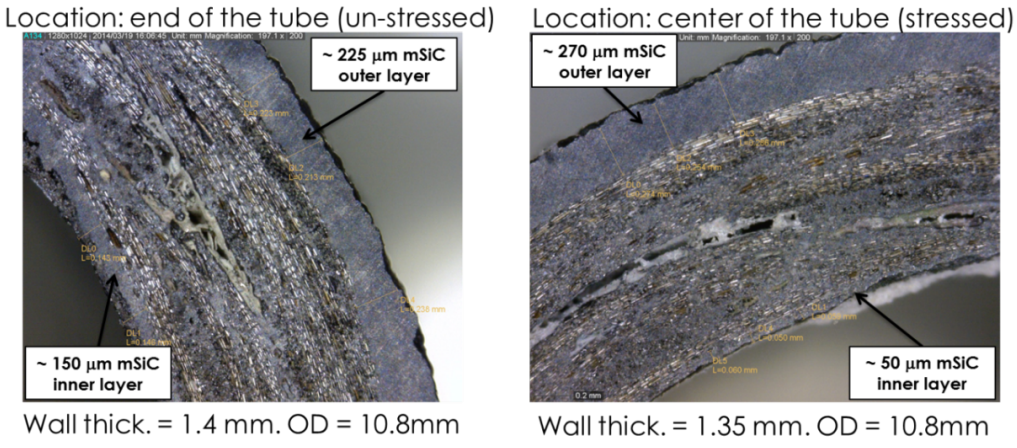

Figure 83: Cross-section of multi-layered SiC-SiC tube used for permeability tests

For the as-fabricated sample, a permeability test was performed for six days with no helium breakthrough at room temperature. The leak detector reading never rose above the 1.0 x 10^{-12} atm/cc-sec reading which is the baseline lowest reading level for the detector used, and well below the permeability requirement.

This specimen was then subjected to hoop stress applications through the use of an expanding plug. After each stress application, a permeability test was performed. Stresses through the sample wall were calculated using two methods. First, as the wall thickness was greater than 10% of the inner radius, a thick walled approximation was used. The equation used for the thick-walled approximation is given as follows, and gives stress as a function of radial position through the tube wall.

$$\text{Thick-walled Stress Equation: } \sigma_c = [(p_i r_i^2 - p_o r_o^2) / (r_o^2 - r_i^2)] - [r_i^2 r_o^2 (p_o - p_i) / (r^2 (r_o^2 - r_i^2))]$$

This gives a rough approximation of the stress through the tube wall, but does not consider the varying structure through the wall thickness (monolithic and composite layers). To account for this, a representation of the tube structure was modeled using ANSYS, and the FEA results were used to predict the stresses as a function of position through the wall thickness.

The applied mechanical loads and corresponding internal pressures are given in Table 19, along with calculated inner and outer diameter stresses using the thick walled approach. Leak rates were measured after each stress application, and the measured leak rates as well as the permeability test duration are also given in Table 19. Permeability was maintained until at least an internal pressure of 38.3 MPa, and was lost between 38.3 MPa and 45.8 MPa.

Table 19: Leak rate measurements as a function of applied stress

INSTRON Load (N)	Internal Pressure (MPa)	ID Stress (MPa)	OD Stress (MPa)	Leak Rate (atm cc/sec)	Permeability test duration
0	0	0	0	<1.0E-12	144 hrs
674	7.8	32	23	<1.0E-12	12 hrs
1,013	15.1	53	37	<1.0E-12	12 hrs
1,366	22.1	75	52	<1.0E-12	12 hrs
1,774	30.3	101	70	<1.0E-12	12 hrs
2,175	38.3	127	89	<1.0E-12	12 hrs
2,550	45.8	151	106	>1.0E-4	Seconds

The stress profile across the cladding wall thickness as calculated using the ANSYS model is given in Figure 84.

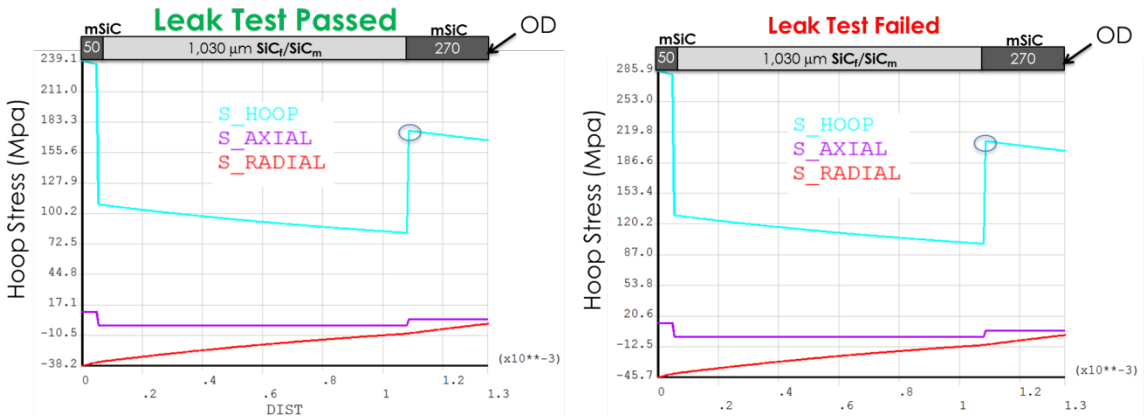

Figure 84: Stress simulation through multilayered structure before and after hermeticity was lost

From the FEA analysis, the peak stresses in the monolithic layers (which maintain hermeticity) are higher than those predicted by the thick walled approach. After the last stress application when the tube still retained hermeticity, the peak stress through the wall thickness was 127 MPa using the thick walled approach, while the peak stress in the outer SiC monolithic layer was 175 MPa as determined using the ANSYS model. Hermeticity was lost after an application of 151 MPa using the thick walled approach and between 175 MPa and 205 MPs using the ANSYS model. The exact stress at which hermeticity was lost cannot be determined, as it occurred at some point after the application of a 2175 N load and during the increase in load up to 2550 N.

A region of the same tube sample which had not been subject to applied stresses was then loaded to failure using a standard quasi-static, uninterrupted expanding plug test. The stress-strain plot for this test is shown in Figure 85, and stresses were calculated using the thick walled approach. The sample PLS was ~122 MPa on the outer surface and ~170 MPa on the inner surface, and the sample ultimate strength was 217 MPa on the outer surface and 303 MPa on the inner. The ANSYS model was also used and indicated a peak stress in the composite at failure of ~240 MPa and a peak stress in the outer monolith of ~400 MPa.

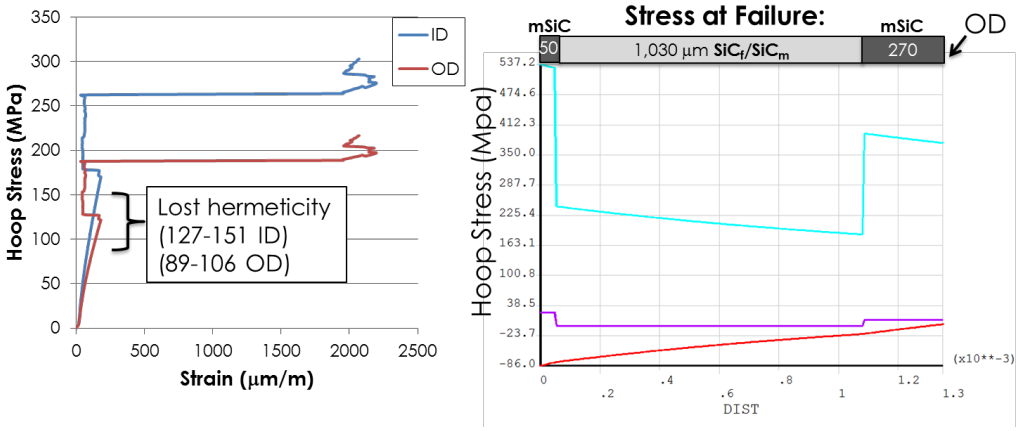

Figure 85: Inner and Outer stress-strain curves and stress simulation through the multilayered structure

Additional tube specimens containing four iterations of the monolithic outer CVD SiC layer were also fabricated for incremental loading and permeability testing. These samples contained a baseline sample (over-coated by a single thick monolithic layer), and three variants. For the first, the monolithic SiC layer was instead deposited as three individual layers, separated by thin pyrolytic carbon layers. An example of this multiple monolithic layer structure is shown in Figure 86, revealing the potential of the pyrolytic carbon layers to deflect cracks. The second variant was similar to the first, however, the carbon layers separating the monolithic SiC layers were thicker and were themselves separated by a very thin SiC layer (the separation layer was itself a multi-layer). The final variant incorporated a layer of lower density SiC within the monolithic SiC layer, but was otherwise similar to the baseline structure. One additional control sample was included, which was an all-composite tube with no over-coat. With the exception of the uncoated tube, all samples were measured and confirmed hermetic before additional testing.

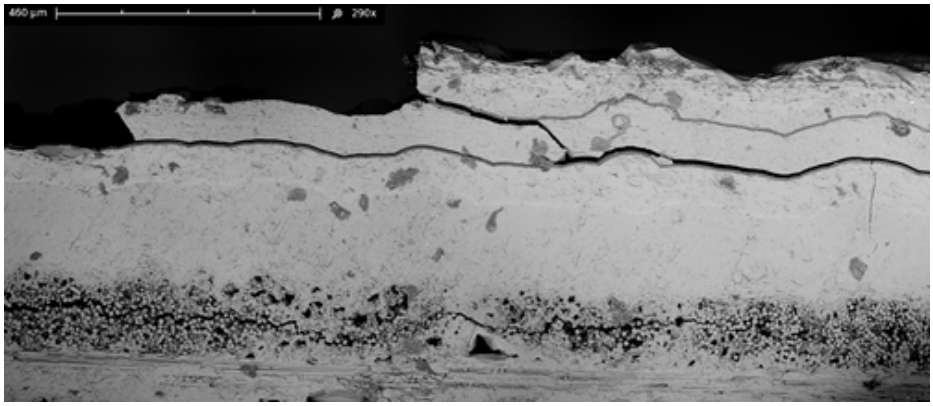

Figure 86: Multilayered monolithic layer showing crack deflection between layers

Specimens from each of these samples were first tested using the expanding plug test coupled with acoustic emission detection. This established the PLS, and the acoustic events occurring at and near the PLS. Following specimens from each sample were then incrementally loaded using the expanding plug technique to different increasing stress levels. After each load application, the specimen was rechecked for hermeticity. If the specimen remained impermeable, it was subjected to an increased stress application, and if the sample had cracked and developed a leak, it was subjected to a regular quasi-static expanding plug test until failure.

The uncoated control tube was measured first (and tested all the way to failure). The stress-strain plot and corresponding acoustic emission events are sown in Figure 87. Note that only the region of the stress-strain curve in the vicinity of the PLS is shown in this and the following plots. The PLS for this set of samples was relatively low compared to other tubes fabricated for other aspects of this project, and the PLS of the uncoated specimen tested here was 75 MPa, which was typical of this set of samples. Also of note is the number of acoustic emission events occurring at low stresses (below the PLS), starting around ~40 MPa.

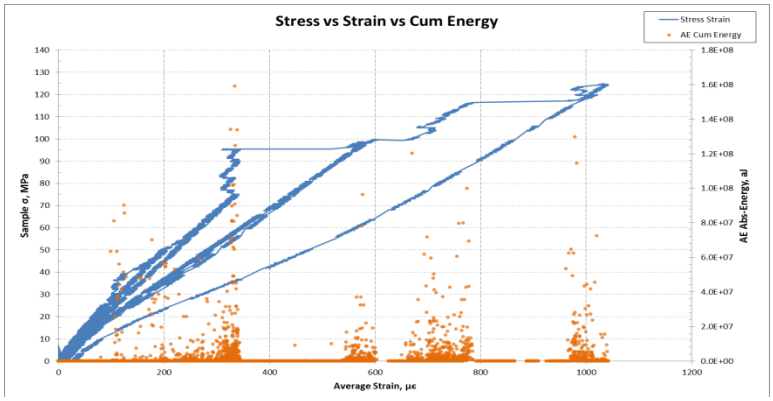

Figure 87: Acoustic Emission events and Stress-Strain plot for an uncoated SiC-SiC tube

The baseline over-coated sample was tested in a similar way, and also tested with incrementally applied loads until hermeticity was lost. Although the PLS was ~75 MPa, major acoustic emission events occur at roughly 50-55 MPa, which coincides with the point at which hermeticity was lost. The stress-strain curves for the acoustic emission tests and for each incremental loading test are shown in Figure 88, and the stress range at which hermeticity was lost is highlighted in yellow.

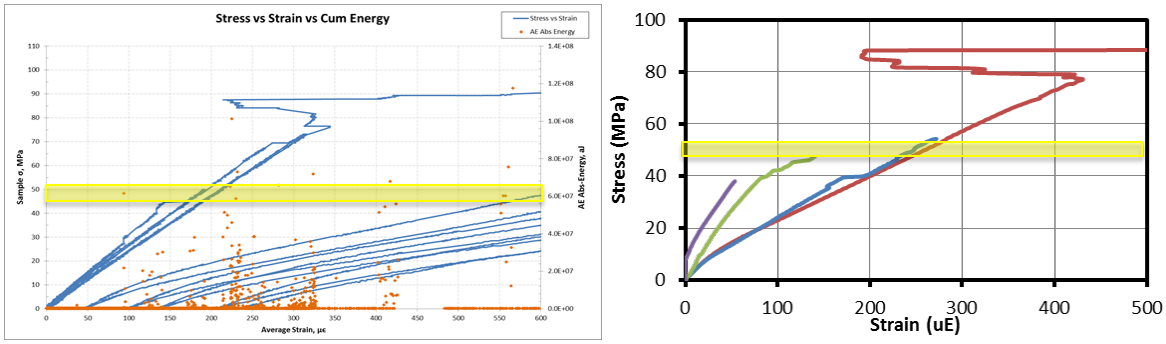

Figure 88: Acoustic emission results and stress-strain plots for baseline over-coating method

The first over-coating variant substituted three individual monolithic layers for the single layer in the base line case, and the three layers were separated by pyrolytic carbon layers. Here the PLS was roughly the same as in the baseline case (~80 MPa), and hermeticity was lost at a stress level roughly 70% of the PLS, between 55 MPa and 60 MPa (Figure 89). This stress level was also associated with increased frequency and magnitude of acoustic emission events.

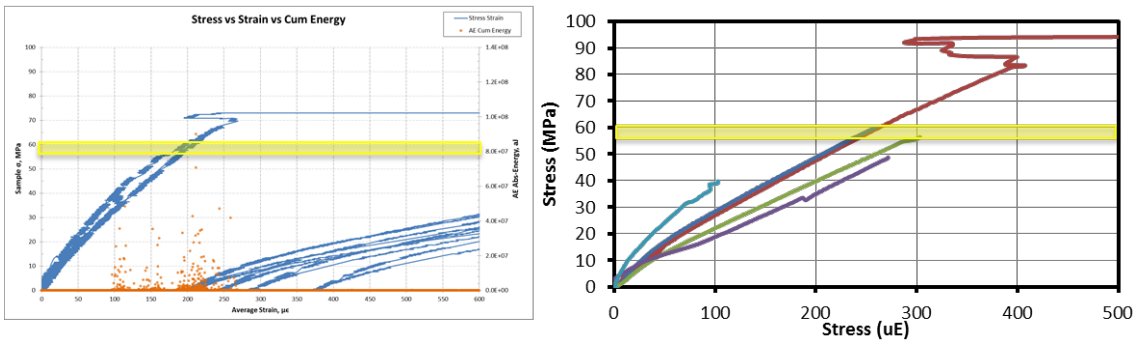

Figure 89: Acoustic emission results and stress-strain plots for first over-coating variant

The second variant, which included multiple monolithic layers and had a more distinct carbon layer separating them was found to remain impermeable to a higher stress, and only lost hermeticity at a stress level roughly corresponding to the PLS (~80 MPa). There were several larger acoustic emission events observed prior to the PLS on this sample, and prior to the loss of hermeticity (Figure 90).

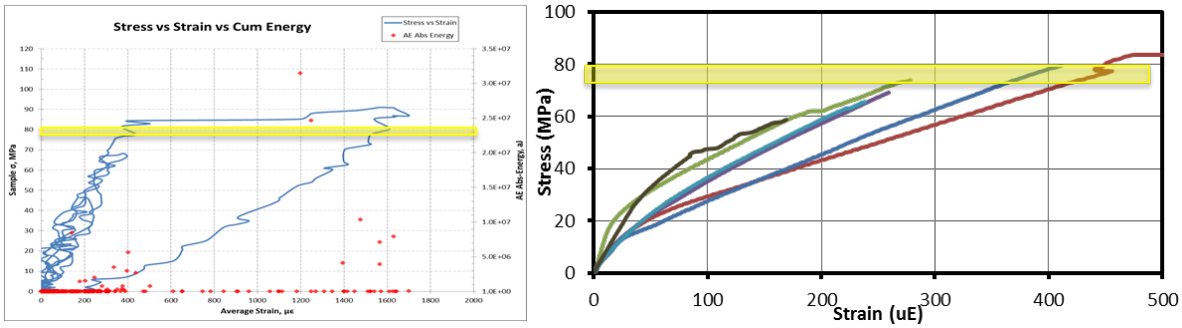

Figure 90: Acoustic emission results and stress-strain plots for second over-coating variant

The final variant, incorporating a lower density SiC layer within the monolithic layer, also retained hermeticity until the PLS (~80 MPa). As with the second variant, a number of significant acoustic emission events were recorded prior to the loss of hermeticity, and prior to the PLS (Figure 91).

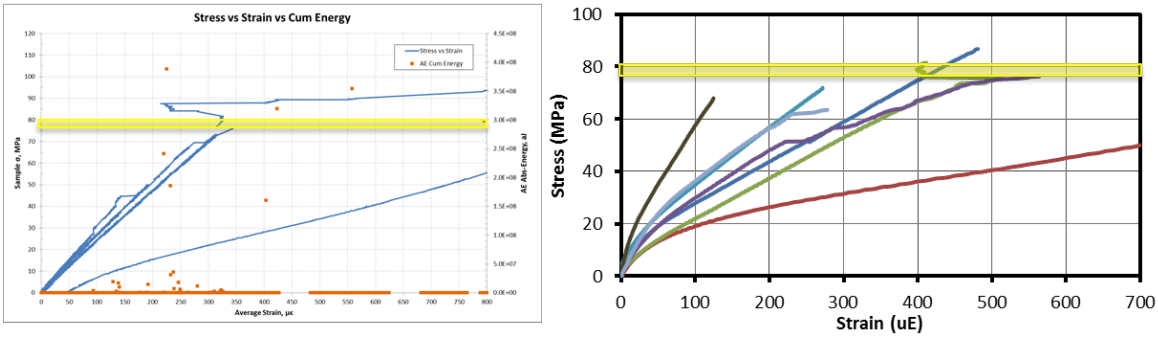

Figure 91: Acoustic emission results and stress-strain plots for third over-coating variant

Overall, the over-coating composited of multiple monolithic layers separated by thicker pyrolytic carbon layers, and the coating containing a lower density SiC layer showed better ability to undergo loading and stresses while retaining hermeticity. Increasing the stress which

can be survived while remaining impermeable is very important for a LWR cladding application, where hermeticity must be ensured to prevent fission gas release. These results show two promising routes towards improving the SiC-based cladding behavior in that aspect. A summary of the permeability readings as a function of applied stress for each structure variant tested is given in Figure 92.

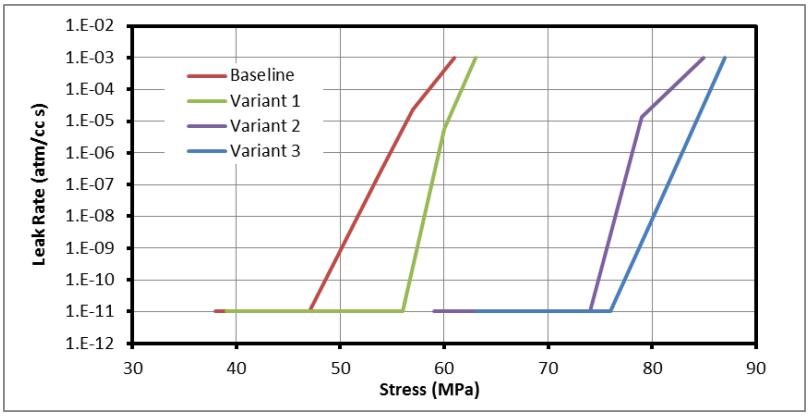

Figure 92: Permeability leak rate measurements for different tube samples as a function of applied stress

5.4. Cladding tube corrosion results and analysis

The SiC-based cladding must exhibit suitable performance in both normal operating conditions (PWR coolant water chemistry), and retain sufficient performance under accident conditions (where high temperature steam exposure is likely). Corrosion testing was performed in autoclave conditions at a Westinghouse facility, under exposure to high temperature steam at MIT, and corrosion with irradiation at the MITR. MIT results are published separately in their reports, but analysis and correlation between corrosion results and fabrication details are presented here.

5.5. Autoclave test results

SiC-SiC tubes were also subjected to corrosion testing in an autoclave (up to 30 days, performed at Westinghouse), and evaluated for mass loss and corrosion after either high temperature steam oxidation or exposure up to 291 days in the MIT reactor in a PWR water chemistry. The autoclave samples were braided with a 3:1 fiber ratio in the hoop to axial direction, and were nominally two inches long and had a small (2.5mm diameter) hole drilled at one end to facilitate support during the exposure. These samples all received a SiC over-coating after being cut to length and Zircaloy tube samples were also included as a reference. Mass change data for the SiC-SiC and Zircaloy samples is presented in Figure 93, and plotted as cumulative mass change normalized to area, and percent mass change normalized to a one month exposure.

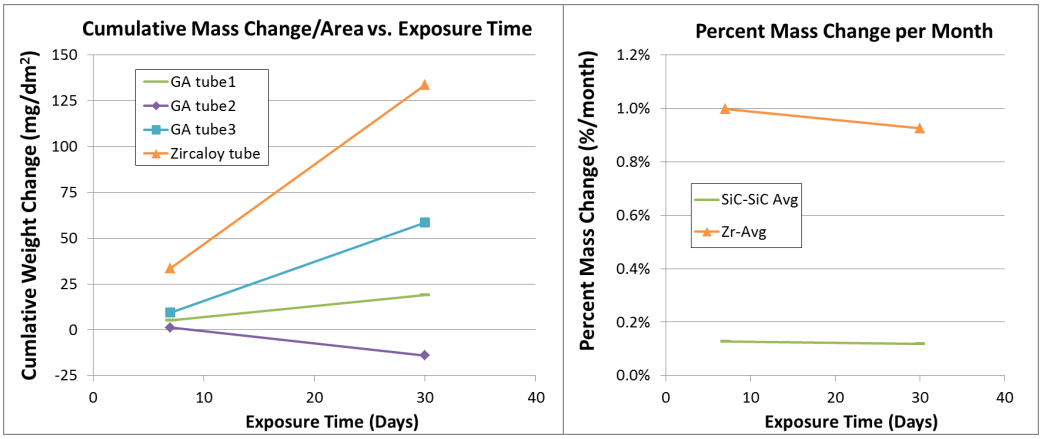

Figure 93: Cumulative mass change and rate of mass change observed for tubular samples in the autoclave test

While some variation was observed between the changes in mass of the SiC-SiC specimens, on average, the rate of mass change (when normalized to either area or exposure time) is much lower than that measured for the Zircaloy reference samples. Average mass change for the SiC-SiC tubes was ~0.1% per month, approximately eight times lower than the Zircaloy samples. This value also represents a ~3x reduction in mass change compared to the previous experiment performed on planar SiC-SiC specimens (when comparing mass loss per month numbers, see section 4.4). This is attributed to better control over the SiC over-coating process in these more recent tube samples.

Optical microscopy was used to examine the surfaces of these samples after the autoclave corrosion test. In general, the samples surfaces were cleaner than the previous planar autoclave samples and the occurrence of surface deposits and debris was reduced. The SiC-SiC was also more uniform in color, with less surface discoloration than observed previously. Some cracks were observed, and there was slight localized discoloration along these cracks, although it could not be determined if the cracks were generated during the autoclave exposure or if they had formed during either the cutting or drilling of the specimens. Chipping and material loss around cut edges (at both the ends of the tubes and at the drilled hole) was minimal. Photographs of a representative specimen are shown in Figure 94.

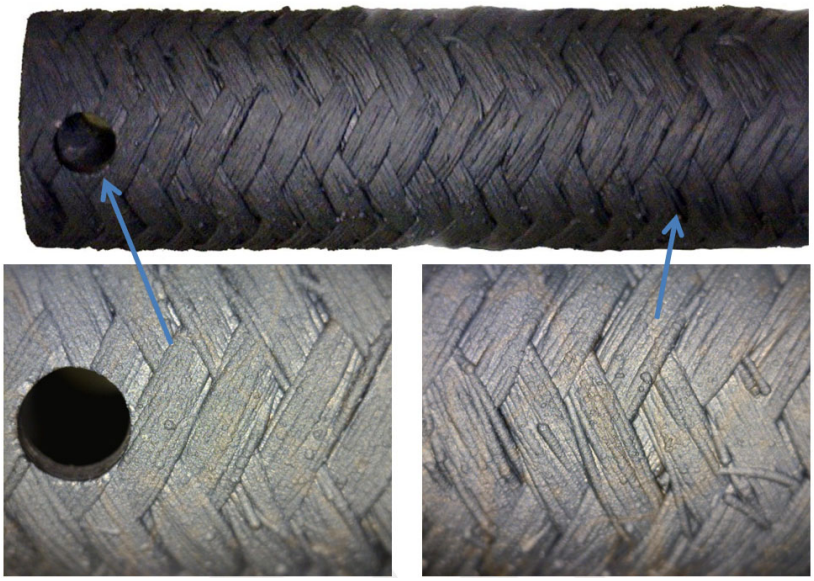

Figure 94: Full and magnified views of SiC-SiC tube sample after autoclave testing

5.6. Analysis of high temperature steam oxidation results

For the corrosion testing at MIT, samples were prepared for both high temperature steam oxidation corrosion testing, and for corrosion testing under irradiation inside the MIT reactor. A total of four specimens were tested under high temperature steam oxidation conditions (48 hours, 1400°C). Under these conditions, the two open ended specimens had mass changes of +66 mg/dm^2 and -13 mg/dm^2. The two specimens which were sealed on one end with an endplug underwent essentially no mass change, with a mass change of 0 and 1 mg/dm^2. From the post-exposure analysis performed by MIT, evidence off oxidation was observed throughout the length of the sample, and there was no significant difference in the oxidation near the surface of the samples and towards the center of the wall thickness. The oxidation observed was a very thin surface oxidation. These results indicate that the preferred pathway for oxidation is stream transport along the interconnected internal porosity. For the specimens with one closed end, the endplug prevented steam to reach the internal porosity, and the additional over-coating these samples received appears to have been sufficient to avoid steam penetration into the internal porosity form the one open end. These results suggest that steam penetration through interconnected internal porosity may not be a significant issue for final fuel rods, which will have both ends sealed with endplugs.

However, some reductions to the mechanical behavior of these oxidized samples were observed, particularly for the open ended samples. These open ended samples failed at stress levels approximately equal to the PLS of the un-oxidized samples, and also exhibited no post-PLS load carrying capability, and did not exhibit typical composite-like failure behavior. In a SiC-SiC composite, the load is transferred to the fibers once the PLS has been exceeded and the matrix begins to crack. The fibers are able to carry significant additional loads, and often the UTS is 2x to 3x higher than the PLS, and the UTS will occur at significantly higher strains than the PLS. In these open ended oxidized specimens, the fact that the failure strength was essentially equal to the PLS and only elastic behavior was observed (no pseudo-ductility), indicates that the oxidation may have affected the load transfer mechanism between the fibers

and the matrix. Oxidized samples had both the matrix and fibers fail simultaneously. One possible cause of this strength loss could be the oxidation of the carbon interphase and also potential oxidation of the SiC fibers. The oxidation of the pyrolytic carbon interphase coatings could have occurred if micro-cracking and steam penetration through the interconnected porosity led to steam attack of the interphase. This steam could also attack the fibers, which, although near-stoichiometric, are slightly carbon rich. Oxidation of the residual carbon in the fibers could have weakened them sufficiently to provide no additional load carrying capacity after the composite matrix began to fail (the PLS), and allowed the failure to proceed rapidly. Additional fracture analysis (fiber pull-out length measurements) and tests (shorter duration steam exposures and/or individual fiber strength measurements for oxidized fibers) would be needed to confirm this mechanism. This issue could be resolved through the use of protective coatings, modified infiltration and/or fiber structure to eliminate interconnected porosity, and through the use of endplugs to prevent steam penetration into the edges of tubes.

The results for the tubes with one end closed were more promising. These samples were tested with the endplug-pushout test method, to assess the overall performance of the tube, endplug, and joint. The specimen with the strong hoop-bias to the fiber structure (GACE-4, 1.65 : 1 fiber ratio in the hoop to axial direction) saw a drop in endplug pushout load of ~32%. However, the sample with the stronger axial bias (GACE-3, 0.64 :1 hoop to axial fiber ratio), only saw a reduction in endplug pushout load of 9%, which for a single test specimen, is too close to the un-oxidized push-out value to be able to conclusively determine if the oxidation had any effect. For the GACE-4 samples in particular, the failure appeared to occur within the composite layer (in the thinner region near the endplug), and MIT reports evidence of oxidation of the fibers at the fracture surface (silica formation). This could confirm the potential mechanism for the reduced behavior of the open ended specimens. Additional details can be found in the MIT report provided for this work.

5.7. Analysis of MITR corrosion results

For the MITR tests, a total of 36 specimens were delivered in two sets. The first set consisted of all open ended tubes (in three groups of eight and one group of four samples), and the second set was delivered later, and consisted of eight tubes sealed at one end with an endplug. The open ended tubes were exposed to either 154 or 291 days of exposure, and the closed end tubes were subjected to 137 days of exposure in PWR conditions in the MIT reactor.

The control (monolithic) samples were removed after 154 days of exposure, saw an average mass loss of 1.4% per month, and exhibited signs of delamination. These samples were composed of a thin-walled Hexoloy SE tube, which was coated by a CVD SiC overcoat. After fabrication of these samples, results were provided which indicated that the irradiation induced swelling of Hexoloy SiC material might be slightly higher (~8%) than that of CVD SiC material (potentially caused by the presence of some sintering additives in the Hexoloy material). Slightly larger swelling of the underlying Hexoloy SE material would result in large tensile stresses in the CVD SiC overcoat, and this could be the potential cause of the delamination observed. For these monolithic samples, the mass loss (normalized as percent change per month) is shown in Figure 95, and compared to data in the literature for monolithic

SiC tubes (composed of a single type of SiC, rather than a mix of CVD and Hexoloy in this current work). The delamination resulted in a large mass loss compared to previous results in the literature, although the differences between sample compositions mean that direct comparison are not possible.

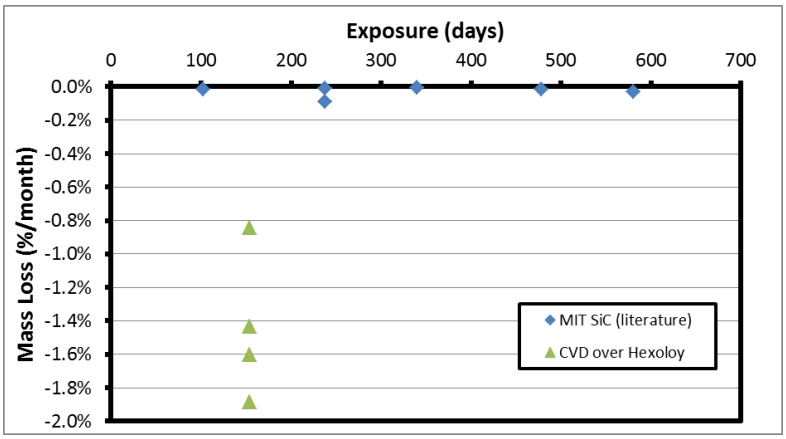

Figure 95: Rate of mass loss in the MITR observed for monolithic samples, compared to literature data

The three sets of open ended tube samples exhibited markedly different behavior, both between sets, and as a function of the variations in overcoat layers applied. Amongst the first set of tubes (GA-1), three received an additional SiC overcoat layer. Those three specimens were exposed for 154 days, and saw an average mass loss of 0.9% per month, compared to the one sample that did not receive that additional coating, which lost 1.9% per month over that same exposure duration. None of the four samples from this set which were exposed for the longer duration (291 days) received the additional over-coating, and those four saw an average mass loss of 3.0% per month, a higher rate compared to the shorter exposure. These samples also appeared to suffer from delamination and resulting material loss, so the overall mass reduction was likely due to both corrosion/dissolution, and material delamination. The GA-2 set of samples had two anomalous specimens; one from the 154 day exposure with an unexpected mass loss roughly 3x higher than others in that set, and one from the 291 day exposure, which saw a mass gain, rather than loss. These specimens were not included in the average calculations, which showed a 1.1% per month average mass loss for the 154 day exposure, and a 0.8% per month average mass loss for the 291 day exposure. For the GA-3 samples (composed of an inner monolith with an outer composite, the results were similar to the GA-2 set of samples, with 1.1% per month average mass loss for 154 days, and 0.9% per month average mass loss for 291 days. There was one sample form this set which received the additional SiC coating, and remained in the reactor for 291 days. A very minor improvement was observed in that sample, which had a 0.7% per month average mass loss compared to 0.9% per month for the samples from the GA-3 set which did not receive that extra coating. The cumulative mass loss results are shown in Figure 96, and the rate of mass loss per month is shown in Figure 97. Additional data is provided in the MIT report on this work.

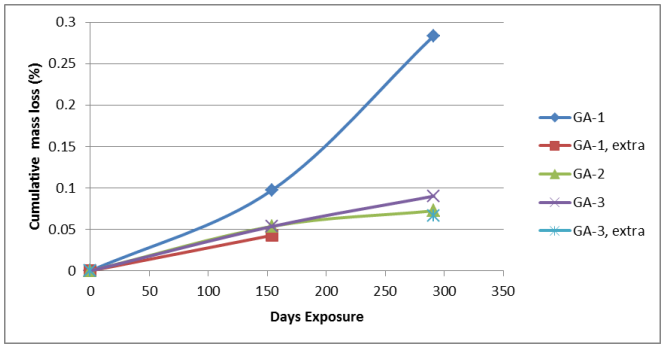

Figure 96: Cumulative mass loss for open ended samples in MITR

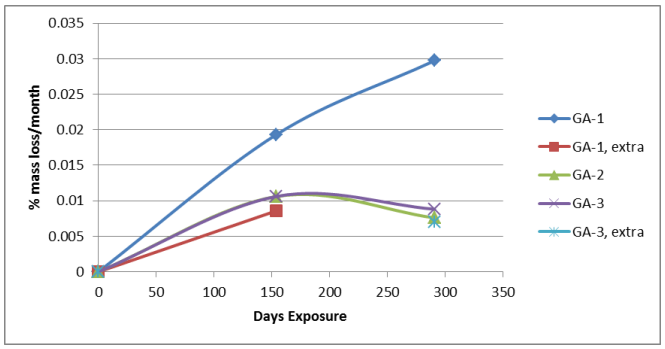

Figure 97: Average rate of mass loss per month for open ended samples in MITR

For the outer monolith open ended samples, it appeared that the largest difference was observed between those samples which received an additional SiC overcoat and those which did not. The additional overcoat (CVD SiC) led to a decrease in corrosion rate with time, rather than an increasing corrosion rate with time for the samples which did not receive the additional coating (GA-1). For the same samples with and without the overcoat (GA-1 at 154 days vs. GA-1 with the extra coating), the overcoat reduced the corrosion rate by over half (1.9% per month to .9% per month). For the samples containing an inner monolith (GA-3), it did not appear that the additional over-coating made as significant of difference, as the rate of mass loss was only slightly reduced (0.9% to 0.7% per month for 291 day exposure). Preliminary analysis indicated that the base overcoat (applied to the GA-1 samples, and some of the GA-3 samples) was not as stoichiometric as the other overcoats applied or the baseline matrix material, and may have contained some excess silicon. This could have led to unanticipated corrosion effects, including accelerated oxidation of the free silicon (to form silica), which could lead to the delamination and faster mass loss observed. Excluding the GA-1 samples which saw higher than expected mass loss, the average rate of mass loss for the remaining samples was 0.9% per month, or ~7.8x faster than the mass loss observed on overcoated tube specimens in the Westinghouse autoclave tests (0.12%/month mass loss). This indicates that the irradiation has a significant contribution to the corrosion mechanism for SiC in PWR water chemistry. Additional details of this testing can be found in the MIT report on this work.

The tubes samples with one closed end were also analyzed and exhibited varying behavior as a function of the tube fiber architecture and over-coating. Unexpected behavior was also observed in the endplug material response to the simulated PWR water chemistry. Upon removal of the samples from the irradiation test capsule, one endplug had detached

(sample GA-TC3-I-1, and one endplug had separated in the middle of the endplug (sample GA-TC3-I-6). The remaining endplugs remained attached to the tubes, but reports from MIT indicate the structural integrity and remaining strength of the endplugs was questionable.

The overall mass change and rate of mass change for the samples sealed at one end with an endplug is shown in Figure 98. The closed end samples with the hoop-biased architecture (GA-TC3-I-5,6,7,8) showed a ~50% higher rate of mass change (2.2% per month) than the corresponding samples with a more axially-biased fiber architecture (1.5% per month). This is consistent with the results for the same architectures in the MIT high temperature steam oxidation test, where the axially-biased samples performed better under steam oxidation than the hoop-biased samples. Differences in fiber architecture could lead to differences in residual porosity, and this could cause the more hoop-biased specimens to be more susceptible to steam or water penetration into the porosity, and lead to higher corrosion and mass loss rates. The best performing samples (amongst both the open ended and closed ended samples) were those axially-bias closed end tubes which received an additional SiC coating composed of some SiC particulate and CVD SiC. These exhibited a mass loss rate roughly 3x lower than the corresponding tube architecture which did not receive that additional coating (0.6% per month compared to 1.5% per month). These mass loss rates under irradiation are between 5x and 18x higher than those observed for the autoclave samples (~0.12% per month), although no sealed specimens were tested in the autoclave. It is also not clear from the results where the contribution to the mass loss came from. The endplugs appeared to degrade, so it is possible that a higher fraction of the overall mass loss than expected came from the endplugs. These results bring into question the performance of a transient eutectic phase SiC material under corrosion in an irradiation environment, and based on this outcome, CVD SiC endplugs will be used in future work.

For these samples, coolant still had access to the inner tube surface through the one open end. This would have a significant effect on mass loss compared to a sample with two closed ends (fully sealed). First, in a fully sealed sample the inner surface would never be exposed to coolant, and this would reduce the expected corrosion by ~41.5% (this corresponds the inner surface area ratio to the inner plus outer surface area ratio for these tubes). Based on this surface area adjustment, the measured 0.6% to 1.5% per month mass loss rate in the MITR could correspond to a 0.35% to 0.88% rate of mass loss per month from only the outer surface. This difference is likely to be even larger than suggested by just the ratio of inner to overall surface areas. In the tube structures tested at MIT, an inner-composite, outer monolith design was used. Monolithic material, with higher density and reduced porosity, is expected to exhibit a lower rate of mass loss than composite material (see Figure 59 and Figure 60). For these samples, with only one end closed, the exposed inner composite surface would likely experience a higher relative rate of mass loss compared to the monolithic coating on the outer surface.

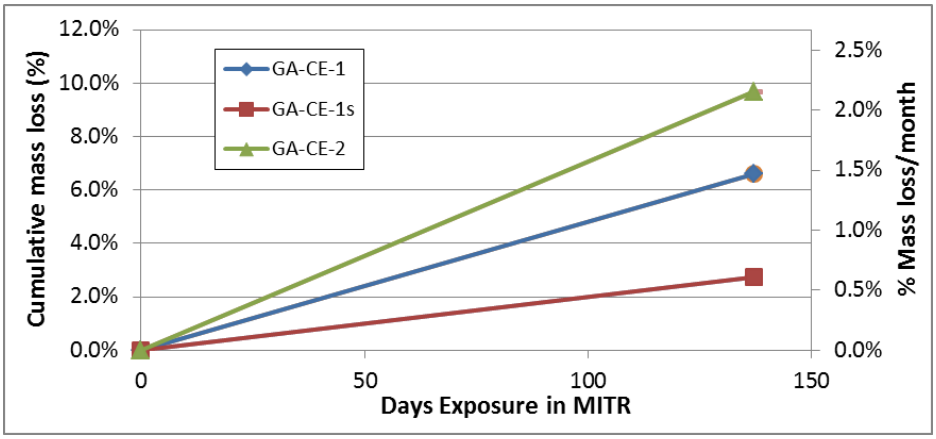

Figure 98: Plot of cumulative mass loss and rate of mass loss for closed end samples under irradiation. The inside of tubes was still exposed to coolant through the one open end.

A closer examination of the x-ray tomography volume reconstructions of the tubes was performed to help identify the cause of the separation of the endplugs in two of the samples (GA-TC3-I-1, 6). First, a typical endplug is shown in Figure 99. The endplug appears well consolidated, and the joint between the endplug and tube is uniform and contains minimal porosity.

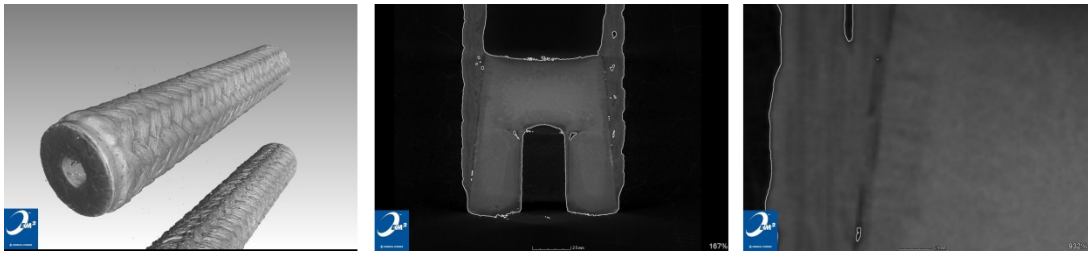

Figure 99: XCT scan of typical GA-TC3-I-X sample, showing good endplug density and alignment

The endplug in sample GA-TC3-I-1 separated from the tube during the irradiation. Closer examination of the as-fabricated endplug indicated large porosity along one side of the endplug (Figure 100). This would have resulted in a weaker joint, and could have also led to water intrusion or accelerated corrosion in this portion of the joint, and eventually causing the endplug to separate.

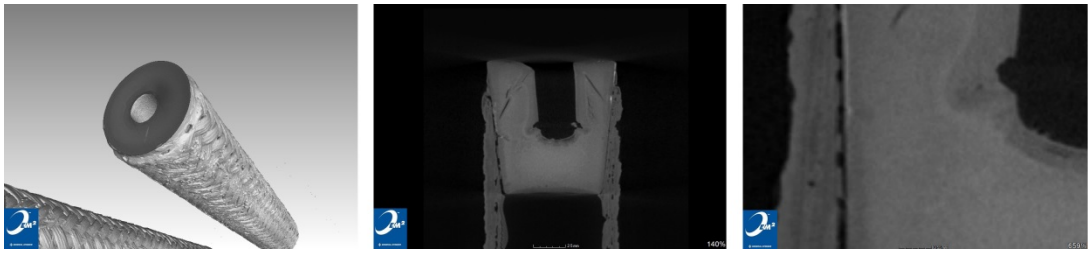
Figure 100: XCT scan of Sample GA-TC3-I-1, showing endplug misalignment and poor joining on one side

The other sample which came out of the reactor with endplug damage was sample GA-TC3-I-6, and in this sample the endplug had fractured, with the lower end (smaller diameter) remaining in the tube, and the upper end separating. Closer examination of the as-fabricated endplug revealed that the plug consolidation in the vicinity of the blind hole was not as dense or uniform as elsewhere in the endplug (Figure 101).

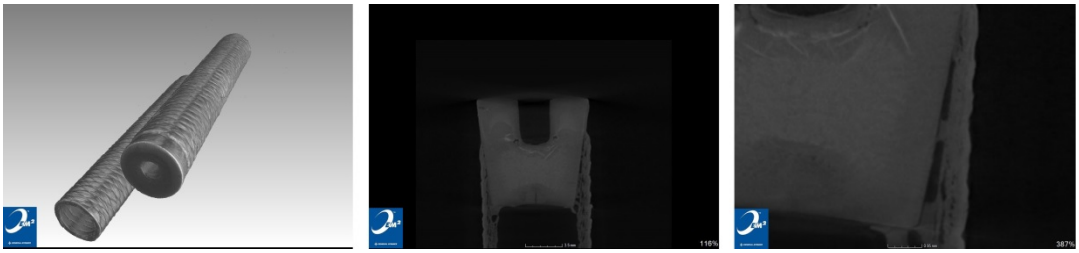
Figure 101: XCT scan of Sample GA-TC3-I-6, showing poor endplug consolidation near blind hole

The blind hole feature was included in the endplugs to accommodate the specimen support approach used by MIT for these tests. It appears that this feature led to non-uniform endplug consolidation, and this geometry could also cause stress concentrations in the vicinity of the end of this hole. The endplug that fractures (from GA-TC3-I-6) appears to have broken at the base of this blind hole, which could likely result from this effect of this feature on the consolidation process.

The overall SiC-SiC tube corrosion results can be compared to literature data (Carpenter, 2010) for other SiC tubes irradiated in the MITR (Figure 102). The SiC-SiC open ended tubes in this work that did not receive the additional SiC coating performed comparably to other SiC tubes irradiated at MIT after the 154 day exposure, but did not perform as well after the longer 291 day exposure. The average rate of mass loss for the other open ended tubes (0.9% per month), was comparable to that reported for other CVI-based SiC-SiC tubes (typically 2% per month or less mass loss rate). The best performing tubes in this current work (the closed end tubes that had received an additional SiC coating), performed about as well as the best set of tubes reported in the literature (0.61% loss per month compared to an average of 0.53% per month for the R7 tubes reported by Carpenter). These results are also not normalized to sample surface area, and a rougher tube (or tube with more open porosity) would have a higher surface area exposed to the water and a higher rate of mass loss would be expected.

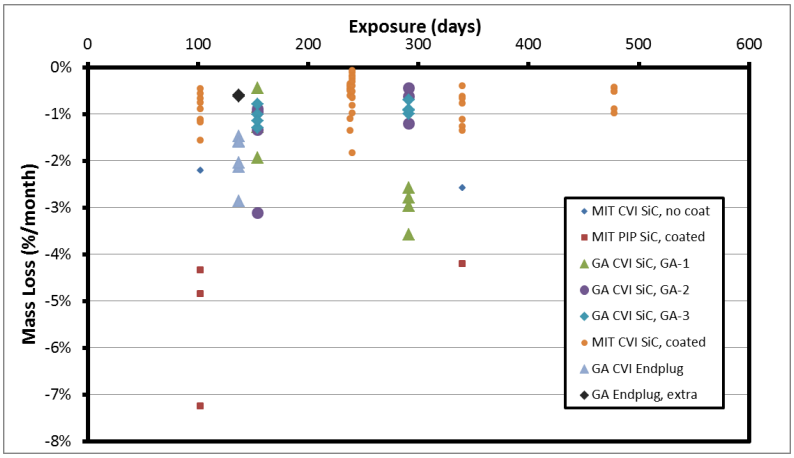

Figure 102: Comparison of irradiation mass loss rate for GA SiC-SiC samples in this work compared to other SiC-SiC samples from the literature (Carpenter, 2010)

Future work to improve the corrosion response of these tubes will look to further improve the as-fabricated tubes (mechanical polishing to smooth and then optimized over-coating to both protect and close open porosity). Other protective coatings will also be evaluated, although the processing route (coating method) must be considered for integration with large scale production, the coating must be compatible with SiC (no delamination), and it must not provide a significantly negative effect on the overall cladding neutronics.

6. SiC Joining Tests (Subtask 9)

The GA high purity SiC-based joining method was evaluated for use in LWR cladding applications as a means to seal the ends of the cladding tube with endplugs. Joint performance was evaluated at room and elevated temperatures, and joint structure was imaged using x-ray tomography. Much of the data presented here was obtained using internal R&D funding as well as funding from DOE-NE0000612 but was leveraged under the ATF development contract to further the ATF project goals.

For larger scale production, uniformity and repeatability will be very important to maximize yield. Improvements to the joining process led to better tolerances and reduced misalignment which resulted in reduced porosity in the joint material. These processing improvements have led to the reduction in the size of the largest pores in the joint by over 50x (Figure 103), as characterized by non-destructive x-ray tomography techniques. With these refinements, there have been corresponding increases in strength and performance.

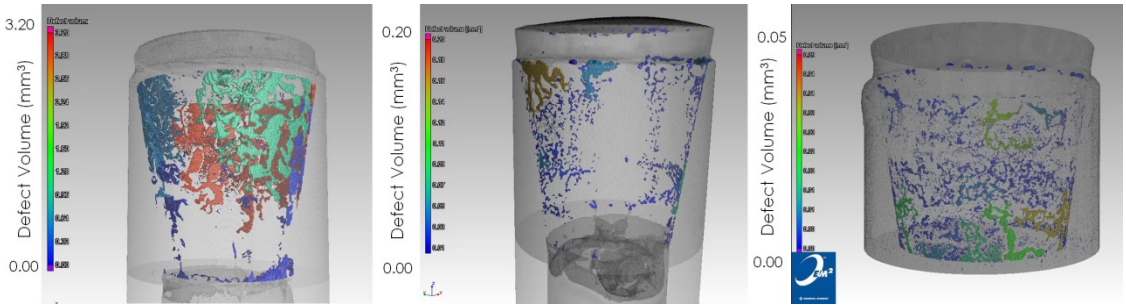

Figure 103: XCT scans of different generations of Joint fabrication. Processing refinements to the right show reduced porosity and improved alignment.

Lengths of tubes sealed on one end with an endplug and this SiC –based joint were evaluated for permeability. Testing was performed using a helium leak detector with a similar procedure to that described in sections 4.3 and 5.3. A leak rate allocation was determined for the geometry, and results for nine sealed specimens are shown in Figure 104. All specimens meet the leak rate requirement, showing this joining procedure can produce reliable, hermetic seals.

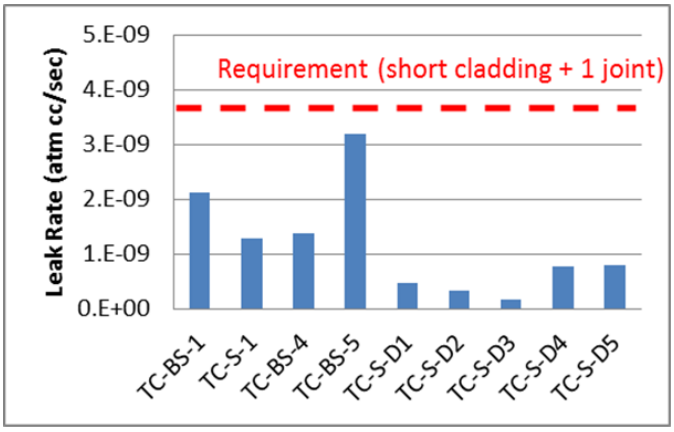

Figure 104: Leak rate measurements for a set of sealed tubes, showing repeatability of joining process

The joints sealing the end of the cladding tubes must also be robust, and survive mechanical and thermal loading without failing or leaking. A sealed tube which had been previously verified to be hermetic was subjected to a series of stress applications. This sample was first taken through a thermal cycling procedure, where it was heated to 1000°C and cooled to room temperature ten times. After this thermal cycling, the sample still met the leak rate requirement, with essentially the exact leak measurement as the as-fabricated part. The sample was then subjected to an additional stress application consisting of loading by expanding plug to a stress corresponding to an internal pressurization of 16.8 MPa, which would be representative of the internal pressure contained by fuel rods at the end of life. The sample still met the leak rate requirement by roughly an order of magnitude after this loading (Figure 105).

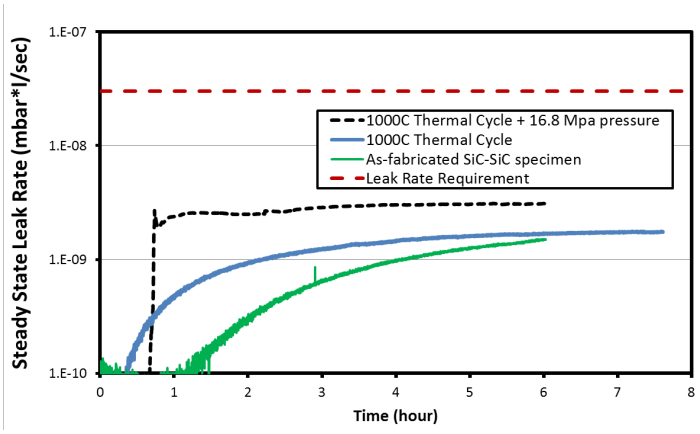

Figure 105: leak rate measurements of sealed tube after thermal and mechanical loading

This internal pressurization at the end of life corresponds to a load on the endplug of ~685N. Additional endplug push-out testing data was performed by MIT, and the SiC-SiC tubes sealed at one end with an endplug required an average of 1534N to fail the endplug/tube/joint assembly. This exceeds the load requirement by more than 2.2x. Even after subjecting the sealed tubes to extended oxidation for 48 hours with steam at 1400°C, the average load required to separate the endplug was 1231N, exceeding the requirement by 1.8x. More details of these results are included in the MIT report.

Future joint development work will focus on modifications to the technique to enable pressurization of the fuel rod (with helium gas to control gap thermal conductivity). This processing as well as the determination of the actual backfill pressure and gas composition needed will be addressed in subsequent phases of the accident tolerant fuel development work. In addition, mechanisms for handling and gripping the fuel components for the assembly process must be established, and modifications to cladding tube and endplug geometry could be implemented as needed.

7. Conclusions

Work performed during this project can be grouped into three main categories: simulation results, measurement of material properties and performance, and assessment of manufacturability and specifications. Conclusions are presented for each of these broad categories.

7.1. Modeling

An axisymmetric, 1-dimensional model for thermo-mechanical stresses in multi-layered cylinders was used to analyze SiC-based claddings for LWRs. The model uses constant, isotropic properties for each layer and includes stresses resulting from temperature and pressure differentials and temperature-dependent swelling. This swelling induces a significant amount of the stresses present in SiC-based LWR cladding. Thermo-mechanical stresses were calculated over the entire range of LWR operating and shutdown conditions.

Different candidate cladding designs were analyzed for stresses and probability of survival over a normal LWR fuel rod operating lifetime. A cladding design composed of an inner composite layer and outer monolithic layer was determined to provide the best probability of survival in LWR operating and shutdown conditions.

To improve the modeling SiC-SiC, a modified stress-strain curve was use to incorporate non-linear behavior of the stress-strain curve. This was done by calculating an effective elastic modulus based on the stress-strain curve. The pseudo-plastic stress-strain behavior that occurs upon exceeding the PLS is particularly important in modeling multi-layer SiC-based cladding tubes. Using experimental data, the statistical variation in the stress-strain curves was incorporated into a probabilistic failure assessment of several cladding concepts.

Based on the results of the model, several conclusions can be drawn:

- Stresses in SiC resulting from irradiation swelling are significantly larger than stresses due to temperature gradient or pressure differential.
- Swelling stresses and thermal stresses oppose each other during reactor operation. This lowers the net stress on the cladding during operation.
- Swelling deformation and its resulting stresses persist after reactor shutdown, and causes the shutdown stress state to be the most severe.
- For fully composite cladding designs, the model predicts stresses that will exceed the composite PLS, leading to matrix cracking and loss of hermeticity. Purely composite cladding concepts are likely insufficient for LWR ATF needs.
- The largest tensile stresses generated by differential swelling are located at the inner wall of the cladding. Inner monolith designs will subject the monolith to these tensile stresses leading to high probability of cracking and leakage.
- This leads to the conclusion that the outer monolith concept is the superior choice for SiC-based cladding. The swelling stresses put a compressive stress on the outer monolith layer, making it very unlikely to fracture.
- Under high stresses, the composite can deform in a pseudo-plastic manner, and this allows loads from internal pressurization during shutdown to be transferred to the compressed monolith while not exceeding the composite UTS, resulting in a low failure probability.
- The variations in the SiC-SiC stress-strain curve must be factored into any failure probability calculation.
- Detailed calculations predict the failure probability of the outer monolith concept is only $6.02*10^{-5}$. In contrast, pure composite and inner monolith concepts will have high failure rates under LWR conditions.
- Sensitivity studies show that 10% changes to distribution parameters and material properties can have large effects on the failure probability. This shows that small improvements to SiC-based cladding can have significant effects in. Improving characteristic PLS and strain past PLS to failure would significantly reduce failure probability. Also, further optimization of fiber architecture and

processing parameters could lead to denser composites with improved thermal conductivity, further reducing likelihood of failure.

The stress and failure probability models provide a framework to efficiently evaluate and optimize tubular CMC components. The results of these models are in agreement with the previous works of Ben-Belgacem and Lee, and they elaborate on their findings with a more in-depth examination of the LWR fuel cycle and SiC-SiC mechanical behavior. This shows that with careful design and optimized manufacturing processes, engineered multi-layer SiC-based claddings are able to meet requirements that could not be achieved by either a fully monolithic or fully composite cladding.

7.2. Material properties and performance

SiC-SiC tubes can be fabricated with high density and controlled fiber architecture to produce high performance cladding material to meet anticipated stress requirements. A series of characterization techniques was applied to thoroughly investigate the performance of both planar and tubular SiC-SiC structures.

- Hoop and axial strengths of SiC-SiC tubes can be carefully controlled though the fiber architecture, and a balanced structure, providing roughly equal hoop and axial strengths, appears to be most suitable for WEC-ATF cladding applications.
- Expected trends of increasing mechanical performance and thermal conductivity with increasing density were observed and confirmed. Relationships between fiber structure and mechanical and thermal properties were identified. Incorporation of an impermeable, monolithic layer improved the thermal conductivity.
- SiC-SiC tube and SiC-based joints showed no reduction in mechanical performance at LWR-relevant temperatures compared to room temperature.
- SiC-SiC tubes and SiC-SiC tubes sealed with an endplug can be made hermetic, and can retain hermeticity after being subjected to mechanical and thermal cycling. With an improved impermeable monolithic coating, hermeticity can be maintained until the PLS of the structure.
- Based on a large set of planar composite data that was analyzed in this work, the strength distribution observed for SiC-SiC specimens could also be well represented by a log-normal distribution, rather than a Weibull distribution. More experimental data will be needed to verify this, but property requirements to meet very low (ppm) failure levels are not as strict with a log-normal distribution.
- Autoclave exposure of SiC-SiC to high temperatures and pressures showed mass change behavior between ~3x and ~8x better than Zircaloy
- High temperature steam oxidation results from MIT showed oxidation progressing down interconnected porosity in open ended tubes, resulting in a loss of pseudo-ductile behavior. Mechanical testing of sealed tubes via endplug push-out testing showed better post-oxidation performance than the open ended tubes (smaller reduction in strength).

- Mass loss data for SiC-SiC tubes irradiated in PWR water chemistry in the MITR was roughly comparable to previous irradiation data in the literature. Earlier tubes suffered from delamination, but this did not appear to occur on later tubes. The experimentally determined mass loss is still higher than desired for LWR cladding applications, and additional efforts to reduce this mass loss are being pursued. Transient eutectic phase SiC material used for the endplugs did not seem to perform well under irradiation, and CVD SiC will be used for future endplugs. Amongst the set of sealed tubes, those with an additional SiC coating had a mass loss rate roughly 3x lower than the rest of the set, showing a potential route towards better corrosion resistance.
- Mass loss data for cladding tubes in the final application (sealed on both ends) will likely be significantly improved compared to these test samples. The test samples had one end open, permitting coolant to access the tube composite inner surface. This added ~42% additional surface area, and the inner surface was composite material, rather than the more corrosion resistant monolithic material on the outer tube surface.

7.3. Current status towards cladding specifications

Work has been done to improve fabrication techniques to reduce fabrication time and increase batch sizes, better meet fuel cladding specifications, and increase yield. Equipment is already in place to manufacture full-size fiber preforms. Polishing, joining, and NDE steps can be adapted to larger, full-size cladding rods with investment in larger-scale equipment, but there is no fundamental challenge associated with performing these steps on longer tubes. Infiltration has been optimized for tubes to reduce processing time by ~40% from the initial baseline and to also increase batch size while maintaining uniformity. Infiltration of full-size tubes will require equipment upgrades, and may require additional process refinements and optimization. However, pervious experience in scaling from 1’ to 3’ tubes has revealed approaches and techniques that can be applied to improve uniformity and ensure that longer tubes can meet the required specifications.

During this work, a list of cladding specifications was provided by Westinghouse in a memo authored by Peng Xu dated January 7th, 2014. This list is reproduced in Table 20, along with a summary of the current progress towards meeting cladding specifications. Most of the mechanical and dimensional specifications have been achieved, although measurements are from smaller-scale tubes, and some measurements are not all from the same tubes. X-ray computed tomography is a powerful tool to characterize these tubes in a non-destructive fashion, and can be used to confirm many of the dimensional tolerances. In the future, determination of defect detection criteria would merit further investigation, as would continued refinements to the tolerances and smoothness of the tube inner surface. Furthermore, while the modeling work shows great promise for the outer monolith cladding design, additional enhancement and material improvement are needed to ensure the anticipated failure rate can match current Zircaloy cladding standards.

Table 20: Summary of current status towards meeting cladding specifications

Item #	Requirement	GA value	Source	Req. Met?	Notes
1	EOL internal pressure <21.4 MPa	~300-600	Hoop test	Yes	21.4 MPa = 107 MPa hoop strength (thin wall approx.). Strength controlled through fiber architecture
2a	ID roughness <1.27μm Ra	6μm	XCT	In progress	For tubes with inner smoothing; mandrel Ra was ~4μm
2b	OD roughness <0.8μm Ra	0.2μm	XCT	Yes	For polished tube. OD roughness can be controlled over a wide range
3a	OD <9.5mm	<9.5	XCT	Yes	OD can be made to desired size
3b	Wall thickness <0.762mm	0.75	XCT	Yes	Wall thicknesses as thin as 0.5mm can be manufactured
3c	ID variation <38μm	89μm	XCT	In progress	Measured from a set of partially polished tubes
3d	OD variation <38μm	32μm, 20μm	XCT	Yes	Standard deviation values, 32μm along the length of tube and 20μm at a given cross-section
4	BOL pellet cladding gap ~190μm	N/A	N/A	N/A	Will depend on WEC overall fuel design
5	Failure rate <5ppm	60	Model	No	Failure rate calculated using stress model and Weibull properties (see section 2)
6	Straightness of <0.00083m/m	0.00082	XCT and GA QA lab	Yes	For 3' long tubes
7	Thickness variation <50μm	47μm	XCT	Yes	Average of nine samples points on three tubes
8	Defect detection	N/A	XCT/AE	In progress	Will need to be developed for SiC-SiC cladding
9	Endplug seal passes He leak test	passes	He leak	Yes	Monolithic endplug, GA SiC-based hybrid joint (as fabricated and thermally and mechanically cycled samples, but this is not yet verified for irradiated material).
10	Circularity deviation <50μm	61μm; 39μm	XCT	Yes	61μm for all-composite, 39μm for outer monolith, from recent polished tubes

8. References:

1. ANSYS Workbench Release 14.5, ANSYS, Inc, Canonsburg, Pennsylvania, United States.
2. ASTM C1239-07: Standard Practice for Reporting Uniaxial Strength Data and Estimating Weibull Distribution Parameters for Advanced Ceramics, ASTM International, West Conshohocken, 2007.
3. ASTM C1323: Standard Test Method for Ultimate Strength of Advanced Ceramics with Diametrally Compressed C-Ring Specimens at Ambient Temperature, ASTM International, West Conshohocken, PA, 2010.
4. ASTM C1341: Standard Test Method for Flexural Properties of Continuous Fiber-Reinforced Advanced Ceramic Composites, ASTM International, West Conshohocken, 2006.
5. ASTM C1683-10(2015), Standard Practice for Size Scaling of Tensile Strengths Using Weibull Statistics for Advanced Ceramics, ASTM International, West Conshohocken, PA, 2015, www.astm.org
6. ASTM C1773: Standard Test Method for Monotonic Axial Tensile Behavior of Continuous Fiber-Reinforced Advanced Ceramic Tubular Test Specimens at Ambient Temperature, ASTM International, West Conshohocken, PA, 2013.
7. ASTM E432-91: Standard Guide for Selection of a Leak Testing Method,; ASTM International: West Conshohocken, PA, 2011.
8. Avincola, V., Shirvan, K., Kazimi, M., Transactions of the American Nuclear Society 110 (2014) 927-930.
9. Bale, H. A., Haboub, A., MacDowell, A. A., Nasiatka, J. R., Parkinson, D. Y., Cox, B. N., Marshall, D. B., and Ritchie, R. O., "Real-time quantitative imaging of failure events in materials under load at temperatures above 1,600C," Nature Materials, Vol. 12, 2013, pp. 40-46.
10. Ben-Belgacem, M., Richet, V., Terrani, K. A., Katoh, Y., and Snead, L. L., "Thermo-mechanical analysis of LWR SiC/SiC composite cladding," Journal of Nuclear Materials, Vol. 447, 2014, pp. 125-142.
11. Birmin, V., in: 1990 InterSociety Conference on Thermal Phenomena, 1990, Las Vegas, NV, USA.
12. Bragg-Sitton, S., “Advanced LWR Nuclear Fuel Cladding System Development Technical Program Plan,” Prepared of US DoC Contract DE-AC07-05ID14517, Dec 2012.
13. Bragg-Sitton, S., Hurley, D., Khafizov, M., Merrill, B., Schley, R., McHugh, K., van Rooyen, I., Katoh, Y., and Shih, C. Silicon Carbide Gap Analysis and Feasibility Study; Idaho National Laboratory: Idaho Falls, 2013.
14. Bragg-Sitton, S., Merrill, B., Teague, M., Ott, L., Robb, K., Farmer, M., Billone, M., Montgomery, R., Stanek, C., Todosow, M., and Brown, N. Advanced Fuels Campaign Light

Water Reactor Accident Tolerant Fuel Performance Metrics; Idaho National Laboratory, 2014.
15. Byun, T.S., Lara-Curzio, E., Lowden, R., Snead, L. L., Katoh, Y., Journal of Nuclear Materials 367-370 (2007) 653-658.
16. Carpenter, D., “An Assessment of Silicon Carbide as a Cladding Material for Light Water Reactors”, Massachusetts Institute of Technology, Cambridge, MA, 2010
17. Causey, R. A., Wampler, W. R., Retelle, J. R., and Kaae, J. L., "Tritium migration in vapor-deposited Beta-silicon carbide," Journal of Nuclear Materials, Vol. 203, 1993, pp. 196-205.
18. Cheng, T., Keiser, J.R., Brady, M.P., Terrani, K.A., Pint, B.A., Journal of Nuclear Materials 427 (2012) 396-400.
19. Deck, C. P., Jacobsen, G., Sheeder, J., Gutierrez, O., Zhang, J., Stone, J., Khalifa, H., Back, C., "Characterization of SiC-SiC composites for accident tolerant fuel cladding", Journal of Nuclear Materials (2015), http://dx.doi.org/10.1016/j.jnucmat.2015.08.020
20. Deck, C., Khalifa, H., Sammuli, B., Hilsabeck, T., and Back, C., "Fabrication of SiC-SiC composites for fuel cladding in advanced reactor designs," Progress in Nuclear Energy, Vol. 57, 2012, pp. 38-45.
21. Deck, C.P., Khalifa, H.E., Back, C.A., Transactions of the American Nuclear Society 106 (2012) 1123-1125.
22. Denwood, F., Ross, J., Hendrich, W. J., Strength testing of monolithic and duplex silicon carbide cylinders in support of use as nuclear fuel cladding, in: Proceedings of the 30th International Conference on Advanced Ceramics and Composites, 2006
23. Development of LWR Fuels with Enhanced Accident Tolerance Task 1 - Technical Concept Description; Westinghouse Electric Company, 2013.
24. Feinroth, H. A Multi-Layered Ceramic Composite for Impermeable Fuel Cladding for Commercial Water Reactors; Gamma Engineering: Rockville, 2008.
25. Final report, “Technology for Joining Silicon Carbide Ceramic Matrix Composites for Nuclear Fuel Cladding,” BEA-INL, Sep 2013. GA-C27672.
26. Ford, L.H., Hibbert, N.S., Martin, D.G., Journal of Nuclear Materials 45 (1972) 139-149.
27. Fuel design data, Nuclear Engineering International, September 2004, 26-35.
28. Gonczy, S. T. and Jenkins, M. G. Mechanical, Thermal and Environmental Testing and Performance of Ceramic Composites and Components, ASTM, West Conshohocken, PA, 2000 Vol. ASTM STP 1392.
29. Gutierrez, O., Khalifa, H. E., Deck, C. P., Back, C. A., and Schleicher, R., "Permeability Measurements for SiC Ceramic Matrix Composites Relevant to LWR," Transactions of the American Nuclear Society, Vol. 110, 2014, pp. 803-806.
30. Hasegawa, A., Kohyama, A., Jones, R. H., Snead, L. L., Riccardi, B., and Fenici , P., “Critical issues and current status of SiC/SiC composites for fusion”, Journal of Nuclear Materials, Vol. 283-287, 2000, pp.128-137

31. Hegeman, J.B.J., van der Laan, J.G., van Kranenburg, M., Jong, M., d'Huslt, D., ten Pierick, P., Fusion Engineering and Design 75-79 (2005) 789-793
32. Jacobsen, G. M., Stone, J. D., Khalifa, H. E., Deck, C. P., and Back, C. A., "Investigation of the C-ring test for measuring hoop tensile strength of nuclear grade composites," Journal of Nuclear Materials, Vol. 452, 2014, pp. 125-132.
33. Jung, P., "Diffusion and retention of helium in graphite and silicon carbide," Journal of Nuclear Materials, Vol. 191-194, 1992, pp. 377-381.
34. Katoh, Y., Kondo, S., Snead, L. L., Journal of Nuclear Materials 382 (2008) 170-175.
35. Katoh, Y., Nozawa, T., Snead, L. L., Ozawa, K., and Tanigawa, H., "Stability of SiC and its composites at high neutron fluence," Journal of Nuclear Materials, Vol. 417, 2011, pp. 400-405.
36. Katoh, Y., Ozawa, K., Shih, C., Nozawa, T., Shinavski, R. J., Hasegawa, A., Snead, L. L., "Continuous SiC fiber, CVI SiC matrix composites for nuclear applications: Properties and irradiation effects", Journal of Nuclear Materials, v.448, n.1-3, pp.448-476 (2014)
37. Katoh, Y., Snead, L. L., Henager Jr., C. H., Nozawa, T., Hinoki, T., Ivekovic, A., Novak, S., Gonzelez de Vicente, S. M., Journal of Nuclear Materials 455 (2014) 387-397.
38. Katoh, Y., Snead, L. L., Nozawa, T., Kondo, S., Busby, J. T., Journal of Nuclear Materials 403 (2010) 48-61
39. Katoh, Y., Snead, L.L., Hinoki, T., Kondo, S., and Kohyama, A., "Irradiation creep of high purity CVD silicon carbide as estimated by the bend stress relaxation method", Journal of Nuclear Materials, Vol. 367–370, 2007, pp.758–763
40. Khalifa, H. E., Deck, C. P., Gutierrez, O., Jacobsen, G. M., and Back, C. A., "Fabrication and characterization of joined silicon carbide cylindrical components for nuclear applications," Journal of Nuclear Materials, Vol. 457, 2015, pp. 227-240.
41. Kim, K. H., Nam, C., Baek, J. H., Choi, B. K., Park, S. Y., Lee, M. H., and Jeong, Y. H. A State-of-the Art Report on Manufacturing Technology of High Burn-up Fuel Cladding; Korea Atomic Energy Research Institute: Taejon, 1999.
42. Kim, W.-J., Kim, D., Park, J. Y., "Fabrication And Material Issues For The Application Of SiC Composites To LWR Fuel Cladding", Nuclear Engineering and Technology, Vol. 45, 2013, pp.565-572
43. Lee, Y. and Kazimi, M., "A structural model for multi-layered ceramic cylinders and its application to silicon carbide cladding of light water reactor fuel," Journal of Nuclear Materials, Vol. 458, 2015, pp. 87-105.
44. Lipetzky, P., Dvorak, G.J., Stoloff, N.S., Materials Science and Engineering: A 216 (1996) 11-19.
45. Lorrette, C., Sauder, C., Chaffron, L., "Progress In Developing SiC/SiC Composite Materials For Advanced Nuclear Reactors", Proceedings of the 18th International Conference on Composite Materials, Jeju Island, Korea August 2011

46. M.I.T., CANES-MIT Workshop on Silicon Carbide Modeling, Cambridge, MA, 2014,
47. MATLAB Release 2011a, The Mathworks, Inc., Natick, Massachusetts, United States.
48. Nozawa, T., Ozawa, K., Tanigawa, H., “Re-defining failure envelopes for silicon carbide composites based on damage process analysis by acoustic emission”, Fusion Engineering and Design, Vol. 88, 2013, pp.2543-2546
49. Nuclear Power Technology Development Section. Thermophysical Properties Database of Materials for Light Water Reactors and Heavy Water Reactors; International Atomic Energy Agency: Vienna, 2006.
50. Parker, W. J., Jenkins, R. J., Butler, C. P., and Abbott, G. L., "Flash Method of Determining Thermal Diffusivity, Heat Capacity, and Thermal Conductivity," Journal of Applied Physics, Vol. 32, 1961, p. 1679.
51. Pint., B. A., Terrani, K. A., Brady, M. P., Cheng, T., Keiser, J. R., “High temperature oxidation of fuel cladding candidate materials in steam–hydrogen environments”, Journal of Nuclear Materials, Vol. 440, 2013, pp. 420-427.
52. Potluri, P., Manan, A., Francke, M., Day, R. J., “Flexural and torsional behaviour of biaxial and triaxial braided composite structures”, Composite Structures, Vol. 75, 2006, pp.377-386
53. Private communications, Ed Lahoda, 2013, 2014.
54. Private communication, Peng Xu, January 7th, 2014
55. Rohmer, E., Couégnat, G., Martin, E., Lorrette, C., Caty, O., “Modelling The Mechanical Properties Of SiCf/SiC Braided Composite Tubes”, Proceedings of the 15th European Conference On Composite Materials (ECCM-15), Venice, Italy, June 2012
56. Ross, D. F. and Hendrich, W. R., "Strength Testing of Monolithic and duplex cylinders of SiC/SiC," Ceramics Engineering and Science Proceedings, Vol. 27, No. 5, 2007, pp. 117-126.
57. Sabiego, M., Sauder, C., David, P., Guéneau, C., Briottet, L., Ingremeau, J. J., Ravenet, A., Lorrette, C., Chaffron, L., Guédeney, P., Le Flem, M., Séran, J. L., “Overview of CEA’s R&D on GFR Fuel Element Design: From Challenges to Solutions,” FR13 Conference, Paris France, March 2013, Paper IAEA-CN-199-282.
58. Shirvan, K., Kazimi, M., Technical and Economic Viability of Ceramic Multi-layer Composite SiC Cladding for LWRs, in IAEA ATF Workshop 2014, ORNL, Oak Ridge, TN, 2014
59. Snead, L. L., Nozawa, T., Katoh, Y., Byun, T.-S., Kondo, S., and Petti, D. A., "Handbook of SiC properties for fuel performance modeling," Journal of Nuclear Materials, Vol. 371, 2007, pp. 329-377.
60. Snead, L.L.., Nozawa, T., Ferraris, M., Katoh, Y., Shinavski, R., Sawan, M., Journal of Nuclear Materials 417 (2011) 330-339.
61. Stone, J. G., Schleicher, R., Deck, C. P., Jacobsen, G. M., Khalifa, H. E., and Back, C. A., "Stress Analysis and Probabilistic Assessment of Multi-layer SiC-based Nuclear Fuel

Cladding," Journal of Nuclear Materials, 2015, http://dx.doi.org/10.1016/j.jnucmat.2015.08.001
62. Terrani, K.A., Pint, B.A., Parish, C.M., Silva, C.M., Snead, L. L., Katoh, Y., Journal of the American Ceramic Society 97 (2014) 2331-2352.
63. Timoshenko, S., Goodier, J., Theory of Elasticity, second ed., McGraw-Hill, New York, 1951.
64. Vasiliev, V., “Composite Pressure Vessels: Analysis, Design, and Manufacturing”, Bull Ridge Publishing, Blacksburg, VA, 2009
65. Watchman, J. B., Cannon, W. R., and Matthewson, M. J. Mechanical Properties of Ceramics, 2nd edition, John Wiley & Sons, Danvers, MA, 2009, pp. 249-275.
66. Whitmarsh, C. L. Review of Zircaloy-2 and Zircaloy-4 Properties Relevant to N.S. Savannah Reactor Design; Oak Ridge National Laboratory: Oak Ridge, 1962.
67. Zhang, J., Khalifa, H. E., Deck, C. P., Sheeder, J., and Back, C. A. "Thermal diffusivity measurement of curved samples using the flash method," submitted to Proceedings of the 39th Int'l Conf & Expo on Advanced Ceramics & Composites, Daytona Beach, FL, 2015.
68. Zhu, S., Mizuno, M., Kagawa, Y., Mutoh, Y., Composites Science and Technology 59 (1999) 833-851.

P.O. BOX 85608 SAN DIEGO, CA 92186-5608 (858) 455-3000

Summary Report of Irradiation of SiC/SiC Composite Cladding Tubes in the MITR Water Loop Under PWR Conditions

Prepared by Dr. Gordon Kohse

MIT Nuclear Reactor Laboratory, In-core Experiments Group

July 2015

1. Introduction

This report summarizes the irradiation and initial post-irradiation examination (PIE) of SiC/SiC composite tubing manufactured by General Atomics under the Westinghouse-led accident tolerant fuel development project. This tubing is a candidate material for PWR fuel cladding and was exposed in the MITR water loop under conditions closely resembling those that would be encountered in a commercial PWR, including temperature, coolant chemistry, neutron flux and spectrum and gamma irradiation intensity. This report briefly describes the irradiation facility and sample fixturing, provides an irradiation history and corrosion weight loss data for all the samples. Typical pre and post irradiation photographs of each sample type at two exposure levels are included. A full photographic archive of all post-irradiation samples is available.

2. Irradiation Exposure

The irradiation of these samples was performed in a water loop installed in the MITR 6 MW research reactor as shown in Figure 1. The samples are contained within an autoclave in the core region of the reactor. Two types of samples were exposed – unsealed tubes approximately 10 mm diameter by 25 mm long and tubes with one end sealed approximately 10 mm diameter by 65 mm long. These samples were fixtured in capsules for irradiation as shown in Figure 2. Table 1 summarizes the test matrix for the irradiation, which was carried out in two stages, with an interim exchange of some of the samples. As shown in the table, unsealed tubes were irradiated in two capsules, one containing 16 tubes and irradiated for the first irradiation stage, the other containing 12 tubes and irradiated for both irradiation stages. The single-end sealed tubes were irradiated in a capsule containing 8 tubes and exposed for the second irradiation stage. Based on the exposures and calculations of the neutron flux in the assembly using a benchmarked MCNP model, the fast neutron fluence (E>.1 MeV) was approximately 1.2 x 10^{21} n/cm^2 for Capsule 1 samples, 2.0, 2.1 and 2.3 x 10^{21} n/cm^2 for Capsule 2 samples in Tiers 3, 2 and 1, respectively, and 1.2 and 1.3 x 10^{21} n/cm^2 for Capsule 3 samples in Tiers 1 and 2, respectively. Plots of the loop temperature and reactor power for the duration of the run are provided in the Appendix.

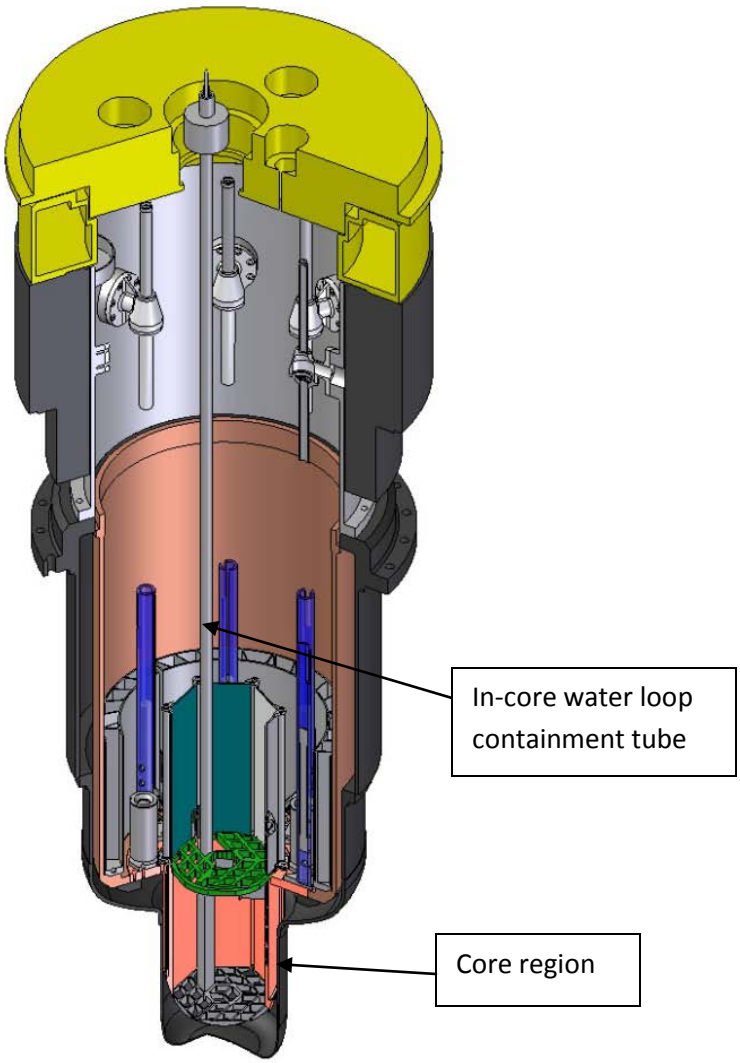

Figure 1. Cutaway model of the MITR core showing the ICSA assembly installed in an in-core position. Reactor fuel elements not show for clarity.

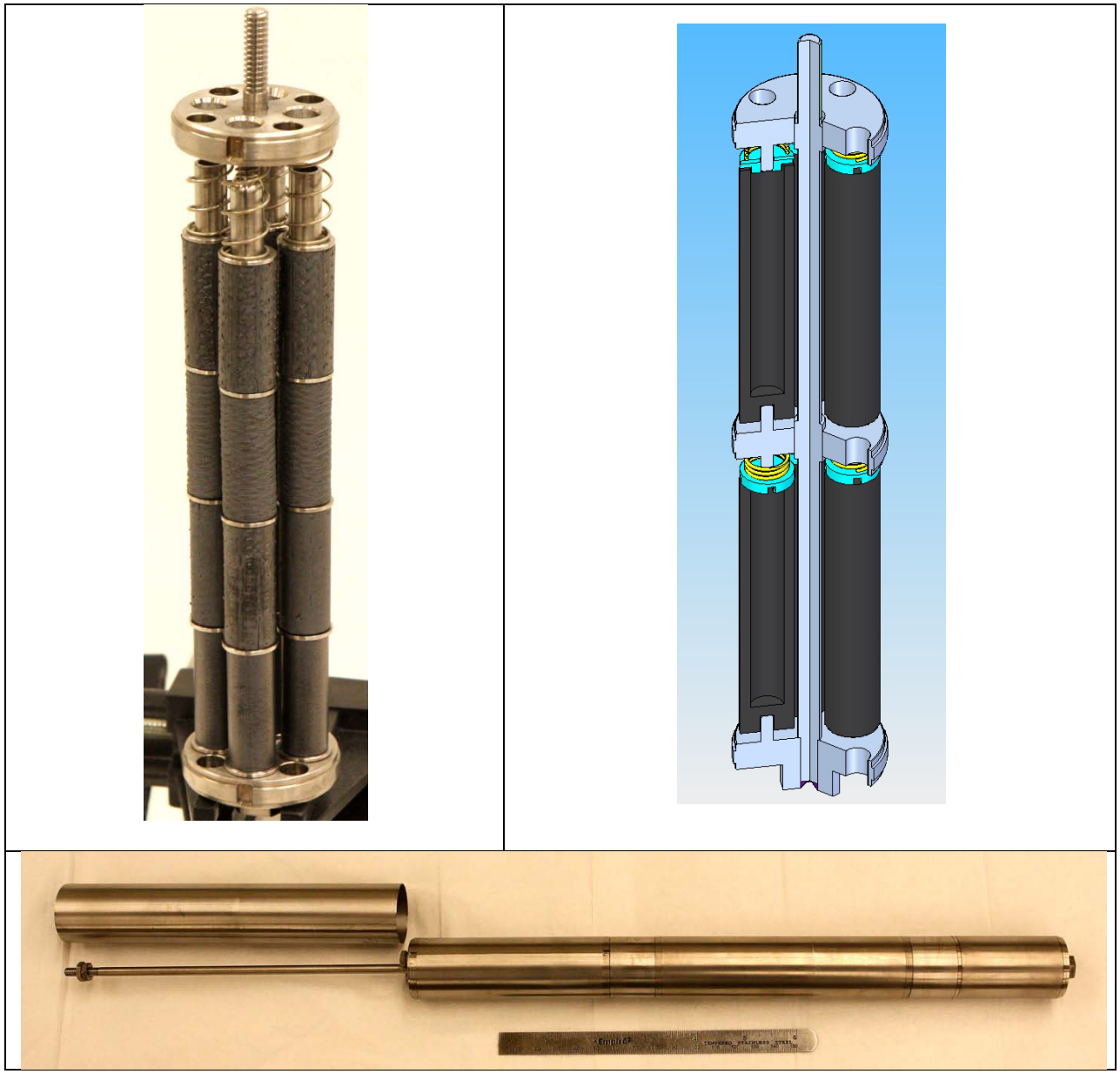

Figure 2. Sample fixturing and rig assembly for the SiC/SiC tube sample irradiations. Shown on the upper left is one of the irradiation capsules containing 16 unsealed tubes and on the upper right is the irradiation capsule for the 8 tubes with one end sealed. Note that the “flow shrouds” are not in place in the upper photographs. The lower photograph shows the full sample stack for the first stage of the irradiation with flow shrouds in place. From left to right (top to bottom of the core as installed) there is a spacer shroud, a three-tier capsule with 12 tubes, the four tier capsule with 16 tubes and a capsule containing coated coupons (not addressed in this report). Between the first and second irradiation stages the four-tier capsule was removed and replaced with the sealed tube capsule.

Table 1. Test matrix for the irradiation of SiC/SiC composite tubes.

	Sample A	Sample B	Sample C	Sample D	Exposure
Capsule 1	Unsealed Tubes				4/10/2014- 10/6/2014 572 MWd 154 hot days
Tier 1	GA-4-01	GA-4-02	GA-4-03	GA-4-04	
Tier 2	GA-1-01	GA-1-02	GA-1-03	GA-1-04	
Tier 3	GA-2-01	GA-2-02	GA-2-03	GA-2-04	
Tier 4	GA-3-01	GA-3-02	GA-3-03	GA-3-04	
Capsule 2	Unsealed tubes				4/10/2014- 5/8/2015 1239 MWd 291 hot days
Tier 1	GA-2-05	GA-2-06	GA-2-07	GA-2-08	
Tier 2	GA-3-05	GA-3-06	GA-3-07	GA-3-08	
Tier 3	GA-1-05	GA-1-06	GA-1-07	GA-1-08	
Capsule 3	Capped tubes (one end)				
Tier 1	GA1-TCJ-I-1	GA1-TCJ-I-2	GA1-TCJ-I-3	GA1-TCJ-I-4	10/23/2014- 5/8/2015 667 MWd 137 hot days
Tier 2	GA1-TCJ-I-5	GA1-TCJ-I-6	GA1-TCJ-I-7	GA1-TCJ-I-8	

3. Post-Irradiation Examination Results

Sample Photographs

Figures 3-7 show typical photographs of each of the tube types pre and post irradiation. For GA1, GA2 and GA3 tubes there are two irradiated states corresponding to exposure in Stage 1 only and for the full run duration, all other samples have only one irradiated state.

Figure 3. Photograhs of GA1 tubes: left to right GA1-01 unirradiated, GA1-01 after Stage 1 exposure and GA1-?? after Stage 1 and Stage 2 exposure.

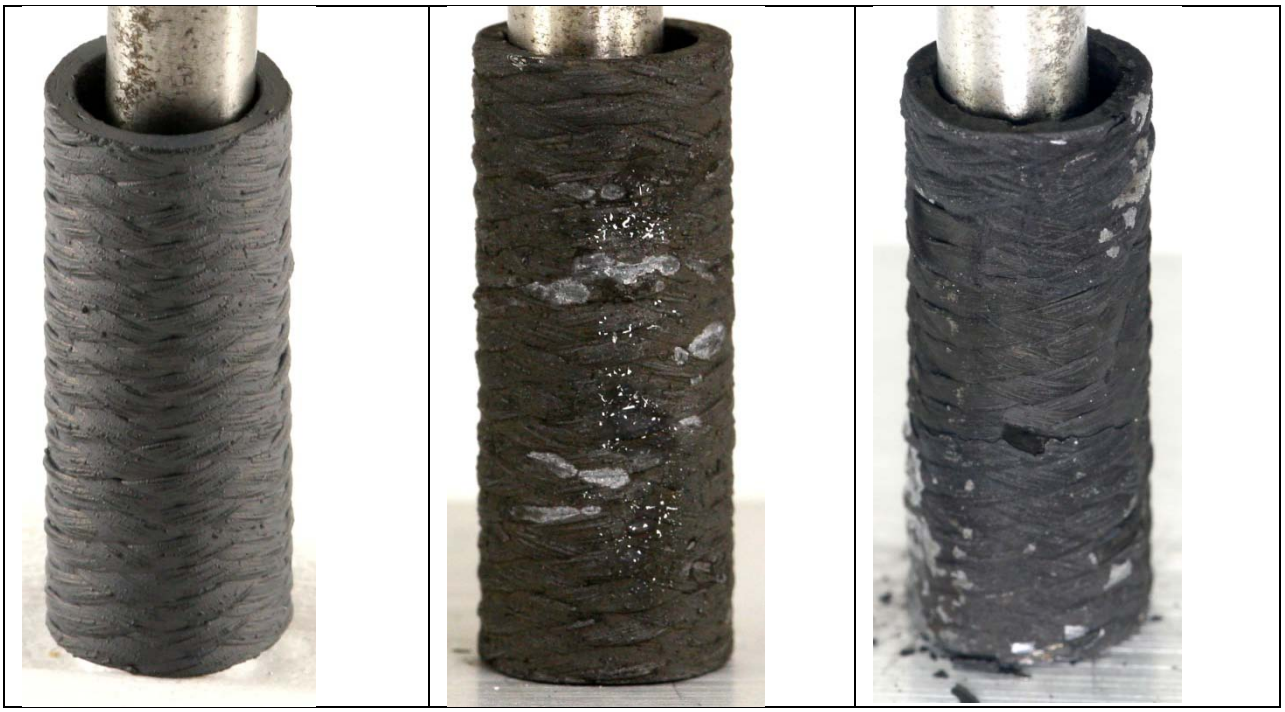

Figure 4. Photographs of GA2 ubes: left to right GA2-01 unirradiated, GA2-01 after Stage 1 exposure and GA2-08 after Stage 1 and Stage 2 exposure.

Figure 5. Photographs of GA3 tubes: left to right GA3-01 unirradiated, GA3-01 after Stage 1 exposure and GA3-05 after Stage 1 and Stage 2 exposure.

Figure 6. Photographs of GA4 tubes: GA4-01 unirradiated and GA4-01 after Stage 1 exposure.

Figure 7. Photographs of GA end-sealed tubes: above - GA1-TCJ-I-1 unirradiated, below – after Stage 2 irradiation, left to right, GA1-TCJ-I-1 (end cap separated completely from tube during capsule disassembly), GA1-TCJ-I-6 (end cap broke at bottom of mounting hole but lower section remained bonded to tube), GA1-TCJ-I-2, GA1-TCJ-I-3. Note that the end caps remained bonded for samples 2, 3, 4, 5, 7, and 8.

Weight Loss Results

All samples were weighed before and after irradiation exposure. In each case, the samples were baked at 150 °C before weighing and bake and weigh cycles were repeated until no decrease in weight was observed. The weight loss results for all the unsealed tube samples are presented in Table 2 and those for the end-sealed tubes are presented in Table 3. Note that for the end-sealed samples (1 and 6) where the end-cap separated either completely or partially, the post-irradiation weights include the separated portion of the end caps. Most of the samples exhibited some flaking of material and it must be assumed that the total weight losses are composed of both corrosion and mechanical loss of material. We currently have no explanation for the apparent weight gain of GA-2-06 during exposure.

Table 2. Weight loss results for unsealed SiC/SiC sample tubes at two different exposure times in the MITR water loop. All weights are in grams.

	572 MWd Exposure					1239 MWd			
Sample	PreIrrad	PostIrrad	Loss	Avg Loss	Sample	PreIrrad	PostIrrad	Loss	Avg Loss
GA-1-01	2.6794	2.4181	0.2613	0.1539	GA-1-05	2.6750	1.9197	0.7553	0.7550
GA-1-02	2.6597	2.5996	0.0601		GA-1-06	2.7476	2.0700	0.6776	
GA-1-03	2.7285	2.6116	0.1169		GA-1-07	2.6127	1.9189	0.6938	
GA-1-04	2.7425	2.5652	0.1773		GA-1-08	2.6125	1.7190	0.8935	
GA-2-01	2.3490	2.2431	0.1059	0.1975	GA-2-05	2.4863	2.3375	0.1488	0.1781*
GA-2-02	2.4635	2.3453	0.1182		GA-2-06	2.3378	2.5378	-.2000	
GA-2-03	2.5265	2.1291	0.3974		GA-2-07	2.4412	2.1598	0.2814	
GA-2-04	2.4928	2.3243	0.1685		GA-2-08	2.4473	2.3433	0.1041	
GA-3-01	2.9474	2.7971	0.1503	0.1583	GA-3-05	2.9683	2.6852	0.2832	0.2513
GA-3-02	2.9803	2.7851	0.1952		GA-3-06	2.9685	2.7071	0.2615	
GA-3-03	2.9716	2.7991	0.1725		GA-3-07	2.9281	2.6731	0.2550	
GA-3-04	2.9130	2.7980	0.1150		GA-3-08	3.0793	2.8736	0.2056	
GA-4-01	1.2287	1.1762	0.0525	0.0916					
GA-4-02	1.2671	1.1753	0.0918						
GA-4-03	1.2570	1.1552	0.1018						
GA-4-04	1.2613	1.1410	0.1203						

*This average result excludes the anomalous weight gain measured on GA-2-06.

Table 3. Weight loss results for SiC/SiC composite sample tubes with one end sealed.

Sample	PreIrrad	PostIrrad	Loss	Avg Loss
GA-TC3-I-1	7.7970	7.2464	0.5506	0.5273*
GA-TC3-I-2	7.6101	7.1085	0.5015	
GA-TC3-I-3	7.5495	7.3403	0.2092	
GA-TC3-I-4	7.6634	7.4568	0.2066	
GA-TC3-I-5	6.9949	6.0958	0.8991	
GA-TC3-I-6	7.0361	6.5339	0.5022	
GA-TC3-I-7	7.1970	6.5074	0.6896	
GA-TC3-I-8	7.1844	6.5268	0.6576	

*The average weight loss result excluded samples 1 and 6.

Weight Loss Observations

The weight loss results will be supplemented, and possibly better explained and understood, by dimensional measurements and SEM observations that are ongoing. In the meantime, it is possible to discern some trends in the data. First, for most of the sample sets, there is considerable variation in the weight loss from sample to sample. This may be a result of mechanical losses, or of the flaking and "layer failure" that is observed in some of the photographs. Efforts to correlate individual sample weight losses with defects visible in the photographs are currently under way. GA1, GA2 and GA3 materials display markedly different behavior with respect to weight loss progression from the Stage 1 exposure to the Stage 1 plus Stage 2 exposure. The weight loss for GA1 samples is approximately five times higher after the full run compared to the Stage 1 samples, although the exposure time and fluence is only approximately double. The weight losses for the four GA4, high-exposure samples show less sample to sample variation than at the lower exposure. Conversely, the GA2 samples show approximately the same average weight loss after the full exposure as they do at the midpoint. The behavior of the GA3 samples is more predictable, with the weight loss approximately doubling with approximately double the exposure and with relatively low sample to sample variation.

Appendix to Summary Report of Irradiation of SiC/SiC Composite Cladding Tubes in the MITR Water Loop Under PWR Conditions

Revised 9/24/2015

This Appendix consists of 5 plots, each showing a 3-month time span plot of reactor power and in-core water loop temperature. The plots cover the time during which the 2 phases of irradiation of Accident Tolerant Fuel Samples were irradiated.

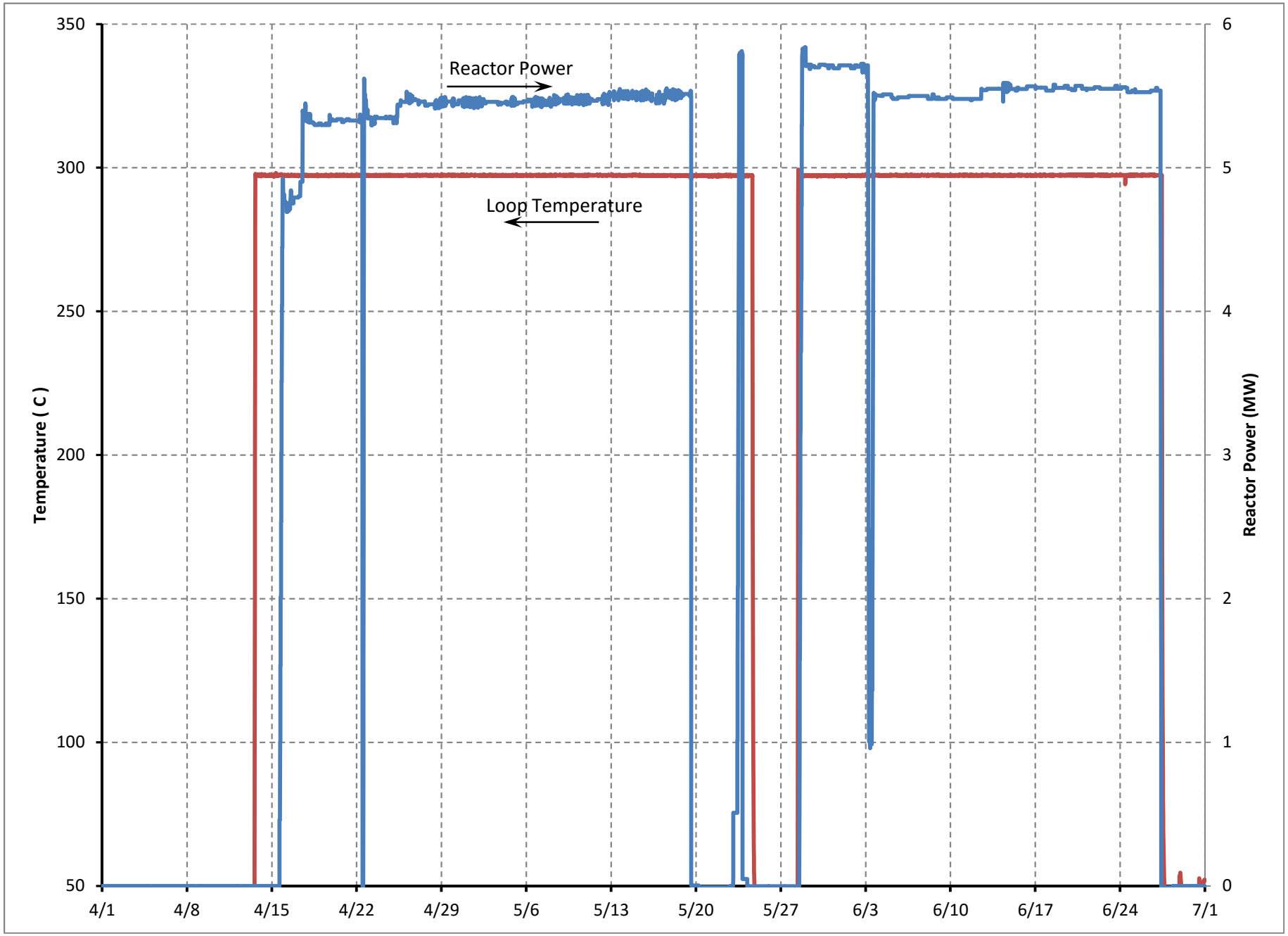
Reactor Power
Loop Temperature
Temperature (C)
Reactor Power (MW)
350
300
250
200
150
100
50
6
5
4
3
2
1
0
4/1
4/8
4/15
4/22
4/29
5/6
5/13
5/20
5/27
6/3
6/10
6/17
6/24
7/1

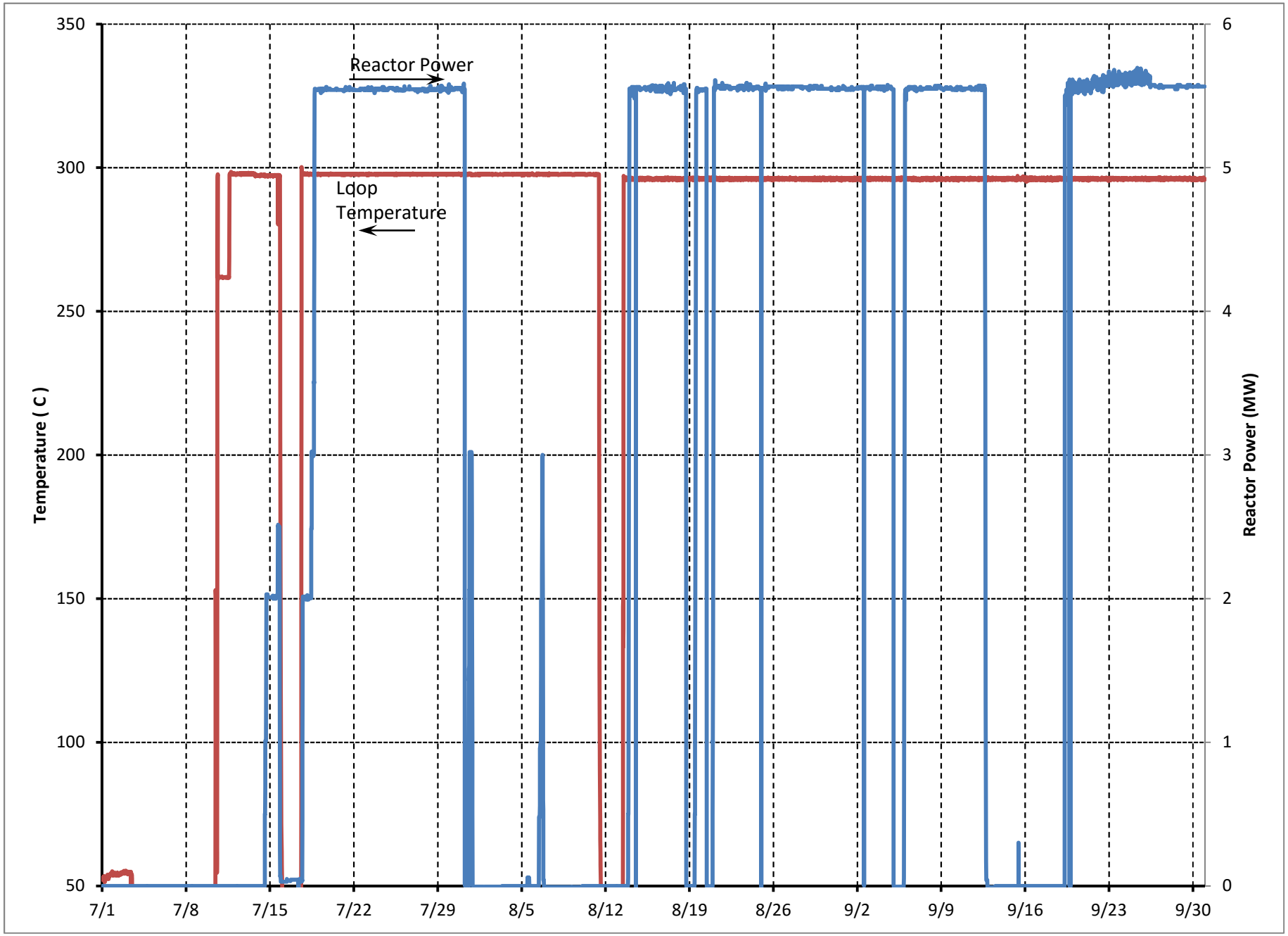
Reactor Power
Loop Temperature
Temperature (C)
Reactor Power (MW)
350
300
250
200
150
100
50
6
5
4
3
2
1
0
7/1
7/8
7/15
7/22
7/29
8/5
8/12
8/19
8/26
9/2
9/9
9/16
9/23
9/30

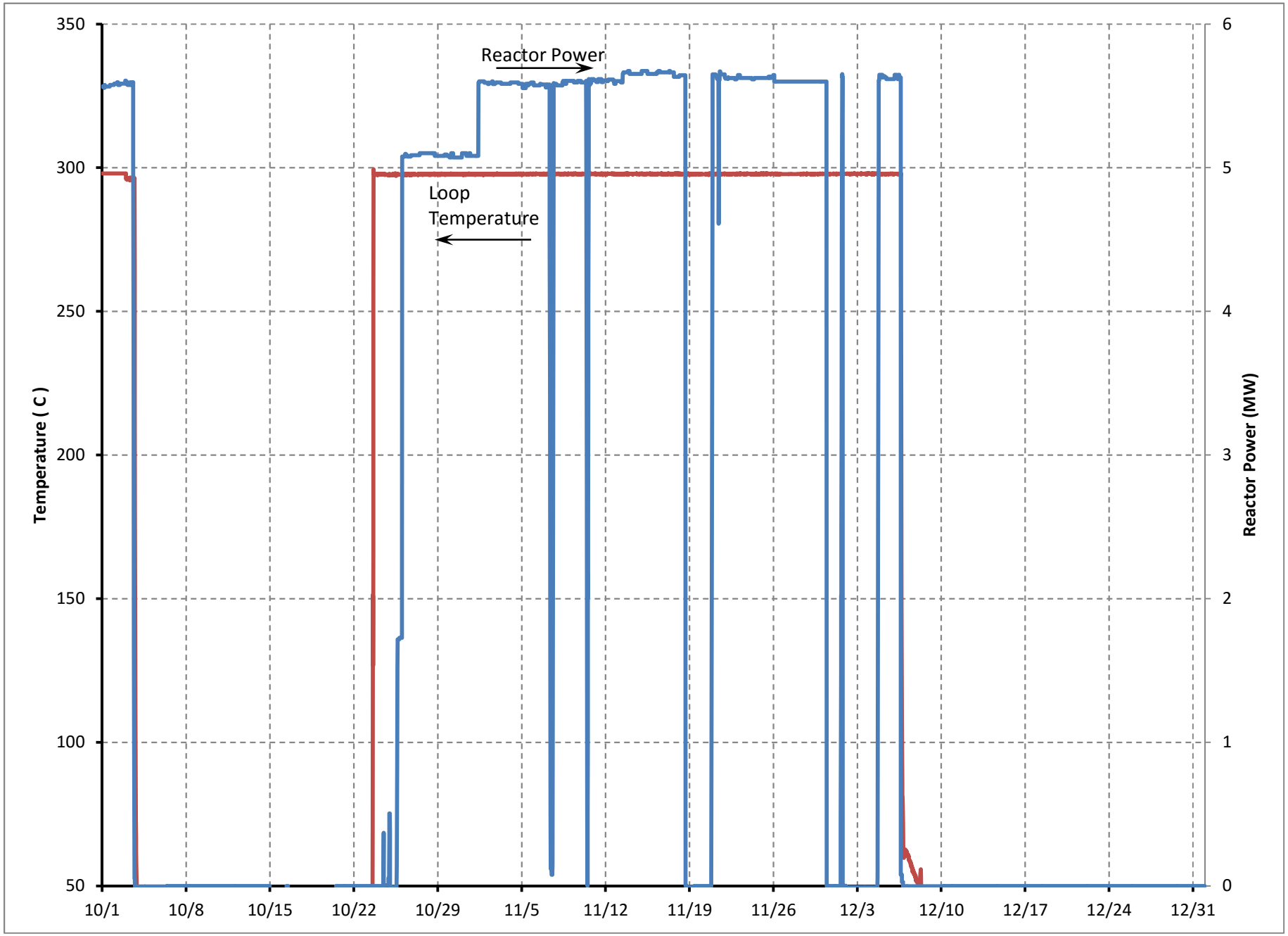
Reactor Power
Loop
Temperature
Temperature (C)
Reactor Power (MW)
350
300
250
200
150
100
50
6
5
4
3
2
1
0
10/1
10/8
10/15
10/22
10/29
11/5
11/12
11/19
11/26
12/3
12/10
12/17
12/24
12/31

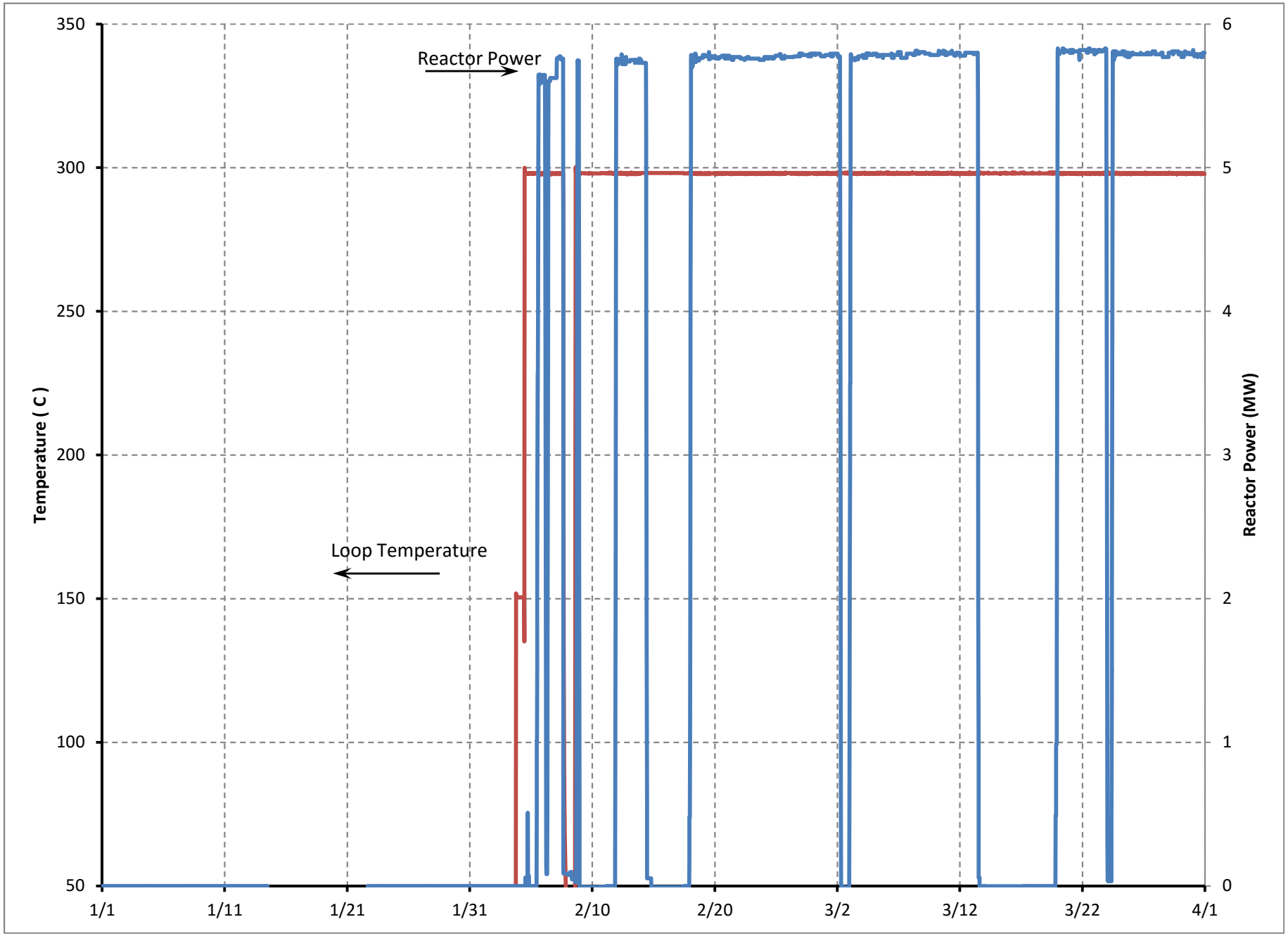
Reactor Power
Loop Temperature
Temperature (C)
Reactor Power (MW)
350
300
250
200
150
100
50
6
5
4
3
2
1
0
1/1
1/11
1/21
1/31
2/10
2/20
3/2
3/12
3/22
4/1

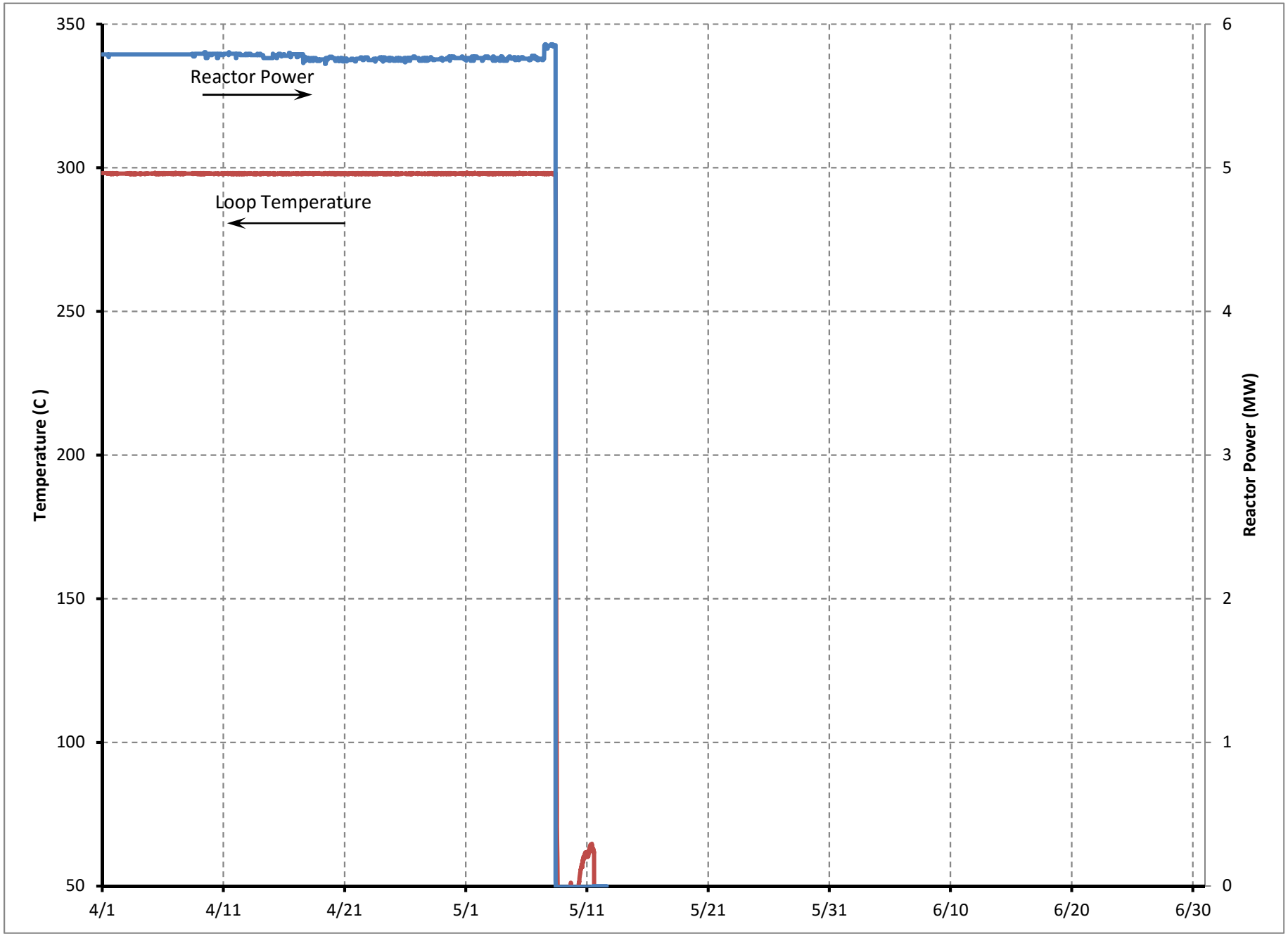
Reactor Power
Loop Temperature
Temperature (C)
Reactor Power (MW)
350
300
250
200
150
100
50
6
5
4
3
2
1
0
4/1
4/11
4/21
5/1
5/11
5/21
5/31
6/10
6/20
6/30

High Temperature Oxidation and Quench Studies of Accident Tolerant LWR Fuels – SiC/SiC CMC Tube Samples

Final Report

September 23, 2015

by Gregory Daines & Pierre Guenoun, Research Assistants, MIT

Prof. Mujid Kazimi	Director, Center for Advanced Nuclear Energy Systems (CANES) TEPCO Professor of Nuclear Engineering – posthumously authored Director, Kuwait MIT Center for Natural Resources and the Environment MIT Nuclear Science and Engineering Department
Dr. Thomas McKrell	Director, CANES Experimental Laboratory Research Scientist MIT Nuclear Science and Engineering Department
Dr. Edward Lahoda	Westinghouse Technical Lead
Dr. Frank Boylan	Westinghouse Project Manager

MIT Project # 6926954

MIT
Massachusetts Institute of Technology

Contents

List of Figures

List of Tables

I. Executive summary

In this work, five different series of Silicon Carbide (SiC) SiC/SiC ceramic matrix composite (CMC) cladding architectures are assessed under simulated loss-of-coolant accident (LOCA) conditions. The five series are denominated WEC[1]01 196, WEC01 198, WEC01 200, GAOE[2] and GACE[3]. For each series, sample performance is assessed under high temperature steam oxidation (oxidation at 1,400°C for 48 hours under a steam flow rate of 6 g/min) and thermal shock (quenching from 1,200°C into 100°C and 90°C water). Finally, the strength and ductility of the samples were evaluated and compared against control samples. Performance is quantified by a regimen of weight measurement, optical analysis, scanning electron microscopy (SEM) analysis, energy dispersive spectroscopy (EDS) analysis and mechanical strength analysis (yield stress, failure stresses, elastic moduli, and failure strain).

Section VI provides a summary comparison of the samples performance. Detailed conclusions are provided in section VII. Briefly, those conclusions are as follows:

1. The thermal shock was observed to only have a small impact on the mechanical and microstructural characteristics of all samples. Strength testing revealed that the failure stresses of the cladding samples was scattered but was not significantly influenced by thermal shock. Furthermore, SEM analysis failed to detect microcracks or other signs of material degradation following thermal shock. Overall, multilayer SiC composite cladding was observed to be resilient to thermal shock.
2. High temperature steam oxidation led to silica buildup in the inner voids of the CMC layer of all samples resulting in a net weight gain of the samples and in the embrittlement of the SiC/SiC CMC region. For all oxidized Westinghouse samples, sudden and catastrophic failure was observed as the CMC layer failed immediately upon inner monolith failure. Post oxidation, those samples showed a reduction in strength from 250 MPa to 180 MPa while the absence of pseudo-ductility resulted in the failure strain dropping from 0.3% to 0.03%. For the GA samples, failure stress fell from 580MPa as-received to 230MPa post oxidation, and these samples also experienced a ten times reduction in strain at failure. SiC/SiC composites achieved much better performance than typical Zr or steel claddings as the oxidative embrittlement was non-frangible in nature thereby maintaining a coolable geometry after failure. Additionally, zirconium alloys are nearly completely consumed after 15 minutes at 1200C and here we are comparing to SiC that has seen 1400C for 48 hours.
3. The GAOE series (composed of a CMC layer with thin 200 µm outer monolith layer) offered the best performance with a failure hoop stress reaching 600 MPa as-received and higher than 200 MPa after oxidation.
4. The three Westinghouse series (with an inner monolith/CMC/outer EBC) all behaved in a similar way with an inner monolith failure hoop stress reaching 250 MPa as-received. However, the CMC layers behaved differently. Series 196 and 200 exhibited pseudo ductility while monolith and CMC layers of series 198 failed simultaneously in a brittle manner. It

[1] WEC: Westinghouse Electric Company
[2] GAOE: General Atomics Open Ended
[3] GACE: General Atomics Closed One End

cannot be correlated to the weaving pattern since series 198 and 200 have a similar weaving pattern (three tows) while series 196 is made of two tows.

5. Endplug joining appears as a possible limitation. Endplug joint burst strength was estimated by uniaxial loading to approximately 30 MPa as-received. The GACE-B endplug sample/architecture performed poorly compared to the GACE-A. The GACE-B endplug strength drops after quenching (by more than 50%) and less severely after oxidation (by 25%). While the GACE-A endplug strength was largely unaffected. It appears as though fiber weave/architecture could play a role in this trend. Looking at the typical 14 MPa plenum pressure limit for a LWR, the SiC monolithic endplug joint withstanding 30 MPa seems satisfactory. However, plenum pressure could be much higher with SiC cladding as the absence of creep closing the fuel-cladding gap, the radial swelling of SiC and its low thermal conductivity will raise the plenum temperature, and hence the pressure.

A limited number of samples, one or two per each test condition, were tested in this work. Accordingly, it is strongly suggested that more samples be tested to strengthen these conclusions. Also, differences in sample fabrication could also be influencing the results.

Additionally, performance under irradiation must be assessed before drawing conclusive judgement on SiC/SiC composites' potential as fuel cladding material. This work is in progress under a separate project.

II. Introduction

1. Test Matrix

Five different series of Silicon Carbide (SiC) SiC/SiC ceramic matrix composite (CMC) cladding designs are assessed under simulated loss-of-coolant accident (LOCA) conditions: WEC01 196, WEC01 198, WEC01 200, GAOE and GACE. For each series, high temperature steam oxidation, thermal shock and mechanical strength tests were conducted to assess sample performance. Weight measurement, optical analysis, scanning electron microscopy (SEM) analysis, and energy dispersive spectroscopy (EDS) analysis are used to quantify performance. In such a manner, the influence of high temperature oxidation and thermal shock are assessed and related to the design choices.

Oxidation is performed at 1400˚C for 48 hours under a steam flow rate of 6 g/min. Thermal shock consists of quenching specimens at 1200˚C into 100˚C saturated water or 90˚C water. Finally, failure stress measurement is performed by the internal pressurization of the tubular specimen through the expansion of a polymer plug. Failure modes are determined via ceramographic analysis. Figure 1 illustrates the test matrix.

Sample Designation	As Received Analysis	Hight Temperature Oxidation 6g/min, 1400C, 48h	Quench Process 1200C->100C; 1200C->90C	Burst Process
	Optical, SEM & EDS Analysis; Weight	Optical, SEM & EDS analysis; Weight	Optical, SEM & EDS Analysis; T/H Analysis	Optical, SEM & Stress-Strain Analysis
WEC01 196.1.19	×	×		×
WEC01 196.1.27	×			×
WEC01 196.1.26	×		×	×
WEC01 196.1.20	×		×	×
WEC01 198.1.16	×		×	×
WEC01 198.1.23	×		×	×
WEC01 198.1.24	×			×
WEC01 198.1.25	×	×		×
WEC01 200.1.14	×		×	×
WEC01 200.1.24	×		×	×
WEC01 200.1.25	×			×
WEC01 200.1.23	×	×		×
GAOE 1	×	×		×
GAOE 2	×			×
GAOE 3	×	×		×
GAOE 4	×	×		×
GAOE 5	×		×	×
GAOE 6	×		×	×
GACE-A 1	×		×	×
GACE-A 2	×			×
GACE-A 3	×	×		×
GACE-B 4	×	×		×
GACE-B 5	×		×	×
GACE-B 6	×			×
GACE -B 7	×	To Be Determined		
GACE-B 8	×		×	×

Figure 1: Test Matrix

2. Description of the samples

The SiC cladding sample designs explored in this work fall into two categories: The WEC01 designation refers to three-layered SiC specimens while the GA designation describes two-layered SiC specimens.

i. Westinghouse samples

The Westinghouse (WEC01) samples consist of three layers: an inner monolith layer, a fibrous layer, and an outer SiC environmental barrier coating (EBC) layer. High purity beta-phase SiC forms the inner monolith layer whose role is to contain fission gases and retain hermeticity of the fuel rod. It is synthetized by chemical vapor deposition (CVD) and represents 1/6 of the total wall thickness of the samples.

The next layer is a SiC/SiC Ceramic Matrix Composite (CMC) that accounts for 2/3 of the total wall thickness of the samples. Tows consisting of around 500 mono-filament beta silicon carbide fibers are wrapped around the inner monolith layer to add tensile strength to the sample and allow for pseudo-ductility. For the WEC01 samples, the tows used are Hi-Nicalon Type S with a single layer of pyrolytic carbon added at the fiber/matrix interphase for decoupling. Beta silicon carbide was added to fill the voids between the tows by the chemical vapor infiltration (CVI) process.

The outermost 1/6 of the total wall thickness is made of another monolith layer. This EBC layer contributes to hermeticity and mainly prevents corrosion of the CMC layer. Westinghouse constructed the EBC overcoat using high-purity beta-phase deposited via CVD. Additionally, because the samples were cut from a longer tube stock, the ends of the samples were CVD coated with SiC in an attempt to seal the cut faces. This thin (~ 60µm thick) layer would not be present in service.

Three WEC01 architectures are investigated for this report. First, the weaving pattern of the CMC layer of series 196 differs from weaving pattern in both series 198 and 200. Indeed, series 196 is arranged in a herringbone pattern, sometimes referred as plain-weave pattern, where two sets of tows are interlaced with an angle of about 90º. However, the CMC layer for series 198 & 200 is made of three distinct sets of tows: one running axially and two crossing each other symmetrically (+/- 60 degree angle). Series 198 and 200 differ based on dimensions, with series 200 being thicker and of a larger diameter than series 198. Additionally, the sample architectures differ in tow spacing, as shown by “D” in Figure 2.

Table 1 below provides the details of the WEC01 architectures and Figure 2 illustrates the differences.

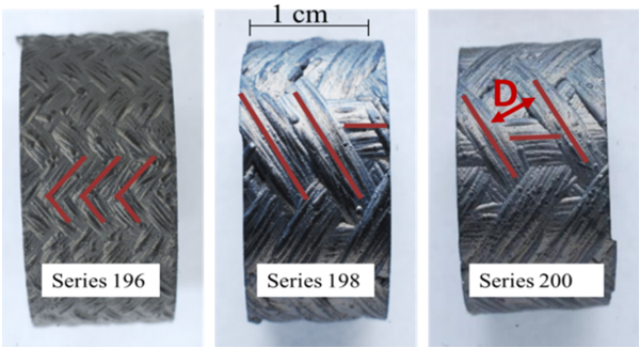

Figure 2: Optical view of the different WEC Designs

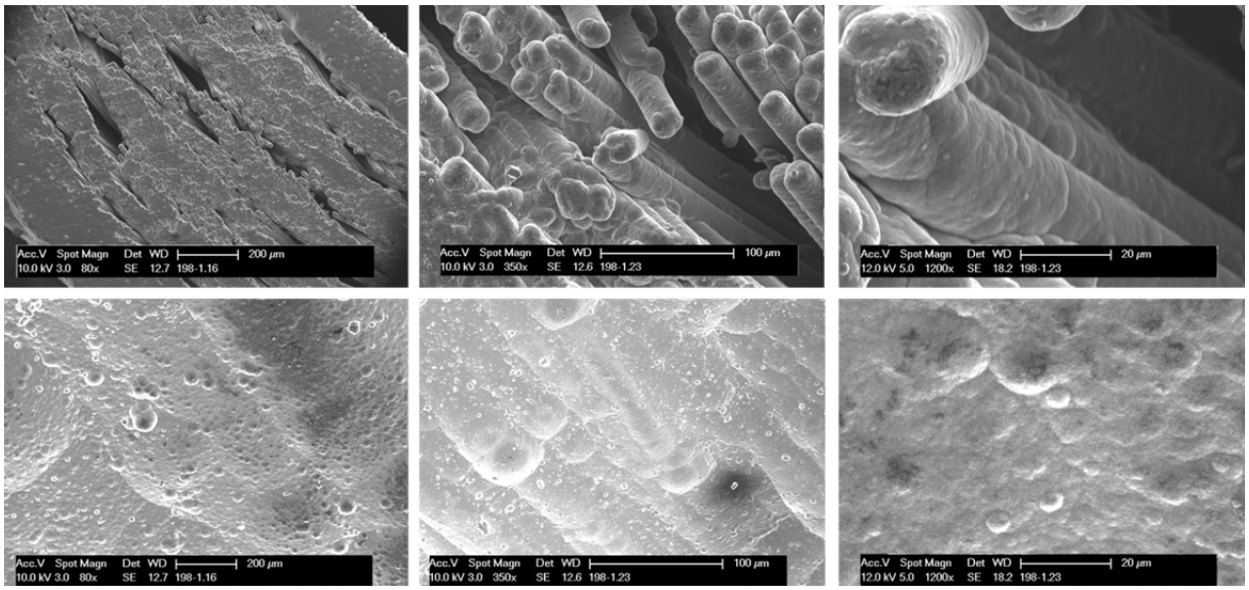

Figure 3: As-received SEM views of 198.1.23
Top: cross-section, Bottom: lateral view

The SEM work presented in Figure 3 illustrates the design of the Westinghouse samples. The upper row shows the cross section of the sample with three increasing magnifications: *80, *350, *1200. From the figure, the three-layer structure with inner monolith, CMC and outer EBC can be observed. The CMC layer is made of several interlaced tows of elliptical cross section (major axis: 1mm, minor axis: 200µm). The tows are made of approximately 500 filaments (10-15 micron diameter) that can be seen in the rightmost two images in the upper row of Figure 3. Additionally, voids between the tows and at the interface of the different layers can be observed. The roughness of the lateral surface of the sample (bottom row) arises from the woven pattern of the tows.

ii. GA samples

The GA designated specimens have an inner CMC layer and an outer monolith layer. The CMC layer for the GA open ended samples (GAOE) is similar to the CMC layer for the WEC01 196 series, with two tows in a herringbone pattern. GACE samples are sealed on one end of the tube with a SiC end plug and have two distinguishable CMC architectures: GACE-A architecture has three tows (similar to WEC01 198 & 200 series) whereas GACE-B has only two tows (similar to WEC01 196 & GAOE). Figure 4 illustrates the different tow patterns present in the GA samples. Similar to the Westinghouse samples, the GA samples have been coated by the CVD process with a thin SiC layer to protect the cut faces. For the GACE series, efforts will focus on assessing the end plug joint performance under LOCA conditions. Table 1 provides architecture details for all samples.

GACE-a GACE-b

Figure 4: Architectures of GACE samples

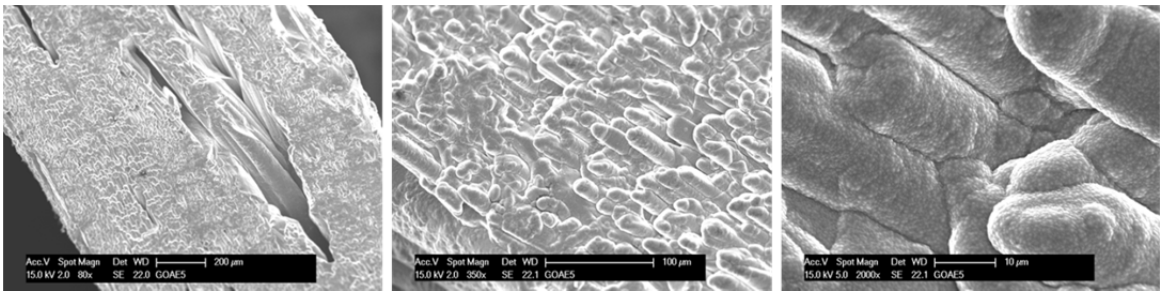

Figure 5: SEM cross section of GAOE6

Figure 5 is a cross-sectional view of sample GAOE6, representative of GAOE series. From the SEM analysis, it appears that the GAOE samples are less porous than Westinghouse samples and also have a higher SiC-matrix density. A fine pebble structure constitutes the SiC CVD overcoat. The nomenclature used to describe the samples in future publications are presented in Table 1. The summary of all the results is presented in Section VI.

Table 1: Designs, dimensions, and nomenclature of the specimens

		General Architecture					Dimensions				
		Global	CMC layer				Geometry		Ratio of the Different Layers		
		Structure	Weaving Pattern	Helicoidal Pitch (mm)	Interlace Angle	Unit Distance D between // tows	OD (mm)	ID (mm)	Inner Monolith	CMC	EBC
WEC	**196**	Tri-layer	Herringbone / Plain weave	25	90˚	0.96 mm	13.6	8.4	0.16	0.67	0.17
	198	Tri-layer	Three Tows	35	110˚	2.66 mm	11.7	8.1	0.16	0.67	0.17
	200	Tri-layer	Three Tows	40	100˚	3.18 mm	12.8	8.3	0.16	0.67	0.17
GA	**GAOE**	Duplex	Herringbone / Plain weave	15	120˚	1.47 mm	10.8	9.4	0	0.83	0.17
	GACE-A	Duplex + End Plug	Three Tows	30	100˚	1.80 mm	10.5	7.8	0	0.83	0.17
	GACE-B	Duplex + End Plug	Herringbone / Plain weave	6	150˚	1.22 mm	10.4	7.8	0	0.83	0.17

Current Nomenclature	Publication Nomenclature (XY-Z) Where X=#Layers, Y=Weave, Z= Thin CMC or Sealed
WEC01-196	Tri-Layer Plain (TP)
WEC01-198	Tri-Layer Axial Thin (TA-T)
WEC01-200	Tri-Layer Axial (TA)
GAOE	Bi-Layer Plain (BP)
GACE-A	Bi-Layer Axial Sealed (BA-S)
GACE-B	Bi-Layer Plain Sealed (BP-S)

III. As-Received Sample Characterization

1. Procedure

A destructive burst test was conducted to measure the failure hoop stress of the as-received samples. A cylindrical incompressible plug made of polyurethane was fitted in the inner space of the tubular samples and was axially strained at a constant rate of 1mm/min by a cylindrical metal insert attached to an Instron 8501 100kN load frame (Figure 6). In this manner the samples were internally pressurized by the expansion of the polyurethane plug. As the plug radially expanded, it loaded the tubular sample's inner surface until failure. Custom plugs were machined so that the volume of the plug was at best equal to the inner volume of the specimen.

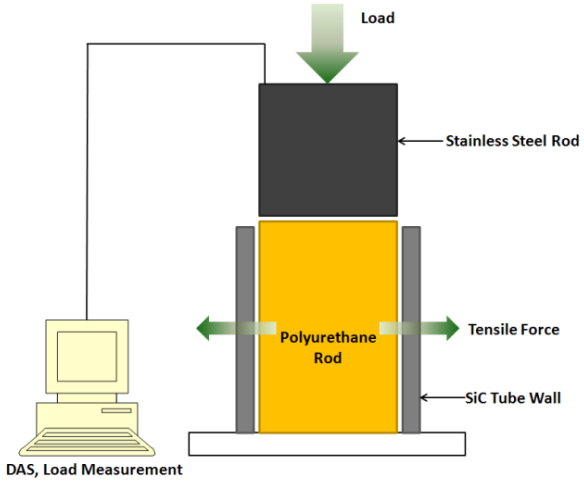

Figure 6: Schematic of the burst test

Two quantities were measured during the experiment. First, the load was retrieved from the load frame to be used to determine the internal pressure of the samples. Second, the hoop strain was measured at the outer surface of the sample using 2mm dual parallel grid strain gages (Omega SGD-2/1000-DY13) by means of a Wheatstone bridge.

The strain gage implementation was validated by measuring the Young's modulus of tubular samples of steel, aluminum and brass under similar burst test conditions. During the strain gage validation, zinc stearate was implemented to lubricate the plug and enhance the accuracy of the test.

2. Inner Pressure vs Displacement

Load and displacement of the metal insert were directly retrieved from the load frame. Under the assumption that the polyurethane plug behaves as an incompressible fluid (γ=0.5), the load registered by the load frame was used to calculate the inner pressure exerted by the plug onto the inner wall of the tubular specimens. Figure 7 shows the evolution of the inner pressure as the metal insert compresses the plug at a constant displacement rate.

Two failure modes were observed for the Westinghouse samples. The first failure mode was observed in samples 196.1.27 and 200.1.25, which broke in two stages. It is believed that the inner monolith broke

first ($p_{in} = 67\ MPa$ for sample 196.1.27) leading to uneven loading and subsequent tilting. During a second charging phase, the entire sample broke ($p_{in} = 115\ MPa$). The two stage failure of sample 200.1.25 is more clearly visible on the stress-strain curve that will be presented below. Sample 198.1.24 did not exhibit this two-stage breaking pattern but rather broke in a single crack.

For GAOE 2, no intermediate failure was observed due to the sample's lack of an inner monolith layer. Additionally, the GAOE 2 sample didn't experience catastrophic failure: the sample conserved some load carrying capacity after failure because the crack didn't cut entirely through the length of the sample. Instead, fragments of the sample dissociated and became loose, but the remainder of the sample was intact. This way, the intact parts of the samples could still potentially carry some load.

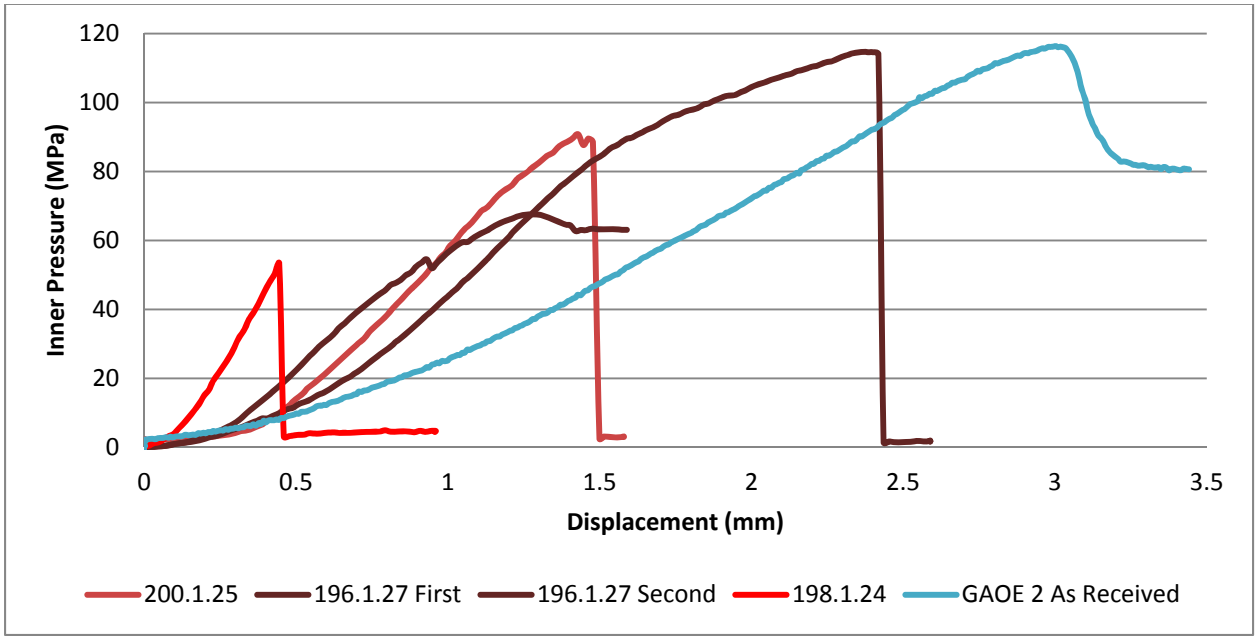

Figure 7: As-Received Samples, Inner Pressure vs Displacement

3. Optical and SEM Analysis

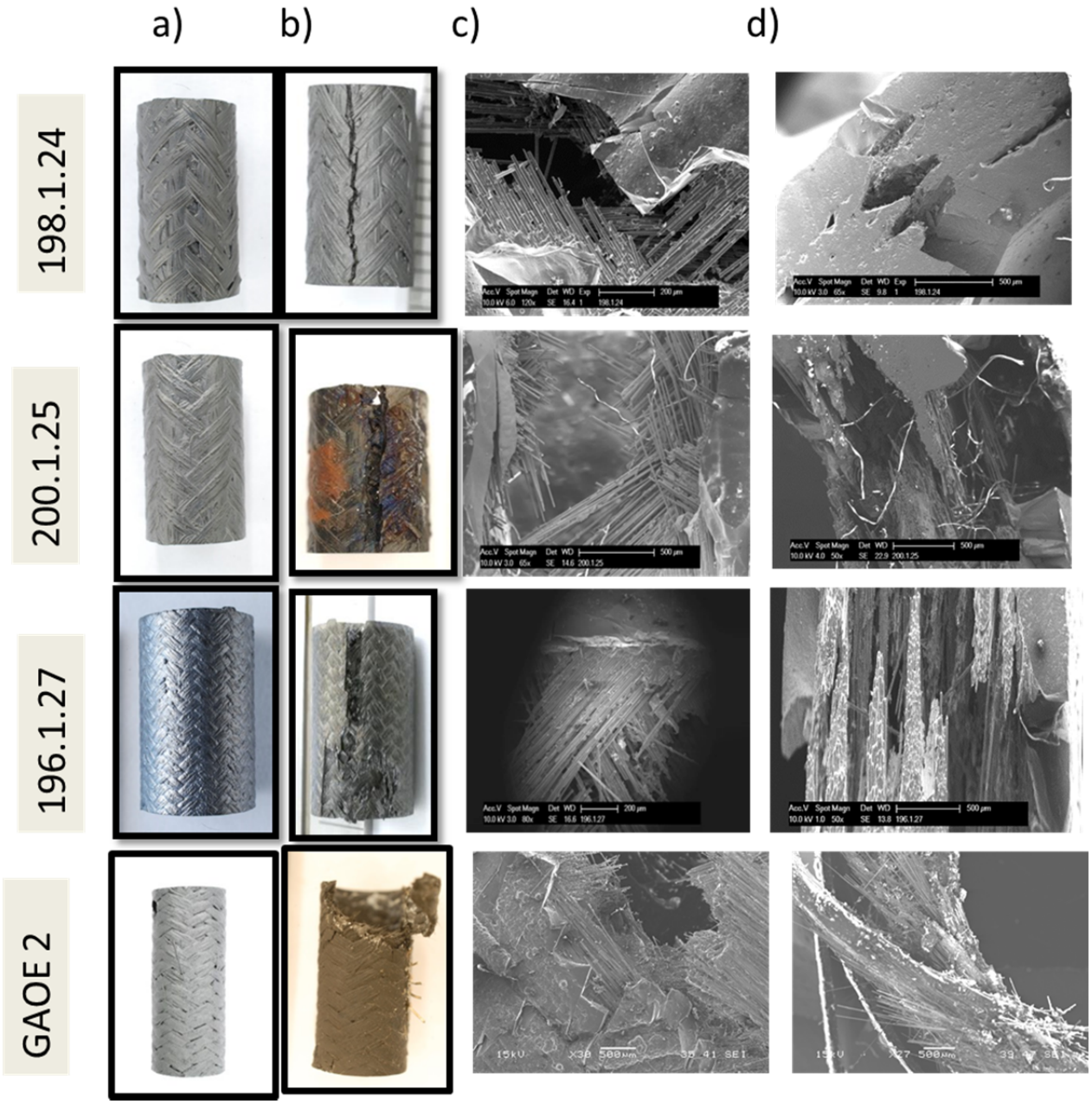

Figure 8: Optical and SEM analysis of the failure modes for the Westinghouse samples and GAOE 2
a) Lateral View As-Received (scale: 1.5 cm)
b) Post Burst Lateral view
c) Lateral SEM view
d) Top SEM view of the crack

Figure 8 presents the burst results for the as-received open ended Westinghouse and GA samples. For the as-received samples the failure crack propagated around the tows instead of cutting through the tows. Such behavior is clearly visible on column d) of Figure 8 for sample 198.1.24 or 196.1.27. Apart from this characteristic zig-zag pathway, the morphologies of the cracks fall into three distinct categories:

1. Sample 198.1.24 has a sharp, narrow crack. The inner monolith and CMC layers remained united and both layers catastrophically failed in a single crack (first row of Figure 8). Fracture is typically brittle and non-frangible.
2. Samples 196.1.27 and 200.1.25 showed wider cracks with more shearing. The inner monolith detached while the CMC region lost its matrix. As a result, opened tows are clearly visible on the SEM images (2nd and 3rd row of Figure 8). Presumably, micro cracks propagated in the CMC and stopped at the fiber-matrix interface, breaking the matrix into pieces. As a result, fibers disassembled from both the matrix and e bundles. The crack is wider than the crack observed in sample 198.1.24 (above). In this case the samples exhibit pseudo-ductility.
3. Finally, the failure mode of GAOE 2 was different from the WEC01 samples because GAOE 2 was made of almost only fibers (with only a thin 200 µm EBC layer on the outer surface). Upon failure, a piece of the sample detached from the sample and the contours of the crack loosely followed the direction of the weaving pattern. Presumably, the matrix was destroyed between the tows, thereby allowing for easier gliding of the tows and final rupture of the sample. The sample experienced pseudo-ductility.

It is believed that two possible loading regimes occurred. As long as the monolith was intact, both inner monolith and CMC layers shared the load (for the Westinghouse samples). With a strong interface bonding between the CMC and monolith layers, the CMC was able to share the load with the monolith. This mode is qualified as the shared-loading regime. Then, once the monolith failed, the CMC must withstand the load without contribution from the monolith. This regime, characterized by the inability of the monolith to share the load, is the fiber-loading regime. As will be discussed below, it is believed that the fracture will be either brittle or pseudo-ductile depending on the stress level at which the transition from shared-loading to fiber-loading occurs. This differentiates the behavior of 198.1.24 from failure of both 196.1.27 and 200.1.25. Those two loading regimes are also visible when looking at the evolution of the inner pressure as a function of displacement (analogous to time) as shown on Figure 9. On the loading curve of sample 196.1.26 (Figure 9), this shared-loading regime is observable for a metal insert position between approximately 0 and 0.75 mm. After monolith failure, characterized by a sudden drop in internal pressure, the fiber-only loading regime can be observed until complete failure of the sample.

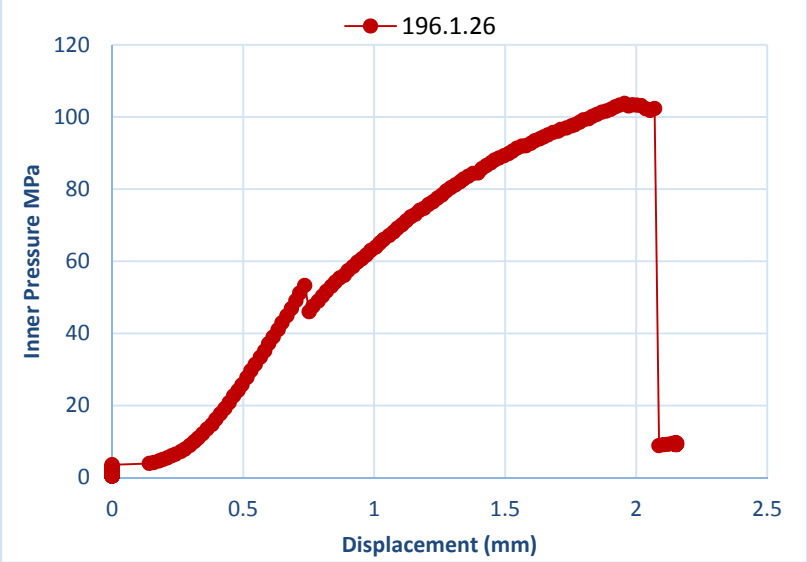

Figure 9: Illustration of the two steps loading regimes

4. Mechanical Model

This section presents the two modelling approaches to describe the shared-loading and fiber-loading regimes as can be observed on Figure 9 (above). Because the strain gages are positioned on the outer surface of the sample, it is necessary to relate the hoop stress on the outer surface to the internal pressure measured from the load frame by the mean of mechanical modelling.

From the observation of the failure modes, two models were developed: the shared-loading regime and the fiber-only loading regime. The first one intends to describe the behavior of a specimen when both the inner monolith and the CMC layer contribute to the load. On the other hand, the second model (fiber-only regime) assumes that the monolith layer does not contribute to the loading. That is, only the CMC layer is modelled. This second model is used for the GAOE samples since they don't have inner monolith but also for the Westinghouse samples once their inner monolith failed.

For the shared-loading regime, the sample is treated as a two layer structure (monolith layer and CMC layer, the EBC is treated as an extension of the CMC layer) with a perfectly bonded interface. As such, stress and strain at any point in the two concentric tubes can be calculated as a function of the internal pressure p_i, the external pressure p_o and the interfacial pressure p_s using Hooke's law and the thick cylinder equation in each region.

The general form of the thick cylinder equation is:

$$\sigma_\theta(r) = \frac{p_i r_i^2 - p_o r_o^2}{r_o^2 - r_i^2} - \frac{r_o^2 r_i^2 (p_o - p_i)}{r^2\left(r_o^2 - r_i^2\right)} \quad (4.1)$$

With p_i, p_o, r_i, r_o the inner and outer pressure and the inner and outer radii respectively for a general thick wall.

In our system, the boundary conditions of the system are:

No external pressurization: $p_o = 0$
Internal pressure p_i known (calculated from the load frame output)
Ideally bonded interface until monolith failure (strain is continuous)

Internal pressure is calculated through the load frame output. To start, $p_{load} = \frac{F}{\Sigma}$ where $\Sigma = \pi {r_i}^2$ is the inner cross section of the tubular sample and F the force recorded by the load frame. Treating the plug as an incompressible fluid leads to $p_i = p_{load}$.

It should be noted that $r_i$is the inner radius, r_s is the position of the interface and r_o is the outer radius. The compatibility equation (continuous strain at the interface) will allow for the back calculation of the internal pressure. The thick wall equation in each layer yields for $r = r_s$:

$$\sigma_{mono,s} = \frac{p_i r_i^2 - p_s r_s^2}{r_s^2 - r_i^2} - \frac{r_i^2 (p_s - p_i)}{\left(r_s^2 - r_i^2\right)} \quad (4.2)$$

$$\sigma_{fiber,s} = \frac{p_s (r_o^2 + r_s^2)}{r_o^2 - r_s^2} \quad (4.3)$$

Hooke's law coupled with continuity of hoop strain yields at the interface ($r = r_s$):

$$\sigma_{mono} = E_{mono}\epsilon_{mono} \quad and \quad \sigma_{fiber} = E_{fiber}\epsilon_{fiber} \quad (4.4)$$

$$\epsilon_{mono} = \epsilon_{fiber} <=> \frac{1}{E_{fiber}} \frac{p_s(r_o^2 + r_s^2)}{r_o^2 - r_s^2} = \frac{1}{E_{mono}} \left(\frac{p_i r_i^2 - p_s r_s^2}{r_s^2 - r_i^2} - \frac{r_i^2 (p_s - p_i)}{(r_s^2 - r_i^2)} \right) (4.5)$$

From where p_s can be deduced:

$$p_s = \frac{2r_i^2}{r_s^2 + r_i^2 + \frac{E_{mono}}{E_{fiber}} (r_s^2 - r_i^2) \frac{(r_s^2 + r_o^2)}{(r_o^2 - r_s^2)}} p_i \ (4.6)$$

Once p_s is known, the hoop stress at any generic position can be expressed:

$$\sigma_{mono} = \frac{p_i r_i^2 - p_s r_s^2}{r_s^2 - r_i^2} - \frac{r_s^2 r_i^2 (p_s - p_i)}{r^2 (r_s^2 - r_i^2)} \quad (4.7) \text{ for } r < r_s$$

$$\sigma_{fiber} = \frac{p_s r_s^2}{r_o^2 - r_s^2} + \frac{r_s^2 r_o^2 p_s}{r^2 (r_o^2 - r_s^2)} \ (4.8) \ \text{ for } r \geq r_s$$

Hoop strain is then back calculated using Hooke's law:

$$\epsilon_{mono} = \frac{\sigma_{mono}}{E_{mono}} \ \ and \ \ \epsilon_{fiber} = \frac{fiber}{E_{fiber}} \ (4.9)$$

To perform those calculi, it is necessary to know the elastic moduli of the monolith and the CMC layers. The value of the monolith modulus was taken from (1):

$$E_{mono} = 460 \ GPa$$

An initial guess for the fiber modulus was also made based on the same reference (1):

$$E_{fiber} = 220 \ GPa$$

Fed with those moduli values, this model allows the estimation of the hoop stress at the OD knowing the inner pressure of the sample (equations *(4.6)* and *(4.8)*). Independently, strain is also measured. Accordingly, it is possible to use this estimated stress (derived from p_i) with the experimental strain to determine a fiber elastic modulus.

As a precaution, one must insure that the fiber elastic modulus observed on the stress-strain curve (post modeling) equals the modulus that fed the mechanical model (pre-modeling, equation *(4.6)*). That way, the mechanical model remains consistent with the experimental Hooke's law observed. To do so, iterations on the fiber elastic modulus were implemented until convergence (no more than three iterative steps were needed).

<u>For the fibers only charging region</u>

When the model presented above is not relevant (GAOE samples or failed monolith), the thick wall model was simply implemented to describe the CMC layer.

In the case of the GAOE samples, the thick wall cylinder equation directly applies and yields:

$$\sigma_\theta(r) = \frac{p_i r_i^2 - p_o r_o^2}{r_o^2 - r_i^2} - \frac{r_o^2 r_i^2 (p_o - p_i)}{r^2 (r_o^2 - r_i^2)} \ (4.10)$$

Since $p_o = 0$, we get:

$$\sigma_\theta(r) = \frac{p_i r_i^2}{r_o^2 - r_i^2} + \frac{r_o^2 r_i^2 p_i}{r^2 (r_o^2 - r_i^2)} \ (4.11)$$

In this case, there is no need for an initial guess for the fiber elastic modulus. It is directly measured on the stress strain-curve.

For the Westinghouse samples, this model applies when the inner monolith breaks. The inner radius becomes r_s and the pressure: $p_s = p_i$.

$$\sigma_\theta = \frac{p_i r_s^2}{r_o^2 - r_s^2} + \frac{r_s^2 r_o^2 p_i}{r^2(r_o^2 - r_s^2)} \quad (4.12)$$

At last, it is necessary to define how failure is calculated. Because strain was measured on the OD, all the stress-stain curves are plotted at that point with a perceived failure hoop stress at that point. However, levels of stresses are higher in the ID than in the OD. Therefore, the failure must initiate at the ID and the failure stress is the stress at this point (ID). As such, we calculated the failure stress as the stress in the ID at the moment of failure. The energy and momentum released by the local failure at the ID position triggers the failure of the outer layers (up to the OD) even if the stress levels at those points were slightly below the failure hoop stress.

5. Mechanical Results

Although the burst tests of the as-received samples 196.1.27 and 198.1.24 were performed prior to the implementation of strain gages, the burst tests of the as-received samples 200.1.25 and GAOE 2 were performed with strain gages implemented. The strain gages were implemented such that they measured the hoop strain on the outermost surface of the sample.

Because the strain gages were implemented on the outer surface of the samples, the stress-strain curves presented in the work represent the outer surface. However, the failure stresses presented in this work reflect the peak calculated stresses in the samples, which occur on the inner surfaces of the sample layers. Therefore, the failure stresses observed in the stress-strain curves are always lower than the peak failure stresses experienced by the samples as reported in the tabulated data.

Endplug pushout testing was performed following General Atomics procedure (2) which consists of uniaxial loading of the endplug (Figure 10). The burst strength reported is obtained by dividing the peak force by the internal area of the sample as shown in equation 5.1. The burst strength is analogous to the internal pressure required to result in joint failure.

$$Burst\ Strength = \frac{Peak\ Load}{\pi * r_i^2} \quad (5.1)$$

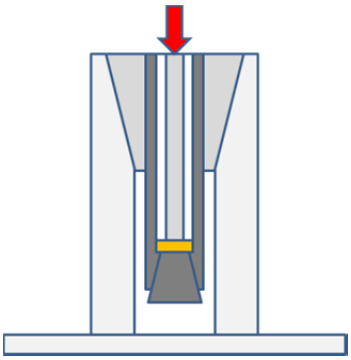

Figure 10: GA endplug pushout test set-up

i. Series 196

Figure 11 presents the internal pressure versus displacement curves obtained for the as-received sample 196.1.27. The first loading curve experienced monolith failure but was terminated prior to fiber failure due to plug leakage. The plug leakage can be observed from the first loading curve by the substantial increase in displacement with negligible increase in internal pressure. For the second loading curve, the sample was loaded until complete sample failure.

Table 2 presents the mechanical properties gathered from the burst testing of sample 196.1.27. The failure plenum pressure is defined at the inner monolith failure, as the sample losses hermeticity once it the monolith fails. In parenthesis is the pressure at total failure.

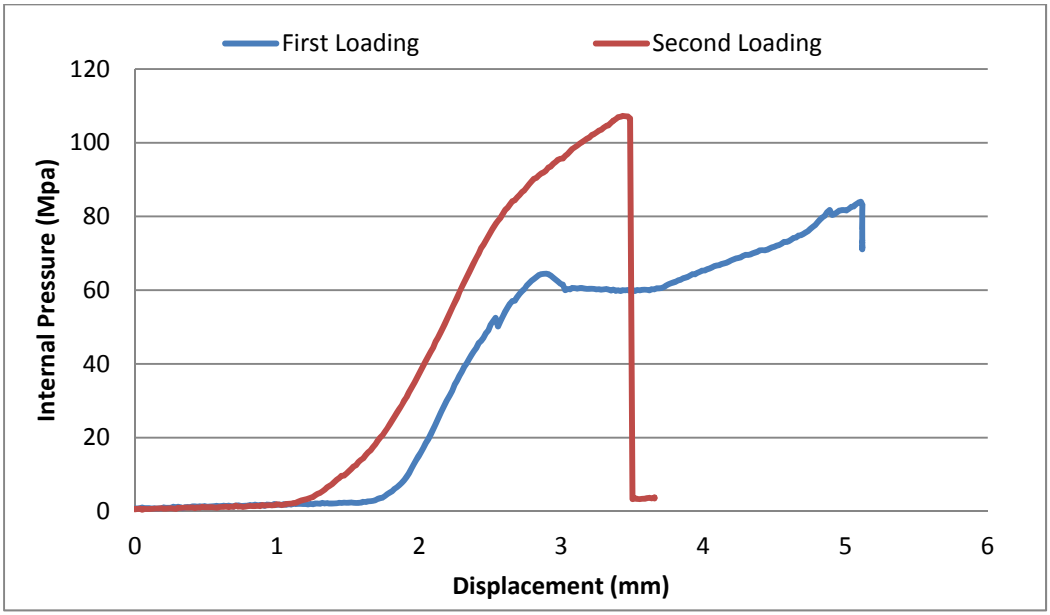

Figure 11: Internal Pressure vs Displacement curves for as-received sample 196.1.27

Table 2: Mechanical characteristics of sample 196.1.27

	196.1.27 As-Received
Failure Hoop Stress ID Monolith	249 MPa
Failure Hoop Stress ID Fibers	267 MPa
Failure Plenum Pressure (Total Failure)	64 MPa (107 MPa)

ii. Series 198

Figure 12 presents the internal pressure versus displacement curve for the burst test of the as-received sample 198.1.24. From the curve, only one distinct loading regime can be identified. Furthermore, the steep slope of the loading curve indicates a stiff sample with little yielding.

Table 3 presents the mechanical characteristics obtained for the as-received sample 198.1.24. Because the fiber region failed simultaneously as the monolith region, the precise failure stress for the fiber region could not be determined. However, the limits for the failure stress of the fiber region were determined based on the stress of the fibers during shared loading with the monolith and the stress of the fibers during fiber-only loading at the moment of sample failure.

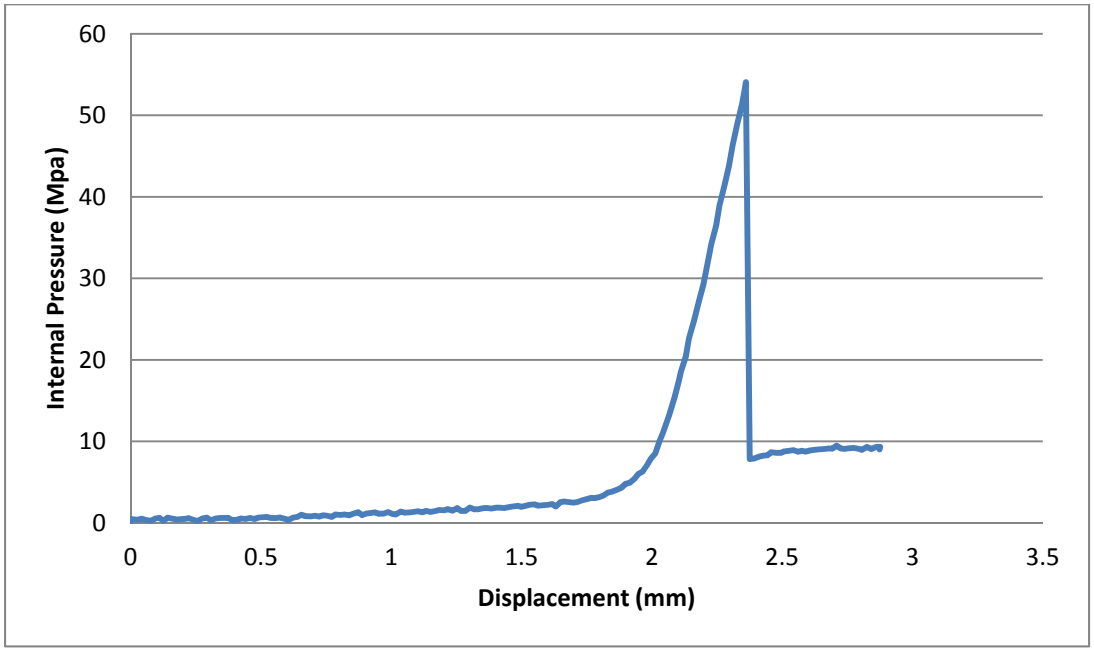

Figure 12: Internal Pressure vs Displacement curve for as-received sample 198.1.24

Table 3: Mechanical characteristics of as-received sample 198.1.24

	198.1.24 As-Received
Failure Hoop Stress ID Monolith	267 MPa
Failure Hoop Stress ID Fibers	115-232 MPa
Failure Plenum Pressure (Total Failure)	54 MPa (54 MPa)

iii. Series 200

Multiple tests were performed on sample 200.1.25. Test 1 loaded the sample with the monolith intact and was terminated at plug leakage from the bottom. Test 2 loaded the sample with the monolith intact, but experienced monolith failure and the transition to fiber-only loading before being terminated. Test 3 loaded the sample with the failed monolith until complete failure of the sample.

The mechanical model previously described was used to calculate stress for the stress-strain curves. The stress indicated is the calculated stress at the OD of the sample (the location of the strain gage). The resulting stress-strain curve for the outer surface of the sample is shown in Figure 13. Table 4 presents the mechanical characteristics gathered from the stress-strain behavior of sample 200.1.25. The change in elastic modulus of the sample with increasing yielding can be observed.

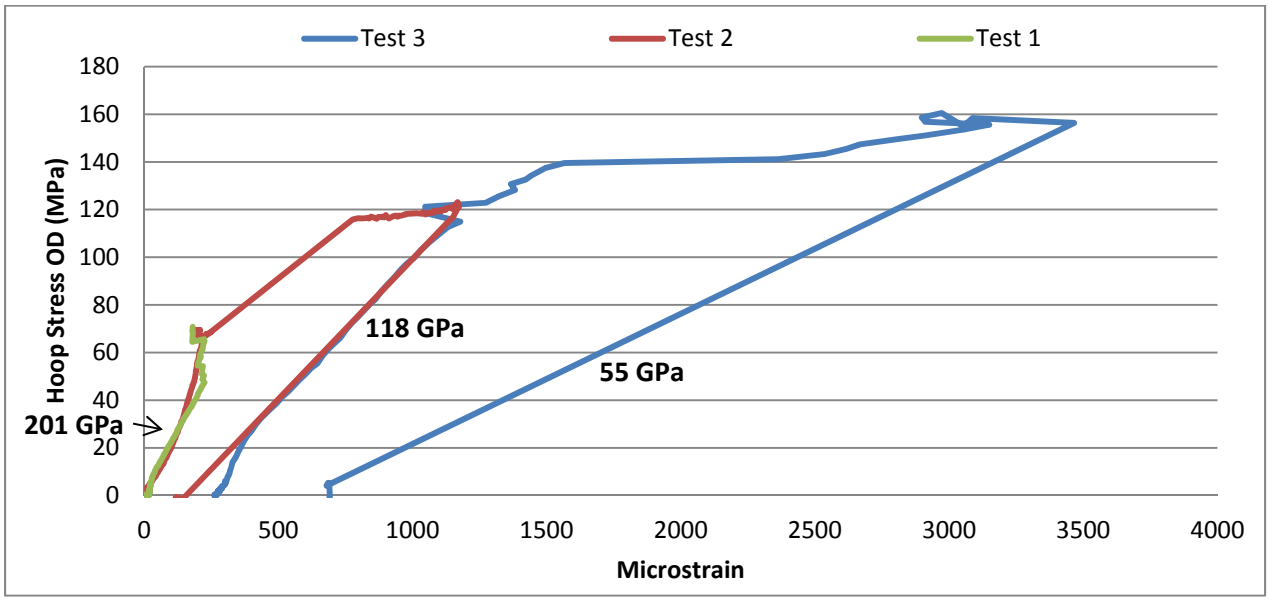

Figure 13: Stress-Strain curve for outer surface of sample 200.1.25 (slopes of elastic regions indicated on curve)

Table 4: Mechanical Characteristics of 200.1.25

	200.1.25		
	Test 1	**Test 2**	**Test 3**
Elastic Modulus	201 GPa	118 GPa	55 GPa
Yield Stress (ID of fibers)	105 – 175 MPa		
Failure Hoop Stress ID Monolith	243 MPa		
Failure Hoop Stress ID Fibers	242 MPa		
Failure Strain	3466 μ-strain		
Failure Plenum Pressure (Total Failure)	60 MPa (82 MPa)		

iv. Series GAOE

One burst test was performed on sample GAOE 2 which loaded the sample to failure. Sample GAOE 2 was treated as a thick-wall cylinder with only one layer (in contrast to the multilayer mechanical model of the Westinghouse samples). Using the thick wall cylinder stress equations, the stress-strain curve was constructed for sample GAOE 2 and is presented in Figure 14. The stress indicated is the stress on the OD of the sample.

Table 5 presents the mechanical properties of sample GAOE 2 gathered from the stress-strain curve. A change in slope can be observed in the GAOE 2 sample. A large increase in strain from 300 to 600 microstrain signalizes the onset of pseudo-ductility in the sample and defines the yielding stress of the fiber region (although the calculated stress at the ID is tabulated).

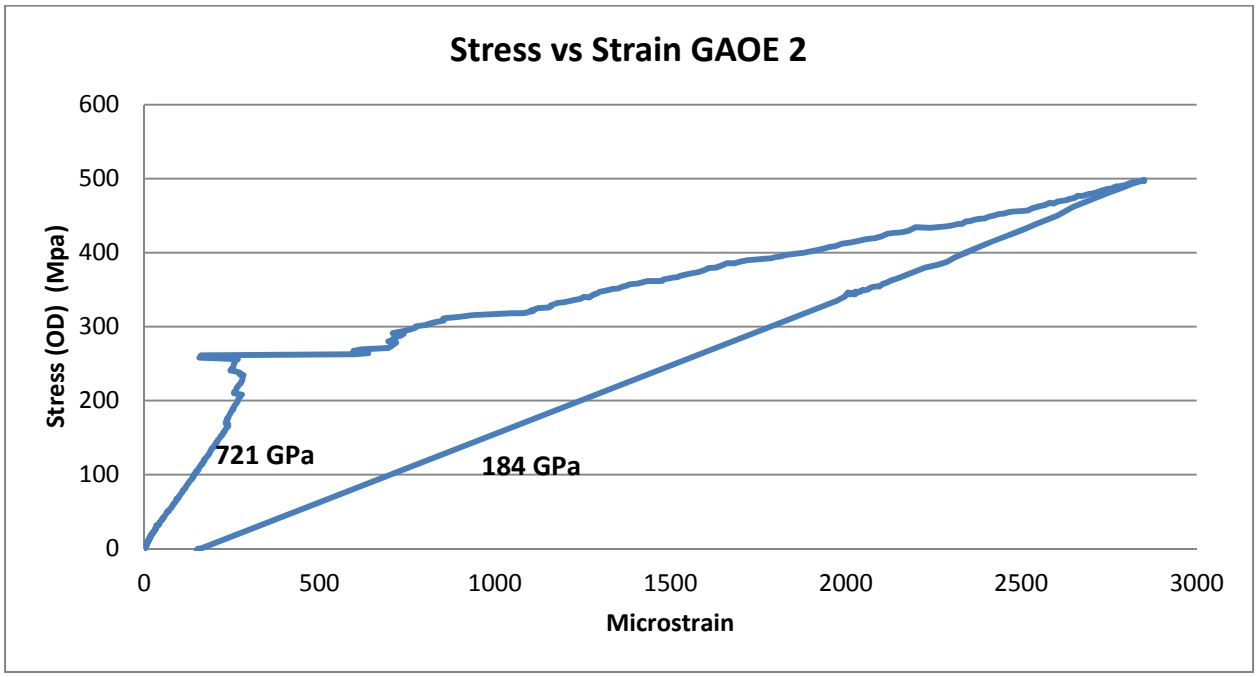

Figure 14: Stress-Strain curve for outer surface of sample GAOE2 (slopes of elastic regions indicated)

Table 5: Mechanical characteristics of GAOE2

	GAOE 2 As-Received
Elastic Modulus	721 GPa
Yield Stress (ID)	304 MPa
Failure Hoop Stress ID	581 MPa
Failure Strain	2851 μ-strain
Failure Plenum Pressure	76 MPa

v. Series GACE-A

An endplug pushout test was performed on the as-received sample GACE 2. The test uniaxially loaded the endplug until failure, which was observed in the joint region, signifying a valid test. Figure 15 presents the load versus pushrod displacement curve for the pushout test.

Table 6 presents the mechanical strength characteristics of the endplug joint for the as-received sample GACE 2. Note that the burst strength is analogous to the internal pressure required to result in joint failure.

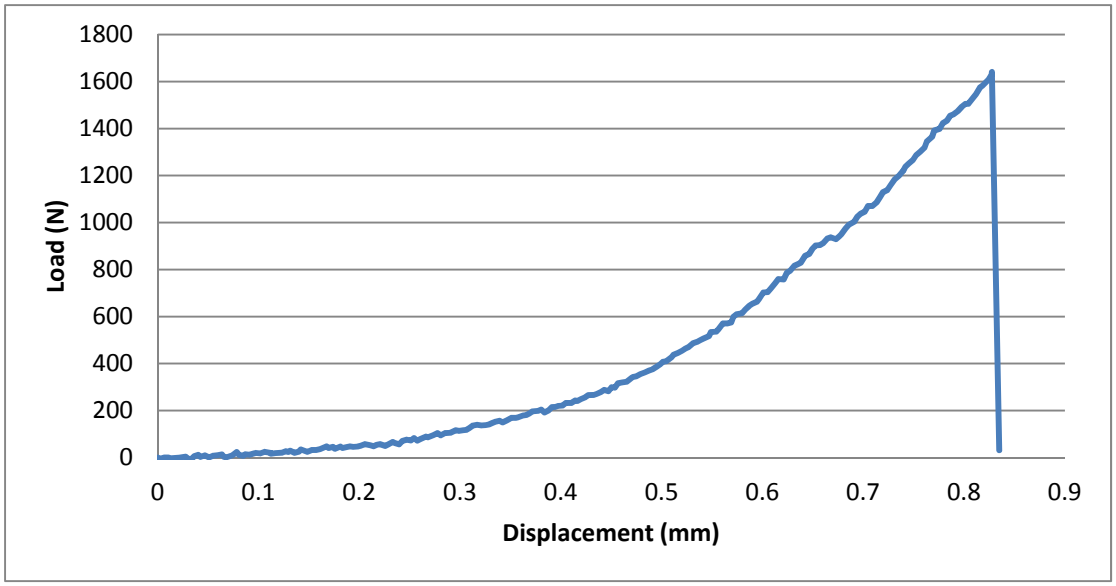

Figure 15: Pushrod load versus displacement curve for GACE 2 pushout test

Table 6: Mechanical characteristics of endplug joint for GACE 2

	GACE 2 As-Received
Peak Load (N)	1641 N
Burst Strength (MPa)	37.1 MPa

vi. Series GACE-B

An endplug pushout test was performed on the as-received sample GACE 6. The test uniaxially loaded the endplug until failure, which was observed entirely in the joint region, signifying a valid test. Figure 16 presents the load versus pushrod displacement curve for the pushout test.

Table 7 presents the mechanical strength characteristics of the endplug joint for the as-received sample GACE 6. Note that the burst strength is analogous to the internal pressure required to result in joint failure.

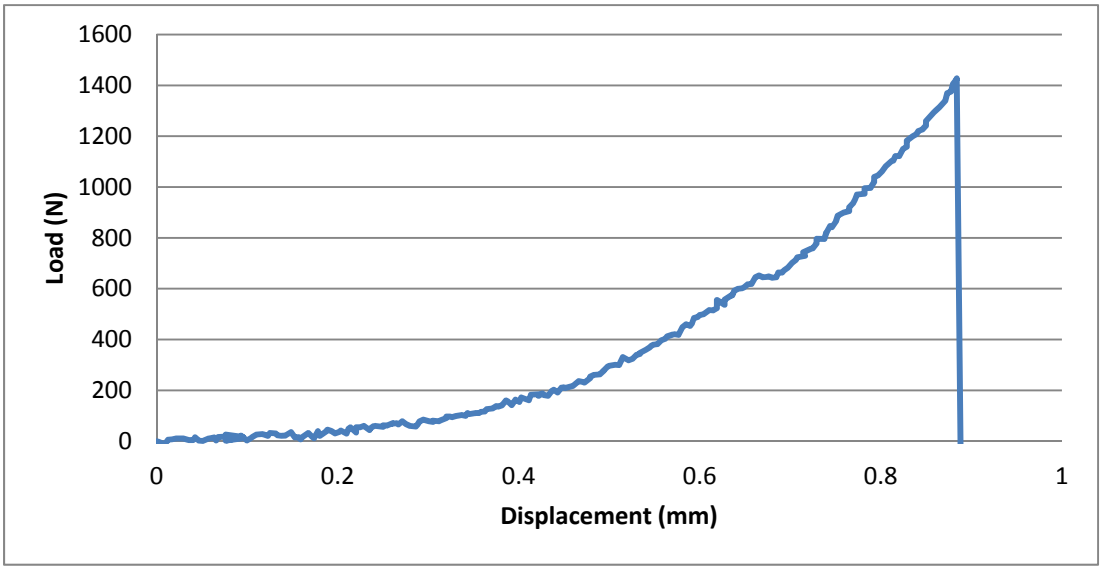

Figure 16: Pushrod load versus displacement curve for GACE 6 pushout test

Table 7: Mechanical characteristics of endplug joint for GACE 6

	GACE 6 As-Received
Peak Load (N)	1428 N
Burst Strength (MPa)	32.3 MPa

6. Failure Characteristics

For the Westinghouse samples, during the initial monolith charging, the samples behaved elastically and were characterized by the monolith and fibers loading simultaneously (as outlined in the mechanical model section above). However once the failure stress of the monolith was exceeded, the monolith failed by suddenly cracking entirely through. Additionally, after the monolith failed small pieces of monolith were observed to detach from the sample. The detachment of small pieces of monolith is attributable to the proliferation of cracking around the initial failure crack and the evident destruction of the interface between the monolith and the fiber region. This was confirmed in tests where loading was reversed shortly after yielding and the samples showed a destroyed inner monolith and an intact CMC.

After monolith failure, some samples could offer resistance to further loading, as observed in the fiber-only loading regions of series 200 or for GAOE 2 (Figure 17). It is also believed from the pressure vs displacement curve that series 196 (Figure 17) had a fiber-only loading regime even though no strain measurements were obtained. During this fiber-only loading stage, the fiber region resisted the load with negligible contribution from the failed monolith. Below the fiber region yield stress, the fiber region behaved linearly-elastically and was characterized by the stretching of the CMC layer without slipping of fibers or destruction of the matrix. However once the fiber region yield stress was exceeded the fibers began to slip across one another as the matrix between the fibers was gradually destroyed. This fiber slipping behavior can be observed in the sudden increases in strain with negligible increases in stress for the stress-strain curve obtained for sample 200.1.25. As the stress increased more of the CVI matrix was destroyed resulting in more fiber slippage. This behavior can be observed in the changing elastic modulus for the stress-strain curve obtained for sample 200.1.25.

Sample failure occurred when the fibers' matrix had been thoroughly destroyed and the fibers, stressed too high, finally fractured. The fiber failure region was characterized by a crack fully penetrating the sample at the radial location of the monolith failure. However, the fiber region did not fail catastrophically and instead only failed at one angular location. Except at the angular location of failure, the fibers were still intact and maintained a geometry very similar to the original geometry of the sample. The stress-strain curve obtained for sample 200.1.25 demonstrates that after complete sample failure, when the stress was relaxed to zero, the sample was only 0.07% strained when compared to 0.28% failure strain.

For sample series 198 the fiber region failed almost immediately after the monolith failed and could not withstand higher internal pressures than those which caused the monolith failure. This behavior is attributable to the cracks formed during monolith failure penetrating through the fibers immediately without crack-blunting. The cracks cause the fibers to fail before the fibers have a chance to exhibit pseudo-ductility, resulting in complete failure of the sample in series 198 upon failure of the internal monolith layer.

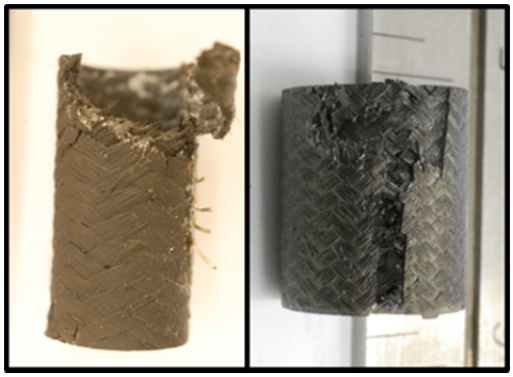

Figure 17: Comparison of Failure Characteristics of GAOE 2 (left) and 196.1.27 (right)

The GAOE 2 sample failure was characterized by complete detachment of large sections of the sample (Figure 14 & Figure 17). When the sample failed, a large fragment of fibers entirely separated from the sample, and much of the remaining material at the site of failure was only very loosely connected to the body of the sample. However, the cracking did not occur along the entire length of the sample as in the Westinghouse samples. Instead, the cracking appeared to follow the contours of the fiber tows until dissipating before traversing the entire length of the sample.

The GAOE 2 (Figure 14 & Figure 17) sample cracking led to near-complete separation of large sections of the sample and resulted in the partial opening of the sample at the site of failure. The Westinghouse sample cracking, although occurring along the entire length of the sample, did not open the interior of the sample.

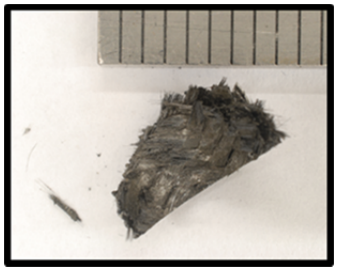

Figure 18: Detached Fragment of GAOE 2

Endplug pushout testing revealed similar failure characteristics for the as-received samples of both architectures tested (GACE-A and GACE-B). The failure of the joint occurred near the top of the endplug with significant debonding of the endplug and tube. After failure, the endplug entirely detached from the tube. Figure 19 shows the similarity in the failure characteristics of the endplug joint after pushout testing of the as-received samples.

Figure 19: Endplug failure characteristics of as-received samples GACE 2 (left) and GACE 6 (right)

7. Conclusion

The mechanical model as presented above was used to calculate the failure hoop stresses of the Westinghouse samples. For the GA samples, the thick-wall cylinder mechanical model was used because the GA samples lacked the distinct inner monolith layer of the Westinghouse samples. Because the inner surface of the samples experienced the highest hoop stress, the ID hoop stress of each layer was tabulated as the failure hoop stress of the respective layer. However, because the strain measurements were taken at the outer surface of the samples, the strain data provided reflects the hoop strain of the OD of the samples during the event of interest (monolith or fiber region failure). The results of the strength testing of the as-received samples are presented in Table 8. The yield stress of the fiber region was calculated for the inside surface of the sample and is presented in Table 9.

Table 8: As-received strength testing

	Monolith Layer		Fiber Layer	
As-Received Sample	**ID Failure Hoop Stress**	**Sample OD Hoop Strain At Event**	**ID Failure Hoop Stress**	**Sample OD Hoop Strain At Event**
196.1.27	249 MPa	No Data	267 MPa	No Data
198.1.24	267 MPa	No Data	115 - 232 MPa	No Data
200.1.25	243 MPa	0.0224 %	242 MPa	0.35 %
GAOE 2	No inner monolith		1190 MPa	0.28%
	Peak Load		**Burst Strength**	
GACE-a 2	1641 N		37.1 MPa	
GACE-b 6	1428 N		32.3 MPa	

Table 9: Fiber yield stress for as-received samples

As-Received Sample	Fiber ID Yield Stress
196.1.27	109 – 161 MPa
198.1.24	115 – 231 MPa
200.1.25	105 – 175 MPa
GAOE 2	612 MPa

The monolith layer failure hoop stress was very similar for all Westinghouse as-received samples. For these samples, the monolith failed at a hoop stress of between 240 and 270 MPa. The fiber region failure hoop stress was similar for samples 196.1.27 and 200.1.25 at 267 and 242 MPa respectively. However, because sample 198.1.24 experienced fiber region failure immediately upon monolith failure the precise fiber region failure hoop stress cannot be ascertained but was calculated to be greater than 115 MPa and lower than 232 MPa, the corresponding hoop stresses for shared-loading and fiber-loading respectively at the instant the monolith failed.

The fiber layer failure behavior of sample 198.1.24 differs markedly from the failure behavior of 200.1.25 and 196.1.27. This is possibly due to the inability of the CMC Fiber layer to effectively resist the cracks initiated during monolith failure due to excessive stress in the fiber region. Immediately after monolith failure, the stress of the fiber region required to contain the internal pressure in 198.1.24 was far higher than in samples 196.1.27 and 200.1.25. It is possible that the fiber-only loading stress was too

high in 196.1.27 at the instant of monolith failure and that the CMC layer was unable to resist the internal energy released by the monolith failure, thereby allowing cracks initiated by monolith failure to propagate through the fibers and result in complete failure of the sample upon monolith failure.

The GAOE 2 sample withstood far higher stresses than those seen in the Westinghouse samples. The peak stress of the GAOE 2 sample was 1190 MPa whereas the fiber failure stress observed in the Westinghouse samples was roughly 260 MPa. Sample GAOE 2 experienced fiber yielding at a stress of 612 MPa.

The endplug joint strength between the two GACE samples was similar, with both joints achieving burst strength of slightly higher than 30 MPa. Because the endplug burst strength is lower than the peak internal pressure observed in the tube sections during burst testing, the endplug joint is likely the weakest part of the cladding.

8. Discussion

The stress calculations rely on the validity of the mechanical model outlined previously in Section 0.4. However, this model relies on several key assumptions whose accuracy is uncertain. One of the principal assumptions is the perfect interface between the monolith and the fiber layers. The model assumes that this interface is capable of perfectly transmitting the radial stress and strain from the monolith layer to the fiber layer. However, if the interface is not perfect then the calculated monolith stress would be lower than the true monolith stress, and the calculated fiber region stress would be higher than the true fiber region stress.

Another important assumption made in the mechanical model is that the fiber region behaves as a continuous material with spatially constant properties. This assumes that at any given instant, every location in the fiber region has the same properties. However, this treatment of the fiber region is highly simplified. The stress-strain behavior of CMC fiber demonstrates that the elastic modulus of the fiber region is not spatially constant but rather depends on the amount of yielding experienced by the CMC at the location of interest. This would result in a true stress distribution with lower stress on the inner surfaces and higher stress on the outer surfaces when compared to the stresses calculated using spatially constant properties.

Moreover, it is assumed that the monolith does not contribute at all to the fiber loading regime once it fails. However, it was observed that the inner monolith was reduced into pieces at the end of the burst test, suggesting that the monolith conserved some capability to carry additional load (otherwise it wouldn't be further reduced in smaller pieces). Therefore, this assumption should be partially relaxed by accounting for a monolith contribution after main failure in future modelling efforts.

Additionally, the calculation of the stress state of the fiber region when the monolith is intact relies on knowing the elastic modulus for the fibers and for the monolith. For samples 196.1.27 and 198.1.24 the elastic modulus of the fiber region was not known, and therefore the elastic modulus determined for sample 200.1.25 was used (200 GPa). However, for all samples the elastic modulus of the monolith layer was not experimentally measured; therefore the value of 460 GPa was used from literature. Were the

true elastic moduli different from those used in the calculations, the true stress distributions would be different from those presented.

Finally, edge effects of the experimental set-up should be accounted for. In particular, plug leakage on the upper end of the samples leads to stress concentration at that position, resulting in preferential failure from the top.

Because only one sample in each Westinghouse series (196, 198, and 200), only one sample in the GAOE series, and only one sample in each GACE architecture series were tested as-received, there are too few samples to provide meaningful statistics on the distribution of true population as-received mechanical properties. Only by testing more samples could the population's true distribution of mechanical properties be determined.

IV. Thermal Shock Experiments

1. Procedure & Results

The thermal shock experiments attempt to reproduce the conditions associated with the restoration of coolant flow following a LOCA accident. Prior to the restoration of coolant flow, the fuel rod temperature increases owing to the lack of coolant flow. Indeed, if the coolant remains stagnant in the core it may altogether evaporate, thereby exposing the fuel rods. Once the emergency core cooling system is reactivated, the onrush of water at near-atmospheric conditions results in severe thermal shock to the previously exposed fuel rods.

The experimental setup, shown in Figure 20, involves a quartz tube which rises from a water pool to the heart of a furnace capable of 1500°C. A pneumatic actuator drives the alumina sample holder from the furnace into the water. The entire quenching process is recorded with a high speed video camera (around 1000 frames per second). The recording is used to quantify the different heat transfer regimes involved throughout the quenching process.

In the thermal shock tests, specimens are heated to 1200°C and then quenched into either 100°C saturated or 90°C (10°C subcooled) water depending on the test criteria. All specimens survived the thermal shocks without any visible mechanical deterioration (although the sample appearance changed, see below). In particular, whereas pure monolith samples used to shatter upon quenching into 100°C water (1), the inner monolith (for the Westinghouse samples) and the EBC do not show any visible sign of mechanical degradation. Similarly, the fibers' ends also remain intact. All thermal shock samples were burst tested after quenching to investigate degradation of mechanical properties. None of the thermal shock samples exhibited significant degradation of mechanical properties when compared to the as-received samples.

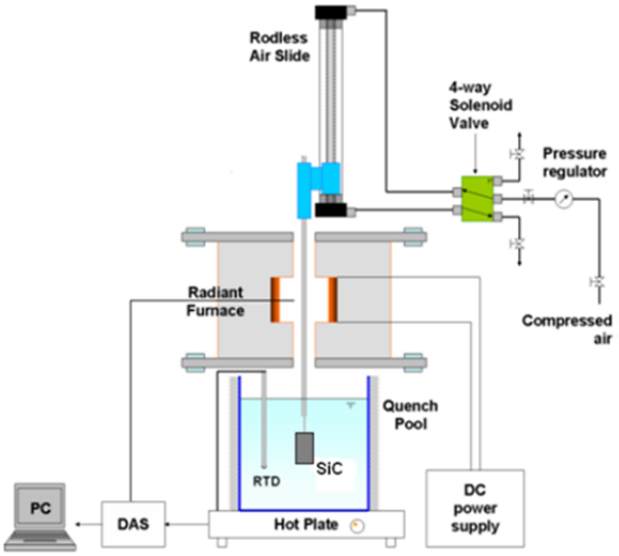

Figure 20 (right): Schematic of Thermal Shock Facility

2. Thermal-Hydraulic Analysis

All of the samples were observed to behave in a similar manner. First, the specimen entered the quenching water carrying a layer of air. Because of the air and the high temperature of the sample, the sample began film boiling. Except for the GACE samples, the Leidenfrost point was achieved after approximately 10 seconds, with a quench front starting at the bottom of the sample and progressing to the top of the sample in two to three seconds. For the GACE samples, due to the presence of the endplug that allows for retention of more heat, film boiling lasted approximately 30 seconds before the Leidenfrost point was achieved, with the quench front progressing from the top of the sample to the

bottom (this results from the latent heat associated with the end plug at the bottom). As the sample rewetted, heat was transferred by nucleate boiling until complete cooling. Also, no major difference was observed between 100°C and 90°C thermal shocks. Figure 21 illustrates this behavior for sample 196.1.26 quenched from 1200°C into 90°C water.

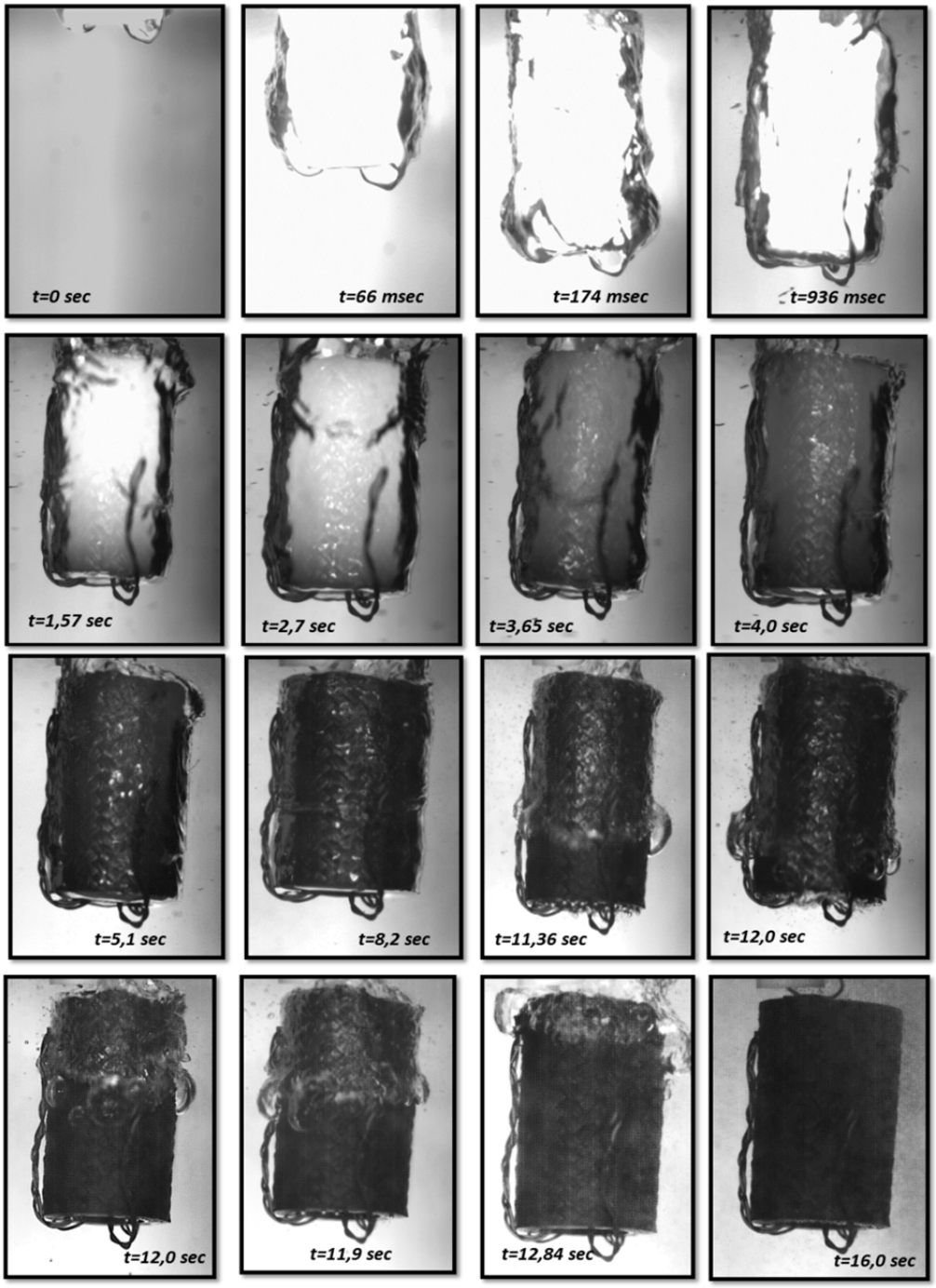

Figure 21: Quench of 1200°C 196.1.26 into 90°C water, quench from is first seen at t = 11.36 seconds

3. Optical & SEM analyses

i. Westinghouse Samples

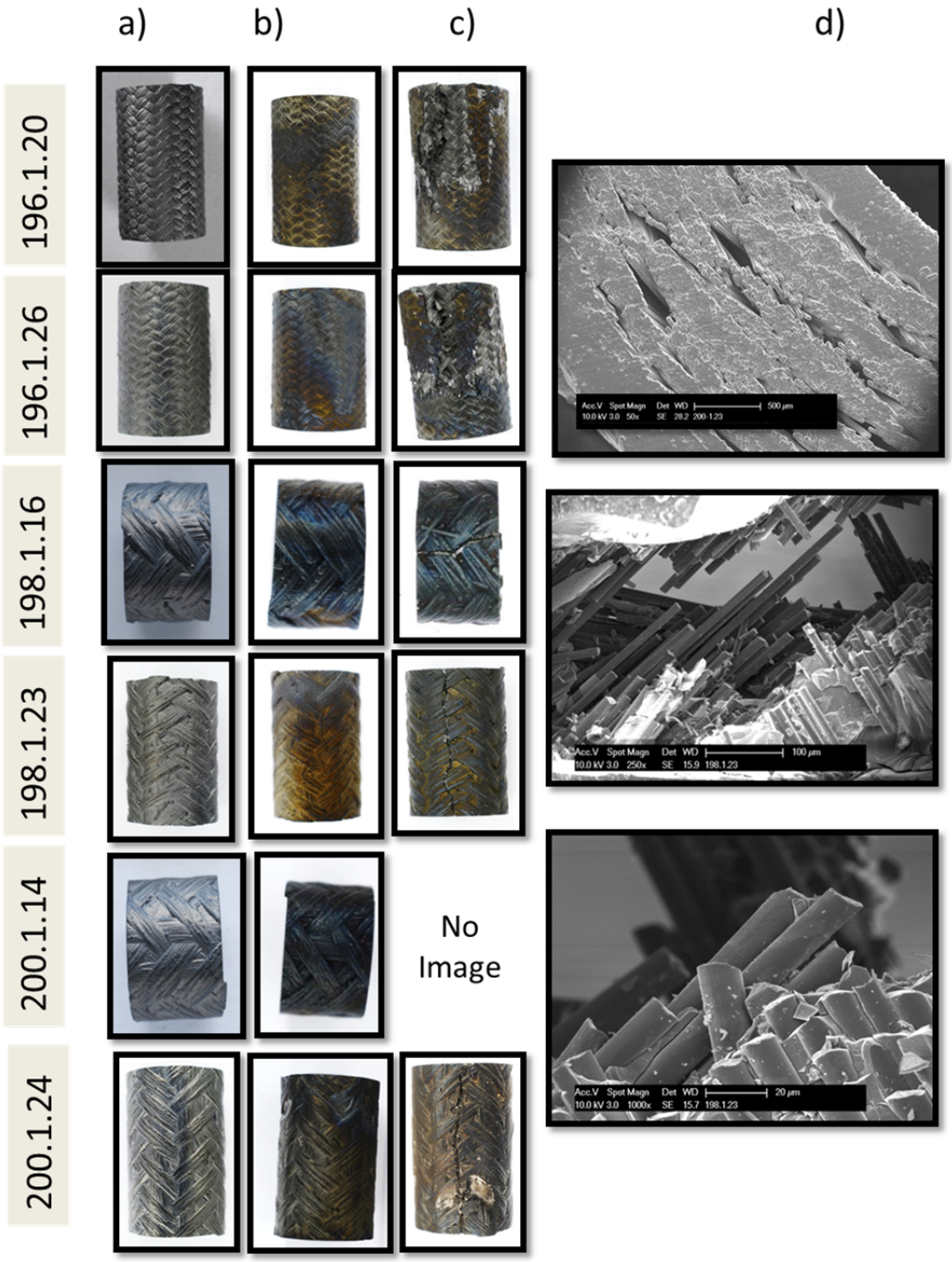

Figure 22: Optical and SEM analysis of quench characteristics of Westinghouse samples
a) as-received lateral view
b) post quench lateral view
c) crack after quench & burst
d) SEM images of the sample 198.1.23: cross section as-received and views of the post burst test crack

Following quenching, surfaces of the samples exhibited discoloration (Figure 22 columns a and b), betraying the presence of an oxide layer. Oxide layers with a thickness similar to the wavelength of visible light can create such a discoloration: therefore, the oxide layer was likely about 0.5 microns thick. SEM analysis (see Figure 22 column d as an illustration) revealed that the underlying structure of the sample was unaffected by the quenching, with no signs of failure or breaking detected.

ii. GA Samples

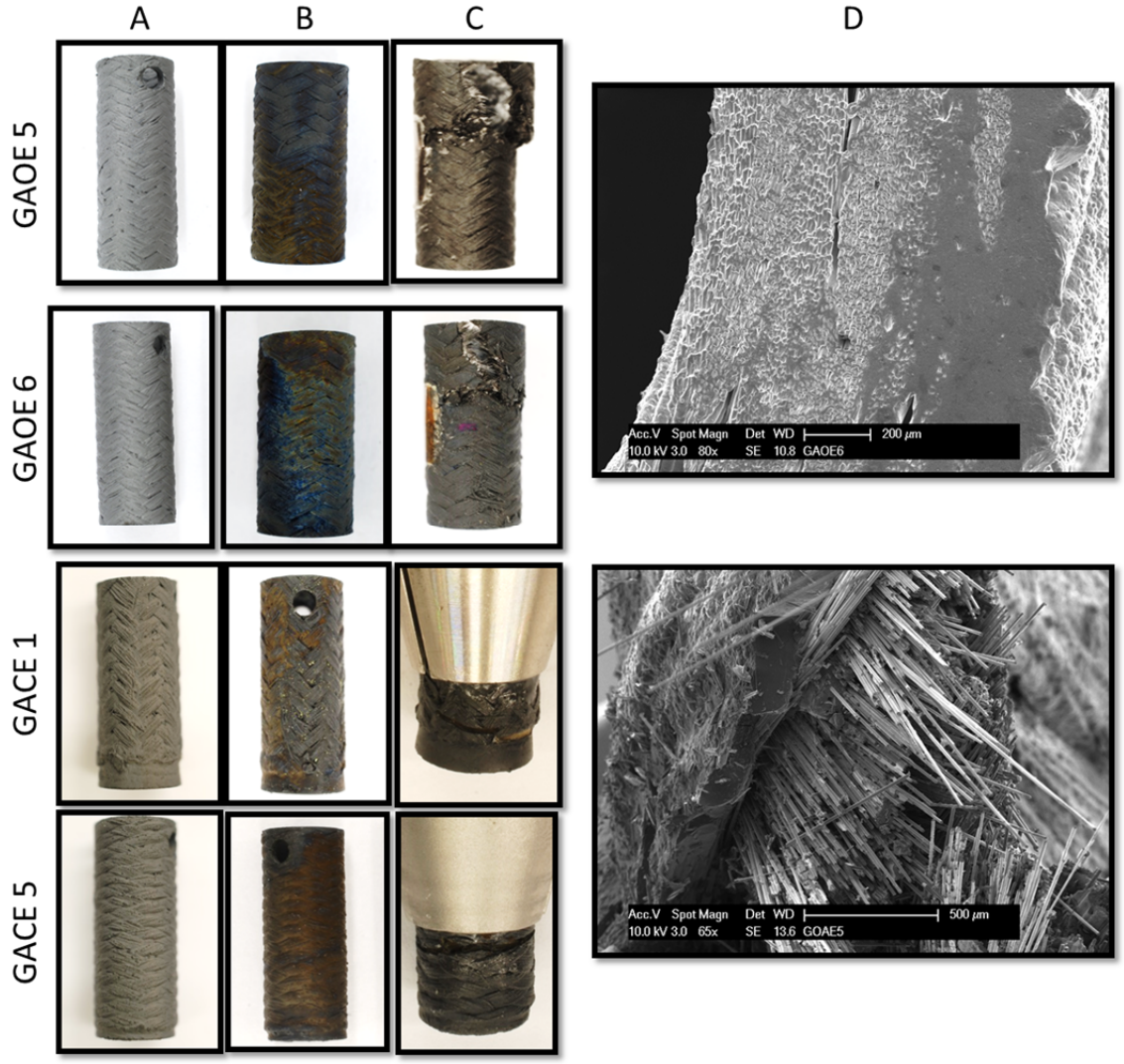

Figure 23: Optical and SEM analysis of quench characteristics of GA samples
a) as-received lateral view
b) post quench lateral view
c) crack after quench & burst
d) SEM images of the GAOE samples: cross section as-received and view of the post burst test crack

Following quenching, the surfaces of the GA samples appeared discolored (Figure 23 columns a and b), similar to the discoloration observed in the Westinghouse samples. SEM analysis failed to reveal any microcrack development (Figure 23 column d).

iii. Observations

Following the thermal shock, the samples exhibited the same failure modes as for the non-quenched samples. Series 196 failure involved fiber yielding and destruction of the matrix, leading to large strains at failure and a reduction of matrix and EBC to pieces. Similarly, series 198 quenched samples behaved similar to the as-received sample: the three layers failed simultaneously in a clear and sharp crack with very little fiber yielding. Column d) illustrates the failure mode of sample 198. Looking into the crack, fibers tows broke at the same position as the matrix. Also, the crack does not extend more than 200 µm. Finally, series 200 quenched samples exhibited the same characteristics as the as-received samples. However, the burst of 200.1.14 was unsuccessful (partly attributable to the sample's small size): the inner monolith broke on one side leading to leaking of the plug. With this leaking, it was impossible to reach internal pressure high enough to break the sample thoroughly.

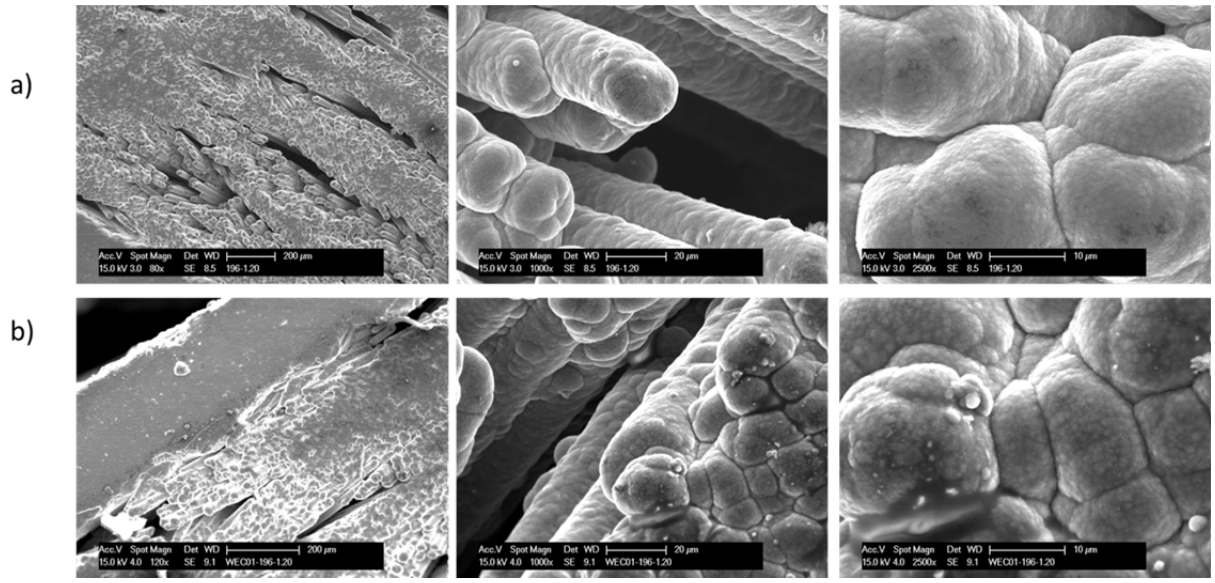

Figure 24: SEM comparison of as-received and quenched sample 196.1.20
a) as-received
b) quenched

No micro crack development was visible after the thermal shock treatment. Figure 24 compares sample 196.1.20 as-received (top row) and after quenching (bottom row). Even the tip of the fibers that were entirely exposed to the water didn't develop visible cracks. This leads to the conclusion that the SiC composites used in the samples are relatively insensitive to quenching. This could explain why the same failure modes were observed regardless of whether the samples underwent thermal shock.

4. Mechanical Results

This section discusses the influence of the thermal shock on the mechanical properties of the various series of samples. For all series except GACE-B, quenching in either 90°C or 100°C water has not shown significant influence on the mechanical properties of the samples (yield or ultimate failure strength).

The data, presented in Figure 25, shows that samples quenched in 90°C versus 100°C water behave similarly. For instance, samples 196.1.26 (light blue) and 196.1.20 (dark blue) failed at similar internal pressures (110-120 MPa) and their inner monolith failed at similar pressures (50 MPa) despite different quenching temperatures. However, the GAOE samples did exhibit variation in the failure strength at different quench temperatures. Despite these observations, the small number of samples doesn't allow for more statistically quantitative conclusions. The singular behavior of Sample 198.1.16 (light red) likely comes from its small height (6 mm as compared to 20 mm for the other samples): less than 1/4 of the unit cell of the weaving pattern is contained in this short sample, the significance of this data point is questionable.

Additionally, the characteristics of each series can still be captured after the quench. Indeed, from the quench testing it was observed that series 198 behaved the closest to a monolith SiC sample (exhibiting stiff loading and little strain) while series 200 was the closest to the full CMC behavior of the GAOE samples. These results are similar to the observations made during the as-received testing and indicate that the quenching process has little impact on the mechanical properties of the samples.

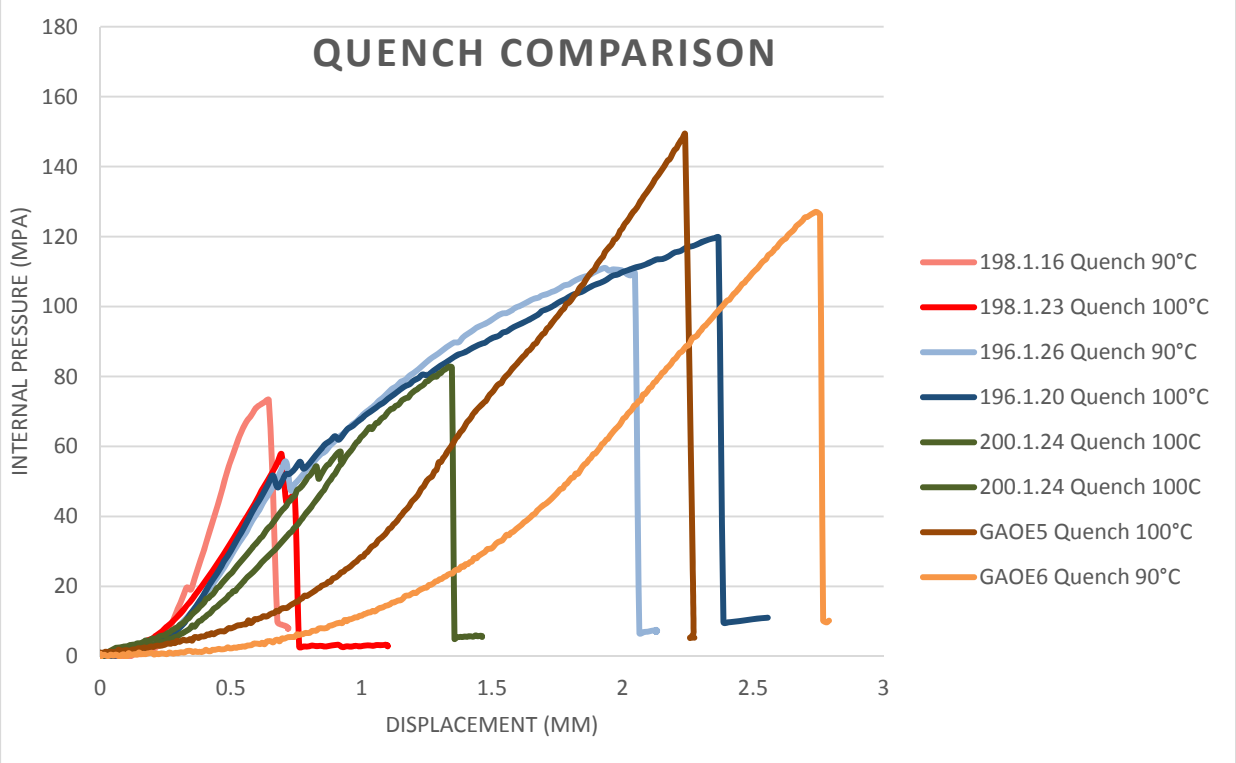

Figure 25: Internal pressure vs Displacement for quench samples

i. Series 196

Figure 26 presents the internal pressure versus displacement curves for the as-received and quenched samples in the series 196. Similar behavior was observed for the samples, although the sample quenched at 90°C failed at a slightly lower internal pressure than the sample quenched at 100°C.

Table 10 presents the mechanical results of the quench testing for series 196. No significant difference in mechanical properties was observed between the as-received sample and the quenched samples.

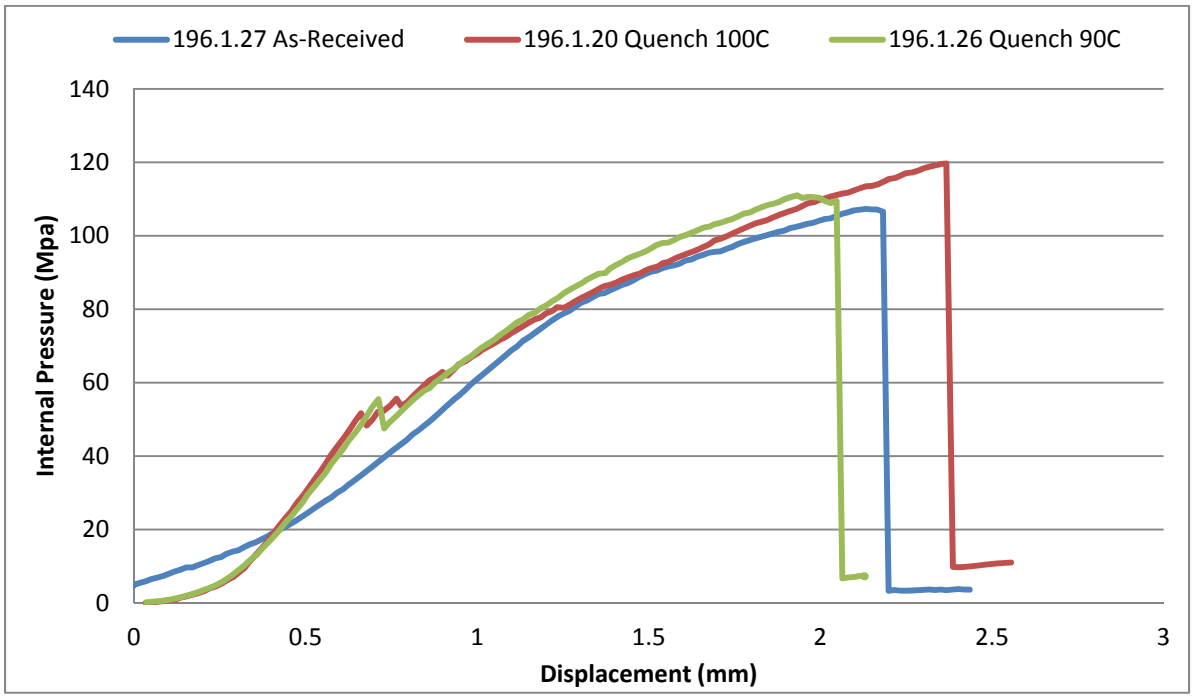

Figure 26: Internal Pressure vs Displacement curves for as-received and quenched series 196

Table 10: Mechanical properties of series 196

	196.1.27 As-Received	196.1.20 Quench 100°C	196.1.26 Quench 90°C
Failure Hoop Stress ID Monolith	249 MPa	193 MPa	207 MPa
Failure Hoop Stress ID Fibers	267 MPa	279 MPa	260 MPa
Failure Plenum Pressure (Total)	64 (107) MPa	49 (110) MPa	53 (102) MPa

ii. Series 198

Figure 27 presents the internal pressure versus displacement curves for the as-received and quenched samples in the series 198. Similar behavior was observed for the samples, although the sample quenched at 100C failed at a significantly lower internal pressure than the sample quenched at 90°C.

Table 11 presents the mechanical results of the quench testing for series 196. No significant difference in mechanical properties was observed between the as-received sample and the quenched samples.

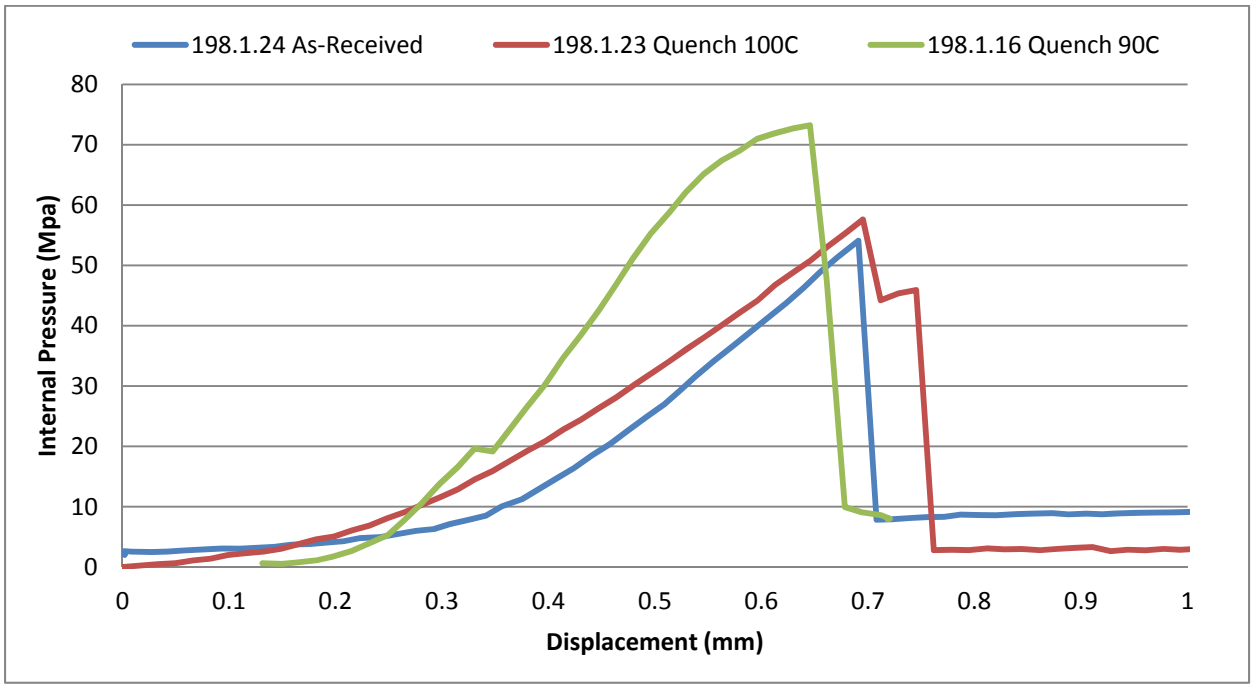

Figure 27: Internal Pressure vs Displacement curves for as-received and quenched series 198

Table 11: Mechanical properties of series 198

	198.1.24 As-Received	198.1.23 Quench 100°C	198.1.16 Quench 90°C
Failure Hoop Stress ID Monolith	267 MPa	305 MPa	378 MPa
Failure Hoop Stress ID Fibers	115-232 MPa	134-232 MPa	167-292 MPa
Failure Plenum Pressure (Total)	54 (54) MPa	56 (56) MPa	67 (67 MPa)

iii. Series 200

Figure 28 compares the stress-strain curves of as-received and quenched samples at the OD of the sample while Table 12 summarizes their mechanical properties. A similar elastic modulus was observed for both the as-received sample and the two quenched samples.

Sample 200.1.14 experienced the detachment of large fragments of monolith after monolith failure at the same radial location as the strain gage. Therefore, after monolith failure the strain measurements for 200.1.14 were corrupted by the concentration of stress on the fibers at the location of monolith detachment. Additionally, due to the short size of sample 200.1.14 and the large size of the detached monolith fragments, plug leakage prevented successful bursting of the sample.

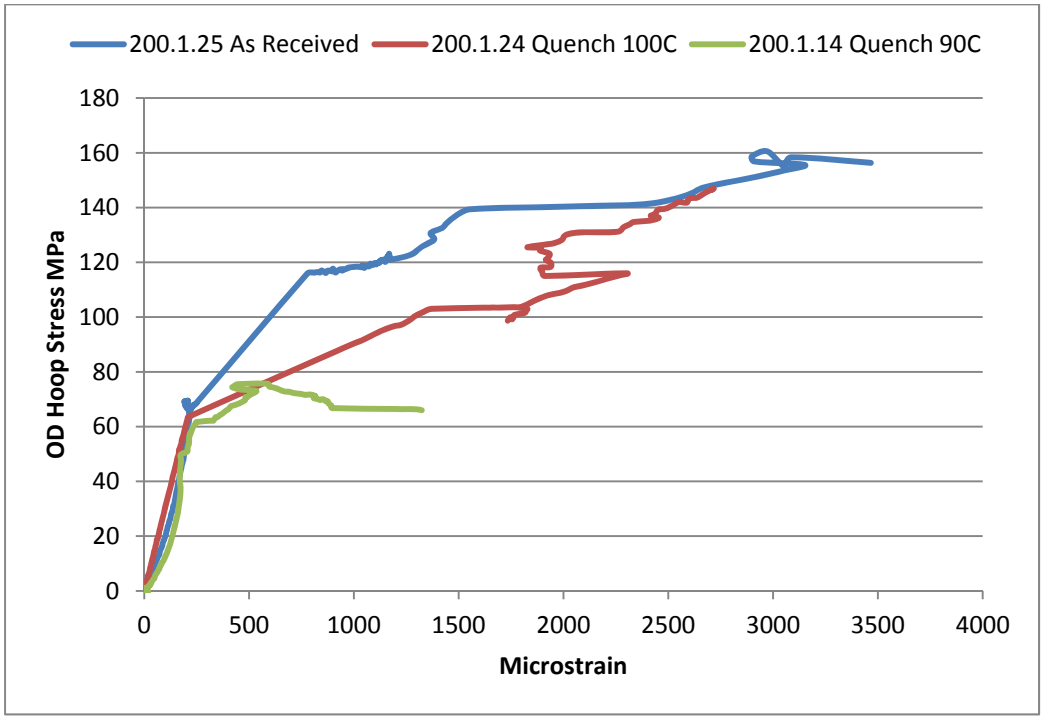

Figure 28: Stress-strain curve for as-received and quench series 200

Table 12: Mechanical properties of series 200

	200.1.25 As-Received	200.1.24 Quench 100°C	200.1.14 Quench 90°C
Elastic Modulus (First Loading)	201 GPa	300 GPa	240 GPa
Failure Hoop Stress ID Monolith	229 MPa	165 MPa	215 MPa
Failure Hoop Stress ID Fibers	252	225	No data
Failure Strain	3470 µ-strain	2700 µ-strain	No data
Failure Plenum Pressure (Total)	60 (82) MPa	51 (53) MPa	58 (-) MPa

Similar to the GAOE samples, the initial elastic modulus and the yield stress showed little dependence on the thermal shock. Furthermore, the pseudo-ductile behavior is also observed.

iv. Series GAOE

Figure 29 presents the stress-strain curve at the OD of the sample for the GAOE series. Sample GAOE 2 was burst as-received and is used as a reference case for the two quenched samples, GAOE 5 & 6 (the analysis of GAOE 2 was presented above). The effect of quenching on the elastic modulus is difficult to evaluate because significant variation was observed in the moduli of the quenched samples (Table 13). The yield stress was observed to decrease by 7% for both quenched samples. However, this difference cannot be attributed to the thermal shock because of the lack of repeated results. Finally, as for all stress-strain curves obtained, a slight decrease in strain at a constant load can be observed just before the first large crack nucleates (signaled by the large jump in strain).

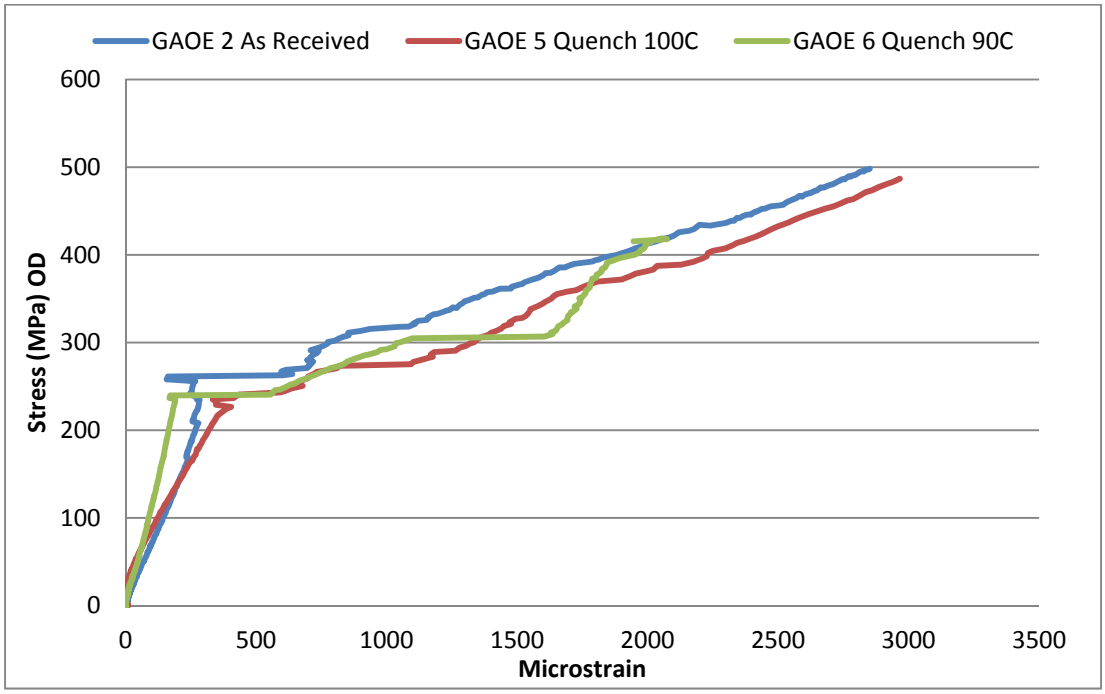

Figure 29: Stress- Strain Curve Series GAOE, OD

Table 13: Mechanical properties of GAOE series

	GAOE 2 As-Received	GAOE 5 Quench 100C	GAOE 6 Quench 90C
Elastic Modulus	721 GPa	679 GPa	1159 GPa
Yield Stress (ID)	304 MPa	283 MPa	282 MPa
Failure Hoop Stress ID	473 MPa	572 MPa	492 MPa
Failure Strain	2375 µ-strain	2966 µ-strain	1945 µ-strain
Failure Plenum Pressure	76 MPa	86 MPa	73 MPa

v. Series GACE-A

Figure 30 presents the load versus pushrod displacement curves for the pushout tests of the GACE-A series. Sample GACE 2 underwent pushout testing as-received and is used as the reference case for the pushout test of the quenched sample GACE 1.

Table 14 presents the mechanical strength characteristics of the endplug joint for the GACE-A series. Note that the burst strength is analogous to the internal pressure required to result in joint failure. Although the observed burst strength of the quenched sample was 8% lower than that of the as-received sample, the burst strengths are similar and the difference cannot be attributed to quenching due to the lack of a large dataset.

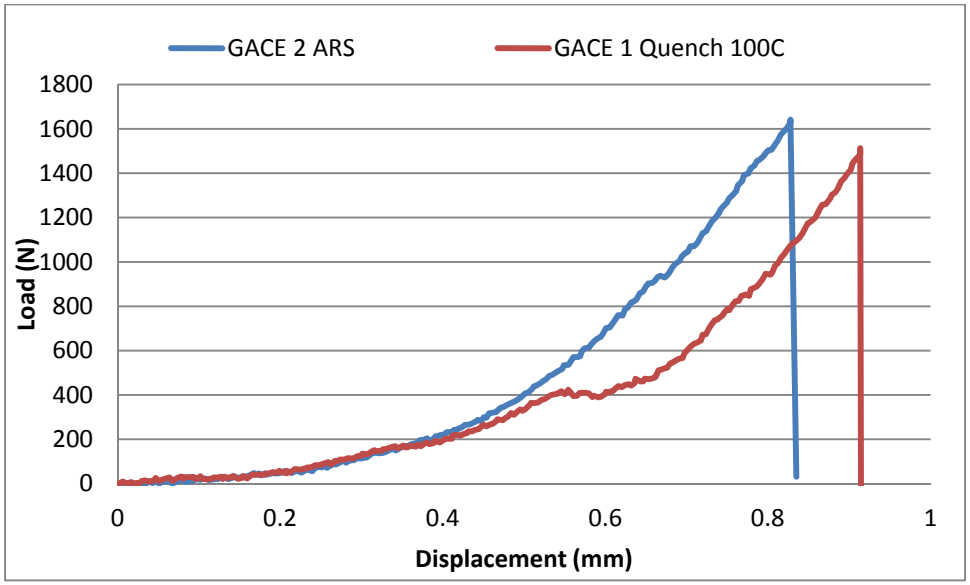

Figure 30: Pushrod load versus displacement curves for GACE-A series pushout test

Table 14: Mechanical properties of endplug joint for GACE-A series

	GACE 2 As-Received	GACE 1 Quench 100C
Peak Load	1641 N	1513 N
Burst Strength	37.1 MPa	34.2 MPa

vi. Series GACE-B

Figure 31 presents the load versus pushrod displacement curves for the pushout tests of the GACE-B series. Sample GACE 6 underwent pushout testing as-received and is used as the reference case for the pushout test of the quenched sample GACE 5.

Table 15 presents the mechanical strength characteristics of the endplug joint for the GACE-B series. Note that the burst strength is analogous to the internal pressure required to result in joint failure. The observed burst strength of the quenched sample was 78% lower than that of the as-received sample, suggesting that quenching may lead to mechanical degradation of the joint for the GACE-B series. However, X-Ray Computed Tomography (XCT) analysis revealed that the as-received joint in the GACE 5 sample was weaker than the joint in the GACE 6 sample due to the presence of voids in the joint region. XCT analysis is further discussed in section IV.7.

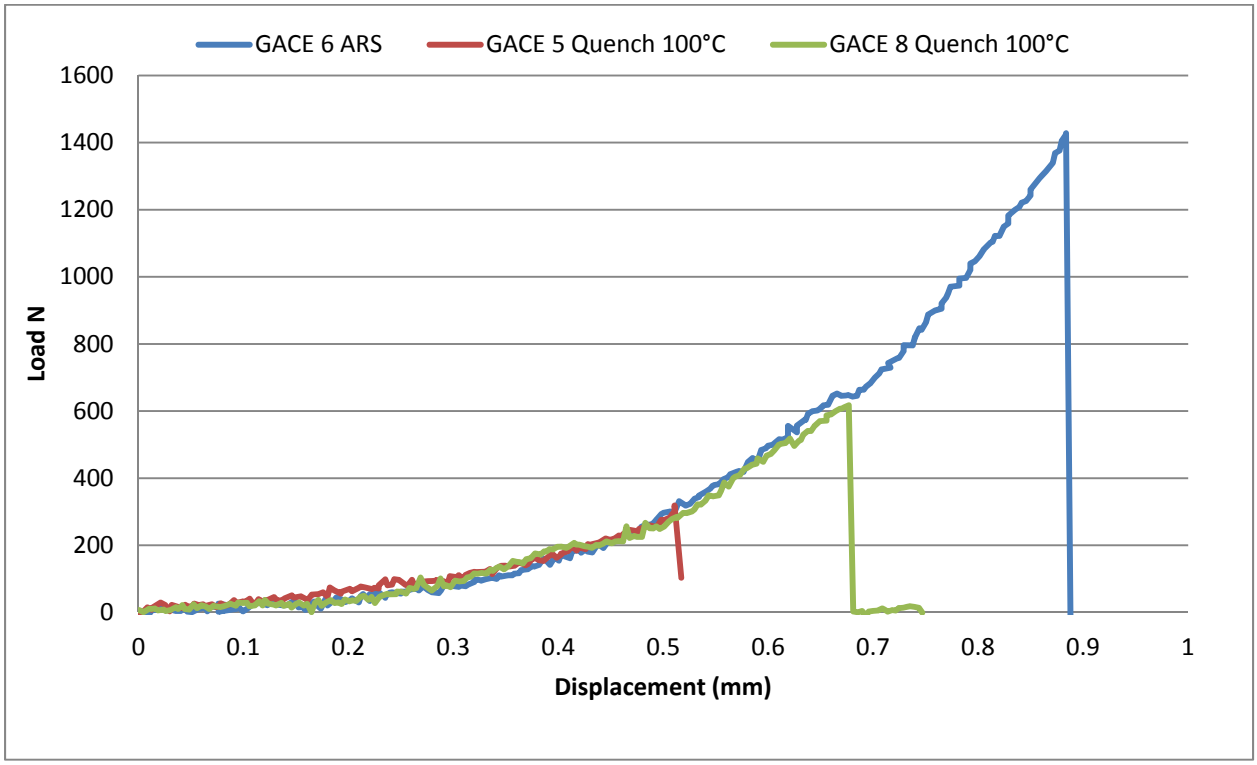

Figure 31: Pushrod load versus displacement curve for GACE-B series pushout test

Table 15: Mechanical properties of endplug joint for GACE-B series

	GACE 6 As-Received	GACE 5 Quench 100C	GACE 8 Quench 100C
Peak Load	1428 N	318 N	617 N
Burst Strength	32.3 MPa	7.2 MPa	14 MPa

5. Quenched Failure Characteristics

All of the quenched samples, with the exception of the GACE-B series, behaved very similarly to the as-received samples and did not show significant mechanical degradation due to the quenching. Burst failure strength for quenched samples occurred at stresses comparable to the failure stresses observed in the as-received samples, and the failure modes for the quenched samples were similar to the as-received failure modes. Figure 32 shows the comparison between the cracking characteristics of the quenched and the as-received samples for the different series.

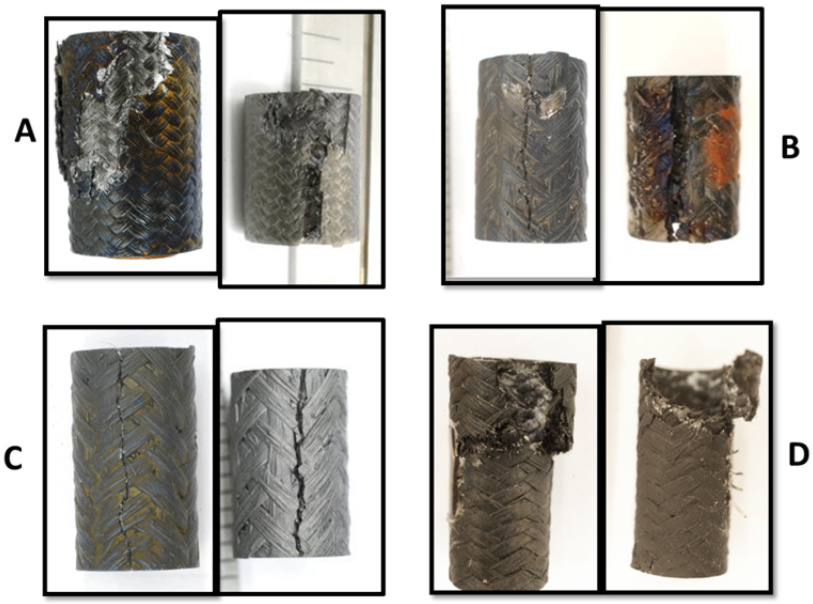

Figure 32: Comparison of cracking behavior between pairs of quenched samples (left half of paired pictures) and as-received samples (right half of paired pictures) A) Series 196, B) Series 200, C) Series 198, D) Series GAOE

Figure 33 shows top (row a) and lateral (row b) views of GAOE 5's crack. Tows and individual fibers decouple from their matrix and become independent from it as the matrix falls apart. Tows are then able to glide and an important amount of yielding is observed. SEM images for sample GAOE 6 are similar and not reported here.

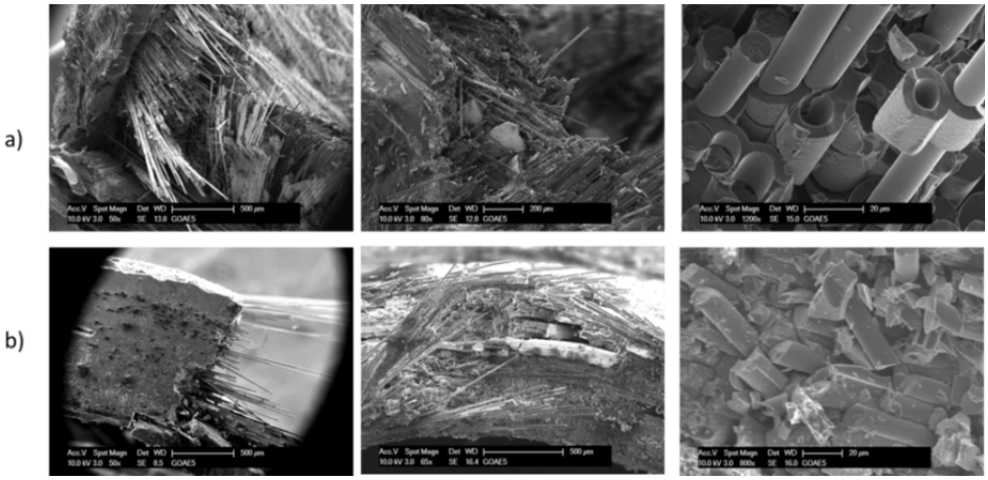

Figure 33: Failure mode of GAOE 5 a) top view b) lateral view

Figure 34 illustrates the different behaviors that were observed and described below. In the upper row sample 196.1.20 shows large shearing and yielding of the fibers whereas in the second row sample 198.1.16 shows that it broke in a brittle manner. That is, the matrix and fibers were bonded until failure, resulting in a sharp crack.

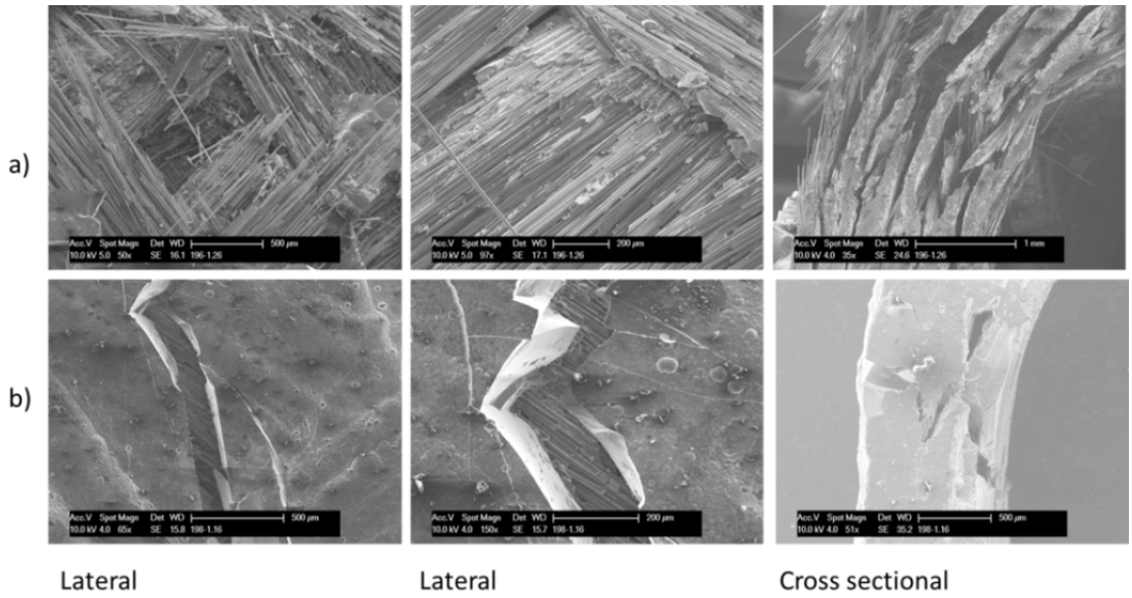

Figure 34: SEM comparison of 196.1.20 (top) and 198.1.16 (bottom)
Lateral: lateral view of the crack; Cross sectional: upper view of the crack

Endplug pushout testing revealed that quenching had little effect on the strength and failure characteristics of the endplug joint for the GACE-A series. However, quenching was observed to significantly reduce the strength of the endplug joint for the GACE-B series. Figure 35 shows the comparison between the failure characteristics of the GACE-A and GACE-B series. From the figure, it can be observed that the failure characteristics of the endplug joint is very similar between the as-received and quenched samples in the GACE-A. However, the GACE-B series exhibited different failure characteristics of the endplug joint between the as-received and the quenched samples. XCT comparison of the samples in their as-received state shows significantly more joint voids on the quenched sample compared to the as-received sample. Lack of joint material has a twofold effect reducing the joint strength and reducing tube maximum bearing load as the tube section is reduced due to its scarf. This large difference in strength prompted a repeat quench test of this architecture to investigate if the difference is related to quenching or joint quality. The second sample quenched with higher joint quality still revealed significant reduction in joint strength, leading to the conclusion that quenching degrades strength.

Figure 35: Endplug joint failure comparison for GACE-A and GACE-B series

6. Conclusion

The thermal shock experiments were conducted to simulate the rewetting of the fuel rods following a LOCA accident. Samples heated to 1200°C were quenched into 100°C water and 90°C water to explore possible quenching conditions.

All samples survived the thermal shock and, despite their observed discoloration (revealing the development of an oxide layer), no significant degradation of mechanical properties was observed except with the GACE-B series. Furthermore, SEM analysis of the open-ended samples showed no crack development in either the monolith or the CMC (both matrix and fibers) layers. As a result, all quenched samples except in the GACE-B series exhibited the same failure characteristics as the as-received samples. Series 196, 200, and GAOE failure involved fiber yielding while for series 198 the three layers failed simultaneously in a sharp crack.

For all the samples except the GACE-B series, the thermal shock experiment results were similar to the as-received results. The negligible impact of quenching conditions on the mechanical properties could stem from the film boiling heat transfer mechanism. Video analysis revealed that samples undergo almost exclusively film boiling. The development of the film layer protects the samples from thermal gradients and limits thermal stresses. Therefore, the development of the film layer helped protect the integrity of the samples during the thermal shock experiments.

The difference in the effects of quenching between the GACE-A and GACE-B series demonstrates that the sample architecture likely is an important factor in the resilience of the sample's endplug joint to quenching. Furthermore, quenching behavior is different for the cladding samples near the endplug joint because the large latent heat of the endplug prolongs boiling at the joint location. This mechanism may enhance the thermal stresses at the joint location and result in the weakening of sample at the endplug region.

Table 16 presents the mechanical properties for the as-received and quenched samples. For the samples of the WEC01 series, the failure hoop stress was calculated using the mechanical model presented previously. The failure hoop stress of the monolith layer was calculated in the shared-load regime whereas fiber layer failure occurs in the fiber-only loading regime. Note that strain data was not

gathered for many of the samples as the strain measurement technique was not yet in place. Because the GA samples don't have an inner monolith they are modelled as single thick wall cylinders.

Table 16: Mechanical properties of as-received and quenched samples

		Monolith Layer		Fiber Layer			
Sample	**Water Temp.**	**ID Failure Hoop Stress**	**Sample OD Hoop Strain At Event**	**ID Failure Hoop Stress**	**Sample OD Hoop Strain At Event**	**Elastic Modulus**	**Fiber ID Yield Stress (MPa)**
196.1.27	ARS	249 MPa	No Data	267 MPa	No Data	No Data	109 – 161
196.1.20	100°C	193 MPa	No Data	279 MPa	No Data	No Data	85-124
196.1.26	90°C	207 MPa	No Data	260 MPa	No Data	No Data	91-133
198.1.24	ARS	267 MPa	No Data	115-232 MPa	No Data	No Data	No Yielding
198.1.23	100°C	305 MPa	No Data	134-232 MPa	No Data	No Data	No Yielding
198.1.16[4]	90°C	167 MPa	No Data	167-292 MPa	No Data	No Data	No Yielding
200.1.25	ARS	243 MPa	0.02%	242 MPa	0.35%	201 GPa	105 – 175
200.1.24	100°C	165 MPa	0.02%	226 MPa	0.27%	300 GPa	100-152
200.1.14[5]	90°C	215 MPa	No Data	No Data	No Data	No Data	No Data
GAOE 2	ARS	No Inner Monolith		581 MPa	0.28%	721 GPa	305
GAOE 5	100°C			572 MPa	0.30%	612 GPa	266
GAOE 6	90°C			492 MPa	0.19%	1174 GPa	276

		Peak Load	**Burst Strength**
GACE-A 2	ARS	1641 N	37.1 MPa
GACE-A 1	100°C	1513 N	34.2 MPa
GACE-B 6	ARS	1428 N	32.3 MPa
GACE-B 5	100°C	318 N	7.2 MPa

[4] Sample 198.1.16 was very short and didn't contain an entire weave pattern. Therefore, significance of the result is questionable.

[5] Sample 200.1.14 was very short and didn't contain an entire weave pattern. Therefore, significance of the result is questionable.

7. Discussion

The stress calculations rely on the validity of the mechanical model outlined previously. Therefore, as outlined in the as-received section, assumptions are made regarding the monolith-fiber interface and mechanical properties of the monolith and fiber regions.

Because only two samples in each Westinghouse series (196, 198, and 200), only two samples in the GAOE series, only two samples in the GACE-B series, and only one sample in the GACE-A series were quench tested, there are too few samples to provide meaningful statistics on the distribution of true population as-received mechanical properties. Only by testing more samples could the population's true distribution of mechanical properties be determined, but the testing does show suggest that quenching has a minimal impact on the mechanical strength of most samples, and only the GACE-B endplug joint strength showed a significant impact of quenching

The results of the pushout test of the quenched sample GACE 5 suggested a severely weakened joint. However, XCT analysis of the samples prior to testing suggested that the joint in GACE 5 was inherently weaker than the joint of GACE 6, as shown in Figure 36. Therefore, the inherent weakness of the GACE 5 joint confounds the results of the quench testing and makes it difficult to determine the extent of the mechanical degradation due to the quenching.

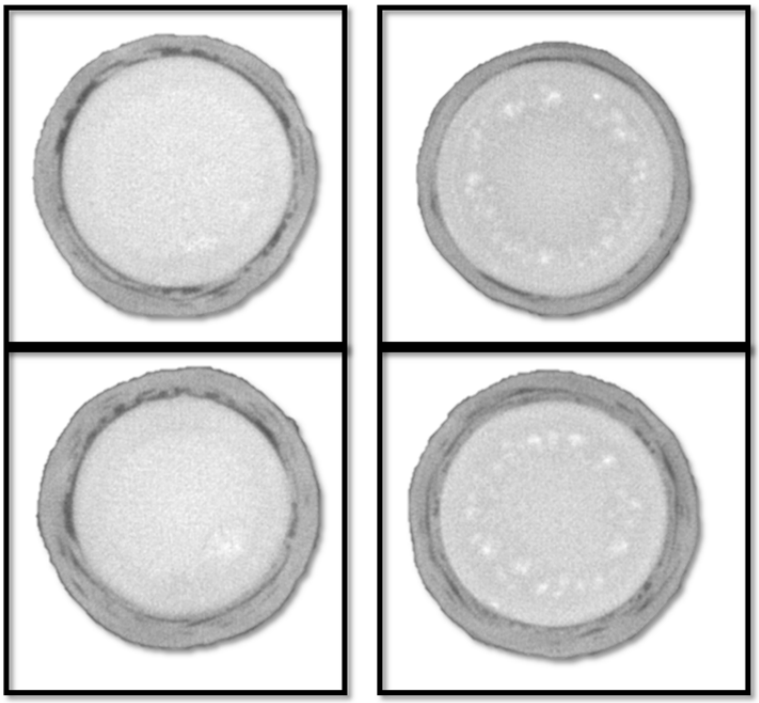

Figure 36: XCT scans of the joint region in GACE 5 (before quenching) (left) and GACE 6 (tested as-received) (right) showing more voids in the joint of GACE 5

V. High Temperature Oxidation Experiments

1. Procedure

The facility used to perform high-temperature steam oxidation tests of the samples consists of a sealed pool of boiling water feeding steam inside a quartz tube through a succession of heaters with the ultimate temperature reaching 1400˚C. The steam then passes across a sample, with the steam flow rate, sample oxidation time, and oxidation temperature predetermined based on the testing criteria. Thermocouples measure the temperature of the heating stages and the temperature of the steam flowing across the sample. The furnaces at each heating stage have closed-loop temperature control and the steam generator is powered by a DC power supply, thereby allowing for accurate control of the steam flow rate. This facility was built specifically for this project.

Testing was performed by suspending the sample in the high-temperature sample furnace as the steam was passed across the sample surface. The sample was positioned vertically in the center of the quartz tube and steam was allowed to pass across both the inner and outer surfaces for all samples. Although the close ended samples had their plug facing the steam flow, steam could enter from the top open end of the sample. After the oxidation test the sample was removed and allowed to air-cool. The sample weight was taken prior to oxidation, and the weight was again taken after oxidation. Additionally, after testing, the burst strength of the open ended samples was measured, and the samples were examined via SEM both before and after oxidation.

2. Optical and SEM Analysis

i. Westinghouse Samples

Figure 37 compares optical (columns A and B) and SEM views (columns C and D) of pre and post oxidized Westinghouse samples. Discoloration was observed on the surfaces of the samples after oxidation. The oxidation characteristics for the Westinghouse samples are outlined in Table 17.

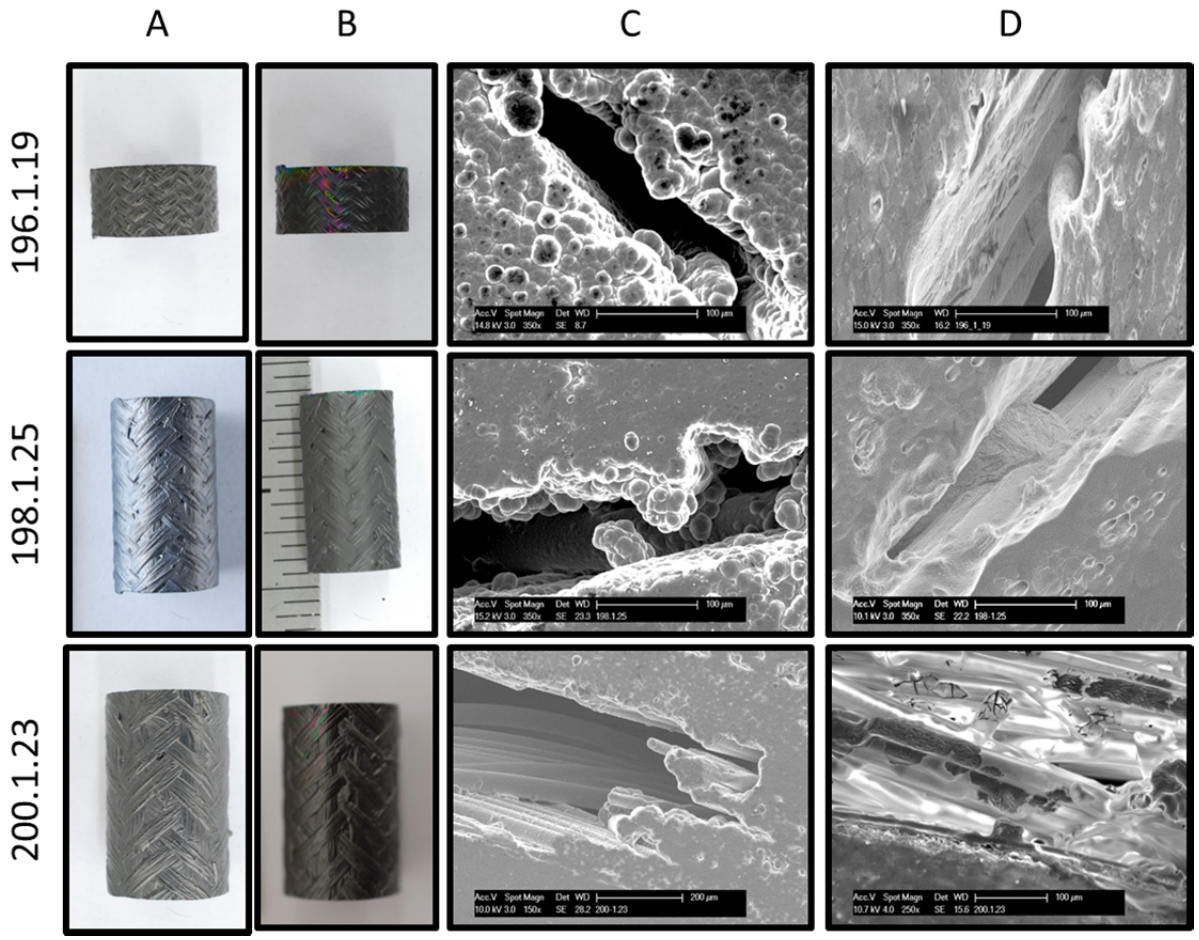

Figure 37: Optical and SEM analysis of oxidation characteristics of Westinghouse samples
A) Lateral view of as-received samples
B) Lateral view of oxidized samples (Note: for 198.1.25 ruler divisions are 1/16")
C) Cross Section SEM view of as-received samples
D) Cross Section SEM view of oxidized samples

Table 17: Table of Westinghouse sample oxidation characteristics

Sample	Steam Flow Rate	Oxidation Temperature	Oxidation Period	Weight Change
196.1.19	6.1 g/min	1400°C	48 hours	+0.65 mg/cm^2
198.1.25	3.9 g/min	1400°C	48 hours	-0.12 mg/cm^2
200.1.23	6.0 g/min	1400°C	48 hours	+0.73 mg/cm^2

ii. GA Samples

Figure 38 compares optical (columns A and B) and SEM views (columns C and D) of pre and post oxidized Westinghouse samples. Discoloration was observed on the surfaces of the samples after oxidation.

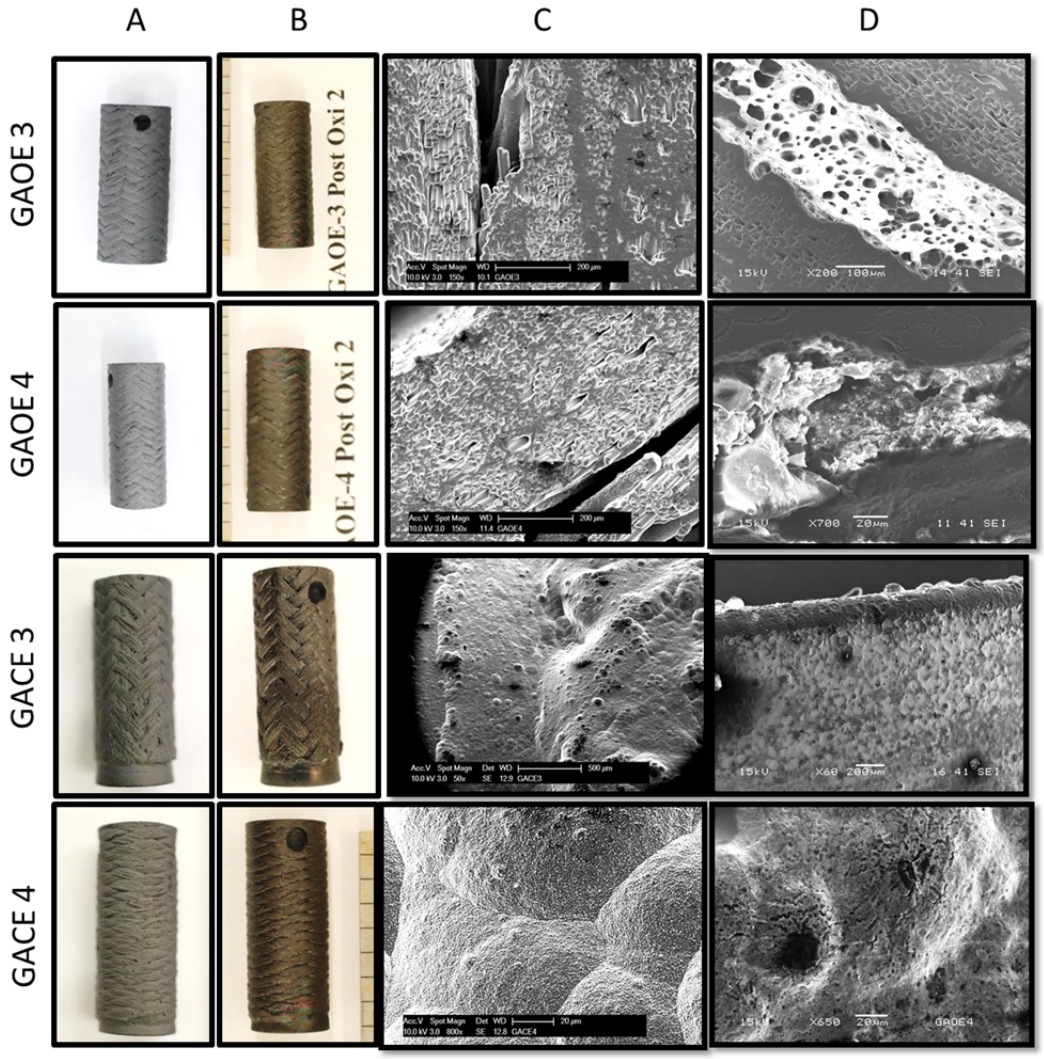

Figure 38: Optical and SEM analysis of oxidation characteristics of GA samples
A) Lateral view of as-received samples
B) Lateral view of oxidized samples
C) Cross Section (GAOE) and Lateral view of plug joint (GACE) SEM view of as-received samples
D) Cross Section (GAOE) and Lateral (GACE) SEM images of oxidized samples showing silica formations

The oxidation characteristics of the GA samples are outlined in Table 18.

Table 18: Table of oxidation characteristics of GA samples

Sample	Steam Flow Rate	Oxidation Temperature	Weight Change
GAOE 3	6.1 g/min	1400°C	+0.66 mg/cm^2
GAOE 4	6.1 g/min	1400°C	-0.13 mg/cm^2
GACE-A 3	6.1 g/min	1400°C	0.00 mg/cm^2
GACE-B 4	6.0 g/min	1400°C	0.01 mg/cm^2

iii. Observations

Samples 196.1.19 and 200.1.23 experienced a weight gain during oxidation, whereas sample 198.1.25 experienced a weight loss (See Table 17). The erroneous steam flow rate for sample 198.1.25 (3.9 g/min instead of the intended 6.0 g/min) originated from a problem with the heating element of the oxidation column. Weight change for SiC is typically a balance between oxidation and volatilization: at sufficient oxygen activity, a protective silica (SiO_2) layer is formed but in the presence of water silica turns into volatile Si(OH).

As such, oxidation could either lead to weight gain or weight loss depending on the flow conditions. For precisely similar conditions as run here, Lee (1) has observed a normalized weight loss of -4.6 mg/cm^2 on monolith SiC. It is believed that the difference stems from the presence of voids and cavities in the inner SiC/SiC CMC layer allowing for the accumulation of silica in the inner layers where the steam stagnates preventing sufficient water for the SiO_2 volatilization to Si(OH). The growth of silica layers on the inner surfaces of SiC/SiC CMC composites ultimately results in a global weight gain. This hypothesis is supported below via SEM analysis.

The GAOE 3 sample experienced a weight gain whereas the GAOE 4 sample experienced a weight loss. Additionally, neither GACE sample experienced an appreciable weight change. Cross-sectional SEM analysis of the GACE samples, shown in Figure 39, revealed that the GACE samples had fewer and less pronounced crevices between fiber tows when compared to the Westinghouse samples 200.1.23 and 196.1.19. Both Westinghouse samples experienced weight gain whereas the GACE samples exhibited very little appreciable weight change. This behavior can possibly be attributed, in part, to the inability of the oxidizing atmosphere to penetrate the crevices and form an interior oxide. This data supports the previous analysis in Section 2.i. Figure 39 illustrates the differences between the cross-sectional views of various as-received samples.

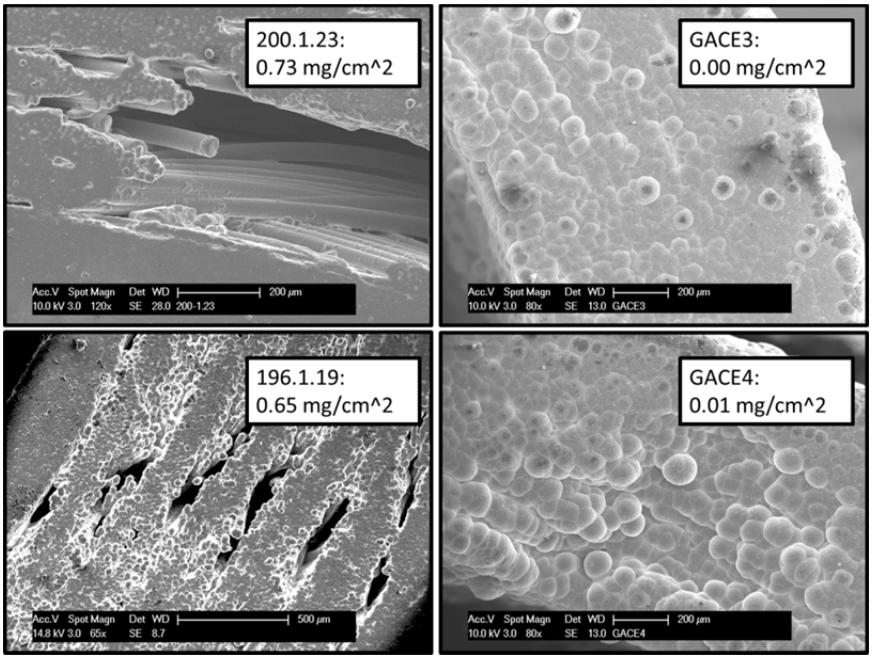

Figure 39: As-received cross-sectional SEM images of various oxidized samples

Despite the difference in weight changes between the samples, the optical and SEM analysis revealed similar characteristics among the samples. Optically, the oxidized samples all appear much darker and less lustrous than the as-received samples. SEM analysis of the sample cross section exposed to the steam (Figure 40, note that this was the as-received cut face) revealed that, during oxidation, the exposed fibers were coated with what is believed to be silica. Because the deposits observed in the cross section were recessed, EDS was unable to be performed on them. However, the deposits observed in the cross-section views are morphologically similar to deposits observed on the lateral faces that were analyzed by EDS (see below). Silica deposits similar to those seen in Figure 40 were analyzed by EDS in Figure 43. The deposition of a smooth silica layer softened many of the rough features of the fiber region observed in the pre-oxidation samples. The silica layer blankets the fibers, effectively binding them together. Additionally, fibers directly exposed to the steam flow exhibited severe cracking and corrosion.

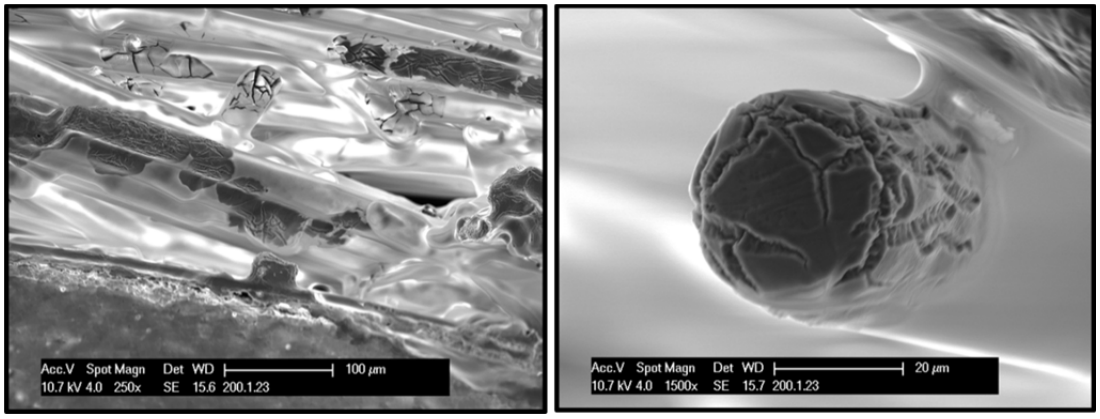

Figure 40: SEM images of sample 200.1.23 showing what is believed to be silica-coated fibers (left) and corrosion cracking of fiber (right)

SEM analysis of the as-received samples (Figure 41) did not reveal any of the blanketing material on the fibers nor did it reveal cracking along the fibers as observed in the oxidized samples. The as-received fibers are bound only by the SiC matrix and the surface of the fibers is rough and lacks the cracks observed in the oxidized samples.

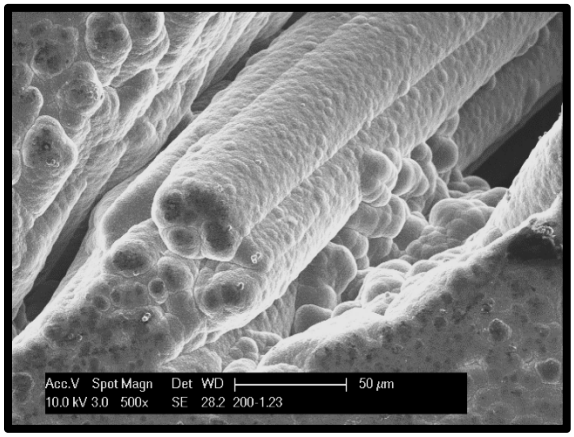

Figure 41: SEM image of sample 200.1.23 prior to oxidation showing as-received fiber structure and fiber texture

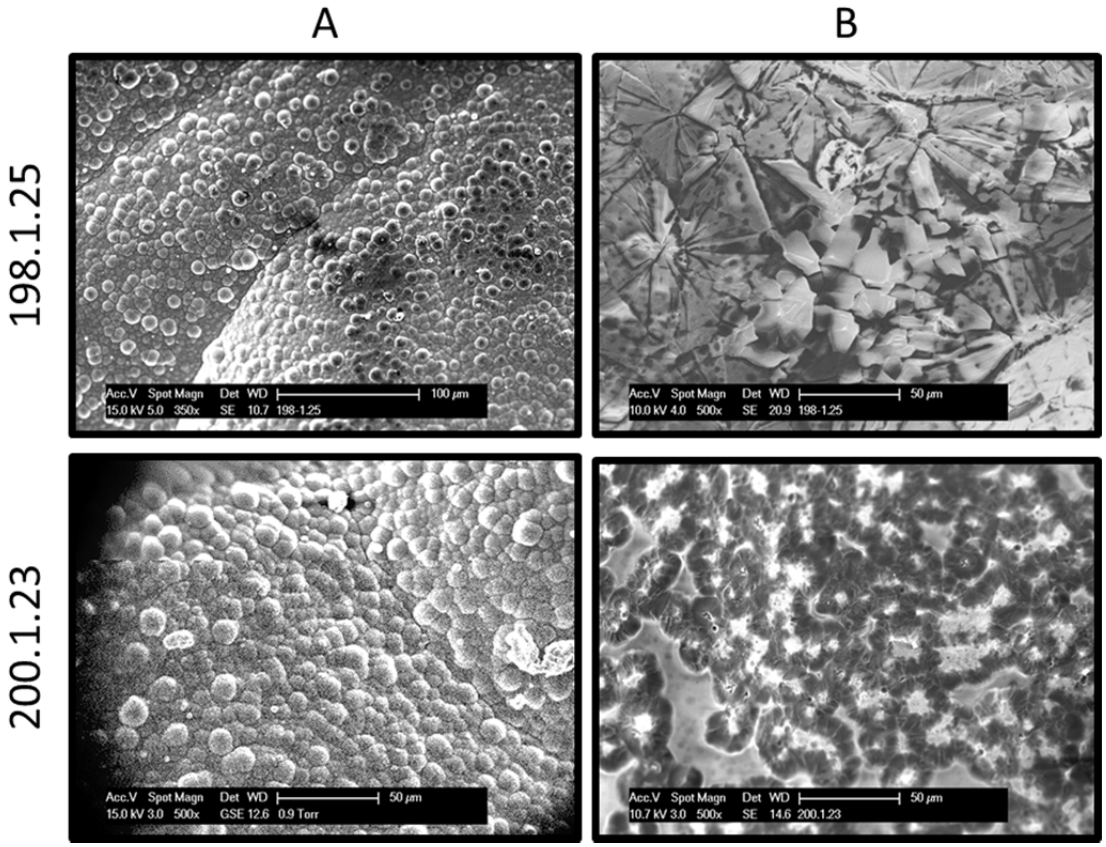

Figure 42: SEM lateral view of A) As-received sample and B) Oxidized sample

SEM analysis of the lateral view of the samples also revealed dispersed and speckled localized microstructural changes during oxidation. The as-received samples exhibited a rough texture with characteristic round bumps that can be found covering almost the entire surface (Figure 42 column A). However the oxidized samples revealed speckled points with a flatter texture whereby the bumps were softened or altogether erased by large flat, smooth, or blocky areas (Figure 42 column B). This behavior is attributable to the formation of a silica layer on the surface of the sample and the oxidation of the SiC directly exposed to the oxidizing atmosphere. EDS analysis performed on the oxidized samples revealed the presence of oxygen in the oxidized samples indicative of silica (Figure 43). The oxygen is attributed to the formation of silica induced by the oxidation of the SiC.

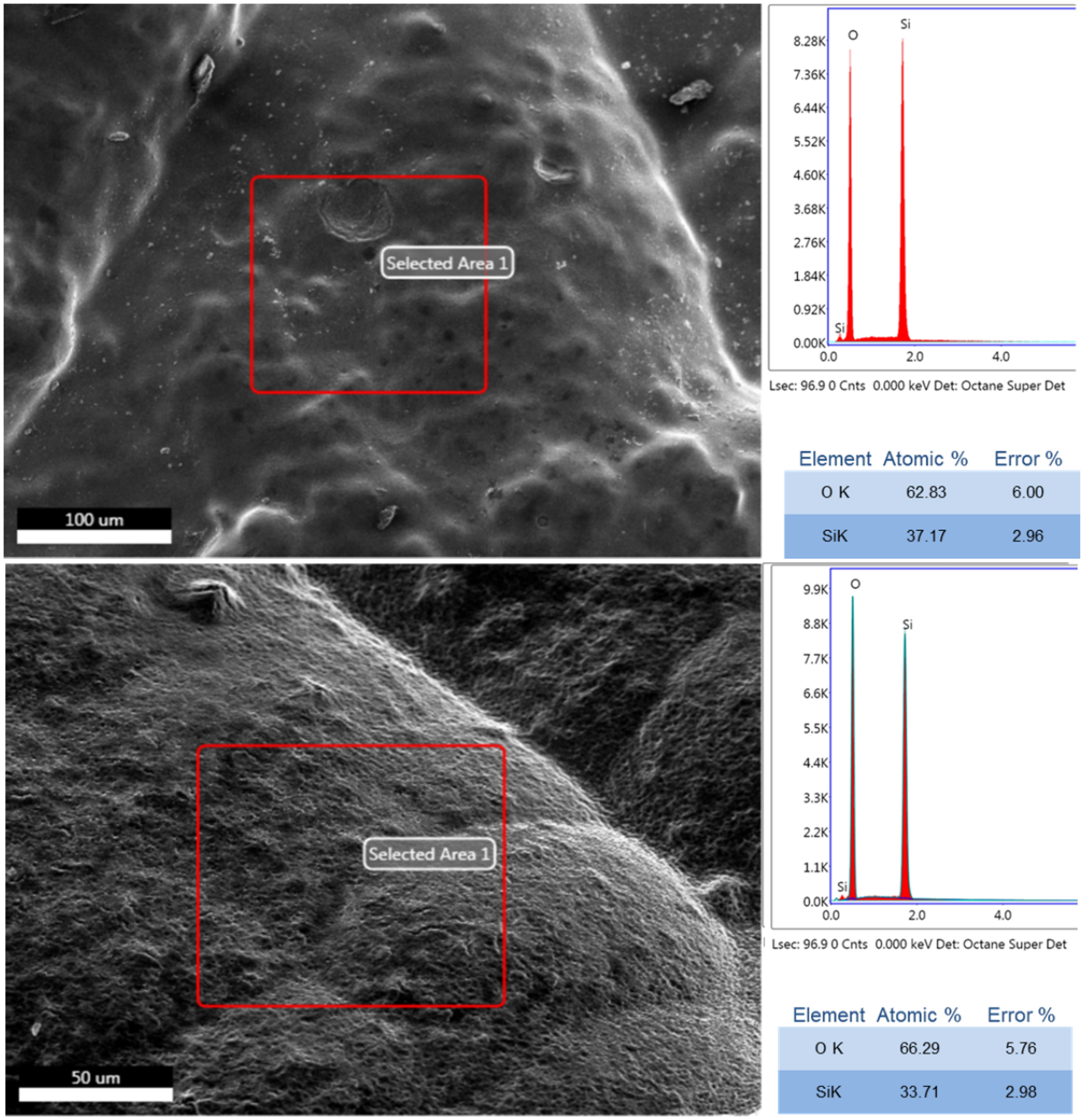

Figure 43: EDS analysis of silica coating on lateral surface of oxidized sample GAOE 3 (top) and 198.1.25 (bottom) showing oxygen to silicon ratio of approximately 2 to 1

Silica was observed to cover sections of the lateral surface of the oxidized samples. The silica formed either a smooth layer (Figure 43, top) or a pitted and cracked layer (Figure 43, bottom). Similar silica morphology was observed in the cross-section of the oxidized samples, as seen in Figure 40 above.

Although the silica was observed to produce a relatively homogenous coating over the samples as shown in Figure 43, it was also observed to form irregular scales and block-like formations on the exposed surfaces of the samples (Figure 44). Although EDS analysis was unable to be performed on the deposit observed in between fiber tows in cross-section of the sample, similar deposits were observed

and analyzed via EDS on the lateral surfaces of the samples, thus corroborating the hypothesis of silica buildup in the voids between fiber tows in the cross-section of the sample.

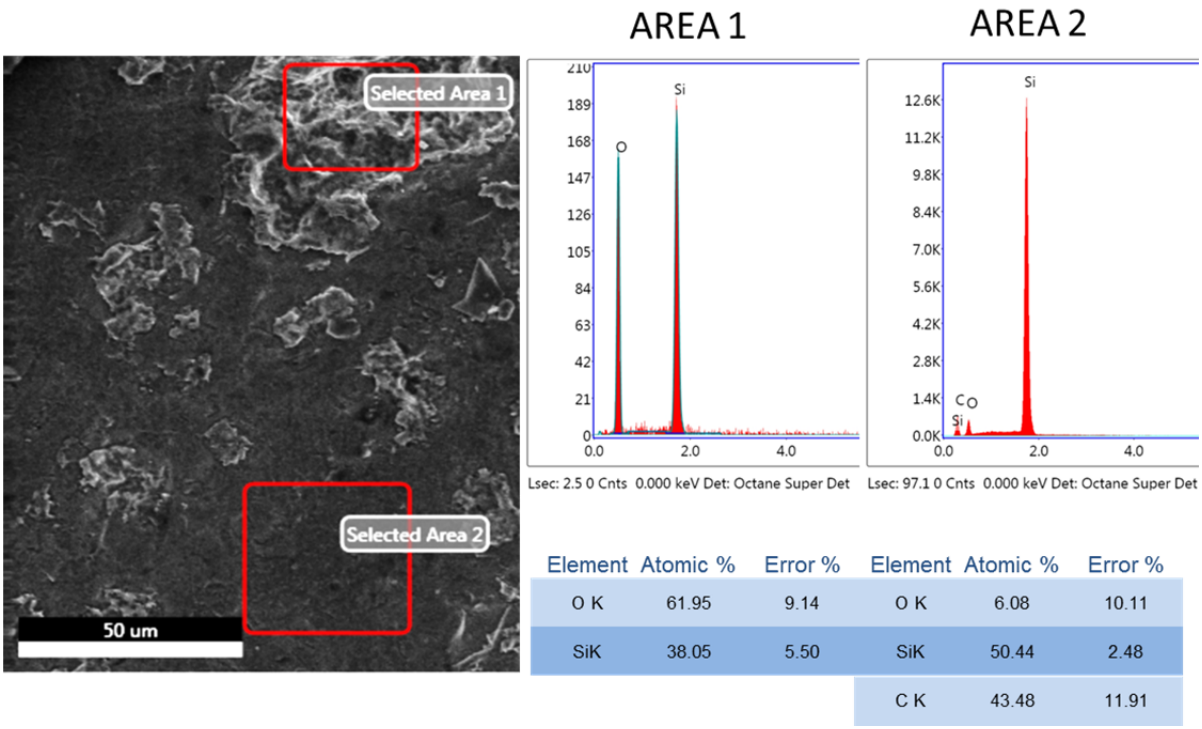

Element	Atomic %	Error %	Element	Atomic %	Error %
O K	61.95	9.14	O K	6.08	10.11
SiK	38.05	5.50	SiK	50.44	2.48
			C K	43.48	11.91

Figure 44: EDS analysis of irregular formations on lateral face of oxidized sample 200.1.23 showing silica (area 1) and silicon-carbide (area 2). Similar deposits were observed in the cross-section of the oxidized samples

Similar deposits to the silica in area 1 of Figure 44 were observed in the voids in the cross-section of the oxidized samples. Figure 45 shows such a deposit seen in GAOE 4, although because the void was recessed within the sample EDS was unable to be performed on it.

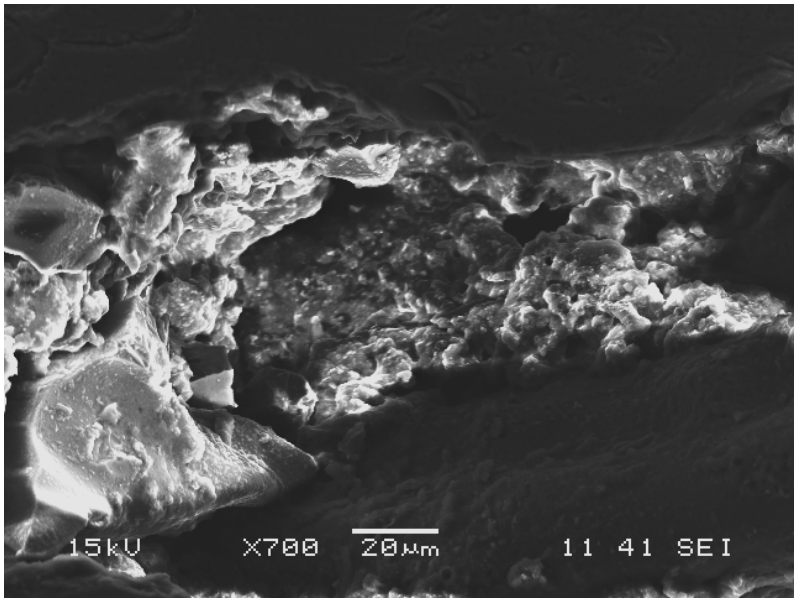

Figure 45: Deposit believed to be silica in the void between fiber tows in the cross-section of oxidized sample GAOE 4

Silica was observed to form in the endplug joint of the close-ended samples (Figure 46, top). However, silica was also observed on the inward-facing side of the endplug (Figure 46, bottom), indicating that the sample was oxidized from the inside as well as from outside (due to the fact that only one end of the GACE samples is closed).

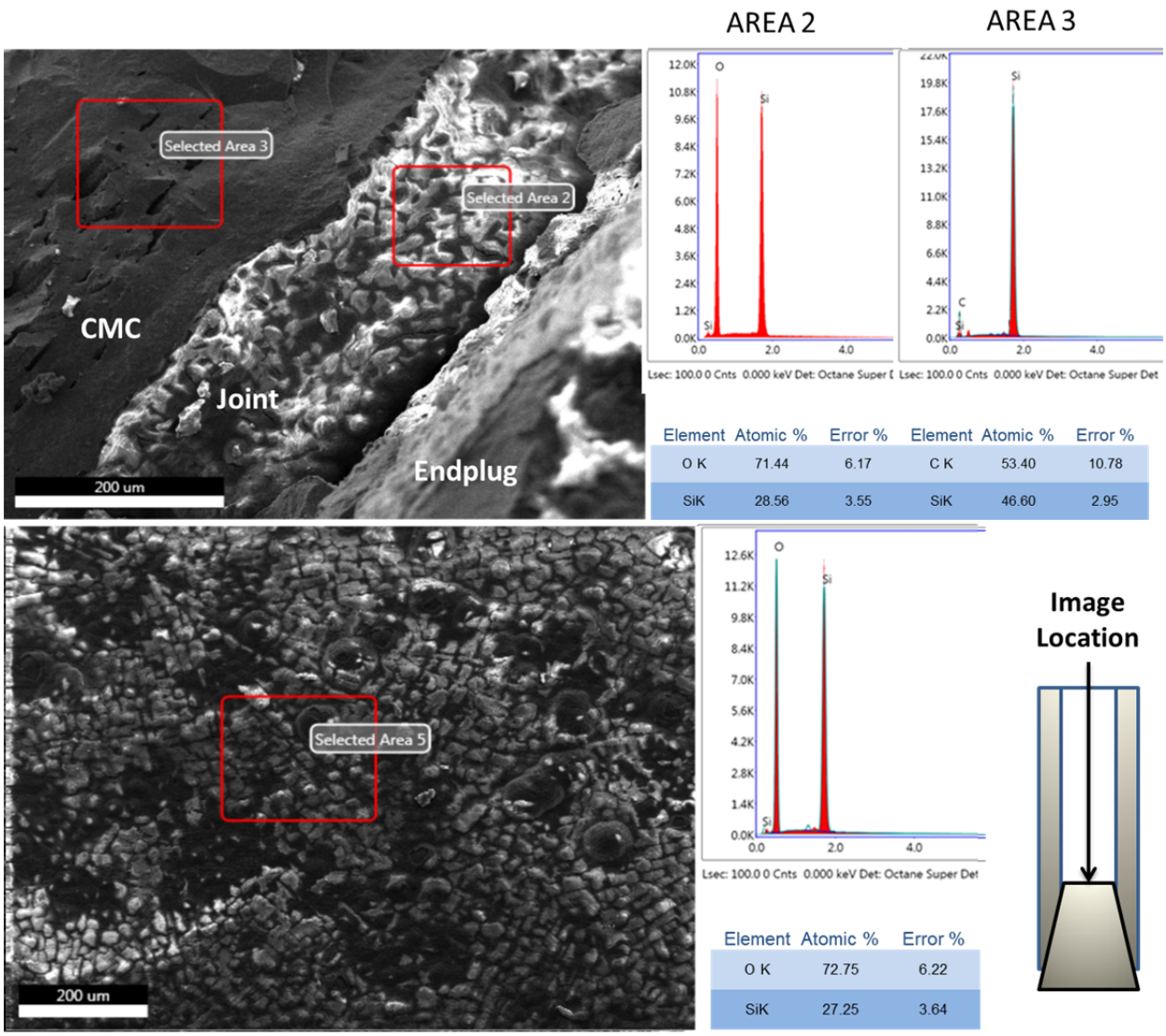

Figure 46: EDS analysis showing silica in the endplug joint but not in surrounding CMC layer (top) and silica buildup on the inside-facing surface of the endplug (bottom)

3. Mechanical Results

The influence of high-temperature steam oxidation on the mechanical behavior of the samples is investigated in this section. From the results, oxidation does impact the mechanical properties of the samples and results in brittle samples that do not exhibit the pseudo-ductility of the as-received and quenched samples.

The raw data for all oxidized samples is shown in Figure 47 and demonstrates that the oxidized sample behave similarly with only one distinct loading regime and complete sample failure upon termination of the first loading regime. Additionally, the slopes of all curves are similarly steep when compared to the fiber-only loading regimes observed in the as-received samples. Sample 200.1.23 failed at the highest pressure, with sample 196.1.19 failing at the next highest pressure and sample 198.1.25 failing at the lowest pressure. This behavior can be attributed to the difference between wall thickness and diameter between the sample series.

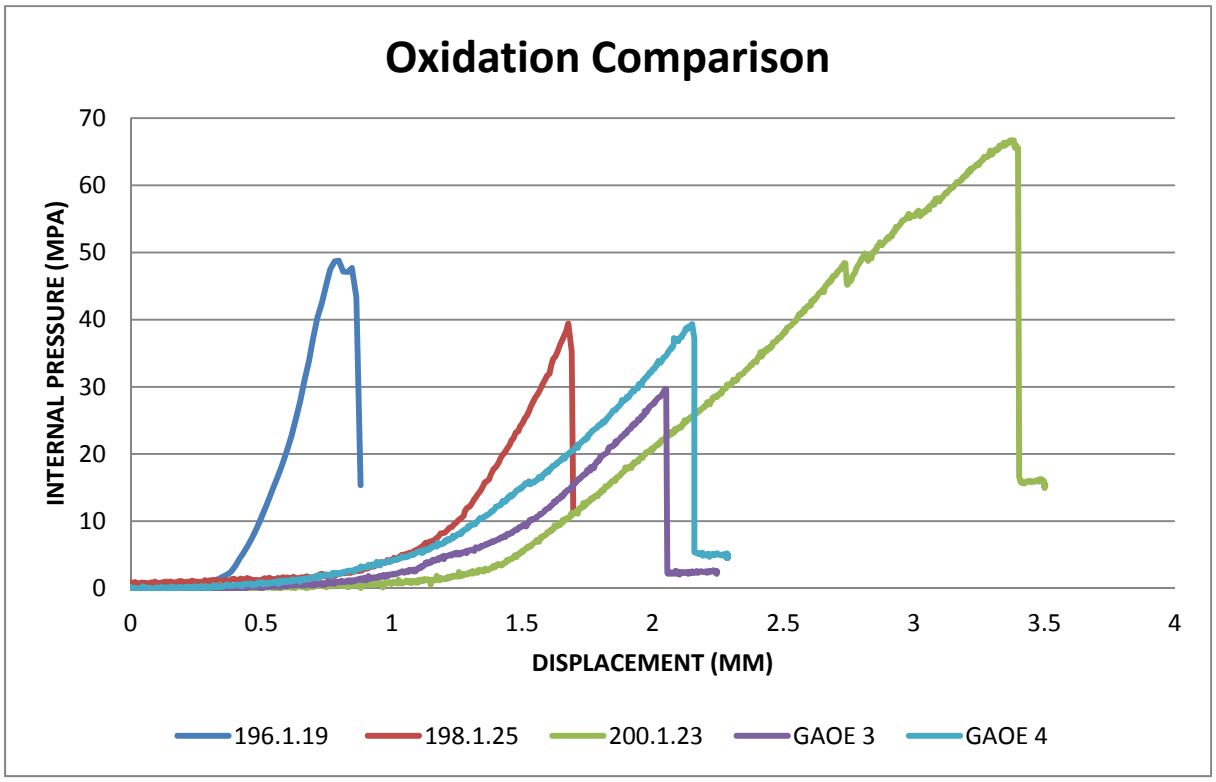

Figure 47: Internal pressure vs displacement for oxidized samples

i. Series 196

Figure 48 presents the internal pressure versus displacement curves for the oxidized sample 196.1.19 and the as-received sample 196.1.27. From the curves, it can be observed that the oxidized sample only exhibits a single loading regime in contrast to the two distinct loading regimes observed in the as-received sample. Furthermore, the oxidized sample failed at a significantly lower pressure than the failure pressure of the as-received sample.

Table 19 presents the mechanical characteristics for the oxidized sample 196.1.29 and the as-received sample 196.1.19. It can be observed that the oxidized sample was significantly weaker than the as-received sample, failing at stresses far lower than those witnessed by the as-received sample.

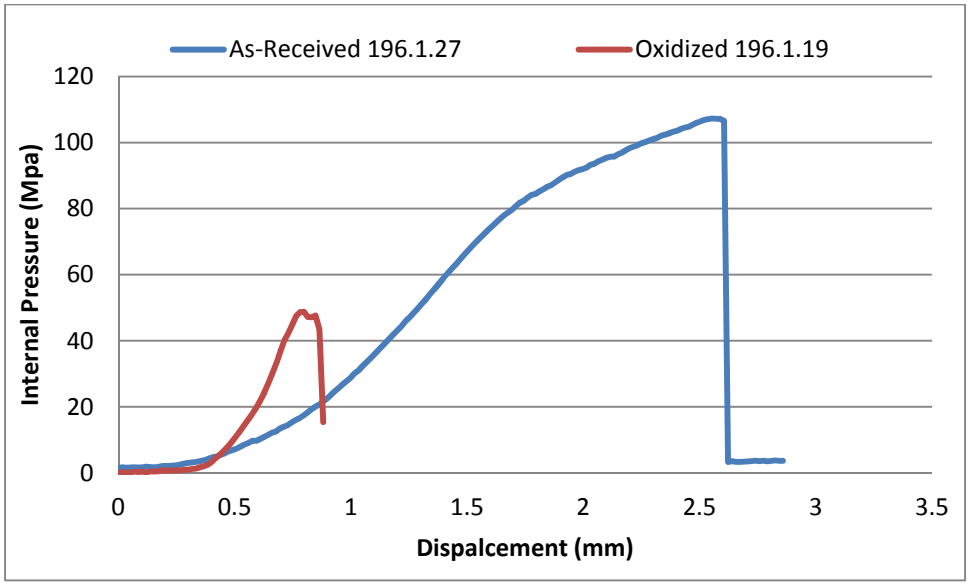

Figure 48: Internal Pressure vs Displacement Curve Comparison for Series 196

Table 19: Mechanical Characteristics for Series 196

	196.1.27 As-Received	196.1.19 Oxidized
Failure Hoop Stress Monolith ID	249 MPa	183 MPa
Failure Hoop Stress Fiber ID	267 MPa	78-120 MPa
Failure Plenum Pressure [MPa]	64 (107) MPa	49 (49) MPa

ii. Series 198

Figure 49 presents the OD stress-strain curve of sample 198.1.25 (left) and the comparison of the internal pressure versus displacement curves (right). The stress-strain curve for the as-received sample in series 198 was not obtained. No yielding was observed in the stress-strain curve, and instead the curve is linear until the complete failure of the sample. Such behavior demonstrates the brittle behavior of the oxidized sample 198.1.25. From the internal pressure versus displacement curves, similar behavior can be observed for both the as-received sample and the oxidized sample.

Table 20 shows the mechanical characteristics comparison between the oxidized sample and the as-received sample for series WEC01.198. The oxidized sample 198.1.25 failed at stresses approximately 30% lower than the failure stress for the as-received sample 198.1.24.

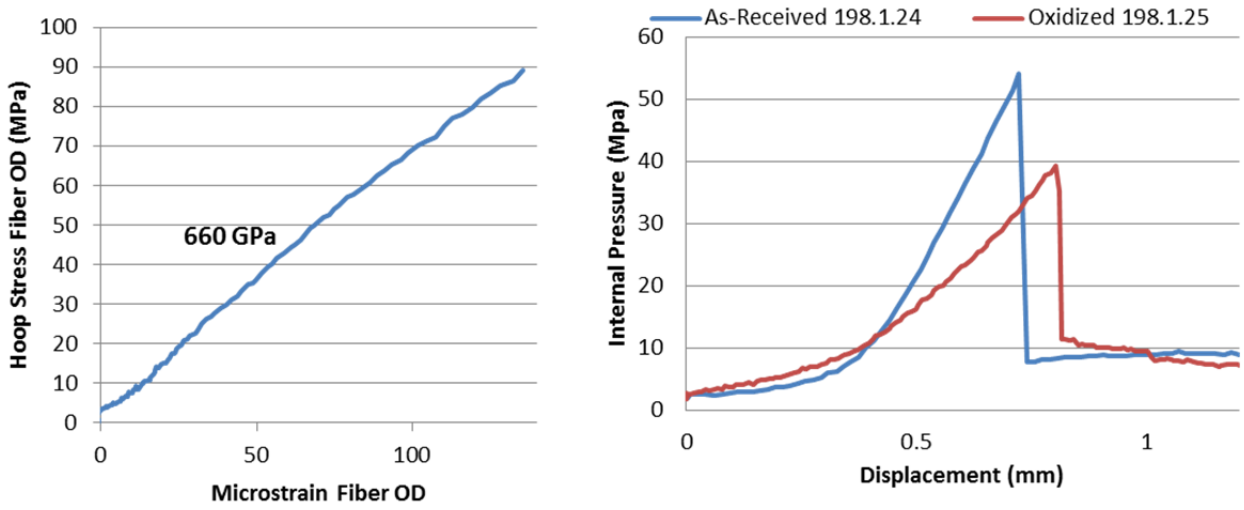

Figure 49: Stress-Strain Curve for OD of Oxidized Sample 198.1.25 (Left, Slope of Elastic Region Indicated) Internal Pressure vs Displacement Curve Comparison for Series 198 (Right)

Table 20: Mechanical Characteristics of Series 198

	198.1.24 As-Received	198.1.25 Oxidized
Elastic Modulus	No Data	660 GPa
Yield Stress (ID)	No Yielding	No Yielding
Monolith Failure ID Stress	267 MPa	192 MPa
Fiber Failure ID Stress	115 – 231 MPa	83 – 162 MPa
Failure Strain	No Data	135 µ-strain
Failure Plenum Pressure [MPa]	54 (54) MPa	39 (39) MPa

iii. Series 200

Figure 50 presents the OD stress-strain behavior comparison between the oxidized sample 200.1.23 and the as-received sample 200.1.25. For the stress-strain curve for sample 200.1.23, the strain gage failed before the termination of the burst test due to cracking of the glue bonding the strain gage to the sample. Therefore, the stress-strain curve for sample 200.1.23 is estimated after the point of strain gage failure based on observation of the stress-strain behavior for other oxidized samples. The estimation is based on the measured elastic modulus for the sample 200.1.23 when the strain gage was functional and the brittle, non-yielding behavior observed in other oxidized samples. The estimated stress-strain curve terminates at the stress of sample failed.

Table 21 shows the comparison of mechanical properties between the oxidized sample 200.1.23 and the as-received sample 200.1.25. It can be observed that the oxidized sample failed at a stress 48% lower than the failure stress for the as-received sample. The elastic modulus for the oxidized sample was steeper than the modulus of the as-received sample, although the moduli were fairly similar.

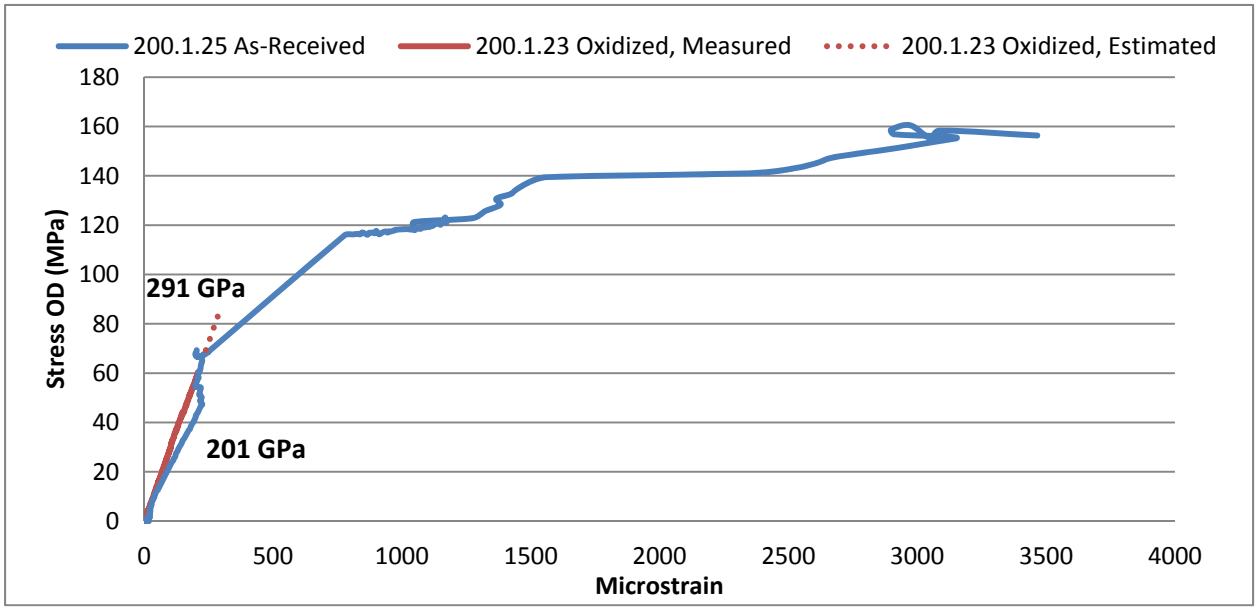

Figure 50: Stress-Strain Curve Comparison for OD of Series 200 (Slopes of Elastic Regions Indicated)

Table 21: Mechanical Characteristics of Series 200

	200.1.25 As-Received	200.1.23 Oxidized
Initial Elastic Modulus	201 GPa	291 GPa
Yield Stress (ID)	105-175 MPa	No Yielding
Monolith Failure ID Stress	243 MPa	169 MPa
Fiber Failure ID Stress	242 MPa	90 – 145 MPa
Failure Strain (OD)	3466 μ-strain	Estimated at 286 μ-strain
Failure Plenum Pressure [MPa]	60 (82) MPa	68 (68) MPa

iv. Series GAOE

Figure 51 presents the OD stress-strain behavior comparison between the GAOE samples. The oxidized samples, GAOE 3 and GAOE 4, are compared against the as-received sample GAOE 2. No yielding was observed for the oxidized samples and the failure stress was significantly lower than the failure stress for the as-received sample. The elastic moduli for the oxidized samples were similar to each other but were both smaller than the elastic modulus of the as-received sample. Whereas GAOE 3 failed without the decreases in strain observed in the as-received sample's initial loading curve, GAOE 4 experienced slight decreases in strain shortly before failure.

Table 22 shows a comparison of the mechanical properties between the oxidized samples GAOE 3 and GAOE 4 with the as-received sample GAOE 2. It can be observed that the oxidized samples had slightly different properties from each other: GAOE 3 had an elastic modulus of 550 GPa and a failure stress of 203 MPa, whereas GAOE 4 had an elastic modulus of 501 GPa and a failure stress of 262 MPa. The failure stress of both oxidized samples was approximately 60% lower than the failure stress for the as-received sample.

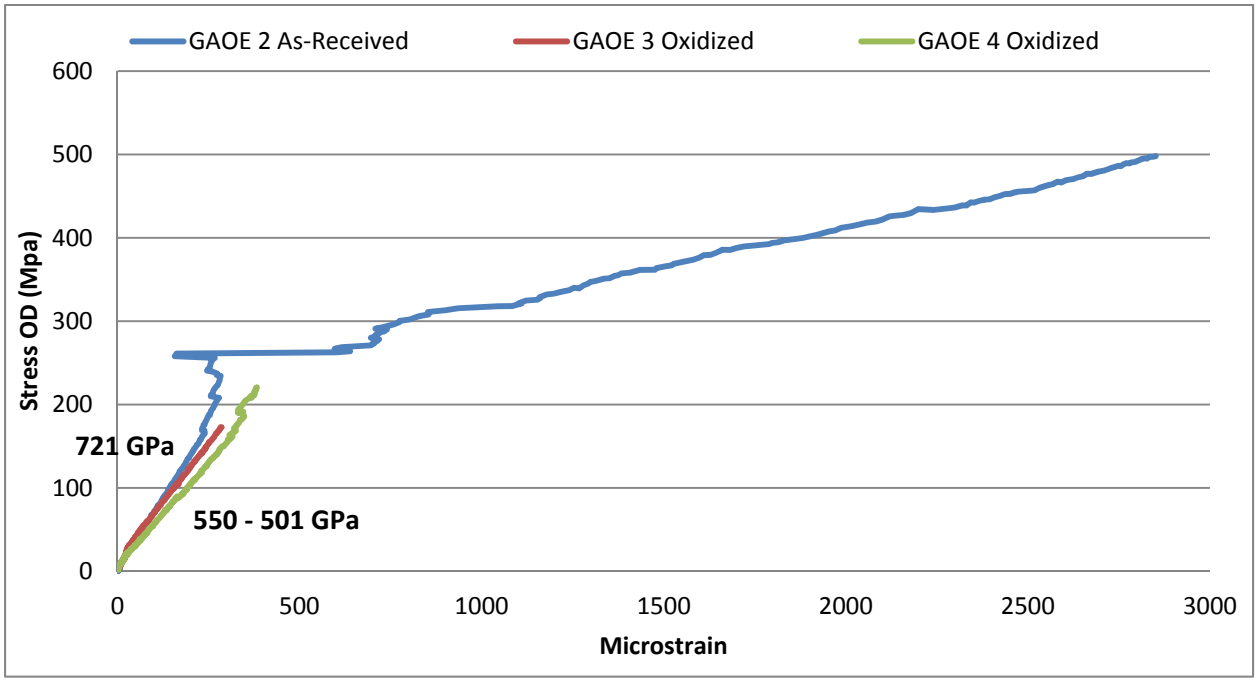

Figure 51: Stress-Strain Curve Comparison for OD of Series GAOE (Slopes of Elastic Regions Indicated)

Table 22: Mechanical Characteristics of Series GAOE

	GAOE 2 As-Received	GAOE 3 Oxidized	GAOE 4 Oxidized
Elastic Modulus	721 GPa	550 GPa	501 GPa
Yield Stress (ID)	304 MPa	No Yielding	No Yielding
Failure ID stress	581 MPa	203 MPa	262 MPa
Failure Strain (OD)	2851 µ-strain	286 µ-strain	383 µ-strain
Failure Plenum Pressure [MPa]	76	30	39

v. Series GACE-A

Figure 52 presents the load versus pushrod displacement curves for the pushout tests of the GACE-A series. Sample GACE 2 underwent pushout testing as-received and is used as the as the reference case for the pushout test of the oxidized sample GACE 3.

Table 23 presents the mechanical strength characteristics of the endplug joint for the GACE-A series. Note that the burst strength is analogous to the internal pressure required to result in joint failure. Although the observed burst strength of the oxidized sample was 9% lower than that of the as-received sample, the burst strengths are similar and the difference cannot be attributed to oxidation due to the lack of a large dataset.

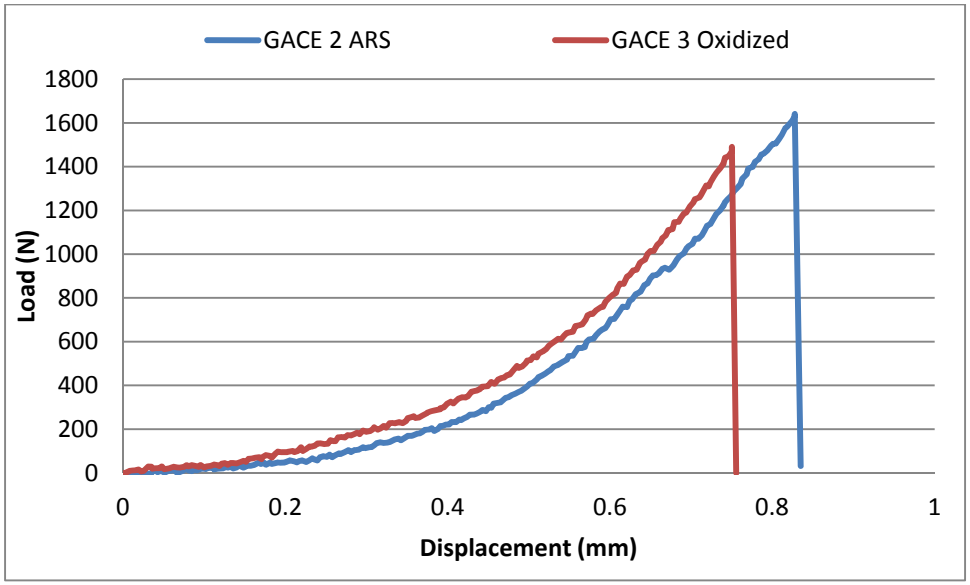

Figure 52: Pushrod load versus displacement curves for GACE-A series pushout tests

Table 23: Mechanical properties of endplug joint for GACE-A series

	GACE 2 As-Received	GACE 3 Oxidized
Peak Load	1641 N	1490 N
Burst Strength	37.1 MPa	33.7 MPa

vi. Series GACE-B

Figure 53 presents the load versus pushrod displacement curves for the pushout tests of the GACE-B series. Sample GACE 6 underwent pushout testing as-received and is used as the as the reference case for the pushout test of the oxidized sample GACE 4.

Table 24 presents the mechanical strength characteristics of the endplug joint for the GACE-B series. Note that the burst strength is analogous to the internal pressure required to result in joint failure. The observed burst strength of the oxidized sample was 32% lower than that of the as-received sample, suggesting that oxidation results in significant mechanical degradation of the joint for the GACE-B series.

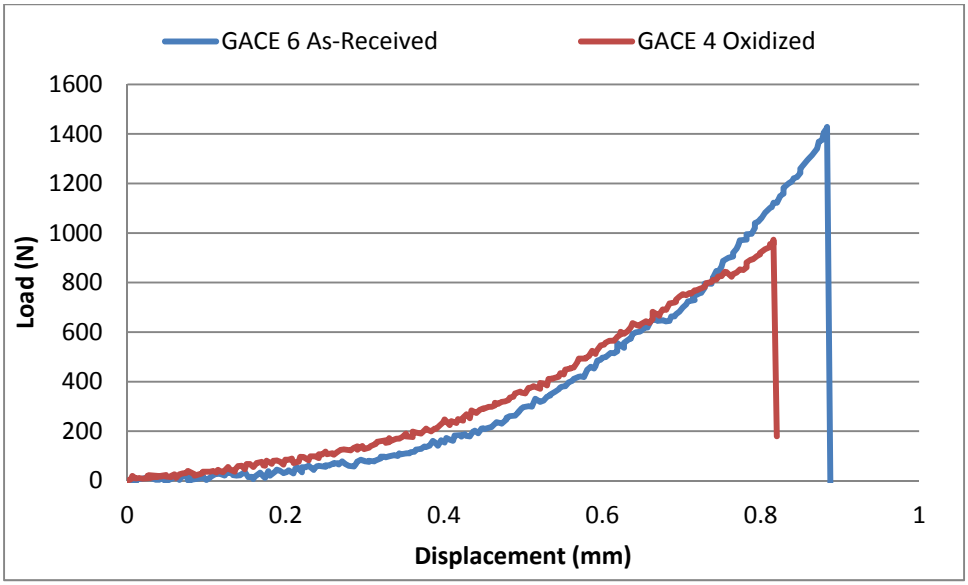

Figure 53: Pushrod load versus displacement curves for GACE-B series pushout tests

Table 24: Mechanical properties of endplug joint for GACE-B series

	GACE 6 As-Received	GACE 4 Oxidized
Peak Load	1423 N	972 N
Burst Strength	32.3 MPa	22.0 MPa

4. Oxidized Failure Characteristics

For the oxidized Westinghouse samples, during the initial monolith charging, the samples behaved elastically and were characterized by the monolith and fibers loading simultaneously as outlined in the mechanical model section (see Section 0.4 above). However, once the failure stress of the sample was exceeded, the monolith and the fiber region both failed by suddenly cracking entirely through the sample's thickness. The cracking behavior betrays the non-frangible embrittlement of the CMC layer.

When the samples failed, both the monolith and fiber regions failed simultaneously. The fiber region did not exhibit pseudo-ductility, and the failure strain was very low compared to the as-received samples. Sample failure was characterized by a single crack running along the entire length of the sample without large deformation of the sample. Whereas the as-received samples, when burst, exhibited deformation of the fiber tows and a wider crack, the oxidized samples displayed almost no deformation of the fibers and had a very narrow crack. Figure 54 presents the comparison between the cracking behavior for the as-received samples and the oxidized samples.

Figure 54: Comparison of cracking behavior between pairs of oxidized samples (left half of paired pictures) and as-received samples (right half of paired pictures)
A) Series 196, B) Series 200, C) Series 198, D) Series GAOE
Note the wider crack for the as-received samples.

Oxidation was not observed to have a significant impact on the mechanical strength of the endplug joint for the GACE-A series, but oxidation was observed to weaken the endplug joint for the GACE-B series. The failure characteristics of the endplug joint for the oxidized samples were different from those of the as-received samples, with the debonded surface of the oxidized samples showing remains of the fiber structure still attached to the endplug in contrast to the relatively smooth debonded surface for the as-received samples. The different failure characteristics observed between the as-received and the oxidized samples may be attributable to failure occurring within the CMC region, allowing for the

retention of fragments of the CMC region on the surface of the endplug. The characteristics of the debonded region for the oxidized GACE-B sample were especially different from the as-received debonded region, exhibiting pronounced texture similar to the weave pattern of the CMC layer. It is important to keep in mind that the scarf joint significantly reduces the load bearing section of the tube in the joint region.

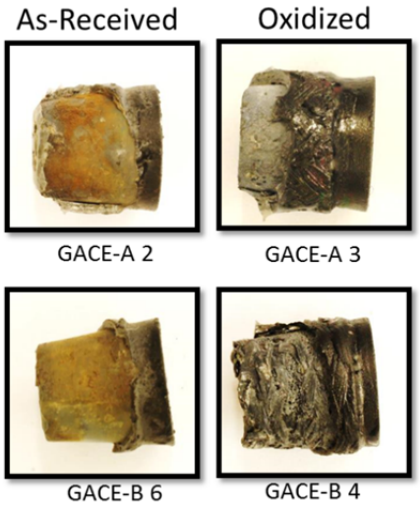

Figure 55: Endplug joint failure comparison for GACE-A and GACE-B series

SEM analysis of the lateral view of the endplug for the oxidized sample GACE 4 revealed that the endplug carried oxidized fibers with it during the pushout, as shown in Figure 56. This suggests that the oxidation weakened the CMC and failure occurred within the CMC region instead of within the joint.

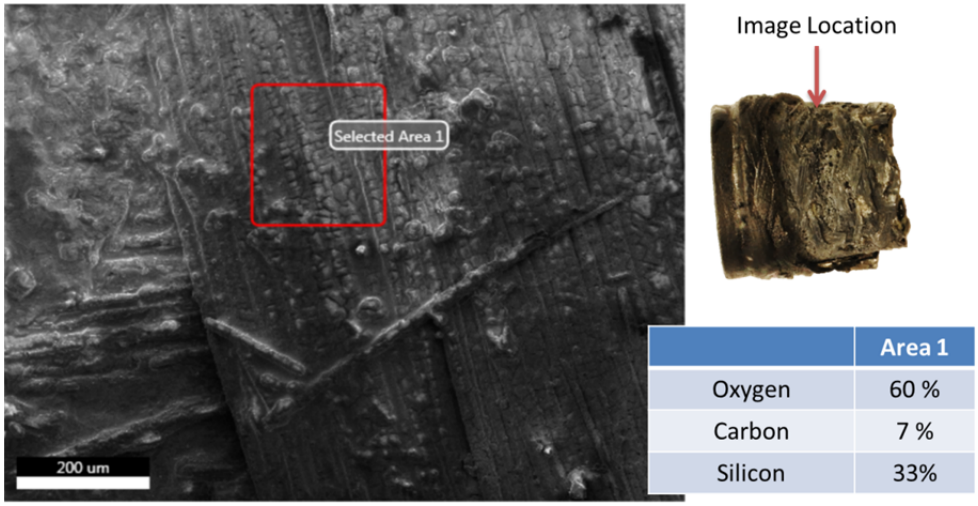

	Area 1
Oxygen	60 %
Carbon	7 %
Silicon	33%

Figure 56: SEM lateral view of endplug showing silica-coated fibers on the endplug after pushout

5. Conclusion

The mechanical model as presented above was used to calculate the failure hoop stresses of the Westinghouse samples with the monolith layer, whereas the thick-wall cylinder model was used for the GA samples (with no monolith). Because the inner surface of the samples experienced the highest hoop stress, the innermost surface hoop stresses were used as the failure hoop stresses of the layers. However, because the strain measurements were taken at the outer surfaces of the samples, the strain data provided reflects the hoop strain of the outermost surface of the samples during the event of interest (monolith or fiber region failure). The results of the burst testing of the oxidized samples are presented in Table 25 (Note: the GAOE samples are treated without a monolith layer).

Table 25: Table showing results of oxidized sample burst testing (Note: the GA samples are treated as without a monolith)

	Monolith Layer		Fiber Layer			
Sample	**ID Failure Hoop Stress**	**Sample OD Hoop Strain At Event**	**ID Failure Hoop Stress (ID)**	**Hoop Strain At Failure (OD)**	**Elastic Modulus**	**Yield Stress ID (MPa)**
196.1.27 ARS	249 MPa	No Data	267 MPa	No Data	No Data	109 – 161
196.1.19 Oxi.	183 MPa	No Data	78 – 120 MPa	No Data	No Data	No Yielding
198.1.24 ARS	267 MPa	No Data	115 - 232 MPa	No Data	No Data	No Yielding
198.1.25 Oxi.	192 MPa	0.014 %	83 – 169 MPa	0.014 %	660 GPa	No Yielding
200.1.25 ARS	243 MPa	0.022 %	242 MPa	0.35 %	201 GPa	105 – 175
200.1.23 Oxi.	169 MPa	0.03%[6]	90-145 MPa	0.03%[7]	291 GPa	No Yielding
GAOE 2 ARS	No Monolith Layer		581 MPa	0.28%	721 GPa	305
GAOE 3 Oxi.			202 MPa	0.03 %	550 GPa	No Yielding
GAOE 4 Oxi.			262 MPa	0.04 %	501 GPa	No Yielding
	Peak Load		**Burst Strength**			
GACE 2 ARS	1641 N		37.1 MPa			
GACE 3 Oxi.	1490 N		33.7 MPa			
GACE 6 ARS	1428 N		32.3 MPa			
GACE 4 Oxi.	972 N		22.0 MPa			

For the determination of the stress, the elastic modulus of the monolith layer was assumed to be unchanged from the as-received samples, but the elastic modulus of the fiber region was iterated upon until it converged with the measured elastic modulus. The resulting fiber region converged elastic moduli are also presented in Table 25.

The fibers were not observed to yield and therefore fiber yield stress is not tabulated. The monolith layer failure hoop stress was very similar for all Westinghouse as-received samples. For these samples, the monolith failed at a hoop stress of between 240 and 270 MPa. However, because all the Westinghouse oxidized samples experienced fiber region failure immediately upon monolith failure the precise fiber region failure hoop stress cannot be ascertained (because the mechanical model changes

[6] Estimated value based on strain data gathered prior to sample failure
[7] Estimated value based on strain data gathered prior to sample failure

from shared-loading to fiber-only loading) but was calculated to be greater than 115 MPa and less than 232 MPa, the corresponding hoop stresses for monolith-fiber and fiber-only loading respectively at the instant the monolith failed.

The fiber region failure behavior of the oxidized samples differs markedly from the fiber region failure of the as-received samples. This is likely due to the buildup of silica on the fiber region, thus binding the fibers together and preventing the fibers from gliding and exhibiting pseudo-ductility. Immediately after monolith failure, the stress of the fiber region required to contain the internal pressure in the oxidized samples coupled with the shock of the sudden failure of the monolith layer resulted in sudden failure of the fiber region without the characteristic pseudo-ductility observed in the as-received samples. Oxidizing the samples causes the fibers to remain bound in the matrix and results in a brittle but non-frangible fiber region.

6. Discussion

The stress calculations rely on the validity of the mechanical model outlined previously. Therefore, as outlined in the as-received section, assumptions are made regarding the monolith-fiber interface and mechanical properties of the monolith and fiber regions.

An important aspect of the calculation of the stresses of the oxidized samples is knowledge of the elastic modulus for the fibers and for the monolith. The stress distribution is dependent on the elastic moduli for the different layers in the sample. For the as-received samples and quenched samples, the elastic modulus of the fiber region was measured from the stress-strain curves and, corresponded well with published data (3), was used in the mechanical model along with the published modulus for the monolith (4). However, because the stress-strain behavior for the oxidized samples is markedly different from the behavior of as-received and quenched samples, the elastic moduli for the monolith and fiber regions were unknown. For calculation of the stresses, the elastic modulus for the monolith layer was assumed to be unchanged from the as-received elastic moduli. To validate this assumption, pure monolith elastic modulus was measured on as-received and oxidized samples. No change in the modulus was observed. However, the elastic modulus of the fiber region was iterated until it converged with the measured elastic modulus of the fiber region.

Because only one sample in each Westinghouse series (196, 198, and 200), only two samples in the GAOE series, and only one sample in each GACE series were oxidized, there are too few samples to provide meaningful statistics on the distribution of true population as-received mechanical properties. Only by testing more samples could the population's true distribution of mechanical properties be determined. However, oxidation does appear to have a significant impact on the mechanical properties of all of the sample series except the GACE-A endplug joint strength.

VI. Series Comparison

1. Series 196

Table 26: Mechanical results for series 196

	Monolith Failure		Fiber Failure			Failure Plenum Pressure
	ID Hoop Stress	OD Hoop Strain	ID Yield Hoop Stress	ID Ultimate Hoop Stress	OD Ultimate Hoop Strain	Monolith (Total)
As-Received 1 Sample Tested	249 MPa	No Data	109 – 161 MPa	267 MPa	No Data	64 (107) MPa
Quenched 2 Samples Tested	200 MPa[8]	No Data	88 – 129 MPa[8]	270 MPa[8]	No Data	51 (106) MPa
Oxidized 1 Sample Tested	183 MPa	No Data	No Yielding	78 – 120 MPa	No Data	49 (49) MPa

2. Series 198

Table 27: Mechanical results for series 198

	Monolith Failure		Fiber Failure			Failure Plenum Pressure
	ID Hoop Stress	OD Hoop Strain	ID Yield Hoop Stress	ID Ultimate Hoop Stress	OD Ultimate Hoop Strain	Monolith (Total)
As-Received 1 Sample Tested	267 MPa	No Data	No Yielding	115 – 231 MPa	No Data	54 (54) MPa
Quenched 2 Samples Tested	236[8]	No Data	No Yielding	151 - 262 MPa[8]	No Data	62 (62) MPa
Oxidized 1 Sample Tested	192 MPa	0.02%	No Yielding	83 – 169 MPa	0.02%	39 (39) MPa

[8] Value based on average of all quenched samples in series

3. Series 200

Table 28: Mechanical results for series 200

	Monolith Failure		Fiber Failure			Failure Plenum Pressure
	ID Hoop Stress	OD Hoop Strain	ID Yield Hoop Stress	ID Ultimate Hoop Stress	OD Ultimate Hoop Strain	Monolith (Total)
As-Received 1 Sample Tested	243 MPa	0.02%	105 - 175 MPa	242 MPa	0.35%	60 (82) MPa
Quenched 1 Sample Tested[9]	165 MPa	0.13%	100-152 MPa	225 MPa	0.27%	50.8 MPa
Oxidized 1 Sample Tested	169 MPa	0.03%[10]	No Yielding	90 – 145 MPa	0.03%[10]	68 (68) MPa

4. Series GAOE

Table 29: Mechanical results for series GAOE

	Yielding		Ultimate Failure		Failure Plenum Pressure
	ID Hoop Stress	OD Hoop Strain	ID Hoop Stress	OD Hoop Strain	
As-Received 1 Sample Tested	305 MPa	0.03%	581 MPa	0.28%	76 MPa
Quenched 2 Samples Tested	271 MPa[8]	0.03%[8]	532 MPa[8]	0.25%[8]	34.5 MPa
Oxidized 2 Samples Tested	No Yielding	No Yielding	232 MPa[11]	0.03%[11]	80 MPa

[9] Although sample 200.1.14 was quenched, it was too short to be successfully burst. This data is from 200.1.24.
[10] Estimation based on strain data gathered prior to sample failure
[11] Value based on average of all oxidized samples in series

5. Series GACE-A

Table 30: Mechanical results for series GACE-A

	Peak Load	Burst Strength
As-Received 1 Sample Tested	1641 N	37.1 MPa
Quenched 1 Sample Tested	1513 N	34.2 MPa
Oxidized 1 Sample Tested	1490 N	33.7 MPa

6. Series GACE-B

Table 31: Mechanical results for series GACE-B

	Peak Load	Burst Strength
As-Received 1 Sample Tested	1428 N	32.3 MPa
Quenched 2 Sample Tested	468 N	10.6 MPa
Oxidized 1 Sample Tested	972 N	22.0 MPa

7. Overall

Table 32 presents the comparison of the mechanical properties between the different series tested. From the results, the monolith failure strength was observed to decrease during quenching, although there is variation in the exact decrease in failure stress. However, the monolith was observed to weaken by approximately 30% during the oxidation testing. Similarly, there is variation in the effect of the quenching on the fiber failure strength, although the fibers were observed to weaken by approximately 60% during oxidation (except for series 198 where the fibers weakened by approximately 30%). Performance of the endplug was observed to be dependent on sample architecture, with GACE-A series being more resistant to the corrosion tests than the GACE-B series.

Table 32: Comparison of Results between Series

		Series 196	Series 198	Series 200	GAOE
Monolith	Ultimate Failure Hoop Stress[12]	249 MPa	267 MPa	243 MPa	-
	Reduction in Strength, Quench[13]	-20%	-12%	-22%	-
	Reduction in Strength, Oxidation[14]	-27%	-28%	-30%	-
Fiber	Ultimate Failure Hoop Stress[12]	267 MPa	115 to 231 MPa	242 MPa	581 MPa
	Reduction in Strength, Quench[13]	+1%	+13% to +31%	-11%	-8%
	Reduction in Strength, Oxidation[14]	-55% to -71%	-28%	-40% to -63%	-60%
			GACE-A	**GACE-B**	
Endplug Joint	Burst Strength[12]		37.1 MPa	32.3 MPa	
	Reduction in Strength, Quench		-8%	-78%	
	Reduction in Strength, Oxidation		-9%	-32%	

Figure 57 presents the observed monolith ultimate failure stresses for the three Westinghouse sample series. Both quenching and oxidation were observed to decrease the monolith failure stress. Note the GA samples are not shown because they do not have an inner monolith layer.

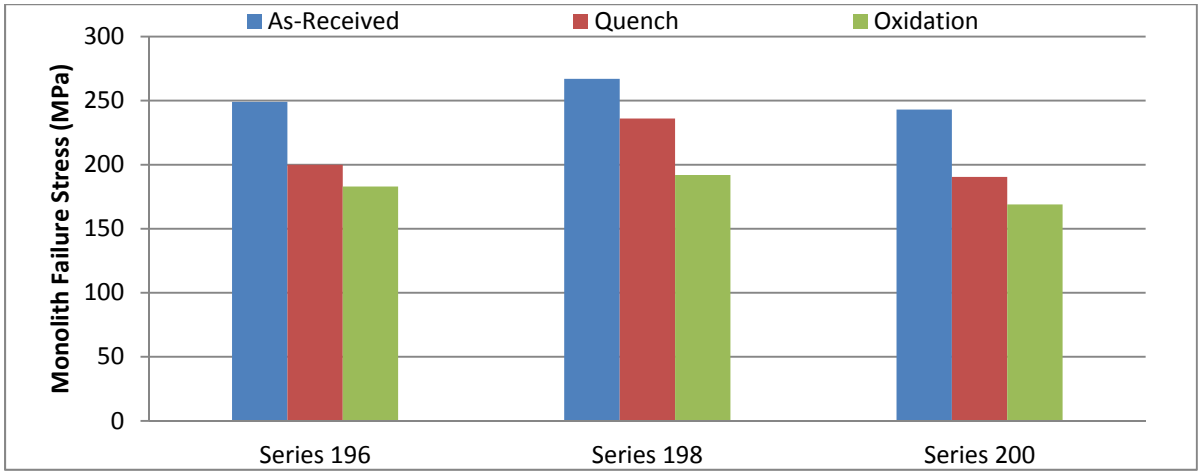

Figure 57: Comparison of monolith failure stress

[12] For as-received sample
[13] Value based on average of all quenched samples in series
[14] Value based on average of all oxidized samples in series

Figure 58 presents the observed fiber failure stress for all sample series. Because several of the properties could not be precisely determined a range of possible values (reflected by the split bars, with the lower bar representing the lower end of the range and the higher bar representing the higher end of the range) are presented, with the precise observed fiber failure stress observed for the samples lying somewhere within the range. It can be observed that quenching had varying results on the samples, although the quenching was observed to be less impactful on the fiber strength than on the monolith strength. However, oxidation was observed to significantly decrease the fiber failure strength (although conclusions are difficult for series 198 due to the range of possible values observed).

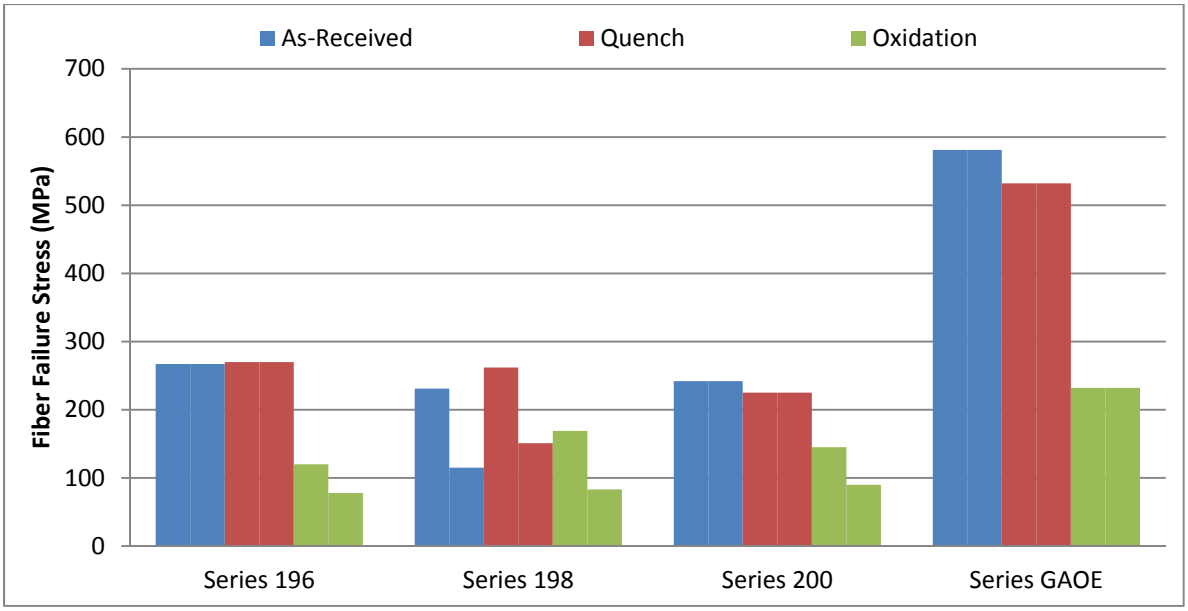

Figure 58: Comparison of fiber failure stress (note that the range of possible values is reflected by the split bars)

Figure 59 presents the observed endplug burst strength for the GACE-A and GACE-B series. From the figure, the influence of architecture on endplug joint strength can be observed, with the GACE-A series exhibiting little decrease in strength due to testing, whereas the GACE-B series shows substantial decrease in strength with testing.

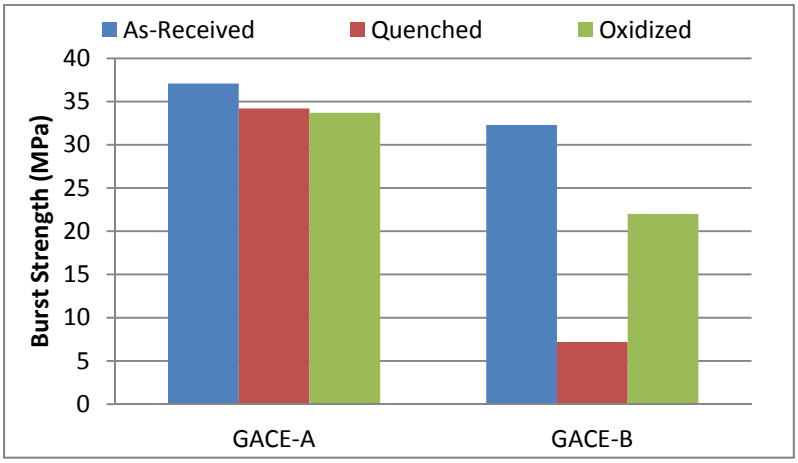

Figure 59: Comparison of endplug joint burst strength

VII. Conclusion

The preliminary results presented in this study do not involve irradiation. Therefore, no definitive conclusion can be drawn yet regarding the potential of SiC/SiC composites for nuclear fuel cladding. It must also be noted that these conclusions are being drawn on a limited number of samples, typically one or two per test condition. Additionally, differences in sample fabrication could also be influencing the results.

1. As-Received Analysis

The behavior of the as-received samples fall into two categories: the behavior observed in the Westinghouse and the behavior observed in the GAOE samples. For all of the Westinghouse samples, the inner monolith layer failed for similar stresses (around 250 MPa) while the CMC layer failed below 270 MPa (Table 33). However variation was observed in the behavior of the CMC layer: sample 198 – because of its geometry- experienced stresses in the fiber region sufficient to result in the simultaneous failure of both the fiber layer and the inner monolith, whereas series 196 and 200 layers had more de-correlated fiber and monolith failure behavior. In that sense, series 198 didn't exhibit any pseudo-ductility while series 196 had the closest behavior to a fiber-only specimen. The differences observed between the three series are more attributable to the differences in the samples' dimensions rather than the differences in design, and all three series fall under the same general behavioral category; with the monoliths failing at a similar stress. Because hermeticity is lost when the inner monolith breaks, the inner monolith failure should be seen as a critical event that decreases the performance of such samples. However, the failure resulting in a single crack allows for maintaining a coolable geometry.

Series GAOE was observed to be much stronger than the Westinghouse series. Sample GAOE 2 reached more than twice the failure stress of the Westinghouse samples and the fibers yielded at 300 MPa, compared to around 150MPa for the Westinghouse samples. However, as the GAOE 2 failure was characterized by the detachment of relatively large fiber fragments, its failure mode is not compatible with the conditions of a primary coolant loop because debris would be released into the core which might block coolant channels.

Both as-received endplug joint tests revealed similar burst strengths of slightly more than 30 MPa. Withstanding such a plenum pressure seems satisfactory looking at the current 14 MPa plenum pressure limit. However, since fuel temperature will be higher with SiC cladding (lower thermal conductivity than Zr, no creep to close the fuel-cladding gap and radial selling emphasizing this gap), fuel rods will likely be expected to withstand higher pressures, making the endplug join a central question.

Table 33: As-Received Sum up Mechanical Table

	Monolith Layer		Fiber Layer		
As-Received Sample	**ID Failure Hoop Stress**	**Sample OD Hoop Strain At Event**	**ID Failure Hoop Stress**	**Sample OD Hoop Strain At Event**	**Fiber ID Yield Stress**
196.1.27	249 MPa	No Data	267 MPa	No Data	109 – 161 MPa
198.1.24	267 MPa	No Data	115 - 232 MPa	No Data	115 – 231 MPa
200.1.25	243 MPa	0.0224 %	242 MPa	0.35 %	105 – 175 MPa
GAOE 2	No Inner Monolith		581 MPa	0.28%	305 MPa

	Peak Load	**Burst Strength**
GACE 2	1641 N	37.1 MPa
GACE 6	1428 N	32.3 MPa

2. Influence of Quenching

All samples that underwent thermal shock survived, even when harsher conditions were tested (90°C water). In particular, no quench-induced micro cracks could be detected during the SEM analysis. Moreover, non-frangible failure mode was still observed which satisfies the NRC requirement of maintaining coolable rod geometry.

The lack of repetition of the tests prevents definitive conclusions on the impact of quenching on the monolith and CMC layer failure hoop stress. However, from the samples that were tested, fiber yield stress was observed to decrease by 10-20% with quenching whereas the failure hoop stress was observed to be more stable. From the stress-strain curves in Section IV, quenching appears to have a slight impact on the overall mechanical behavior of the samples.

The design of the GAOE series seems more promising as the failure stress of the fiber region was around twice that of the strongest of the Westinghouse design. The series also exhibits a more predictable behavior with quenching and would allow for more confidence in potential predictive models. However, the GAOE fragmentation failure mode would potentially release debris in the primary coolant loop, possibly restricting subchannel flow.

The endplug joint strength in the GACE-A series was not observed to be significantly affected by the quenching. However, the endplug joint strength in the GACE-B series was observed to decrease by 78% and 55 % after quenching. This suggests that architecture may have an important influence on the resilience of the endplug joint.

Because only one as-received and two quench sample in each Westinghouse series (196, 198, and 200), only two samples in the GAOE series, and only one sample in each GACE series were tested both as-received and quenched, there are too few samples to provide meaningful statistics on the distribution of mechanical properties. Only by testing more samples could the population's true distribution of mechanical properties be determined.

Table 34: Thermal Shock Summary table

		Monolith Layer		Fiber Layer			
Sample	**Water Temp.**	**ID Failure Hoop Stress**	**Sample OD Hoop Strain At Event**	**ID Failure Hoop Stress**	**Sample OD Hoop Strain At Event**	**Elastic Modulus**	**Fiber ID Yield Stress (MPa)**
196.1.27	ARS	249 MPa	No Data	267 MPa	No Data	No Data	109 – 161
196.1.20	100°C	193 MPa	No Data	279 MPa	No Data	No Data	85-124
196.1.26	90°C	207 MPa	No Data	260 MPa	No Data	No Data	91-133
198.1.24	ARS	267 MPa	No Data	115-232 MPa	No Data	No Data	No Yielding
198.1.23	100°C	305 MPa	No Data	134-232 MPa	No Data	No Data	No Yielding
198.1.16[15]	90°C	167 MPa	No Data	167-292 MPa	No Data	No Data	No Yielding
200.1.25	ARS	243 MPa	0.02%	242 MPa	0.35%	201 GPa	105 – 175
200.1.24	100°C	165 MPa	0.02%	226 MPa	0.27%	300 GPa	100-152
200.1.14[16]	90°C	215 MPa	No Data	No Data	No Data	No Data	No Data
GAOE 2	ARS	No Inner Monolith		581 MPa	0.28%	721 GPa	305
GAOE 5	100°C			572 MPa	0.30%	612 GPa	266
GAOE 6	90°C			492 MPa	0.19%	1174 GPa	276

		Peak Load		**Burst Strength**
GACE 2	ARS	1641 N		37.1 MPa
GACE 1	100°C	1513 N		34.2 MPa
GACE 6	ARS	1428 N		32.3 MPa
GACE 5	100°C	318 N		7.2 MPa
GACE 8	100°C	617 N		14.0 MPa

[15] Sample 198.1.16 was very short and didn't contain a complete weave pattern unit cell. Therefore, significance of the result is questionable.

[16] Sample 200.1.14 was very short and didn't contain a complete weave pattern unit cell. Therefore, significance of the result is questionable.

3. Influence of Oxidation

Oxidation was shown to result in the formation of silica on the exterior surfaces of the specimens and also in the inner voids of the CMC (as has been shown on the optical and SEM images). As a result, a normalized weight change from 0 to 0.7 mg/cm^2 (likely depending on sample porosity) was observed. This chemical change reduced the hoop stress of the monolith layer for the Westinghouse samples from around 250 MPa for the as-received samples to roughly 180MPa after oxidation. Still, those performances largely surpass those of actual Zr cladding under oxidation. Moreover, coolable geometry is still guaranteed after oxidation.

Additionally, all the Westinghouse oxidized samples experienced fiber region failure immediately upon monolith failure. The precise fiber failure hoop stress cannot be measured (due to the simultaneous failure of the monolith) but the two models previously described (monolith-fiber and fiber-only loadings) give respectively minimum and maximum estimations of this hoop stress. Table 35 reports those values and shows a drop in strength of up to a 60%. Because the CMC failed right after the inner monolith, no yielding is observed. Similarly, whereas the as-received 196, 200 and GAOE series samples would experience up to 0.3% strain at failure, after oxidation only a 0.03% strain at failure was observed.

The absence of pure fiber region loading is likely due to the buildup of silica on the fiber matrix interface, thus binding the fibers and preventing the fibers from gliding and exhibiting pseudo-ductility. Immediately after monolith failure, the stress of the fiber region required to contain the internal pressure in the oxidized samples coupled with the shock of the sudden failure of the monolith layer resulted in sudden failure of the fiber region without the characteristic pseudo-ductility observed in the as-received samples. Oxidizing the samples caused the fibers to remain bound in the matrix and resulted in a brittle fiber region.

The endplug joint strength testing revealed that sample architecture has an impact on the corrosion resistance of the joint. The GACE-A series showed little decrease in the strength of the joint due to oxidation, whereas the GACE-B series showed significant weakening of the joint due to oxidation.

Because only one sample in each Westinghouse series (196, 198, and 200), only two samples in the GAOE series, and only one sample in each GACE series were tested both as-received and oxidized, there are too few samples to provide meaningful statistics on the distribution of mechanical properties. Only by testing more samples could the population's true distribution of mechanical properties be determined.

Table 35: Oxidation Mechanical results

	Monolith Layer		Fiber Layer			
Sample Denomination	**ID Failure Hoop Stress**	**Sample OD Hoop Strain At Event**	**ID Failure Hoop Stress (ID)**	**Hoop Strain At Failure (OD)**	**Elastic Modulus**	**Yield Stress ID (MPa)**
196.1.27 ARS	249 MPa	No Data	267 MPa	No Data	No Data	109 – 161
196.1.19 Oxi.	183 MPa	No Data	78 – 120 MPa	No Data	No Data	No Yielding
198.1.24 ARS	267 MPa	No Data	115 - 232 MPa	No Data	No Data	No Yielding
198.1.25 Oxi.	192 MPa	0.014 %	83 – 169 MPa	0.014 %	660 GPa	No Yielding
200.1.25 ARS	243 MPa	0.022 %	242 MPa	0.35 %	201 GPa	105 – 175
200.1.23 Oxi.	169 MPa	0.03%[17]	90-145 MPa	0.03%[18]	291 GPa	No Yielding
GAOE 2 ARS	No Monolith Layer		581 MPa	0.28%	721 GPa	305
GAOE 3 Oxi.			202 MPa	0.03 %	550 GPa	No Yielding
GAOE 4 Oxi.			262 MPa	0.04 %	501 GPa	No Yielding

	Peak Load	**Burst Strength**
GACE 2 ARS	1641 N	37.1 MPa
GACE 3 Oxi.	1490 N	33.7 MPa
GACE 6 ARS	1428 N	32.3 MPa
GACE 4 Oxi.	972 N	22.0 MPa

4. Recommendations for design

Of the different designs analyzed, the GAOE design offers the best mechanical properties. Its failure hoop stress reaches almost 600 MPa as-received and remains significantly stronger than the Westinghouse samples after both oxidation and quenching. Additionally, the normalized weight change after oxidation for the GAOE samples was approximately 2 orders of magnitude smaller than for the Westinghouse samples. Further ceramographic analysis will allow for better characterization of the chemical changes during oxidation.

The improved behavior of the GAOE samples comes from the monolith layer positioning on the outside of the sample. Setting the monolith at the outer surface allows the fibers to contribute more substantially to the loading and therefore alleviate the monolith loading. On the inside, the monolith covers much of the contribution of the fibers. Moreover, an outer monolith plays both the roles of hermeticity barrier and EBC which allows reducing the needed cladding thickness. With an inner layer design - as such in the Westinghouse samples - the monolith layer undergoes maximal tensile stress and fails before fibers significantly contribute to loading. Once the monolith fails, the material is no longer reliable because hermeticity is lost and debris is generated.

Thus, future design should involve two layers with SiC/SiC CMC as an inner layer and an outer SiC monolith. Because the Westinghouse samples behavior was dominated by the monolith layer, it was more difficult to observe the influence of the weaving architecture. However, several studies (5) (6) suggest that higher failure hoop stress can be achieved with a circumferentially oriented weave versus

[17] Estimated value based on strain data gathered prior to sample failure
[18] Estimated value based on strain data gathered prior to sample failure

an axial weave. Therefore, a plain weave pattern with a 60°-70° angle from the axial direction is suggested. However, axial tows would allow the tubing and the joint to withstand higher axial stress, so more investigation would need to be performed on the axial strength of the tubing and the joint to identify an optimal architecture.

Endplug joint testing revealed that the endplug joint fails at an internal pressure far lower than that which was observed to cause failure of the open-ended samples. This suggests that the endplug could be the weakest part of the SiC cladding and that the joint strength should be enhanced. Furthermore, because architecture was observed to influence the joint strength, more architectures should be investigated to determine the best weave pattern for endplug joint performance.

VIII. Bibliography

1. **Lee, Y., McKrell, T. and Kazimi, M.** *Safety of Light Water Reactor Fuel with Silicon Carbide Cladding.* Cambridge : CANES, 2014. MIT-ANP-TR-150.

2. *Fabrication and characterization of joined silicon carbide cylindrical components for nuclear applications.* **Khalifa, H., C. Deck, O. Gutierrez, G. Jacobsen, and C. Back.** s.l. : Journal of Nuclear Materials, 2014, Vol. 457, pp. 227-240.

3. **Shinavski, R., Katoh, Y. and Snead, L.** *Mechanical, Thermal and Electrical Properties of Nuclear Graded Silicon Carbide Composites.* Oak Ridge, Tennessee : Oak Ridge National Laboratory, 2008. pp. 14-18. DOE-ER-0313/44 .

4. *Handbook of SiC properties for fuel performance modeling.* **Snead, L. L., Nozawa, T., Katoh, Y., Byun, T.-S., Kondo, S., & Petti, D. A.** s.l. : Journal of Nuclear Materials, 2007, Vol. 371.

5. *Fabrication and measurement of hoop strength of SiC triplex tube for nuclear fuel cladding applications.* **D. Kim, , HG. Lee, JY Park, WJ. Kim.** s.l. : Journal of Nuclear Materials, 2015, Vol. 458.

6. *Ingluence of winding angle on the strength and deformation of filament-wound composite tubes subjected to uniaxial and biaxial loads.* **P. D. Soden, R. Kitching, P. C. Tse, Y. Tsavalas.** Manchester : Composites Science and Technology, 1993.

Overview of Properties and Performance of Uranium-Silicide Compounds for Light Water Reactor Applications

A.T. Nelson, J.T. White, D.D. Byler, J.T. Dunwoody, J.A. Valdez and K.J. McClellan

Los Alamos National Laboratory
P.O. Box 1667
Los Alamos, NM, 87545
atnelson@lanl.gov

INTRODUCTION

The uranium-silicon binary system possesses a range of compounds that have been historically investigated and utilized to a limited extent as nuclear reactor fuels. Of the multiple compounds, U_3Si and U_3Si_2 are most familiar; their high uranium densities have made them an intriguing choice for incorporation into composite plate fuels in research reactors and other low power core redesigns where retained neutronic performance was desired at lower enrichments [1]. This increased uranium density compared with uranium dioxide (UO_2) has made them attractive to a new generation of nuclear fuels research driven by the renewed push for accident-tolerant light water reactor (LWR) fuels. A higher uranium density may motivate incorporation of U-Si phases into composite fuels that utilize secondary phases with the goal of increasing coping time during a cladding breach before fission products and/or actinides are released. Additionally, development of fuels containing higher uranium densities than those of reference UO_2 could facilitate utilization of alternative cladding materials that offer improved high temperature performance than zirconium alloys but incur neutronic penalties.

Surveys of the existing property databases of candidate U-Si compounds revealed that very little is known of even the more common uranium silicides with respect to their thermophysical and thermodynamic performance. The absence of such data challenges development of potential fuel forms or modeling of reactor operation under hypothesized core loadings that include U-Si fuel forms. Furthermore, consideration of potential off-normal scenarios requires even more specific knowledge of the thermodynamic stability and reaction kinetics of U-Si compounds when they are exposed to diverse stimuli such as oxidizing environments or prolonged contact with cladding materials. The literature is largely devoid of any information on these critical details necessary to hypothesize the performance of U-Si compounds as LWR fuels.

An experimental campaign was undertaken at Los Alamos National Laboratory in 2012 in order to provide this data and facilitate evaluation of the potential of U-Si compounds for LWR applications. In the case of the uranium-rich U_3Si and U_3Si_2 compounds that have seen more extensive service as research reactor fuels, this work focused on a more critical evaluation of their thermophysical properties to temperatures near their melting points. These compounds have seen limited characterization at temperatures low relative to those anticipated of an LWR fuel, but even here appreciable scatter is present [2]. Lesser-studied compounds such as USi and U_3Si_5 have received virtually no attention from previous researchers regarding their thermal conductivity, heat capacity, and thermal expansion as a function of temperature. Accurate knowledge of these properties is essential to modeling of heat transport in reactor systems.

The renewed focus on accident tolerance has also emphasized consideration of the off-normal performance of materials in nuclear reactor systems. The dominant focus has been understanding evolutions expected during a loss of coolant accident (LOCA). During a breach of cladding (brought about by a LOCA, cladding defect introduced during manufacturing, or failure during long term storage), the fuel will be exposed to high temperatures and water vapor. The potential availability of oxygen, hydrogen, or nitrogen may also dictate behavior. Aside from low temperature U_3Si studies [3], no attention has been given to understanding the oxidation kinetics of U-Si compounds under such environments at high temperature. Experimental investigation of these aspects of thermodynamic stability has also been undertaken for each of the four U-Si compounds.

Finally, exploratory studies of other factors critical to LWR deployment of U-Si compounds have begun. The compatibility of these compounds with both conventional nuclear fuels (i.e. UO_2 and UN) and other oxidation resistant materials at high temperature will be discussed. Stability of solid fission product silicide compounds (opposed to the more familiar oxides) will be presented with respect to high burnup applications. Finally, issues and potential solutions encountered during scaling of techniques employed for fabrication of high-purity uranium-silicides in the laboratory (10^{-2} kg) to the test irradiation environment (10 kg), and finally to possible commercial use (10^6 kg) will be examined.

METHODOLOGY

Characterization of the properties of U-Si compounds first required synthesis of high purity material for each of the compositions. The four compounds targeted for

investigation in this work were U_3Si, U_3Si_2, USi, and U_3Si_5. Although additional silicon-rich U-Si compounds do exist, it was desired to limit the investigation to these four in order to retain U-densities above or reasonably near those of UO_2. Arc melting was used to produce all materials investigated here. Depleted uranium metal and an excess of silicon (necessary to account for volatilization in the molten state) were combined in the arc melter and melted multiple times in order to maximize homogenization. The buttons of each material were then solutionized at roughly 80% of each compound's melting point for 50-80 hours in gettered argon atmospheres. Gettered argon ($P_{O2} < 10^{-16}$ atm) was found necessary; even ultra-high purity argon ($P_{O2} \approx 10^{-6}$ atm) was observed to quickly oxidize the materials at moderate temperatures. Solutionization at high temperature was found necessary to eliminate second phases resulting from the peritectic transformations encountered upon cooling from the melt.

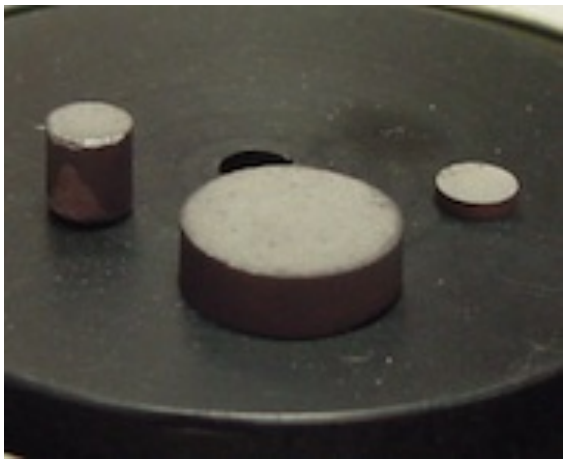

Fig. 1. Photograph of U_3Si_5 pellets produced using powder metallurgy route. The large center pellet is roughly 10 mm in diameter.

Processing of starting materials produced as described above into forms sufficient for thermal analysis and oxidation studies varied depending on the specific compound. U_3Si was found to possess ductility comparable to a metal. As such, is was possible to machine specimens of U_3Si using common fabrication techniques. The other three compounds were far more brittle and dictated use of powder metallurgy techniques. The heat-treated U_3Si_2, USi, and U_3Si_5 buttons were first milled into a fine powder and then pressed into the necessary cylindrical geometries. Sintering was performed in gettered argon atmospheres. The precise conditions varied between U_3Si_2, USi, and U_3Si_5, but required 24-48 hour isothermal holds at temperatures similar to those employed in the heat treatment steps. The fabrication routes used were found to result in materials in excess of 96% the theoretical density of the compounds and substantially free of second phases. Figure 1 shows a photograph of U_3Si_5 pellets fabricated for thermophysical property measurements.

Thermophysical property measurement of all four U-Si compositions was performed to approximately 100 K below the melting point. Thermal expansion was measured using dilatometry, the specific heat capacity was determined using differential scanning calorimetry and the ratio method, and the thermal diffusivity was measured using laser flash analysis. The thermal conductivity of each sample was calculated by taking the product of the temperature-dependent density, the specific heat capacity, and the thermal diffusivity. All measurements were again made under flowing gettered argon.

Finally, the oxidation and other relevant reactions were measured using thermogravimetric analysis. This technique provides the weight change of a sample *in situ* during exposure to controlled atmospheres at elevated temperatures. Samples of each compound were placed on platforms or shallow crucibles and heated to various test temperatures under gettered argon. After the temperature profile was switched to an isotherm at the desired point, the test atmosphere was introduced to the system and the sample's response recorded. The test atmospheres included oxygen, water vapor, hydrogen, nitrogen, and varying partial pressures of the above.

RESULTS

The thermophysical properties determined for the four U-Si compounds as a function of temperature provide data vital for consideration of their use in LWR applications. In the case of U_3Si and U_3Si_2, fair agreement was found with the limited low temperature data as illustrated in Figure 2. In addition to the data itself, verification of the high temperature behavior of the materials was possible. The existence of a high temperature phase transformation within U_3Si has been disputed historically [4], but was clearly visible in all data obtained in this study.

The oxidation behavior of the U-Si compounds was found to be quite poor, even when compared to other ceramic nuclear fuels generally considered to have inferior resistance to oxidation. As mentioned previously, property measurement at temperatures above roughly 800K required very low partial pressures of oxygen to avoid severe degradation. This effect is shown even more dramatically in Figure 3, where the response of U_3Si_2 and U_3Si_5 to synthetic air is plotted against that of UN and UO_2. This measurement was made during dynamic heating at 2.5 K/min in order to illustrate the approximate

temperature where severe oxidation begins to occur for the four materials. Figure 3 shows that both U_3Si_2 and U_3Si_5 begin oxidizing at the lowest temperature of the four materials. Both U_3Si_2 and UN experience extreme exothermic oxidation reactions (observable as the ducktail when the data is plotted against temperature).

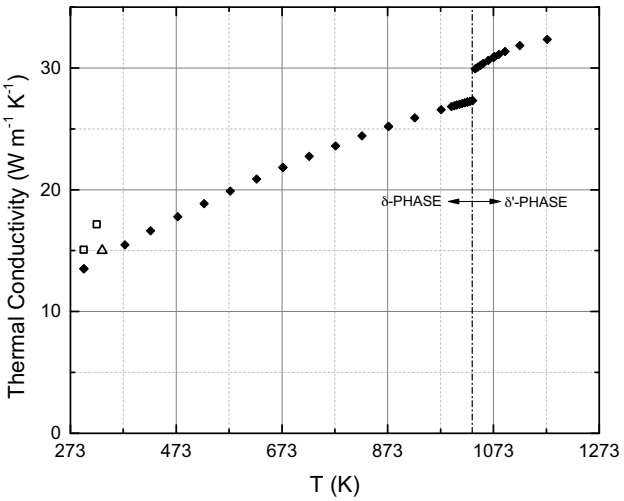

Figure 2. Thermal conductivity of U_3Si measured in this study (black diamonds) compared to available literature values (open markers).

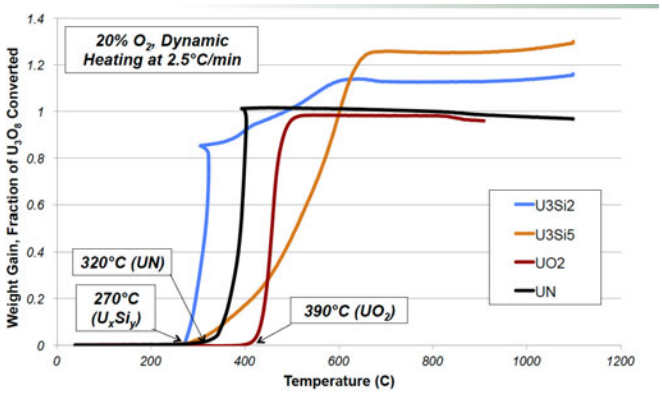

Figure 3. Comparison of the oxidation of U_3Si_2 and U_3Si_5 in synthetic air compared with UO_2 and UN. Oxidation data is expressed in terms of conversion to U_3O_8; the silicide compounds exceed unity on this scale as their conversion is to U_3O_8 and SiO_2.

Kinetic data describing the oxidation and resulting structure of these compounds will be presented and discussed. These results are important not only in considering possible service in water vapor containing environments, but also in evaluating the feasibility of fabrication on an industrial scale. Analogous studies executed in high nitrogen and hydrogen environments will also be summarized. Discussion will conclude with preliminary experimental results that address the stability of U-Si compounds as a component of the larger fuel-cladding system where the thermochemical stimuli under consideration expand considerably.

REFERENCES

1. Y-S. KIM, "Uranium intermetallic fuels (U-Al, U-Si, U-Mo)," in: R. Konings (Ed.), *Comprehensive Nuclear Materials.* 3, 391, (2012).

2. R. WILLIAMS ET AL. "Thermal conductivities of U_3Si and U_3Si_2-Al dispersion fuels," *Thermal Conductivity.* 11, 271, (1988).

3. K-H. KANG ET AL., "Oxidation behavior of U_3Si (3.9 wt.% Si) in air at 250-400C," *Journal of Nuclear Materials* 228, 220, (1996).

4. A. BERCHE ET AL., "Thermodynamic study of the U-Si system," *Journal of Nuclear Materials* 389, 101. (2009).

Thermal Analysis of Accident Tolerant Fuel Materials

Introduction and Experimental Approach

The proposed U bearing Accident Tolerant Fuel (ATF) forms UN, U_3Si_2, and composites of the two compounds, offer significant potential for improvement as LWR fuel over the current nuclear fuel standard UO_2, specifically in thermal conductivity and fissile content. However these compounds have never before been applied as fuel for LWR use, specifically in high density pellet form. Significant investigation and understanding of these compounds is required to transition them to functional LWR fissile fuel.

To this effect, an experimental thermal analysis investigation of these two compounds was undertaken to quantitatively determine the response of these compounds to elevated temperatures in inert and oxidizing atmospheres. A Netzsch 449 F3 Jupiter simultaneous thermal analyzer (STA) was used to measure reaction temperatures and energetics of these reactions as a function of temperature and atmosphere using thermogravimetry (TG) and differential scanning calorimetry (DSC). TG and DSC signals were collected individually (TG) or simultaneously (TG + DSC) in gettered He, synthetic air (20% O_2 - balance He), and ~100% water vapor. Fuel material samples were heated at 10°C/min to 1250°C, held for ~10 minutes, and then cooled to room temperature. This constant heating rate experiment allows for quantitative determination of reaction temperatures and energies, which can then be used to guide isothermal hold thermal analysis experiments at temperatures around the reaction temperatures. For this investigation, samples of UO_2 were analyzed in addition to U_3Si_2 and UN for relative comparison. Considering the historic and continued future standard that UO_2 represents as a LWR fuel in both fabrication and operation, it is important to understand the differences between UO_2 and the two proposed non-oxide fuel materials.

Experimental Results

Figure 1 presents typical TG and DSC signals as a function of time for a constant 10°C/min ramp to 1250°C, 10 min. hold at 1250°C, and subsequent cooling for UO_2 powder. Note that there are 2 mass increase steps in the TG signal and 2 energy valleys in the DSC signal. These results confirm previous results that the oxidation of UO_2 to U_3O_8 is a 2-step reaction and that both reactions are exothermic. (1) Figure 2 presents typical TG and DSC signals as a function of time for a constant 10°C/min ramp to 1250°C for U_3Si_2 powder and Figure 3 presents similar TG and DSC signals for UN powder. Note that in Figures 2 and 3, both TG and DSC signals show single mass increase steps and 1 energy valley indicating that U_3Si_2 and UN oxidize to U_3O_8 as single step, exothermic reactions.

Table 1 presents thermal analysis results for UO_2 in powder and pellet form and Table 2 presents thermal analysis results for U_3Si_2 and UN in powder form only. These results include the following measured values using the indicated techniques.

value measured	technique
Δ mass, in % of initial	TG
$T_{ox,\,i}$, oxidation reaction initiation temperature in °C	TG and DSC
RXN enthalpy, reaction enthalpy in μVs/mg	DSC

Pellet material analysis was performed using TG only due to the size of typical sectioned pellet samples. Additionally, TG only was used for analysis in water vapor due to equipment restrictions when using the water vapor furnace.

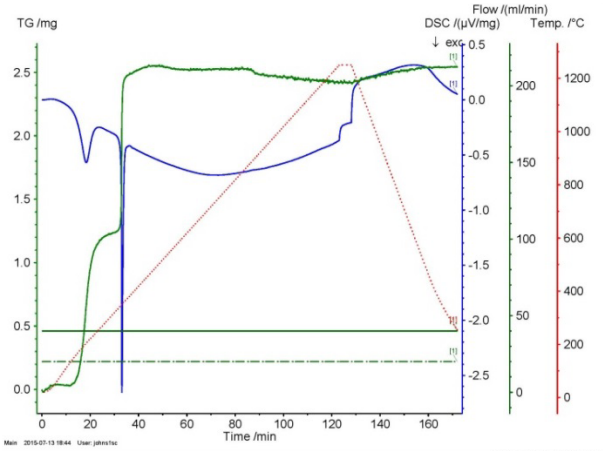

Figure 1. Typical TG + DSC signal for 10°C/min ramp to 1250°C for UO_2 powder. Red plot is sample temperature in °C, green plot is TG data mass gain in mg, and blue plot is DSC data in µV/mg.

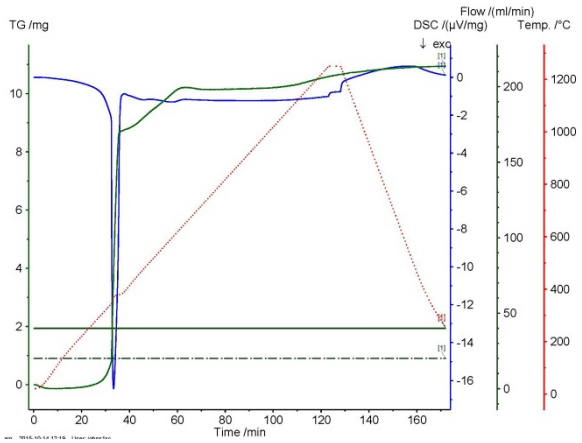

Figure 2. Typical TG + DSC signal for 10°C/min ramp to 1250°C for U_3Si_2 powder. Red plot is sample temperature in °C, green plot is TG data mass gain in mg, and blue plot is DSC data in µV/mg.

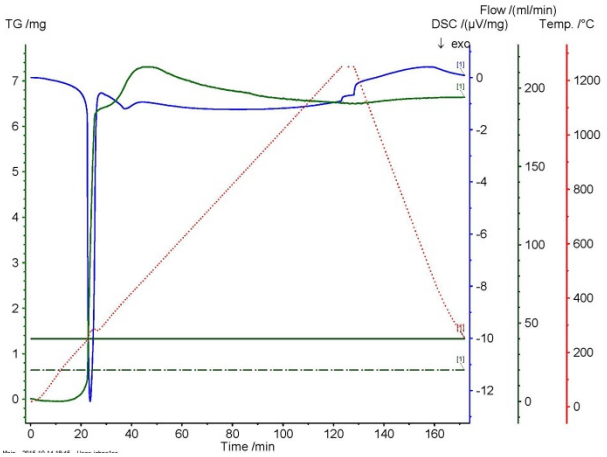

Figure 3. Typical TG + DSC signal for 10°C/min ramp to 1250°C for UN powder. Red plot is sample temperature in °C, green plot is TG data mass gain in mg, and blue plot is DSC data in µV/mg.

material	atmosphere	Δ mass (%)			$T_{ox, i}$ (°C)		RXN enthalpy (µVs/mg)			samples tested	comments
		rxn 1	*rxn 2*	total	*rxn 1*	*rxn 2*	*rxn 1*	*rxn 2*	total		
UO_2 powder	gettered He	-	-	0.345	-	-	-	-	-	4	no oxidation reaction
	20% O_2 – 80% He	1.64	1.79	3.43	164	348	-115	-125	-240	3	two step oxidation reaction
UO_2 pellet	gettered He	-	-	0.023	-	-	-	-	-	4	no oxidation reaction
	20% O_2 – 80% He	-	-	3.96	453	-	-	-	-	3	single step oxidation reaction

Table 1. Thermal analysis results for UO_2 powder and sintered pellet form.

material	atmosphere	Δ mass (%)	$T_{ox,i}$ (°C)	RXN enthalpy (μVs/mg)	*samples tested*	comments
U_3Si_2 powder	20% O_2 – 80% He	21.14	351	-2969	4	single step oxidation reaction
	steam (5 gm/hr)	16.74	429	-	1	single step oxidation reaction
UN powder	20% O_2 – 80% He	10.98	253	-1929	3	single step oxidation reaction
	steam (5 gm/hr)	6.89	351	-	1	single step oxidation reaction

Table 2. Thermal analysis results for U_3Si_2 and UN in powder form.

Results Discussion

For UO_2 tested in both powder and pellet forms, no oxidation reaction was observed when heating to 1250°C in gettered He. The He cover gas used is actively gettered to an O_2 level on the order of 10^{-12} ppm of O_2. These results prove that it is possible to suppress the oxidation reaction of U at elevated temperatures in a sufficiently O_2 free environment.

Both U_3Si_2 and UN are shown to exhibit single step oxidation reactions in synthetic air to the stable U oxide U_3O_8. The reaction sequence for these 2 compounds can be expressed as follows.

$$U_3Si_2, UN \;\; \text{-->} \;\; U_3O_8 \qquad \text{(i)}$$

In comparison, UO_2 exhibits a two-step oxidation reaction to U_3O_8 and this reaction sequence can be expressed as follows. (1)

$$UO_2 \;\; \text{-->} \;\; U_3O_7 \;\; \text{-->} \;\; U_3O_8 \qquad \text{(ii)}$$

For the work performed here, only UO_2 was tested in sintered pellet form and this material exhibited a single step oxidation reaction as shown in table 1. A speculative reason for this result is that a certain amount of U_3O_8 powder is added to UO_2 powder as a sintering aide during fuel pellet fabrication and the U_3O_8 content could suppress the UO_2 --> U_3O_7 reaction step. U_3Si_2 and UN were not analyzed in sintered pellet form because it was determined that oxidation of these materials in solid form was too exothermic and literally threw sample material out/off of the sample holder in the STA during the oxidation reaction.

Results presented in table 1 show that UO_2 gains 3 to 4% of its original mass during oxidation to U_3O_8 as either powder or pellet form in synthetic air. Compared to UO_2, U_3Si_2 and UN powders gain significantly more mass during oxidation to U_3O_8, approximately 21 and 11% of initial mass respectively in synthetic air as shown in table 2. Additionally, U_3Si_2 and UN powders gain approximately 17 and 7 % of initial mass during oxidation to U_3O_8 in steam also shown in table 2. Qualitatively, the larger mass gain of U_3Si_2 and UN during oxidation compared to that of UO_2 can be explained in that U_3Si_2 and UN are non-oxide compounds of U. UO_2 is already an oxide form of U, however not the equilibrium oxide U_3O_8. Thus, more O_2 is consumed during the oxidation of U_3Si_2 and UN than during the oxidation of UO_2 to U_3O_8 because UO_2 is in a non-equilibrium oxide state. Materials balance calculations would confirm these experimental results.

Tables 1 and 2 present the temperatures at which the oxidation reaction initiates ($T_{ox,i}$) for UO_2, U_3Si_2, and UN in synthetic air, and in steam for U_3Si_2 and UN. For UO_2, $T_{ox,i}$ is presented for both the first and second steps of the reaction. Also shown in Table 1, the enthalpy of these 2 oxidation reaction steps are relatively the same. So it can be stated that oxidation of UO_2 powder begins at approximately 165°C with a second step in the oxidation reaction at 348°C. Note that the single step oxidation reaction in synthetic air for sintered UO_2 in pellet form was determined to be 453°C. Presently, it is not clear why $T_{ox,i}$ for solid UO_2 is so much higher than

that of powdered UO_2. The $T_{ox,\,i}$ of U_3Si_2 is 351°C and that of UN is 253°C both in synthetic air with values shown in table 2. Additionally, the $T_{ox,\,i}$ of U_3Si_2 and UN in steam are 429 and 351°C respectively. Thus the temperatures at which UO_2, U_3Si_2, and UN in powder form oxidize can be ranked as follows.

$$T_{ox,\,i}\ (\text{syn. air}) = UO_2 < UN < U_3Si_2$$
$$T_{ox,\,i}\ (\text{steam}) = UN < U_3Si_2$$

These results indicate that of the fuel compounds analyzed in this work, U_3Si_2 has the highest resistance to oxidation as a function of temperature in both synthetic air and steam. As stated previously, solid sintered pellet form of U_3Si_2 and UN were not analyzed in this work because their oxidation reactions are too exothermic. Future analysis of these materials in solid, sintered form would be most beneficial since this is the form of an LWR fuel pellet,

The enthalpy of the oxidation reactions for all three fuel compounds in synthetic air are presented in tables 1 and 2. All oxidation reactions are exothermic; i.e.; negative reaction enthalpy values. These values for UO_2, U_3Si_2, and UN in powder form oxidized in synthetic air can be ranked as follows.

$$\text{RXN enthalpy (syn. air)} = UO_2 << UN < U_3Si_2$$

Here the reaction enthalpy of UO_2 is presented as the sum of the values of the first and second steps of the oxidation reaction to U_3O_8 and this value is one order of magnitude smaller than the reaction enthalpy's of U_3Si_2 and UN. Note that reaction enthalpy's in steam were not determined because these values are measured using DSC and the DSC sample support cannot be used in the STA water vapor furnace. Clearly, all three U bearing fuel compounds analyzed here oxidize exothermically with the non-oxide fuel compounds (U_3Si_2 and UN) exhibiting very exothermic oxidation reactions.

Summary

The experimental analysis results presented here clearly show the reactive nature of U bearing fuel compounds. While the current LWR fuel standard UO_2 does oxidize exothermically at relatively low temperature, the proposed ATF fuel compounds U_3Si_2 and UN oxidize at higher temperatures but are one order of magnitude more reactive as measured by the oxidation reaction enthalpy. While these results were generated on *powder* form of these compounds, it is offered that the relative $T_{ox,\,i}$ and oxidation reaction enthalpy's should extrapolate to solid pellet form. Obviously this requires experimental proof.

All experiments in this study were performed on monolithic fuel compound materials. It has been proposed that composites of U_3Si_2 and UN could improve the resistance to reaction with water of these fuel materials. Based on the results of this work, compositing U_3Si_2 and UN will have very little or no effect on the oxidation resistance of these two compounds. While U_3Si_2 does oxidize at a higher temperature than UN, the reaction of U_3Si_2 to U_3O_8 is more exothermic than UN. Thermal analysis work to determine the $T_{ox,\,i}$ and oxidation reaction enthalpy of composites of U_3Si_2 and UN, either in powder or sintered pellet form, should be performed.

An important conclusion from this work is that, while UO_2 is a reactive fuel material and requires proper handling during processing, the proposed ATF fuel compounds U_3Si_2 and UN are significantly more reactive. Thus proper precautions should be taken during the processing and handling of these compounds and experimental efforts such as presented here can be helpful.

References

1. McEachern R.J. and Taylor, P., "A Review of the Oxidation of Uranium Dioxide at Temperatures Below 400°C", AECL-11335, January 1997, Atomic Energy of Canada Limited.